Poly (Lauryl Methacrylate): spread monolayers and bulk configuration

Reynolds, Ian

Poly (Lauryl Methacrylate): Spread Monolayers and Bulk Configuration

by

Ian Reynolds

College of St. Hild and St. Bede

A thesis submitted for the Degree of Doctor of Philosophy at the University of Durham

October 1995

CONTENTS

3. MONOLAYERS AND SURFACE PRESSURE ISOTHERMS

4. NEUTRON REFLECTIVITY

5. SURFACE QUASI - ELASTIC LIGHT SCATTERING

MEMORANDUM

The work reported in this thesis has been carried out at the Durham site of the Interdisciplinary Research Centre in Polymer Science and Technology and the Rutherford Appleton Laboratory in Oxfordshire between October 1992 and July 1995. This work has not been submitted for any other degree either in Durham or elsewhere and is the original work of the author unless otherwise acknowledged.

STATEMENT OF COPYRIGHT

FINANCIAL SUPPORT

I gratefully acknowledge the provision of a grant from the Engineering and Physical Science Research Council and the additional funding from the Interdisciplinary Research Centre in Polymer Science and Technology to support the work described herein.

ACKNOWLEDGEMENTS

A great number of people have contributed to this work, directly or indirectly, and I am grateful to them all. Firstly, thanks are due to Prof. Randal Richards for his "character building" supervision and his words of wisdom (RTFM, bugger, ...)

The synthesis lab wouldn't have been a safe place without the guidance of Tom Kiff and thanks also go to Gorden Forrest, for size exclusion chromatography and differential scanning calorimetry measurements, Julia Say and Dr. Alan Kenwright who ran and helped analyse the NMR spectra.

The neutron experiments would not have been possible without the expert guidance of a number of instrument scientists at the Rutherford Appleton Laboratory, these are: Dr. Jeff Penfold, Dr. John Webster and Dr. David Bucknall on CRISP and Dr. Steve King on LOQ. While on the subject of neutron experiments, thanks must go to Brian Rochford and Stella Peace, both of whom had the "privilege" to stay up all night at RAL.

My time in the IRC would not have passed so quickly and enjoyably without the many people, past and present, who have made it an enjoyable place to work.

The support from my family has been invaluable and knowing that Dawn was always there, despite the ups and downs during the writing of this thesis, made this all possible.

Finally, how would I have got through the last three years without the extra curricular activities supplied by that group of entertaining people, otherwise known as "The Lads". To name names, in no particular order, "The Lads" consisted of Richard "Captain Birds Eye" Towns, Steve "Carssy" Carrs, Brian "Reptile, man of a thousand chat up lines" Rochford, Gary "Taggart" McGeorge, Don "Fives (attempting to lose)" Davison, Michael "Pecky" Jeschke, and lastly honorary membership goes to Nick "Ronnie" Haylett.

Poly (Lauryl Methacrylate): Spread Monolayers and Bulk Configuration

Ian Reynolds

Ph.D. Thesis 1995

Abstract

Deuterated variations of poly(lauryl methacrylate) (PLMA) have been synthesised, this involved the initial synthesis of the monomer (LMA). This was achieved by a transesterification reaction between methyl methacrylate and lauryl alcohol using either hydrogenous or deuterated materials depending on which part of the resulting LMA monomer was to be deuterated.

The physical properties of PLMA and LMA spread monolayers have been investigated using surface pressure - area isotherms and surface quasi - elastic light scattering (SQELS). The isotherms for PLMA show that the thermodynamic state of the polymer is poorer than theta conditions and no variation occurs with changes in temperature. LMA shows a drastic change in the nature of the isotherm as the temperature is varied. This has been attributed to the formation of lenses and the variation caused by temperature is due to a change in the rate of migration of the LMA molecules. The SQELS results show that the PLMA monolayer displays the characteristics of a Voigt solid model and shows no viscous relaxation processes. SQELS has also been used to demonstrate the biphasic nature of the monolayer at low surface concentrations, the size of the polymer 'islands' has been estimated to be in the range of 5 to 20mm. SQELS from LMA monolayers showed that the two higher surface concentrations gradually converted into the same state as that obtained for the low

surface concentration which produced negative surface pressures and transverse shear viscosities.

Neutron reflectivity has been used to determine the organisation of the polymer and monomer at the interface. By using the isotopic variations and applying the kinematic approximation, the distribution of the methacrylate and lauryl ester components of the molecules has been determined. For the polymer, the lauryl ester groups and the methacrylate backbone region could be described by a Gaussian distribution with a standard deviation of circa 16Å and 6Å respectively and little change in the structure occurred for surface pressures of 0.5, 5 and 10mN m^{-1}. For the monomer, the apparent surface concentration decreased with time, although for each initial surface concentration the final surface concentration was roughly the same, possibly due to an equilibrium between lenses of LMA and bare subphase.

The solid phase configuration of PLMA was investigated by carrying out small angle neutron scattering experiments, the results of which were to be compared with the scattering calculated from computer generated models. However, it proved impossible to produce the computer models, so only a limited amount of information could be obtained from the experiments.

1. INTRODUCTION

1.1 Historical Background and General Introduction

The study of monomolecular films (or monolayers) is by no means a recent development. As early as 1765 Benjamin Franklin observed the wave damping properties of oil spread on water when he placed one teaspoon of oil on a pond and calmed half an acre[1]. The foundations for modern day studies of monolayers were laid in the 1890s when Pockels [2] began experimenting with a primitive trough and she developed many of the techniques which are regarded as standard today, such as containing films by barriers and the importance of cleanliness. Pockels observed that there was little change in the surface tension of fatty acid monolayers until they were confined to an area corresponding to about 20Å^2 per molecule. In 1899 Rayleigh [3] provided an interpretation of Pockels observations which was that at the point where the surface tension began to decrease the molecules of the film material were just beginning to touch each other. A picture was developing of the surface film which consisted of the molecules of the film material floating on the water surface, with little interaction until they actually came into contact with each other. It was also noted in these early experiments that the monolayer could exert a physical force on a floating barrier, for example, a loosely floating circle of thread was stretched taut to a circular shape when some surface active material was spread inside the circle of thread.

In 1917 Langmuir [4] developed a new trough to study monolayers which consisted of two barriers, one which was rigid but adjustable, the other which was floating on the water. The floating barrier was connected to a knife edge suspension which enabled the force acting on the barrier to be determined. Using this trough Langmuir found that the limiting area was the same for a range of fatty acids, namely 21Å^2 per molecule, for chain

lengths varying from 16 to 26 carbon atoms. This provided the first insight into the molecular organisation at the air - water interface as the interpretation of this observation was that the hydrophilic head groups were immersed in the water with the alkyl chains being perpendicular to the interface. The process of transferring the floating monolayer onto a solid substrate was developed by Langmuir in conjunction with Blodgett [5] and it was demonstrated that it was possible to construct multilayer Langmuir - Blodgett films.

The interest in the field subsided around the mid 1900s until the early 1960s when it was demonstrated that monolayers could be used to construct precise supermolecular structures. More recently, with the introduction of new techniques to investigate the structure and properties of monolayers, a revival in the study of monolayers has occurred as the applications which involve monolayers and interfacial properties increases, for example, the surface absorption behaviour of surfactants in solution, the properties of emulsions and the stabilisation of colloidal dispersions. The air - water interface provides a simple system to study the behaviour of molecules which can be related to the behaviour in more complex situations. Poly(lauryl methacrylate) (PLMA) was chosen for this study for two reasons, firstly to determine the effect of the large lauryl substituent on the properties and surface organisation of the polymer backbone compared to that of poly(methyl methacrylate) [6,7]. Secondly the structure of PLMA consists of hydrophilic and hydrophobic regions similar to low molecular weight surfactants, so it provided a good system on which to apply the kinematic approximation (section 4.1.2) for the analysis of neutron reflectivity data to determine if the same level of detail was accessible for polymer monolayers as that obtained for surfactants. In addition to the work on PLMA monolayers, the monomer was also investigated to compare the properties and structure of a monolayer with the same chemical composition but without the restrictions placed on the organisation of the monolayer due to the polymer backbone.

As an aside to the work on monolayers of PLMA the solid phase configuration of the polymer has been investigated using small angle neutron scattering. The configuration of polymer molecules in the bulk state is determined by the potential energy change as rotation takes place about main chain bonds which confines the molecules to a discrete number of possible configurations. For poly(methyl methacrylate) such experiments have been carried out and the results compared to the scattering calculated for a molecular model constructed using rotational isomeric state calculations [8]. This allows the visualisation of the polymer chain configuration as it would be in the solid state.

The techniques used in this study of monolayers were surface pressure - area isotherms, surface quasi - elastic light scattering (SQELS) and neutron reflectivity. An introduction and theoretical background to each technique is given at the beginning of each chapter, so only a brief summary of the uses of each technique is given here.

1.2 Surface Pressure - Area Isotherms

In recent times the advent of scaling laws to describe the relationship between the surface pressure of a monolayer, π (where $\pi = \gamma_o - \gamma$, γ_o = surface tension of clean water and γ = measured surface tension with monolayer present) and the surface concentration (section 3.2.2) has led to a flurry of activity, both theoretically and experimentally, to determine the scaling exponents that govern the properties of polymer chains in two dimensions. The values obtained for the exponent υ which relates the radius of gyration $R_{g,2}$ to the degree of polymerisation indicates the thermodynamic state of the monolayer, values around 0.76 being indicative of good solvent conditions and a range of values from 0.505 to 0.59 have been predicted for θ conditions. υ is determined from the region of the isotherm analogous to the semi dilute region in three dimensions where the chains just begin to interact and the surface pressure increases. Previous equation of state methods to determine the thermodynamic properties of monolayers required the investigation of extremely low surface concentrations where surface pressure measurements are difficult. In 1980 Vilanove and Rondelez [9] made use of the scaling laws for the first time to characterise polymer monolayer thermodynamics when they extracted υ for poly(vinyl acetate) and poly (methyl methacrylate), obtaining values of 0.79 and 0.56 respectively.

Takahashi *et al* [10, 11] investigated monolayers of poly(methyl acrylate) at various temperatures between 16.5 and 45 °C and reported transitions from good solvent to θ solvent and even to collapse. This was observed in their values of υ, which varied between 0.77 at 25 to 45 °C and 0.51 at 18 °C, and also in low concentration studies where the value of the second virial coefficient changed from positive (above 25 °C), to zero (at 18 °C) and to negative (at 16.5 °C) values. However, Vilanove *et al* [12] were

unable to reproduce these observations even though both sets of experiments were carried out on the same samples and they concluded that the observation of the transition in monolayer behaviour was due to contamination, as the surface pressure reached values in excess of 10mN m^{-1} at surface concentrations as low as 0.35mg m^{-2}, whereas in Vilanove's work this occurred at surface concentrations of 0.7mg m^{-2}. Further evidence that the observation of the transition was incorrect is given by the narrow temperature range over which it took place (7 °C). Ranges for such transitions have been calculated to be circa 60 °C for chains with a molecular weight of 10^4 and 23 °C for chains with a molecular weight of 10^5.

In the same paper Vilanove *et al* repeated their earlier experiments on PMMA and they found a value of υ equal to 0.53 and a negative second virial coefficient which indicates that the monolayer is in less than theta conditions. This placed a lower limit on the value of υ for monolayers in the theta state and discounts theoretical predictions of υ for the theta state which are less than 0.53. The difference in the two sets of results was attributed to the successive addition method used for the monolayer deposition which does not allow accurate control of the surface concentration, offers no protection against the possibility of solvent retention within the monolayer and supposes that the monolayer is able to reach equilibrium quickly and that there are no trapped entanglements between chains.

Much of the work carried out on monolayers uses analogies to the three dimensional state. Kawaguchi and Nishida [13] used this principle to compare the compatibility of polymer chains at the air - water interface to the bulk phase blends of polymers. They used binary mixtures of poly(ethylene oxide) (PEO), poly(methyl acrylate) (PMA), poly(vinyl acetate) (PVAc) and poly(methyl methacrylate) (PMMA). In the bulk phase blends of PEO and PMMA as well as PMA and PVAc are compatible, while PMMA and PVAc blends are incompatible. In the two dimensional case to

determine if the polymers are compatible the isotherms are obtained for the homopolymer monolayers and for the binary mixtures with differing mole fractions. At any surface pressure, if the plot of the area per polymer segment as a function of mole fraction for the binary monolayer matches that calculated by adding the areas of the pure components (determined from the monolayers of the pure polymers) weighted by their mole fractions, then the surface areas are additive and the mixed film can be regarded as an ideal mixture or as a completely immiscible mixture in the entire mixture range. To confirm whether the mixture is completely incompatible or ideally miscible the collapse surface pressures as a function of mole fraction can be considered. The collapse pressure of an ideal mixture depends on the composition, whereas for completely immiscible mixtures it is independent of composition.

For the PEO / PMMA binary mixture a negative deviation from the ideal linear plot of mean areas versus mole fraction is obtained indicating that the intermolecular interaction between PEO and PMMA is attractive and the mixture is non - ideally miscible and stable. The compatibility is confirmed by the composition dependence of the collapse pressure. For PVAc and PMA the mean areas lie on the ideal additive line and the collapse pressure varies with composition, both indicating that the polymers are ideally mixed. This ideal behaviour has been attributed to the similar chemical structures of the polymers. PVAc and PMMA binary mixtures produced mean areas that were above the ideal line indicating that they are thermodynamically less stable than the two pure polymer monolayers and they repel each other. This was accompanied by a collapse pressure which was similar to that for PVAc over the range of mole ratios used. PEO and PVAc produce a negative deviation in the area plot indicating that they are non - ideally compatible, however, above 10mN m^{-1} the mixtures become incompatible as the collapse pressures become the same as that for PVAc and there is no variation with

composition. This study indicates that the mixture behaviour in two dimensions correlates with that obtained in the bulk state.

In 1985 Malcolm [14] observed the flow behaviour of monolayers of synthetic polypeptide and found that there was a surface pressure gradient formed during compression. Barnes and Peng [15] carried out a study of vinyl stearate (VS) and poly(vinyl stearate) (PVS) to see if such gradients formed in other polymer monolayers. They measured the surface pressure at various points along the length of the trough parallel to the compression direction and found that a surface pressure gradient formed for PVS (π highest close to the compressing barrier and decreased linearly with distance away from the barrier) but not for VS. This was attributed to the high molecular weight of the polymer which slows the rate of diffusion of the molecules on the water surface and to the slow rearrangement of the polymer segments. The spreading technique and the method of compression effect the nature of the gradient formed. Even spreading and spreading at the fixed end of the trough yielded isotherms that were almost the same, whereas spreading near the moving barrier produced significantly higher surface pressures at all stages of the compression and the surface pressure began to increase at larger areas than for the other two methods. This reflects a greater inhomogeneity in the initial distribution of the film. The inhomogeneity could be reduced by using symmetric compression with two barriers and also by using step wise compression as opposed to continuous compression, although even when 90 minutes were left between compression steps relaxation was not complete and a surface pressure gradient remained. These observations bring into question earlier isotherms obtained for PVS [16 - 18] because the film close to the barrier will begin to collapse well before the surface pressure near the fixed end of the trough reaches a high value. Therefore, it is likely that the earlier isotherms of PVS refer to films that are partially collapsed at moderate and high pressures. The surface pressure gradient reflects the fact that macromolecules tend to remain in or near

the region where they are deposited, so this can explain the apparent annealing effect observed by O'Brien *et al* [17]. They reported that when a PVS monolayer was compressed and held at 33mN m^{-1} for 3 hours, the areas in subsequent compression isotherms were considerably lower than for an unannealed film. It is more likely that this observation is due to the failure of the compressed film to expand properly when the barrier was moved back.

Surface pressure gradients have also been observed in PMMA monolayers [19] and Barnes and Peng have shown that the presence of stearic acid in PMMA monolayers greatly reduced the surface pressure gradient, which disappeared when the mole fraction of stearic acid was above 0.3 [20]. This has been attributed to the stearic acid acting as a monomeric surfactant which behaves as a 'lubricant' and facilitates the flow of the monolayer during compression and allows the surface pressure gradient to relax more rapidly and more completely. Another method to improve the homogeneity of polymer monolayers is to change the molecular architecture of the main polymer chain [21]. For polymers with a main chain with long hydrophobic side chains the homogeneity can be improved by introducing longer, more flexible hydrophilic links into the main polymer chain. This allows the polymer to modify its structure and facilitate the packing of the long side chains.

1.3 Surface Quasi - Elastic Light Scattering (SQELS)

The trend of comparing three dimensional polymer behaviour with that in two dimensions is the basis behind the development of SQELS as it enables the viscoelastic properties of polymers in two dimensions to be investigated and this is an important area of study in three dimensions for polymers as the practical importance of the mechanical behaviour in the processing and utilisation of rubbers, plastics and fibres increases. Viscoelastic materials can be considered as those which display elastic and viscous characteristics to some extent. The classical theory of elasticity deals with mechanical properties of elastic solids for which stress is always proportional to strain in small deformations but independent of the rate of strain or the strain history (Hooke's law). The classical theory of hydrodynamics deals with properties of viscous liquids for which the stress is proportional to the rate of strain but independent of the strain itself (Newton's law). These two categories are ideal situations, although they can be approached for solids with the application of infinitesimal strains and for liquids with the application of infinitesimal rates of strain. If finite strains are applied to solids (especially those soft enough to be deformed substantially without breaking) the stress - strain relations are more complicated (non Hookean). Similarly, in steady flow with finite strain rates, many fluids (especially polymeric solutions and melts) exhibit deviations from Newton's law (non Newtonian flow). The dividing line between infinitesimal and finite depends on the material under study.

Even if both strain and rate of strain are infinitesimal a system may exhibit behaviour that combines liquidlike and solidlike characteristics. For example, a material that is not quite solid does not maintain a constant deformation under constant stress but continues to slowly deform with time, or creeps. When such a material is constrained at constant deformation the stress required to hold it diminishes gradually or relaxes. A

material that is not quite liquid may, while flowing under constant stress, store some of the energy input instead of dissipating it all as heat. It may recover part of its deformation when the stress is removed (elastic recoil). When such materials are subjected to sinusoidally oscillating stress, the strain is neither exactly in phase with the stress (as it would be for a perfectly elastic material) nor 90° out of phase (as it would be for a perfectly viscous liquid) but is somewhere in between. Some of the energy input is stored and recovered in each cycle and some is dissipated as heat. Materials that exhibit such characteristics are called viscoelastic.

In polymeric systems the mechanical behaviour is dominated by viscoelastic phenomena which is not too surprising considering the complicating molecular rearrangements that must occur when any macroscopic deformation takes place. In the deformation of a hard solid, such as diamond or sodium chloride, atoms are displaced from their equilibrium positions in fields of force that are quite local in character. Other mechanical phenomena reflect structural imperfections involving distances discontinuously larger than atomic dimensions. In an ordinary liquid, viscous flow reflects the change with time, under stress, of the distribution of molecules surrounding a given molecule and for this too the relevant forces and processes of readjustment are quite local in character. In a polymer, each flexible molecule pervades an average volume much greater than atomic dimensions and is continually changing the shape of its contour under the action of Brownian motion. Rearrangements on a local scale that involve small parts of the molecule occur relatively fast and only provide a small contribution to the deformability of the material under stress (the compliance). The larger the part of the molecule involved in a molecular rearrangement the more sluggish the movement and the larger its contribution to the deformation. This shows that measurements of viscoelastic properties of polymers imparts information about the nature and rates of the configurational rearrangements and the interaction of the

macromolecules in both their short range and long range interactions, this being true in two dimensions as well as in three dimensions.

The technique of SQELS has been developed over the last fifteen years or so, even though the earliest predictions of surface scattering caused by surface corrugations had been around since 1913, as described by Von Smoluchowski [22] and calculated by Mandlestam [23]. Vrij [24] developed a theory for the scattering of light polarised normal to the interface for soap films and presented limited results to support his interpretation of interfacial corrugations dependent on the balance of electrostatic and van der Waal's stabilising forces in the films. Further progress of the technique was hindered by the optical technology available at the time.

The development of laser optics increased the practicality of SQELS and in 1967 Katyl and Ingard [25] were able to demonstrate the spectral modification of light scattered by a liquid surface. Also around this time the existence of two distinct modes of capillary evolution, termed propagating and overdamped, was confirmed [26] and the validity of the dispersion equation was verified [27]. A major advance in the detection of the small frequency shifts caused by surface fluctuations was the use of a diffraction grating for the generation of heterodyne beat signals by Hård *et al* [28] which enabled the simultaneous detection of scattered and reference light at a particular wavenumber. The technique was developed for time domain correlation methods by Byrne and Earnshaw [29 - 31] and then Hård and Neuman [32] improved the use of the grating by placing it before the liquid surface and refocussing the diffraction spots at the surface which provides beam mixing at the surface. This method also provided a simple method of wave number selection by selecting different diffraction orders and this set up is now the preferred design for SQELS experiments. SQELS has been applied to the study of simple liquids (water [31], ethanol [33]) and to liquids covered with monolayers and surfactant solutions, examples of which are referred to in chapter 5.

1.4 Neutron Techniques

To carry out successful neutron experiments a source of neutrons with a suitable flux is required. There are two methods for producing neutrons, nuclear reactors and more recently pulsed accelerator sources became available and all of the neutron experiments carried out in this work involved the use of a pulsed source. The pulsed sources use heavy energetic particles (800MeV protons) to chip neutrons from heavy nuclei, hence the term spallation neutron source from the verb to 'spall'. Each proton produces around 25 to 30 neutrons which is a high yield, however the cost of accelerating protons to the energies required to overcome the short range nuclear and electrostatic repulsive forces is high. The protons are accelerated by a combination of a linear accelerator and a synchrotron ring and then 'kicked' out towards the target in short bursts producing pulses of neutrons.

Another feature common to all neutron experiments is the convention of expressing results as a function of scattering vector Q. This is equal to the wavevector change that occurs during the scattering process and can be represented pictorially as is shown in figure 1.1. This depicts a scattering event in terms of the neutron wavevectors, each of magnitude $2\pi/\lambda$ and pointing in the direction of travel of the neutrons. As the neutron does not exchange energy with the scattering material (elastic scattering) the wavelength remains the same and only its direction changes. Therefore, the magnitude of the initial wavevector ($\mathbf{k}_i$) is unchanged and equals the magnitude of the final wavevector ($\mathbf{k}_f$). The scattering vector (Q) is sometimes known as the momentum transfer, which can be understood by recalling that momentum, mv, is given by h/λ, by substituting for λ one obtains $mv = hk/2\pi$, so the change in momentum during the scattering process is just $hQ/2\pi$.

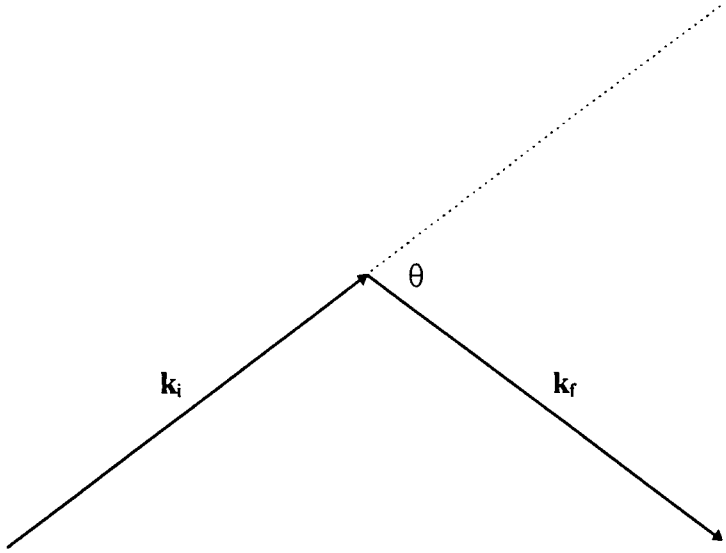

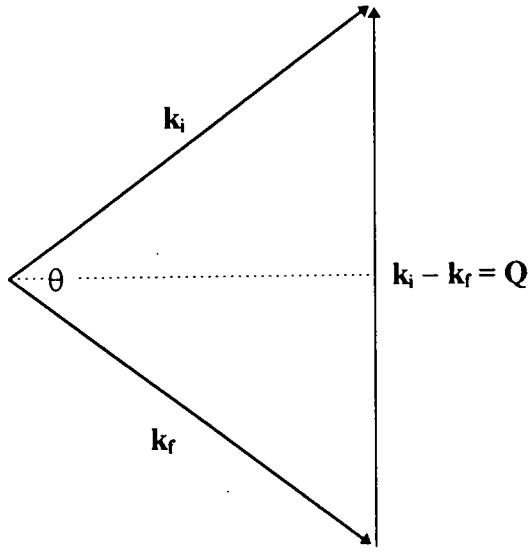

$k_i = k_f = 2\pi/\lambda$

$Q = 2k_i \sin\theta/2$

$= (4\pi/\lambda) \sin\theta/2$

$Q = 2k_f \sin\theta/2$

$k_i = |\mathbf{k}_i|$
$k_f = |\mathbf{k}_f|$
$Q = |\mathbf{Q}|$

Figure 1.1: Relationship between wavevectors and scattering vector for elastic scattering

1.4.1 Neutron Reflectivity

The earliest observation of the total reflection of slow neutrons was by Fermi and coworkers in the years after the Second World War [34]. However, since then until more recent times when Steyerl [35] and Handel [36] pointed out the potential uses of reflection as a surface probe, little attention was paid to the area. The first major development in the field of neutron reflectivity was made in 1976 when Hayter, Penfold and Williams [37] observed interference of reflected neutrons from magnetised metal films using the IN11 instrument on the high flux reactor of the Institut Laue Langevin (ILL), Grenoble, France. This was followed in 1981 by Hayter *et al* [38] spelling out for the first time a range of potential applications of interest to surface chemists which have since been fulfilled. Hayter *et al* presented arguments and examples based on optical matrix calculations for reflectivity from fatty acid multilayers and liquid - vapour interfaces as well as presenting preliminary experimental data for films on solid glass substrates obtained on the adapted small angle scattering instrument D17 at ILL.

The technique became more widely available for the analysis of surfaces when a dedicated reflectometer was constructed (CRISP) at the Rutherford Appleton Laboratory, Didcot, Oxfordshire. Crisp has been used for the study of a wide range of interfacial systems and this led to the development of other reflectometers. The usefulness of neutron reflectivity in the characterisation of many interfacial systems has been demonstrated. Solid and liquid surfaces; solid - solid, liquid - solid and liquid - liquid interfaces; magnetic, conducting and semi - conducting films and biological membranes have all been studied.

Examples of the work carried out on solid surfaces include chemical vapour deposition on silicon to form silicon oxide and silicon nitride layers [39], Langmuir - Blodgett films [40] and a variety of thin magnetic films studied using spin polarised

neutrons, for example ferromagnets [41] and superconductors [42]. Polymer surfaces have also received a large amount of attention. Solution cast films [43] have been investigated and surface ordering in solution spun cast films of poly(styrene-d-methyl methacrylate) diblock copolymers has been observed. The polymer - polymer interface has been studied for the cases of hydrogenous/deuterated bilayers of poly (styrene) [44], immiscible [45] and miscible [46] polymer pairs, while Jones *et al* [47] have investigated the surface segregation of deuterated poly(styrene) in blends with its hydrogenous analogue.

The interfacial structure of surfactants has been studied by neutron reflectivity, this being an area of practical and industrial relevance. Thomas and his co - workers have been prominent in this field having studied surfactant adsorption at the air - solution interface for decyltrimethylammonium bromide[48], tetradecyltrimethylammonium bromide[49], ethylene glycol monododecyl ethers [50] and sodium dodecyl sulphate [51]. Insoluble surfactants have also been studied as spread Langmuir films [52] as these materials are of interest as the precursors of Langmuir - Blodgett films. The adsorption of surfactants at the solution - solid interface has been investigated [53] using quartz as the solid as it is transparent to long wavelength neutrons so the physically inaccessible interface can be probed.

Similar work to that carried out on low molecular surfactants has been also been carried out using polymers. The interfacial structure at the solution - air interface for poly(ethylene oxide) solutions has been investigated [54], as has the adsorption of various polymers in organic solvents at the interface with quartz and mica [55 - 57]. The organisation of spread monolayers of polymers has been determined using neutron reflection. PMMA monolayers were studied by Henderson *et al* [58,59] which display a tactic effect on the monolayer organisation and recently monolayers of a diblock copolymer of PMMA and PEO were studied [60,61].

1.4.2 Small Angle Neutron Scattering (SANS)

The theory necessary for the design of neutron scattering spectrometers was available almost as soon as the neutron was discovered in 1932. The first reactors were built in the forties and fifties and the first scattering experiments followed soon afterwards. However, until the seventies, there was very little use of the technique in the field of polymer science due to the lack of access to suitable facilities and a lack of know - how as the first experimentalists to use the technique were solid state physicists, so it took time for information about the possibilities of the technique to spread to people in other areas. Also, the techniques used in polymer science need good resolution, so a high neutron flux and efficient detectors are required, the first high flux reactors were built in the late sixties and the technology for constructing area detectors was developed in the early seventies. The application of SANS in polymer science has increased so much since the seventies that now about 60% of all the experiments carried out on the SANS spectrometer at the Rutherford - Appleton Laboratory (LOQ) are in the fields of colloid and polymer science.

SANS has been used to study the stabilisation of colloidal dispersions by investigating the adsorbed layers of polymers or surfactants which stabilise the dispersed material by creating steric repulsions between neighbouring particles if they approach each other. SANS can determine how thick the adsorbed layer is and how much polymer or surfactant is adsorbed by using selective deuteration to reduce the contribution to the scattering from the substrate and to enhance the scattering from the adsorbed layer. Other work has been carried out on the latex films formed by the drying of aqueous dispersions of poly(urethane) and poly(acrylate) latices stabilised by nonyl phenyl ethoxylate surfactant [62]. This is an important area of study as it forms the basis of the new, more environmentally friendly water based paints. Similarly, emulsion systems can

be studied, for example the structure of water/cyclohexane/AOT microemulsions as a function of counter ion have been investigated [63] (where AOT is the di-octyl ester of sodium sulphosuccinic acid which is an anionic surfactant and acts as an emulsifying agent) where the oil phase was deuterated cyclohexane to enhance the neutron contrast of the system.

The kinetics of transesterification in copolyesters has been investigated using SANS, as demonstrated in a study of an ABC random copolyester of hydroxybenzoic acid, hydroquinone and isophthalic acid [64]. Two variations of the polymer were used, one which was fully hydrogenous and another with the hydroxybenzoic acid and hydroquinone residues deuterated, these were then mixed in 50:50 ratio and heated to various temperatures for different times and then quenched, resulting in samples with different extents of transesterification. The principle of the experiment was that as transesterification took place the deuterated residues would become distributed over all the coployester molecules in the sample. This would lead to a decrease in the apparent molecular weight of the polymer as determined from the SANS, which would be dominated by the scattering from the deuterated residues.

Polymer blends have received attention as they have enormous technological potential as the basis of new low cost, high performance materials and adhesives. However, very few pairs of homopolymers are miscible in one another due to the fact that the combinational entropy contribution on mixing tends to be so low only a small positive enthalpy of mixing is required to produce phase separation. This can be overcome by adding compatibilisers, which are block copolymers with each block having an affinity for one of the homopolymers. The copolymer segregates to the interface between the homopolymers where it lowers the interfacial tension by altering the local molecular structure. This can be followed by SANS as demonstrated by Higgins *et al* [65] who investigated the compatibilising effect of a symmetric diblock copolymer of

poly(styrene) and poly(methyl methacrylate) on the morphology of an immiscible 50:50 blend of deuterated poly(styrene) and hydrogenated poly(methyl methacrylate).

1.5 Overview of This Work

The original intention of the project was to investigate the effect of the long ester side chain on the properties and organisation of the polymer compared to PMMA and also to investigate the effect of tacticity on the interfacial characteristics of PLMA. This final objective proved impossible to accomplish due to difficulties encountered in the synthesis of the polymers, this is covered in chapter 2. The subsequent chapters cover each technique used, comprising of an introduction to the technique, how the experiments were carried out, results, discussion and finally conclusions. In the case of the surface pressure - area isotherm, surface quasi - elastic light scattering and neutron reflectivity chapters, they are divided into two sections, the first covers the experiments on PLMA monolayers and the second on LMA monolayers. The final chapter draws together the overall conclusions and contains suggestions for further work.

1.6 References

1. Franklin, B., *Philosophical Transactions of the Royal Society*, 445, **64**, 1774
2. Pockels, A., *Nature*, 437, **43**, 1891
3. Lord Rayleigh, *Phil. Mag.*, 337, **48**, 1899
4. Langmuir, I., *Am. Chem. Soc.*, 1848, **39**, 1917
5. Blodgett, K.B., *Physical Review*, 391, **55**, 1939
6. Henderson, J.A., Richards, R.W., Penfold, J., Shackleton, C., Thomas, R.K., *Polymer*, 3284, **32**, 1991
7. Henderson, J.A., Richards, R.W., Penfold, J., Thomas, R.K., *Acta Polymer*, 184, **44**, 1993
8. Hopkinson, I., Kiff, F.T., King, S.M., Richards, R.W., *Polymer*, 1722, **35**, 1994
9. Vilanove, R., Rondelez, F., *Phys. Rev. Letts.*, 1502, **45**, 1980
10. Takahashi, A., Yoshida, A., Kawaguchi, M., *Macromolecules*, 1196, **15**, 1982
11. Takahashi, A., Yoshida, A., Kawaguchi, M., *Macromolecules*, 956, **16**, 1983
12. Vilanove, R., Poupinet, D., Rondelez, F *Macromolecules*, 2880, **21**, 1988
13. Kawaguchi, M., Nishida, R., *Langmuir*, 492, **6**, 1990
14. Malcolm, B.R., *J. Colloid Interface Sci.*, 520, **104**, 1985
15. Barnes, G.T., Peng, J.B., *Langmuir*, 578, **6**, 1990
16. Fort, T., Alexander, A.E., *J. Colloid Sci.*, 190, **14**, 1959
17. O'Brien, K.C., Lando, J.B., Long, J., *Langmuir*, 51, **1**, 1985
18. Letts, S.A., Fort, T., Lando, J.B., *J. Colloid Interface Sci.*, 64, **56**, 1976
19. Barnes, G.T., Peng, J.B., *Langmuir*, 1749, **7**, 1991
20. Barnes, G.T., Peng, J.B., *Langmuir*, 3090, **7**, 1991
21. Barnes, G.T., Peng, J.B., Schuster, A., Ringsdorf, H., *Thin Solid Films*, 16, **210**,

1992

22. Von Smoluchowski, M., *Ann. Physik*, 609, **41**, 1913

23. Mandlestam, L., *Ann. Physik*, 609, **41**, 1913

24. Vrij, A., *J. Colloid Sci.*, 1, **19**, 1964

25. Katyl, R.H., Ingard, U., *Phys. Rev. Lett.*, 64, **19**, 1967

26. Katyl, R.H., Ingard, U., in *In Honour of P.M. Morse*, Eds. Freshbach, H., Ingard, U., MIT Press, Cambridge, Mass., 1969

27. Cruchon, D., Meunier, J., Bouchiat, M.-A., *C.R. Acad. Sci. Paris*, 422, **268B**, 1969

28. Hård, S., Hamnerius, Y., Nilsson, O., *J. Appl. Phys.*, 3433, **47**, 1976

29. Byrne, D., Earnshaw, J.C., in *Lasers in Chemistry*, Ed. West, M.A., Elsevier, Amsterdam, 1977

30. Byrne, D., Earnshaw, J.C., *J. Phys. D: Appl. Phys.*, 207, **10**, 1977

31. Byrne, D., Earnshaw, J.C., *J. Phys. D: Appl. Phys.*, 1133, **12**, 1979

32. Hård, S., Neuman, R.D., *J. Colloid Int. Sci.*, 73, **115**, 1987

33. Earnshaw, J.C., McGivern, R.C., *J. Phys. D: Appl. Phys.*, 82, **20**, 1987

34. Fermi, E., Zinn, W., *Phys. Rev.*, 103, **70**, 1946

35. Steyerl, A., *Z. Physik.*, 169, **253**, 1972

36. Handel, P.H., *Z. Physik.*, 7, **252**, 1972

37. Hayter, J.P., Penfold, J., Williams, W.G., *Nature*, 569, **262**, 1976

38. Hayter, J.P., Highfield, R.R., Pullman, B.J., Thomas, R.K., McMullen, A.I., Penfold, J., *J. Chem. Soc., Farad. Trans. 1*, 1437, 77, 1981

39. Ashworth, C.D., Messoloras, S., Stewart, R.J., Wilkes, J.G., Baldwin, I.S., Penfold, J., *J. Phys. D: Appl. Phys.*, 1862, **22**, 1989

40. Highfield, R.R., Thomas, R.K., Cummins, P.G., Gregory, D.P., Mingins, J., Hayter, J.B., Scharpf, O., *Thin Solid Films*, 165, **99**, 1987

41. Buhaenko, M.R., Grundy, M.J., Richardson, R.M., Roser, S.J., *Thin Solid Films*, 253, **159**, 1988

42. Felcher, G.P., Kampwirth, R.T., Gray, K.E., Felici, R., *Phys. Rev. Lett.*, 1537, **52**, 1984

43. Felici, R., Penfold, J., Ward, R.C., Olsi, E., Matacotta, C., *Nature*, 523, **329**, 1987

44. Russell, T.P., Karim, A., Mansoor, A., Felcher, G.P., *Macromolecules*, 1890, **21**, 1988

45. Fernandez, M.L., Higgins, J.S., Penfold, J., Ward, R.C., Shackleton, C., Walsh, D.J., *Polymer*, 1923, **29**, 1988

46. Fernandez, M.L., Higgins, J.S., Penfold, J., R.C., Shackleton, C., Walsh, D.J., *Polymer*, 2146, **31**, 1990

47. Composto, R.J., Stein, R.S., Kramer, E.J., Jones, R.A.L., Mansour, A., Karim, A., Felcher, G.P., *Physica B*, 434, **156 & 157**, 1989

48. Lee, E.M., Thomas, R.K., Penfold, J., Ward, R.C., *J. Phys. Chem.*, 381, **93**, 1989

49. Simister, E.A., Lee, E.M., Thomas, R.K., Penfold, J., *J.Phys. Chem.*, 1373, **96**, 1992

50. Lu, J.R., Li, Z.X., Su, T.J., Thomas, R.K., Penfold, J., *Langmuir*, 2408, **9**, 1993

51. Lu, J.R., Simister, E.A., Lee, E.M., Thomas, R.K., Penfold, J., Rennie, A.R., *Langmuir*, 1837, **8**, 1992

52. Bradley, J.E., Lee, E.M., Thomas, R.K., Willatt, A.J., Gregory, D.P., Penfold, J., Ward, R.C., Waschkowski, W., *Langmuir*, 821, **4**, 1988

53. Lee, E.M., Thomas, R.K., Rennie, A.R., Penfold, J., Cummins, P.G., Staples, E.J., *Chem. Phys. Lett.*, 196, **162**, 1989

54. Rennie, A.R., Crawford, R.J., Lee, E.M., Thomas, R.K., Crowley, T.L., Roberts, S., Qureshi, M.S., Richards, R.W., *Macromolecules*, 3466, **22**, 1989

55. Cosgrove, T., Heath, T.G., Phipps, J.S., Richardson, R.M., *Macromolecules*, 94, **24**, 1991

56. Lee, E.M., Simister, E.A., Thomas, R.K., *Langmuir*, 1031, **6**, 1990

57. Satija, S.K., Majkrzak, C.F., Russell, T.P., Sinha, S.K., Sirota, E.B., Hughes, G.J., *Macromolecules*, 3860, **23**, 1990

58. Henderson, J.A., Richards, R.W., Penfold, J., Shackleton, C., Thomas, R.K., *Polymer*, 3284, **32**, 1991

59. Henderson, J.A., Richards, R.W., Penfold, J., Thomas, R.K., *Acta Polymer*, 184, **44**, 1993

60. Rochford, B.R., Gissing, S.K., Richards, R.W., *Colloids and Surfaces A: Physiochemical and Engineering Aspects*, 171, **86**, 1994

61. Rochford, B.R., Richards, R.W., Webster, J.R.P., *Faraday Discuss.*, 263, **98**, 1994

62. Sanderson, A.R., Crowley, T.L., Morrison, J.D., Barry, M.D., Morton-Jones, A.J., Rennie, A.R., *Langmuir*, 2110, **8**, 1992

63. Eastoe, J., Fragnetto, G., Robinson, B.H., Towey, T.F., Heenan, R.K., Leng, F.J., *J. Chem. Soc., Faraday Trans.*, 461, **88**, 1992

64. MacDonald, W.A., McLenaghan, A.D.W., McLean, G., Richards, R.W., King, S.M., *Macromolecules*, 6164, **24**, 1991

65. Higgins, J.S., Rostami, S., Bucknall, D.G., *Polymer*, 4419, **33**, 1992

2. SYNTHESIS OF POLY(LAURYL METHACRYLATE)

2.1 Introduction

Four isomers of poly(lauryl methacrylate) (PLMA) were synthesised using monomer which was either hydrogenous or deuterium labelled at different parts. The deuterium labelling was necessary for the neutron reflectivity experiments, so that the maximum possible information about monolayer organisation could be obtained. The four isomeric polymers are shown schematically in figures 2.1(a) to (d).

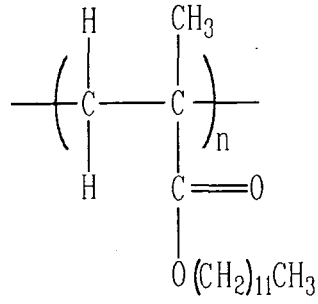

Figure 2.1(a): Fully hydrogenous (HMHL)

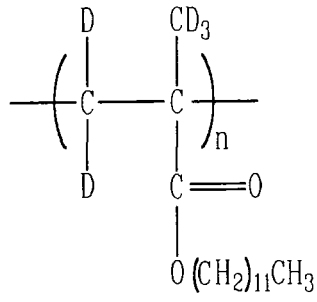

Figure 2.1(b) Deuterated methacrylate backbone with hydrogenous lauryl ester groups (DMHL)

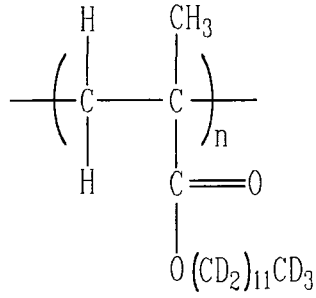

Figure 2.1(c) Hydrogenous methacrylate backbone with deuterated lauryl ester groups (HMDL)

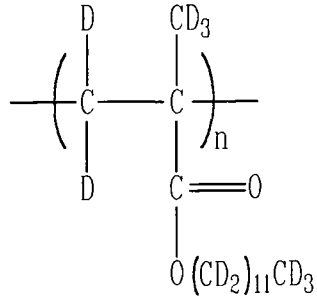

Figure 2.1(d) Fully deuterated (DMDL)

2.2 Synthesis of Fully Hydrogenous PLMA

2.2.1 Anionic Polymerisation

Originally it was hoped to use anionic polymerisation as the means of synthesising PLMA. This method is a living polymerisation, characterised by the absence of a termination step. If all impurities which are able to react with the carbanions are excluded from the system, then propagation should continue until all the monomer present has been consumed, leaving the carbanion intact and still active. The living ends are terminated by adding methanol or a mixture of methanol and ethanoic acid. This method was the preferred route since it enables control of the molecular weight and the polydispersity of the polymer.

The lauryl methacrylate (LMA) monomer (100ml) was washed with three 50ml aliquots of 10% sodium hydroxide and then with two aliquots of water to remove the hydroquinone inhibitor. The LMA was then run off into a conical flask containing calcium chloride and allowed to stand over night, then it was decanted and vacuum distilled, discarding the first 10mls. To purify the monomer further it was dried over calcium hydride, vacuum degassed and then filtered off from the calcium hydride under an argon atmosphere.

The LMA was transferred via a canulla to a pre-weighed vessel so a known amount was used for the polymerisation (17.87g). The initiator used was diphenyl hexyl lithium (DPHL) which was prepared by mixing secondary butyllithium (1.1M 163μl) with a slight excess of diphenyl ethene DPE (38μl). This was done by injecting the DPE and then the secondary butyllithium into THF under an argon atmosphere. A bright red solution of DPHL was produced. DPHL was chosen to be the initiator as the sterically

hindered, less basic nature of the carbanion prevents attack at the carbonyl group [1, 2] and had been used previously for the polymerisation of higher methacrylates [3].

The reaction flask was rinsed with acetone and dried by evacuation using a water pump. The apparatus was attached to the vacuum line and evacuated to a pressure of 1×10^{-6} mbar and heated. The reaction flask was then further cleaned by rinsing with living polystyryl lithium in benzene to remove any remaining polar impurities on the glass. Following this and after complete removal of the polystyryl lithium from the reaction volume, about 100mls of THF was vacuum transferred into the polymerisation apparatus. The reaction flask was then placed under an argon atmosphere and cooled to -78°C. DPHL (63.9µl) was injected into the THF followed by the LMA via a canulla. The deep red colour disappeared almost immediately. After 1 hour the reaction was killed by injecting a 50/50 mixture of methanol and ethanoic acid (total volume = 500µl) and the solution was precipitated into methanol but no polymer was present. A second attempt was carried out with the initiator being added to the monomer solution, this was also unsuccessful.

The lack of success was most likely due to monomer purity[3]. Higher alkyl methacrylate monomers are generally synthesised via transesterification of methyl methacrylate with the appropriate alcohol, which in most cases has a similar boiling point to the resulting methacrylate and, therefore, cannot be distilled off (b.p. of LMA = 280°C, b.p. of lauryl alcohol = 268°C). Alcoholic impurities are present in most commercially available methacrylates and these lead to termination. Calcium hydride does not react appreciably with these higher alcohols, therefore, most higher methacrylates cannot be used for anionic polymerisation. The problems encountered with the anionic polymerisation route to PLMA may have been possible to overcome with more synthetic work, however, as the objective of this work was to study the

physical properties of PLMA this method was abandoned as samples were needed immediately to commence the studies of the monolayer properties of PLMA. Attention turned to free radical polymerisation techniques.

2.2.2 Free Radical Polymerisation

Free radical polymerisation does not require the same stringent conditions as anionic polymerisations, so any alcoholic impurities do not affect the polymerisation of higher methacrylates.

This is a chain growth polymerisation which is not living as it contains termination steps. The free radical polymerisation process is characterised by three distinct stages:

1. Initiation - the reactive species responsible for propagation is formed (reaction of monomer and initiator)

2. Propagation - the monomer molecules react specifically and exclusively with the reactive group at the end of the polymer chain

3. Termination - the reactive group at the end of the growing chain is lost

Termination can occur in two ways:

(a) Combination

$$M_n^{\cdot} + M_m^{\cdot} \longrightarrow P_{(n+m)}$$

(b) Disproportionation

$$M_n^{\cdot} + M_m^{\cdot} \longrightarrow P_n + P_m$$

where $M^{\cdot}$ = propagating chains

P = polymer

n and m = number of monomer units

The initiator used was azobisisobutyronitrile (AIBN) which decomposes to produce radical species. The crude initiator was purified by recrystallising it from warm methanol.

The LMA was washed with sodium hydroxide and water and then vacuum distilled. LMA (50.66g 0.199mol) and 500mls of 2-butanone solvent were placed in a 1l 2-neck flask fitted with a reflux condenser and a nitrogen purge inlet. The amount of initiator added was 0.5% of the moles of LMA present. Therefore, 0.001 moles (0.16g) of AIBN were used. The LMA solution was purged with nitrogen and then heated to reflux with the nitrogen purge continuing. A solution of the AIBN initiator in 2-butanone was then added. This was left to reflux for six hours, by which time the solution had increased in viscosity, an indication that polymerisation had occurred. The solution was cooled and the polymer was precipitated out by pouring the solution into methanol. The methanol was decanted off leaving behind the PLMA as a viscous, tacky mass which was removed and dried in a vacuum oven at 40°C and less than 1mbar. From this polymerisation, 29.2g of PLMA were obtained, corresponding to a yield of

58%. SEC analysis in THF (calibrated with poly(styrene standards) the $\overline{M}_W$ was 38 600 and the $\overline{M}_n$ 19 100, corresponding to a polydispersity of 2.00.

To obtain polymer samples with a narrower polydispersity, the PLMA was fractionated. This was done by fractional precipitation by the addition of methanol to a solution of the polymer in 2-butanone. PLMA (14.80g) was dissolved in 1.5l of solvent and then transferred to a separating funnel with 3 B24 sockets which had a pear shaped blister blown into it just above the tap. A mechanical stirrer was placed in the middle socket and the other two were stoppered except when methanol was introduced. The funnel was then placed into a temperature controlled water bath, which was set at 25°C. The stirrer was switched on and the first portion of methanol was added using a 25ml pipette which had its tip bent so as to direct the methanol into the vortex created by the stirrer and at such a rate that it dispersed without any build up of high local concentrations of precipitant.

After the addition of 39mls of methanol the solution became turbid due to the first fraction of the highest molecular weight, least soluble polymer precipitating out. The water bath was then raised in temperature until the solution became clear again as it became homogeneous. The water bath was then allowed to cool down to 25°C with the stirrer removed. This was then left overnight for the precipitated polymer to settle to the bottom. However, the amount of methanol necessary to give a reasonable fraction size was not known and a trial and error process was used to determine the correct amount. A further 50 mls of methanol were added to the first fraction as no precipitate was collected after the first 39mls had been added as this was insufficient to precipitate enough polymer to flow down and settle at the bottom of the funnel as the PLMA tended to stick to the walls of the funnel.

IR PLMAR
FILE /data/curdat/iry08decb
RUN ON Dec 8 92
SOLVENT CDCl3
OBSERVE C13

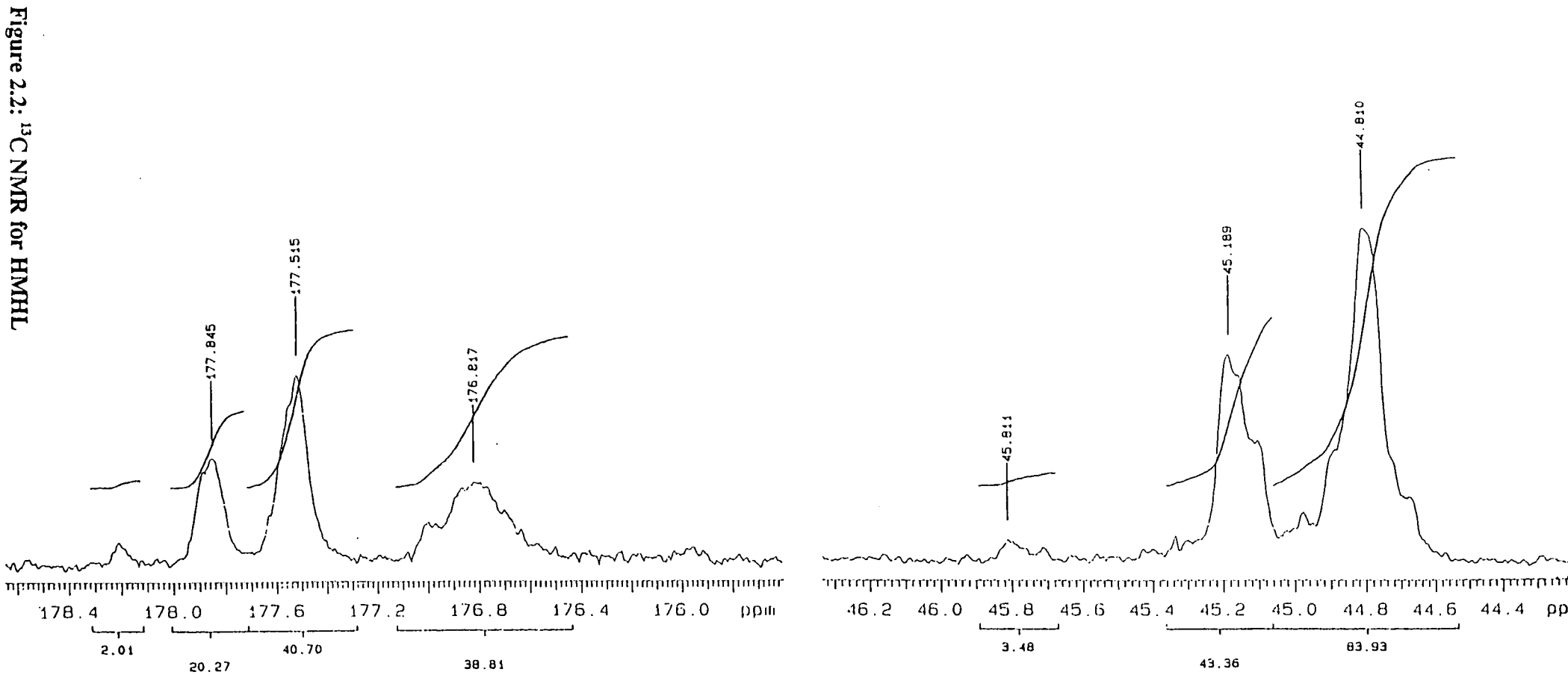

Figure 2.2: ^{13}C NMR for HMHL

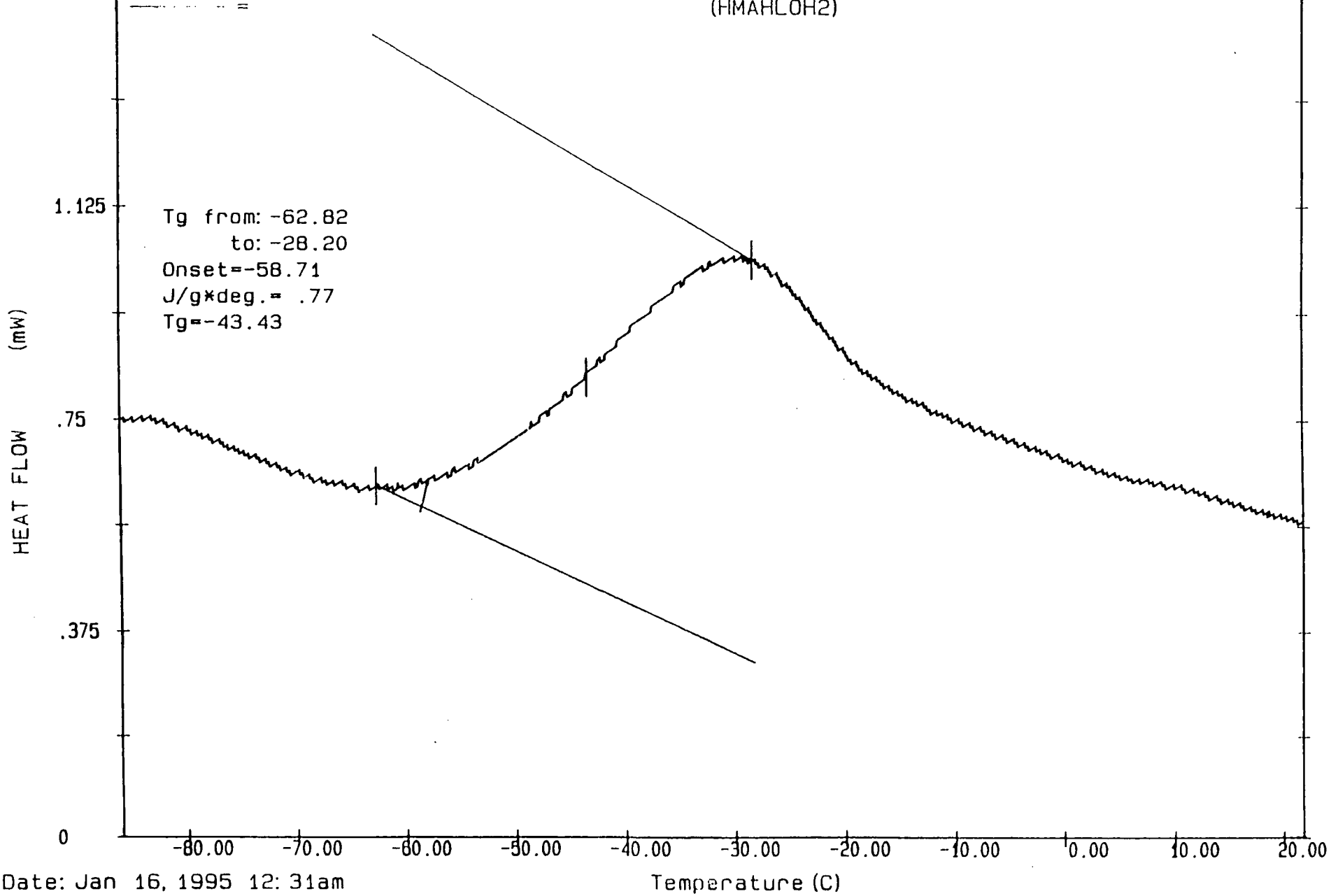

Figure 2.3: DSC trace for HMHL

2.3 Synthesis of Deuterated Variations

Various procedures were attempted to synthesise the deuterated variations. All the reactions that were attempted were carried out using hydrogenous material to check if the reactions were proceeding as expected before using the deuterated versions of the reagents.

2.3.1 Synthesis of Deuterated Variations of the Monomer by Esterification

By esterifying methacrylic acid and lauryl alcohol all three variations of the monomer could be synthesised by esterifying deuterated methacrylic acid with hydrogenous lauryl alcohol (DMHL), hydrogenous methacrylic acid with deuterated lauryl alcohol (HMDL) and deuterated methacrylic acid with deuterated lauryl alcohol (DMDL). These monomers could then be polymerised as for the fully hydrogenous material.

As the deuterated material is expensive it would be desirable for all the deuterated material to react. Therefore, for the synthesis of DMHL and HMDL the hydrogenous material would be used in excess and for DMDL, equal molar amounts would be used. To check if the reactions worked for both conditions, hydrogenous material was used with excess alcohol and then excess acid.

The procedure for the esterification was as follows:

In a 50ml round bottom flask, methacrylic acid, lauryl alcohol, toluene, hydroquinone, concentrated sulphuric acid and a few anti-bumping granules were placed

(see tables 2.2 and 2.3 for quantities). A Dean and Stark apparatus was attached to the flask. This was used to separate the water produced in the reaction so as to drive the equilibrium towards ester formation. The reaction mixture was then heated to reflux and the solution became a deep red colour.

The reaction mixture was then cooled, diluted with diethyl ether and washed with sodium carbonate solution until the organic layer was neutral. The ether solution was then washed with a saturated sodium chloride solution and dried with magnesium sulphate. The ether solution was filtered and the solvent ether removed under reduced pressure. The resulting solution was then distilled under vacuum to give pure lauryl methacrylate.

This process was first carried out using excess lauryl alcohol and the quantities used are given in table 2.2.

ATTEMPT	1		2	
	MASS /g	MOLES	MASS /g	MOLES
METHACRYLIC ACID	1.31	0.015	1.37	0.016
LAURYL ALCOHOL	5.69	0.031	5.89	0.032
TOLUENE	6.20	–	6.00	–
HYDROQUINONE	0.26	0.0024	0.25	0.0023
SULPHURIC ACID	0.20	0.0020	0.21	0.0021

Table 2.2: Amounts of reagents used for esterification with excess lauryl alcohol

Attempt 1 was refluxed for six hours and washed with 10% sodium carbonate solution, however, when this was added no separation occurred after shaking so this attempt was aborted.

Attempt 2 was also refluxed for six hours, however, it was washed with 5% sodium carbonate. Separation was achieved with the aqueous layer a dark brown colour and the ether layer orange/brown. Sodium carbonate solution in 30ml portions was added until no gas evolution was evident and the ether layer was neutral. The ether layer was removed and the resulting solution was distilled under vacuum producing 1.23g of pure lauryl methacrylate which corresponds to a yield of only 32.3%.

The esterification was next tried using excess methacrylic acid. The amounts used are shown in table 2.3.

Attempt	1		2		3		4	
	Mass (g)	Mole	Mass (g)	Mole	Mass (g)	Mole	Mass (g)	Mole
Methacrylic Acid	3.33	0.039	3.46	0.040	3.53	0.041	3.58	0.042
Lauryl Alcohol	5.27	0.028	5.35	0.029	5.27	0.028	5.28	0.28
Toluene	5.52	–	10.16	–	13.32	–	5.23	–
Hydroquinone	0.31	0.003	2.09	0.019	5.25	0.048	0.33	0.003
Sulphuric Acid	0.25	0.003	0.42	0.004	0.33	0.003	0.23	0.002

Table 2.3: Amounts of reagents used for esterification with excess methacrylic acid

Attempt 1 was refluxed for six hours and the same washing procedure was used as for the previous attempt 2. 2.67g of lauryl methacrylate were produced, corresponding to a yield of only 37.1%. In an attempt to increase the yield, attempt 2 was refluxed overnight for a total of twenty four hours. The same washing procedure was undertaken, however, during the distillation a white solid was produced in the condenser which was polymerised methacrylic acid. In an attempt to inhibit this, more than twice the amount of hydroquinone was added for attempt 3, but no lauryl methacrylate was isolated. Attempt 4 was a repeat of attempt 1 to try and repeat the

successful reaction, however, no lauryl methacrylate was isolated this time. Due to the low yields and poor reproducibility of these reactions a new approach was undertaken.

2.3.2 Transesterification of PMMA and Lauryl Alcohol

This process used PMMA synthesised using anionic techniques, so the molecular weight could be controlled and the polydispersity kept low. Therefore, PLMA could be synthesised with a known molecular weight and polydispersity as these two were initially determined by the PMMA sample used, whereas producing the LMA monomer and then free radically polymerising it has less control over molecular weight and produces high polydispersities. The transesterification reaction is an equilibrium reaction and therefore, the methanol produced has to be removed to increase the yield of the transesterified polymer.

The first method for the transesterification was as follows:

PMMA (3.01g 0.03mol of monomer units) was dissolved in 100mls of toluene in a 250ml round bottom flask. To this solution was added 11.20g (0.06 mol) of lauryl alcohol and a catalytic amount of sodium methoxide (~2ml) which was produced by adding sodium metal to dry methanol (which was produced by refluxing with magnesium and iodine - see section 2.3.5 for more detail). A Dean and Stark separator, of the type which returns the bottom layer, was fitted to the round bottom flask. A plug of glass wool was placed in the bottom U-bend of the separator and the column was then filled with calcium chloride to absorb the methanol produced and return the toluene to the reaction vessel. A condenser was fitted to the top of the separator and the reaction mixture heated to reflux for five hours.

The solution was allowed to cool and then concentrated by removing some of the toluene under reduced pressure. This solution was then precipitated into methanol and a white powdery precipitate was produced, which was presumably PMMA. The lack of reaction could possibly have been caused by too short a reflux, the methanol not being removed or lauryl alcohol being absorbed by the calcium chloride.

A second attempt was carried out using 4A molecular sieves instead of calcium chloride as these are selective to the absorption of methanol and not lauryl alcohol. The reaction was left to reflux for 22 hours. During the reflux the polymer came out of solution where the solvent had evaporated from the sides of the flask. This left a stiff clear gel stuck to the sides of the flask.

A second method was then attempted. This involved the continuous distillation of toluene to take off the methanol and continuous addition of more sodium dried toluene. PMMA (3.20g 0.032 mol) was placed in a 500ml 2-neck round bottom flask and dissolved in 170mls of toluene, then a distillation head, thermometer, condenser and receiver adapter were connected. A dropping funnel was placed in the side arm for the addition of more toluene. Lauryl alcohol (11.16g 0.06 mol), which had been stood over 4A molecular sieves, was then added and sodium metal was added directly to the reaction flask. The reaction mixture was initially distilled for three hours and allowed to cool. The solution was then rotary evaporated to about a 5% solution (~65mls) and precipitated into methanol. A fine white precipitate was produced (PMMA) so this was redissolved in toluene and distilled for a further eight hours. However, as before the polymer came out of solution on the walls of the flask.

Due to the problems of heating the polymer solution outlined above attention again turned to the monomer.

2.3.3 Transesterification of MMA and Lauryl Alcohol

Four possible methods to carry out this reaction were found:

1. Otera *et al*[4] used novel distannoxanes ($X-Sn(Bu)_2-O-Sn(Bu)_2-Y$ X = Cl, -N=C=S Y=OH) as catalysts for transesterification of α,β–unsaturated esters. The disadvantages of this method were that the catalyst is not easily obtainable and the reaction solution of the ester and alcohol would need to be heated at reflux and this could lead to polymerisation of the monomer.

2. Seeback *et al*[5] used titanium (IV) alkoxides as catalysts for transesterifications of functionalised esters. This method also required heating of the reaction solution and used the alcohol as the solvent which would be a draw back when using deuterated lauryl alcohol due to the cost.

3. Yazawa *et al*[6] reacted carboxylic esters with boron tribromide at room temperature. When amines were added to the solution the corresponding amide was produced and if alcohols were added to the solution the corresponding ester would be produced (transesterification). Although this reaction was simple it had not been used with any large alcohols.

4. Meth-Cohn[7] has used n-butyl lithium to transesterify aromatic and α,β–unsaturated methyl esters. This reaction has been used with methyl acrylate and large alcohols, menthol and borneol. For primary alcohols an excess of the alcohol was found to be required for good yields, however, polymerisable compounds are best used in

excess and also if the alcohol is expensive and/or difficult to separate from the product ester (both of which facts are true in this case) then an excess of methyl ester is best. The considerations outlined above indicate that if this method was used then an excess of methyl ester would be the favoured route.

The method of Meth-Cohn was the one which was chosen to carry out the transesterification, due to the simple reagents used, the straight forward method and as elevated temperatures were not required. The method was as follows:

Lauryl alcohol was weighed into a 250ml 2-neck round bottom flask and then anhydrous THF was added. A magnetic stirrer was placed in the flask and then a nitrogen supply was connected to the top neck and turned on, the side arm was stoppered. The flask was placed into an ice bath and the n-butyl lithium was injected via the side arm and then a few minutes later a pre-weighed amount of methyl methacrylate was added. The amounts used are shown table 2.4.

The reaction was left stirring for about six hours by which time a clear gelatinous precipitate (LiOH) had formed in the solution. This was filtered off from the solution and rinsed with THF. The filtrate was then rotary evaporated to remove the THF leaving lauryl methacrylate. The success of the reaction can be shown by comparing the NMR spectra of LMA purchased to make the fully hydrogenous polymer and the monomer synthesised via the transesterification. The ^{1}H and ^{13}C NMR of the two samples of LMA are shown in figures 2.4 and 2.5 (a) and (b). The spectra show identical features and the ^{1}H and ^{13}C NMR peaks for both samples can be assigned as shown in tables 2.5 and 2.6. There are trace impurities in the synthesised LMA and these are observed at 1.8 and 3.6 - 3.7ppm in the ^{1}H spectrum, 25.9, 32.9, 63 and 68ppm in

the ^{13}C spectrum. These resonances can be attributed to the presence of alcoholic impurities, the peak at 1.8ppm in the ^{1}H spectrum is due to the alkyl part of the alcohol and the peaks at 3.6 - 3.7 are due to the protons on the carbon adjacent to the oxygen. Such impurities also account for the observations in the ^{13}C spectrum, with the 25.9 and 32.9ppm peaks corresponding to the alkyl groups and the 63 and 68ppm peaks corresponding to the carbons adjacent to the oxygen.

By using varying combinations of hydrogenous and deuterated methyl methacrylate and lauryl alcohol the three deuterated variations of the monomer were synthesised. The ^{1}H NMR spectra of the deuterated monomers are shown in figures 2.6 to 2.8 and show that the deuteration is as expected. For DMHL (figure 2.6) the peaks at 1.9ppm, corresponding to the α methyl, 5.5 and 6.1ppm, corresponding to the cis and trans protons on the double bond, are not present due to them being deuterated. The alkyl region remains the same as for the fully hydrogenous variation. For HMDL (figure 2.7) the opposite occurs, with the alkyl proton region disappearing and the peaks for the α methyl and hydrogens on the double bond being clearly visible. For DMDL (figure 2.8), as expected, there are no peaks present due to hydrogenous monomer.

MONOMER PREPARED	HMHL	DMHL	HMDL	DMDL
AMOUNT OF MMA g (mol)	2.51 (0.025)	2.70 (0.025)	2.22 (0.022)	2.05 (0.019)
AMOUNT OF LOH g (mol)	3.81 (0.020)	3.78 (0.020)	3.75 (0.018)	3.20 (0.015)
AMOUNT OF 2M BuLi ml (mol)	10.0 (0.020)	10.0 (0.020)	8.9 (0.018)	7.6 (0.015)
AMOUNT OF THF (ml)	90	90	90	90
AMOUNT OF LMA PRODUCED g (mol)	4.23 (0.017)	3.52 (0.014)	3.92 (0.014)	3.87 (0.014)
% YIELD	85	70	79	91

Table 2.4: Amounts of reagents used to synthesise each monomer and yields obtained

SHIFT (ppm)	N° OF PROTONS (FROM INTEGRALS)	ASSIGNMENT
0.8	3	CH_3 at end of side chain
1.3	18	$(CH_2)_9$ bulk of side chain
1.6	2	CH_2 - CH_2 -O group in side chain
1.9	3	α CH_3
4.1	2	CH_2 - O - C = O
5.5	1	trans H - C = C - C = O
6.1	1	cis H - C = C - C = O
7.3	–	$CDCl_3$

Table 2.5: ^{1}H NMR peak assignments for LMA

SHIFT (ppm)	ASSIGNMENT
14 - 32	12 alkyl carbons in side chain
65	α CH_3
77	$CDCl_3$
126	$H_2C=$
137	$=C$
168	$C=O$

Table 2.6: ^{13}C NMR peak assignments for LMA

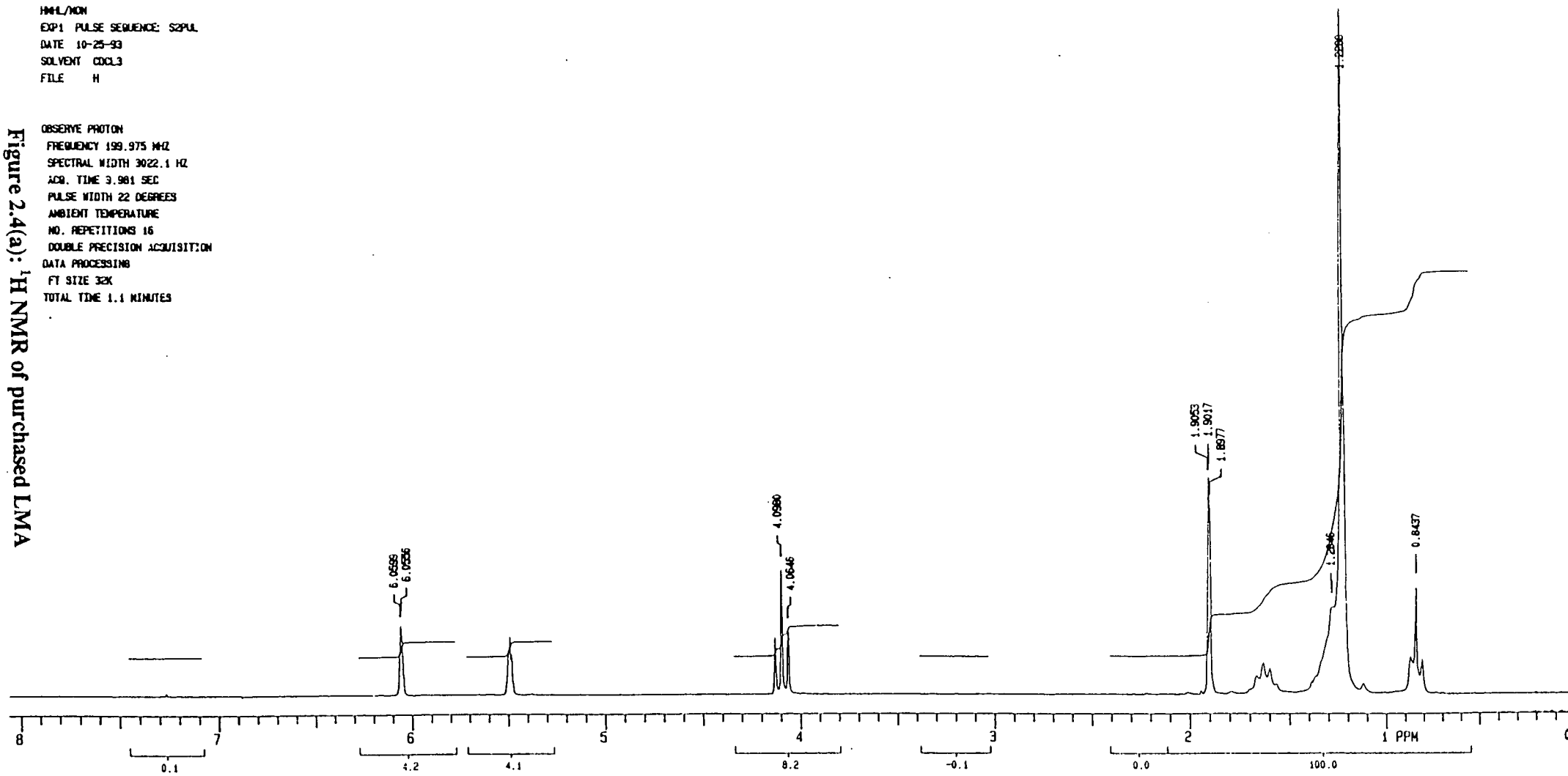

Figure 2.4(a): ^{1}H NMR of purchased LMA

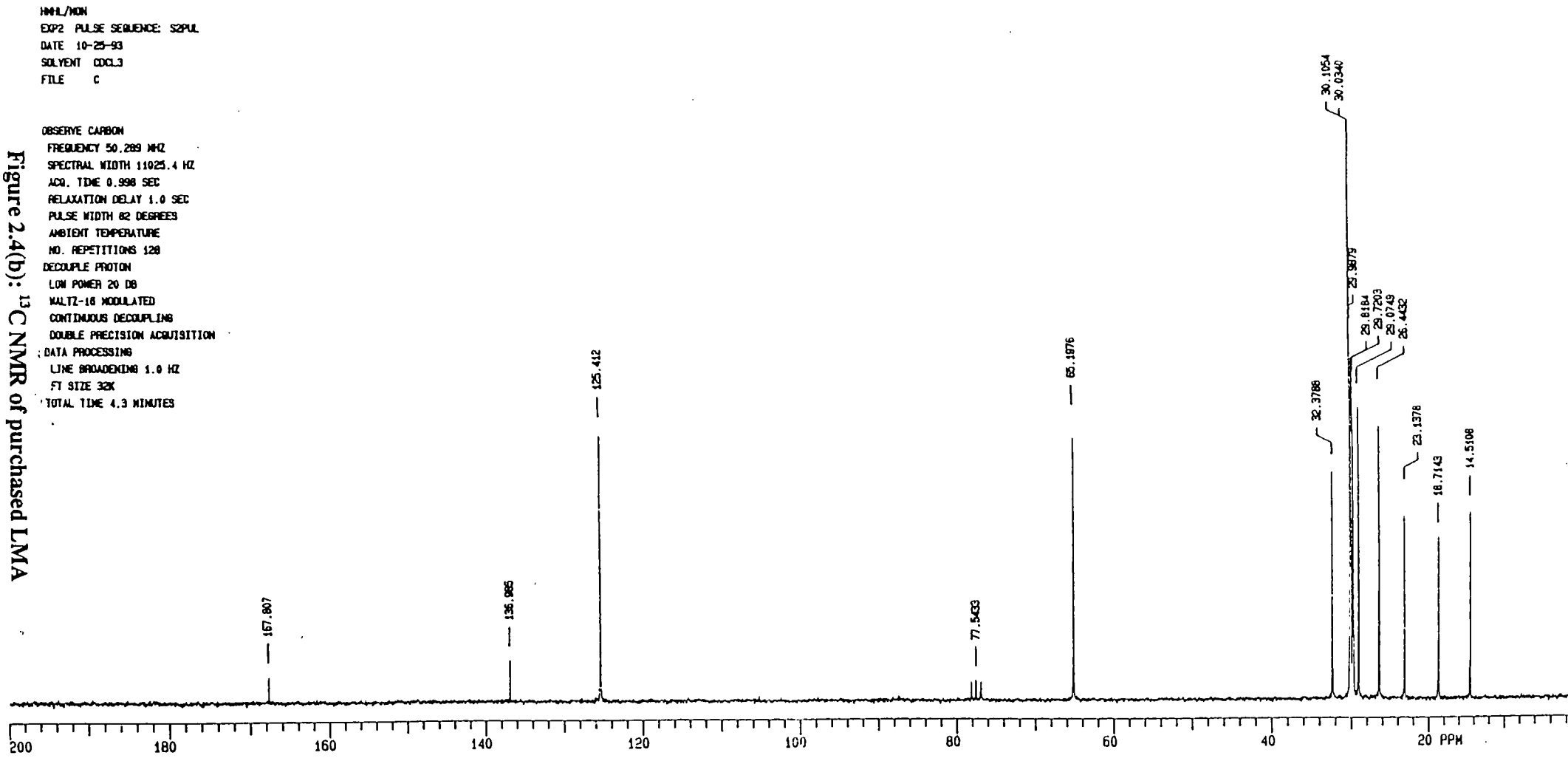

Figure 2.4(b): ^{13}C NMR of purchased LMA

IR LMA Trans
FILE /data/curdat/irs02juna.fid
RUN ON Jun 2 93
SOLVENT CDCl3

OBSERVE H1
Frequency 399.952 MHz
Spectral width 5000.0 Hz
Acquisition time 3.744 sec
Relaxation delay 0.000 sec
Pulse width 2.0 usec
Ambient temperature
No. repetitions 64
Double precision acquisition
DATA PROCESSING
FT size 65536
Total acquisition time 4 minutes

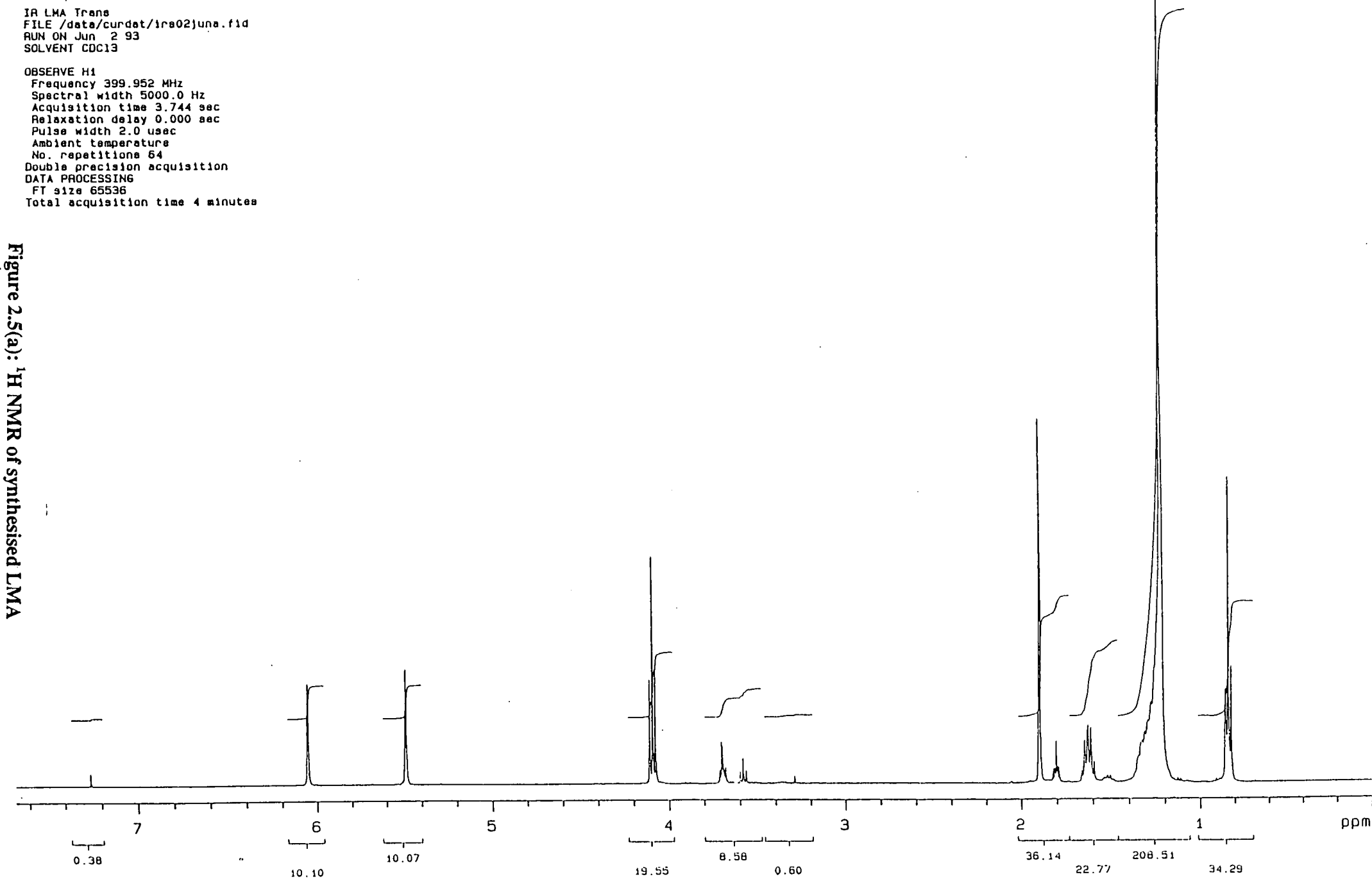

Figure 2.5(a): ^{1}H NMR of synthesised LMA

IR LMA Trans
FILE /data/curdat/irs02junb.fid
RUN ON Jun 2 93
SOLVENT CDCl3

OBSERVE C13
Frequency 100.577 MHz
Spectral width 25000.0 Hz
Acquisition time 1.199 sec
Relaxation delay 3.000 sec
Pulse width 8.9 usec
Ambient temperature
No. repetitions 512
DECOUPLE H1
High power 40
Decoupler continuously on
WALTZ-16 modulated
Double precision acquisition
DATA PROCESSING
Line broadening 0.8 Hz
FT size 131072
Total acquisition time 35 minutes

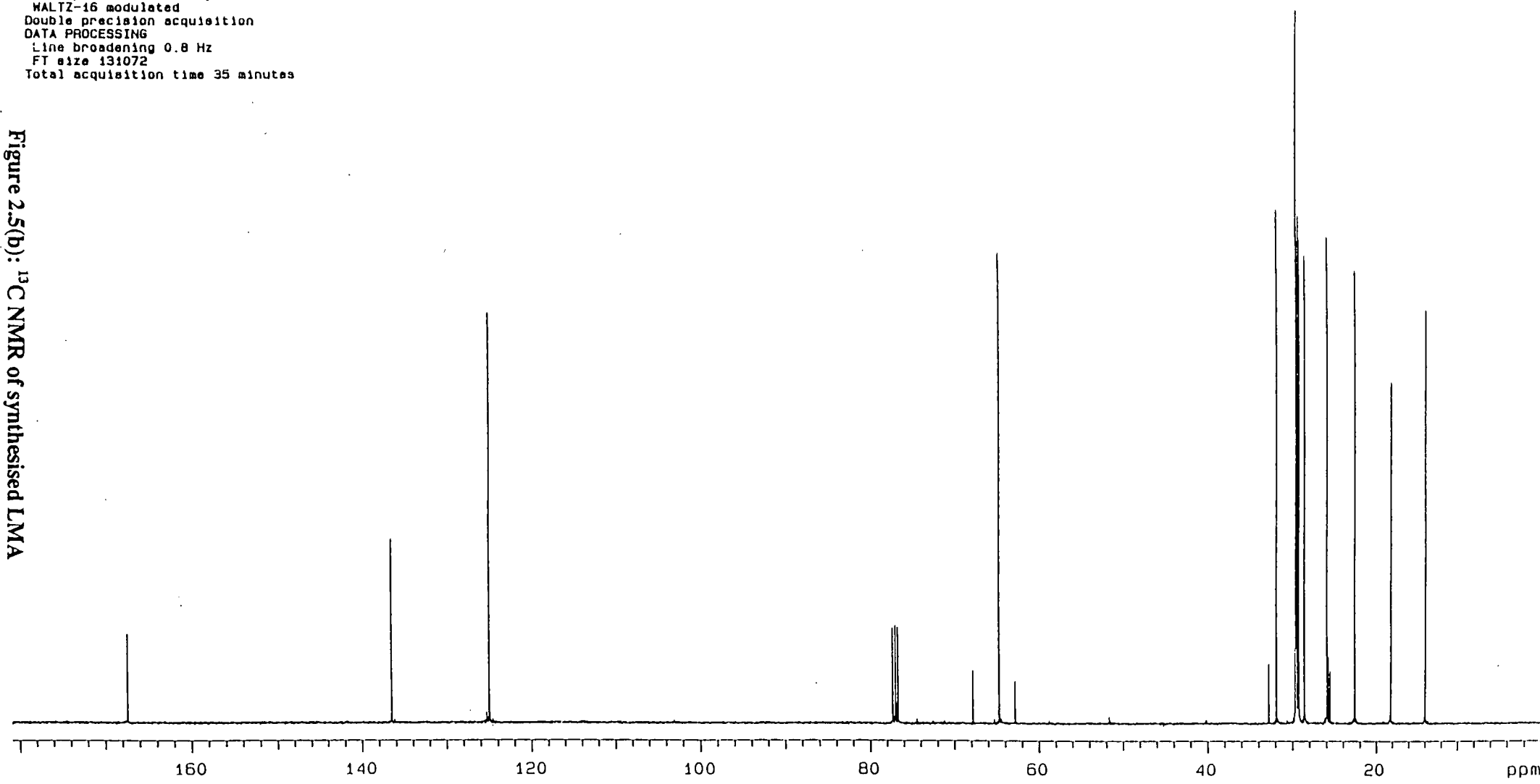

Figure 2.5(b): ^{13}C NMR of synthesised LMA

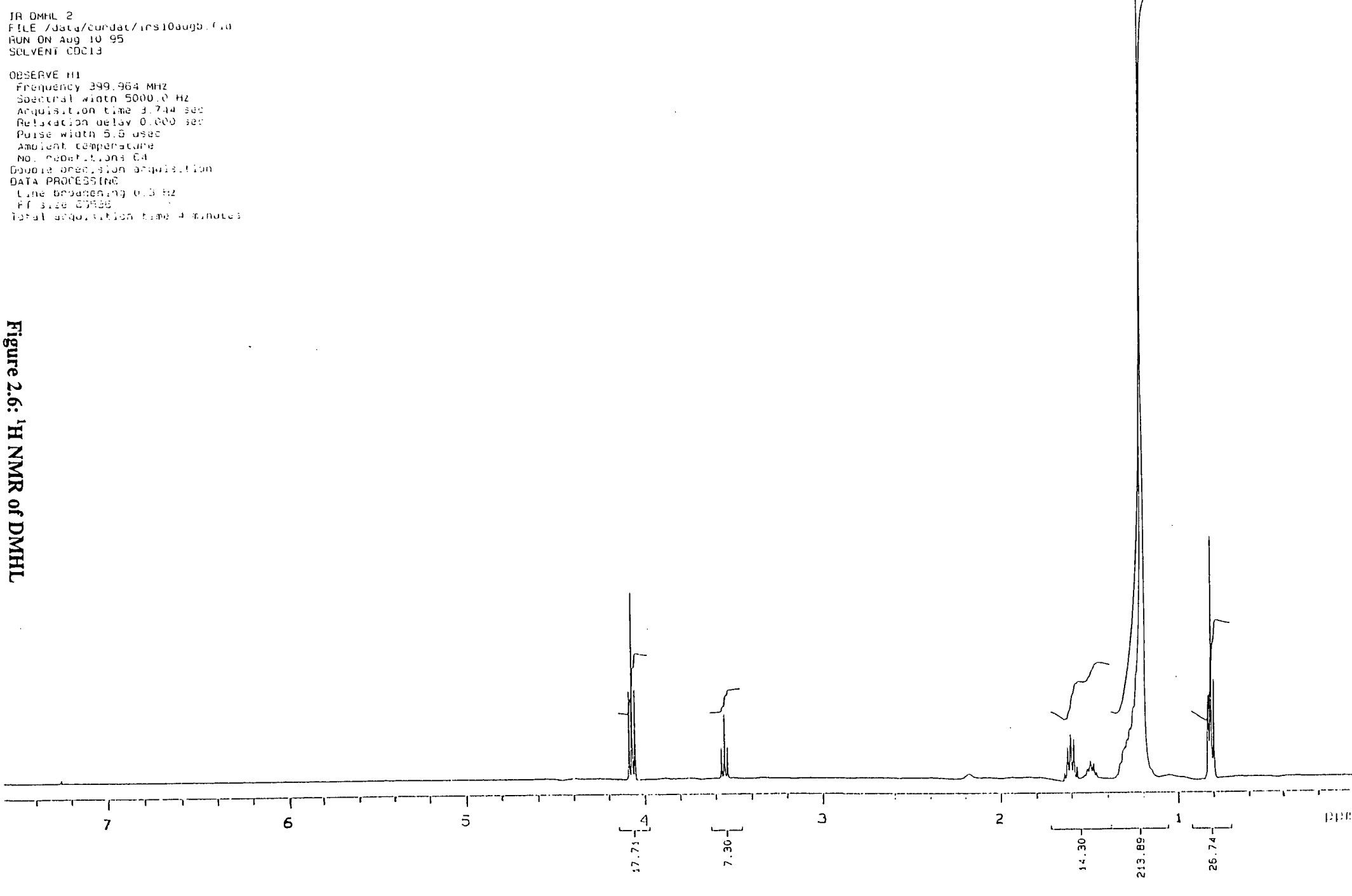

Figure 2.6: ^{1}H NMR of DMHL

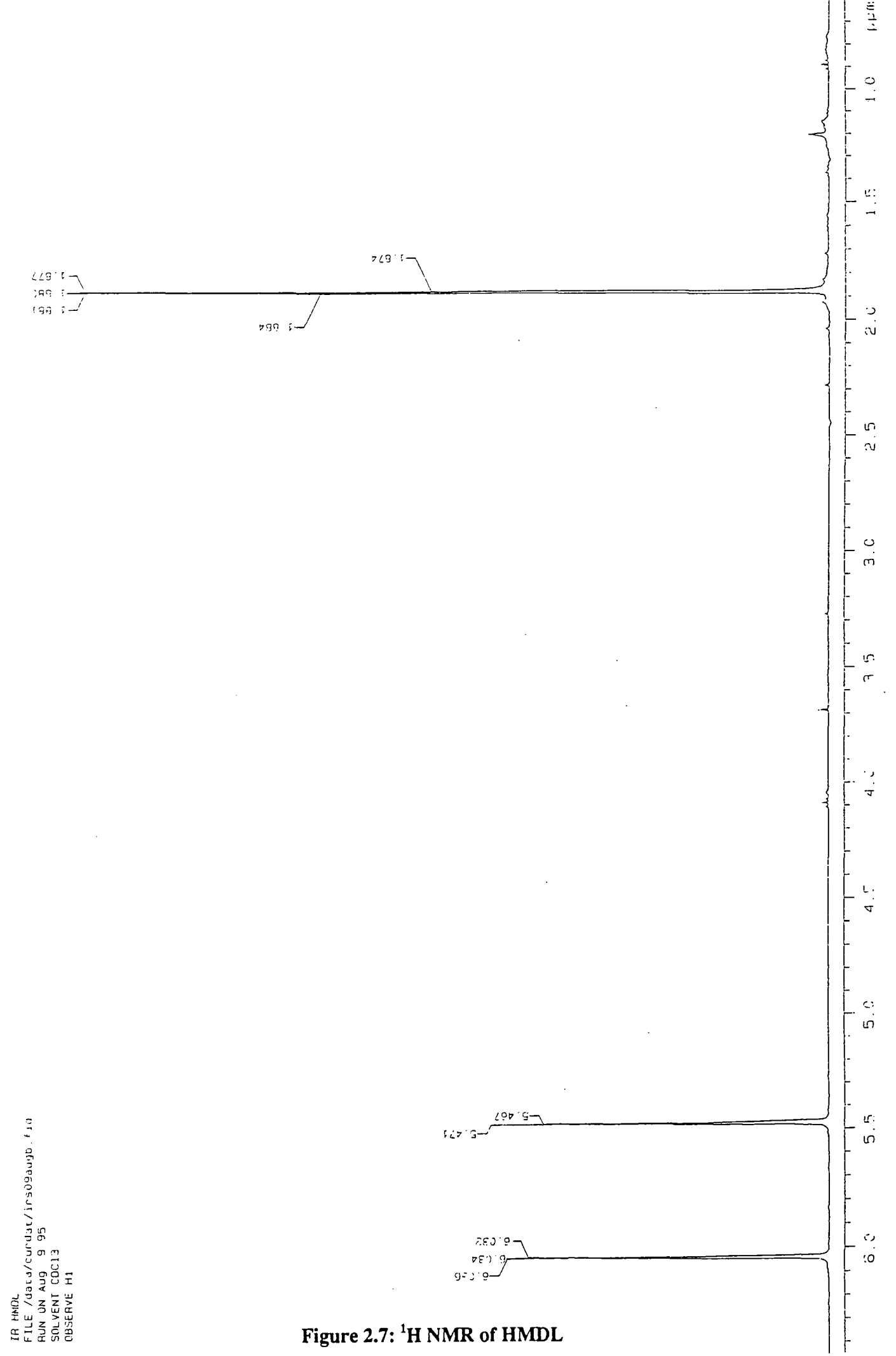

Figure 2.7: ^{1}H NMR of HMDL

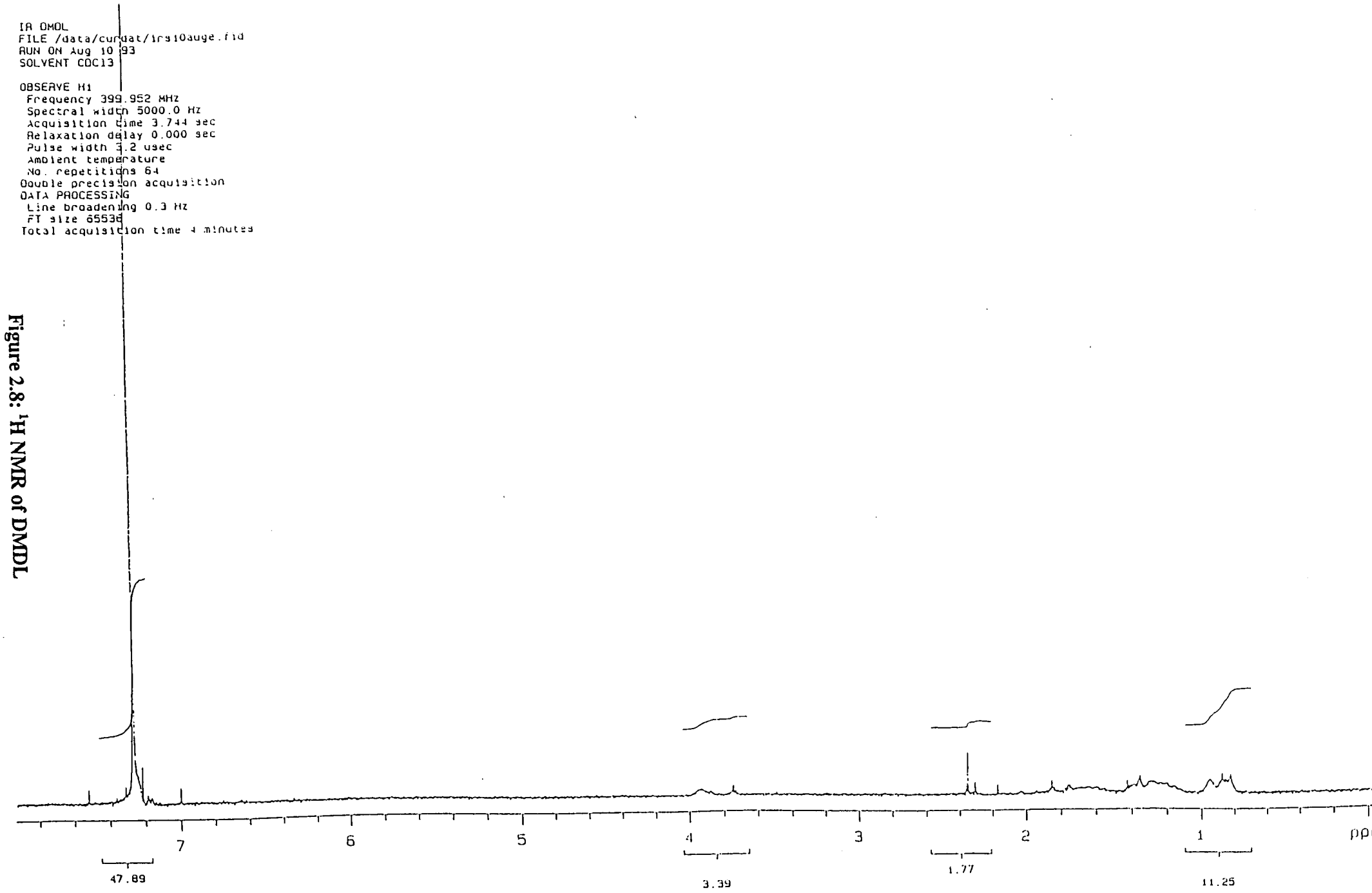

Figure 2.8: ^{1}H NMR of DMDL

2.3.4 Polymerisation of deuterated variations of LMA

Each monomer was polymerised using a procedure similar to that for the hydrogenous material (section 2.2.2) except on a much smaller scale. Table 2.7 shows the quantities of reagents used and the polymer produced for each polymerisation.

MONOMER POLYMERISED	DMHL - 1	DMHL - 2	HMDL	DMDL
AMOUNT OF LMA g (mol)	2.22 (0.009)	1.29 (0.005)	2.60 (0.009)	2.70 (0.010)
AMOUNT OF AIBN g (mol)	0.007 (4.29×10^{-5})	0.004 (2.49×10^{-5})	0.009 (5.24×10^{-5})	0.008 (4.90×10^{-5})
AMOUNT OF MEK ml	20	13	26	27
AMOUNT OF PLMA g	1.06	0.56	0.91	1.03
% CONVERSION	48	43	35	38

Table 2.7: Amounts used for polymerisations and polymer produced

The first polymer produced (DMHL - 1) was bimodal with a small amount of high molecular weight polymer (~700 000), but mainly consisting of PLMA with a molecular weight of about 10 000. This was thought to occur due to AIBN initiator being added to the cold reaction solution. This polymerisation was repeated with the AIBN added to the refluxing solution. The polymer was again bimodal although the

amount of high molecular weight polymer had decreased (high molecular weight ~530 000, low molecular weight ~18 000). DMHL - 1 was fractionated and the first fraction was isolated and dried (DMHL -1 Fr1). The SEC results for each polymer are given in table 2.8.

POLYMER	$\overline{M}_w$	$\overline{M}_n$	$\overline{M}_w/\overline{M}_n$
DMHL - 1	15 500	8 000	1.90
DMHL - 1 Fr1	165 100	111 700	1.48
DMHL - 2	29 800	15 400	1.94
HMDL	62 900	44 300	1.42
DMDL	81 700	55 300	1.48

Table 2.8: Molecular weights and polydispersities of the deuterated polymers

The traces obtained from DSC measurements of each polymer are shown in figures 2.9 to 2.11. The T_g for each polymer was −59.3°C for HMDL, −42.2°C for DMHL and −52.8°C for DMDL. The T_g values for the isotopic variations of PLMA occur in two groups, DMHL and HMHL have a T_g between −42 and −43°C, whereas for HMDL and DMDL the T_g is between −52 and −59°C. This may be explained by considering the values of $\overline{M}n$ obtained for the polymers, DMHL and HMHL have $\overline{M}n$ values which are approximately twice those for HMDL and DMDL, hence the movement of the chains will be more restricted for DMHL and HMHL

The tacticity of HMDL was determined in the same way as for the fully hydrogenous polymer and the ^{13}C NMR spectrum is shown in figure 2.12. HMDL was found to be 69% syndiotactic and 31% atactic. No isotactic signals were observed, this could be due to the poor signal to noise ratio of the spectrum which may lead to the

swamping of the signal or the lack of any isotactic sequences in the polymer. The tacticity for DMHL and DMDL can not be found in this way due to the lack of the relevant carbon peaks which occurs because of the presence of deuterium instead of hydrogen which results in the loss of the nuclear Overhauer effect. The T_g for DMHL and DMDL are in the same range as for HMHL and HMDL, indicating that their tacticties will probably be similar to those for HMHL and HMDL.

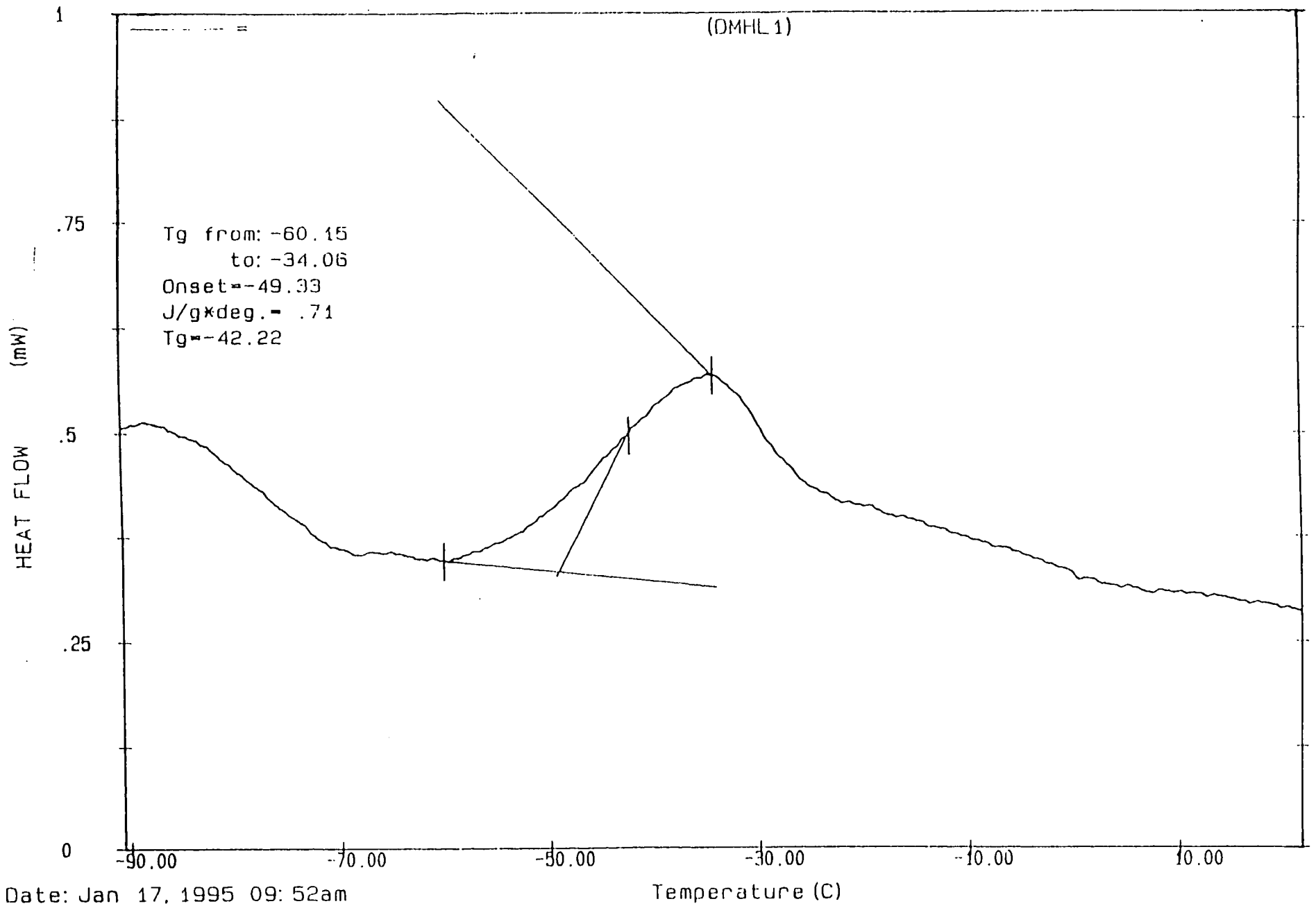

Figure 2.9: DSC trace of DMHL

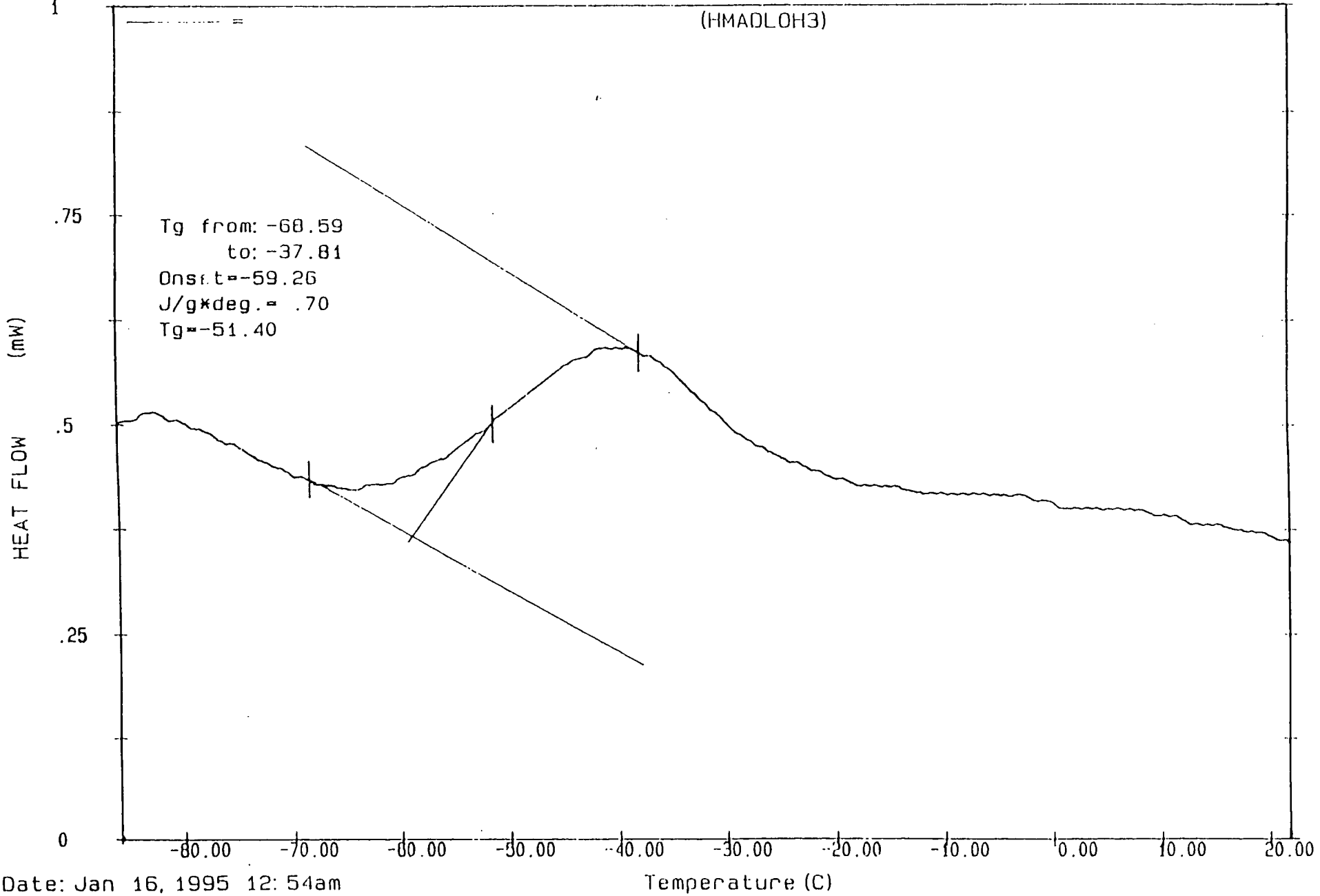

Figure 2.10: DSC trace of HMDL

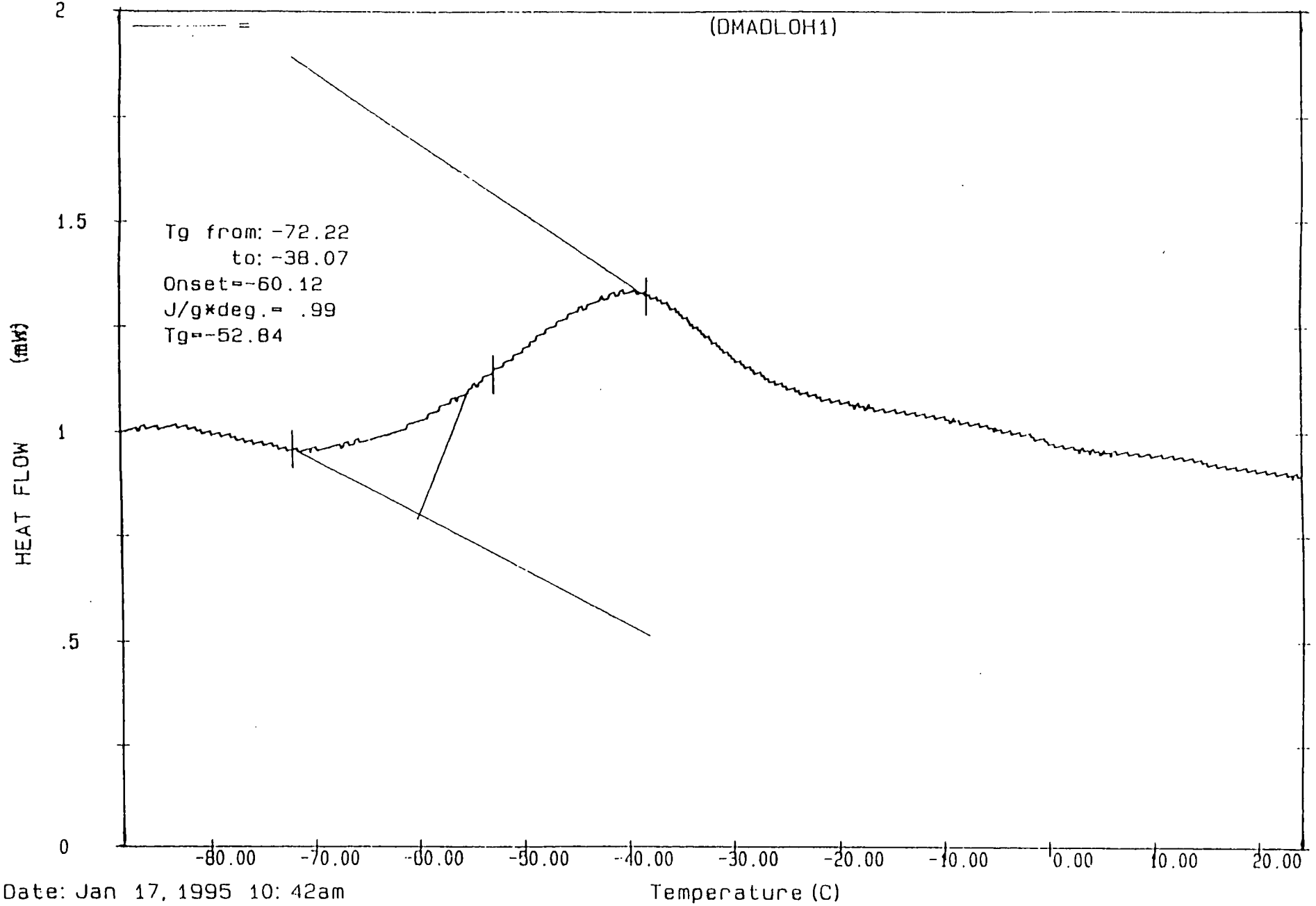

Figure 2.11: DSC trace of DMDL

Figure 2.12: ^{13}C NMR of polyHMDL

2.3.5 Synthesis of Deuterated Lauryl Alcohol

The synthesis of deuterium labelled LMA requires deuterated lauryl alcohol. The latter was produced by the reduction of deuterated lauric acid using lithium aluminium deuteride. Initial reactions were carried out using hydrogenous equivalents.

First Attempt

Lauric acid (5g 0.025 mol) was dissolved in about 20mls of anhydrous THF and then poured into a pressure equalising dropping funnel. Lithium aluminium hydride (1.14g 0.03 mol) was placed in a two neck 250ml round bottom flask, 50 mls of anhydrous THF were added to this and a magnetic stirrer was also added. The dropping funnel was placed in the side arm and a double surface condenser in the top. A nitrogen inlet was placed in the top of the condenser with an outlet to a bubbler. The nitrogen was turned on and the solution was stirred for fifteen minutes. The lauric acid solution was then added dropwise at such a rate so that the reaction was not too vigorous.

Once all the solution was added the stirring was continued for a further fifteen minutes and then the excess lithium aluminium hydride was decomposed by the addition of ethyl acetate (~15mls). The solution was filtered through a glass sinter, however, some of the precipitate passed straight through, so a second filtration was carried out, but it proved impossible to filter out all the precipitate.

Second Attempt

Lauric acid (5.25g 0.026 mol) and lithium aluminium hydride (1.20g 0.032 mol) were used in the same set-up. The reaction was left for one and a half hours and then terminated using ethyl acetate. The reaction mixture was filtered through a glass sinter with about a 1cm thick celite bed on it. This removed most of the precipitate, however, a fine white precipitate remained in the THF solution. The THF was removed in an attempt to isolate the lauryl alcohol, but no product was present after the removal of the solvent.

One possibility which might have been causing the reduction to fail was that in the reduction of acids there is a tendency for the lithium salt, $RCO_2^-Li^+$ to separate from the solution and stop the reduction. This can be overcome by converting the acid to the methyl ester, when initial nucleophilic attack by AlH_4^- is followed by elimination of OR' (where R'= methyl group). It was decided to try the reduction on the methyl ester of lauric acid. The ester was prepared using boron trifluoride-methanol complex and carried out in dry methanol which was produced as follows:

Magnesium powder (5g) and iodine (0.5g) were placed in a 1.5l round bottom flask and then 500mls of A.R. methanol were added. A splash head adapter for downward distillation was fitted to the round bottom flask and a condenser was placed into this and a nitrogen supply attached. The nitrogen was turned on for thirty minutes and then the methanol was refluxed. The magnesium (activated by the iodine) reacts with the methanol to produce methanolate, $Mg(OMe)_2$, which then reacts with any water present to produce insoluble $Mg(OH)_2$ and dry methanol. To collect the

methanol, a two-neck round bottom flask was attached to the splash head adapter outlet side arm, the second neck had a silica guard tube placed in it. The tap on the outlet side arm was then opened for collection of the methanol as it refluxed.

The esterification was carried out as follows:

Lauric acid (5.22g 0.026 mol) was heated under reflux for two hours with 3.90g (0.039 mol) of boron trifluoride-methanol complex in 30mls of dry methanol. The reaction was allowed to cool and then poured into a saturated sodium hydrogen carbonate solution (19.69g of $NaHCO_3$) in order to destroy the excess boron trifluoride-methanol complex. The methyl laurate was extracted using four 40ml portions of ether, which was then removed under reduced pressure. The resulting ester was distilled under vacuum, coming off at 132-134^{o}C at 0.03mmHg (literature value 262^{o}C at 766mmHg corresponding to 132-134^{o}C at 0.03mmHg - Aldrich) producing 4.60g (82.4% yield).

Reduction of Methyl Laurate

The first two attempts were similar to the previous attempts for the acid. The same problems with the precipitate occurred.

For the third attempt, 5.04g of methyl laurate in 30 mls of anhydrous THF and 4.04g of lithium aluminium hydride were used. The reaction was refluxed for two hours and killed using x mls of water, 3x mls of 10% sodium hydroxide and then x mls of water, where x equals the number of grams of lithium aluminium hydride used. This was much more efficient at killing the reaction and also formed a much thicker white precipitate which was easily filtered off on a celite bed. The THF was then removed

from the filtrate and 0.61g of lauryl alcohol were produced, corresponding to a yield of only 13% which was too low for the reduction of the deuterated compound.

Reduction in Diethyl Ether

A change in solvent from THF to sodium dried diethyl ether was the next variation that was tried. Lauric acid (5.01g) was dissolved in about 15mls of ether and placed in a pressure equalising dropping funnel. Lithium aluminium hydride (3g) was placed in a 500ml two-neck round bottom flask, then about 120mls of ether were added to this and a magnetic stirrer was added. The dropping funnel and double surface condenser were put in place and a nitrogen supply was attached. The flask was put in an ice bath, stirring started and the lauric acid solution was added at such a rate so that the ether refluxed gently. Once all the acid solution was added the bath was warmed up to $40^{o}C$ and the reaction was refluxed for six hours. The reaction was terminated using 3mls of water, 9mls of 10% sodium hydroxide and 3mls of water. This left a clear colourless solution with a thick white precipitate. This was then filtered out on a celite bed and rinsed with more ether. The solvent was removed and 2.76g of lauryl alcohol were produced, corresponding to a yield of 60%.

This method was selected for use with the deuterated lauric acid. The latter was reduced in two batches, the first consisted of 5.60g (0.0251 mol) of d-lauric acid, the second 4.35g (0.0195 mol) of d-lauric acid. The first reaction had 3.50g (0.083 mol) of lithium aluminium deuteride and the second had 2.81g (0.067 mol). Both of these were left to reflux for ten hours and then terminated as before using water/sodium hydroxide/water. The first reduction produced 4.52g of d-lauryl alcohol (85% yield) and the second produced 3.38g (82% yield).

2.4 Synthesis References

1. Freyss, D., Rempp, P., Benoit, H., *J. Polymer Sci., Letter*, 217, **2**, 1964
2. Wiles, D.M., Bywater, S., *Trans. Faraday Soc.*, 150, **61**, 1965
3. Allen, R.D., Long, T.E., McGrath, J.E., *Synthesis of Tactic Poly(Alkyl Methacrylates) Homo and Copolymers,* from, *Advances in Polymer Synthesis,* Eds. Cuthbertson and McGrath, Philadelphia, 1985
4. Otera, J., Yano, T., Kawabata, A., Nozaki, H., *Tetrahedron Letters,* 1986, **27**, 2383
5. Seebach, D., Hungerbuhler, E., Naef, R., Schnurrenberger, P., Weidmann, B., Zuger, M., *Synthesis.*, 138, **No. 2**, 1982
6. Yazawa, H., Tanaka, K., Kariyone, K., *Tetrahedron Letters,* 1974, **46**, 3995
7. Meth-Cohn, O., *J Chem. Soc., Chem. Commun.*, 6951986, **No. 9**, 1986

3. MONOLAYERS AND SURFACE PRESSURE ISOTHERMS

3.1 Monolayers

A monolayer is formed on the surface of the subphase by depositing the substance under study dissolved in a suitable solvent. The spreading solution is applied to the surface in small drops and the solvent is allowed to evaporate which leaves the molecules free to move in a two-dimensional plane. The process of spreading can occur in a number of ways. Usually a thin film is formed by the spreading solution while the film forming material attains its favoured configuration at the air/water interface and the solvent then evaporates, leaving behind the monolayer. In some cases the deposited droplet does not spread over the subphase but a thin film of dilute solution of monolayer forming material spreads from its edges and as solvent evaporates, more film spreads from the droplet.

Spontaneous spreading continues until the surface pressure is greater than the equilibrium spreading pressure, which depends on the relative magnitude of the forces tending to hold the molecules at the air/water interface and those holding it within the droplet. If the subphase area is large the material will spread completely; in such a case the surface pressure would be less than the equilibrium spreading pressure. If the equilibrium spreading pressure is exceeded the droplets will not disperse and they will be observed floating on the water.

The structure of the monolayer on the subphase depends on the characteristics of the molecules forming the monolayer. If the molecule has hydrophilic and hydrophobic groups, i.e. they are amphiphilic, (e.g. surfactants), then the molecules orientate themselves so that the hydrophilic groups are in the water subphase and the hydrophobic

groups are in the air above the subphase. For macromolecules the situation is more complex as in any molecule there may be numerous hydrophilic and hydrophobic groups either distributed evenly along the chain length or in blocks of each type. Therefore, parts of the macromolecule will be attracted to the water and other parts repelled by the water and the resulting chain configuration will depend on how the hydrophilic and hydrophobic groups are distributed along the chain.

Molecules in a solution are subject to attractive forces, in the bulk solution these forces are equilibrated. However, at the surface the forces are unequal and the net effect is to pull the peripheral molecules into the bulk of the solution. Thus if the surface was expanded, molecules would have to be taken from the bulk to the surface, going against the net inward pull, so work would be required to expand the surface and this gives rise to surface tension (γ). The surface tension can be defined as the work required to expand the surface isothermally by unit area (Joules per square meter) or as the force required to extend the interface by unit length (Newtons per meter). The tendency of surface-active molecules to accumulate at interfaces favours expansion of the interface and hence lowers the surface tension as less work is required to accomplish the same expansion compared to a clean interface.

3.2 Surface Pressure Isotherms

3.2.1 Qualitative Interpretation

The characteristics of a monolayer on the water surface are studied by measuring the changes in surface tension upon compressing the monolayer. The reduction of the surface tension from the value for the clean water surface is known as the surface pressure (π). Pressure readings are made by means of a Wilhelmy plate attached to a pressure sensor and when the plate is suspended with the lower edge just touching the water surface it is pulled down into the bulk water subphase by the surface tension. When a surface active material is added to the interface, the surface tension decreases, hence the force pulling down on the Wilhelmy plate is reduced and the change in surface tension can be detected. The plot of surface pressure versus area per molecule is known as a pressure-area isotherm, the shape of which is characteristic of the molecules making up the film and provides a two - dimensional 'fingerprint'.

The classical interpretation of the surface pressure data[1] has been to draw analogies with three-dimensional phases. Depending on the rate of change of surface pressure with the decrease in area per molecule (reflecting the interactions between molecules in the layer; how far apart they are and how easily they can move for example) the film behaviour has been described as gaseous, liquid expanded or condensed, or solid

For non-polymeric materials, such as long chain acids and surfactants, the transitions between phases are well observed. At very large areas per molecule very little or no surface pressure is discernible. As the film is compressed, at some point the molecules are brought closer together so that they feel some influence from each other. This results in an increase in surface pressure, corresponding to the transition to liquid

film behaviour. Liquid films are divided into two categories, expanded and condensed. For an expanded type film the initial rise in the surface pressure is observed at a larger area per molecule than for a condensed film and the rate of increase is generally more gradual. As the film is further compressed the molecules are eventually brought so close together that further compression becomes difficult. The film becomes very stiff and the surface pressure rapidly increases in this solid phase and if the film is compressed beyond a certain point, catastrophic collapse occurs, accompanied by a sudden fall in the surface pressure as molecules distort out of the plane of the layer. Alternatively, particularly for the more flexible expanded type films, instead of catastrophic collapse the surface pressure value may plateau in the highly compressed state as molecules dip into the subphase or are excluded into the bulk solution to relieve the strain on the monolayer.

For polymeric materials the situation is less straightforward. The limiting area per molecule (extrapolated from the initial slope of the liquid region of the isotherm) has long been used to infer the nature of packing of molecules at the surface, (e.g. the area per molecule for a range of fatty acids with varying chain length were all found to be equal, indicating that they were all packed perpendicular to the interface) but, for polymers it is not clear what the limiting area obtained from the isotherm refers to. It is usually interpreted as the area per segment of the polymer chain, however, this area may not be due solely to the monomer dimensions and may be influenced by the polymer chain configuration. Despite the complications for polymeric monolayers compared to low molecular weight materials, many polymer films have been studied and classified as either liquid expanded or condensed. Among the former are poly(vinyl acetate)[2,3], poly(2-vinyl pyridine)[4], poly(ethylene oxide)[5], poly(propylene oxide) and poly(vinyl alkyl ethers)[6]. Among the latter are poly(methyl methacrylate)[7,8] and poly(vinyl benzoate)[9]. Systematic trends in some homologous series of polymers have been noted. For example,

in the poly(alkyl acrylates) and (alkyl methacrylates), a trend of increasingly expanded behaviour is observed with increasing alkyl group size from methyl to butyl[1,2].

3.2.2 Quantitative Interpretation

Recently there has been a revival of interest in monolayers due to the development of new theoretical approaches to prediction and interpretation of experimental results. Apart from the pioneering efforts of Crisp[1,2], the earliest attempt to develop a quantitative theory for the description of polymer monolayers according to the molecular interactions occurring at the interface was by Singer[10], using the theory of polymer solutions developed by Huggins[11], Singer derived the expression:

$$\pi = \frac{Nk_BT}{A_0}\left[\ln\left(A/A - A_0\right) + \left(N - 1/N\right) z/2 \ln\left(1 - 2A_0/zA\right)\right] \qquad 3.1$$

where N = degree of polymerisation

k_B = Boltzmann constant

T = temperature

A = surface area for which the surface pressure equals π

A_0 = extrapolated area at zero pressure

z = co-ordination number of the monomer units in the chain, when z = 2 the chain is rigid and when z = 4 the chain is flexible

This equation can be successfully applied to protein and synthetic polymer monolayers by assuming values of z for each separate monolayer. In most cases the values of the co-ordination number assigned to fit the experimental data to Singer's equation were unreasonably small for two - dimensional lattices.

Davies[12] defined a quantity $\omega = z - 2$, where ω is the interchain cohesion from van der Waals forces between polymer segments, as a measure of flexibility or unfolding

of polymer molecules at interfaces depending on the cohesive force between segments and discussed the behaviour of the monolayers in terms of ω. Kawai[13] pointed out that this theory makes no allowance for entropic effects on the chain flexibility caused by the strictures placed on chain configuration by the interface and that the reason for z appearing to give a good representation of the degree of flexibility of polymer molecules was due to the difference in molecular configurations between condensed and expanded films. Frisch and Simha[14,15] modified Singer's treatment to allow for chain looping and crossovers in pseudo-two-dimensional systems. Cohesive forces between polymer segments play an important role in the behaviour of the molecules at the air - water and therefore, in the nature of the surface pressure - area isotherm. In Singer's treatment of polymer monolayers no consideration of cohesive forces between polymer segments was included. Motomura and Matuura[16] derived a new equation of state that took into account the cohesive forces between the polymer

$$\frac{\pi}{\pi_0}=\frac{z}{2}\left\{1-\frac{2}{z}\left(1-\frac{1}{r}\right)\frac{A_0}{A}\right\}-\ln\left(1-\frac{A_0}{A}\right)-\frac{z}{2}\ln\frac{\left\{1-\frac{2}{z}\left(1-\frac{1}{r}\right)\frac{A_0}{A}\right\}(\beta+1)-2\left\{1-\frac{2}{z}\left(1-\frac{1}{r}\right)\right\}\frac{A_0}{A}}{\left(1-\frac{A_0}{A}\right)(\beta+1)} \qquad 3.2$$

where $\pi_0 = kT / A_0$, r is the number of segments in one molecule and β is given by

$$\beta=\left[\frac{\left\{1-\frac{2}{z}\left(1-\frac{1}{r}\right)\right\}\left(1-\frac{A_0}{A}\right)\frac{A_0}{A}}{\left\{1-\frac{2}{z}\left(1-\frac{1}{r}\right)\frac{A_0}{A}\right\}^2}(\eta^2-1)+1\right]^{1/2} \qquad 3.3$$

where $\eta = \exp(\omega / zkT)$

This equation of state has been used to compare the calculated behaviour to the experimental isotherms for poly (vinyl acetate) (PVAc), poly (methyl acrylate) (PMA) and poly (methyl methacrylate) (PMMA). For PVAc and PMA equation 3.2 fitted the isotherm at low surface pressures (< 6mN m^{-1}) and above this there was appreciable deviation, possibly due to the segments of the polymer chains being reversibly and partially squeezed out of the plane of the subphase. For PMMA, which forms condensed monolayers, the calculated isotherm only agrees with the experimental values around the region where the surface pressure increases. Where the experimental surface pressure is zero the equation predicts negative surface pressures.

In the last few years there was a breakthrough in the understanding of the observed surface pressure data with the development of two-dimensional scaling theories analogous to those for three-dimensions by de Gennes[17]. The concept of scaling theory will be discussed first, before their application to two-dimensions. The scaling theory involves the concept of dilute and semi-dilute polymer solutions and the existence of a crossover between these two states at a concentration c^*, where chain overlap just begins to occur. For good solvents, c^* is expressed as:

$$c^* \cong N/R_g^3 = a^{-3} N^{1-3\upsilon} = a^{-3} N^{-4/5} \qquad 3.4$$

where N = degree of polymerisation, tending towards infinity

R_g = radius of gyration

a = monomer length

υ = critical exponent

A corresponding polymer volume fraction ϕ^* may also be defined as the threshold where overlap just begins to occur

$$\phi^* \sim N^{-4/5} \qquad 3.5$$

For dilute solutions, where $c < c^*$, Flory[18] has shown that the coils behave as separate hard spheres of radius R_g and the following equation of state is observed:

$$\pi/T = c^2/N + A_2c_2^2 + ... \qquad 3.6$$

where the second virial coefficient A_2 has the dependence:

$$A_2 \cong R_g^3N^{-2} \sim N^{-1/5} \qquad 3.7$$

In the semi-dilute region where the coils overlap but the polymer volume fraction ϕ is still low, so that $\phi^* < \phi < \phi^{**}$ (where ϕ^{**} is the polymer volume fraction at which transition to concentrated solution behaviour occurs), the chain overlaps necessitate the introduction of an excluded volume interaction term. The scaling law in this case is:

$$\pi/T = c/N\, f_\pi\,(cR_g^3/N) = c/Nf_\pi\,(c/c^*) \qquad 3.8$$

where $f_\pi(x)$ is a dimensionless function so that:

$$\lim_{x \to \infty} f_\pi(x) = \text{constant } x^m = \text{constant } (\phi/\phi^*)^m = \text{constant } \phi^m N^{4m/5} \qquad 3.9$$

In terms of ϕ and N, this gives

$$a^3\pi/T = \text{constant } \phi^{m+1} N^{(4m/5)-1} \qquad 3.10$$

Since all thermodynamic properties are independent of degree of polymerisation in this region, m must equal 5/4 giving

$$a^3\pi/T = \text{constant } \phi^{9/4} \qquad 3.11$$

The three dimensional theories outlined briefly above have also been expressed in forms where the dimensionality is explicitly included by Daoud and Jannink[19] and des Cloizeaux[20]. These expressions may be applied to the two-dimensional "solution" case encountered in polymer monolayers. In the dilute region the equation of state virial expression is

$$\pi/RT = (\Gamma/M + A_{2,2}\Gamma + ...) \qquad 3.12$$

where $A_{2,2}$ = two-dimensional second virial coefficient

Γ = polymer surface concentration

M = polymer molecular weight

A_2 can be defined in any dimensionality, d, as:

$$A_{2,d} \sim N^{\upsilon d} \tau^{d(\upsilon - \upsilon_\theta)} \Psi_\theta \qquad 3.13$$

where τ = reduced temperature

υ, υ_θ and ψ_θ = critical exponents for the good and theta 2-D solvent cases

Values for these exponents have been predicted by many theoretical methods. E-expansion renormalisation group techniques give $\upsilon = 0.77$[21,22], $\upsilon_\theta = 0.505$[23] and $\psi_\theta = 0.60$[24]. Therefore:

$$A_{2,2} \sim N^{1.34} \tau^{0.88} \qquad 3.14$$

Other theoretical predictions for the value of the υ exponent have been attempted. Mean field theory predicts that in the good solvent regime $\upsilon = 0.75$. Self avoiding walk calculations[25,26] give a similar value for short chains ($N < 18$) whilst Monte Carlo simulations predict $\upsilon = 0.753 \pm 0.004$[27]. The matrix transfer prediction is $\upsilon = 0.7503 \pm 0.0002$[28]. For values of υ_θ, which is the value of υ in the θ state, there is much greater diversity in predictions. The mean field prediction is $\upsilon_\theta = 2/3$ and this considers only ternary interactions, whereas the collapsed chain value of 1/2 is obtained by ideal random walk calculations. Monte Carlo simulations have suggested values between 0.51[29] and 0.59[30]. An indefinitely growing self avoiding walk analysis gives a value of 0.567 ± 0.003[31,32]. Other predictions of 0.59 and 0.55 have been obtained by real space renormalisation[33-35] and transfer matrix methods[36] respectively. The currently accepted values of the exponents are $\upsilon = 0.75$ and $\upsilon_\theta = 0.57$.

The general n-dimensional definition of the crossover polymer concentration between dilute and semi-dilute behaviour is:

$$c^* \sim N/R_{g,d}{}^d \sim N^{1-\upsilon d}\tau^{-d(\upsilon-\upsilon_\theta)}\Psi_\theta \qquad 3.15$$

where

$$R_{g,d} \sim N^{\upsilon}\tau^{(\upsilon-\upsilon_\theta)/\Psi_\theta} \qquad 3.16$$

and $R_{g,d}$ is the radius of gyration in the dimensional space of d. For d = 2 one obtains

$$\Gamma^* \sim N^{-0.54}\tau^{-0.88} \qquad 3.17$$

where Γ^* is the surface concentration at the transition from dilute to semi - dilute behaviour. An equation of state expression was obtained by des Cloizeaux

$$\pi / T \sim c^{\upsilon d(\upsilon d-1)}\tau^{(\upsilon-\upsilon_\theta)d/\Psi_\theta(\upsilon d-1)} \qquad 3.18$$

For d=2, the surface pressure expression is

$$\pi/T \sim \Gamma^{2.85}\tau^{1.64} \qquad 3.19$$

Considering the transition from semi-dilute to concentrated behaviour, Daoud and Jannink produced the following general expression for c^{**}:

$$c^{**} \sim \tau^{(\upsilon_\theta d - 1)/\Psi_\theta} \qquad 3.20$$

Above c^{**} there is chain overlap, but, due to screening, θ conditions hold, corresponding to the semi-dilute region at θ conditions.

π is defined by

$$\pi/T \sim c^{\upsilon_\theta d/(\upsilon_\theta d - 1)} \qquad 3.21$$

For d=2 then

$$\Gamma^{**} \sim \tau^{0.0167} \qquad 3.22$$

where Γ^{**} is the surface concentration at the transition from semi - dilute to concentrated behaviour and

$$\pi/T \sim \Gamma^{101} \qquad 3.23$$

However, this behaviour has never been observed, a fact which has been attributed to out of plane deformation of the monolayer before the concentrated regime can be attained.

3.3 Experimental

Surface pressure isotherms were obtained using a NIMA Langmuir trough (NIMA Technology, Coventry, UK) which consisted of a circular Teflon trough with motorised barriers and a pressure sensor to which a Wilhelmy plate was attached to measure the surface pressure of the spread monolayer on the water surface. The temperature of the trough was controlled by circulating water from a thermostated water bath through a labyrinth of channels in contact with the bottom of the trough. For the polymer and monomer isotherms were obtained over a range of temperatures from 10 to 35°C with increments of 5 °C.

The polymer and monomer were spread on the water subphase from chloroform solutions with a concentration of circa 1.00mg ml^{-1} and typically 20µl of the solution were dispensed on to the subphase, corresponding to an initial surface concentration of circa 0.23mg m^{-2} over the trough area of 900cm^2. After each isotherm was completed the subphase was aspirated until there was no significant change in the surface pressure when the barriers were closed and the value for the surface tension of the water subphase was equal to that for pure water (~ 72.8mN m^{-1}). The monolayer was compressed at a rate of 30cm^2 min^{-1}, although no influence of compression rate up to barrier speeds of 100cm^2 min^{-1} was observed. At each temperature three isotherms were obtained with a new monolayer being used for every run to determine the reproducibility of the isotherms.

Isotherms were obtained for each of the deuterated isomers (polymer and monomer) at 25°C to ascertain whether the hydrogenous and deuterated material behaved in a similar fashion.

3.4 Surface Pressure - Area Isotherms for PLMA

The reproducibility of the isotherms can be demonstrated by comparing a set of three isotherms that were obtained at the same temperature, as shown in figure 3.1.

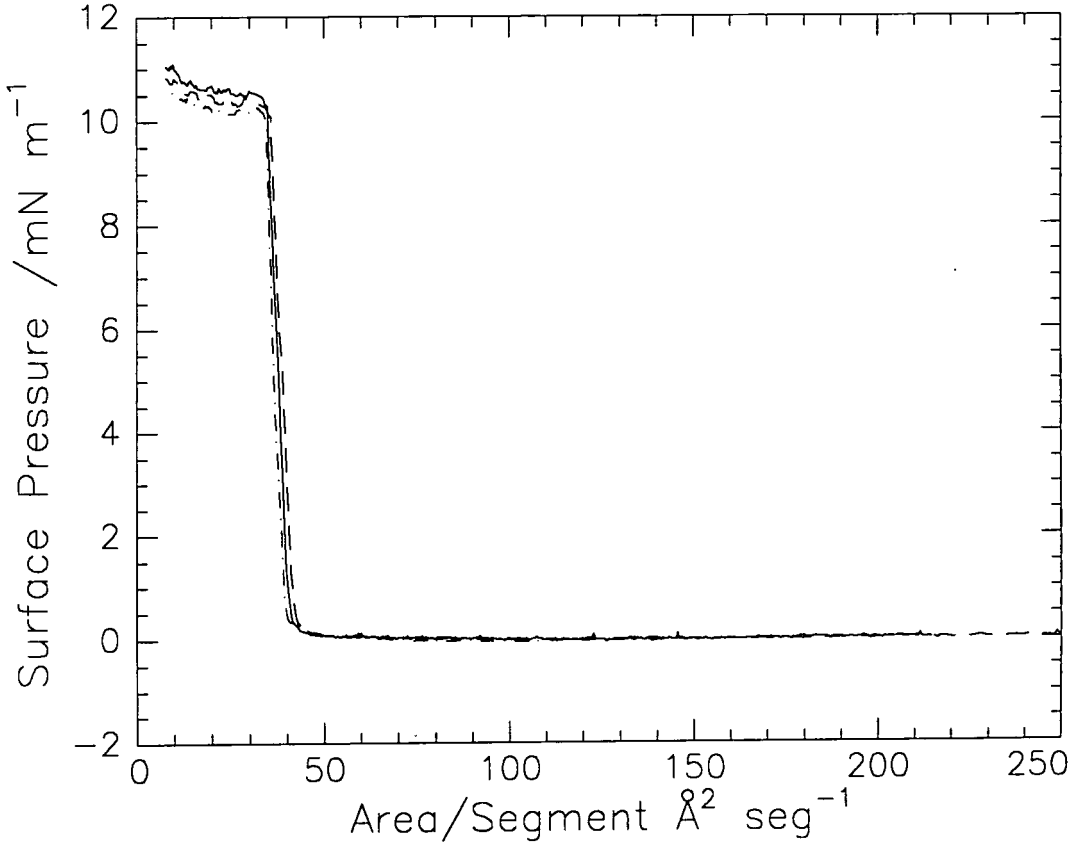

Figure 3.1: Surface pressure - area isotherms for PLMA at 25°C

At low surface concentrations the agreement is excellent and discrepancies begin to occur as the surface pressure begins to increase. The slight differences in the area per segment where the surface pressure increases is due to slight errors in the amount of polymer solution dispensed on to the subphase which leads to errors in the calculated area per segment. The discrepancies in the maximum value of surface pressure obtained are due to the film deforming at the point of maximum surface pressure and this

deformation is entirely random and not reproducible, so the high surface pressure plateau will occur at slightly different values of surface pressure for every isotherm.

The isotherms obtained at each temperature, shown in figure 3.2, clearly show that no temperature dependence occurs within the range of temperatures studied.

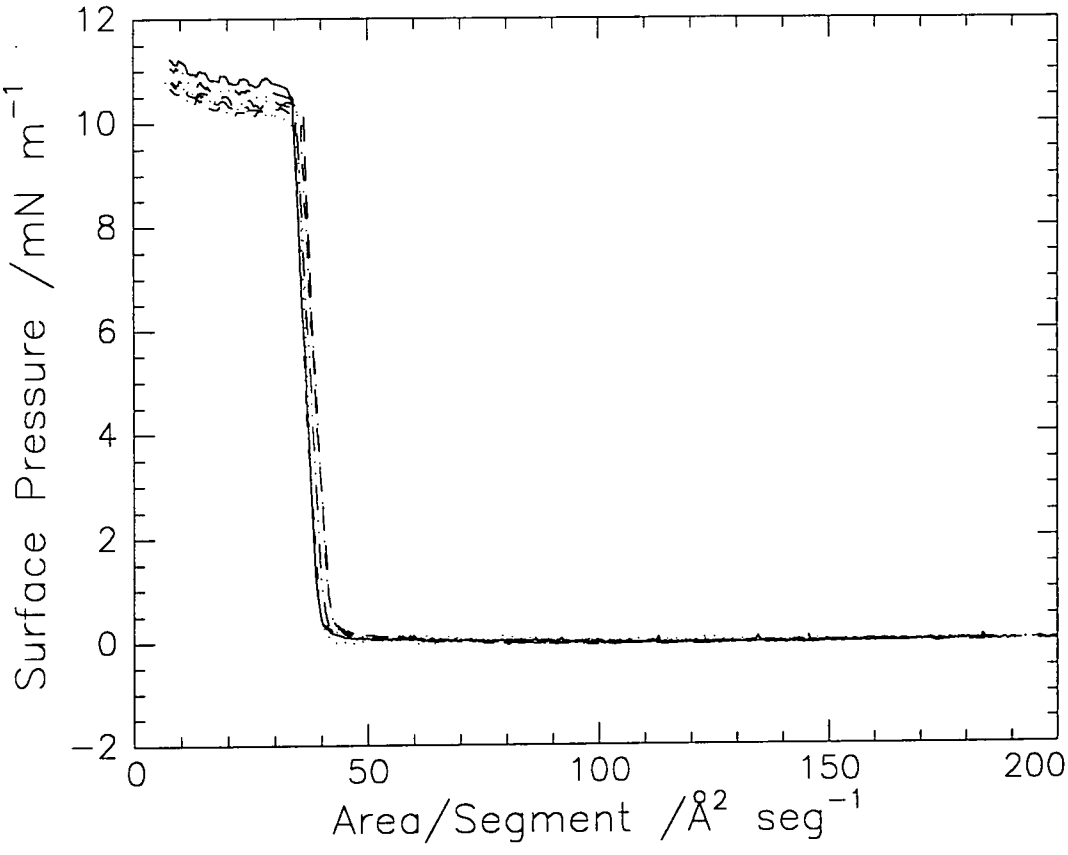

Figure 3.2: Surface pressure - area isotherms for PLMA at 10°C (––), 15°C (– –), 20°C (– · –), 25°C (·····), 30°C (– ·· –) and 35°C (– – ·)

The limiting area per segment can be obtained by extrapolating the steep rise in surface pressure to zero pressure, the intercept on the x axis being the limiting area per segment. The values of the limiting area per segment at each temperature are given in table 3.1. The variation in the values obtained is due to the variation in the position of the increase in surface pressure as mentioned earlier.

TEMPERATURE /°C	AREA PER SEGMENT /±1 $Å^2$ seg^{-1}
10	41
15	43
20	42
25	41
30	43
35	42

Table 3.1: Limiting areas per segment for PLMA at each temperature studied

The values obtained for the limiting area are approximately twice those obtained for straight chain fatty acids for which the areas are due to the close packed molecules perpendicular to the interface, i.e. the cross sectional area of the alkyl chain, therefore, for PLMA there must be a degree of disorder preventing close packing.

The nature of the isotherm is typical of a condensed monolayer, with no increase in surface pressure until large surface coverages are obtained. The characteristics of the isotherm are very similar to those obtained for poly (dimethyl siloxane) spread on water[37] and the same rationale can be used to explain the shape of the isotherm. At large areas (greater than circa 43$Å^2$ seg^{-1}) the polymer exists as 'islands' on the surface, a situation which has also been attributed to spread films of poly (methyl methacrylate) which has similar isotherm characteristics at large areas[38]. The rapid increase in surface pressure occurs at the point where the islands contact each other and a coherent film is formed. The high surface pressure plateau at low areas (less than circa 41$Å^2 seg^{-1}$) corresponds to the islands interpenetrating each other and this is made possible by the fact that PLMA is well above its T_g (circa −50°C), hence the molecules have sufficient mobility to relax and interpenetrate rapidly on contact.

To characterise further the behaviour of the monolayer the surface pressure - area isotherm can be redrawn in terms of the surface concentration instead of the area per segment, as is shown in figure 3.3

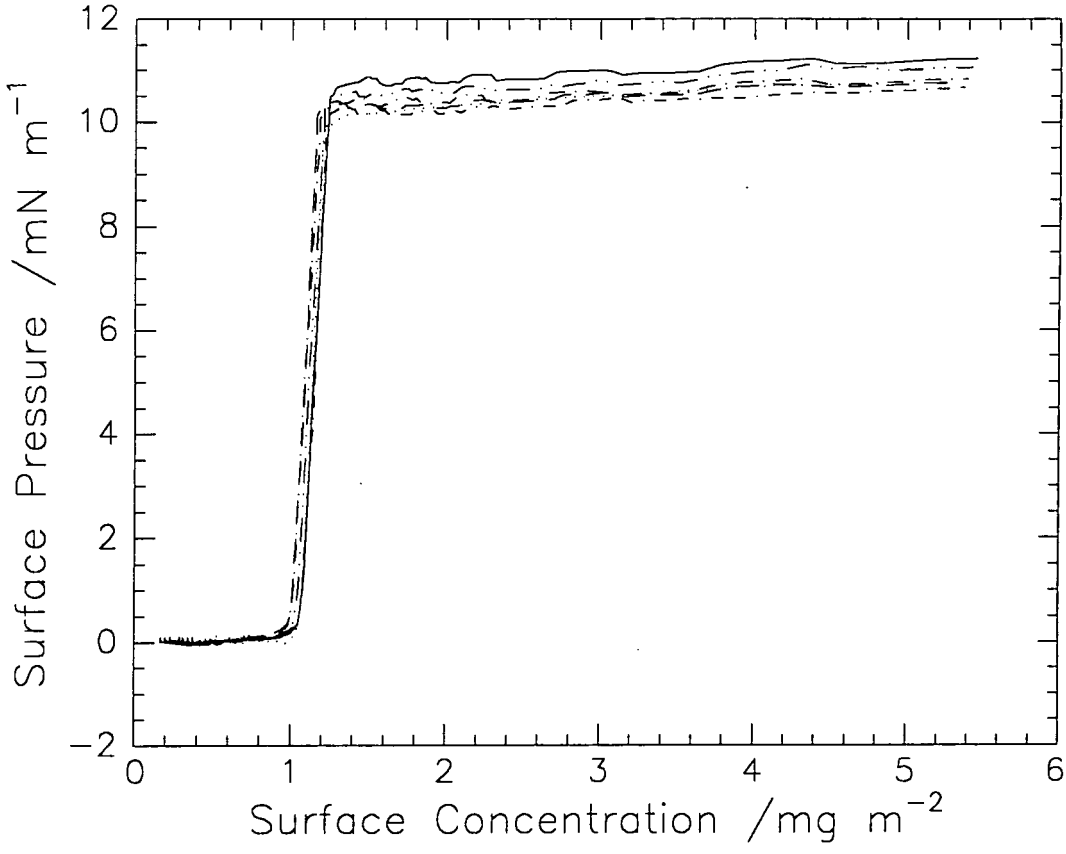

Figure 3.3: Surface pressure - surface concentration isotherms for PLMA at 10°C (––), 15°C (– –), 20°C (– · –), 25°C (·····), 30°C (– ·· –) and 35°C (– – ·)

The value of the critical scaling exponent υ can be obtained by plotting the isotherm data on a double logarithmic scale (e.g.figure 3.4). In the semi - dilute region (where a linear dependence is observed) the scaling law $\pi \alpha \Gamma^{y}$ can be applied, where $y = 2\upsilon/(2\upsilon - 1)$, so from the best fit in this region y can be obtained and υ can be calculated. The value of υ determined at each temperature was equal to 0.53.

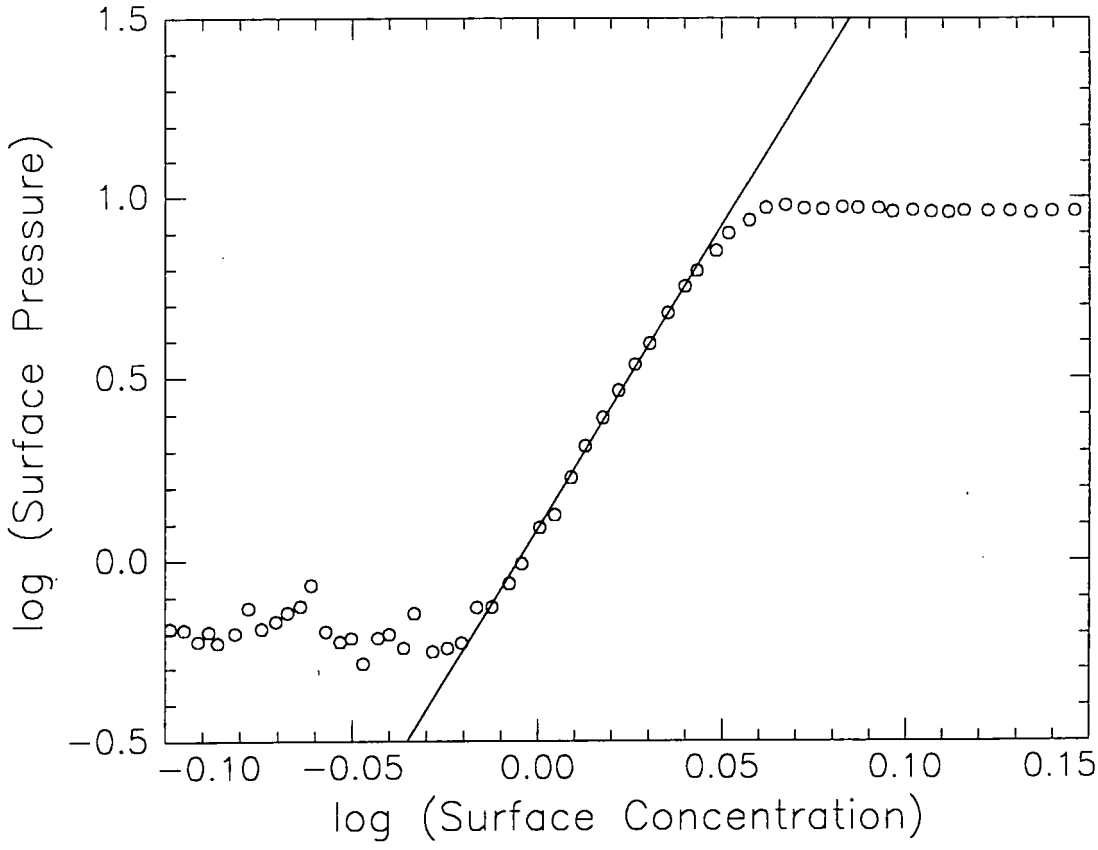

Figure 3.4: Double logarithmic plot of the isotherm data at 25°C

The value of υ relates to the thermodynamic state of the polymer. To recap, when the polymer - subphase interaction is thermodynamically favourable then υ = 0.75 and for two - dimensional theta state conditions, υ is 0.57. The value of 0.53 obtained here suggests that the PLMA molecules are in a collapsed state. The value for PLMA is the same as that obtained for syndiotactic PMMA, whereas isotactic PMMA produces a value of circa 0.77, thus a change in tacticity produces a drastic change in the monolayer properties.

At low values of surface concentration, i.e. in the dilute regime, the behaviour of the polymer molecules on the surface can be described by an equation of state (equation 3.12). By plotting the isotherm data as π / Γ versus Γ (figure 3.5), values of the two dimensional second virial coefficient, $A_{2,2}$, and the polymer molecular weight should be obtainable.

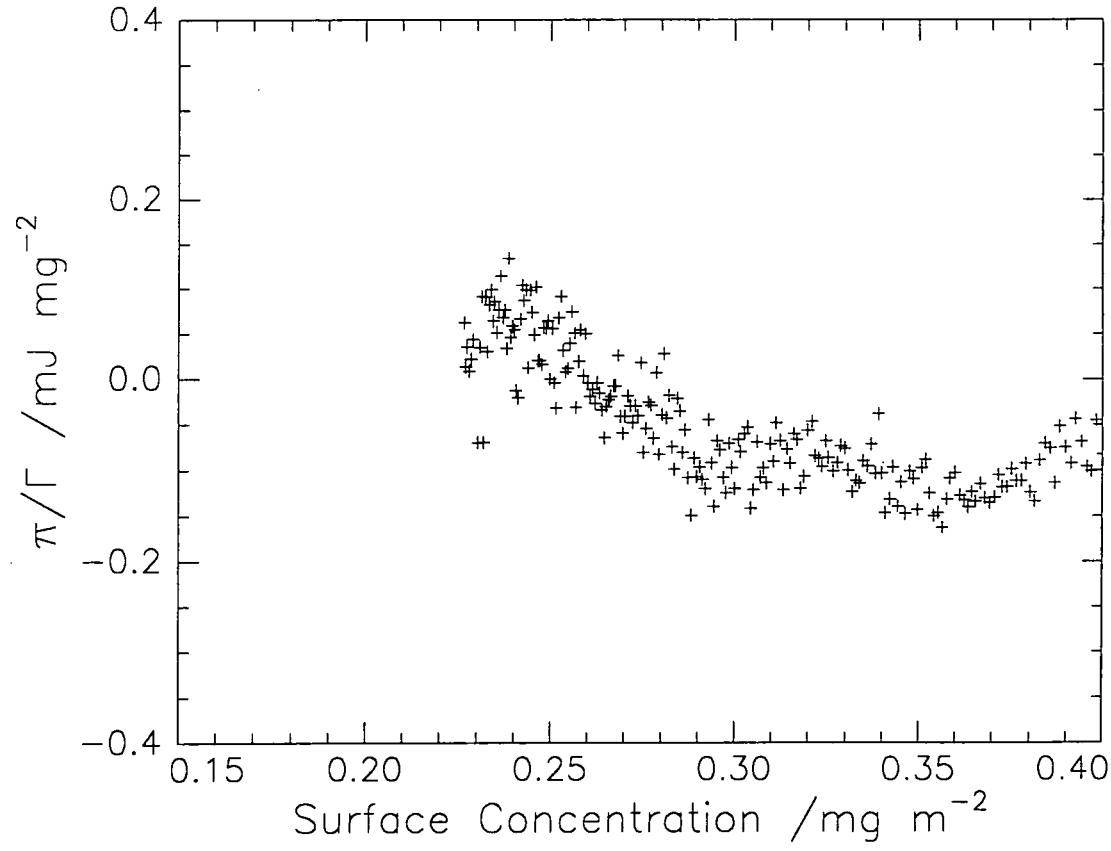

Figure 3.5: Plot of π / Γ versus Γ for PLMA at 25°C

The data quality from the trough in the low surface concentration region is insufficiently precise to allow the evaluation of $A_{2,2}$ and the polymer molecular weight. It is evident that there is a negative slope of the data which indicates that $A_{2,2}$ is negative and confirms that the monolayer is in less than theta conditions with unfavourable chain - solvent interactions.

The equation of state derived by Motomura and Matuura[16] (equation 3.2) has been used to attempt to fit the surface pressure - area isotherm data and the best fits obtained at 25°C are shown in figures 3.6 and 3.7.

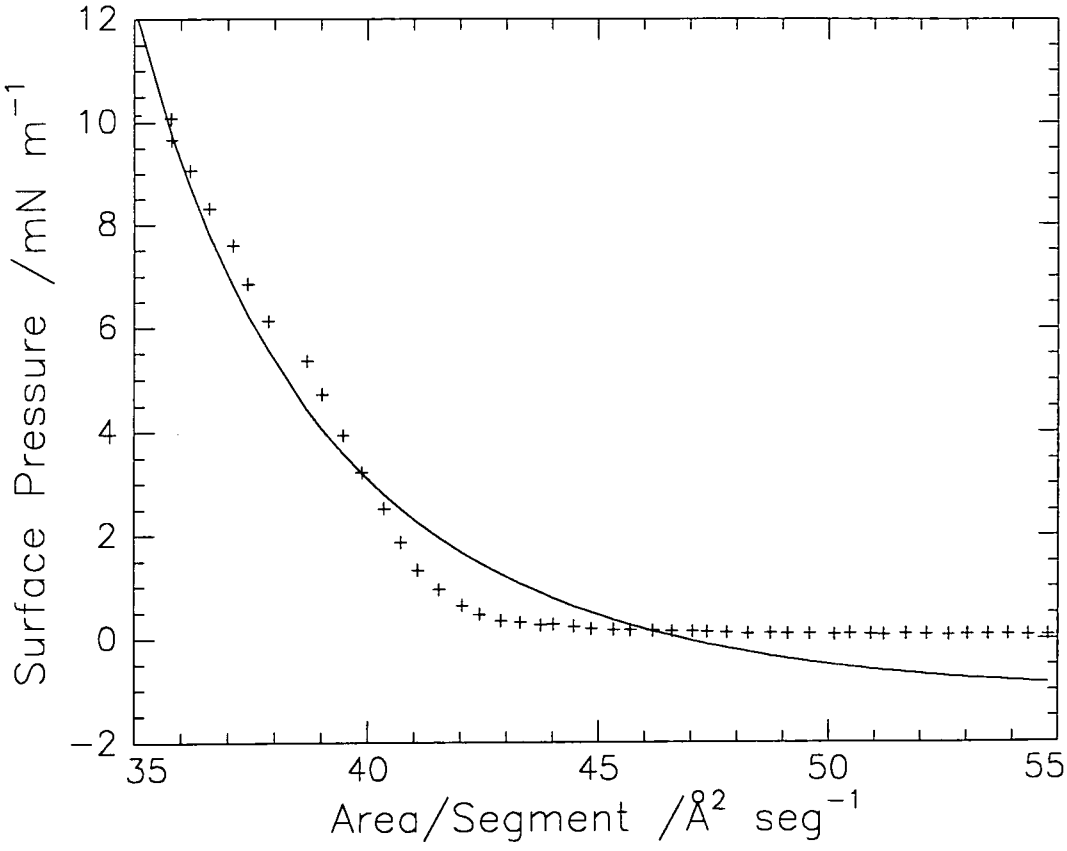

Figure 3.6: Comparison between isotherm data (+) and equation of state (—) with $\omega / kT = 1.2$ and $A_o = 29.3 Å^2$

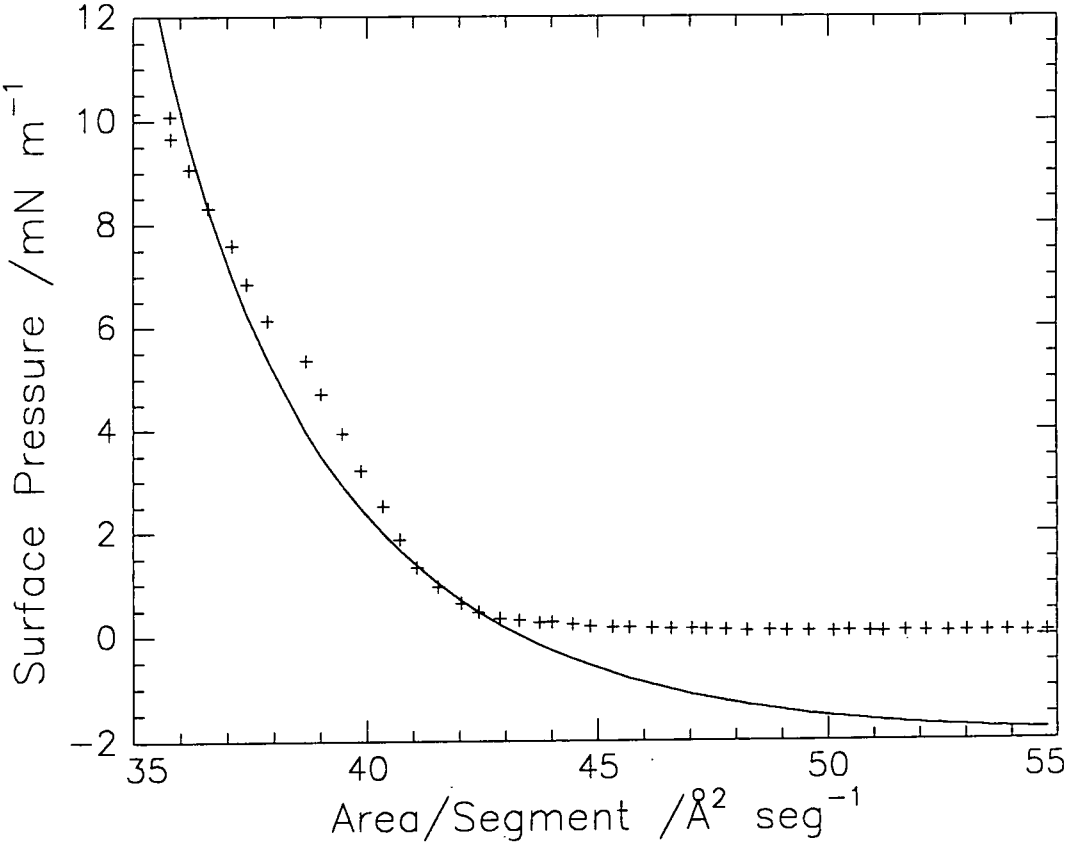

Figure 3.7: Comparison between isotherm data (+) and equation of state (—) with $\omega / kT = 1.3$ and $A_o = 30.3 Å^2$

The equation of state does not fit the experimental data well, this is due to the condensed nature of the isotherm leading to a steeper rise in surface pressure than the equation predicts. The value of ω / kT obtained, which is a measure of the cohesive forces between the monomer segments, is greater than that for PMMA (1.1) and is well above the critical value of 0.864, above which condensation in the monolayer takes place. In order to get a fit close to the experimental increase in surface pressure, negative surface pressures are predicted for areas greater than circa 45Å^2 per segment. This also occurred for PMMA and was attributed to the biphasic nature of the monolayer in this region which results in a long plateau with the surface pressure equal to zero, whereas if the monolayer was expanded, the surface pressure would increase at a lower concentration and more gradually which corresponds to the theoretical behaviour predicted by the equation of state. The values of A_o obtained from the fits to the experimental data are approximately 12Å^2 per segment smaller than the values obtained by extrapolating the isotherm to zero surface pressure. This is due to the inaccurate fit to the data which arises from force fitting the equation of state to the data even though the functional form of the equation does not account for the condensed nature of the monolayer. Alternatively, the theoretical value of A_o obtained from the fits may be nearer the absolute minimum limiting area in a close packed structure, however, this minimum is not achieved experimentally due to randomness and disorder in the structure.

All of the isotherms shown so far have been due to compression of the spread polymer. For low molecular weight materials it is often possible to carry out repetitive compression - expansion cycles to produce a stiffer, compacted monolayer. Such cycles have been carried out on monolayers of PLMA and the resulting isotherms are shown in figure 3.8.

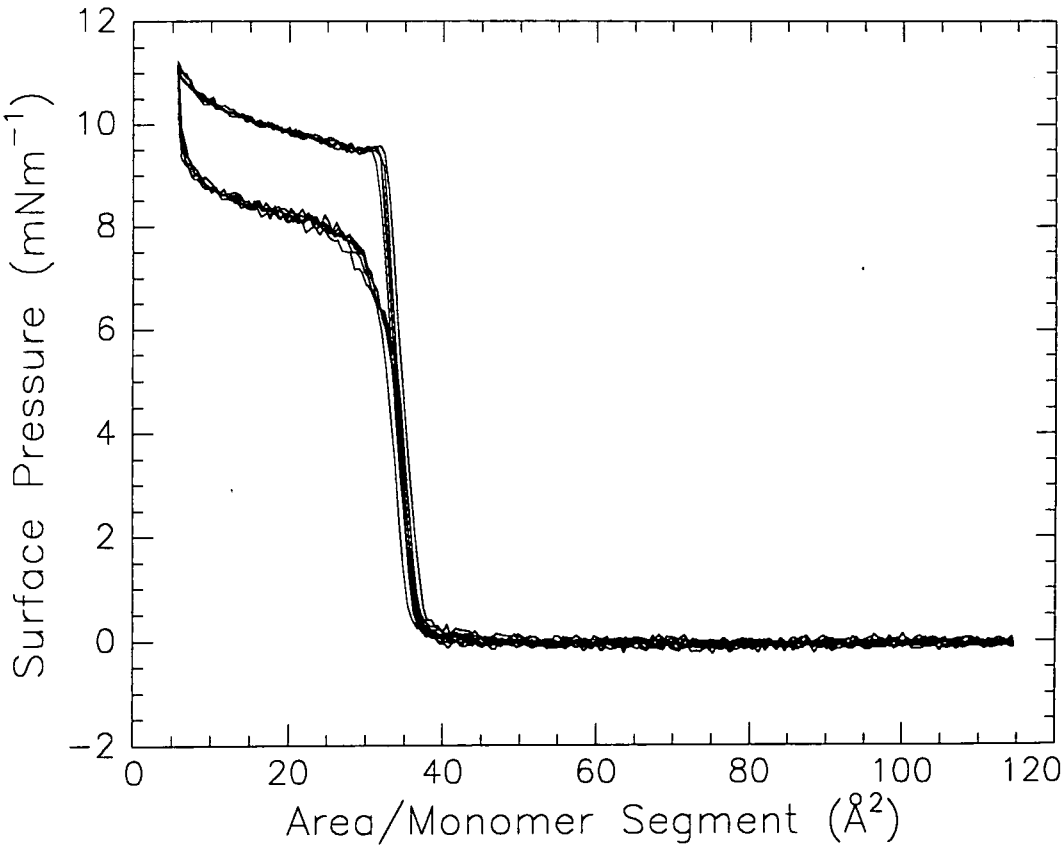

Figure 3.8: Six compression - expansion cycles for PLMA at 25°C

The monolayer shows no change in properties due to the repeated compression - expansion cycles. A closed hysteresis loop is obtained in the high surface pressure region which indicates that the processes occurring during the cycle are reversible with no loss of material or change in structure. This means that the interpenetration of the polymer islands is reversible and as the monolayer is expanded the biphasic nature of the layer is recovered, which behaves as a new monolayer when it is compressed again.

To determine the organisation of the polymer monolayer by neutron reflectivity, it has to be assumed that the deuterium does not alter the physical properties of the monolayer. To prove the validity of this assumption isotherms for each of the deuterated isomeric variation of PLMA were obtained at 25°C. These are shown in figure 3.9 and show no variation apart from that expected due to the factors mentioned earlier.

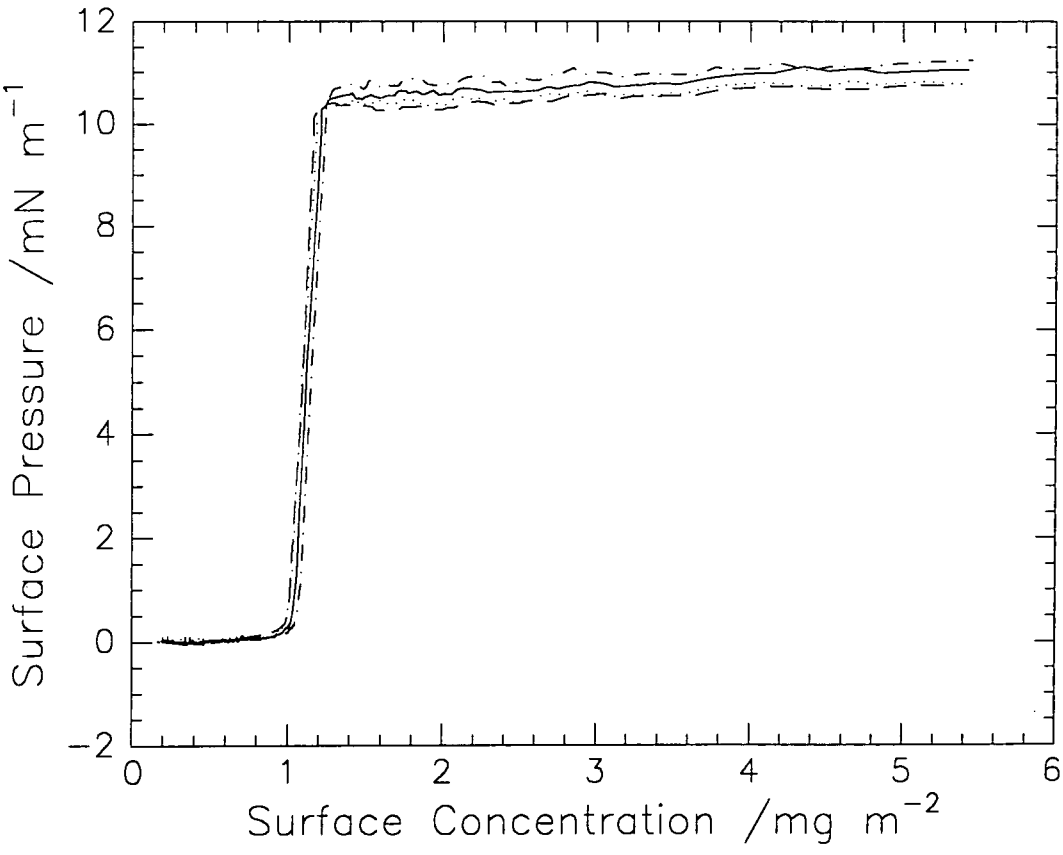

Figure 3.9: Isotherms obtained for the deuterated variations of PLMA at 25°C, HMHL (—), DMHL (– –), HMDL (– · –) and DMDL (·····)

3.5 Surface Pressure - Area Isotherms for LMA

The reproducibility of the monomer isotherms is shown in figure 3.10 where a set of three isotherms obtained at 25°C are compared.

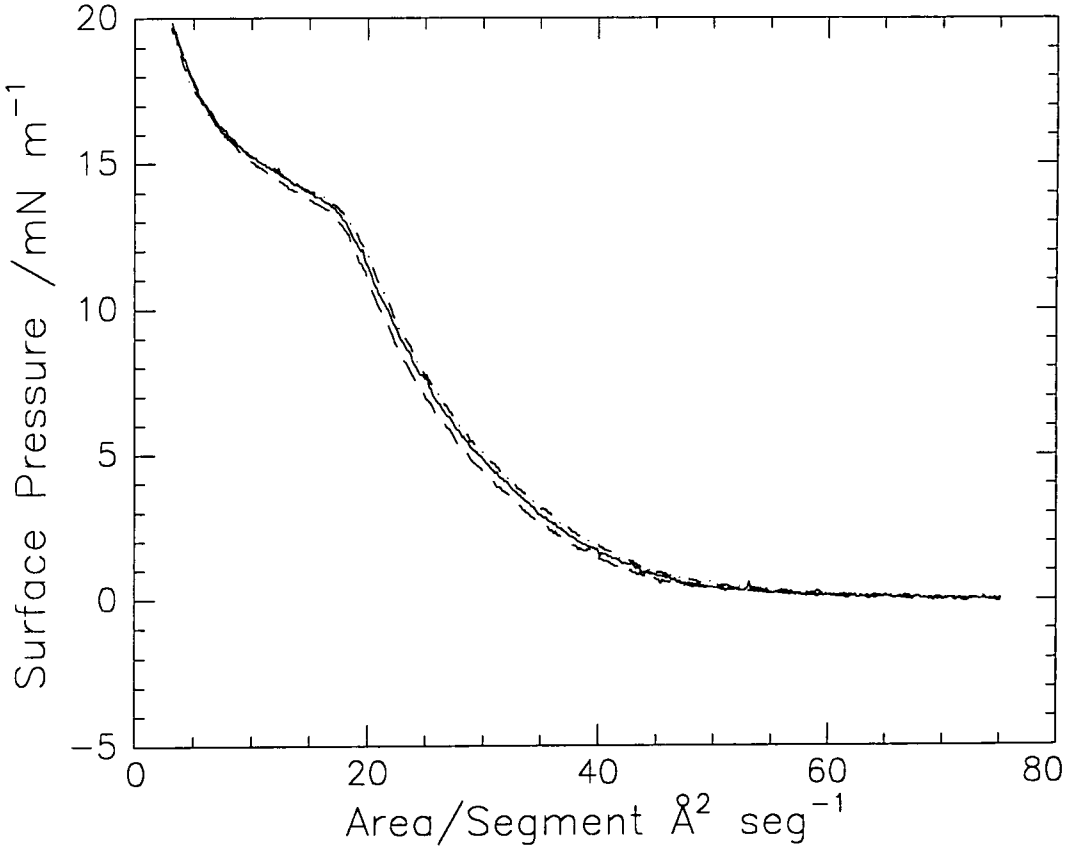

Figure 3.10: Surface pressure - area isotherms for LMA at 25°C

No drastic variation in the isotherms occurs, indicating that LMA produces consistent monolayers with the same structure and properties. The effect of temperature on the monolayers of LMA is shown in figures 3.11 and 3.12 with the data presented in area per segment and surface concentration format respectively.

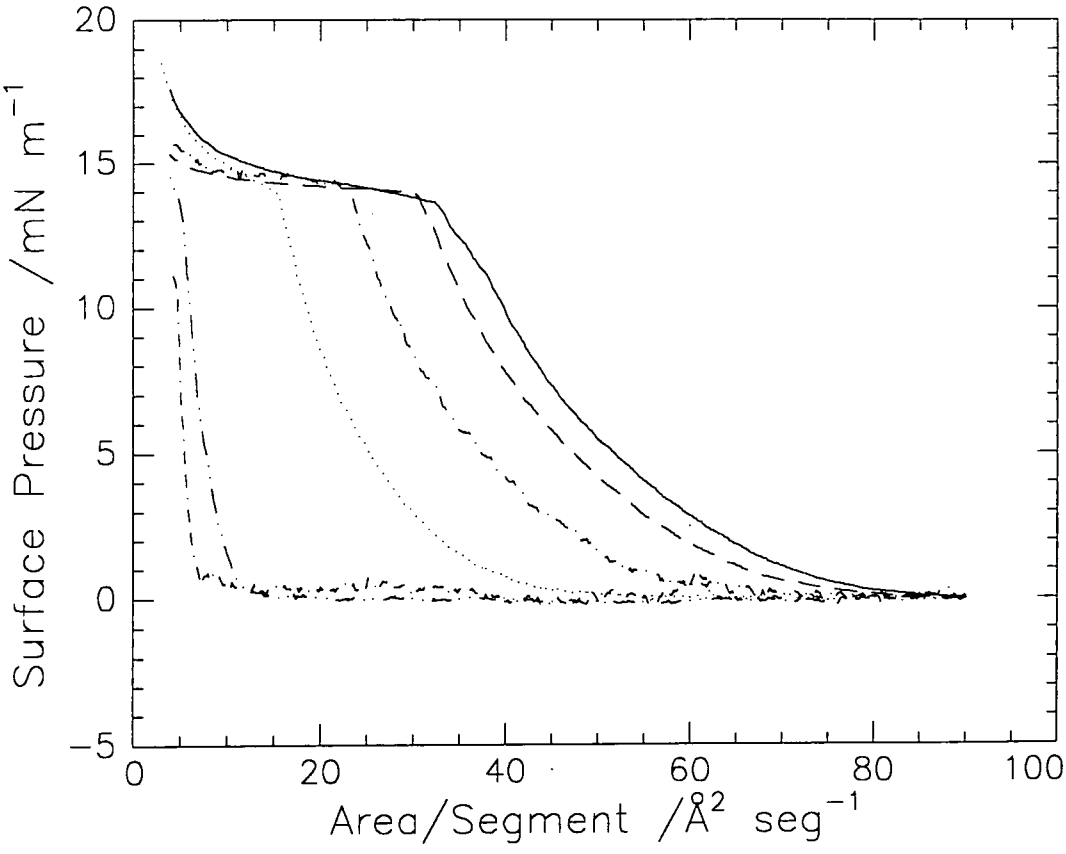

Figure 3.11: Surface pressure - area isotherms for LMA at 10°C (——), 15°C (– –), 20°C (– · –), 25°C (·····), 30°C (– ·· –) and 35°C (– – ·)

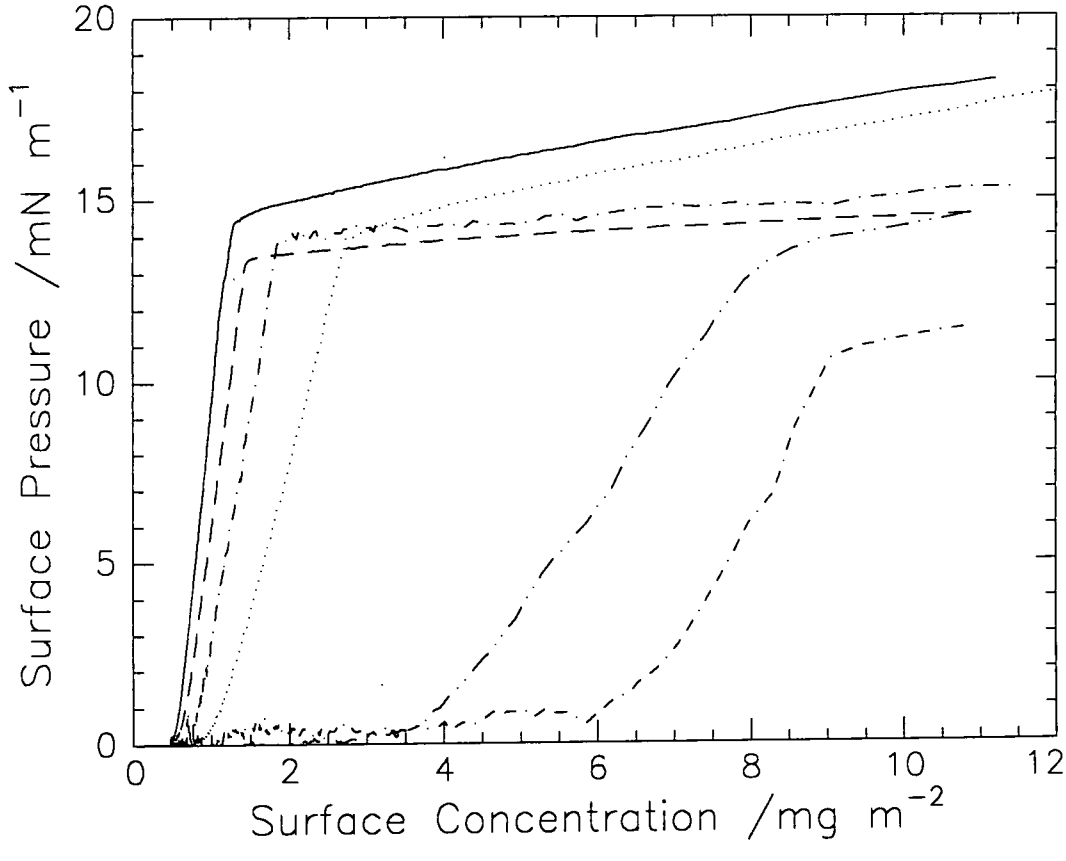

Figure 3.12: Surface pressure - surface concentration isotherms for LMA at 10°C (——), 15°C (– –), 20°C (– · –), 25°C (·····), 30°C (– ·· –) and 35°C (– – ·)

Unlike the polymer, there is a large effect of temperature on the nature of the monolayer and from inspection of figure 3.11 it is clear that the monolayer appears to become more compacted with increasing temperature. This can be quantified by calculating the limiting area per monomer molecule (A_{lim}), however, as the increase in surface pressure is curved in figure 3.11 it is not clear where to extrapolate from, so to overcome this the limiting surface concentration (Γ_{lim}) can be determined from figure 3.12 as the increase in surface pressure in this format appears linear and can be extrapolated to zero surface pressure. The corresponding limiting area can then be calculated from the surface concentration and both values are given in table 3.2.

TEMPERATURE	Γ_{lim} /mg m^{-2}	A_{lim} /Å^2 mon^{-1}
10	0.5	84.3
15	0.6	65.9
20	0.8	55.5
25	1.0	41.3
30	3.4	12.4
35	6.4	6.6

Table 3.2: Limiting surface concentrations and areas for LMA at each temperature

Up to 25°C the LMA monolayer appears to behave as a liquid expanded monolayer, which have limiting areas per molecule in the range 40 to 70Å^2 per molecule. Above this temperature the nature of the isotherm corresponds to that expected for a solid monolayer where the molecules are ordered and compacted together, resulting in low compressibilities. This observation appears to be the reverse of that which would be expected, in 3 or 2 dimensions, of increasing temperature resulting in transitions from solid to liquid and eventually to a gaseous state. Therefore, the effect of temperature on

the LMA monolayer must cause a different effect than simply leading to chain melting. An indication of the effect of temperature can be gained by comparing two isotherms (figure 3.13) obtained at 25°C which were left for different times before compression took place.

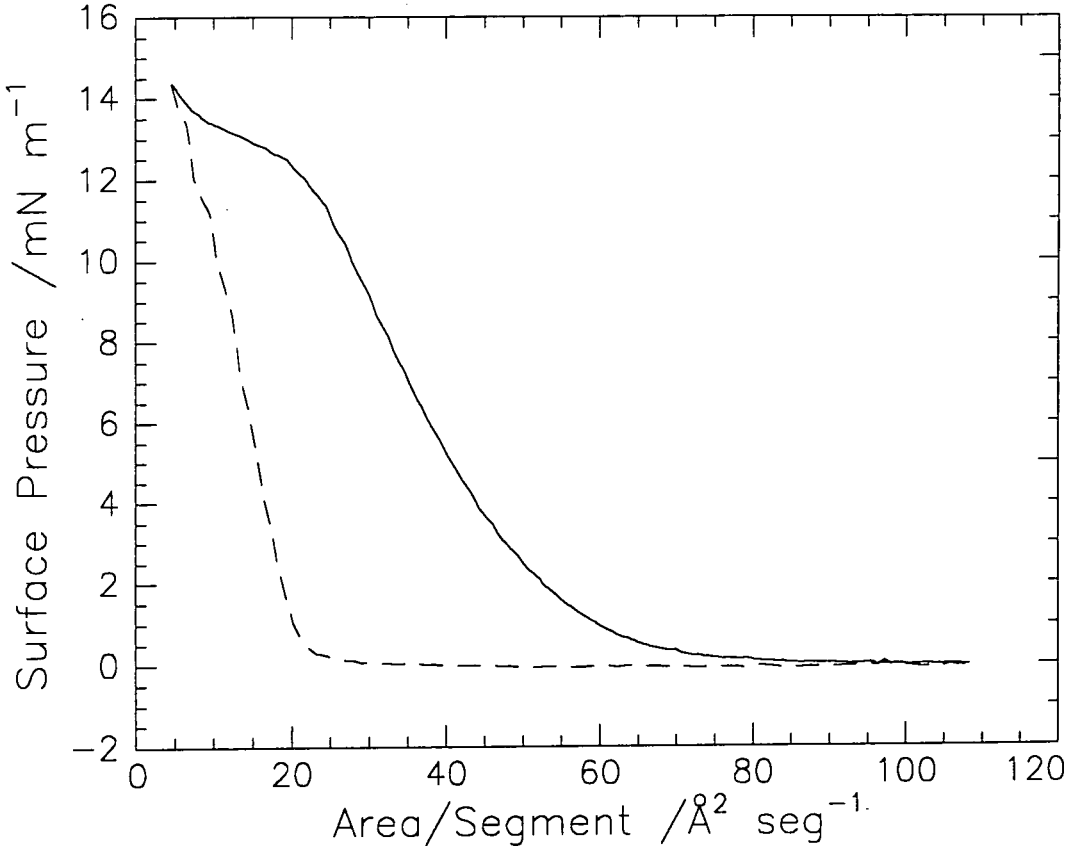

Figure 3.13: Compression isotherms for LMA at 25°C which were left for 10 minutes (—) and 1 hour (– –) before compression

The nature of the isotherm changes depending on the time elapsed before compression is commenced. After 1 hour the isotherm obtained resembled that for a compacted monolayer, similar to those obtained at the higher temperatures. This indicates that there is a dynamic process taking place once the LMA is deposited on to the subphase which changes the monolayer organisation and results in the formation of a condensed monolayer. The effect of temperature is to alter the rate of the dynamic process, so at low temperatures during the 10 minutes allowed for equilibration and

evaporation of solvent, the molecules have insufficient time to obtain the fully condensed state which the molecules prefer, so an isotherm is observed which corresponds to an expanded monolayer. At the higher temperatures the molecules can migrate at a faster rate and form the condensed state within the equilibration period, hence producing an isotherm typical of a condensed monolayer. It appears that the observed temperature effect is kinetic in nature and dominates any effect that might have been expected to occur due to chain melting as is observed for fatty acids and long chain alcohols. This is due to the dominant nature of the hydrophobic lauryl ester groups as they are not balanced by sufficiently hydrophilic groups, so the molecules migrate to minimise contact with the subphase and will form lenses on the water surface.

A series of nine compression - expansion cycles have been carried out on a monolayer of LMA and the isotherms of the first six cycles are shown in figure 3.14.

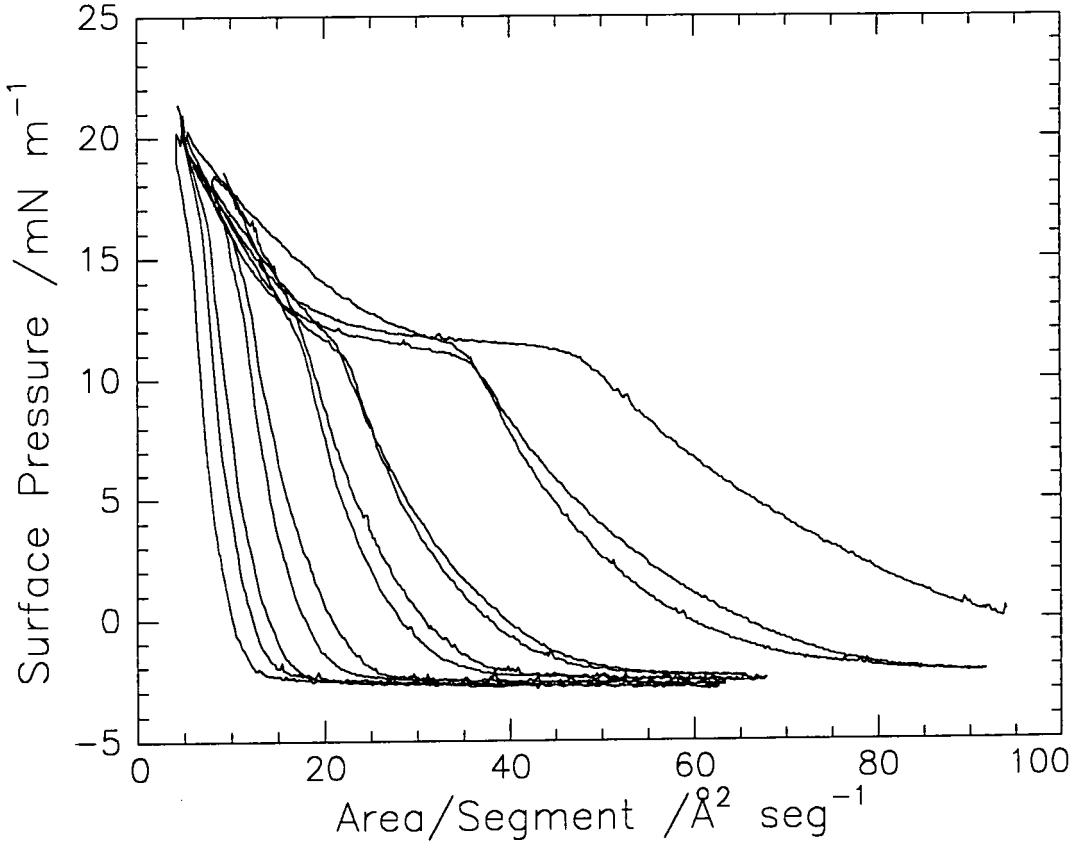

Figure 3.14: Six compression - expansion cycles for LMA

The monolayer becomes more condensed after each cycle, which will be due in part to both the dynamic movement of the molecules and the ordering effect of the successive compressions. A comparison between the first and sixth compression - expansion cycles is shown in figure 3.15

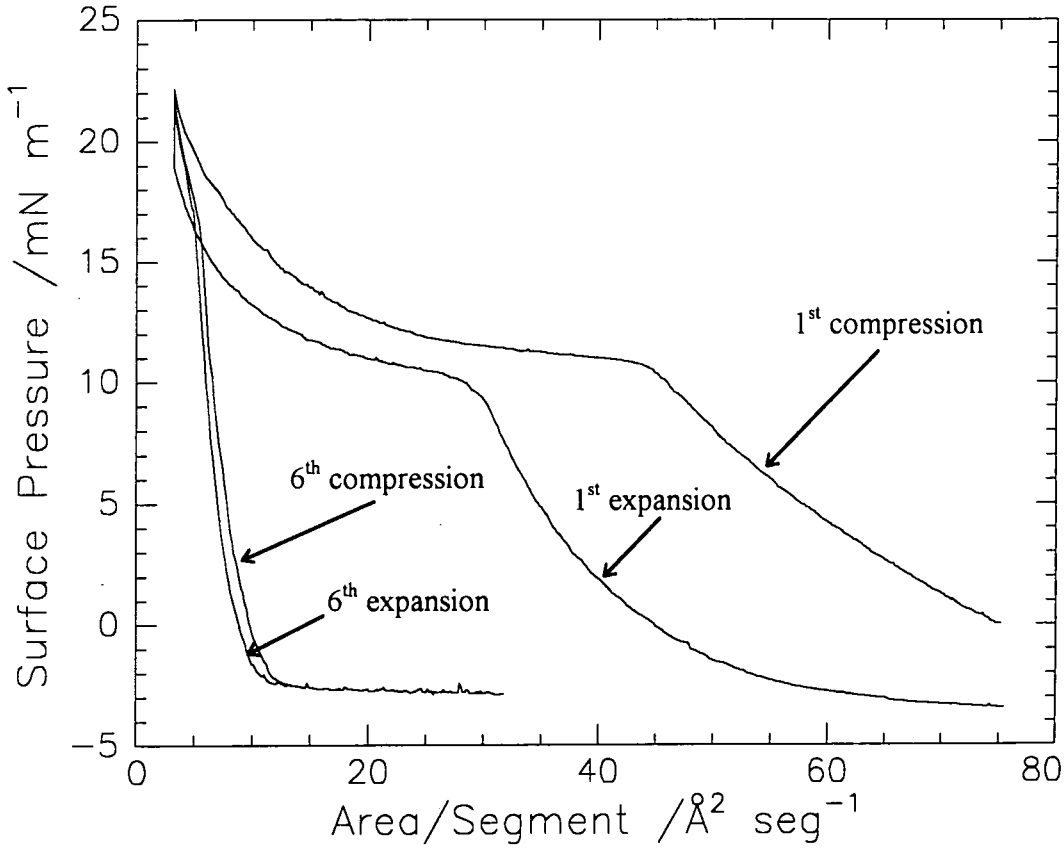

Figure 3.15: 1st and 6th compression - expansion cycle

The most notable feature is the open hysteresis loop produced from the first cycle due to the expansion curve going to negative values of surface pressure, whereas subsequent cycles produced closed loops as they began from negative surface pressure values and returned to the same point. The decrease to negative surface pressures indicates that the surface tension is greater than that for pure water, so additional order and structure must be imparted to the interfacial region. This order is presumably as a result of the migrating LMA molecules which is known to occur over a period of time.

The hysteresis loop obtained on the sixth compression - expansion cycle is reproducible as three additional cycles were carried out after the sixth cycle and they all produced the same loop, shown in figure 3.16.

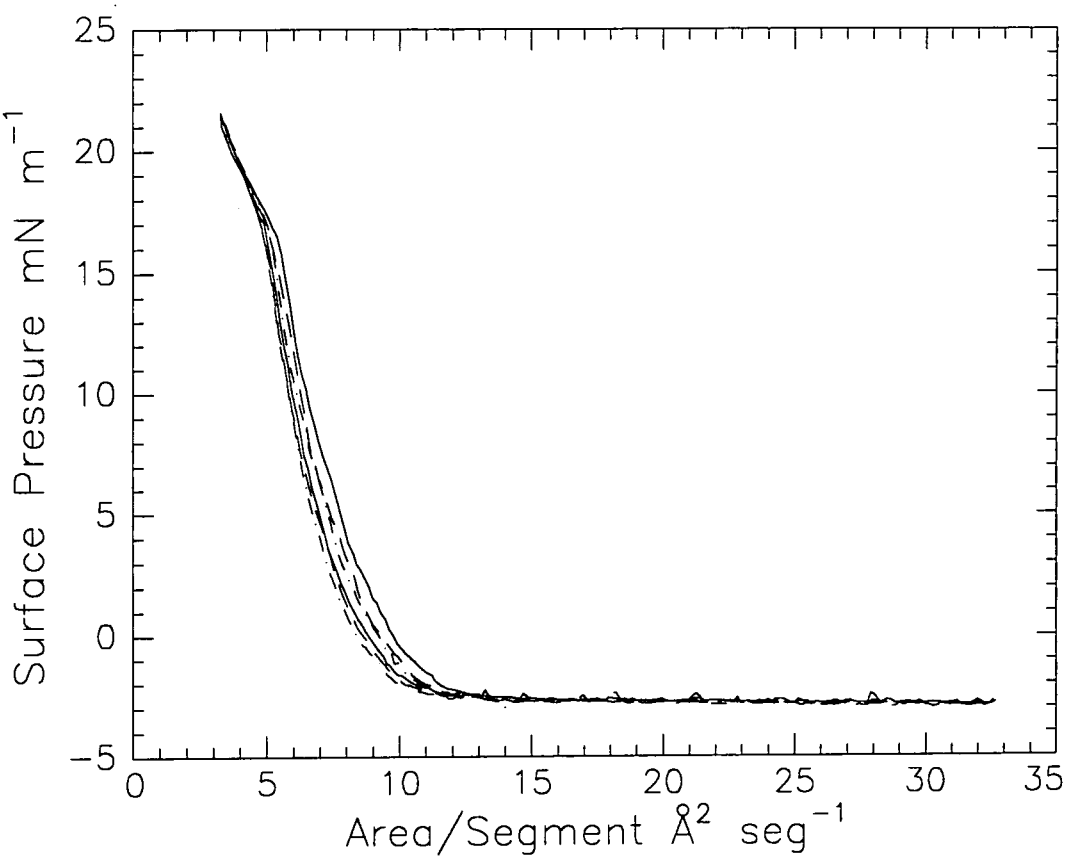

Figure 3.16: 7th (—), 8th (– –) and 9th (– · –) compression - expansion cycles

This indicates that even when the available subphase area is increased, the condensed lenses of LMA do not separate and remain packed tightly together. The dynamic process of the migrating LMA molecules is the characteristic feature which effects the neutron reflectivity and surface quasi - elastic light scattering experiments and is referred to in both sections to account for changes in the experimental observations.

As for the polymer, the effect of the deuterium labelling on the nature of the monolayer has been established by obtaining isotherms for each of the isotopic variations

at 25°C. As is shown in figure 3.17, there is no alteration in the nature of the monolayer due to the presence of the deuterium.

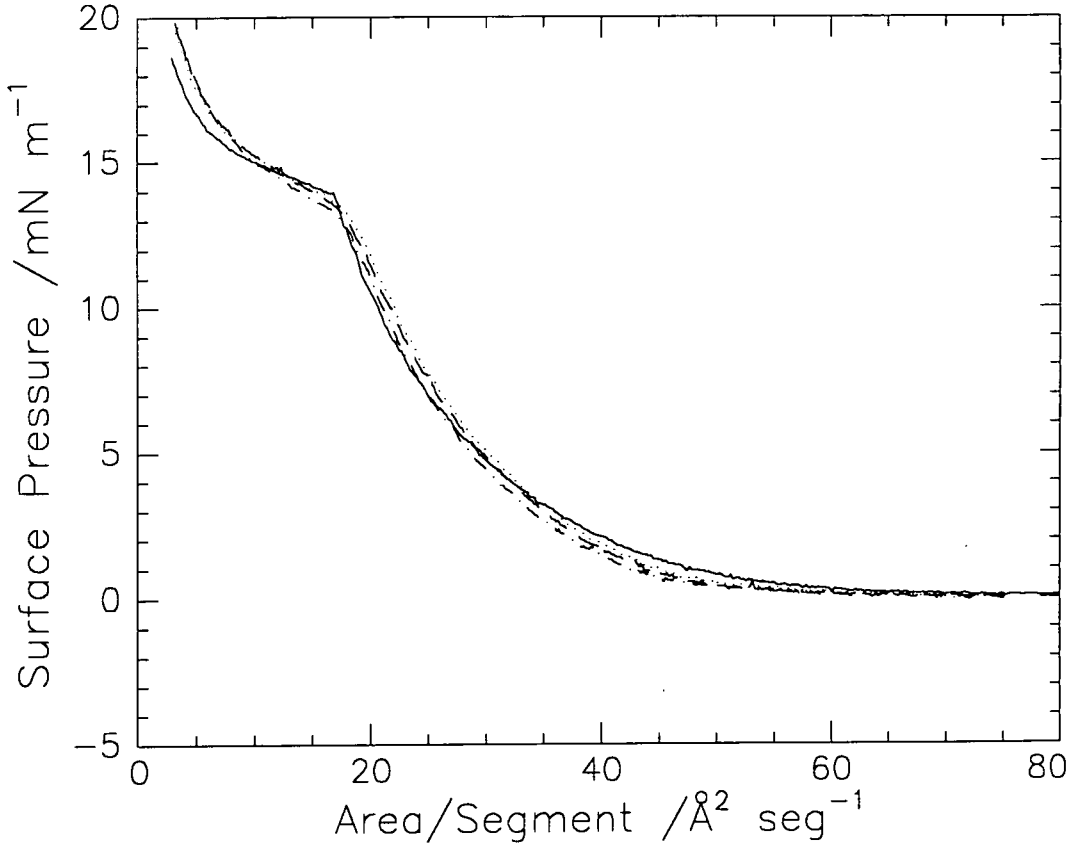

Figure 3.17: Isotherms for the isotopic variations of LMA, HMHL (––), DMHL (– –), HMDL (– · –) and DMDL (·····)

3.6 Conclusions

The nature of PLMA and LMA monolayers is dominated by the hydrophobic lauryl ester groups. This manifests itself as the formation of a condensed PLMA monolayer and dynamic changes in LMA monolayers. The changes observed for LMA monolayers are made possible due to the freedom of movement of the individual molecules, whereas for PLMA, the large chain length prohibits such behaviour and the molecules form larger scale islands which maintain their structure until they are sufficiently compressed to force them to interpenetrate.

3.7 References

1. Crisp, D.J., *J.Colloid Sci.*, 49, **1**, 1946
2. Crisp, D.J., *J.Colloid Sci.*, 161, **1**, 1946
3. Schick, M.J., *J.Polym.Sci.*, 465, **25**, 1957
4. Miller, I.R., *J.Colloid Sci. Suppl.*, 579, **9**, 1954
5. Shuler, R.L., Zisman, W.A., *J. Phys. Chem.*, 1523, **74**, 1970
6. Cockbain, E.G., Day, K.J., McMullen, A.J., *Proc. Intern. Congr. Surface Activity, 2nd, London*, 56, **1**, 1957
7. Beredjick, N., Ries, H.E., Jr., *J. Polym. Sci.*, 564, **62**, 1962
8. Beredjick, N., Ahlbeck, R.A., Kwei, T.K., Ries, H.E., Jr., *J. Polym. Sci.*, 268, **46**, 1960
9. Beredjick, N., *Monomolecular Film Studies of Polymers* in *Newer Methods of Polymer Synthesis and Characterisation*, Ke, B., Ed., Interscience, New York, 1964
10. Singer, S.J., *J. Chem .Phys.*, 872, **16**, 1946
11. Huggins, M.L., *J. Phys. Chem.*, 151, **46**, 1942
12. Davies, J.T., *J. Colloid Sci. Suppl.*, 9, **No.1**, 1955
13. Kawai, T., *J. Polym. Sci.*, 401, **35**, 1959
14. Frisch, H.L., Simha, R., *J Chem. Phys.*, 652, **24**, 1956
15. Frisch, H.L., Simha, R., *J. Chem. Phys.*, 702, **27**, 1957
16. Motomura, K., Matuura, R., *J. Colloid Sci.*, 52, **18**, 1963
17. de Gennes, P.G., *Scaling Concepts in Polymer Physics*, Cornell Univ. Press, Ithaca, New York, 1979
18. Flory, P., *Principles of Polymer Chemistry*, Chap 12, Cornell Univ. Press, Ithaca, New York, 1971

19. Daoud, M., Jannink, G., *J. Phys. (Paris)*, 973, **37**, 1976

20. des Cloizeaux, J., *J. Phys. (Paris)*, 281, **36**, 1975

21. Le Guillou, J.C., Zinn-Justin, J., *Phys. Rev. Lett.*, 95, **39**, 1977

22. Le Guillou, J.C., Zinn-Justin, J., *Phys. Rev .B*, 3976, **21**, 1980

23. Stephen, M.J., McCauley, J.,*J. Phys. Lett.*, 89, **A44**, 1973

24. Stephen, M.J., *J.Phys.Lett.*, 363, **A53**, 1975

25. Grassberger, P.Z., *Phys. B: Condens. Matter*, 255, **48**, 1982

26. Djordjovic, L.V., Majid, I., Stanley, H.E., Dos Santos, R.J., *J. Phys. A: Math. Gen.*, L- 519, **16**, 1983

27. Havlin, S., BenAvraham, D., *Phys. Rev. A*, 2759, **27**, 1983

28. Derrida, B., *J. Phys. A: Math. Gen.*, L - 5, **14**, 1981

29. Baumgartner, A., *J. Phys.*, 1407, **43**, 1982

30. Birshtein, T.M., Buldyrev, S.V., Elyashevitch, A.M., *Polymer*, 1814, **26**, 1985

31. Kremer, K., Lyklema, J.W., *J. Phys. A: Math. Gen.*, 1515, **18**, 1985

32. Kremer, K., Lyklema, J.W., *J. Phys. Rev. Lett.*, 267, **54**, 1985

33. Marqusee, J.A., Deutch, J.M., *J. Chem. Phys.*, 5179, **75**, 1981

34. Dekeyser, R., Maritan, A., Stella, A.L., *J. Chem. Phys.*, 912, **83**, 1985

35. Douglas, J.F., Cherayil, B.J., Freed, K.F., *Macromolecules*, 2455, **18**, 1985

36. Derrida, B., Saleur, H., *J. Phys. A: Math. Gen.*, L-1075, **18**, 1985L-1075

37. Granick, S., Clarson, S.J., Formoy, T.R., Semlyen, J.A., *Polymer*, 925, **26**, 1985

38. Taylor, M.R., Richards, R.W., submitted to *J. Chem. Soc., Faraday Trans 2*

4. NEUTRON REFLECTIVITY

4.1 Theoretical Background

Neutron reflectivity is a recent addition to the techniques for the analysis of surfaces. Neutrons are used to investigate the density (composition) profile in the direction normal to the plane of the layer by measuring the reflected intensity when an incident beam encounters the interface at angles greater than the critical (total reflection) angle. The beam is partially reflected and partially propagated into the medium of the layer and further successive reflections and refractions at compositional differences in the layer lead to interferences in the reflected intensity which are characteristic of the layer composition.

The dominant processes occurring when neutrons impinge on a simple smooth surface (figure 4.1) are specular reflection (angle of incidence equals angle of reflection), transmission and scattering from the bulk. The scattering may result from a variety of processes, for example, incoherent scattering from protons, or coherent scattering from structure in the substrate, typically local liquid or polymer structure, or from larger scale structures such as from individual polymeric species. If the surface is not perfectly smooth, and/or has fluctuations in density and/or in composition, there will also be a non-specularly reflected component to the total reflected intensity.

Since the angle of incidence is small, the pathlength traversed by the beam transmitted through the interface is large and all the transmitted beam is ultimately scattered not just once but several times. This background scattering is a characteristic feature of neutron reflection and is the limiting factor to the spatial or length scale resolution of the technique.

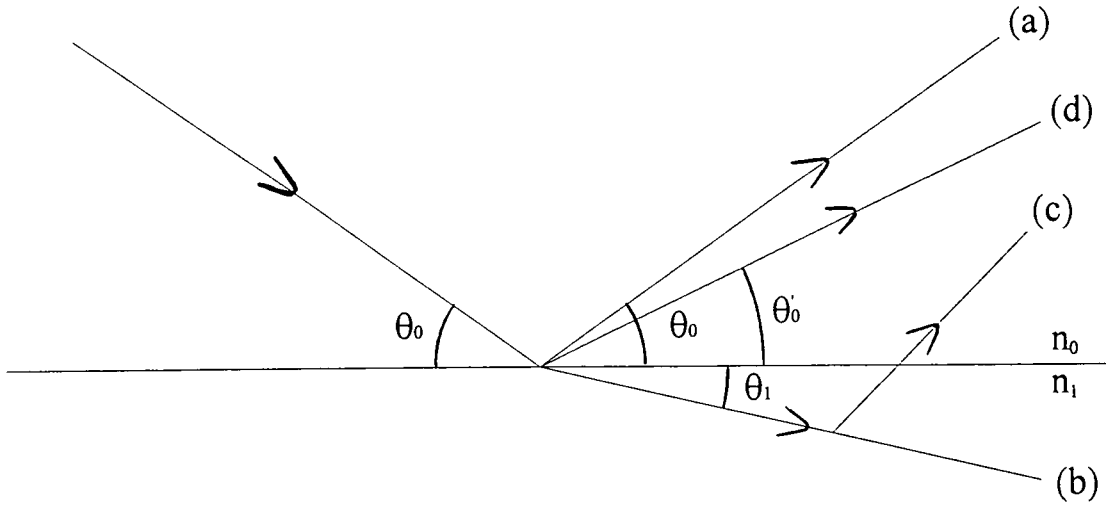

Figure 4.1: The different processes occurring when a neutron beam impinges on a surface, (a) specular reflection, (b) transmission, (c) bulk scattering, (d) non-specular reflection. n_0 and n_1 are the refractive indices of the two media.

Neutron reflectivity involves the measurement of the intensity of a specularly reflected neutron beam as a function of the scattering vector Q (= $(4\pi/\lambda)\sin\theta$) perpendicular to the reflecting surface (λ = wavelength, θ = glancing angle of incidence of neutron beam on the surface). If the incident wavevector is k_0 and the scattered wavevector is k_0', then $Q = k_0' - k_0$. It is the neutron refractive index (n) profile perpendicular to the surface which governs the reflection of neutrons by surfaces and interfaces, and n is given by

$$n = 1 - \lambda^2\left(\frac{\rho}{2\pi}\right) + i\lambda\left(\frac{\rho_a}{4\pi}\right) \qquad 4.1$$

where ρ is the scattering length density and ρ_a is the absorption cross section density. For most polymeric materials ρ_a is negligibly small, so the complex term in equation 4.1 can be ignored. Equation 4.1 shows that the reflection of neutrons depends

on ρ and ρ is determined by the atoms present at the interface and the proportion of each atom type in the interfacial composition

$$\rho = \Sigma\, n_i\, b_i \qquad 4.2$$

where n_i is the number density of species i and b_i is the scattering length of species i. The scattering length is a measure of the strength of the nuclear - neutron interaction and is different for each element, and thus ρ is dependant on the atoms present.

For a wave passing from one medium to another, as shown in figure 4.1, where $\theta_1 < \theta_0$, from Snell's law ($n_0 \cos\theta_0 = n_1 \cos\theta_1$) then $n_1 < n_0$. This is the case for a neutron beam entering a sample from air (n = 1), as most neutron refractive indices for materials are less than 1, albeit by a very small amount ($1\text{-}n \sim 10^{-6}$). When a beam passes from a medium of higher refractive index (n_0) to one of lower refractive index (n_1), the beam will be totally externally reflected when the glancing angle of incidence (θ_0) is less than a critical angle, θ_c. At this angle

$$\cos\theta_c = n_1 / n_0 \qquad 4.3$$

and as n_1 is close to 1, θ_c is small ($< 1^\circ$) and a series expansion can be used for $\cos\theta_c$ in 4.3, giving for small θ_c

$$\theta_c / \lambda = (\rho / \pi)^{1/2} \qquad 4.4$$

The fact that neutron reflection depends on the neutron refractive index, and hence on the scattering length density, allows the manipulation of the reflection by deuterium labelling as hydrogen and deuterium have vastly different scattering lengths, for H, b = -0.374×10^{-4}Å and for D, b = 0.667×10^{-4}Å (the negative value for H indicates a change of phase on the scattering encounter). This technique is widely used in neutron reflectivity work and allows the organisation of the labelled components to be determined as well as allowing the 'correctness' of an assumed model to be checked, as it must fit the reflectivity profiles obtained when the deuterium labelling is altered for the same system, assuming that the deuterium labelling does not alter the properties of the system. Another useful consequence of the values of b for H and D is that a mixture of H_2O and D_2O in the correct proportions (molar ratio of D_2O to H_2O equal to 0.088) will produce water with a scattering length density equal to zero, which is also the value defined for air. This is in effect invisible to neutrons (apart from incoherent scattering) and is termed air contrast matched water (a.c.m.w.). When a monolayer is spread on this subphase, the reflectivity obtained is only due to the molecules in the monolayer and hence information on the monolayer can be obtained by analysis of the reflectivity profile. The converse situation can also be used, with an hydrogenous polymer spread on D_2O, where the reflectivity will be dominated by the subphase signal, hence information on the distribution of the subphase in the monolayer can be determined.

The reflectivity R is defined as the reflected neutron intensity divided by the incident neutron intensity, and for $\theta < \theta_c$ R is unity. For the interface between two bulk media R can be calculated using Fresnel's Law, which states that for incident angles greater than the critical angle for total reflection

$$R = \left| \frac{n_o \sin\theta_o - n_1 \sin\theta_1}{n_o \sin\theta_o + n_1 \sin\theta_1} \right|^2 \qquad 4.5$$

Two methods to obtain information from experimentally determined reflectivity profiles are available, model fitting and the use of the kinematic approximation. These two will be discussed in the following two sections.

4.1.1 Model fitting

The basis of this method is to calculate the reflectivity for a given scattering length density distribution using optical matrix methods. The mathematical description of reflection and refraction from interfacial systems has been considered by several authors [1-3]. For a single film of thickness d at the interface of two bulk media, as is shown in figure 4.2, the reflectivity R can be obtained exactly

$$R = \left| \frac{r_{01} + r_{12} \exp(2i\beta)}{1 + r_{01} r_{12} \exp(2i\beta)} \right|^2 \qquad 4.6$$

where

$$r_{ij} = \left| \frac{n_i \sin\theta_i - n_j \sin\theta_j}{n_i \sin\theta_i + n_j \sin\theta_j} \right|^2 \qquad 4.7$$

r_{ij} is the Fresnel coefficient determining the reflectivity at the ij interface and β is the optical path length of the beam in the film ($\beta = (2\pi / \lambda)\, n_1 d.\sin\theta_1$). This method can be used to construct exact solutions for films of two or three layers, but above this number the complexity of the expressions involved becomes prohibitive.

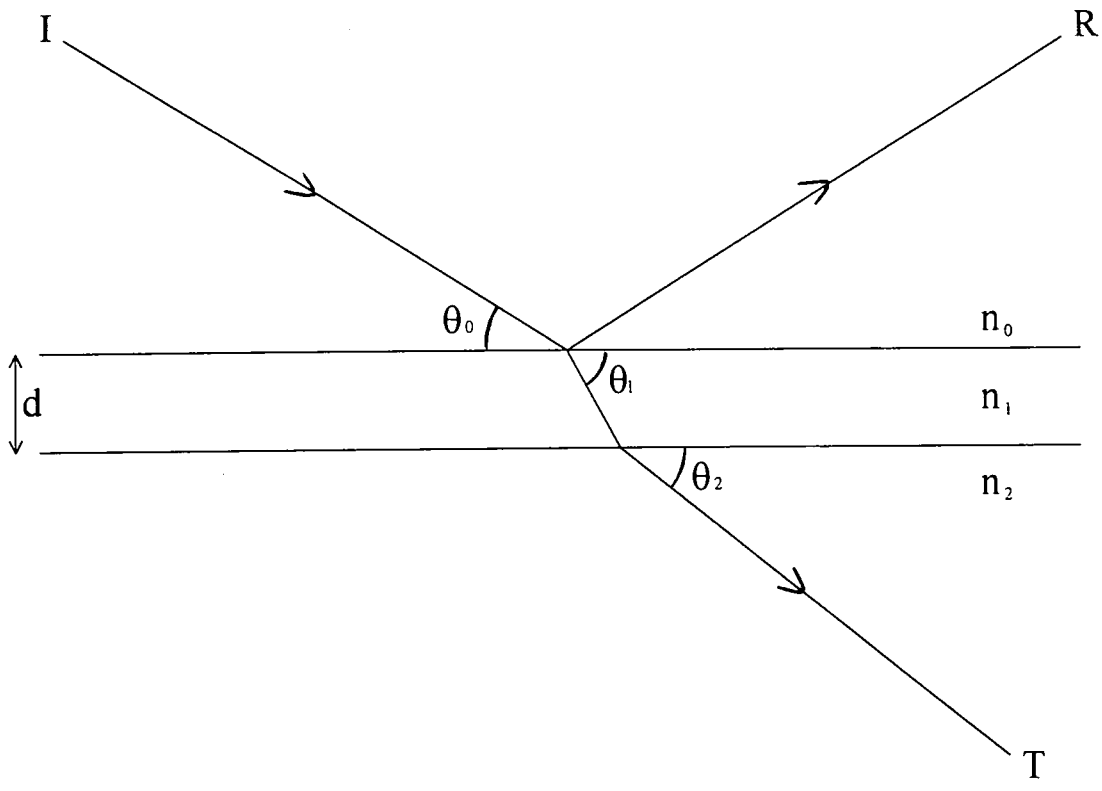

Figure 4.2: Reflection and refraction from a film of thickness d and refractive index n_1 between two media with refractive indices n_0 and n_2. I is the incident beam, R the reflected beam and T the transmitted beam.

A more general method for calculating the reflectivity for an interface is required, and that described by Born and Wolf [1] was the earliest applied to the analysis of reflection data. The Born and Wolf approach approximates the interfacial scattering length density distribution by dividing it into an arbitrary number of layers parallel to the interface, each having a uniform scattering length density but not necessarily the same thickness. Using the condition that the wavefunction for the neutron wave and its derivative must be continuous at each layer boundary, the reflectivity can be calculated by first determining a characteristic matrix $[M_j]$ for each layer.

$$[M_j] = \begin{bmatrix} \cos\beta_j & -(i/q_j)\sin\beta_j \\ iq_j \sin\beta_j & \cos\beta_j \end{bmatrix} \qquad 4.8$$

where $q_j = n_j \sin\theta_j$

The resultant matrix for the reflectivity, $[M_R]$, is obtained from the product of these matrices [1,4] , so for an n layer system

$$[M_R] = [M_1] \times [M_2] \times [M_3] \times \ldots\ldots [M_n] \qquad 4.9$$

and this produces a 2 × 2 matrix

$$[M_R] = \begin{bmatrix} M_{11} & M_{12} \\ M_{21} & M_{22} \end{bmatrix} \qquad 4.10$$

The reflectivity is given by

$$R = \left| \frac{(M_{11} + M_{12} q_s) q_a - (M_{21} + M_{22}) q_s}{(M_{11} + M_{12} q_s) q_a + (M_{21} + M_{22}) q_s} \right|^2 \qquad 4.11$$

where the subscript a refers to the outer air medium, s to the final substrate medium, and M_{ii} are the elements of $[M_R]$.

The description of the reflection may be extended to interfaces which are not perfectly smooth and roughness of the surface generally decreases the specular reflectivity. Croce and Nevot [5] have shown that the reduction in intensity due to

roughness can be accounted for by the application of a Debye - Waller factor for a Gaussian distribution of the interface such that

$$I(\lambda) = I_0(\lambda) \exp(-q_0 q_1 \langle\sigma\rangle^2) \qquad 4.12$$

where $I(\lambda)$ and $I_o(\lambda)$ are the reflected intensity with and without roughness, $\langle\sigma\rangle$ is the root mean square roughness, $q_0 = 2k \sin\theta_0$ and $q_1 = 2k \sin\theta_1$. The application of the Debye - Waller factor for treating surface roughness has been shown to be equivalent to the alternative method used by Born and Wolf, in which they divided the interface into layers with a Gaussian density distribution, however, this becomes unwieldy for more than a few layers. Therefore, the method of Abeles, described by Heavens [2], has become the favoured method for the calculation of the reflectivity from an interface. The process is similar to that of Born and Wolf except that the characteristic matrix for each layer is defined in terms of Fresnel coefficients

$$\left[M_j\right] = \begin{bmatrix} \exp\left(i\beta_{j-1}\right) & r_j \exp\left(i\beta_{j-1}\right) \\ r_j \exp\left(-i\beta_{j-1}\right) & \exp\left(-i\beta_{j-1}\right) \end{bmatrix} \qquad 4.13$$

For n layers, the elements of the resultant matrix M_{11}, M_{21} give the reflectivity as

$$R = \frac{M_{21} M_{21}^*}{M_{11} M_{11}^*} \qquad 4.14$$

To model the roughness at each interface using Abeles' method, a Debye - Waller factor is used to modify the Fresnel coefficients

$$r_{ij}' = r_{ij} \exp (0.5\ q_i\ q_j\ \langle\sigma\rangle^2) \qquad 4.15$$

Using optical matrix methods, the reflectivity of any interface can be calculated exactly and compared to experimentally observed data. To achieve this, a model of the interface has to be assumed, in terms of the scattering length density and thickness of each layer which makes up the model. The fitting of the model to the data then lends itself well to machine fitting, by using least squares fitting with the scattering length density and the thickness as adjustable parameters. Problems associated with this method are in the correctness of the model chosen and the uniqueness of the fit as the thickness and scattering length density are coupled in their action on the resultant reflectivity profile, i.e. the same fit can be obtained by increasing the thickness and decreasing the scattering length density and vice versa. These two problems can be overcome to some extent by using deuterium labelling and different subphases (D_2O and a.c.m.w.) which alter the experimentally obtained reflectivity profiles, however, using the assumption that deuterium labelling does not alter the chemistry of the system, the assumed model of the interface should fit all the experimental reflectivity profiles. The uniqueness of the fit can be tested by using the thickness (d) and scattering length density (ρ) values obtained from the fit to calculate the surface concentration, Γ_c

$$\Gamma_c = m\rho d / N_A \Sigma b_i \qquad 4.16$$

where m is the monomer molecular weight, N_A is Avagadro's number and Σb_i is the sum of the scattering lengths in the monomer unit. This value of Γ_c can then be

compared to the surface concentration calculated from the amount of polymer solution deposited on the subphase and the solution concentration.

4.1.2 Kinematic Approximation

The kinematic approximation method [6] for the analysis of reflectivity data allows a more direct approach to be used and can provide an insight into the relative location of different components at the interface. In the kinematic approximation, the specular component of the reflectivity for weak elastic scattering from a macroscopically flat surface is given by

$$R(Q) = \frac{16\pi^2}{Q^2}\left|\rho(Q)\right|^2 \qquad 4.17$$

where $\rho(Q)$ is the one dimensional Fourier transform of $\rho(z)$, the scattering length density profile perpendicular to the interface

$$\rho(Q) = \int_{-\infty}^{\infty} \exp(iQz)\,\rho(z)\,dz \qquad 4.18$$

An alternative expression to equation 4.17 can be written in terms of the gradient of the composition distribution, $d\rho(z) / dz = \rho'(z)$

$$R(Q) = \frac{16\pi^2}{Q^4}\left|\rho'(Q)\right|^2 \qquad 4.19$$

where

$$\rho'(Q) = \int_{-\infty}^{\infty} \exp(iQz)\left(d\,\rho(z)/dz\right)dz \qquad 4.20$$

This form for R(Q) is advantageous for the analysis of reflectivity data since $Q^4R(Q)$ generally has a strong maximum at a value of Q determined by the layer dimensions being considered. When Q = 0, equation 4.20 reduces to

$$\rho'(0) = \Delta\rho \qquad 4.21$$

where $\Delta\rho$ is the step in scattering length density between the two bulk media. The reflectivity can now be written as

$$R(Q) = R_s(Q)\, h'(Q) \qquad 4.22$$

where

$$R_s(Q) = \left(\frac{16\pi^2}{Q^4}\right)\left|\Delta\rho\right|^2 \qquad 4.23$$

Equation 4.23 is the kinematic expression for the reflectivity of a sharp interface and h'(Q) is a structure factor which modifies $R_s(Q)$ according to the shape and width of the scattering length density across the interfacial region. When $Q\tau$ is much less than 1, τ being the mean width of the interfacial region, $h'(Q) \approx 1$ and the surface profile appears to be sharp. As total reflection occurs when Q is of the order of 10^{-2}Å^{-1}, the reflectivity near the critical angle will appear the same as that for a sharp interface unless the variation of $\rho'(z)$ is over distances greater than circa 10Å. At values of Q above this point, h'(Q) decreases rapidly and R(Q) is depressed below the sharp interface value and broader interfacial regions further depress R(Q).

The structure factor, h'(Q), does not allow the components in the interfacial region to distinguished. This can be achieved by separating the total scattering length density profile perpendicular to the interface into individual contributions from each component, so for the case here for PLMA equation 4.2 can be used to give $\rho(z)$ as

$$\rho(z) = b_b n_b(z) + b_c n_c(z) + b_w n_w(z) \qquad 4.24$$

Where the subscripts refer to the components in the interfacial region, b denotes the methacrylate polymer backbone, c the lauryl side chains and w the subphase water. By taking the one - dimensional Fourier transform of equation 4.24 to obtain $\rho(Q)$ and then substituting into equation 4.17, R(Q) is given by

$$R(Q) = \frac{16\pi^2}{Q^2}\left[\begin{array}{l} b_b^2 h_{bb}(Q) + b_c^2 h_{cc}(Q) + b_w^2 h_{ww}(Q) + \\ 2b_b b_c h_{bc}(Q) + 2b_b b_w h_{bw}(Q) + 2b_c b_w h_{cw}(Q) \end{array}\right] \qquad 4.25$$

where

$$h_{ii}(Q) = \left|n_i(Q)^2\right| \qquad 4.26$$

$$h_{ij}(Q) = \mathrm{Re}\left|n_i(Q)\, n_j^*(Q)\right| \qquad 4.27$$

where $n_i(Q)$ and $n_j(Q)$ are the one - dimensional Fourier transforms of the number density distributions of each species perpendicular to the interface ($n_i(z)$ and $n_j(z)$) and $h_{ii}(Q)$ and $h_{ij}(Q)$ are the self and cross partial structure factors respectively. As referred

to earlier, the reflectivity can be expressed in terms of $\rho'(Q)$ and similarly equation 4.25 can be written in derivative form where

$$h'(Q) = Q^2 h_{ii}(Q) \qquad 4.28$$

and

$$R(Q) = \frac{16\pi^2}{Q^4}\left[\begin{array}{l} b_b^2 h'_{bb}(Q) + b_c^2 h'_{cc}(Q) + b_w^2 h'_{ww}(Q) + \\ 2b_b b_c h'_{bc}(Q) + 2b_b b_w h'_{bw}(Q) + 2b_c b_w h'_{cw}(Q) \end{array}\right] \qquad 4.29$$

The self partial structure factors describe the distributions of each species in the interfacial region, i.e. layer thickness and shape of the layer, and the cross partial structure factors contain information about the relative positions of the various components. In equations 4.25 and 4.29 there are six unknown partial structure factors, therefore, to obtain each of these as a function of Q, six reflectivity profiles must be obtained under different contrast conditions, i.e. where the scattering length density of each component of the polymer and that of the subphase is varied. These different contrast conditions are achieved by using the different isomers of PLMA on subphases of D_2O and a.c.m.w.. A series of simultaneous equations can then be solved to give $h_{ii}(Q)$ and $h_{ij}(Q)$ as a function of Q. When the subphase has a non - zero scattering length density, Crowley [7] has shown that the experimentally obtained reflectivity to be used in solving either equations 4.25 or 4.29 must be scaled by values of the reflectivity calculated for the perfectly smooth subphase using the kinematic reflectivity ($R_k(Q)$ calculated from equation 4.17) and the exact Fresnel reflectivity ($R_f(Q)$ calculated by

optical matrix methods). Thus the reflectivity required when the polymer is spread on D_2O is given by

$$R(Q) = R_k(Q) + \left[\frac{R_{exp}(Q) - R_f(Q)}{1 - R_f(Q)}\right]\left[\frac{1 + \left(1 - Q_c^2/Q^2\right)^{1/2}}{2}\right] \qquad 4.30$$

where Q_c is the critical value of the scattering vector below which total reflection is observed and $R_{exp}(Q)$ is the experimentally observed reflectivity.

A model is required to interpret these partial structure factors, although theoretically the partial structure factor could be Fourier transformed to obtain the distribution of the corresponding species, the data quality is not sufficiently good over a large enough range of Q, due to background limitations, to carry out such a procedure. To obtain the number density and width of the distribution of each component of the polymer at the interface from the self partial structure factors, $h_{bb}(Q)$ and $h_{cc}(Q)$, two models have been used, a uniform distribution and a Gaussian distribution. For a layer of uniform composition given by

$$\begin{aligned} n_i(z) &= n_{i1} \qquad \text{for } -d/2 < z < d/2 \\ n_i(z) &= 0 \qquad \text{for all other } z \end{aligned} \qquad 4.31$$

where d is the thickness of the layer and n_{i1} its number density, $n_i(Q)$ and $h_{ii}(Q)$ are given by

$$n_i(Q) = \frac{2n_{i1}}{Q}\sin(Qd/2) \qquad 4.32$$

$$Q^2 h_{ii}(Q) = 4n_{i1}^2 \sin^2(Qd/2) \qquad 4.33$$

and the surface concentration (in mg m^{-2}) can be calculated by

$$\Gamma_e = [(n_{i1}\, d\, m) / N_A] \times 10^{23} \qquad 4.34$$

For a layer with a Gaussian distribution $n_i(z)$ is given by

$$n_i(z) = n_{i1} \exp(-4z^2/\sigma^2) \qquad 4.35$$

where σ is the full width of the distribution at a height of n_{i1}/e. The partial structure factor is given by

$$Q^2 h_{ii}(Q) = n_{i1}^2 (\pi Q^2 \sigma^2/4) \exp(-Q^2\sigma^2/8) \qquad 4.36$$

and the surface concentration can be calculated by

$$\Gamma_e = \{[(\sigma\, n_{i1}\, \pi^{1/2}/2)m] / N_A\} \times 10^{23} \qquad 4.37$$

For the distribution of the subphase two models of the distribution have been used, a uniform layer and a hyperbolic tangent distribution. For the case where the solvent forms a uniform layer at the interfacial region with a different number density to the bulk then the composition is given by

$$n_w(z) = 0 \qquad z < -d/2$$

$$n_w(z) = n_{w1} \qquad -d/2 < z < d/2$$

$$n_w(z) = n_{w0} \qquad z > d/2 \qquad 4.38$$

where $n_w(z)$ is the variation of the number density of the subphase perpendicular to the interface, n_{w1} is the number density of the subphase in the interfacial region and n_{w0} is the bulk number density of the subphase. The corresponding $n_w(Q)$ and $h_{ww}(Q)$ are given by

$$n_w(Q) = \frac{n_{w1}}{iQ}\exp(iQd/2) + \frac{(n_{w0}-n_{w1})}{iQ}\exp(-iQd/2) \qquad 4.39$$

$$Q^2 h_{ww}(Q) = n_{w0}^2 + 4n_{w1}(n_{w1} - n_{w0})\sin^2(Qd/2) \qquad 4.40$$

For the tanh model, which produces a more gradual decay of the number density, the variation in $n_w(z)$ is given by

$$n_w(z) = n_{w0}\left[1/2 + 1/2\tanh(z/\xi)\right] \qquad 4.41$$

where ξ is the interfacial width parameter. The partial structure factor for the tanh profile is given by

$$Q^2 h_{ww} = n_{w0}^2(\xi\pi Q/2)^2\,\mathrm{cosech}^2(\xi\pi Q/2) \qquad 4.42$$

To obtain the separations between the centres of the distributions calculated from the self partial structure two relationships are used

$$h_{bc}(Q) = \pm (h_{bb}(Q)\, h_{cc}(Q))^{1/2} \cos(Q\delta_{bc}) \qquad 4.43$$

$$h_{iw}(Q) = \pm (h_{ii}(Q)\, h_{ww}(Q))^{1/2} \sin(Q\delta_{iw}) \qquad 4.44$$

where δ is the separation between the two distributions referred to by the subscripts. The $\pm$ sign in equations 4.43 and 4.44 is included to indicate the uncertainty about the phase of the right hand side, i.e. which layer is uppermost. To obtain δ the values of the self partial structure factors in equations 4.43 and 4.44 are calculated using the appropriate equations listed above and the parameters obtained from fits to the experimentally obtained partial structure factors. The cross partial structure factor can then be calculated and compared to the experimental cross partial structure factor and δ is varied until the best fit is obtained.

4.2 Experimental

Neutron reflection experiments were carried out on the Critical ReflectIon SPectrometer, CRISP, at the UK pulsed neutron source, ISIS, at the Rutherford Appleton Laboratories, Didcot, Oxfordshire which is shown schematically in figure 4.3. It operates at a fixed angle, which was set at 1.5° to the horizontal in this case, and a neutron beam with a wavelength distribution of 0.5 to 6.5Å was used. This corresponds to a momentum transfer range of 0.05 - 0.65Å^{-2}. The neutron beam passes through a hydrogen moderator at 25K to reduce the energy of the neutrons and the resulting beam contains a wide spread of energies (and hence wavelengths), so it passes through a beam chopper, 6m from the source, which rotates at 50Hz and selects the desired neutron beam wavelengths, those less than 0.5Å and greater than 6.5Å are rejected. Any other out of sequence neutrons originating from pulses earlier than the primary reference pulse are rejected by nickel frame overlap filtering mirrors. The beam is collimated by adjustable cadmium slits, giving a beam dimension of 40mm wide and 4mm high. The neutron radiation encounters the sample at a distance of 10.25m from the source.

The sample was spread on a Nima Langmuir trough (NIMA Technology, Coventry, UK) which consisted of a rectangular Teflon trough with motorised barriers and a pressure sensor to which a Wilhelmy plate was attached to measure the surface pressure of the spread polymer on the water surface. A Perspex lid covered the trough and quartz windows were fitted to the sides of the lid to enable the passage of the neutron beam. The temperature of the trough was maintained at 298K by circulating water from a thermostated water bath through a labyrinth of channels in contact with the bottom of the trough. The trough was mounted on a height adjustable platform which was attached to the top of a concrete anti-vibration plinth. The overall alignment of the

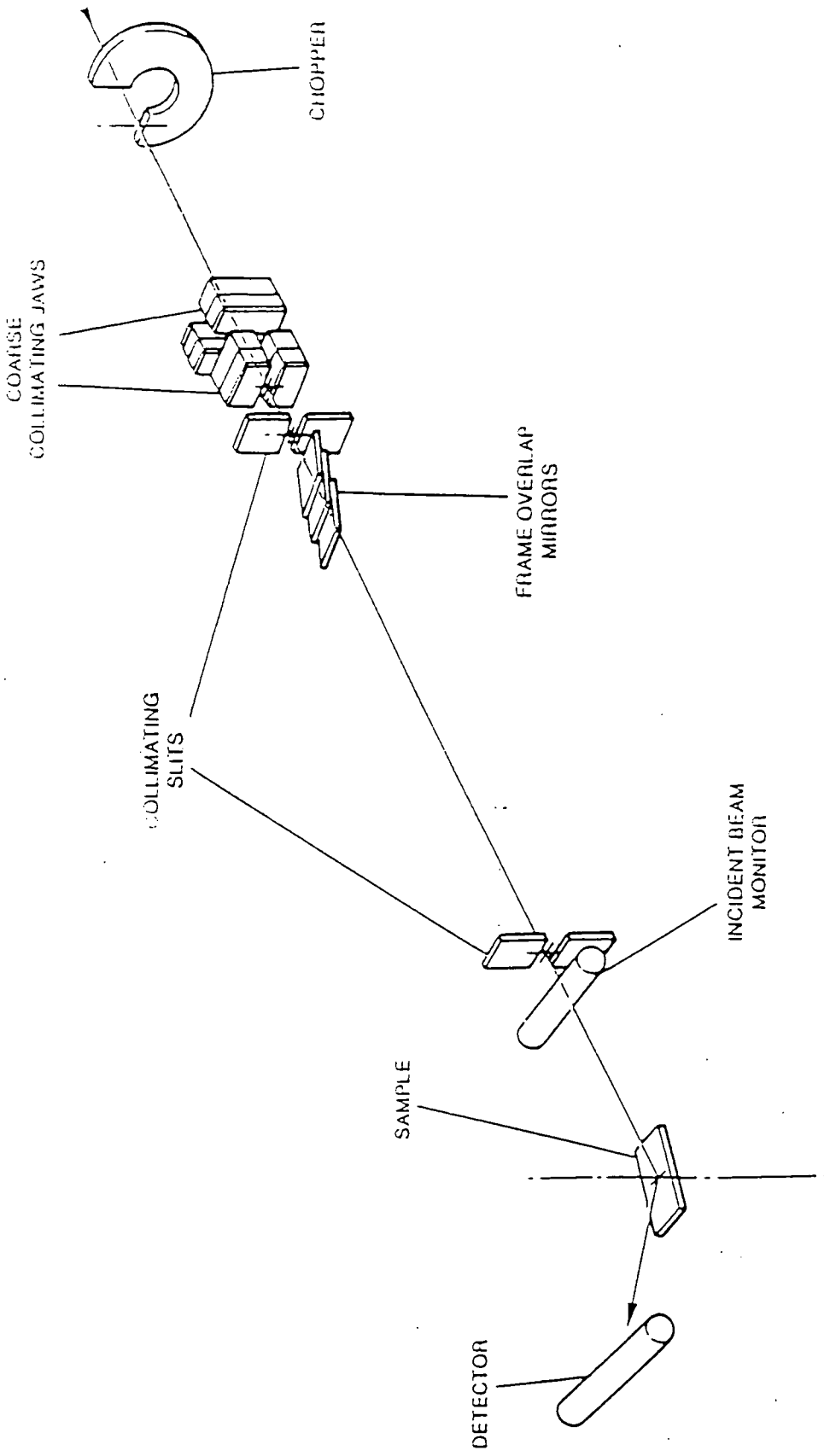

Figure 4.3: Schematic diagram of the CRISP set up

neutron beam path was achieved using a laser beam which was co-linear to the neutron beam path and a single time of flight detector was used to detect the reflected neutrons.

CRISP is a time of flight reflectometer, so called because the reflected beam is analysed as a function of the slightly different arrival times of reflected neutrons of different wavelengths at the detector. This raw data is converted to the corresponding reflectivity by ratioing the reflected intensity to the intensity of the incident beam detected by a beam monitor mounted in the incident beamline. Momentum transfer values were calculated by rebinning the time analysed data packages into corresponding wavelength sets and combining these with the known incident angle. Typical data acquisition times were between 2-3 hours.

For monolayers of PLMA neutron reflectivity profiles were obtained at three surface pressures, 0.5, 5 and circa 10mN m^{-1} (for some of the samples the high pressure plateau fell slightly below 10mN m^{-1}, so the target pressure was reduced to the highest steady pressure obtained) as these pressures correspond to the initial plateau region, the steep rise in surface pressure and the final plateau region of the isotherm. The same surface cleaning procedure used for determination of the surface pressure isotherms was applied and a known volume of polymer solution was deposited onto the subphase. The trough was run under pressure control, which means that the desired pressure is set and then the barriers compress until the pressure is reached and then the barriers move to maintain the target pressure continuously. The target pressures used resulted in the experiments being carried out at very similar surface concentrations, due to the nature of the isotherm, when surface pressures of 0.5, 5 and 10mN m^{-1} are obtained this corresponds to the foot of the transition in the isotherm, half way up the isotherm and the point just where the maximum surface pressure is obtained respectively, and as the transition is so steep, little variation in surface concentration occurs. The amount of

solution deposited was increased for the highest pressure so that the barriers did not have to compress as far to reach the target pressure and thus ensure that the barriers and pressure sensor did not encroach on the neutron beam.

For the monomer, LMA, three surface pressures were used, 0.4, 5 and circa 10mN m^{-1}. After compression the surface pressure began to decrease at a rapid rate to a constant value, the rate and the size of the decrease in surface pressure were too great for the constant pressure technique to be used as it would have resulted in the barriers moving a large amount and at a rapid rate to compensate for the decrease in surface pressure, resulting in the barriers moving into the neutron beam path. Instead the area was held constant once the target pressure was obtained and the surface pressure allowed to decrease. The data acquisition electronics were controlled by a command file which collected data for 15 minutes repetitively and stored each data set separately. It was hoped that changes in surface pressure could be investigated in terms of changes in the organisation at the interface. Typically, six 15 minute runs were carried out at each surface pressure.

All of the isotopic variations of both the polymer and monomer were spread on D_2O, whereas on a.c.m.w. subphase, the fully hydrogenous variations were not used due to the similarity in scattering length density between the fully hydrogenous material ($0.31 \times 10^{-6} Å^{-2}$) and the subphase, which would produce little contrast and therefore virtually no reflectivity. All of the reflectivity data had the incoherent background subtracted which was determined from the flat reflectivity level of the six highest Q points. The data was then normalised by dividing it by a prescale factor which was obtained by fitting the reflectivity for a clean D_2O subphase.

4.3 Neutron Reflectivity from PLMA Monolayers

The reflectivity profiles obtained for all the deuterated polymers spread on a.c.m.w. subphase at each surface pressure are shown in figures 4.4(a) to (c) and as the subphase has $\rho = 0$, the reflectivity profiles obtained are due only to the polymer.

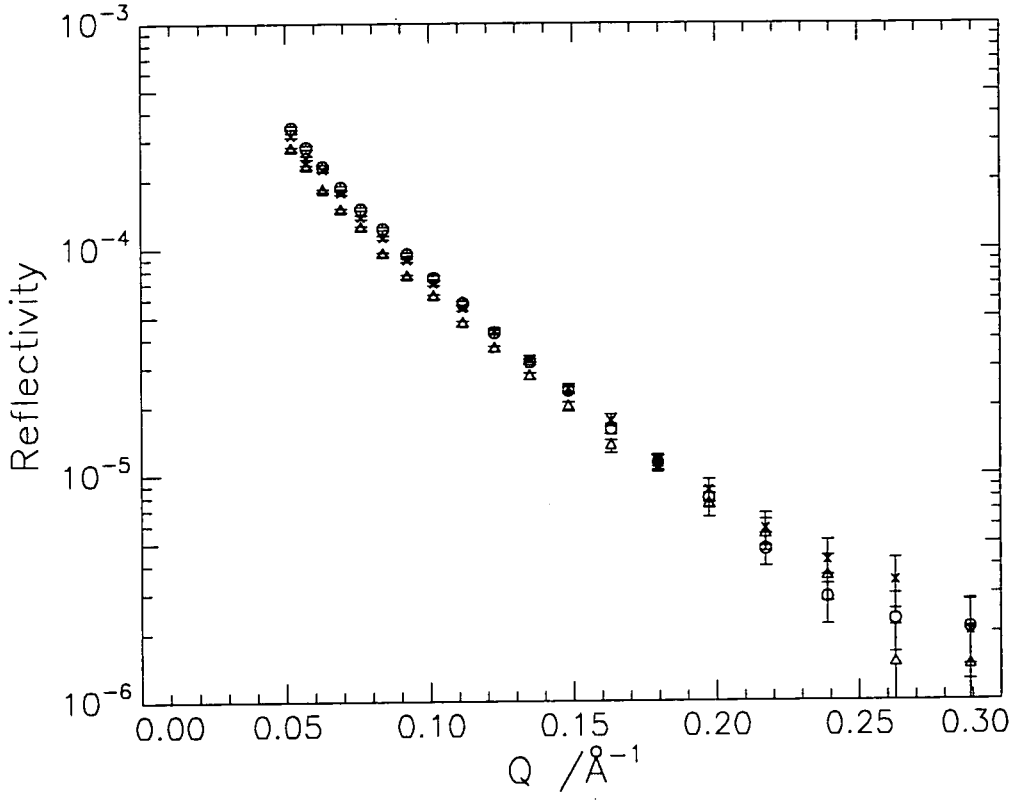

Figure 4.4(a): DMDL on a.c.m.w. subphase at 10mN m^{-1} (o), 5mN m^{-1} (×) and 0.5mN m^{-1} (Δ)

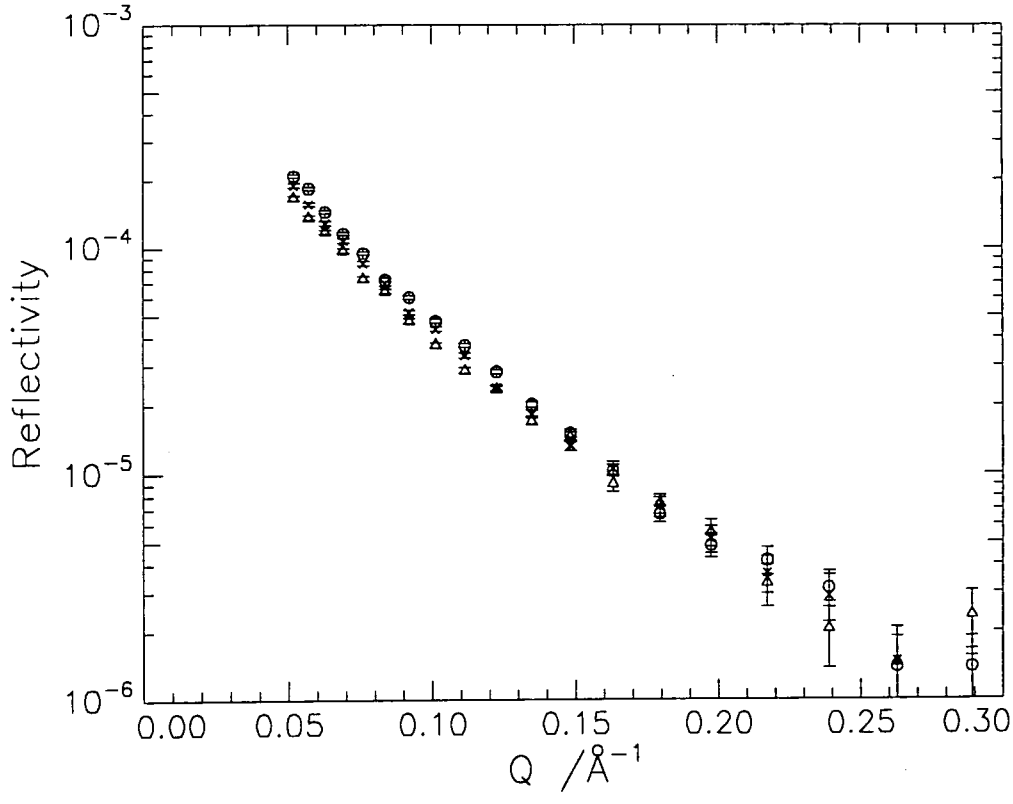

Figure 4.4(b): HMDL on a.c.m.w. subphase at 10mN m^{-1} (o), 5mN m^{-1} (×) and 0.5mN m^{-1} (Δ)

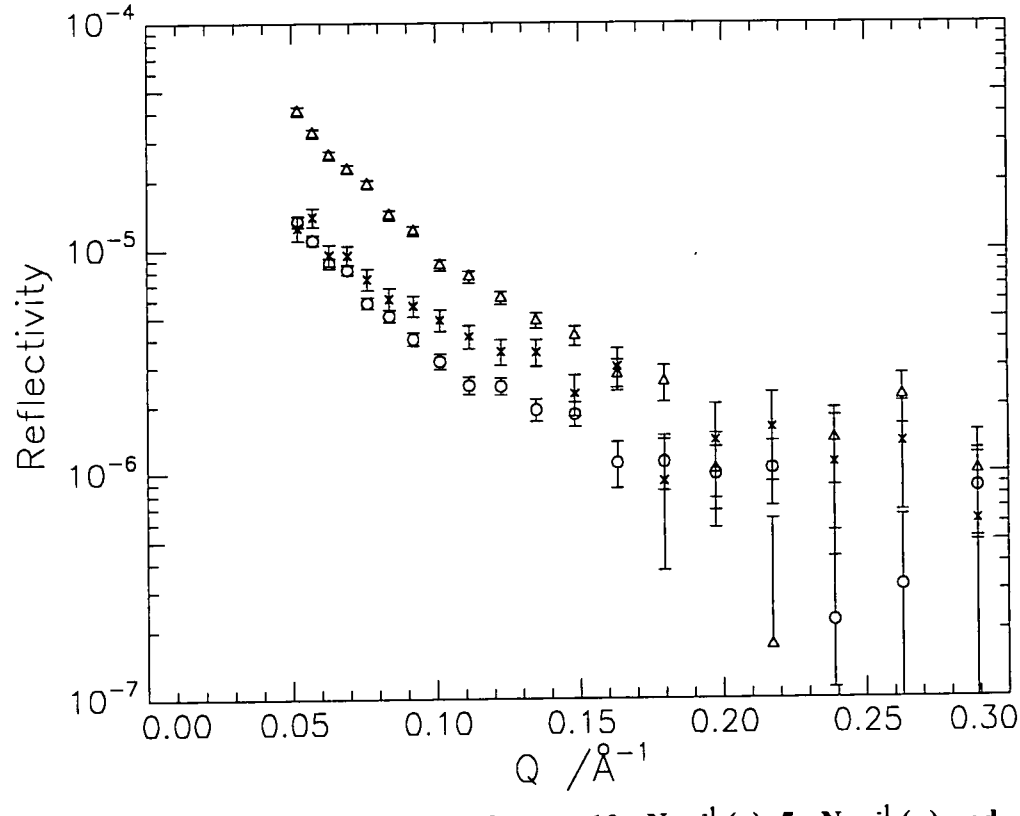

Figure 4.4(c): DMHL on a.c.m.w. subphase at 10mN m^{-1} (o), 5mN m^{-1} (×) and 0.5mN m^{-1} (Δ)

Although the Q range used in the experiments was 0.05 to 0.65Å^{-1}, figures 4.4(a) to (c) only show Q up to 0.3 Å^{-1} because of the large errors for larger Q values due to background subtraction. DMDL and HMDL show little variation in the profiles at each surface pressure, which indicates that, as expected, there is little change in the amount of material at the interface, whereas DMHL, generally has a much lower reflectivity at low Q due to the lower deuterium content in the polymer which resulted in a weaker signal. At 5 and 10mN m^{-1} the data are not too different, whereas at 0.5mN m^{-1} the reflectivity is much higher and this will be referred to later.

The effect of the deuterium labelling can be clearly seen by plotting the reflectivity profiles obtained for each deuterated polymer at a particular surface pressure on the same graph, as is shown in figures 4.5(a) to (c).

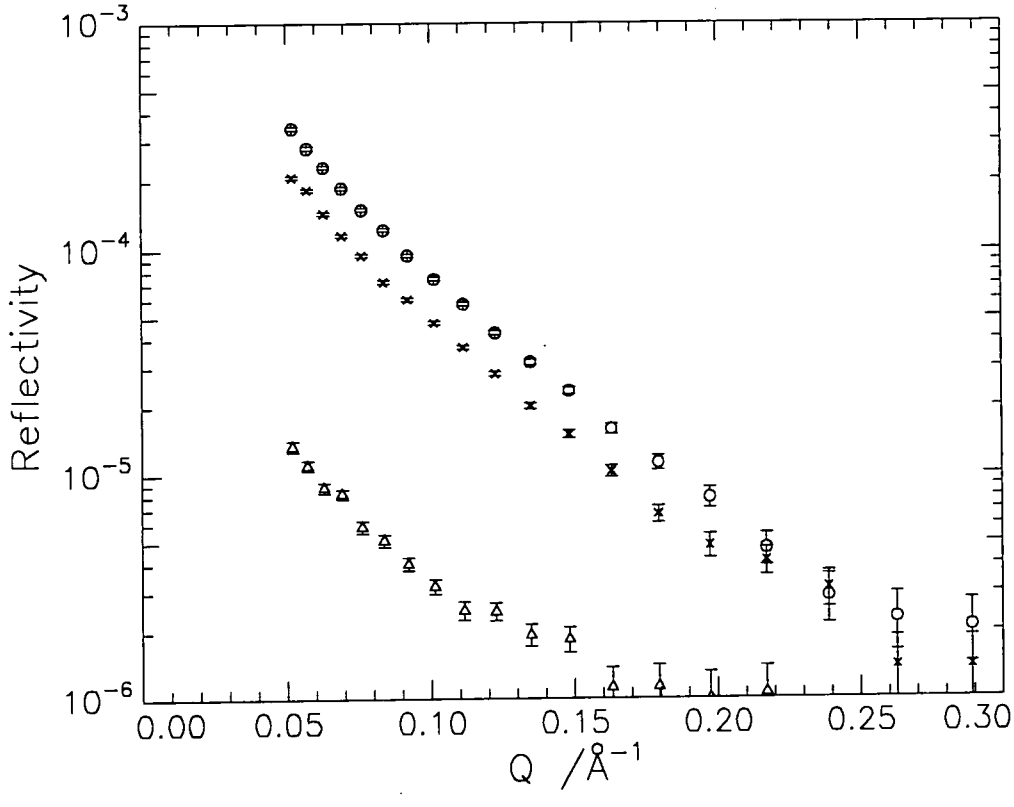

Figure 4.5(a): Reflectivity profiles at 10mN m^{-1} on a.c.m.w. for DMDL (o), HMDL (×) and DMHL (Δ)

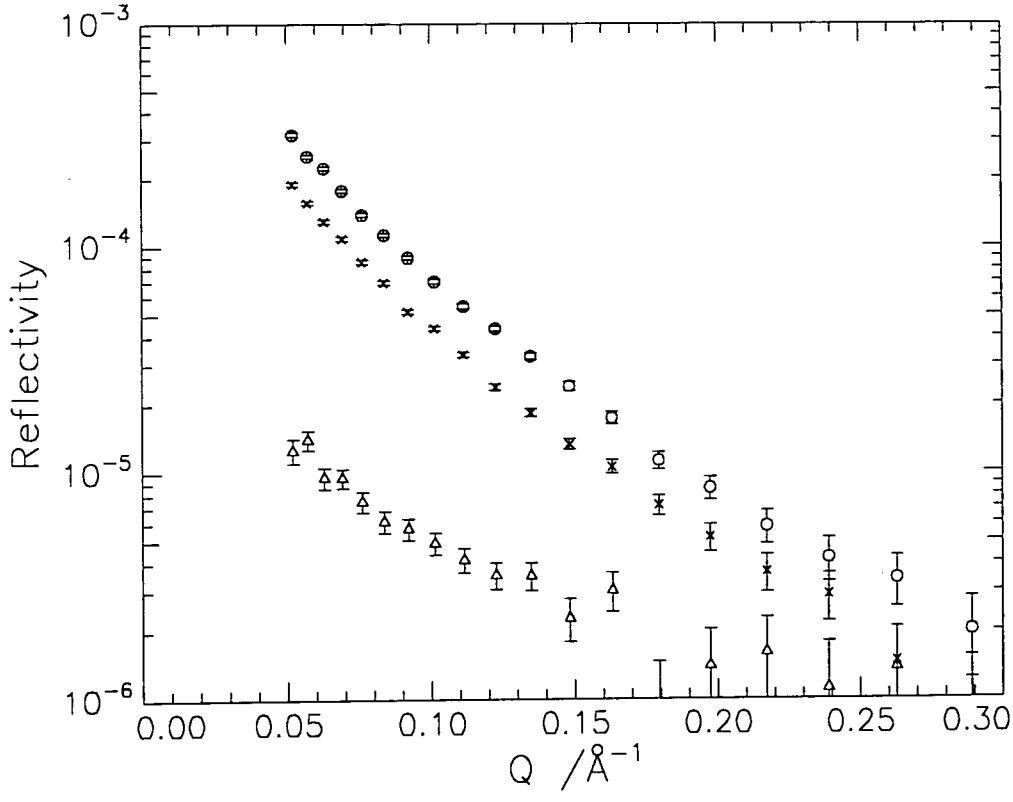

Figure 4.5(b): Reflectivity profiles at 5mN m^{-1} on a.c.m.w. for DMDL (o), HMDL (×) and DMHL (Δ)

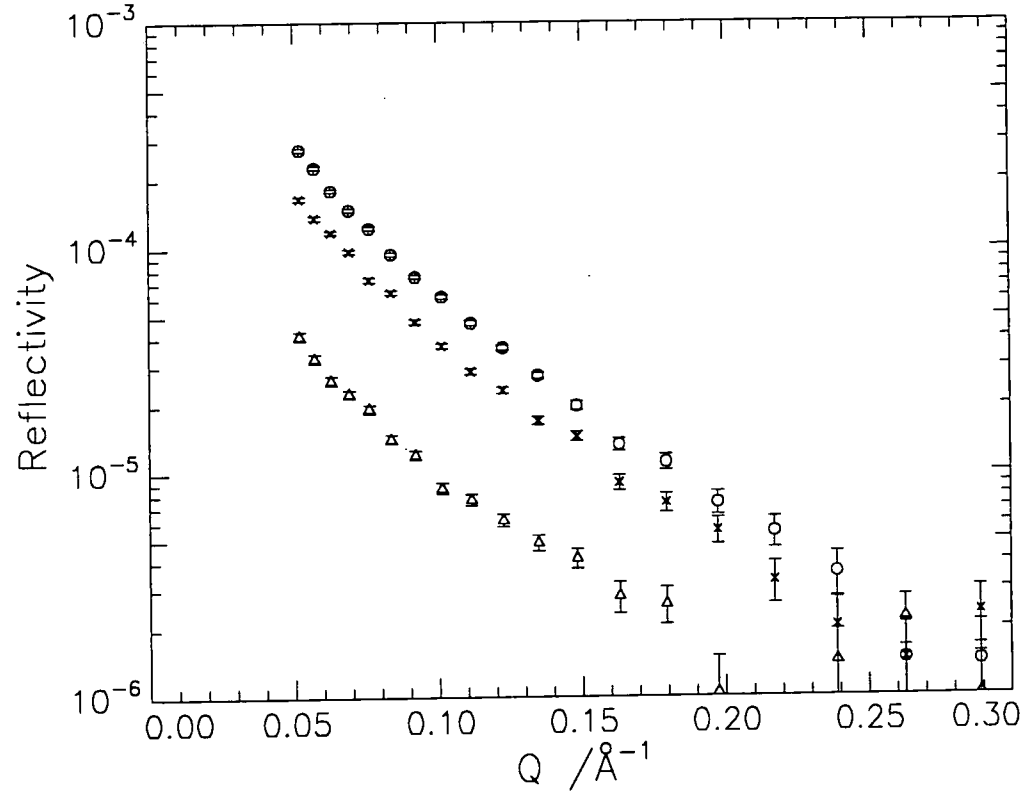

Figure 4.5(c): Reflectivity profiles at 0.5mN m^{-1} on a.c.m.w. for DMDL (o), HMDL (×) and DMHL (Δ)

The trends observed in figures 4.5(a) to (c) reflect the scattering length densities of the constituent parts of the lauryl methacrylate monomer which are given in table 4.1 together with other relevant values of scattering length density.

COMPONENT	SCATTERING LENGTH ($\times 10^{-4}$Å)	SCATTERING LENGTH DENSITY ($\times 10^{-6}$Å^{-2})
D2O	1.92	6.35
H2O	-1.68	-0.56
DMDL	31.80	6.60
HMHL	0.58	0.31
DMHL	5.79	1.46
HMDL	26.61	5.66
HM	1.62	1.20
DM	6.82	5.35
HL	-2.38	-0.26
DL	23.65	7.24

Table 4.1: Scattering lengths and scattering length densities of the components present at the interface

Reflectivity profiles were obtained for all of the isotopic variations on a D_2O subphase and these profiles are shown at each surface pressure and are compared to clean D_2O in figures 4.6(a) to (c).

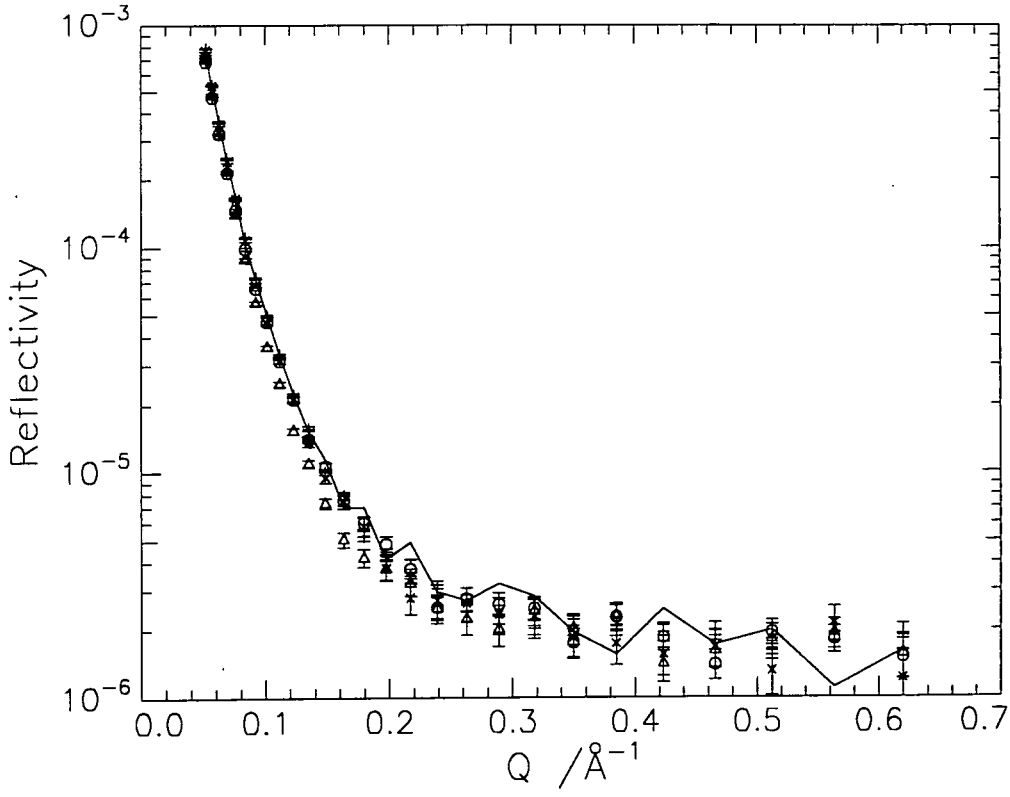

Figure 4.6(a): Reflectivity profiles at 10mN m^{-1} on D_2O subphase for DMDL (o), DMHL (×), HMDL (Δ) and HMHL (+) compared to D_2O (—)

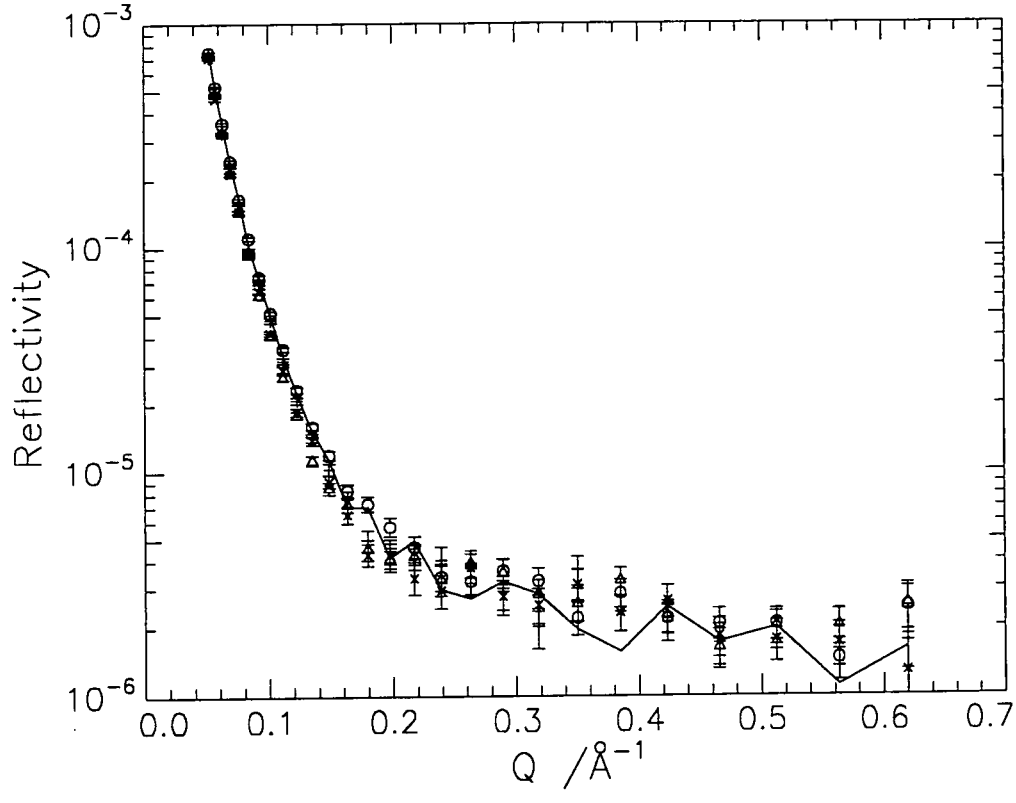

Figure 4.6(b): Reflectivity profiles at 5mN m^{-1} on D_2O subphase for DMDL (o), DMHL (×), HMDL (Δ) and HMHL (+) compared to D_2O (—)

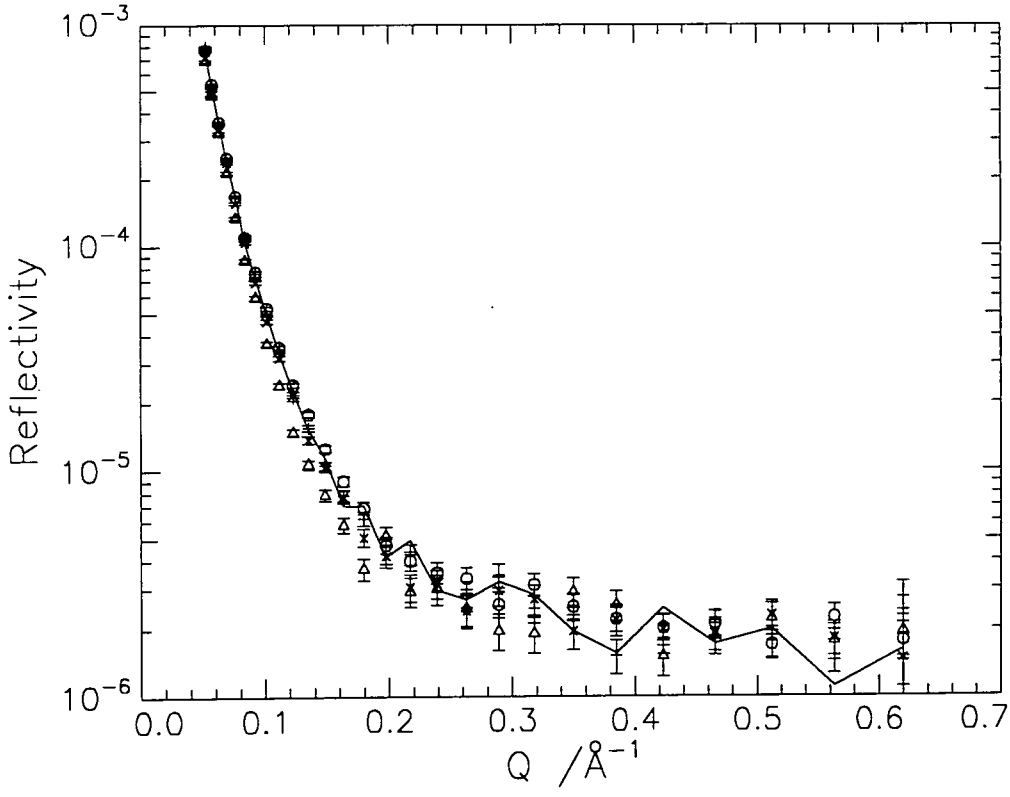

Figure 4.6(c): Reflectivity profiles at 0.5mN m^{-1} on D_2O subphase for DMDL (o), DMHL (×), HMDL (Δ) and HMHL (+) compared to D_2O (—)

Each pressure shows similar characteristics with little deviation from the reflectivity of D_2O, with HMDL being slightly lower in each case.

The first step in the analysis of the profiles was to attempt to fit them with a uniform single layer model of the polymer at the interface, assuming that the polymer backbone and side chains were mixed homogeneously. Examples of the fits obtained are shown in figures 4.7 to 4.13.

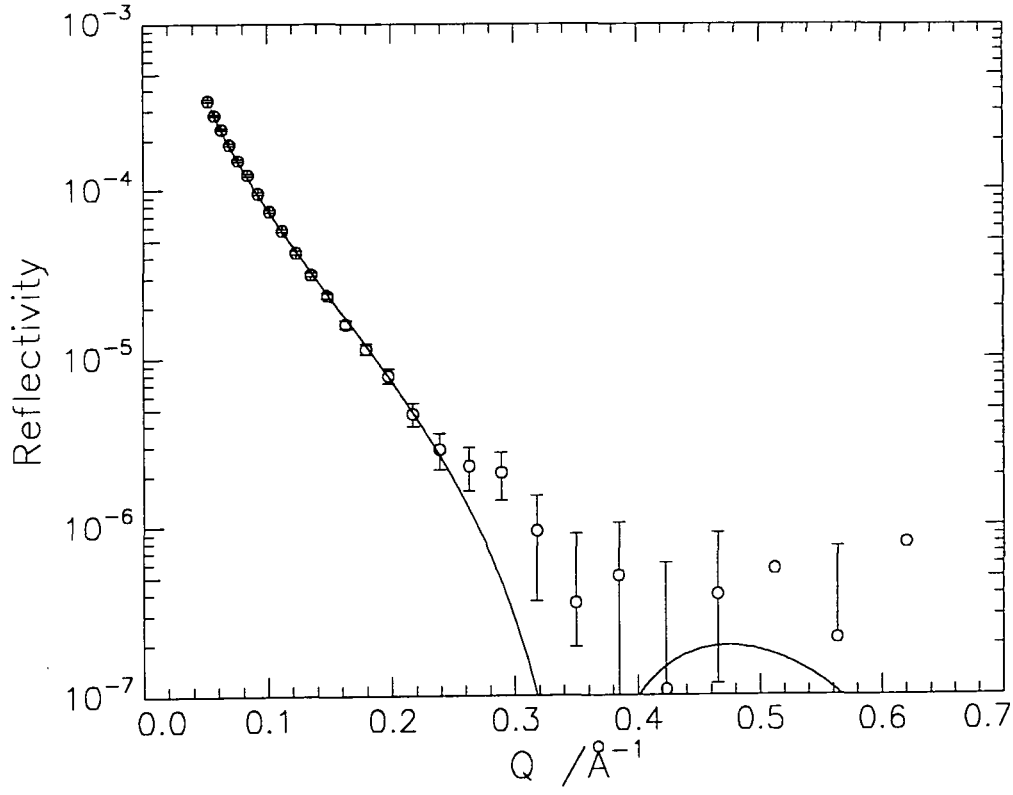

Figure 4.7: Single layer fit to DMDL at 10mN m^{-1} on a.c.m.w. subphase

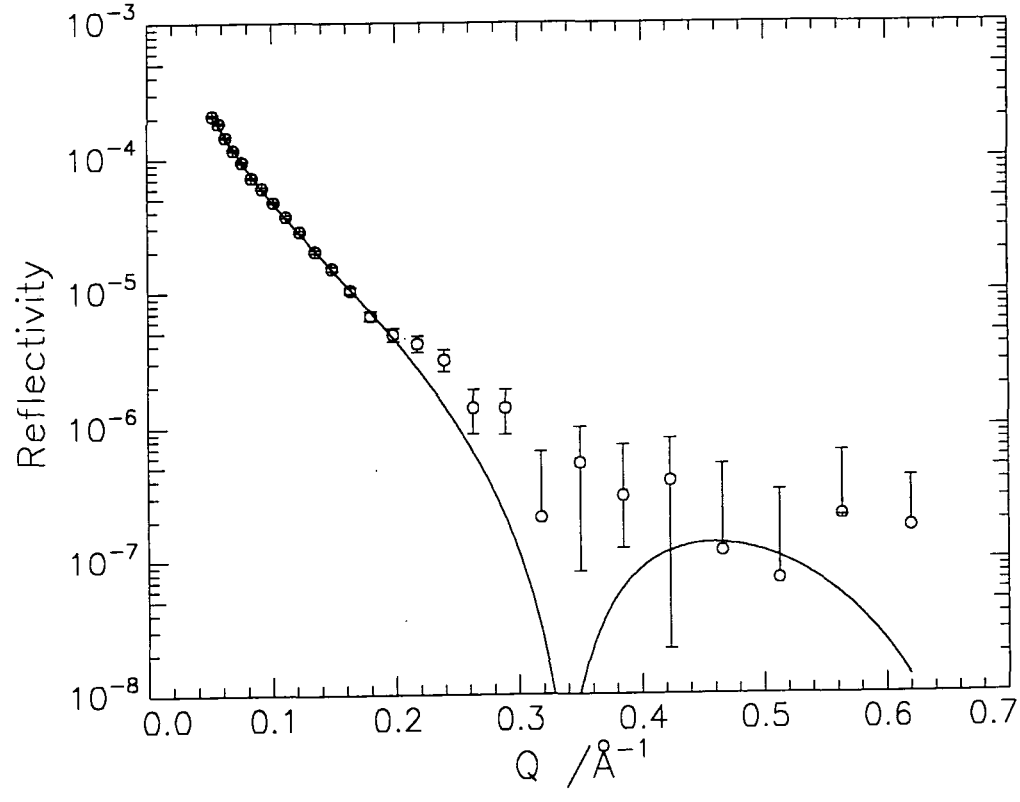

Figure 4.8: Single layer fit to HMDL at 10mN m^{-1} on a.c.m.w. subphase

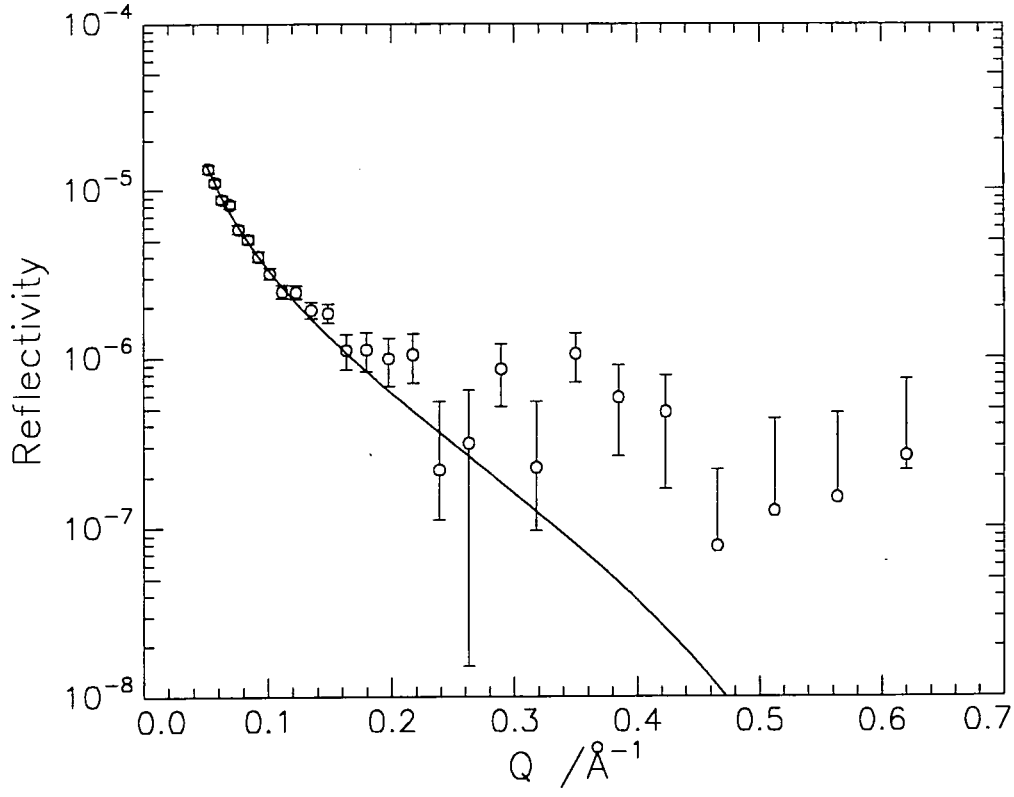

Figure 4.9: Single layer fit to DMHL at 10mN m^{-1} on a.c.m.w. subphase

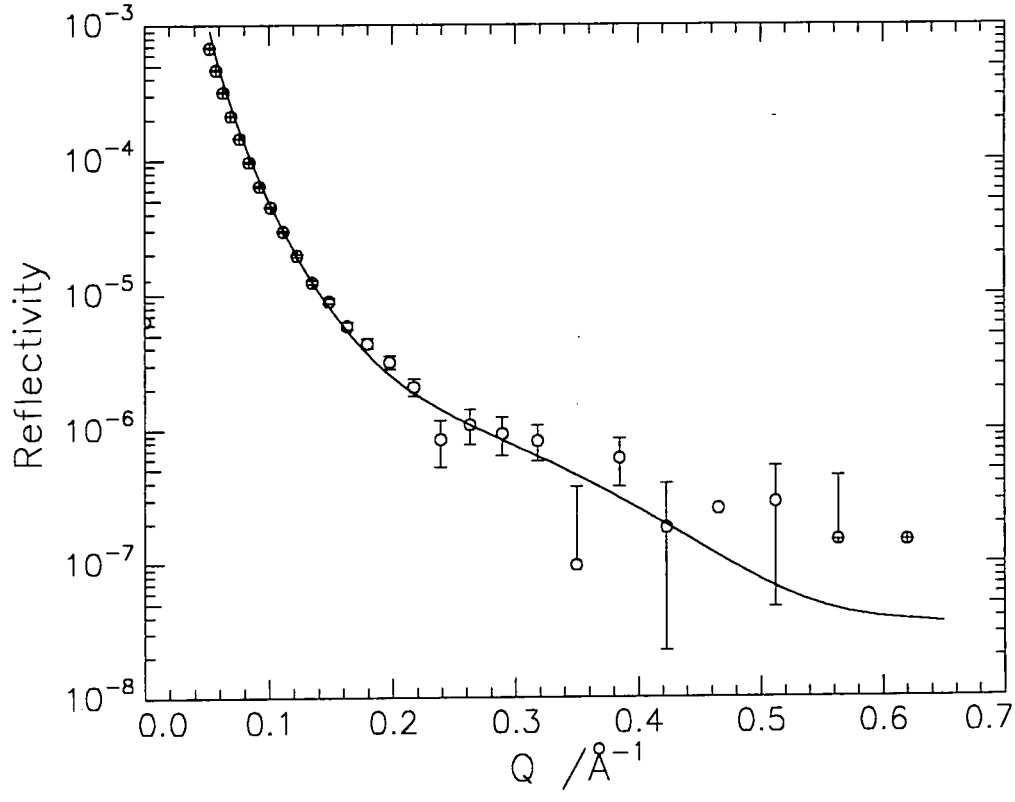

Figure 4.10: Single layer fit to DMDL at 10mN m^{-1} on D_2O subphase

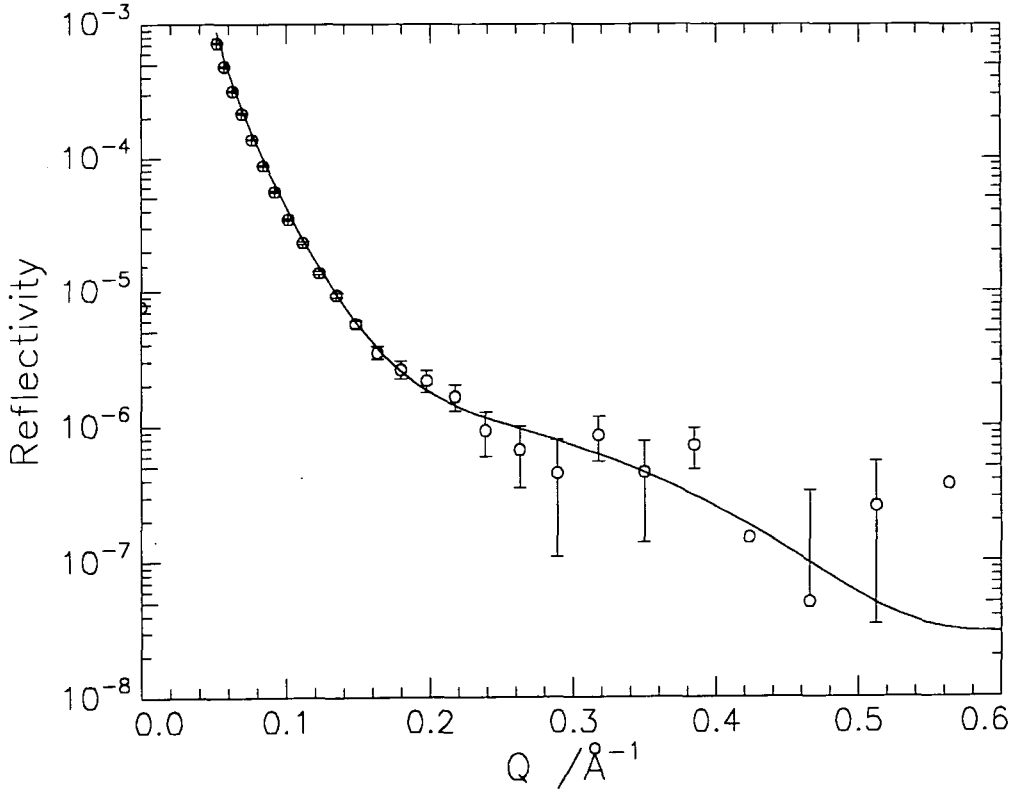

Figure 4.11: Single layer fit to HMDL at 10mN m^{-1} on D_2O subphase

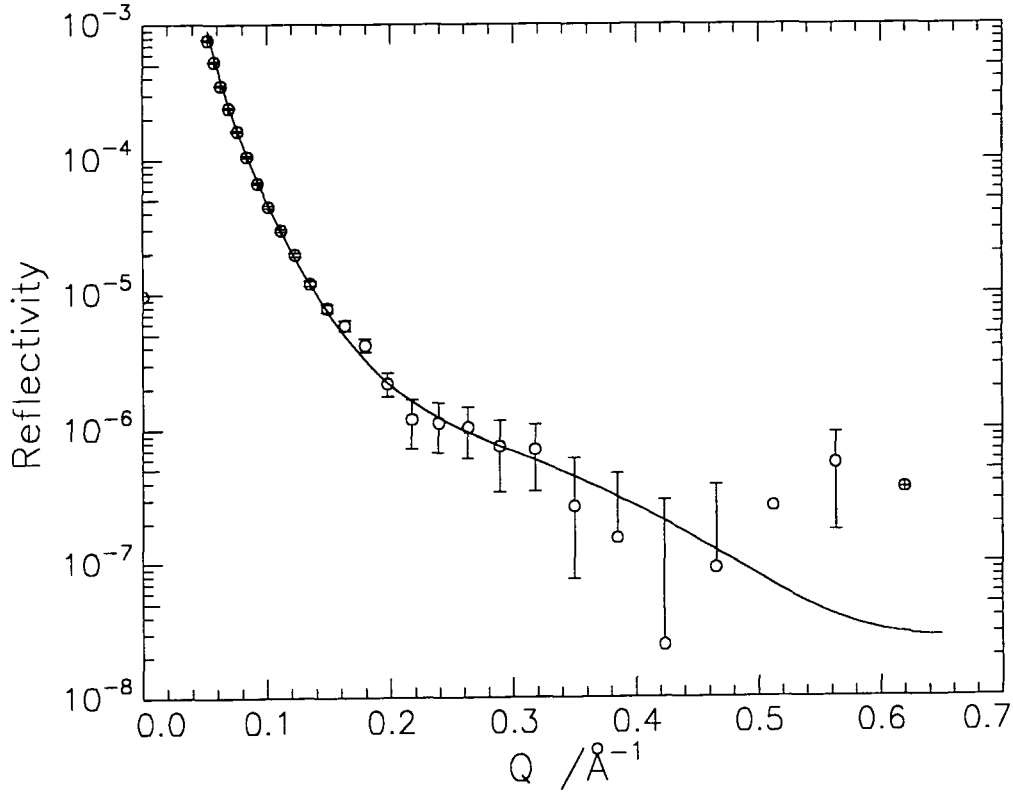

Figure 4.12: Single layer fit to DMHL at 10mN m^{-1} on D_2O subphase

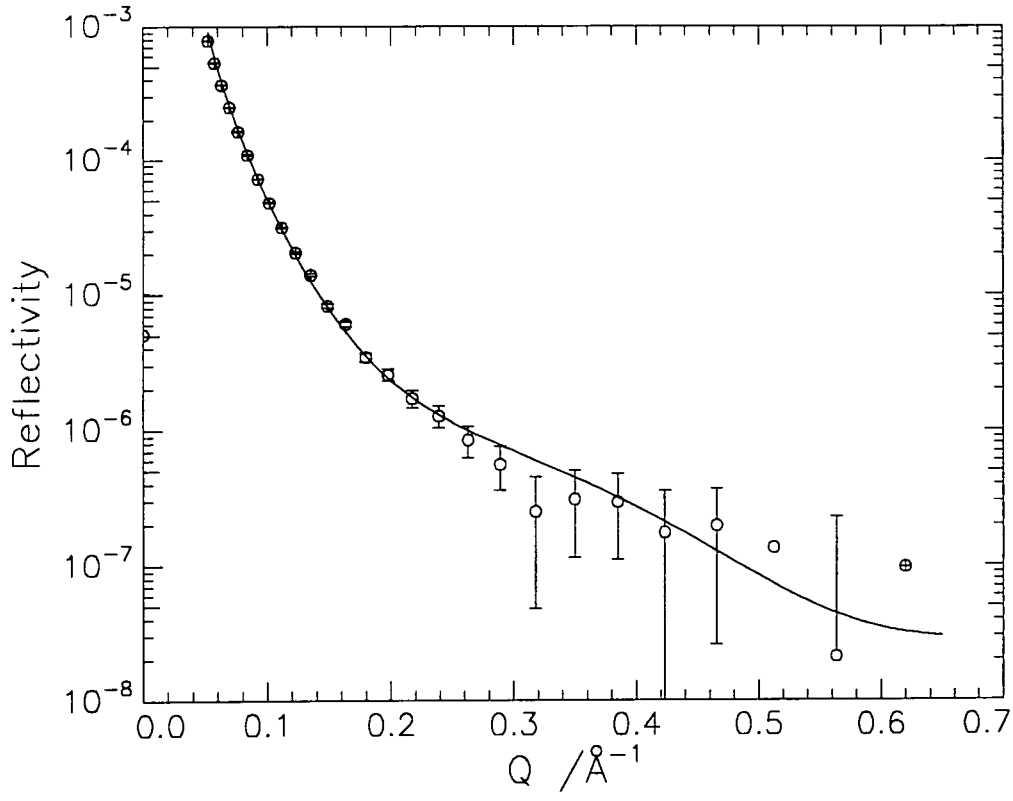

Figure 4.13: Single layer fit to HMHL at 10mN m^{-1} on D_2O subphase

The fits obtained for the polymers on a.c.m.w. subphase deviate from the experimental profiles at Q values of circa 0.2Å^{-1}, whereas on D_2O the fits match the data satisfactorily indicating that on D_2O the interfacial region can be modelled as a single layer. This observation does not mean that the change in subphase has altered the monolayer, it indicates a difference in the nature of the scattering length density profile perpendicular to the interface. On D_2O the monolayer scattering length density profile must resemble a single layer, this could occur if the polymer was mixed homogeneously in the monolayer. However, as this model does not fit the reflectivity data obtained on a.c.m.w., this indicates that the polymer cannot be mixed homogeneously in a single layer, as mentioned in section 4.1, if an assumed model is a good representation of the scattering length density profile it must fit the reflectivity profiles obtained for all isotopic

variations. Therefore, although the scattering length density profile on D_2O must resemble that of a single layer, the polymer components must be segregated into two spatial regions.

Further evidence on the nature of the scattering length density profile on D_2O can be obtained from the values of scattering length density obtained from the fits. The fits were found to be equivalent regardless of whether the high or low values of scattering length density shown in table 4.2 were used. This indicates that not only must the polymer components exist in two spatial regions, the scattering length density profile must resemble that of clean D_2O, hence the monolayer is effectively invisible, therefore, the experimental reflectivity can be fitted with a scattering length density approaching that of air ($\rho = 0$) or that of D_2O ($\rho = 6.35 \times 10^{-6}$ Å^{-2}).

The values of the parameters obtained from the fits to the profiles of the deuterated polymers on a.c.m.w. refer to the polymer only and these are given in table 4.3. As mentioned earlier in section 4.1.1 the values of thickness and scattering length density are coupled and, therefore, the individual values will have a degree of uncertainty. They can, however, be used to calculate the surface concentration using equation 4.16 and then compared to the theoretical surface concentration, calculated from the amount of polymer solution deposited, the solution concentration and the area of the subphase, the comparison of these values is shown in table 4.4.

POLYMER	SURFACE PRESSURE ($mN\ m^{-1}$)	THICKNESS (Å)	ρ ($Å^{-1} \times 10^{-6}$)	ρ ($Å^{-2} \times 10^{-6}$)
DMDL	0.5	19	5.9	0.5
	5.0	22	5.9	0.5
	10.0	18	5.6	0.8
HMDL	0.5	20	5.2	1.1
	5.0	21	5.4	1.0
	10.0	18	5.1	1.2
DMHL	0.5	17	5.5	0.8
	5.0	19	5.5	0.9
	10.0	16	5.5	0.9
HMHL	0.5	20	5.8	0.6
	5.0	21	5.7	0.7
	10.0	16	5.6	0.8

Table 4.2: Thicknesses and scattering length densities from single layer fit of all the polymers on D_2O subphase, the fits were equivalent regardless of which ρ value was used

POLYMER	SURFACE PRESSURE ($mN\ m^{-1}$)	THICKNESS (Å)	ρ ($Å^{-2} \times 10^{-6}$)
DMDL	0.5	16	4.3
	5.0	16	4.6
	10.0	18	4.4
HMDL	0.5	15	3.6
	5.0	17	3.4
	10.0	18	3.4
DMHL	0.5	15	1.8
	5.0	9	1.9
	10.0	11	1.4

Table 4.3: Thicknesses and scattering length densities from single layer fit of deuterated polymers on a.c.m.w. subphase

POLYMER	π (mN m^{-1})	Γ_{EXP} (mg m^{-2})	Γ_{CALC} (mg m^{-2})
DMDL	0.5	1.0	0.9
	5	1.1	1.0
	10	1.2	1.2
HMDL	0.5	1.0	1.0
	5	1.0	1.1
	10	1.1	1.3
DMHL	0.5	2.0	0.9
	5	1.1	1.1
	10	1.1	1.2

Table 4.4: Surface concentrations determined from the fits to the data on a.c.m.w. (Γ_{EXP}) and theoretical calculated surface concentrations (Γ_{CALC})

The values of the surface concentrations are generally in close agreement except for DMHL at 0.5mN m^{-1}, which produced an experimentally determined surface concentration twice that of the theoretical surface concentration. This confirms that there is a problem with this data as can be observed in figure 4.4(c) where the reflectivity profile at 0.5mN m^{-1} is significantly higher than those for the other two pressures. This limits the information that can be obtained at 0.5mN m^{-1} about the polymer organisation to that of the side chains only in the subsequent discussion.

Further evidence that a single layer fit is not valid can be obtained by considering the reflectivity profiles obtained for each polymer on D_2O shown in figures 4.6 (a) to (c). At each surface pressure the profiles are similar to that obtained for D_2O, with HMDL showing the biggest deviation in each case, so for this to occur the scattering length density profile normal to the interface for each polymer spread on D_2O must have a similar distribution to that for a clean D_2O surface, i.e. constant value of 6.35×10^{-6} Å^{-2} in the bulk subphase which decreases sharply at the subphase surface to zero. By

considering the scattering length densities of DMDL and HMHL shown in table 4.1, they could both satisfy this condition as DMDL has a scattering length density similar to that of D_2O and HMHL has a value which is approximately zero, these two situations are shown in figures 4.14 and 4.15. The scattering length density values for DMHL and HMDL produce a step in the interfacial profile of scattering length density (figures 4.16 and 4.17) and would not be expected to produce a reflectivity profile the same as that obtained for D_2O, DMHL would be expected to produce a reflectivity profile which was lower than D_2O and HMDL a profile that was slightly reduced from that of D_2O. These anticipations are made assuming a uniform single layer and the fact that they are not borne out in the experimental profiles supports the view that the polymer components are not homogeneously mixed in the interfacial layer.

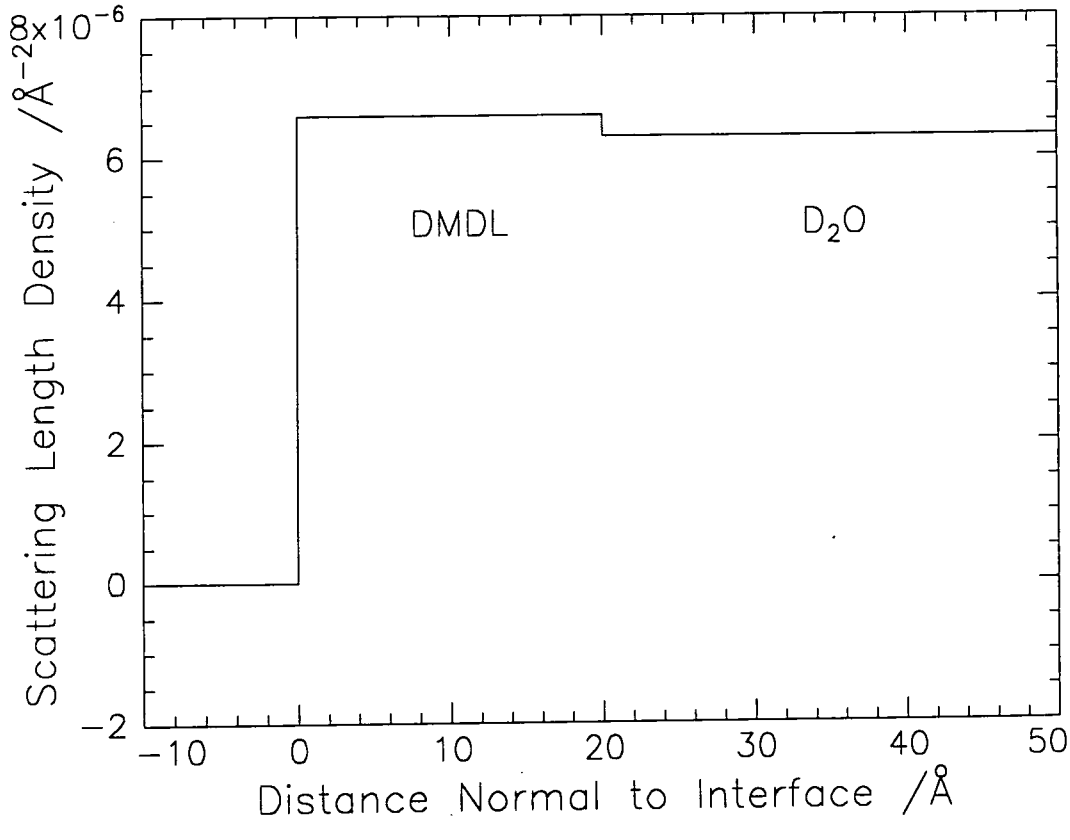

Figure 4.14: Schematic diagram of scattering length density distribution for a single layer model of DMDL on D_2O

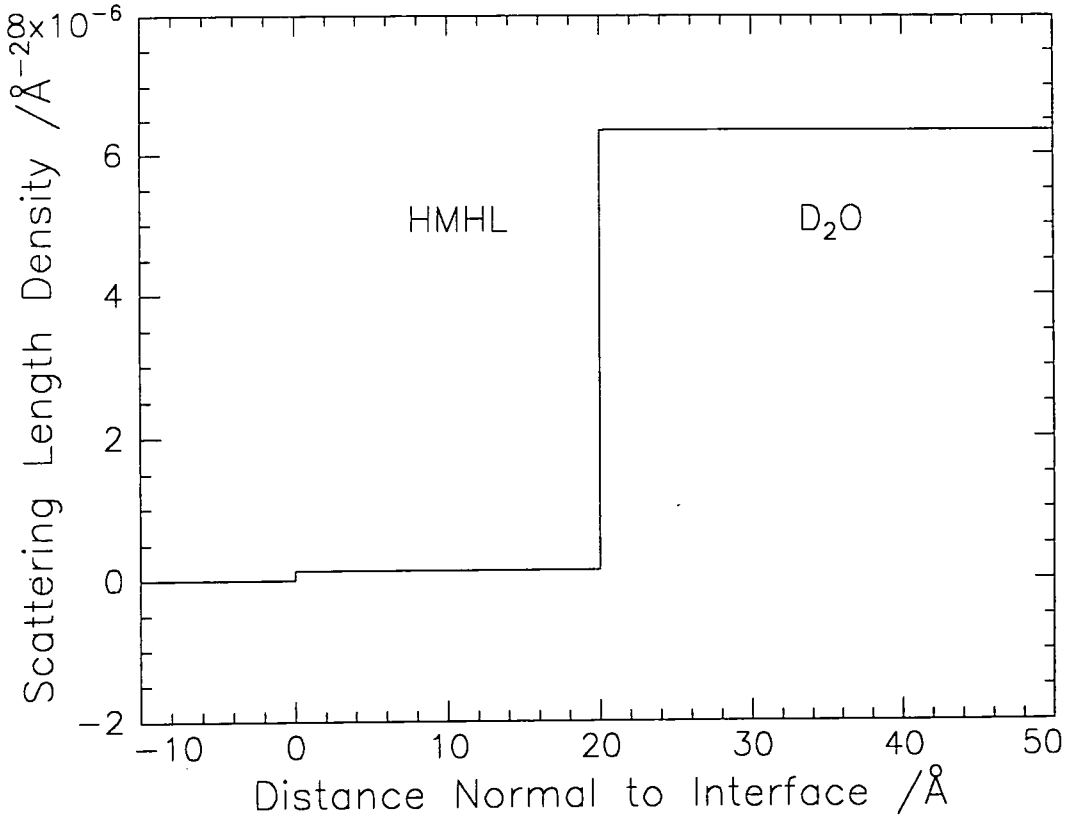

Figure 4.15: Schematic diagram of scattering length density distribution for a single layer model of HMHL on D_2O

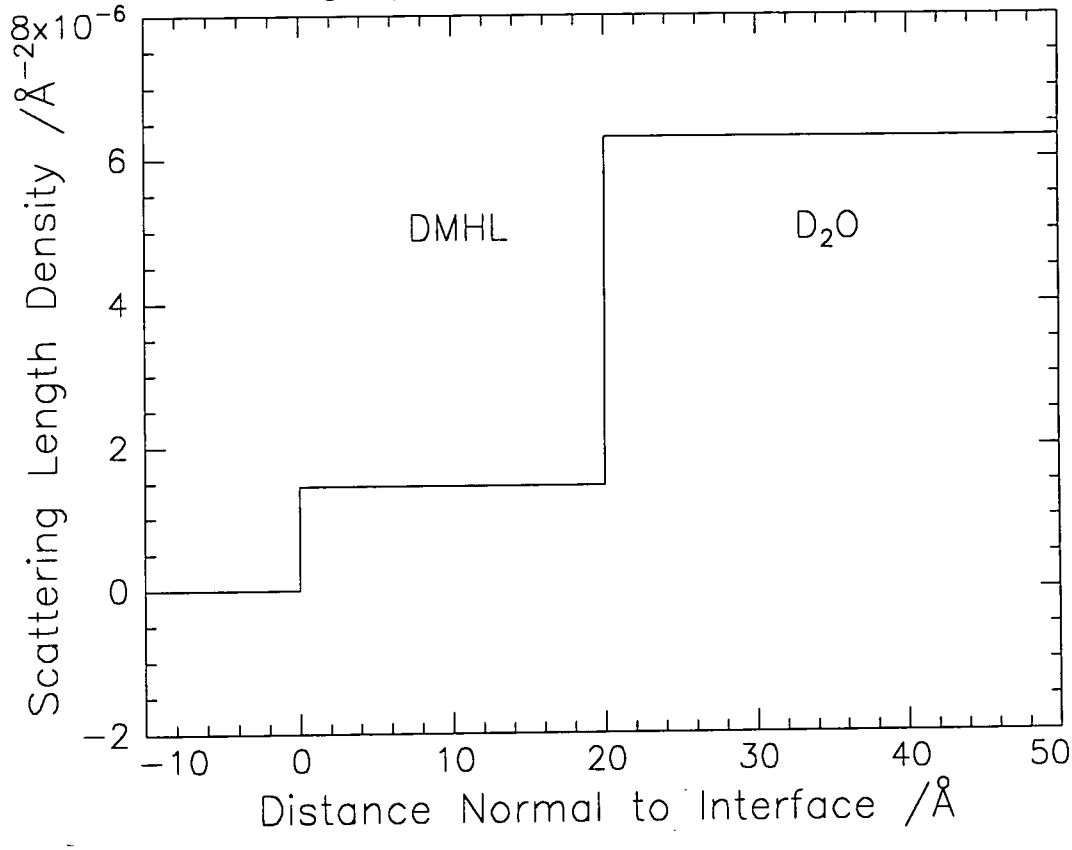

Figure 4.16: Schematic diagram of scattering length density distribution for a single layer model of DMHL on D_2O

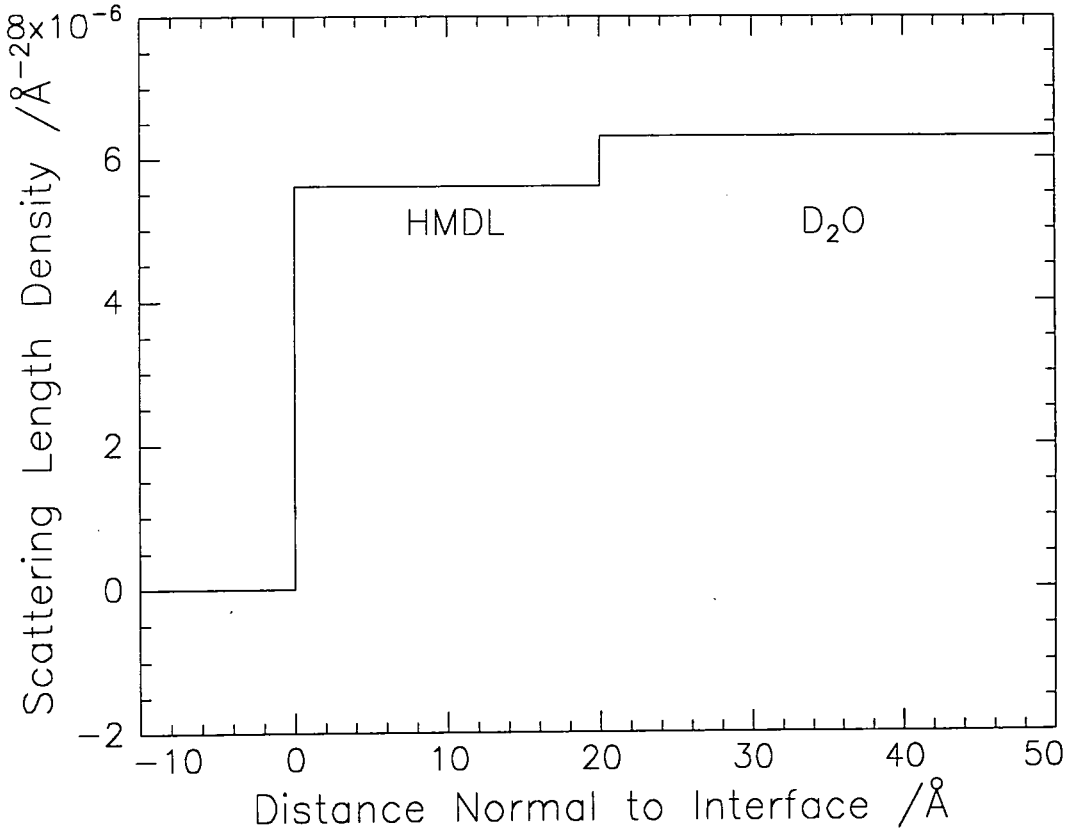

Figure 4.17: Schematic diagram of scattering length density distribution for a single layer model of HMDL on D_2O

As mentioned previously, it is in fact HMDL which produces the greatest deviation from the reflectivity obtained for D_2O and DMHL is little changed from that of D_2O. These observations can be qualitatively accounted for by invoking a two layer model. For DMHL spread on D_2O with the deuterated backbone and hydrogenous side chains occupying different spatial regions, by consideration of the scattering length densities of the component parts of the polymer (DM approaches that of D_2O and HL that of air) a scattering length density distribution at the interface can be achieved similar to that of D_2O as long as the upper layer (i.e. that nearer the air) consists of the hydrogenous side chains, as is shown in figure 4.18.

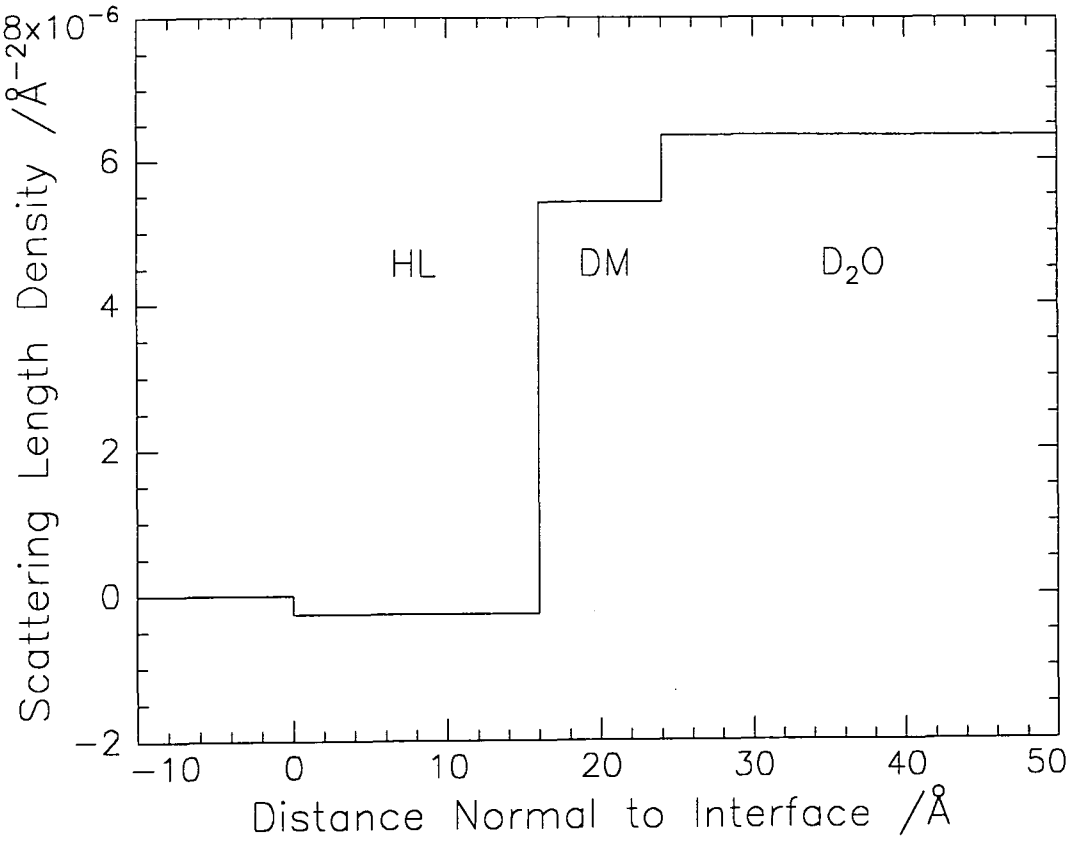

Figure 4.18: Schematic diagram of scattering length density distribution for a two layer model of DMHL on D_2O

Using the assumption that the isotopic substitutions do not alter the structure of the layer, the same positions of the backbone and side chains must persist for HMDL spread on D_2O. This would result in the scattering length density profile shown in figure 4.19 and it can be observed that there is a big trough in the scattering length density distribution which results in a vastly different reflectivity profile, which is shown in figure 4.20 compared to that calculated for DMHL using the model shown in 4.18 and for a sharp D_2O interface.

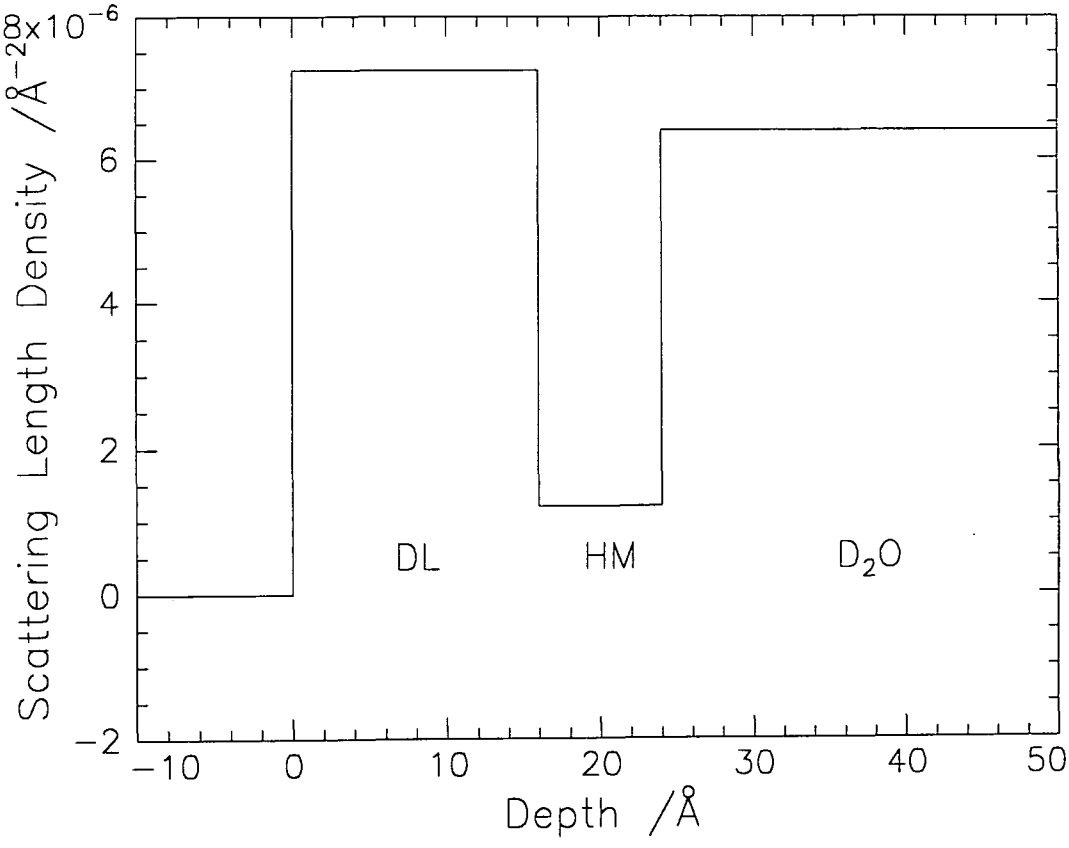

Figure 4.19: Schematic diagram of scattering length density distribution for a two layer model of HMDL on D_2O

From figure 4.20 it is clear that at low Q it is not possible to distinguish between the reflectivities of clean D_2O and DMHL spread on D_2O, which corresponds to the experimental situation shown in figures 4.6(a) to (c), indicating that the model used in figure 4.18 could be a reasonable one, however, the reflectivity calculated for HMDL using the same model proves that it can not be such a simple situation. The results of the single layer fits on a.c.m.w. indicate that the monolayer is penetrated by subphase as the scattering length densities obtained are reduced from the values calculated for each monomer unit due to the presence of a.c.m.w. which has a scattering length density of zero. Assuming that the same is true for a D_2O subphase, then the penetration of the monolayer will result in an increase in the scattering length density of the layer and hence the trough in the scattering length density profile will not be as deep as that shown in

figure 4.19, resulting in a scattering length density profile similar to that of D_2O, shown in figure 4.21. Also, the interfaces between the components at the surface will not be as sharp as the models shown here which will smooth the reflectivity profile considerably and no minima will be present.

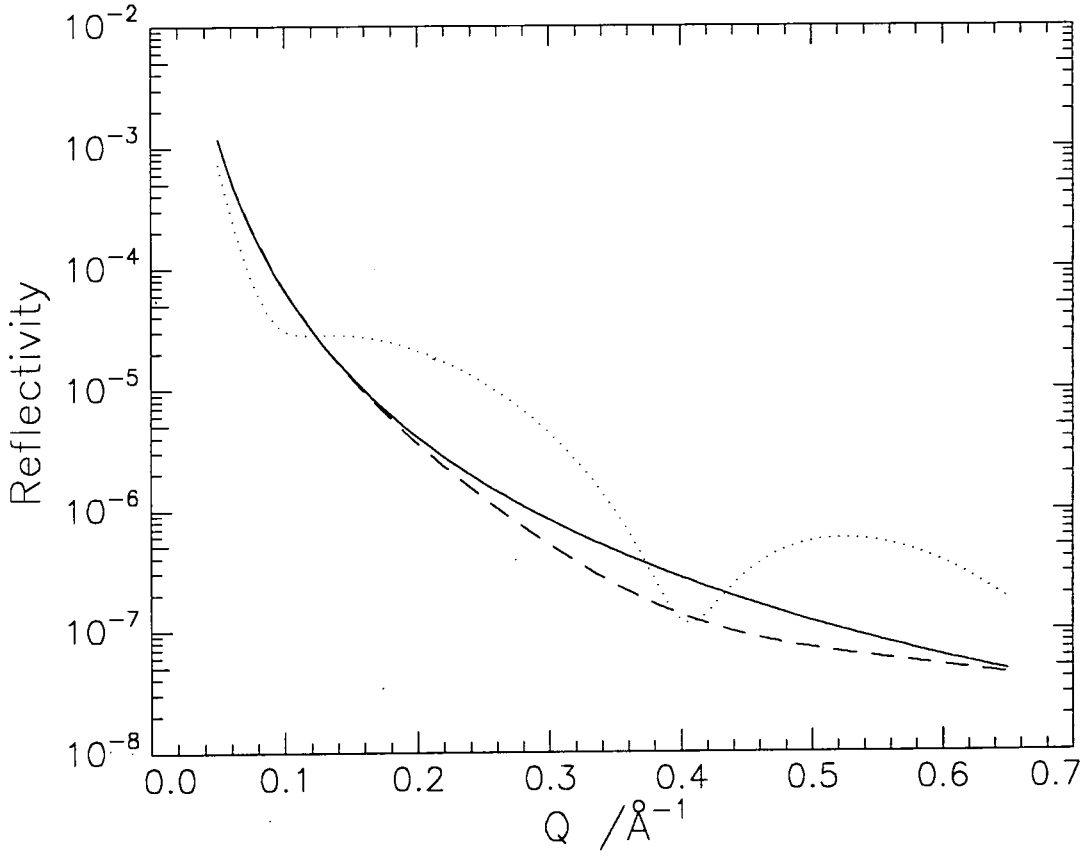

Figure 4.20: Reflectivity profiles calculated for D_2O (—), DMHL(– –) and HMDL (····) using the scattering length density profiles shown in figures 4.18 and 4.19

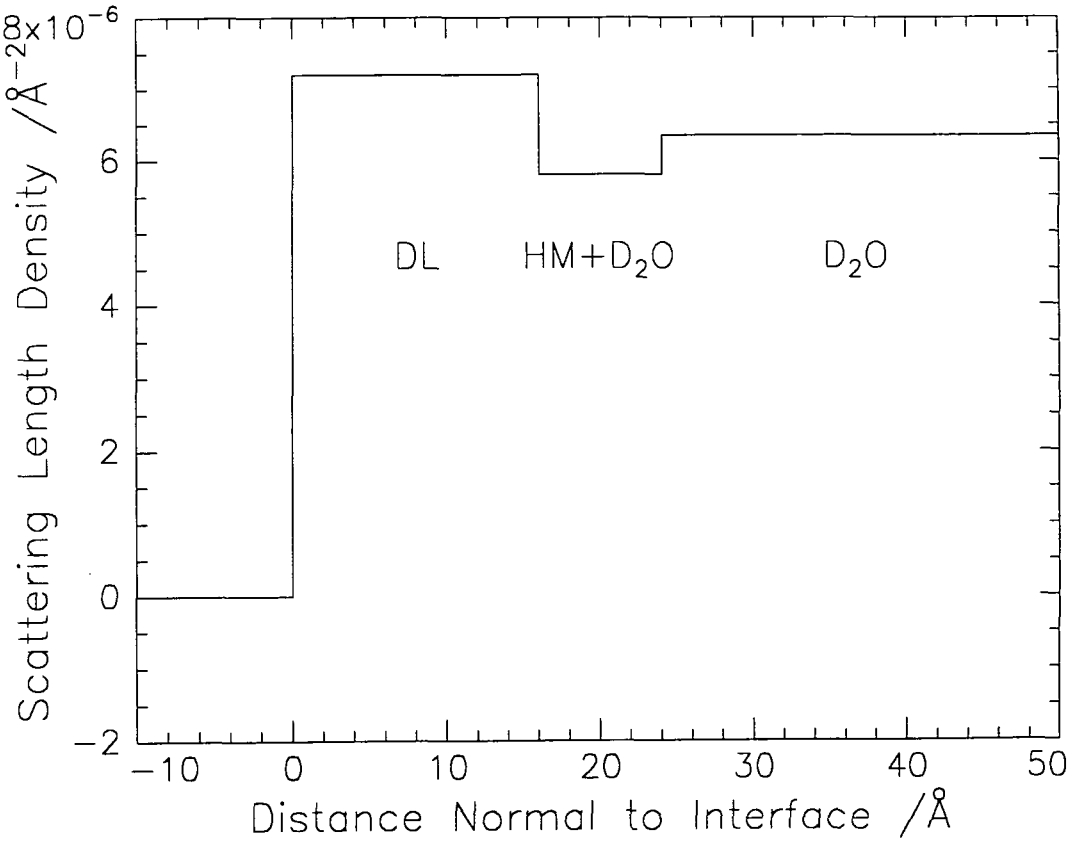

Figure 4.21: Schematic diagram of scattering length density distribution for a two layer model of HMDL on D_2O with penetration of the layer by D_2O

The picture so far of the polymer organisation at the air - water interface is that it arranges itself with the side chains closer to the air and the methacrylate backbone closer to the subphase, which may penetrate the layer. It also appears that the side chains and backbone do not occupy totally separate regions of space normal to the interface and there is a finite extent of intermixing between them.

A two layer model would seem to be a more realistic one than the single layer model and this has been used to fit the reflectivity profiles. All of the parameters were constrained to particular values and manually adjusted until the best fit was obtained. Examples of the fits obtained are shown in figures 4.22 to 4.28 and the values obtained for the thicknesses and scattering length densities of each layer are given in tables 4.5 and 4.6.

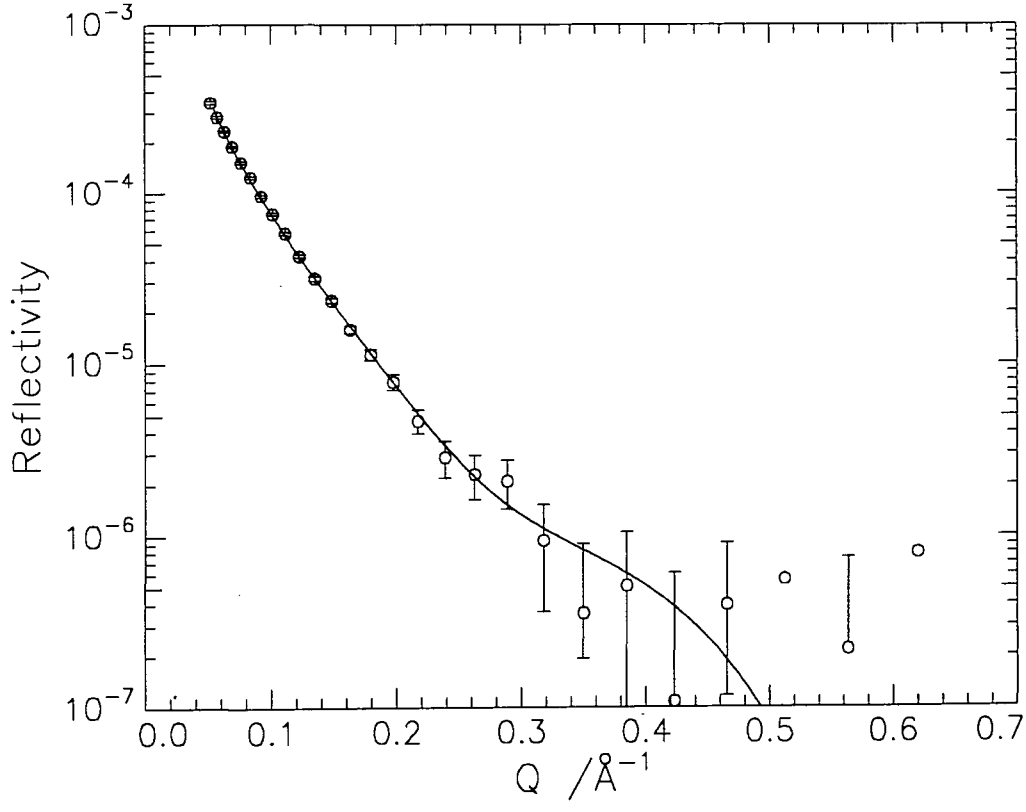

Figure 4.22: Two layer fit to DMDL at 10mN m^{-1} on a.c.m.w. subphase

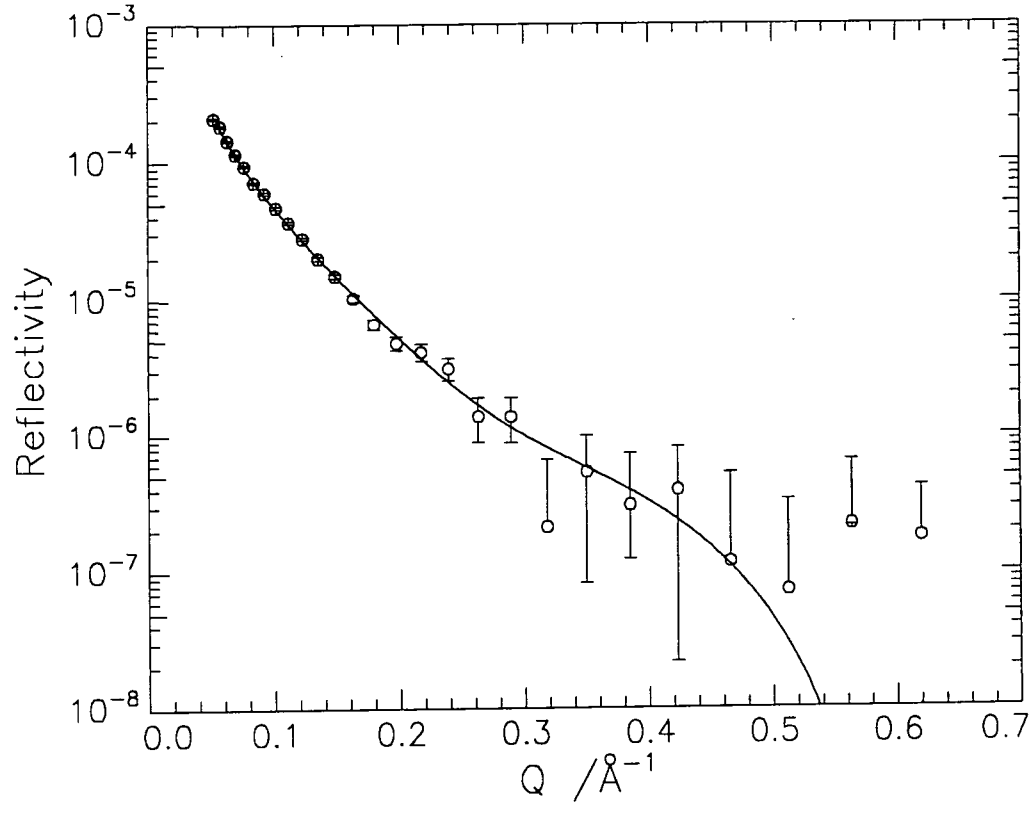

Figure 4.23: Two layer fit to HMDL at 10mN m^{-1} on a.c.m.w. subphase

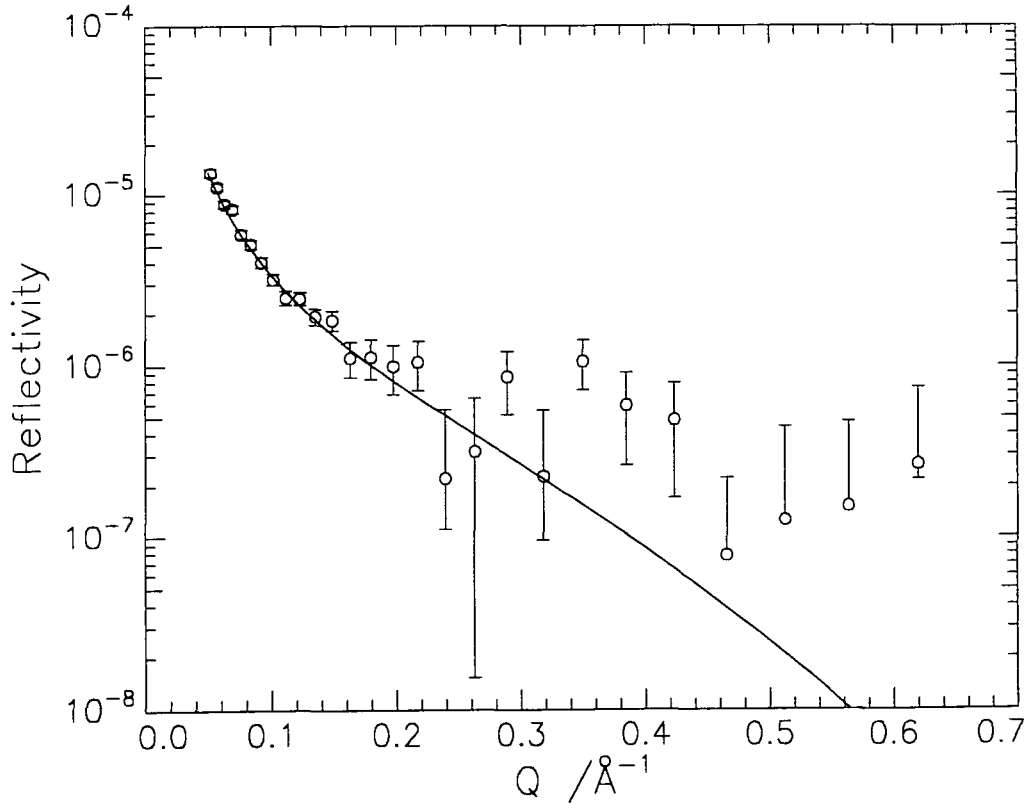

Figure 4.24: Two layer fit to DMHL at 10mN m^{-1} on a.c.m.w. subphase

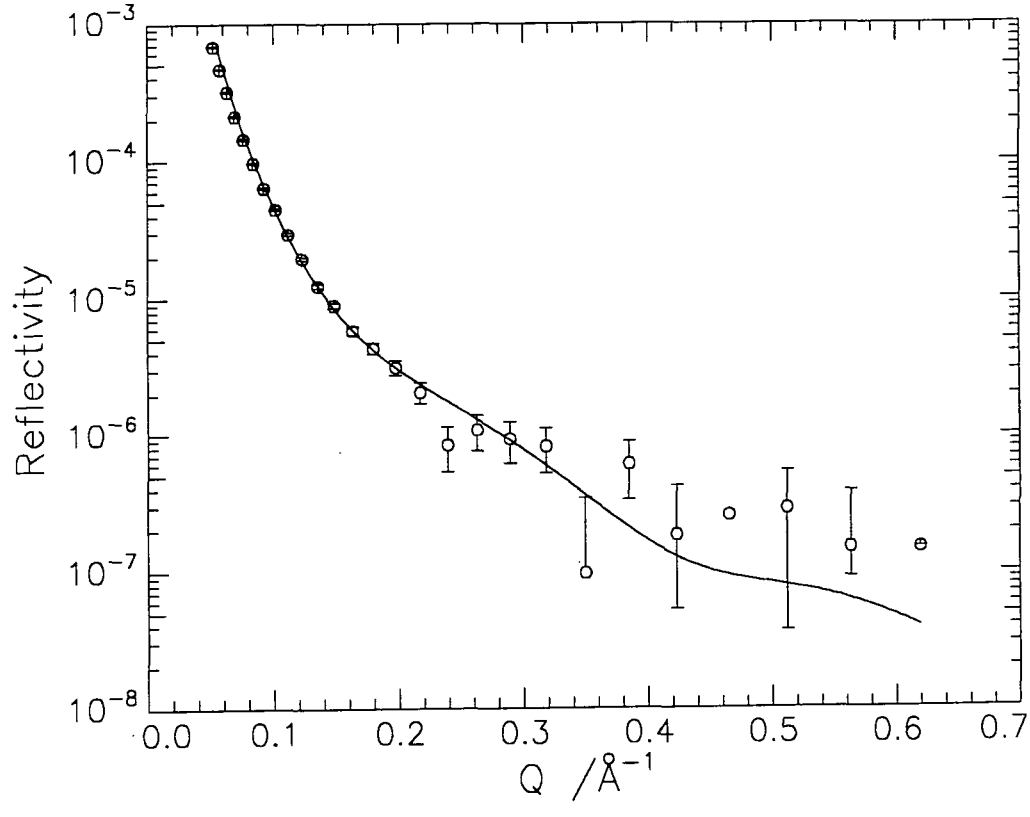

Figure 4.25: Two layer fit to DMDL at 10mN m^{-1} on D_2O subphase

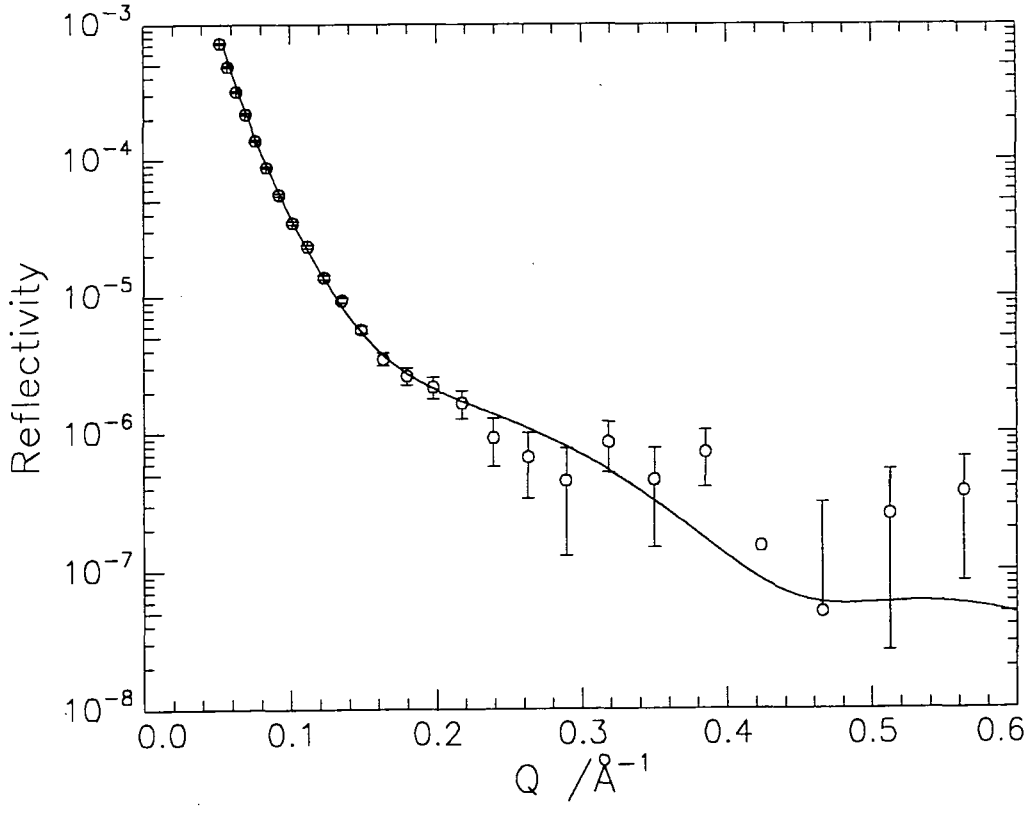

Figure 4.26: Two layer fit to HMDL at 10mN m^{-1} on D_2O subphase

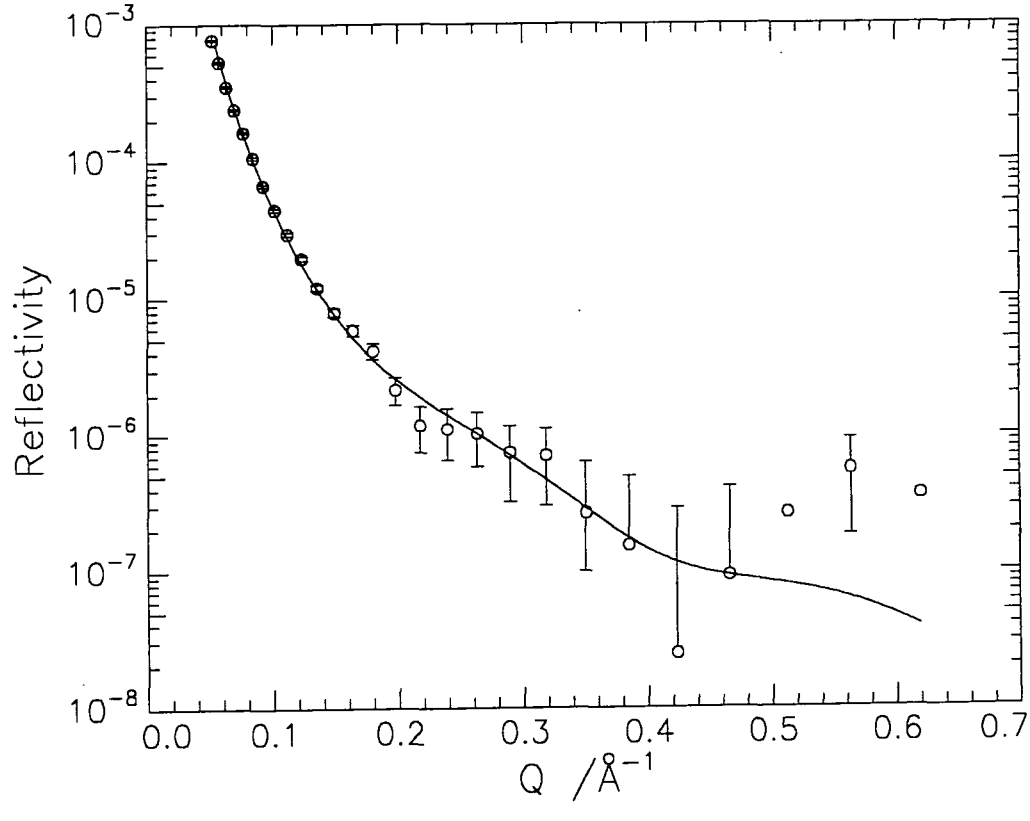

Figure 4.27: Two layer fit to DMHL at 10mN m^{-1} on D_2O subphase

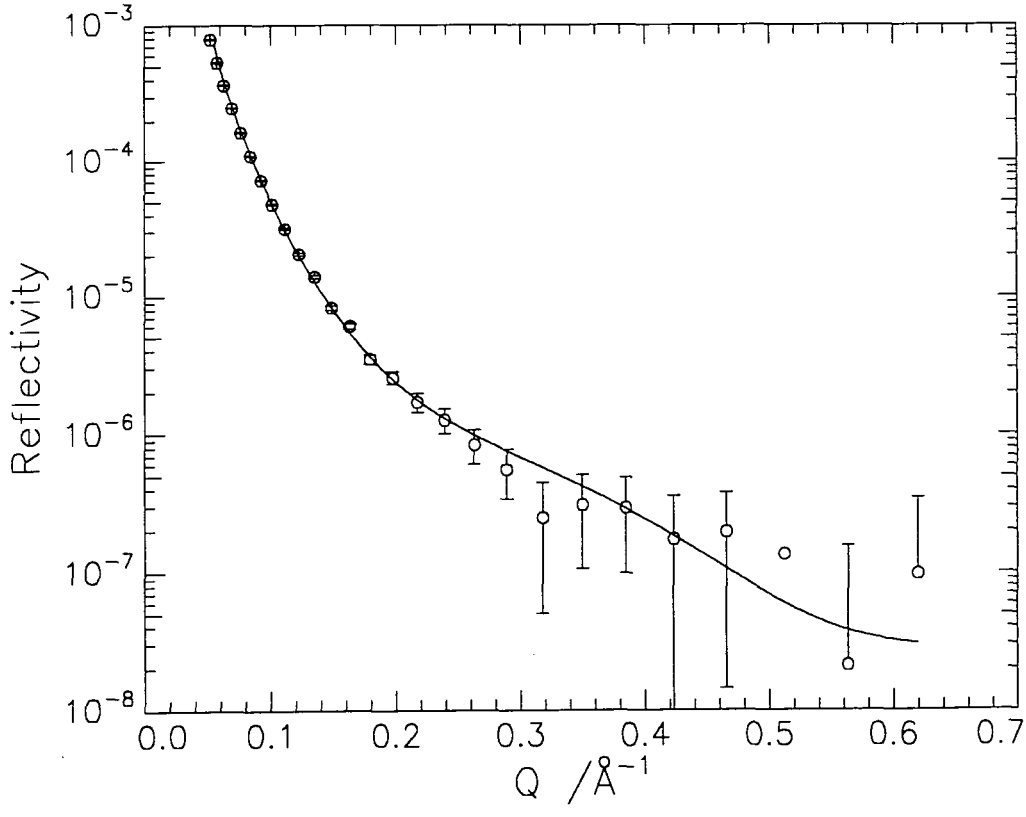

Figure 4.28: Two layer fit to HMHL at 10mN m^{-1} on D_2O subphase

		LAYER 1		LAYER 2	
POLYMER	**π (mN m^{-1})**	**THICKNESS (Å)**	**ρ (Å^{-2} ×10^{-6})**	**THICKNESS (Å)**	**ρ (Å^{-2} ×10^{-6})**
DMDL	0.5	10	5.0	9	2.5
	5.0	10	6.0	10	2.0
	10.0	11	5.7	11	1.7
HMDL	0.5	8	5.0	10	1.5
	5.0	9	5.9	12	1.3
	10.0	11	4.7	11	1.1
DMHL	5.0	9	-0.2	9	2.5
	10.0	11	-0.1	10	1.8

Table 4.5: Thicknesses and scattering length densities from two layer fit of deuterated polymers on a.c.m.w. subphase

		LAYER 1		LAYER 2	
POLYMER	π (mN m^{-1})	**THICKNESS** (Å)	ρ (Å^{-2} $\times 10^{-6}$)	**THICKNESS** (Å)	ρ (Å^{-2} $\times 10^{-6}$)
DMDL	0.5	11	6.0	11	5.9
	5.0	11	6.0	11	5.8
	10.0	11	5.7	11	5.7
HMDL	0.5	12	5.1	12	5.5
	5.0	12	5.3	12	5.6
	10.0	10	5.1	11	5.3
DMHL	0.5	11	5.7	10	5.8
	5.0	10	5.4	10	5.5
	10.0	10	5.5	10	5.7
HMHL	0.5	11	5.7	11	5.8
	5.0	10	5.5	11	5.8
	10.0	12	5.4	10	6.0

Table 4.6: Thicknesses and scattering length densities from two layer fit of all polymers on D_2O subphase

The two layer model produces visibly better fits to the reflectivity profiles obtained on a.c.m.w. compared to the fits obtained using the single layer model. As the two layer model fits the data obtained on D_2O and a.c.m.w. subphases it is a better approximation of the distribution of the polymer at the interface. The parameters obtained from the a.c.m.w. fits are far more informative than those obtained for the polymers spread on D_2O, which show little or no variation as they all have a scattering length density profile similar to that for a clean D_2O subphase. By considering the parameters obtained for DMHL spread on a.c.m.w. it can be concluded that layer 1 primarily contains the lauryl side chains as a negative scattering length density is obtained, however, the value is slightly more positive than would be expected for a pure

hydrogenous layer. This increase in scattering length density may be due to the presence of subphase and/or backbone in the same spatial region as the side chains. Since the likelihood of having a sharp interface between the backbone and side chain regions is small, this argues for the partial mixing of the two components. From the scattering length densities obtained for DMDL spread on a.c.m.w. it is evident that layer 1 (the side chain layer) must contain a proportion of subphase since the fitted scattering length density is less than that of the pure deutero lauryl substituent. Furthermore, it is evident from the fitted scattering length density for layer 2 (the backbone layer) that this layer contains an appreciable quantity of subphase because the scattering length density is much reduced from that calculated for the deuterated methacrylate component. Similar considerations can be used to account for the fitted value obtained for the scattering length density of layer 1 for HMDL spread on a.c.m.w. as for DMDL, whereas for layer 2 the value obtained for the hydrogenous methacrylate group is little changed from the value calculated for this component (1.2×10^{-6} Å^{-2}). This is presumably due to mixing of the layers, with the deuterated side chains penetrating the hydrogenous backbone region and raising the scattering length density of the layer, compensating for the decrease caused by penetration of the backbone layer with subphase. This process of breaking the near surface layer up into a number of lamella regions of varying composition and thickness could be continued to provide a complete description of the spread polymer film. However, for more layers the procedure becomes extremely lengthy and each additional feature must be tested for self consistency by ensuring that when applied to each combination of polymer and subphase, the results obtained in terms of layer thickness and composition are in agreement with each other. Furthermore, with the parameters for each layer being coupled, the more layers that are used introduces greater uncertainty in each value obtained from the fits. At this point attention turns to the use

of the kinematic approximation and partial structure factors to obtain a more direct picture of the polymer organisation at the interface.

As mentioned in section 4.1.2, six partial structure factors are determined by using six different contrast conditions and then these are used to determine the polymer organisation at the interface and in addition to providing the thickness of each near surface layer, the partial structure factors also provide the separation between each layer via the cross partial structure factors. Initially the uniform layer models of the polymer components (equation 4.33) and the interfacial water layer (equation 4.39) were non - linearly least squares fitted the experimentally obtained self partial structure factors to obtain the layer thicknesses and number densities. Examples of the fits obtained are shown in figures 4.29 to 4.31 and the parameters obtained are shown in table 4.7.

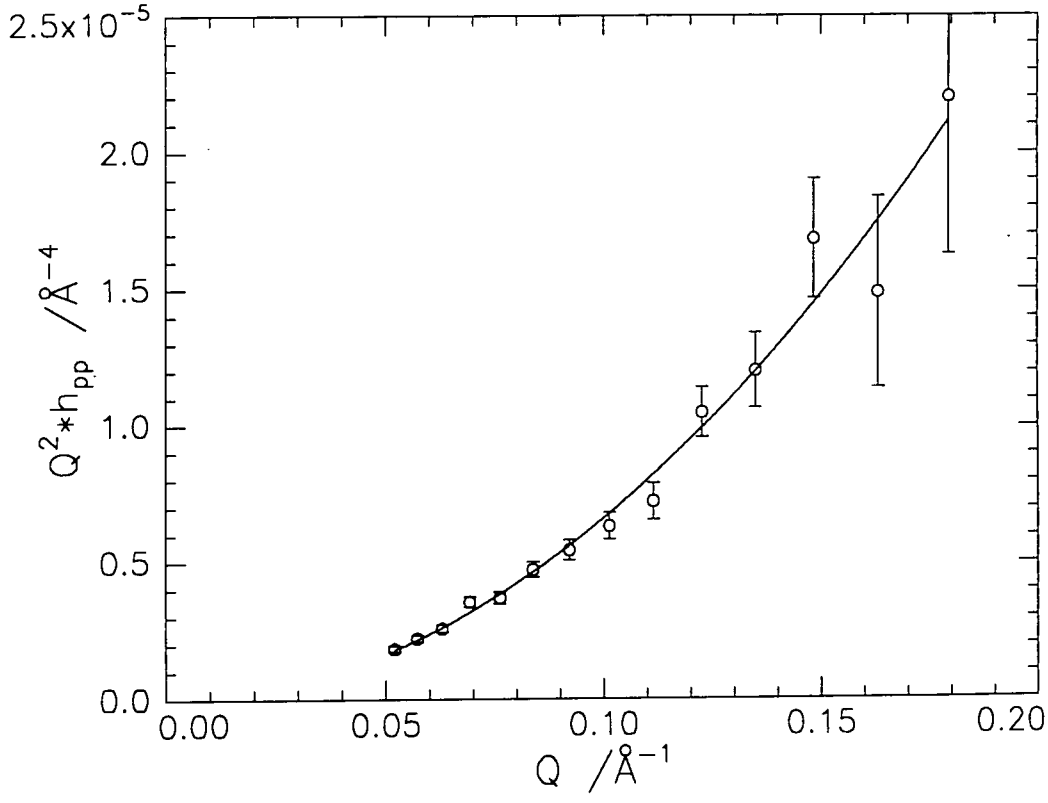

Figure 4.29: Self partial structure factor for the backbone at 10mN m^{-1} fitted using the uniform layer model

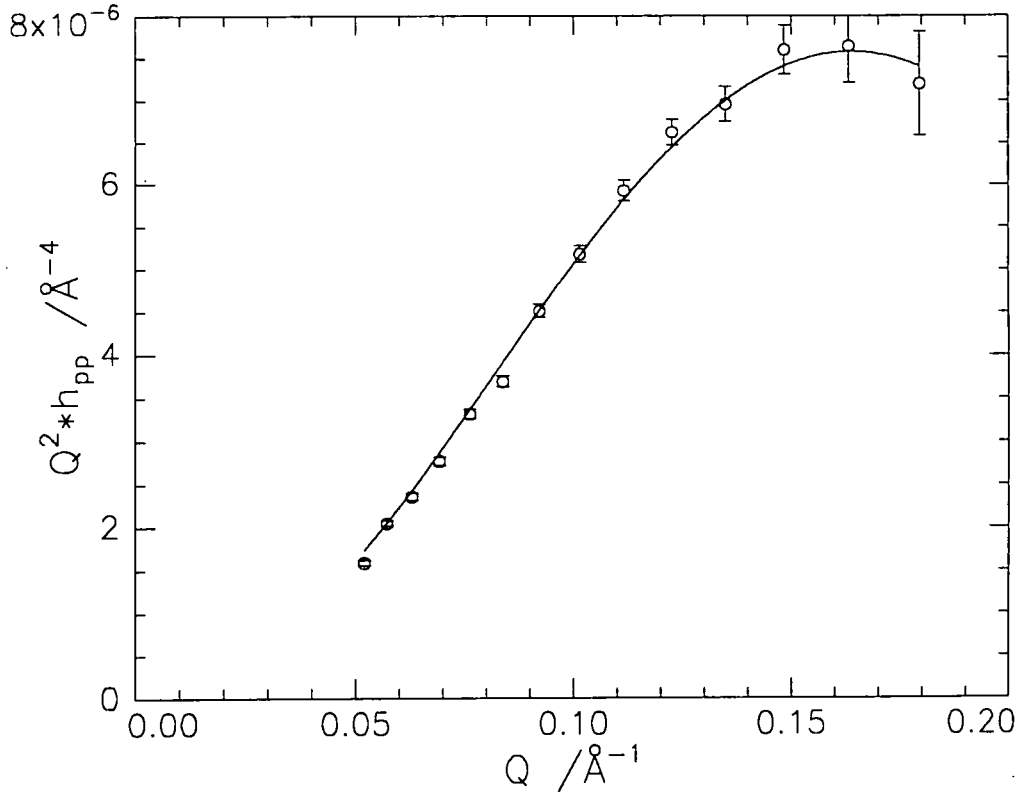

Figure 4.30: Self partial structure factor for the side chains at 10mN m^{-1} fitted using the uniform layer model

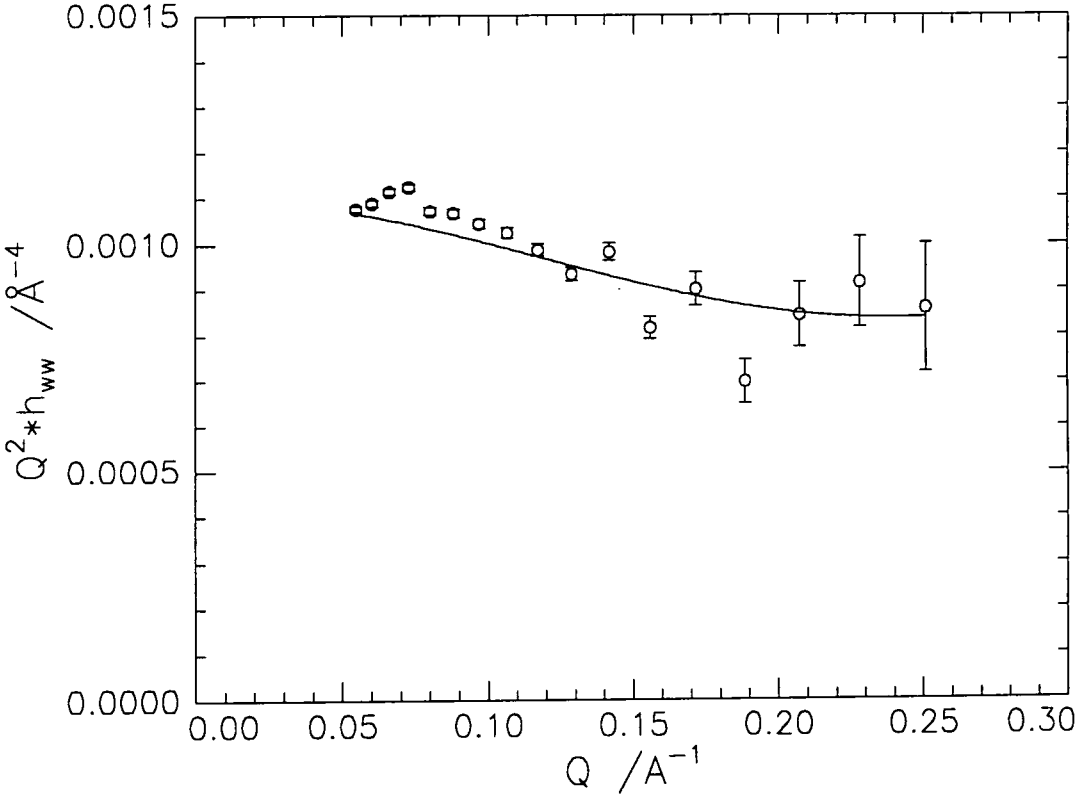

Figure 4.31: Self partial structure factor for the subphase at 10mN m^{-1} fitted using the uniform layer model

π /mN m^{-1}	n_{b1} /10^{-3}Å^{-3}	d_b /Å	n_{c1} /10^{-3} Å^{-3}	d_c /Å	n_{w1} /10^{-3} Å^{-3}	d_w /Å
0.5	–	–	1.4	16	2.0	13
5.0	4.0	8	1.5	15	2.2	13
10.0	3.6	8	1.4	18	2.1	12

Table 4.7: Parameters obtained from uniform model fits of the self partial structure factors

Using equations 4.43 and 4.44, the separation between the centres of each distribution can be determined and examples of the fits of the calculated cross partial structure factor compared to the experimentally determined cross terms are shown in figures 4.32 to 4.34.

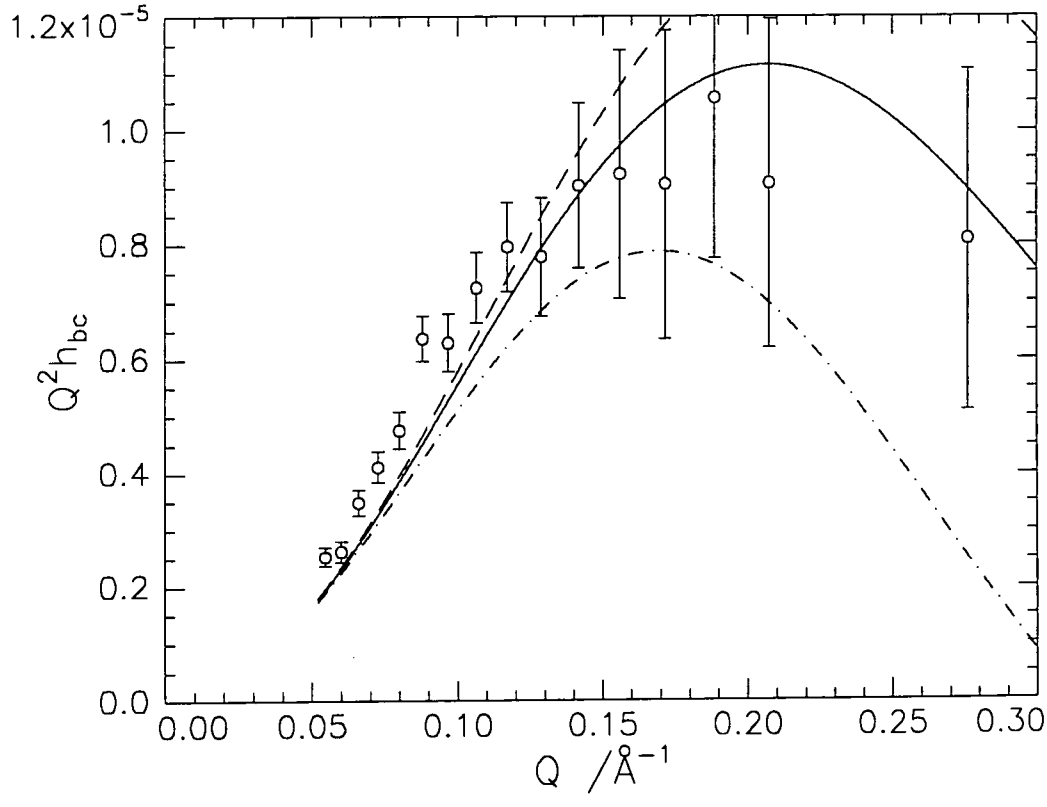

Figure 4.32: Cross partial structure factor for backbone and side chains at 10mN m^{-1}, experimental data (o) and lines are calculated cross terms with different δ, δ = 1Å (– –), δ = 3Å (—), δ = 5Å (– · –)

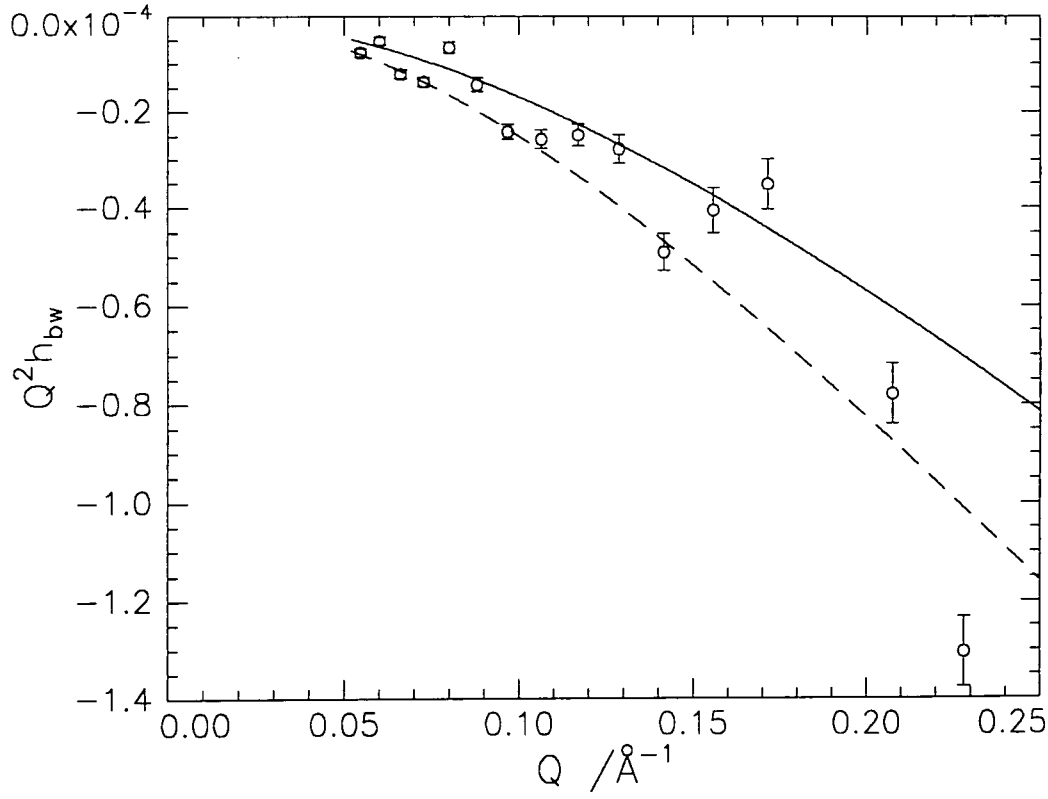

Figure 4.33: Cross partial structure factor for backbone and subphase at 10mN m^{-1}, experimental data (o) and lines are calculated cross terms with different δ, δ = 2Å (—), δ = 4Å (– –)

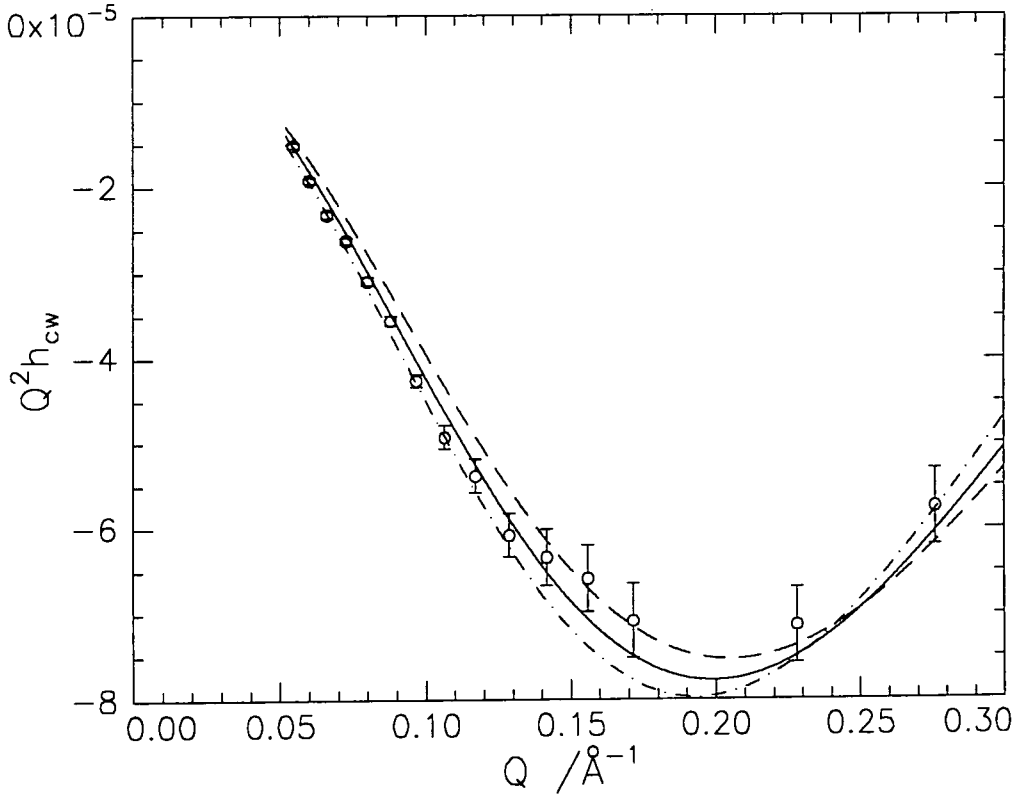

Figure 4.34: Cross partial structure factor for side chains and subphase at 10mN m^{-1}, experimental data (o) and lines are calculated cross terms with different δ, δ = 5.5Å (– –), δ = 6 Å (—), δ = 6.5 Å (– · –)

The cross terms involving the backbone produce more scattered data and less certainty in the value of δ obtained. This is due to the lower reflectivity and poorer signal to noise ratio obtained for DMHL spread on a.c.m.w. which provides the experimental data to allow the backbone self term to be calculated. From the range of values of δ used in the fits, the approximate separations obtained are given in table 4.8.

	SEPARATION /Å		
π (mN m^{-1})	BACKBONE / SIDE CHAIN	BACKBONE / WATER	SIDE CHAIN / WATER
0.5	–	–	6
5.0	3	3	6
10.0	3	3	6

Table 4.8: Separations obtained using uniform layer model for self terms in equations 4.42 and 4.43

Using the values obtained from the self partial structure factors combined with the separations obtained from the cross partial structure factors, it is possible to draw a diagram of the distribution of each component at the interface and this is shown in figure 4.35 at a surface pressure of 10mN m^{-1}. Only this pressure is shown, as from an inspection of the parameters obtained, no change in the positions of the components occurs as the surface pressure changes and the change in the number density of the backbone can not be relied upon due to the poor data quality, resulting in a poor fit and, therefore, uncertainty in the resulting values. The increase in side chain thickness appears to be the only reliable change and is probably due to a slight straightening of the side chains as the monolayer is compressed.

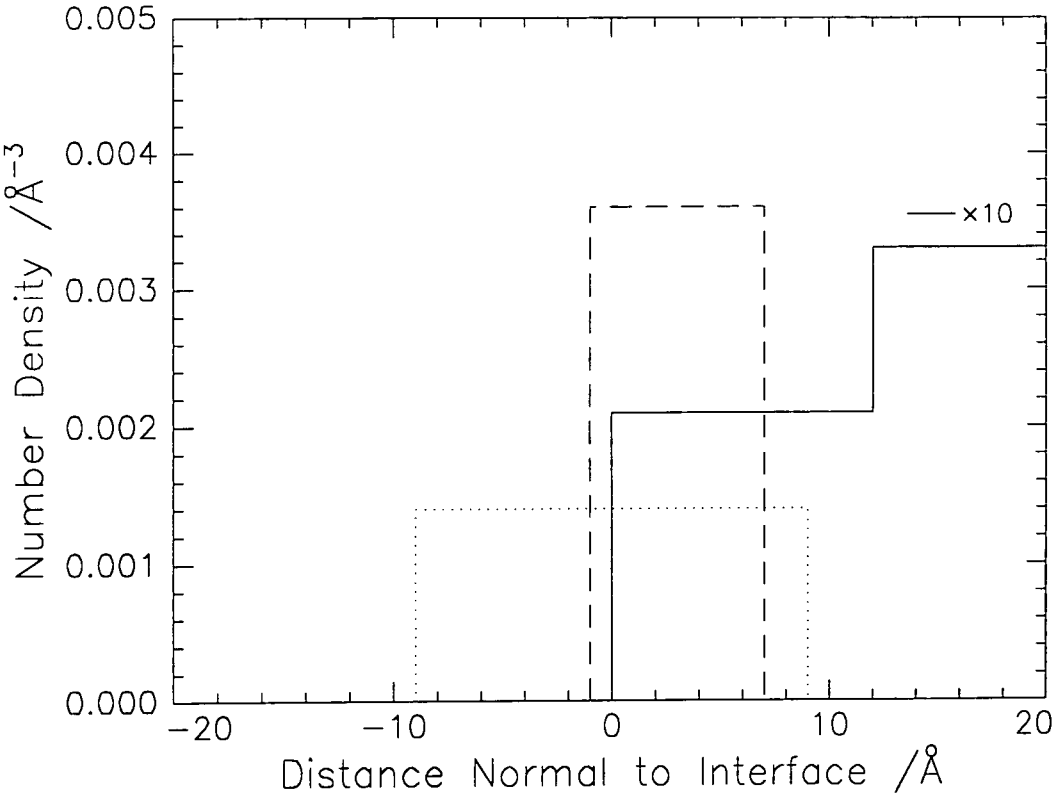

Figure 4.35: Component density distributions predicted by a uniform layer model for the polymer components (···· side chains and – – backbone) and a tanh model for the interfacial subphase region (—)

The uniform layer models of the interfacial components provides an approximate idea as to the positions and distributions of each species, however, it is a fairly unrealistic picture, with the assumption that the density of each component is the same at each point across its distribution. A more realistic description would be to have a more gradual change in the density of the polymer components across the interface, likewise, the change in subphase number density at the interface is more likely to be a gradual change, rather than a step down to a constant level and then down to zero in the air phase. This implies that the use of the Gaussian distribution for the polymer components and the hyperbolic tangent distribution for the interfacial water layer may produce a more realistic picture of the interface.

If a Gaussian model is valid then equation 4.36 can be rearranged to give

$$\ln h_{ii}(Q) = \ln\left(n_{i1}^2 \frac{\pi\sigma^2}{4}\right) - \frac{Q^2\sigma^2}{8} \qquad 4.45$$

and for such a Gaussian distribution the area per molecule at the surface, A, is $2 / (\sigma\, n_{i1}\, \pi^{1/2})$, hence

$$h_{ii}(Q) = A^{-2} \exp(-Q^2\, \sigma^2 / 8) \qquad 4.46$$

hence a plot of ln $h_{ii}(Q)$ as a function of Q^2 (a Guinier plot) should be linear with a slope of $-\sigma^2/8$ and an intercept of -2lnA. A plot of the partial structure factor data at 10mN m^{-1} for the backbone and side chain according to equation 4.46 is shown in figure 4.36.

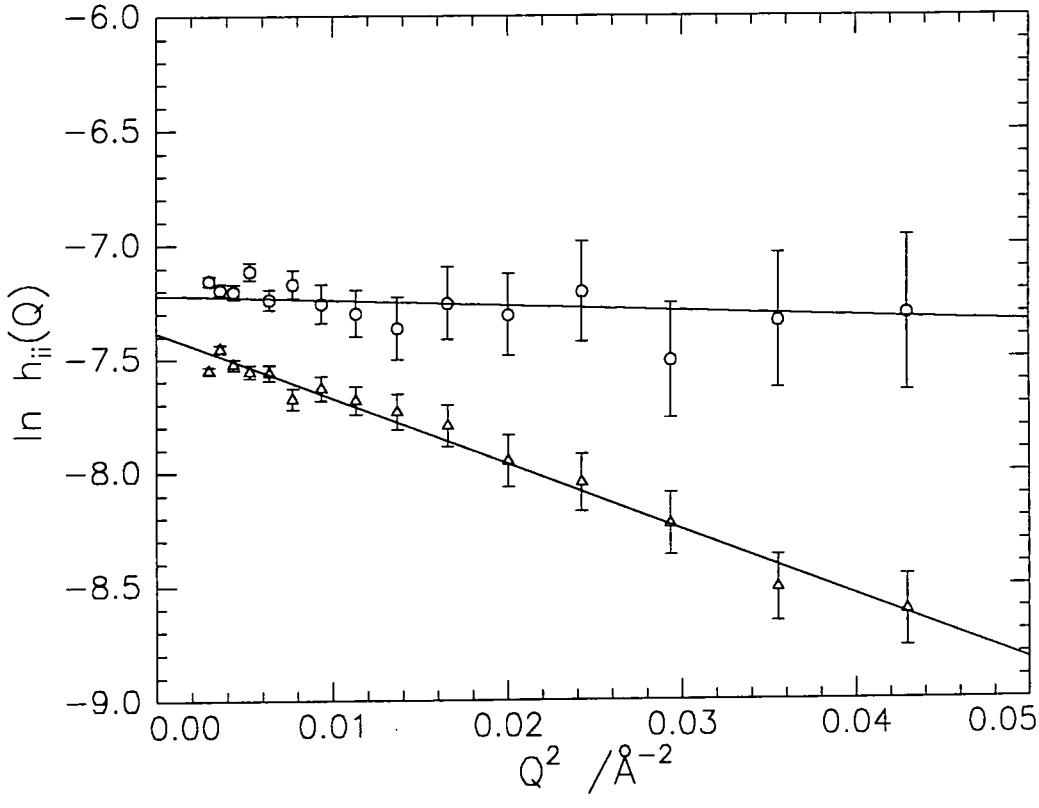

Figure 4.36: Guinier plots of the self partial structure factors of the backbone (o) and side chains (Δ)

Similar plots were obtained for the other surface pressures and they are clearly linear. Equation 4.36 can also be non - linearly least squares fitted to the self partial structure factors with n_{il} and σ as the adjustable fitting parameters in an analogous process to that carried out for the uniform layer model. Examples of the resulting fits are shown in figures 4.37 and 4.38.

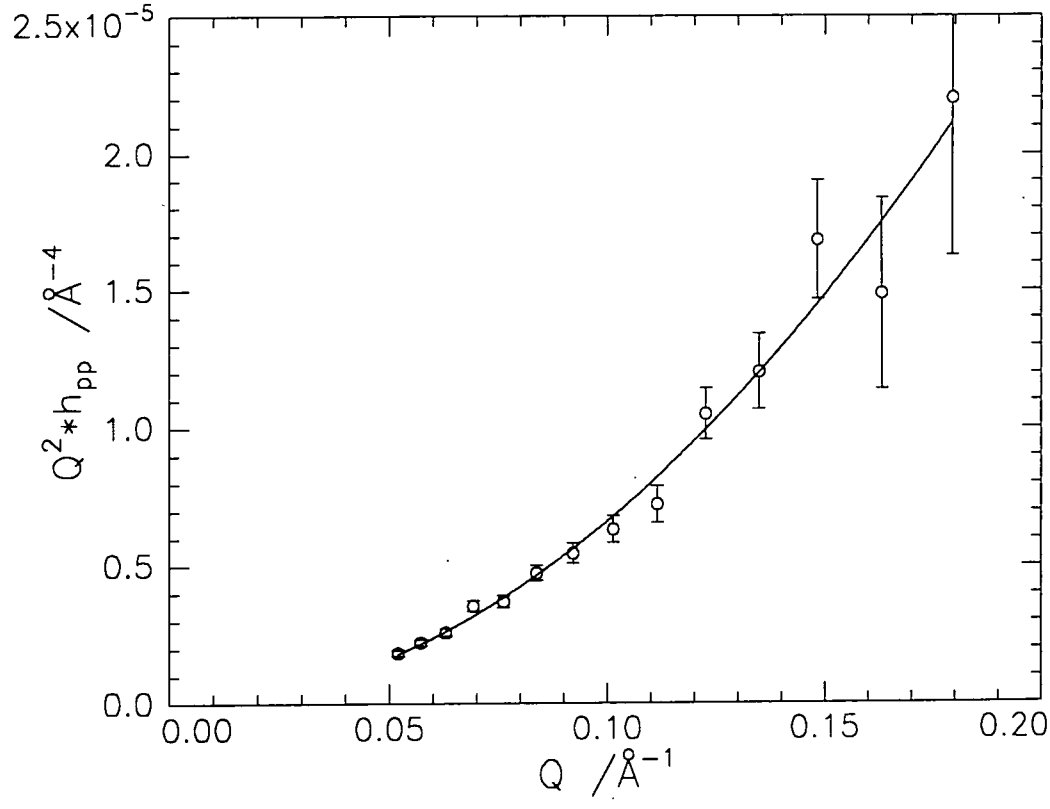

Figure 4.37: Self partial structure factor for the backbone at 10mN m^{-1} fitted using the Gaussian distribution model

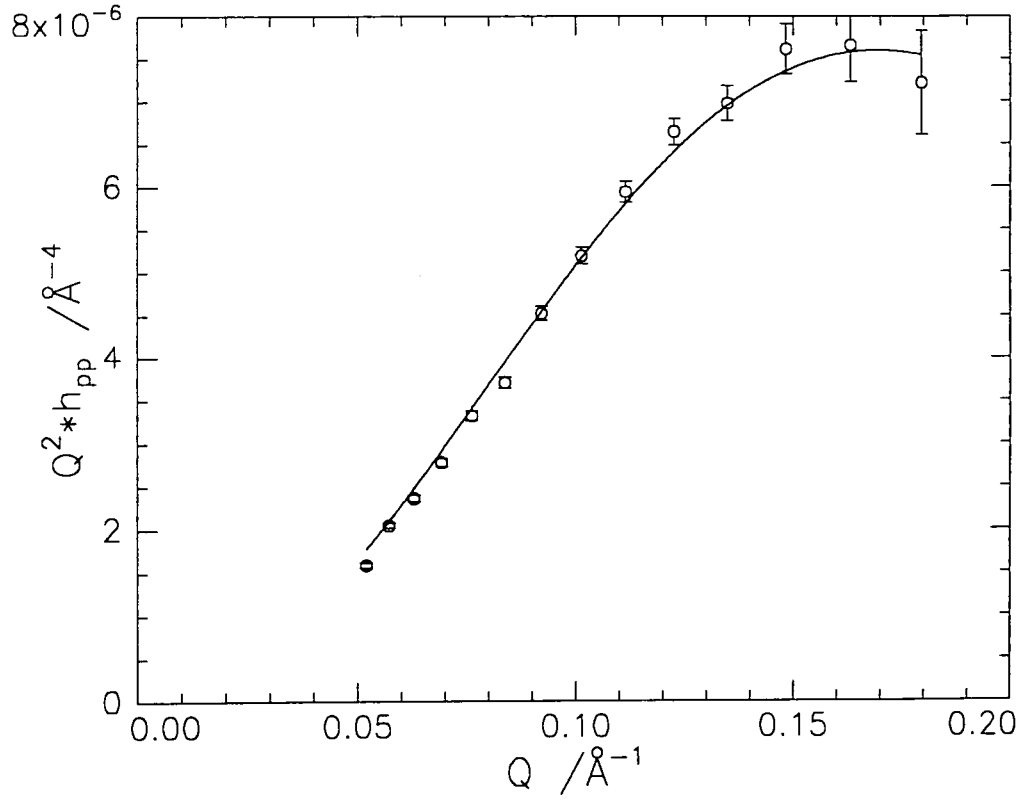

Figure 4.38: Self partial structure factor for the side chains at 10mN m^{-1} fitted using the Gaussian distribution model

Both the Guinier plots and the fitting method give essentially identical values of n_{i1} and σ within experimental error and the values given in table 4.6 were obtained by the fitting method. The water self partial structure factor has been fitted using the tanh profile, with the width parameter, ξ, as the adjustable fitting parameter and an example of the fits obtained is shown in figure 4.39 with the values of ξ determined given in table 4.9.

π /mN m^{-1}	n_{b1} /10^{-3}Å^{-3}	σ_b /Å	n_{c1} /10^{-3} Å^{-3}	σ_c /Å	ξ /Å
0.5	–	–	1.8	14	3
5.0	4.2	9	1.9	14	3
10.0	4.9	6	1.9	16	3

Table 4.9: Parameters obtained from Gaussian and tanh model fits of the self partial structure factors

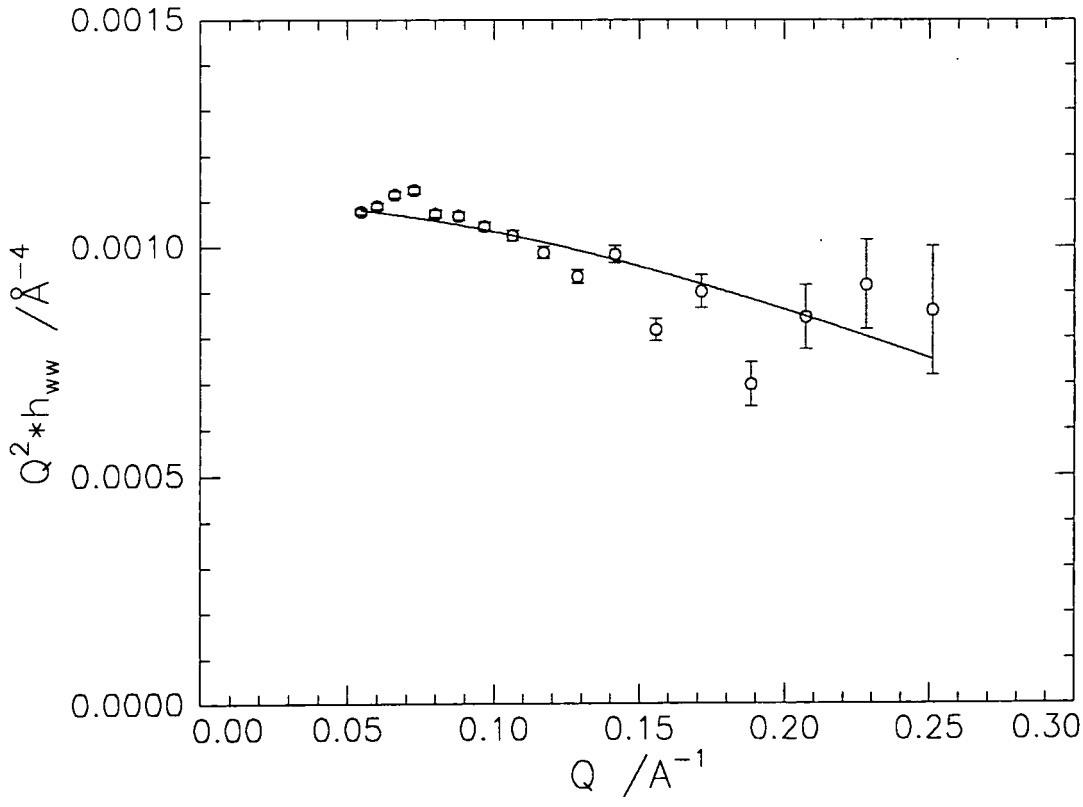

Figure 4.39: Self partial structure factor for the subphase at 10mN m^{-1} fitted using the tanh model

As before, equations 4.43 and 4.44 can be used to calculated the separations between each component, except here the self terms are calculated using the parameters from the self term fits substituted into either the Gaussian distribution for the polymer components or the tanh profile for the subphase. As each model used here produces an almost indistinguishable fit from those produced using the uniform layer model, no change in δ is expected as the calculated cross term will be the same and this is borne out in the values obtained, shown in table 4.10 and examples of the fits are shown in figures 4.40 to 4.42.

π (mN m^{-1})	SEPARATION (Å)		
	BACKBONE / SIDE CHAIN	BACKBONE / WATER	SIDE CHAIN / WATER
0.5	–	–	6
5.0	3	3	6
10.0	3	3	6

Table 4.10: Separations obtained using the Gaussian and tanh models for self terms in equations 4.42 and 4.43

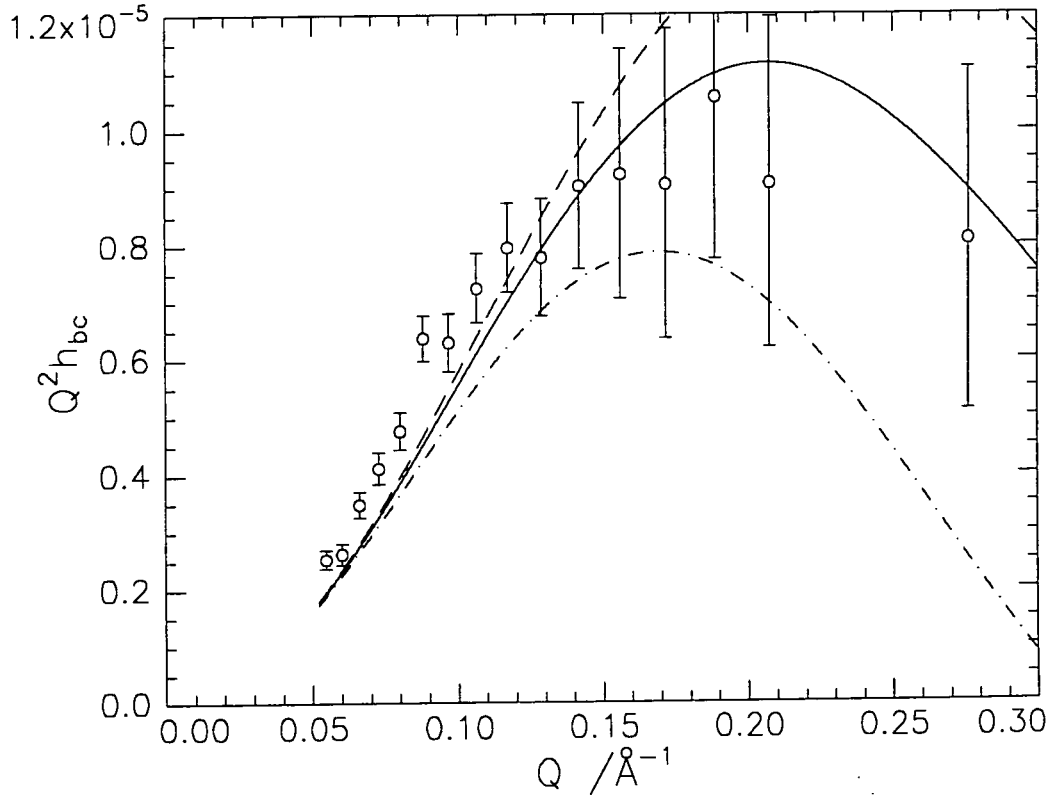

Figure 4.40: Cross partial structure factor for backbone and side chains at 10mN m^{-1}, experimental data (o) and lines are calculated cross terms with different δ, δ = 1Å (– –), δ = 3Å (—), δ = 5Å (– · –)

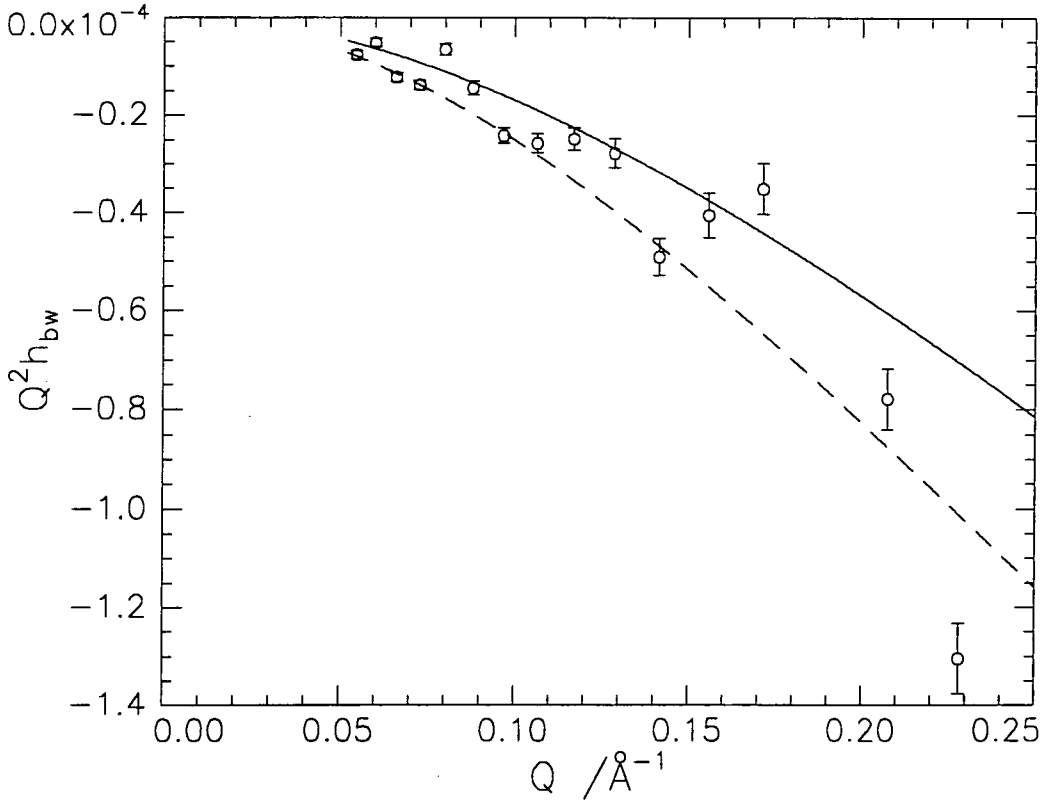

Figure 4.41: Cross partial structure factor for backbone and subphase at 10mN m^{-1}, experimental data (o) and lines are calculated cross terms with different δ, δ = 2Å (—), δ = 4Å (– –)

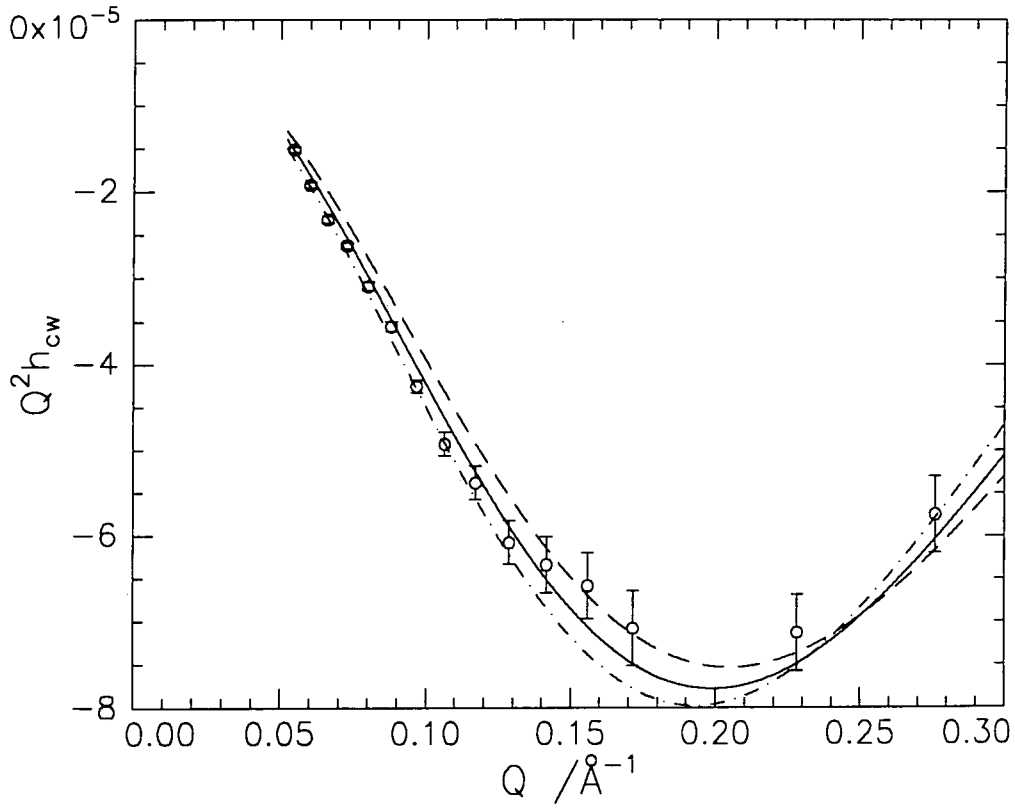

Figure 4.42: Cross partial structure factor for side chains and subphase at 10mN m^{-1}, experimental data (o) and lines are calculated cross terms with different δ, δ = 5.5Å (– –), δ = 6 Å (—), δ = 6.5 Å (– · –)

Using the parameters from the self term fits, the distributions of the polymer components and the subphase at the interface can be calculated. By combining these distributions with the knowledge of the separations, an equivalent distribution diagram as for the uniform layer models can be drawn and this is shown in figure 4.43.

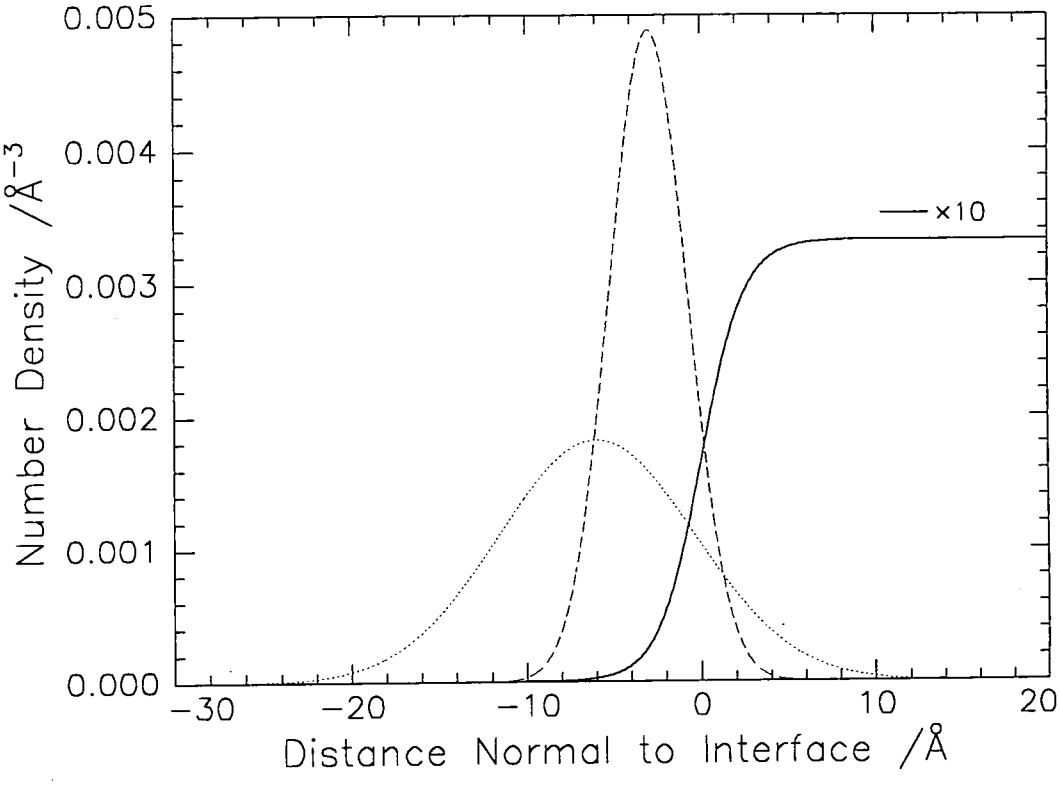

Figure 4.43: Component density distributions predicted by a Gaussian model for the polymer components (···· side chains and – – backbone) and a tanh model for the interfacial subphase region (—)

Although the distribution diagram in figure 4.43 gives a more realistic picture of the interface, the features of the distribution are the same as those obtained using the uniform layer models (figure 4.35). The backbone region is almost completely immersed in the aqueous subphase and this corresponds to the predictions from the two layer model fits to the reflectivity data on a.c.m.w., where the DM layer produced a scattering length density greatly reduced from that expected for a pure DM layer. The immersed

methacrylate backbone is completely different to the organisation observed in spread layers of poly (methyl methacrylate)[8,9] and may be due to the minimisation of contact between the hydrophobic lauryl side chains and the aqueous subphase. Another notable feature of the distributions is the extent of mixing of the spatial regions for the backbone and the side chains, due to circa 50% of the side chain distribution being in the subphase and it is also evident that a small proportion of the side chain distribution extends below the plane of the backbone region. This somewhat surprising observation can be rationalised, albeit qualitatively, with the equilibrium stereochemical configuration of PLMA. Minimisation of the configurational potential energy of four monomer units in a chain sequence of PLMA results in a rotational angle of $\pm$ 120° (all trans configuration has a rotational angle of 0°). This forces the side chains to a lower spatial plane than the main chain segments and hence the side chains sample slightly greater depths than the main chain backbone before sufficient rotations about the bonds in the lauryl substituent enable the hydrophobic methylene units to leave the subphase and protrude into the air. With the main chain backbone being almost completely immersed in the subphase, such a configuration results in a region where both the side chains and backbone reside in the same plane and this accounts for the observation of part of the side chain distribution being in the subphase and mixed with the backbone layer. An attempt to sketch such an arrangement for a short chain section of PLMA is shown in figure 4.44. The two layer thicknesses shown in figure 4.44 indicate the maximum possible range that each component can occupy, determined from the width of the base of the Gaussian distribution for each component. The backbone region for an all trans configuration would be about 8Å thick, so the fact that the backbone can occur in a plane 14Å thick indicates that the backbone is staggered due to rotations about the main chain bonds. This supports the idea that rotations exist along the backbone and consequently force the

side chains into a lower plane, which accounts for the fact that the side chains have such a wide region of possible occupation compared to the all trans side chain length which would be circa 16Å. It is also worth noting that the partial structure factor data includes contributions from thermal fluctuations and the analysis of the data gives the average structure. It is not possible to distinguish between whether the overlap of regions is due solely to main chain configurations producing a staggered arrangement which forces overlap or to the movement resulting from the thermal fluctuations which produces the appearance of each component occupying a greater thickness than it actually does, hence the average picture obtained consists of significant overlap. In reality there is probably a combination of both factors, overlap occurs due to the polymer configurations adopted at the interface and then this is amplified due to the smearing effect of the thermal fluctuations.

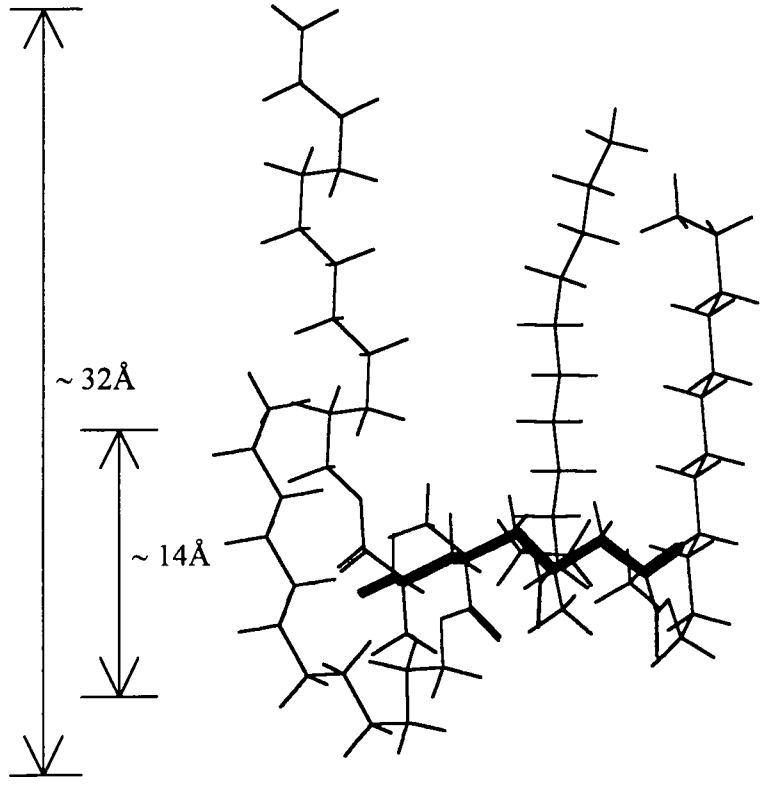

Figure 4.44: Stick model of the arrangement of PLMA at the air / water interface with the backbone shown by the bold line

To demonstrate that the parameters obtained from the partial structure factors for both polymer components are accurate, they can be used to calculate the corresponding reflectivity profile and then compared to the experimental profiles for the partially labelled PLMA monolayers on a.c.m.w.. To achieve this, the parameters obtained from the Gaussian fits to the partial structure factors are used to calculated the distribution in concentration normal to the surface, which can then be divided into a number of uniform layers with varying number density, so in effect the Gaussian distribution is represented by a histogram. The scattering length density for each layer can then be calculated and an optical matrix type calculation can be carried out on this layered structure to obtain the reflectivity. The calculated reflectivity profiles are compared to the experimental profiles in figures 4.45 and 4.46 (a) and (b).

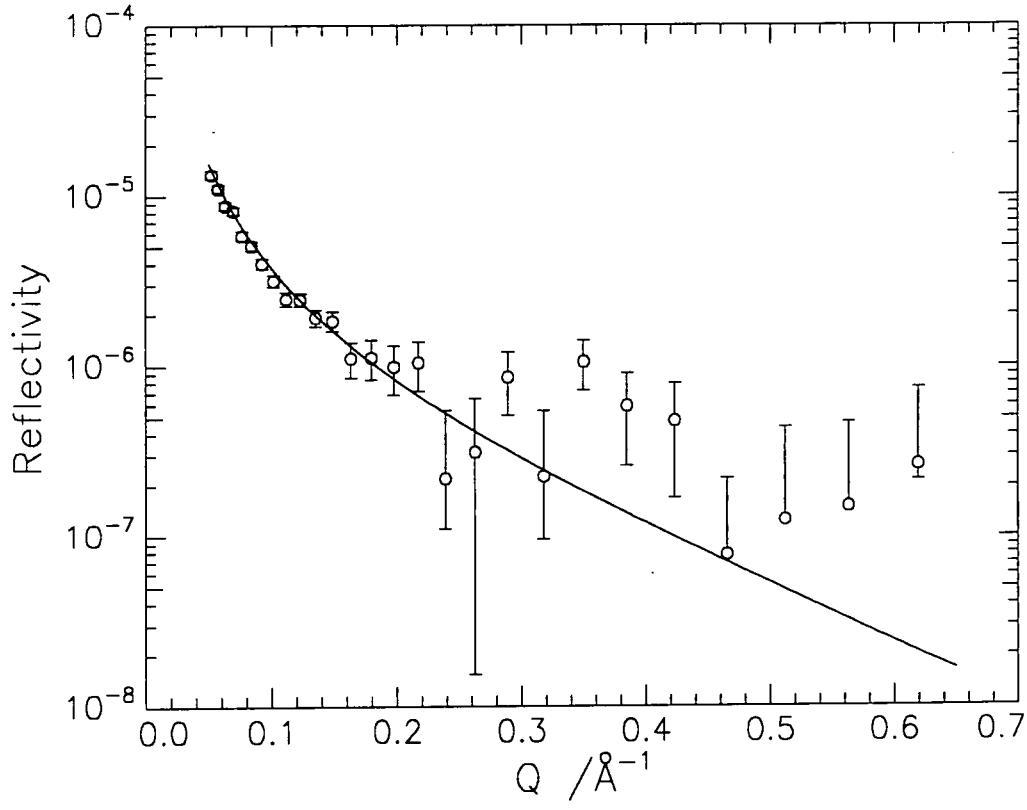

Figure 4.45(a): Calculated reflectivity profile (—) using the parameters for the backbone at 10mN m^{-1} compared to the experimental profile for DMHL at 10mN m^{-1} on a.c.m.w.

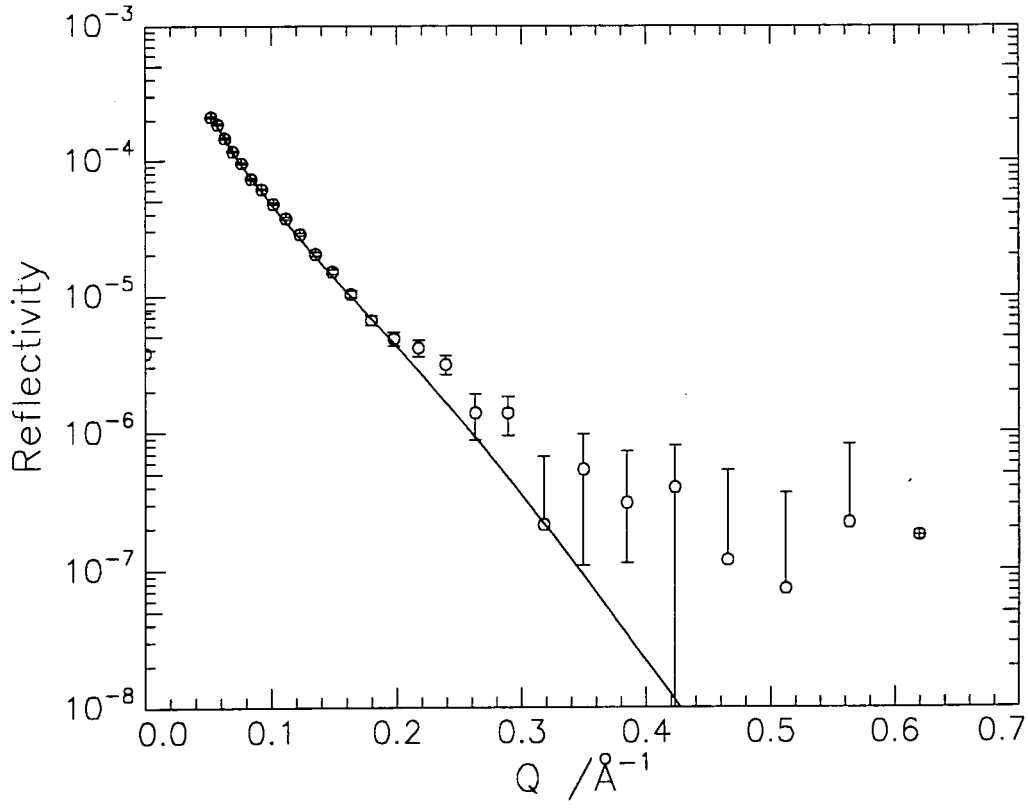

Figure 4.45(b): Calculated reflectivity profile (—) using the parameters for the side chains at 10mN m^{-1} compared to the experimental profile for HMDL at 10mN m^{-1} on a.c.m.w.

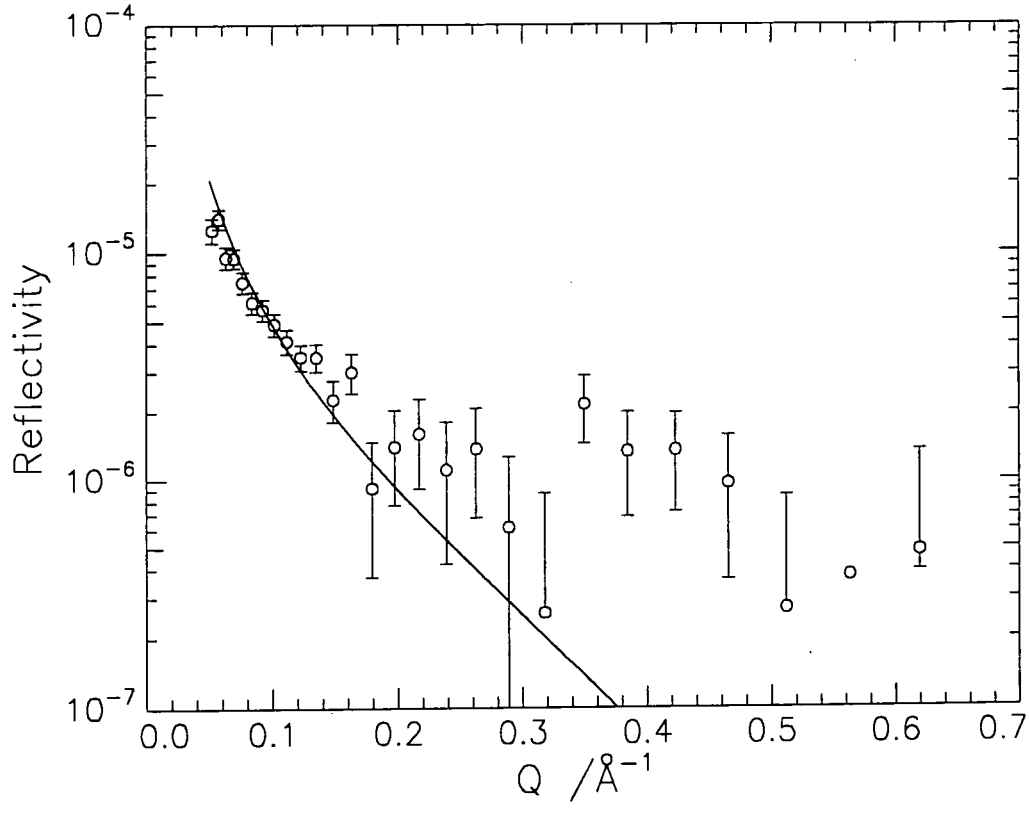

Figure 4.46(a): Calculated reflectivity profile (—) using the parameters for the backbone at 5mN m^{-1} compared to the experimental profile for DMHL at 5mN m^{-1} on a.c.m.w.

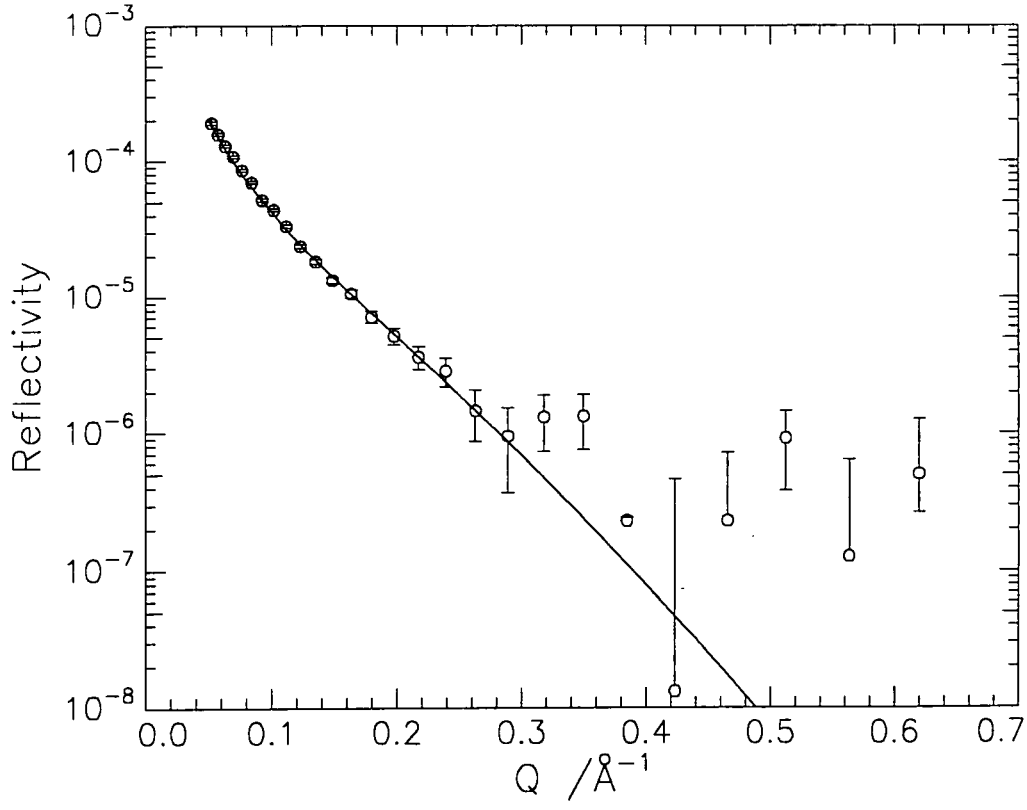

Figure 4.46(b): Calculated reflectivity profile (—) using the parameters for the side chains at 5mN m^{-1} compared to the experimental profile for HMDL at 5mN m^{-1} on a.c.m.w.

There is good agreement between the calculated and experimental profiles up to Q values of circa 0.2Å^{-1} which corresponds to the Q range used in the partial structure factor analysis, so this confirms that the Gaussian distribution parameters are reliable. There is a better agreement for the side chains which is due to the superior data quality which produced more accurate fitting and more reliable parameters, whereas the worst match is for the backbone at 5mN m^{-1} which has the worst data and resulted in parameters which were slightly higher than would have been expected.

Partial structure factors can also be used to calculate the total layer thickness by using a simplified version of equation 4.25 which includes polymer and subphase terms only

$$R(Q)=\frac{16\pi^2}{Q^2}\left[b_p^2 h_{pp}(Q)+b_w^2 h_{ww}(Q)+2b_p b_w h_{pw}(Q)\right] \qquad 4.47$$

Three contrasts are required to obtain each partial structure factor, two of which are DMDL on a.c.m.w. and HMHL on D_2O. By fitting h_{pp}, the total layer thickness and number density are obtained and both the uniform layer and Gaussian models have been used, with the Gaussian model producing visibly better fits, as is shown in figures 4.47 and 4.48.

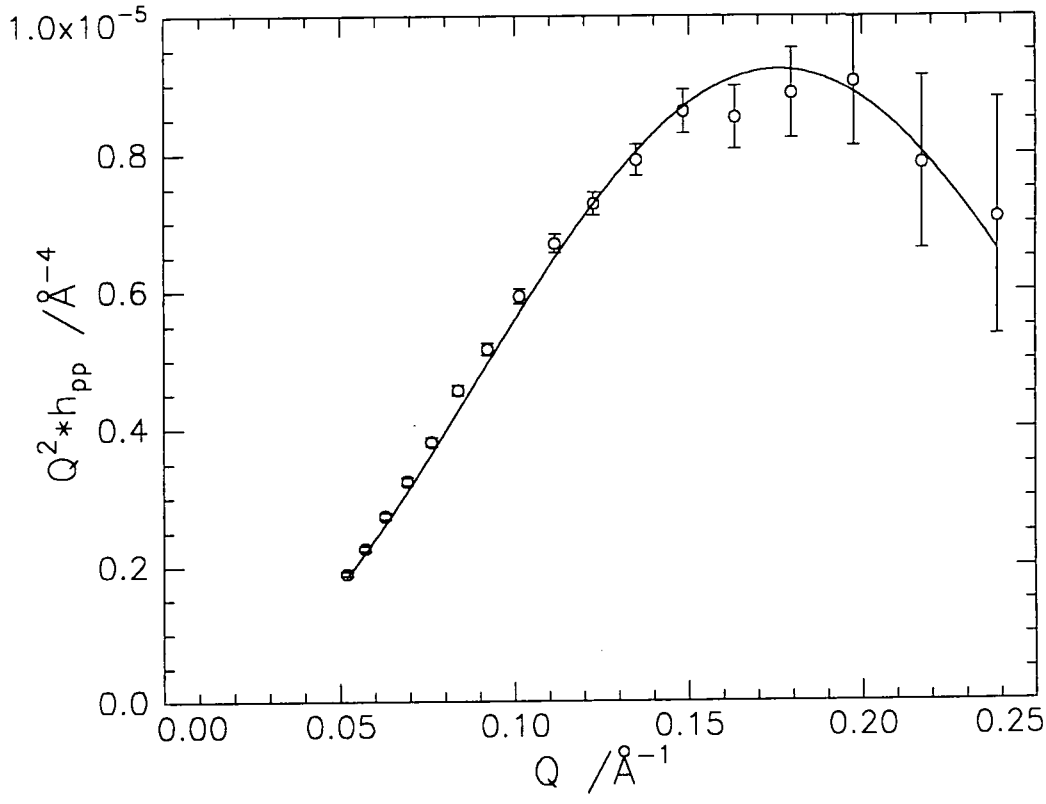

Figure 4.47: Uniform model fit to polymer self partial structure factor at 10mN m^{-1}

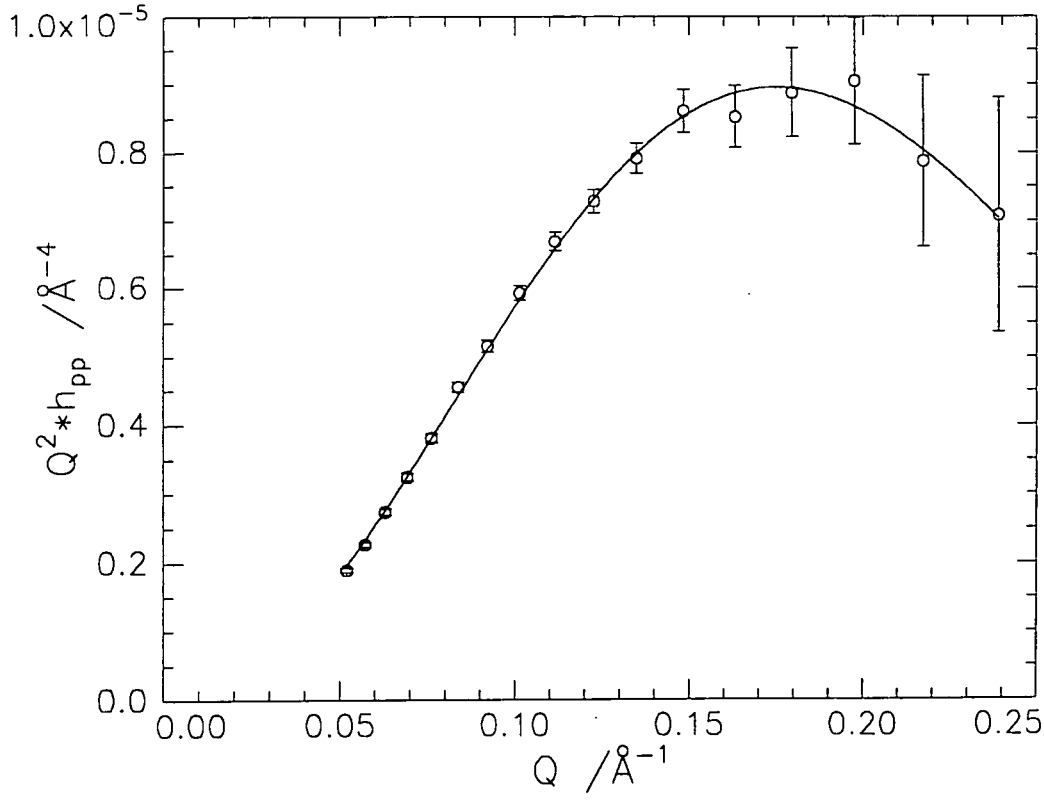

Figure 4.48: Gaussian model fit to polymer self partial structure factor at 10mN m^{-1}

The parameters for each model are shown in table 4.11 together with the surface concentrations determined from the parameters and the theoretical concentrations.

	UNIFORM MODEL			GAUSSIAN MODEL			
π (mN m^{-1})	d (Å)	n_{p1} (10^{-3} Å^{-3})	Γ (mg m^{-2})	σ (Å)	n_{p1} (10^{-3} Å^{-3})	Γ (mg m^{-2})	Γ_{calc} (mg m^{-2})
	15	1.5	1.1	13	2.0	1.1	0.9
	16	1.6	1.2	14	2.1	1.2	1.0
	17	1.5	1.2	14	2.1	1.2	1.2

Table 4.11: Parameters from fits to polymer partial structure factor

These values, in conjunction with the subphase layer thickness (10Å at 0.5mNm^{-1} 13Å at 5mN m^{-1} and 12Å at 10mN m^{-1}) and the separation of the polymer and subphase

distributions (3Å at each surface pressure), can be used to determine the extent of the penetration of the whole polymer monolayer by the subphase[10]. If there is no overlap of the two distributions, i.e. no immersion of polymer monolayer in the subphase, the separation of the two distributions would be the sum of the two half thicknesses. For example, at 10mN m^{-1} the sum is 14.5Å and since the separation is found to be only 3Å, the two components must overlap by 11.5Å, corresponding to 68% immersion of the monolayer. The extent of immersion remained fairly constant at each surface pressure, producing a value of circa 68±5%. The values of the layer thickness are of the same order as those obtained for just the side chain which seems surprising, however this can be explained by considering the overlap of the two polymer components. The extent of the overlap can be estimated by defining it in terms of the proportion of side chains in the backbone region and using the simple equation [11]

$$\phi = \frac{d_c + d_b - 2\delta_{bc}}{2d_c} \qquad 4.48$$

where ϕ is the fraction of the polymer components which overlap. At 10mN m^{-1} using the uniform layer parameters, ϕ equals 0.55, so if the sum of the backbone and side chain thicknesses is taken as the maximum value of the thickness expected for the whole polymer layer (which equals 26Å and assumes no overlap) then taking into account the overlap the thickness expected for the whole polymer reduces to circa 15Å which is in the region of the values obtained from the experiments for the whole layer. The same process can be carried out using the Gaussian parameters which results in the same conclusion. Similarly, the penetration of each polymer component layer by the subphase can be calculated by using the equation

$$\phi = \frac{d_i + d_w - 2\delta_{iw}}{2d_i} \qquad 4.49$$

where the subscript i refers to either the backbone or side chains. For backbone and side chain layers, both the Gaussian and uniform layer models produce similar results, with an amount of penetration of circa 93±5% for the backbone layer and 52±2% for the side chains at surface pressures of 5 and 10mN m^{-1}.

In section 4.1.2 equations 4.34 and 4.37 allow the surface concentrations to be calculated from the parameters obtained for the uniform layer and Gaussian model respectively. If the model is a satisfactory then the surface concentrations should agree with the concentrations calculated from the amount of polymer deposited on the subphase. In addition, due to the constraint imposed by the structure of the polymer, the surface concentrations calculated using the backbone parameters should equal those calculated using the side chain parameters, since for every backbone unit there is a side chain. The values calculated for both models are given in table 4.12 compared to the theoretical values.

π (mN m^{-1})	Γ^{bb}_{calc} (mg m^{-2})	Γ^{sc}_{calc} (mg m^{-2})	Γ^{bb}_{uni} (mg m^{-2})	Γ^{sc}_{uni} (mg m^{-2})	Γ^{bb}_{Gau} (mg m^{-2})	Γ^{sc}_{Gau} (mg m^{-2})
0.5	0.9	1.0	–	1.0	–	1.0
5.0	1.1	1.1	1.3	1.1	1.3	1.1
10.0	1.2	1.3	1.3	1.2	1.1	1.1

Table 4.12: Surface concentrations calculated from uniform layer and Gaussian model parameters compared to theoretical surface concentrations

In table 4.12 the superscripts bb and sc refer to the concentrations calculated from the parameters obtained for the backbone and side chains respectively and the

subscripts show which parameters were used in the calculation. The theoretical surface concentrations (Γ_{calc}) for the backbone and side chains were calculated using the amount of solution deposited onto the subphase for DMHL and HMDL on a.c.m.w. respectively, as it is the reflectivity from these monolayers which determine the partial structure factors for the two components. The surface concentrations determined from the side chain data are in excellent agreement with the theoretical concentrations, whereas the values from the backbone data are not as good, but they are in the correct region. This is solely due to the quality of the reflectivity data obtained for DMHL and HMDL spread on a.c.m.w., HMDL produced good data and therefore the fits to the partial structure factors are more reliable than those for the backbone, DMHL produced very weak reflectivity profiles which results in considerable uncertainty when fitting the partial structure factors. Good agreement between the surface concentrations determined using the backbone and side chain parameters is also obtained, so both of these factors indicate that, within the limitations of the current experiments, both models used for the polymer components represent the distributions adequately and although neither fits the data significantly better than the other, the Gaussian model would seem to be the more realistic. More complicated models could no doubt be used, but this does not seem justified due to the limitations resulting from the data quality. The Gaussian model is the simplest, realistic model which produces the correct results. Similarly, for the subphase, the tanh distribution is the simplest, realistic model to represent the interfacial subphase layer without using over elaborate fitting functions which the data quality does not justify.

As one of the aims of this work was to investigate the effect of the side chains on the organisation of the polymer compared to PMMA, at this point a summary of the organisation of obtained for PMMA[8,9] is necessary. Syndiotactic and atactic PMMA

produced similar surface pressure - area isotherms which were indicative of a condensed monolayer and they both showed a similar organisation at the air - water interface. Syndio- and atactic PMMA showed a constant thickness, circa 18Å, across the concentration range of 0.2 to 2mg m^{-2}, with little penetration of the layer by the subphase, indicating that the polymer mainly exists in the air phase and the theoretical and experimentally determined surface concentrations at each surface concentration studied agreed within experimental error. Isotactic PMMA produced a different surface pressure - area isotherm which indicated that the polymer had favourable interactions with the subphase. A monolayer with a constant thickness of circa 18Å was formed, however, from comparisons of the theoretical and experimentally determined surface concentrations it is evident that not all the polymer is in the air phase. The experimental concentrations are consistently lower than the theoretical concentrations and above circa 1mg m^{-2} the discrepancy approaches 50%. This apparent disappearance of polymer is probably due to the chains departing from the interfacial region as loops or chain ends which penetrate deep into subphase and become too dilute to be observed by the neutrons.

The position of the methacrylate backbone for the mainly syndiotactic PLMA is the exact opposite to that observed for syndiotactic (and atactic) PMMA. This is presumably due to the greater hydrophobicity of the lauryl ester groups compared to the methyl groups in PMMA. The structure for PMMA indicates that the backbone in PLMA would prefer to be in the air phase, however, the more hydrophobic and bulky side chains preclude the backbone from achieving its favoured site. A stereotactic effect is observed for PMMA, but due to the lack of stereoisomers of PLMA the effect of tacticity could not be investigated. Due to the overwhelming hydrophobicity of the side

chains, penetration deep into the subphase would not be expected for isotactic PLMA as was found for isotactic PMMA.

The four surfactants studied by Thomas *et al*, sodium dodecyl sulphate (SDS), tetradecyltrimethylammonium ($C_{14}TAB$), triethylene glycol monododecyl ether ($C_{12}E_3$) [10] and decyltrimethylammonium ($C_{10}TAB$)[12], all showed circa 30% penetration of the interfacial layer by the subphase, in comparison to the value found here for PLMA which was circa 68%. The additional amount of material which is immersed in the case of PLMA is possibly due to the backbone which places restrictions on the positions of the side chains. Whereas the surfactant molecules are all independent, which allows the alkyl chains to go directly into the air phase, the side chains in PLMA can not achieve this as rotations in the backbone force a proportion of the side chains to a lower plane before they can leave the subphase. This will have the effect of increasing the total amount of polymer which is found to be immersed in the subphase.

The distribution of the backbone and side chain components observed here for PLMA is similar to that found for $C_{14}TAB$ absorbed at the air - water interface [13]. The head groups of the molecules are found to be completely immersed in the subphase and circa 45% of the alkyl chains are penetrated by the subphase. The head group region also contains a significant amount of the alkyl chains, which may be a static, permanent structure or the result of dynamic fluctuations which produce this average configuration. Visible changes occurred in the surface structure of $C_{14}TAB$ as the surface coverage changed. At an area per molecule of 62Å^2 the chain layer is thinner (circa 12Å from a Gaussian model) than at areas less than 50 Å^2, where the thickness is fairly constant (circa 16 Å from a Gaussian model), the thinner layer also results in a decrease in the separation between the subphase and the alkyl chains (8 to 6Å). At a molecular area of 43Å^2 there is substantial thickening of the head group region, from 6 to 12Å and this is

accompanied by a decrease in the chain - head group separation from 7 to 5Å. These changes combined with an unchanged thickness of the chain distribution suggests that the closer packing of the molecules leads to a staggering of the head group layer. No such observations were made for PLMA, however, this may be due to the small range in surface concentration studied. The staggering of the head group region in $C_{14}TAB$ is partly due to electrostatic repulsions, whereas for PLMA, such an effect is negligible and the restrictions due to the backbone bonds keep the layer at a fairly constant thickness. Similar features are also observed for the non - ionic surfactant $C_{12}E_2$[11] which has a thickness of 20Å for the whole molecule, 17Å for the alkyl chain region and 11Å for the ethylene glycol region at the critical micelle concentration. These thickness are explained using the same rationale as used here for PLMA, with the two regions overlapping to some extent.

4.4 Neutron Reflectivity from LMA Monolayers

Figures 4.49 to 4.51(a) to (c) show the background subtracted reflectivity profiles obtained for the deuterated variations of LMA spread on a.c.m.w and each figure consists of six 15 minute runs. The key to the points is, o 1st 15min, × 2nd 15min, Δ 3rd 15min, + 4th 15min, <> 5th 15min and • 6th 15min.

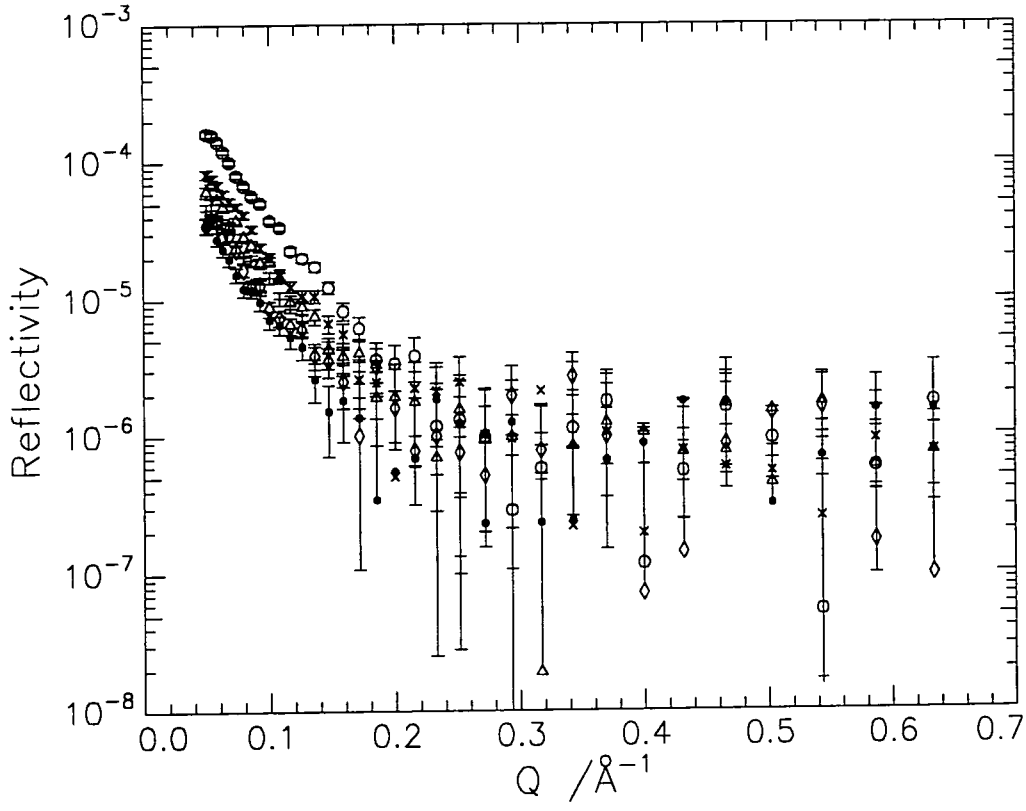

Figure 4.49(a): Reflectivity profiles for DMDL at 10mN m^{-1} on a.c.m.w.

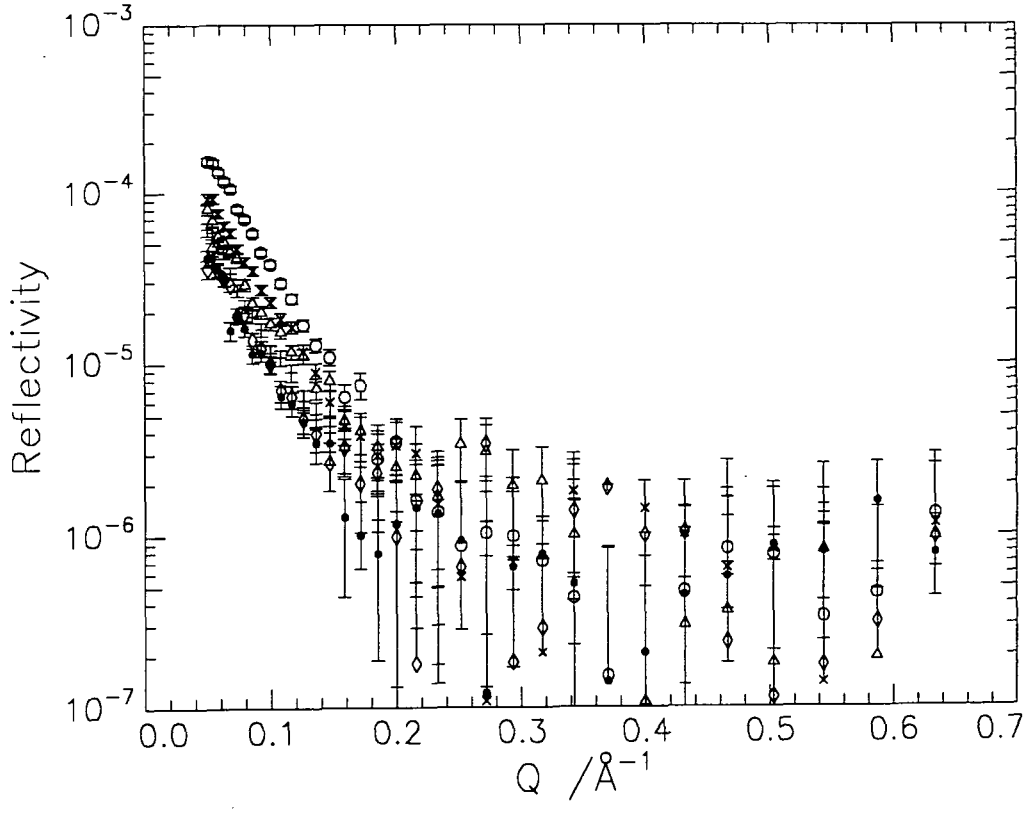

Figure 4.49(b): Reflectivity profiles for HMDL at 10mN m^{-1} on a.c.m.w.

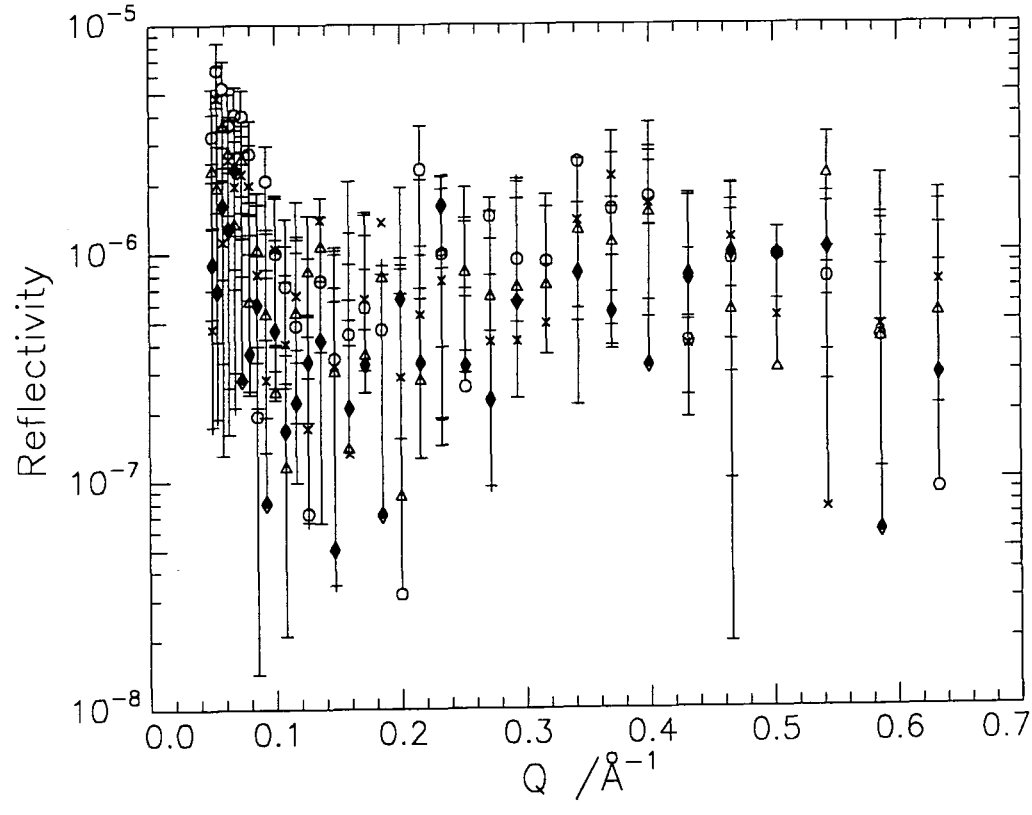

Figure 4.49(c): Reflectivity profiles for DMHL at 10mN m^{-1} on a.c.m.w.

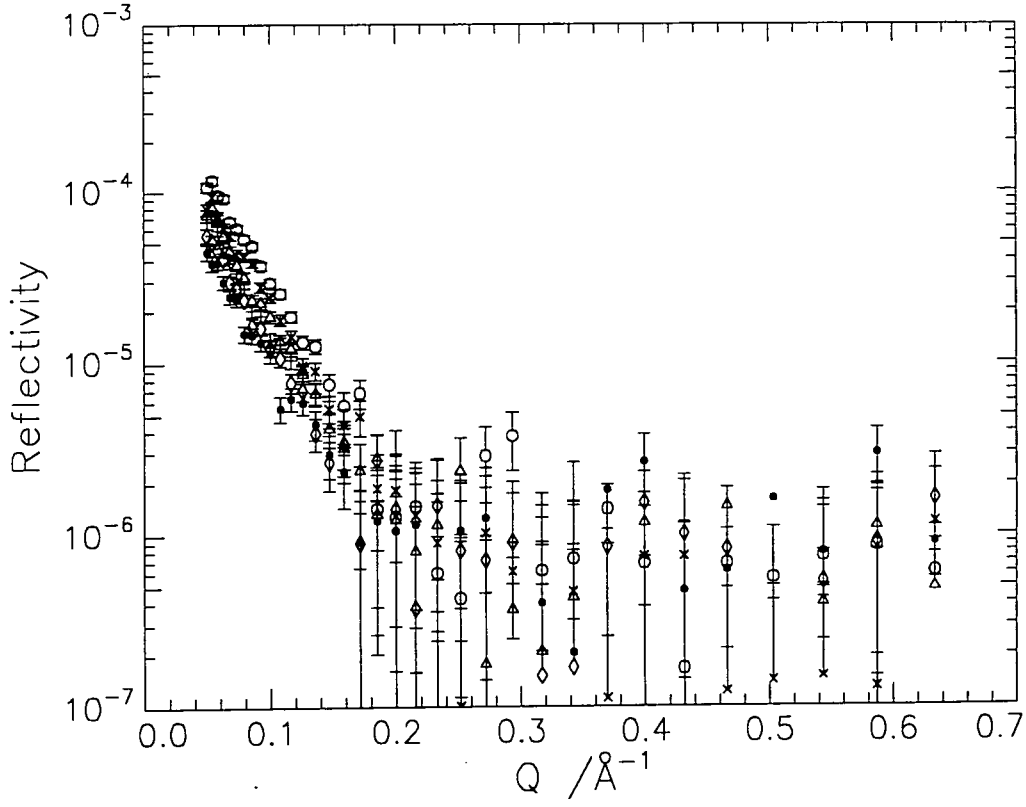

Figure 4.50(a): Reflectivity profiles for DMDL at 5mN m^{-1} on a.c.m.w.

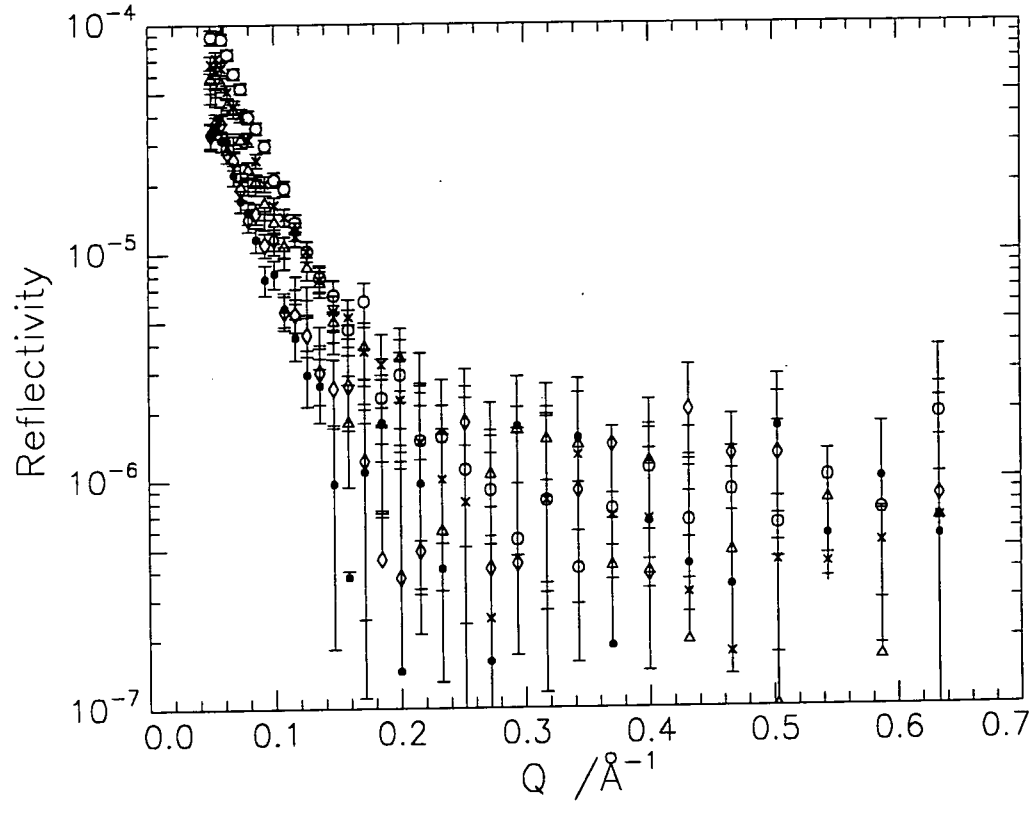

Figure 4.50(b): Reflectivity profiles for HMDL at 5mN m^{-1} on a.c.m.w.

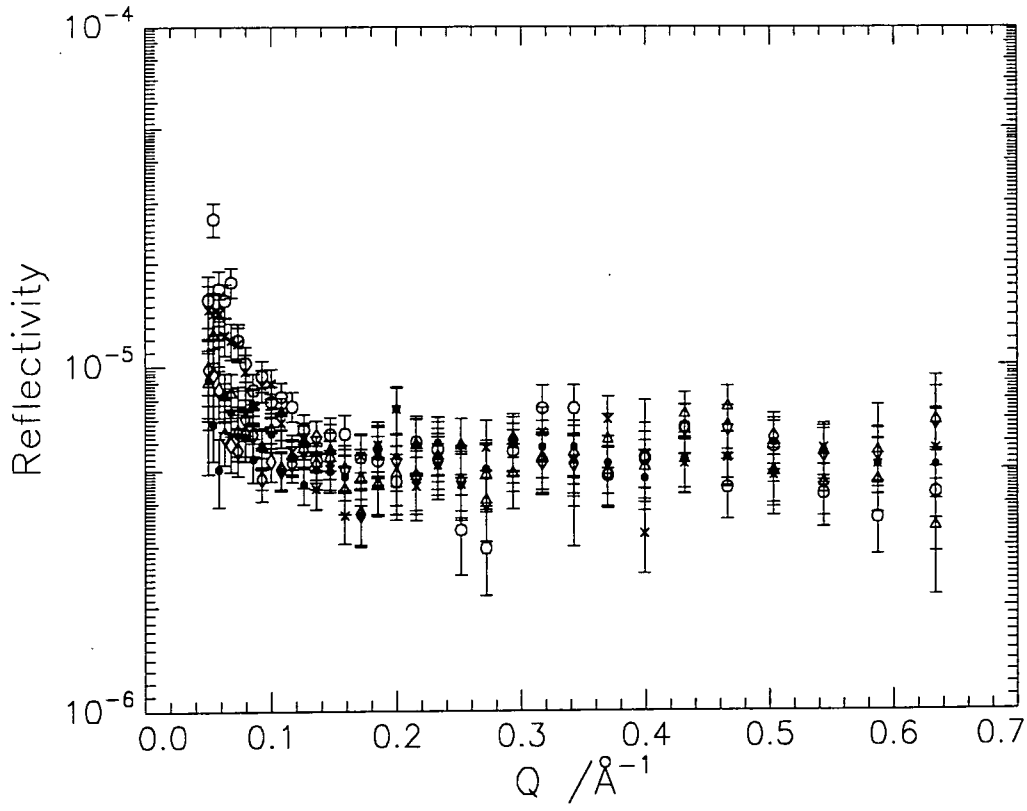

Figure 4.50(c): Reflectivity profiles for DMHL at 5mN m^{-1} on a.c.m.w.

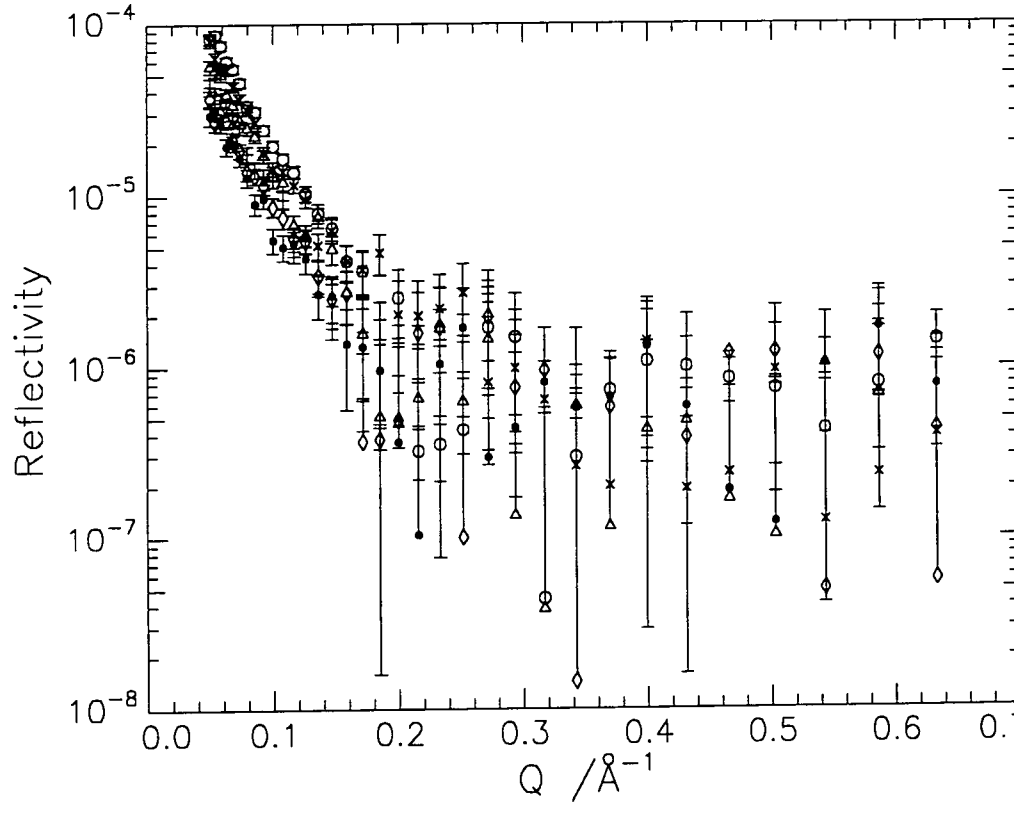

Figure 4.51(a): Reflectivity profiles for DMDL at 0.4mN m^{-1} on a.c.m.w.

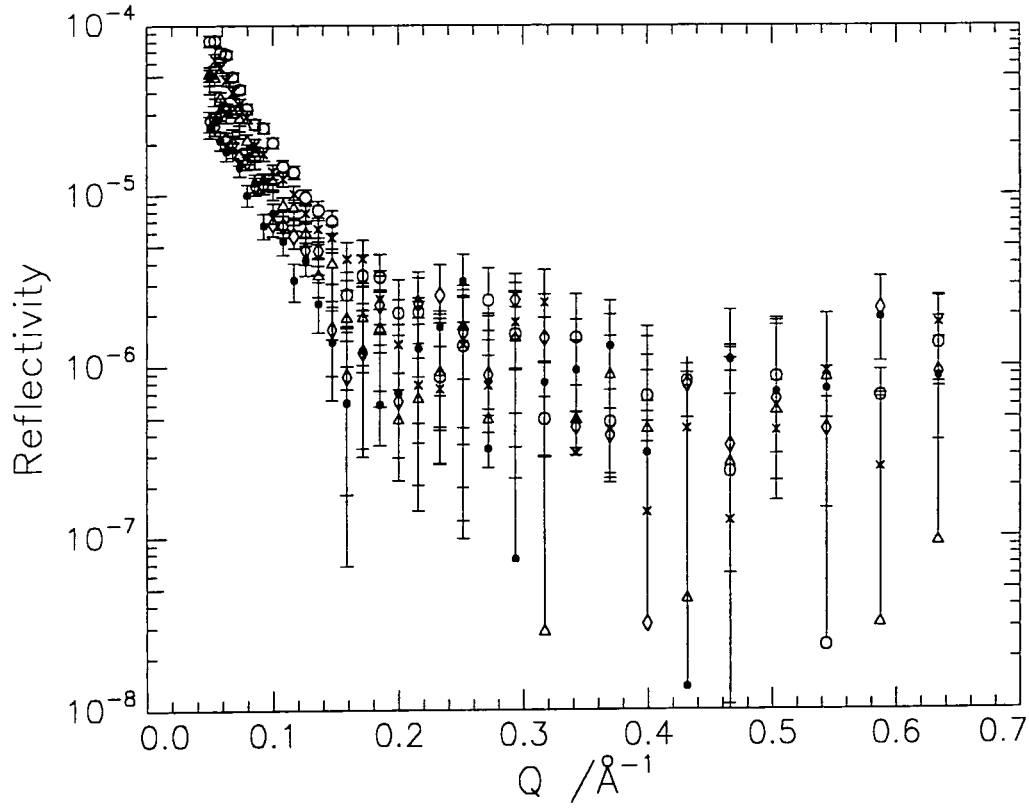

Figure 4.51(b): Reflectivity profiles for HMDL at 0.4mN m^{-1} on a.c.m.w.

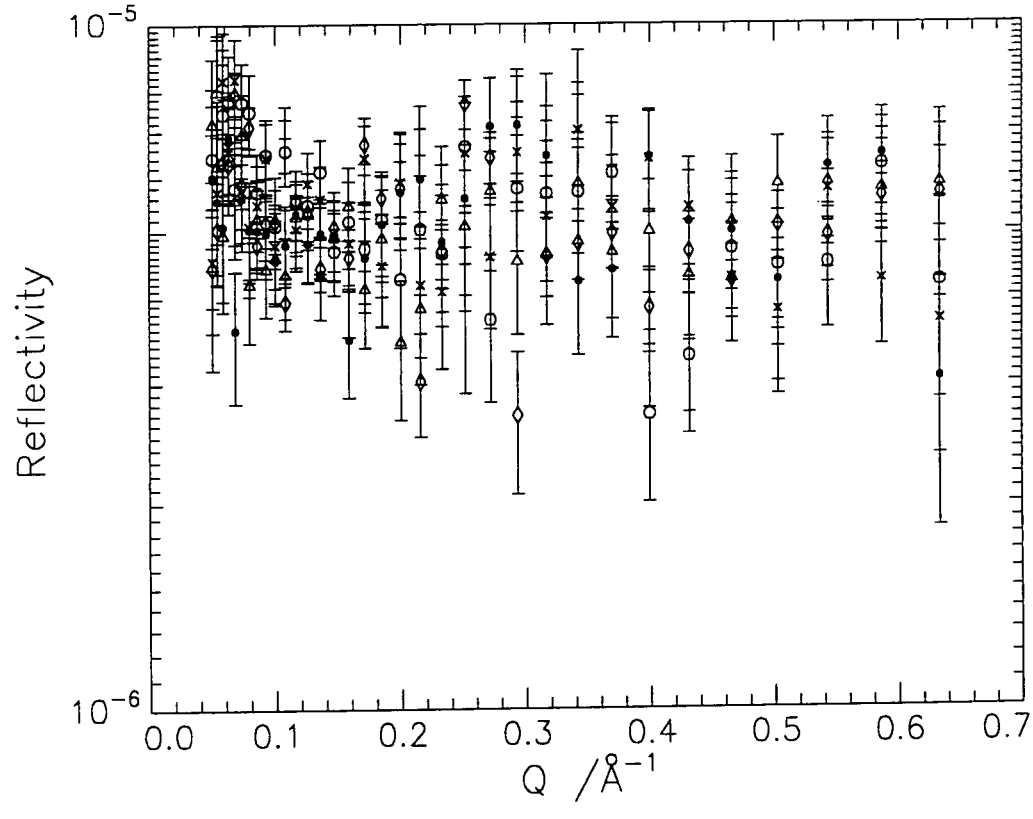

Figure 4.51(c): Reflectivity profiles for DMHL at 0.4mN m^{-1} on a.c.m.w.

The reflectivity for all of the deuterated monomers decreases with time, indicating that the amount of monomer at the interface which is 'visible' to the neutrons decreases. By fitting these profiles with a uniform layer model, the changes can be quantified. Examples of the fits obtained are shown in figures 4.52(a) to (c),4.53(a) to (c) and 4.54(a) and (b), the parameters obtained from the fits are given in tables 4.13 to 4.15. For all the reflectivity profiles, the data above Q of circa 0.3Å^{-1} is unreliable due to the signal merging into the background.

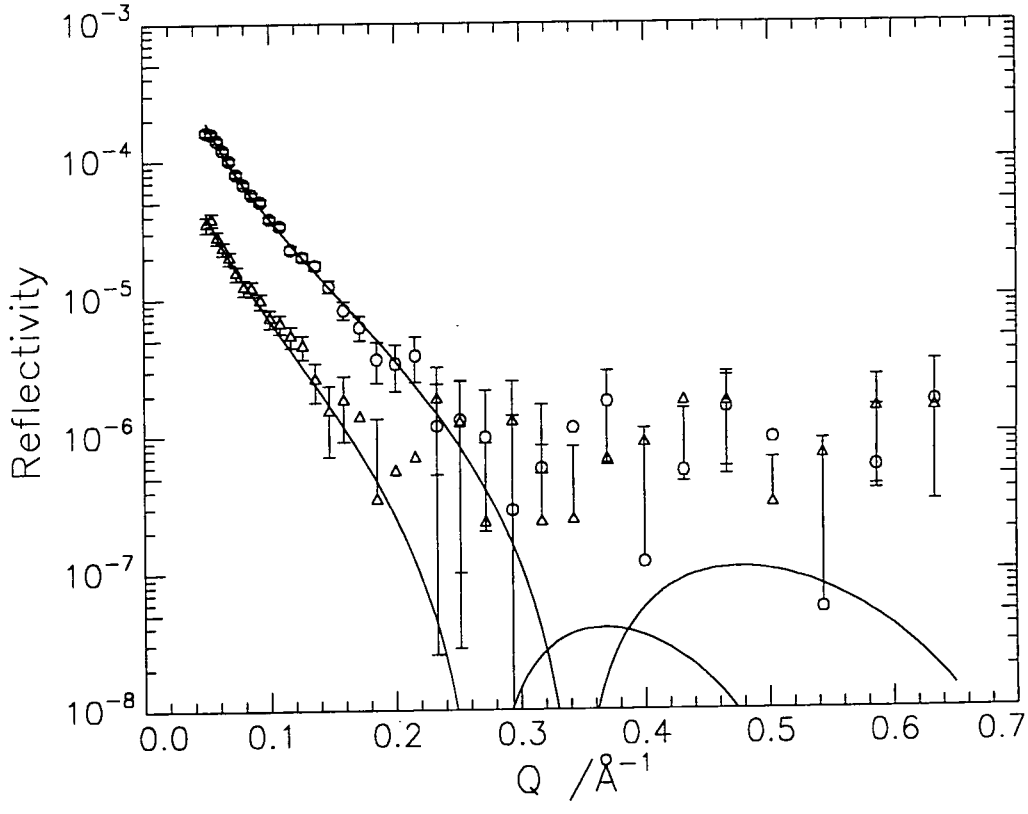

Figure 4.52(a): Reflectivity profiles for DMDL at 10mN m^{-1}, 1st 15 minute run (o), 6th 15 minute run (Δ) and single layer fit (--)

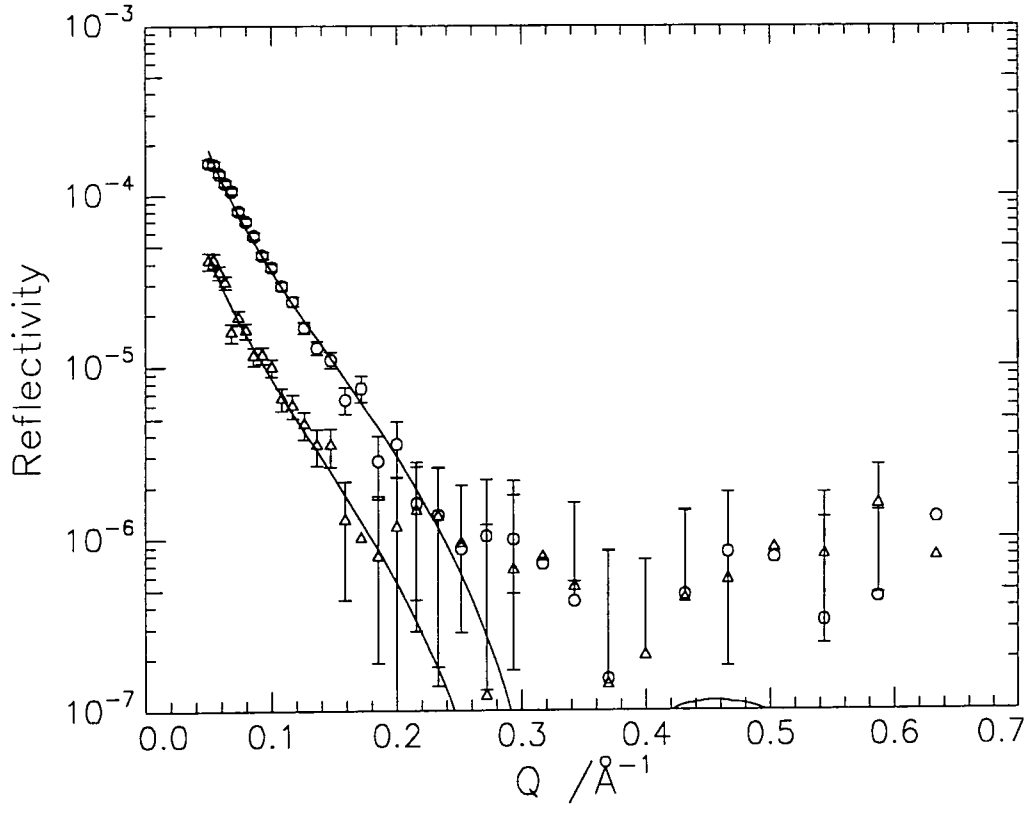

Figure 4.52(b): Reflectivity profiles for HMDL at 10mN m^{-1}, 1st 15 minute run (o), 6th 15 minute run (Δ) and single layer fit (—)

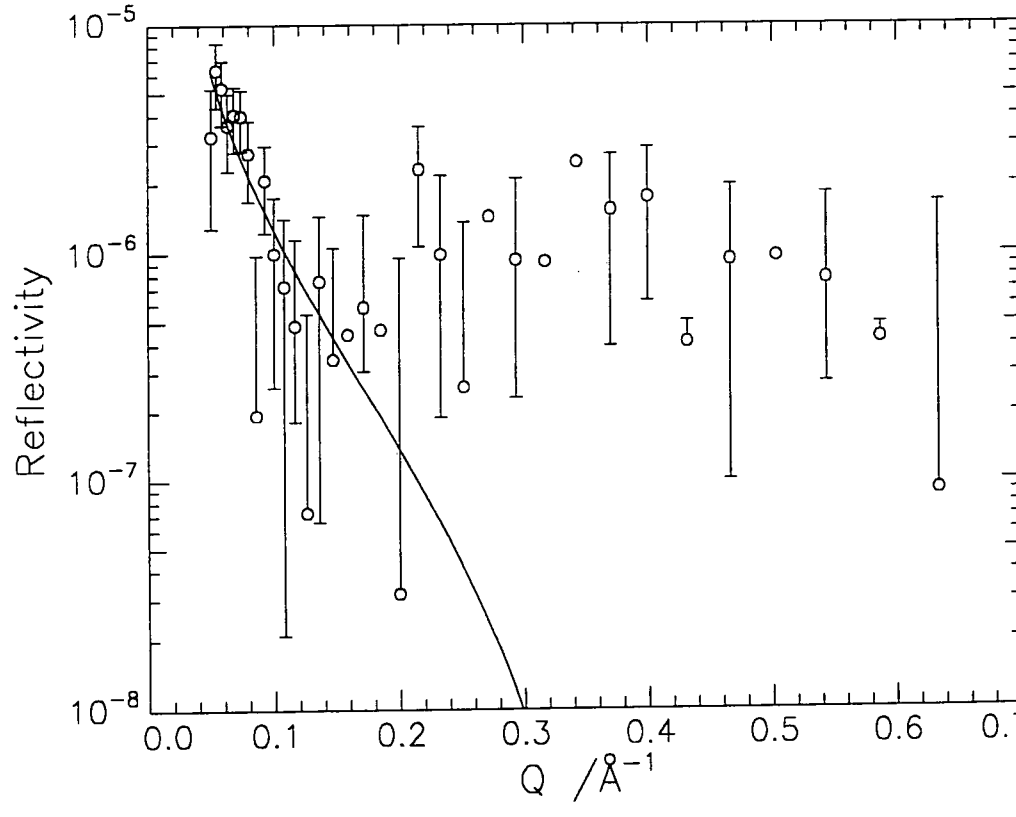

Figure 4.52(c): Reflectivity profiles for DMHL at 10mN m^{-1}, 1st 15 minute run (o) and single layer fit (—)

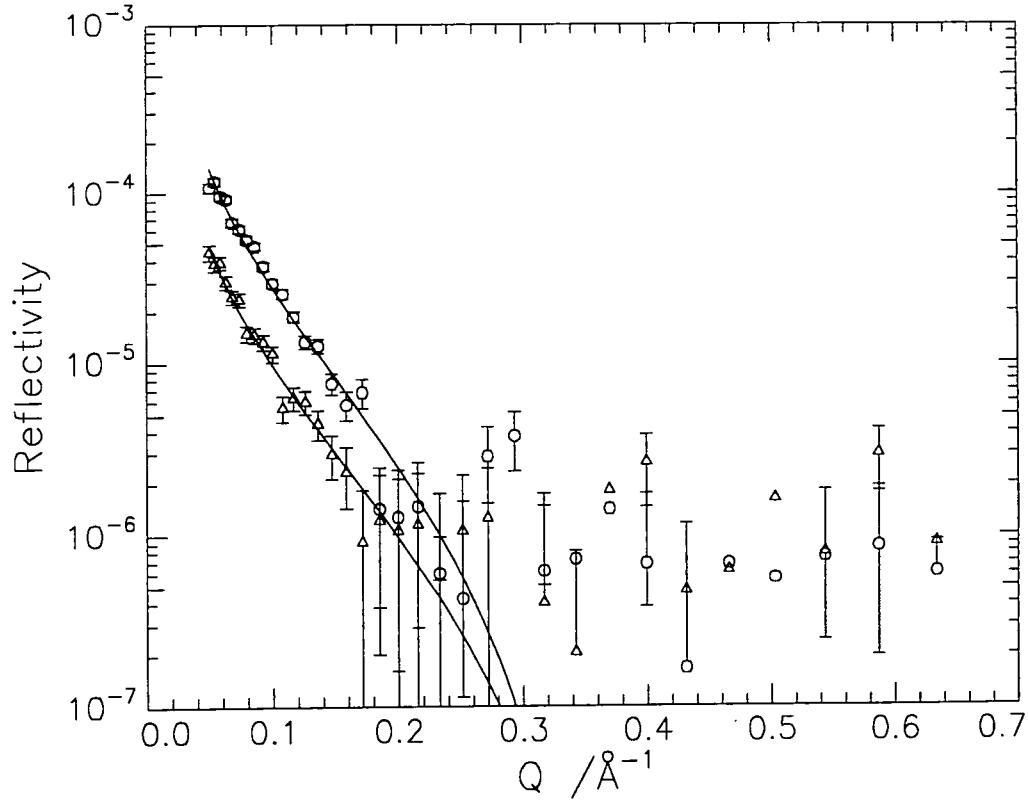

Figure 4.53(a): Reflectivity profiles for DMDL at 5mN m^{-1}, 1st 15 minute run (o), 6th 15 minute run (Δ) and single layer fit (—)

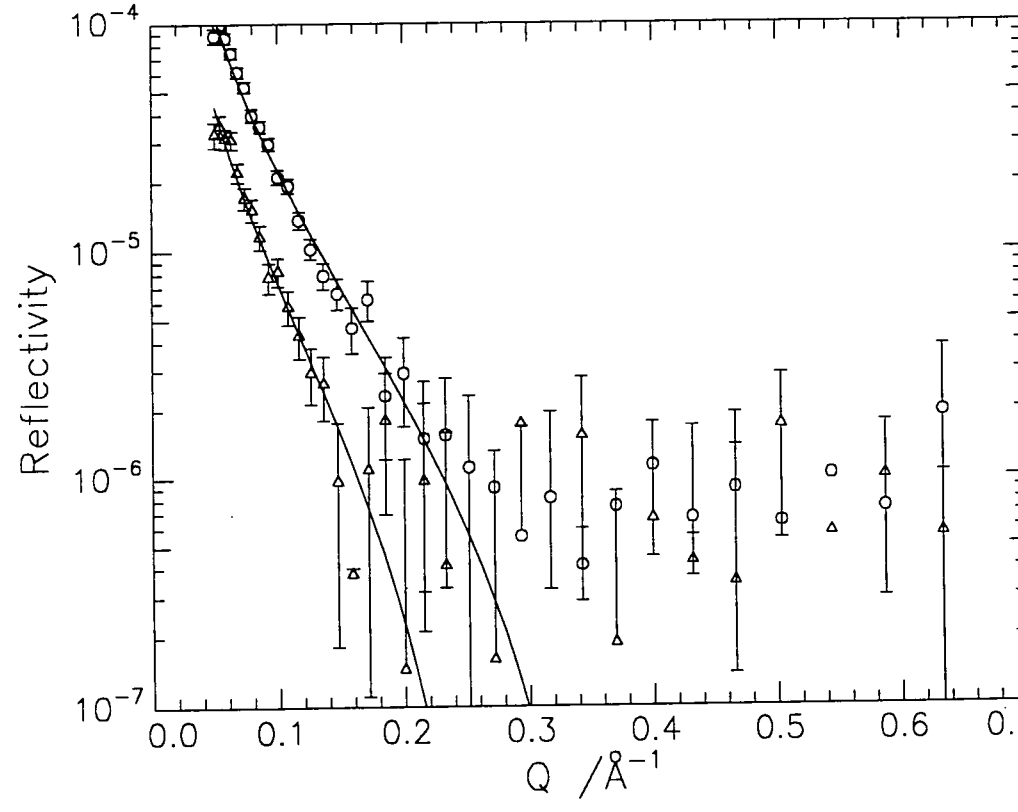

Figure 4.53(b): Reflectivity profiles for HMDL at 5mN m^{-1}, 1st 15 minute run (o), 6th 15 minute run (Δ) and single layer fit (—)

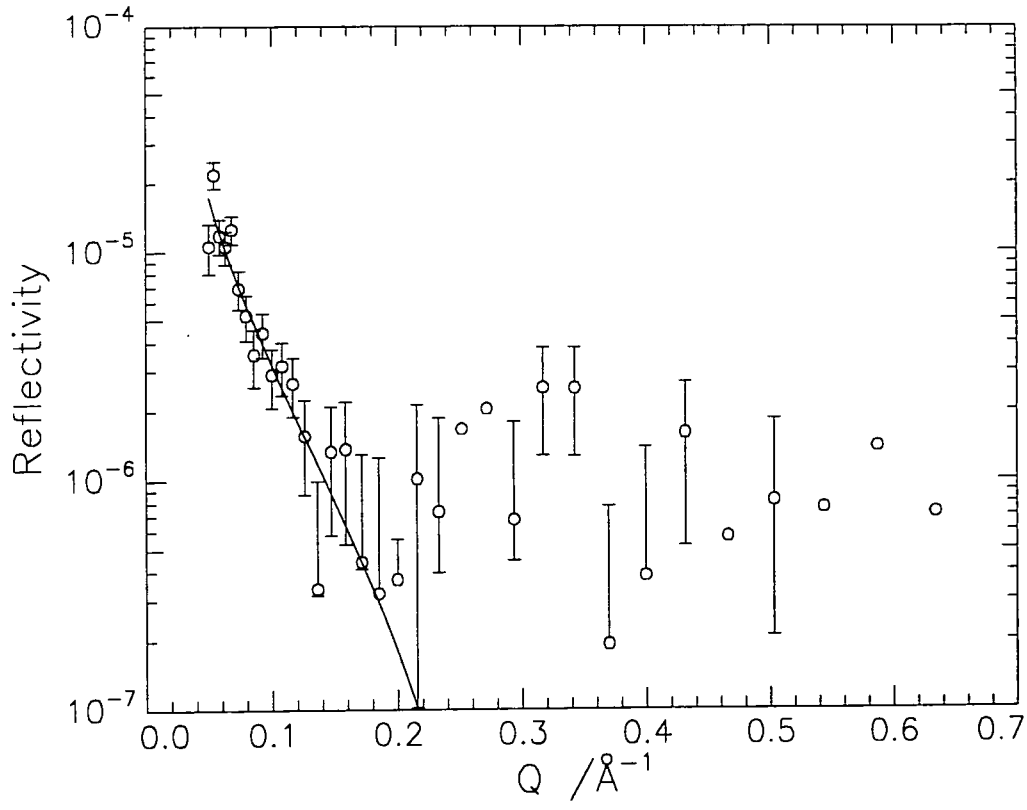

Figure 4.53(c): Reflectivity profiles for DMHL at 5mN m^{-1}, 1st 15 minute run (o) and single layer fit (—)

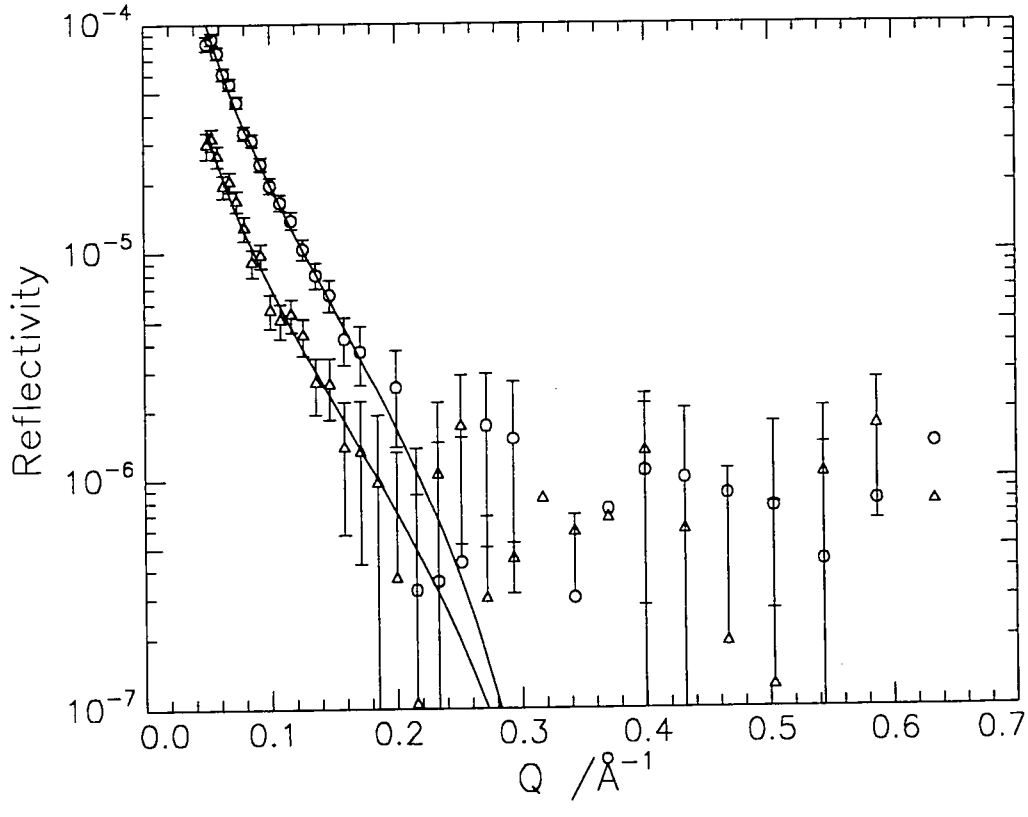

Figure 4.54(a): Reflectivity profiles for DMDL at 0.4mN m^{-1}, 1st 15 minute run (o), 6th 15 minute run (Δ) and single layer fit (—)

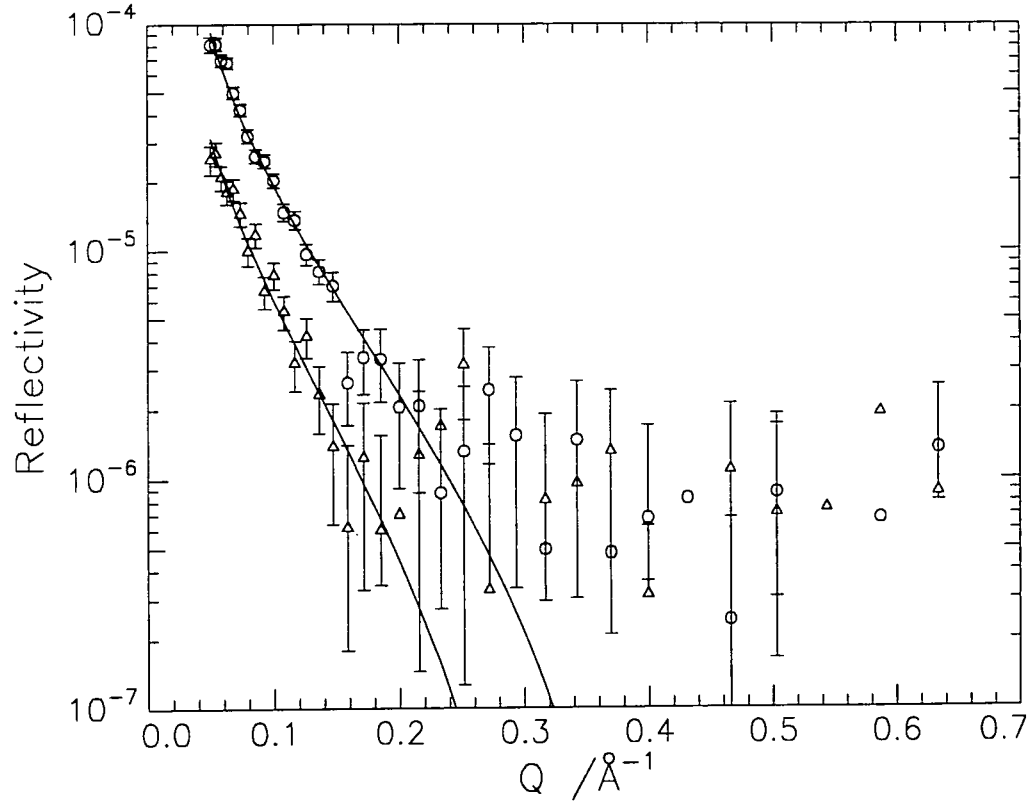

Figure 4.54(b): Reflectivity profiles for HMDL at 0.4mN m^{-1}, 1st 15 minute run (o), 6th 15 minute run (Δ) and single layer fit (—)

MONOMER	RUN NUMBER	d (Å)	ρ (Å^{-2} × 10^{-6})
DMDL	1	18.6	3.1
ρ_{calc} = 6.8 × 10^{-6}Å^{-2}	2	17.6	2.3
	3	17.7	2.05
	4	16.8	1.85
	5	19.5	1.48
	6	23.8	1.13
HMDL	1	19.4	2.9
ρ_{calc} = 5.7 × 10^{-6}Å^{-2}	2	17.7	2.41
	3	9.7	3.61
	4	19.8	1.71
	5	16.3	1.72
	6	21.0	1.34
DMHL	1	17.2	0.59
ρ_{calc} = 1.4× 10^{-6}Å^{-2}			

Table 4.13: Parameters obtained from single layer fits at 10mN m^{-1} on a.c.m.w.

MONOMER	RUN NUMBER	d (Å)	ρ ($Å^{-2} \times 10^{-6}$)
DMDL	1	18.8	2.6
$\rho_{calc} = 6.8 \times 10^{-6} Å^{-2}$	2	18.5	2.3
	3	21.2	1.87
	4	17.3	2.1
	5	18.6	1.7
	6	18.0	1.6
HMDL	1	18.2	2.4
$\rho_{calc} = 5.7 \times 10^{-6} Å^{-2}$	2	16.9	2.2
	3	17.5	2.0
	4	13.0	2.3
	5	20.0	1.39
	6	24.4	1.14
DMHL	1	21.8	0.8
$\rho_{calc} = 1.4 \times 10^{-6} Å^{-2}$			

Table 4.14: Parameters obtained from single layer fits at 5mN m^{-1} on a.c.m.w.

MONOMER	RUN NUMBER	d (Å)	ρ ($Å^{-2} \times 10^{-6}$)
DMDL	1	19.2	2.2
$\rho_{calc} = 6.8 \times 10^{-6} Å^{-2}$	2	13.6	2.6
	3	19.4	1.7
	4	17.9	1.6
	5	17.8	1.5
	6	17.9	1.4
HMDL	1	16.3	2.4
$\rho_{calc} = 5.7 \times 10^{-6} Å^{-2}$	2	14.2	2.4
	3	18.7	1.7
	4	16.8	1.7
	5	14.4	1.7
	6	20.2	1.2

Table 4.15: Parameters obtained from single layer fits at 0.4mN m^{-1} on a.c.m.w.

At 5 and 10mN m^{-1}, the reflectivity for DMHL became too low and merged into the background level after the first 15 minute run, therefore, it was not possible to fit the remaining data. The fits that were obtained for DMHL are not good due to the low reflectivity, so not too much weight should be attached to the parameters obtained. At 0.4mN m^{-1}, the first 15 minute run for DMHL showed no reflectivity above the background level, so no fit for this monomer was obtained at the lowest surface pressure. The individual values of the layer thickness (d) and scattering length density (ρ) show no particular trend, this is due to the coupling of the parameters which leads to the decrease in reflectivity being equally well accounted for by altering either parameter. The scattering length density values obtained are greatly reduced from the calculated value, indicating that a large amount of subphase is contained in the monolayer. The parameters can be used to calculated the apparent surface concentration using equation 4.16 and these are compared to the theoretical surface concentration in tables 4.16 to 4.18. The experimental surface concentrations show a consistent trend and decrease with time, in agreement with the observed decrease in the reflectivity profiles.

The greatest decrease in the experimental surface concentration occurs during the first 15 minutes for each monomer at each surface concentration. The concentration decreases from the theoretical value to circa 0.7±0.1mg m^{-2} within the first 15 minutes and then tends towards a value of 0.4±0.05mg m^{-2}. The surface pressure, which was monitored during the acquisition of the reflectivity profiles, also decreased with time and this is shown in figures 4.55 to 4.57 (a) and (b) compared to the decrease in surface concentration. The decrease in surface pressure follows a similar pattern to that for the surface concentration, i.e. the maximum decrease occurs in the first 15 minutes and then the surface pressure becomes constant at circa -4mN m^{-1}. This behaviour of the surface

tension is the same as that observed in the SQELS study on monolayers of the monomer and is discussed further in the next chapter (section 5.4).

MONOMER	RUN NUMBER	Γ_{exp} (mg m^{-2})	Γ_{calc} (mg m^{-2})
DMDL	1	0.8	1.9
	2	0.6	
	3	0.5	
	4	0.5	
	5	0.4	
	6	0.4	
HMDL	1	1.0	1.8
	2	0.7	
	3	0.6	
	4	0.6	
	5	0.5	
	6	0.5	
DMHL	1	0.8	1.86

Table 4.16: Experimental and theoretical surface concentrations at 10mN m^{-1}

MONOMER	RUN NUMBER	Γ_{exp} (mg m^{-2})	Γ_{calc} (mg m^{-2})
DMDL	1	0.7	1.1
	2	0.6	
	3	0.6	
	4	0.5	
	5	0.5	
	6	0.4	
HMDL	1	0.8	1.1
	2	0.7	
	3	0.6	
	4	0.5	
	5	0.5	
	6	0.5	
DMHL	1	1.3	1.1

Table 4.17: Experimental and theoretical surface concentrations at 5mN m^{-1}

MONOMER	RUN NUMBER	Γ_{exp} (mg m^{-2})	Γ_{calc} (mg m^{-2})
DMDL	1	0.6	0.82
	2	0.5	
	3	0.5	
	4	0.4	
	5	0.4	
	6	0.4	
HMDL	1	0.7	0.80
	2	0.6	
	3	0.5	
	4	0.5	
	5	0.4	
	6	0.4	

Table 4.18: Experimental and theoretical surface concentrations at 0.4mN m^{-1}

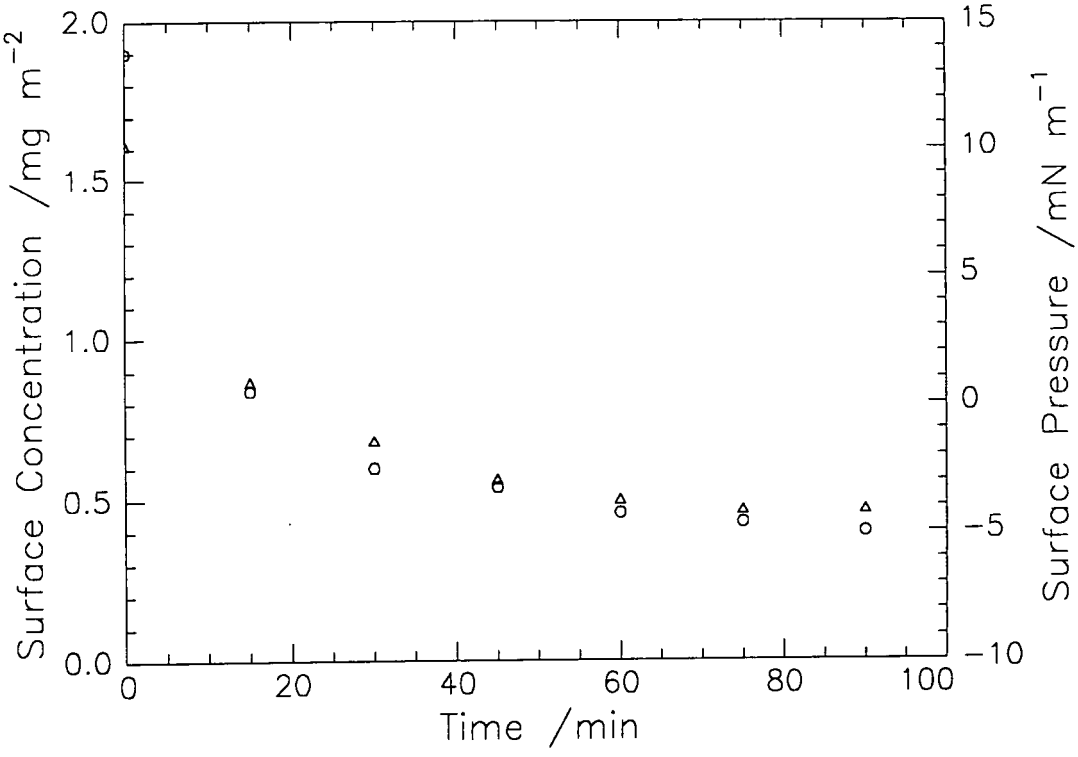

Figure 4.55(a): Change in surface concentration (o) and surface pressure (Δ) with time for DMDL at 10mN m^{-1}

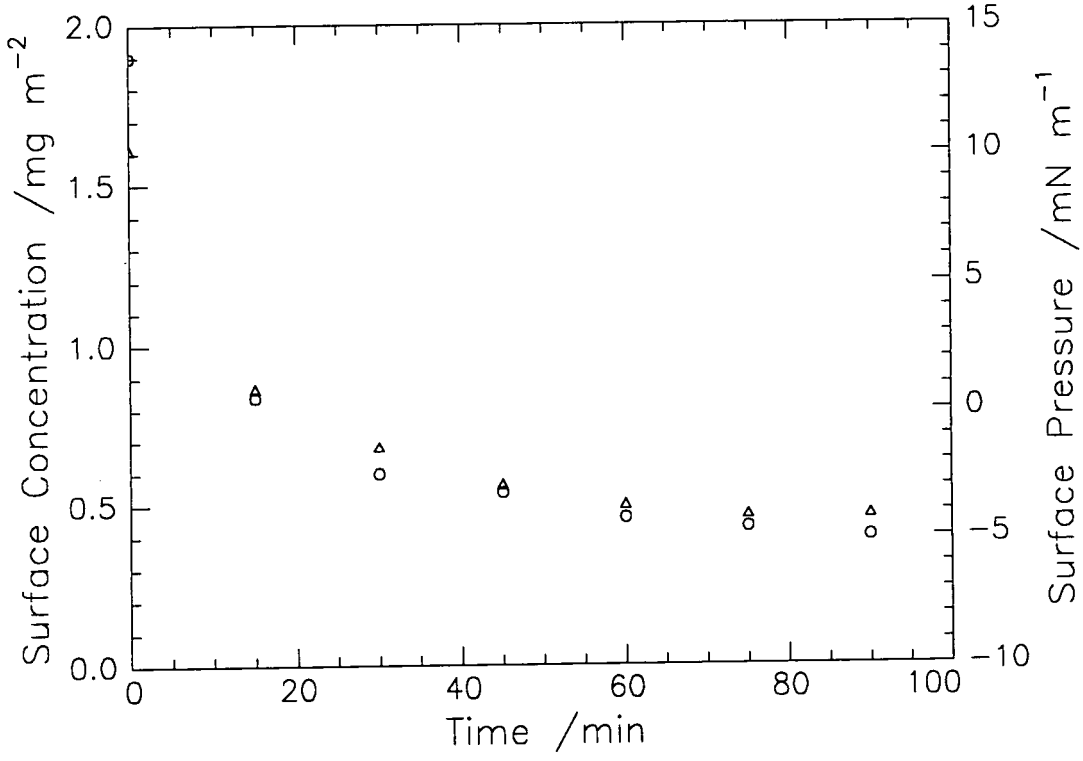

Figure 4.55(b): Change in surface concentration (o) and surface pressure (Δ) with time for HMDL at 10mN m^{-1}

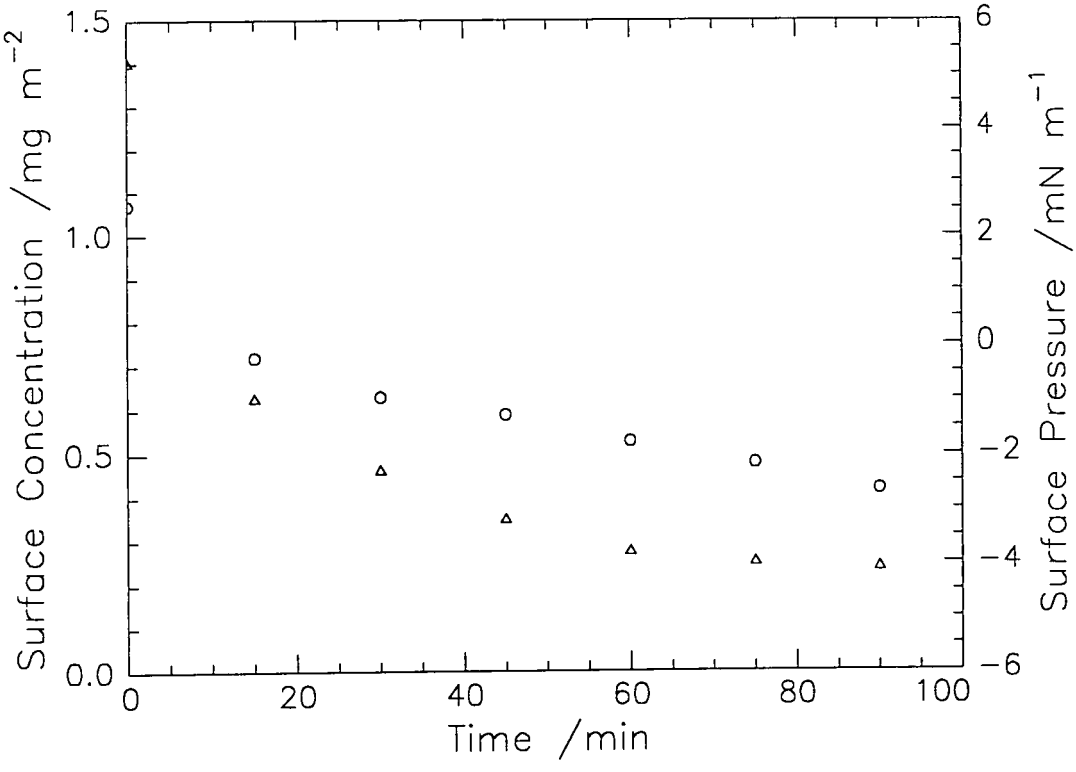

Figure 4.56(a): Change in surface concentration (o) and surface pressure (Δ) with time for DMDL at 5mN m^{-1}

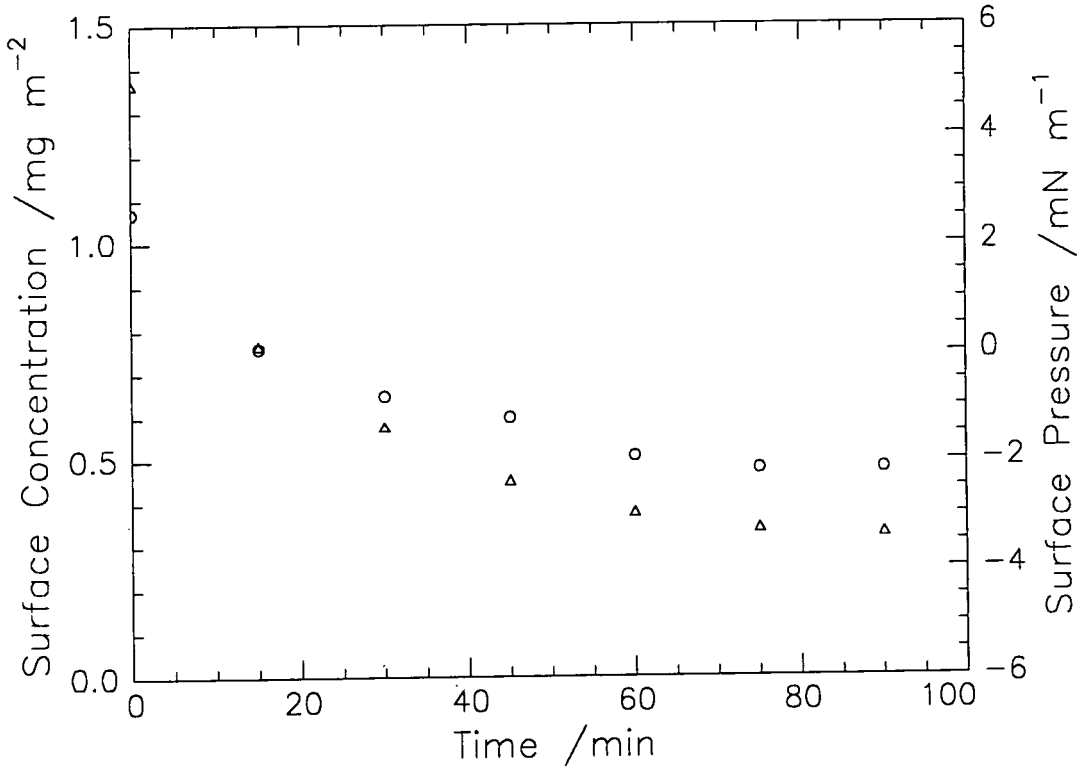

Figure 4.56(b): Change in surface concentration (o) and surface pressure (Δ) with time for HMDL at 5mN m^{-1}

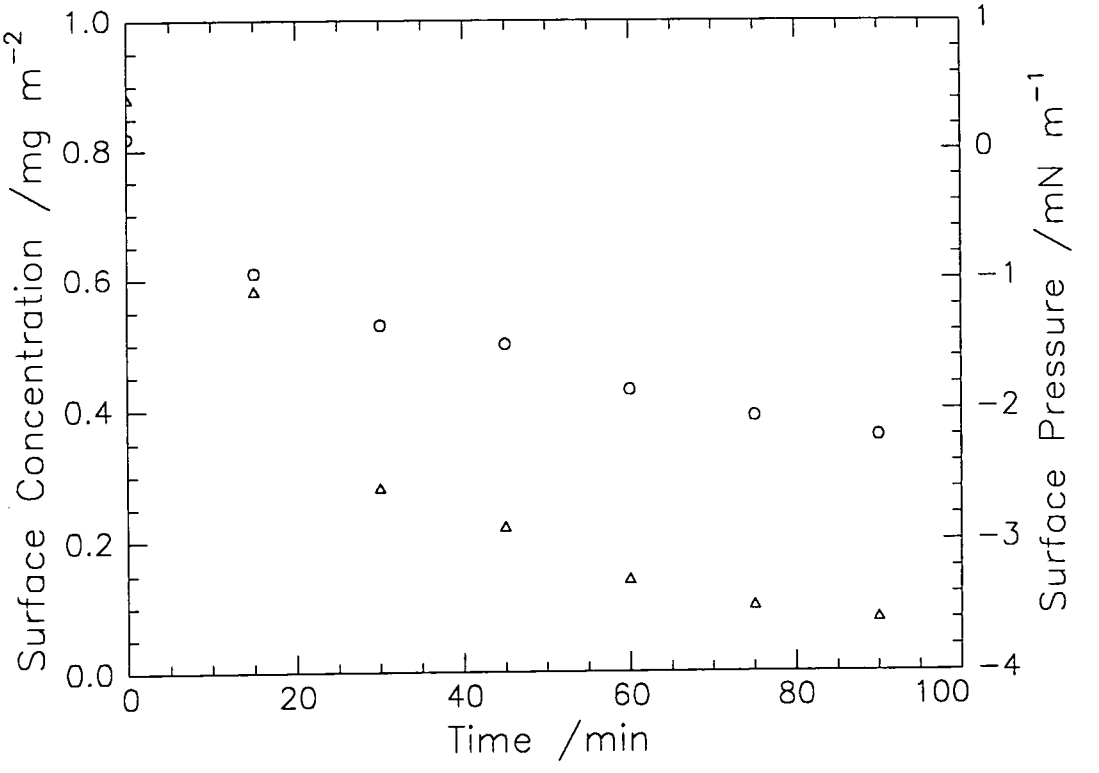

Figure 4.57(a): Change in surface concentration (o) and surface pressure (Δ) with time for DMDL at 0.4mN m^{-1}

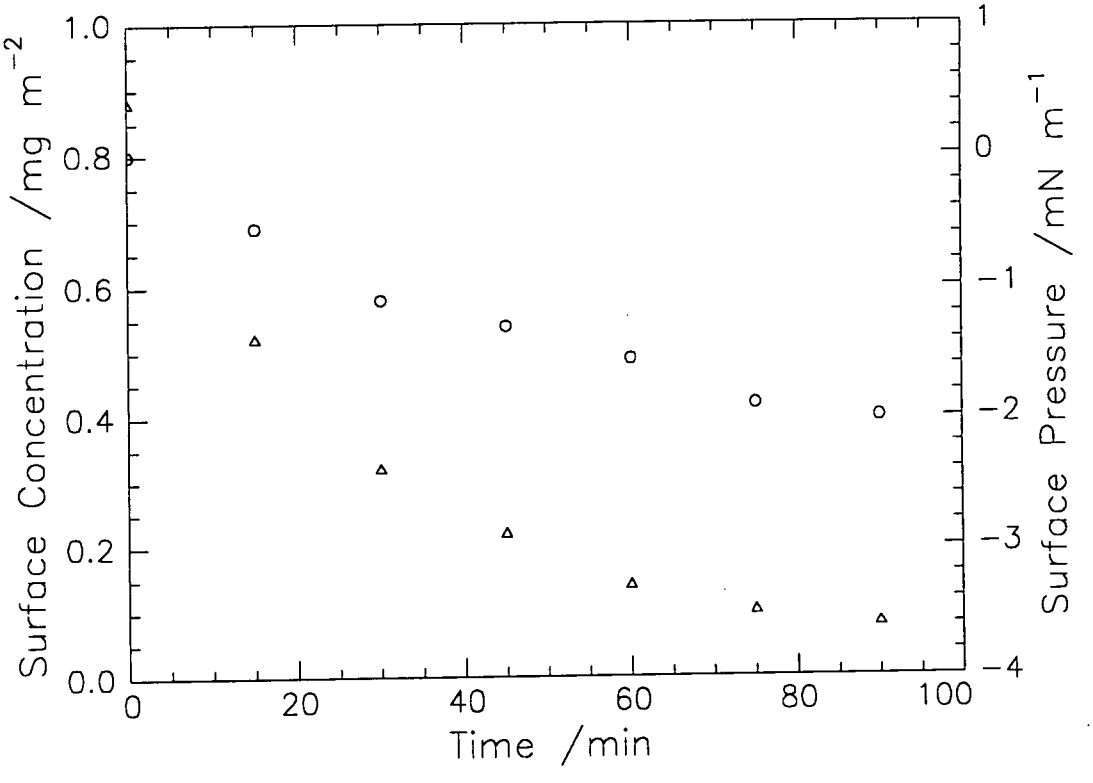

Figure 4.57(b): Change in surface concentration (o) and surface pressure (Δ) with time for HMDL at 0.4mN m^{-1}

The reflectivity profiles obtained for each isotopic variation of LMA spread on D_2O are shown at each surface pressure in figures 4.58 to 4.60(a) to (d). Each figure consists of six 15 minute runs and these are compared to the reflectivity obtained for clean D_2O. The key to the points is, o 1st 15min, × 2nd 15min, Δ 3rd 15min, + 4th 15min, ◇ 5th 15min and • 6th 15min.

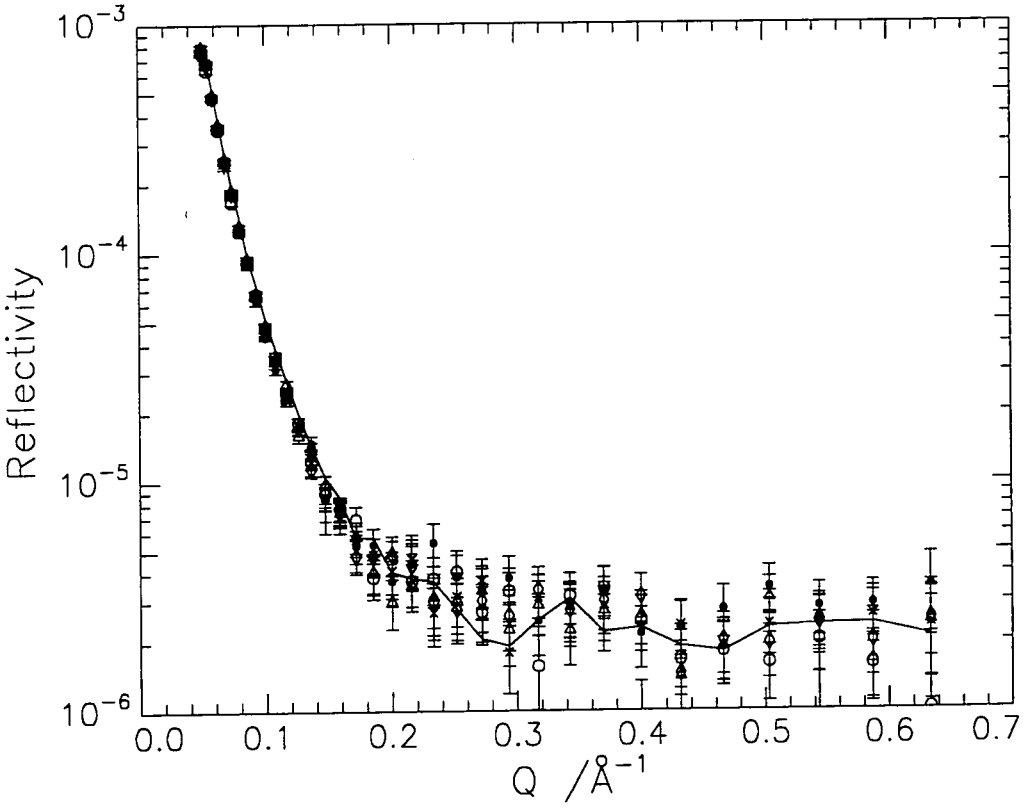

Figure 4.58(a): Reflectivity profiles for DMDL at 10mN m^{-1} on D_2O

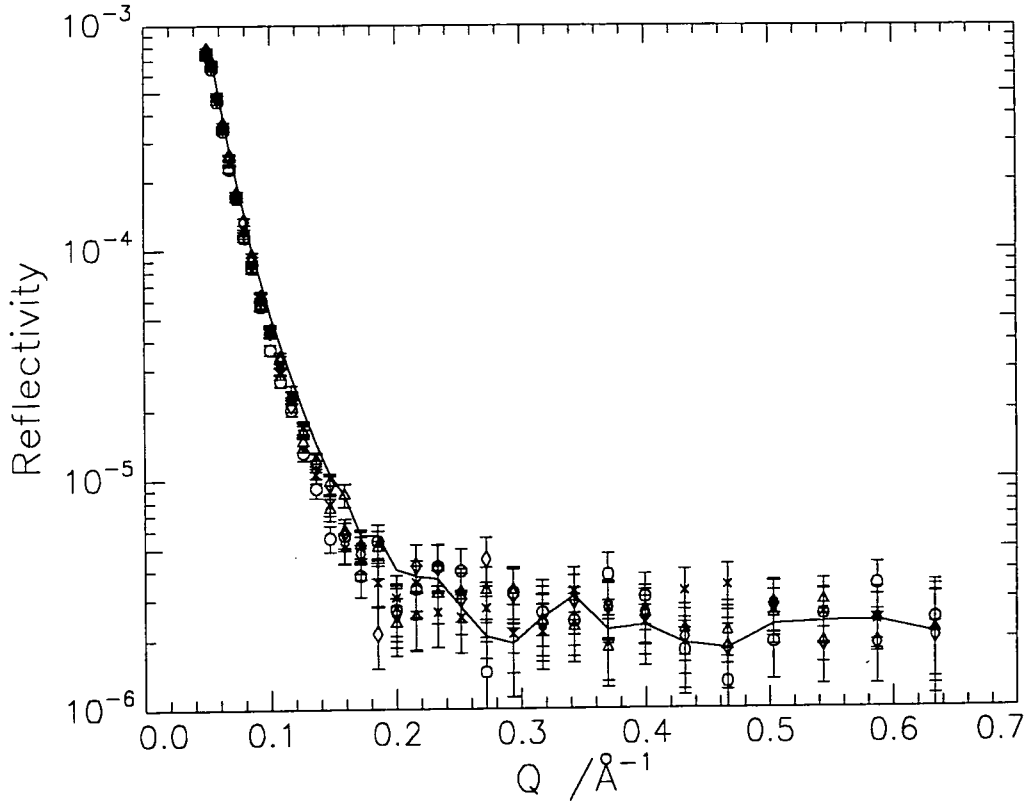

Figure 4.58(b): Reflectivity profiles for HMDL at 10mN m^{-1} on D_2O

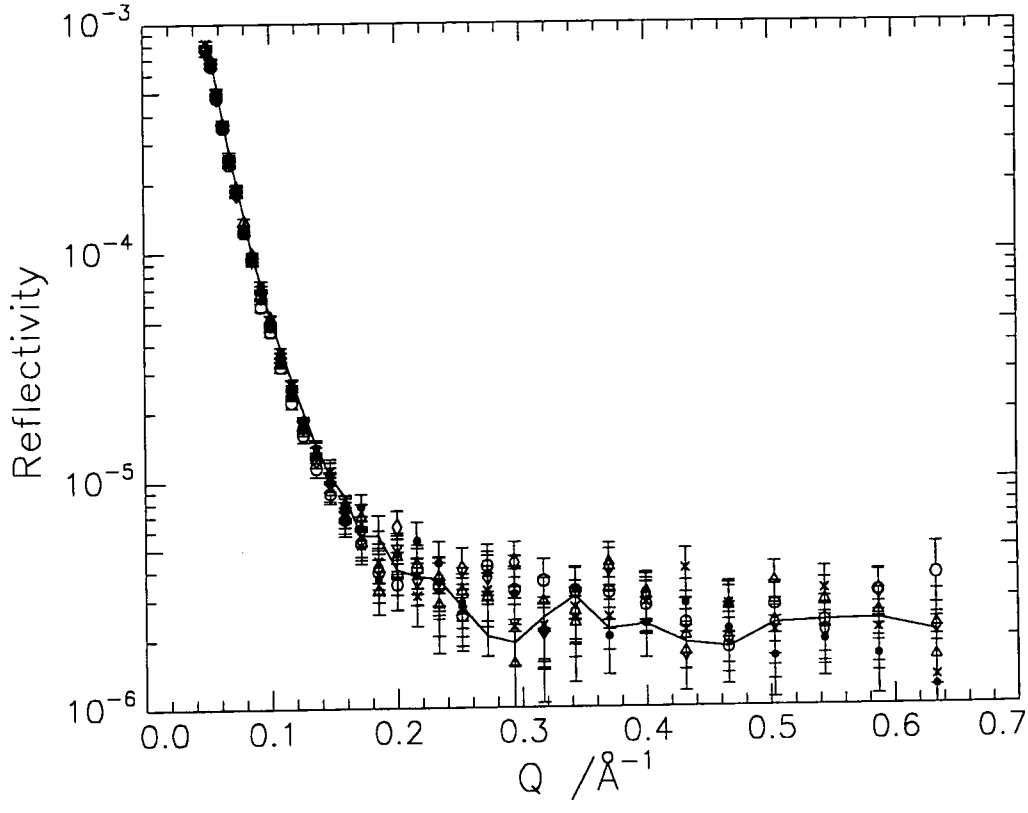

Figure 4.58(c): Reflectivity profiles for DMHL at 10mN m^{-1} on D_2O

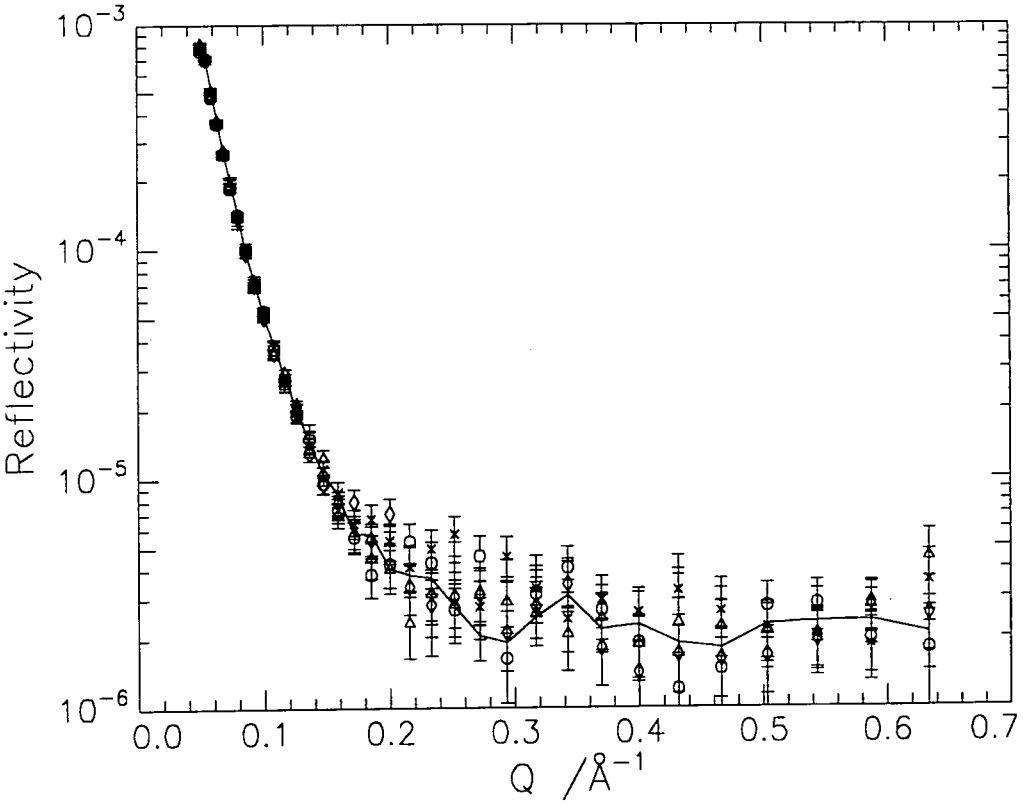

Figure 4.58(d): Reflectivity profiles for HMHL at 10mN m^{-1} on D_2O

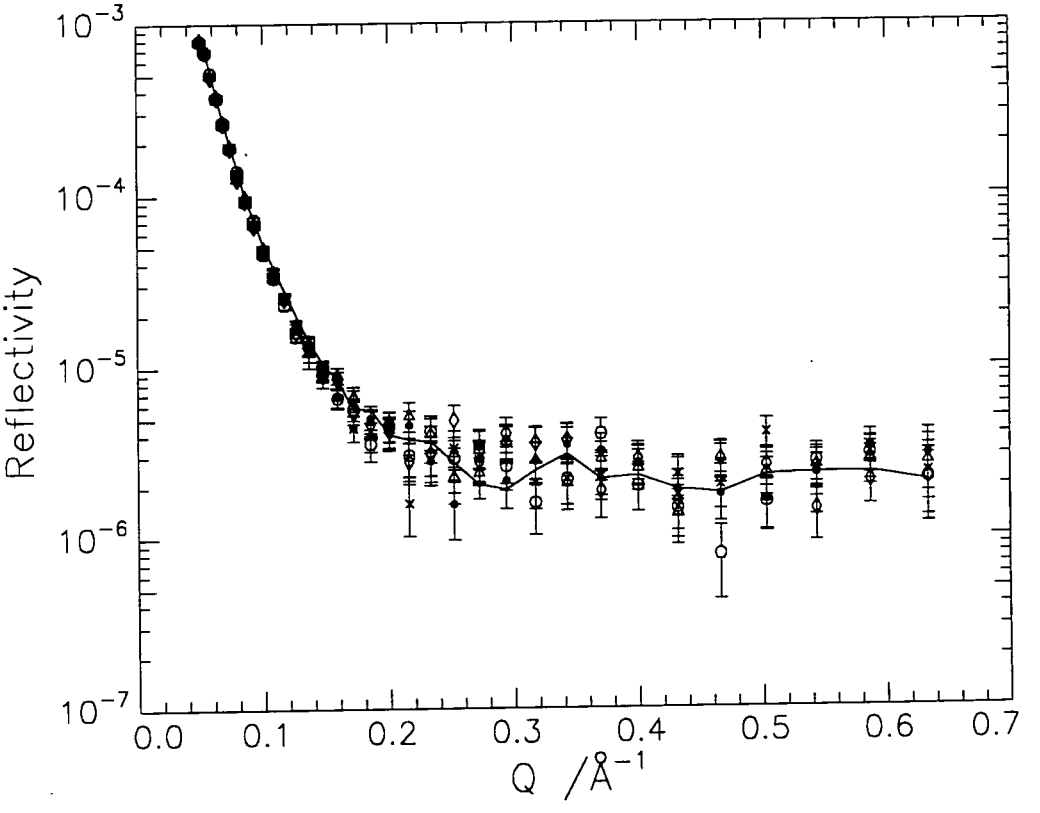

Figure 4.59(a): Reflectivity profiles for DMDL at 5mN m^{-1} on D_2O

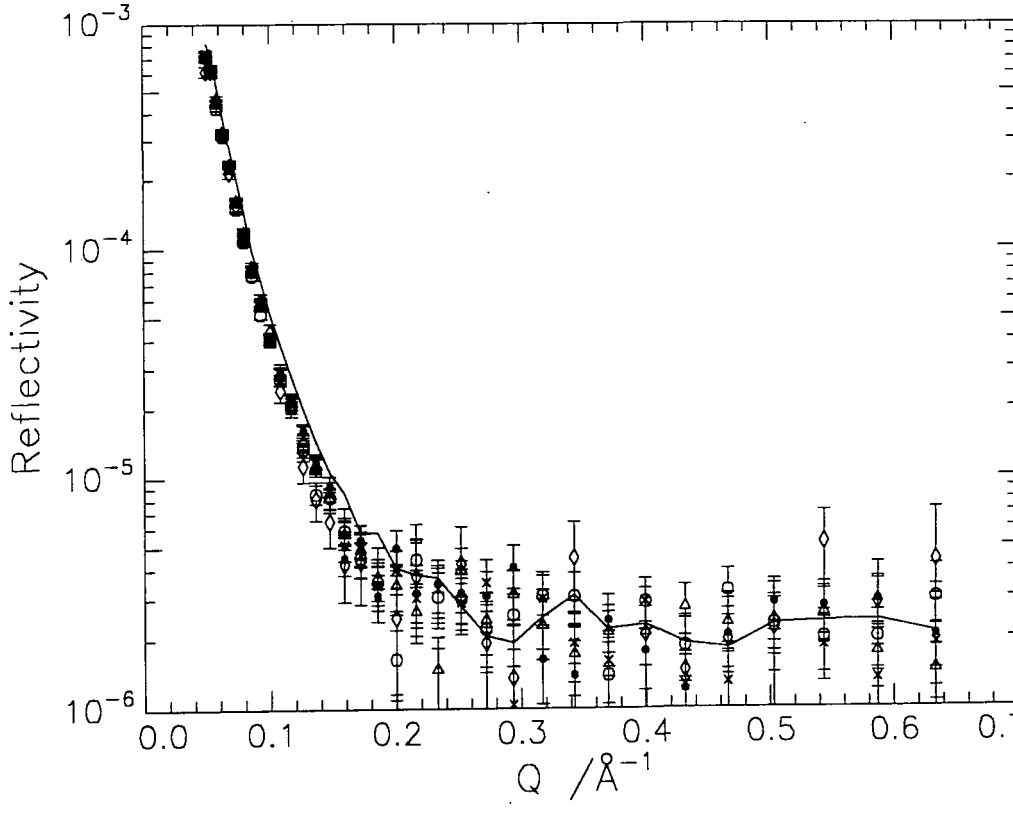

Figure 4.59(b): Reflectivity profiles for HMDL at 5mN m^{-1} on D_2O

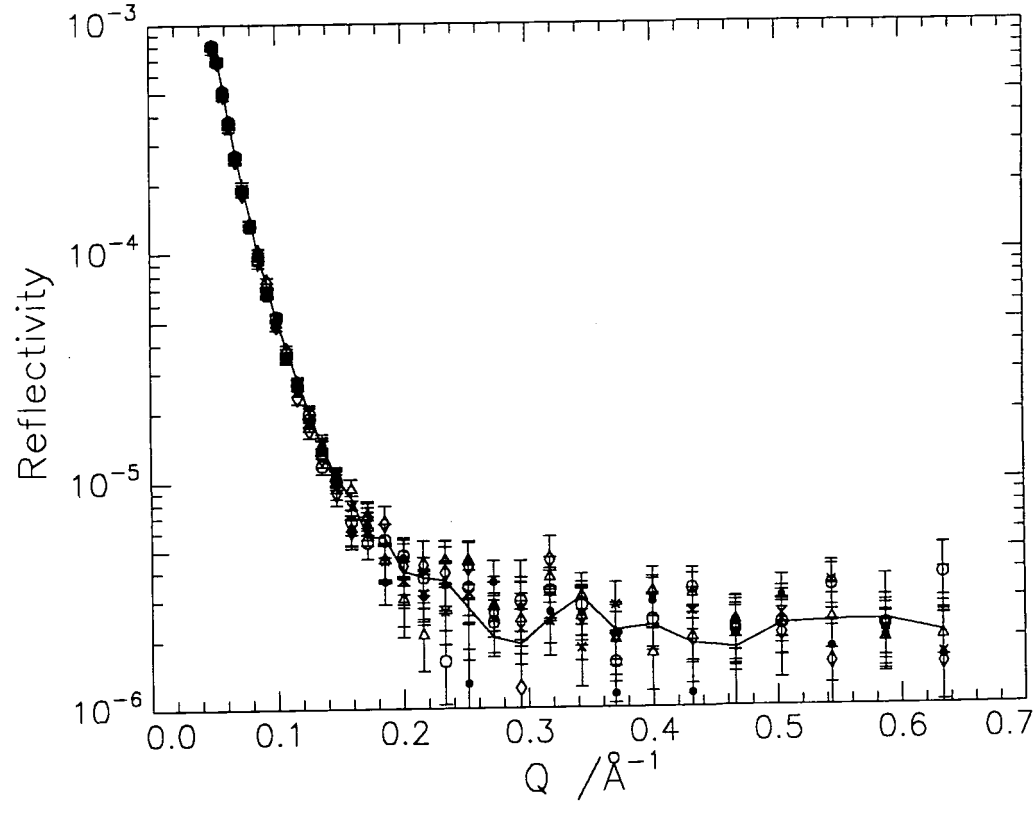

Figure 4.59(c): Reflectivity profiles for DMHL at 5mN m^{-1} on D_2O

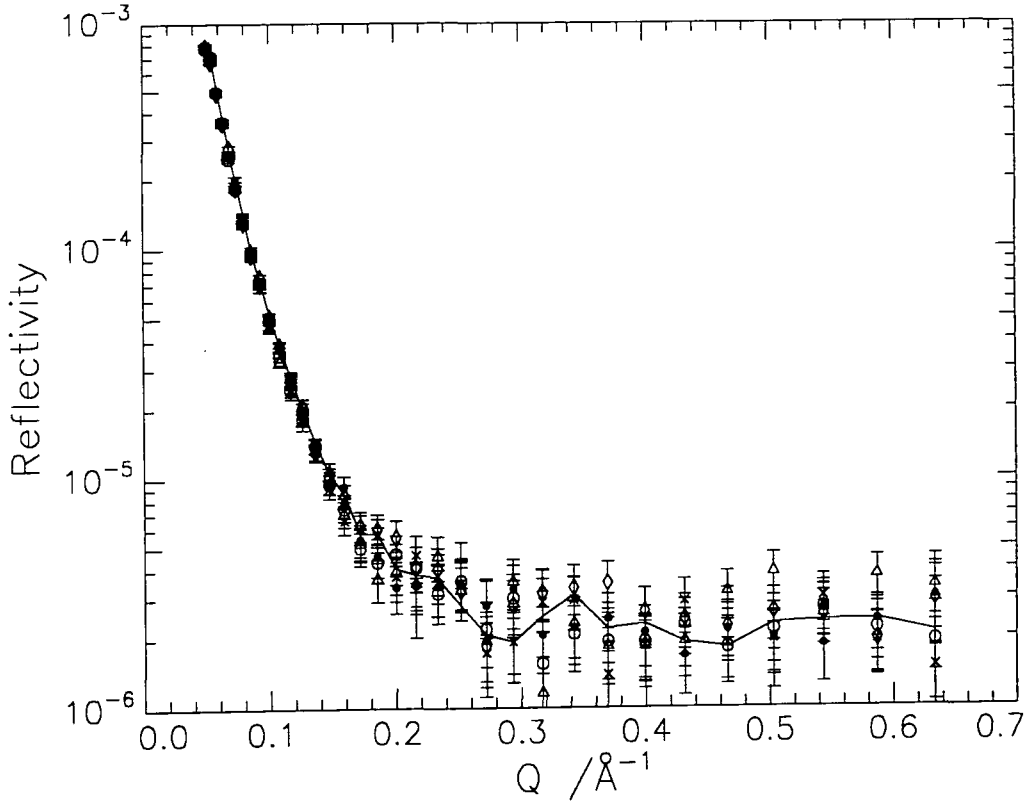

Figure 4.59(d): Reflectivity profiles for HMHL at 5mN m^{-1} on D_2O

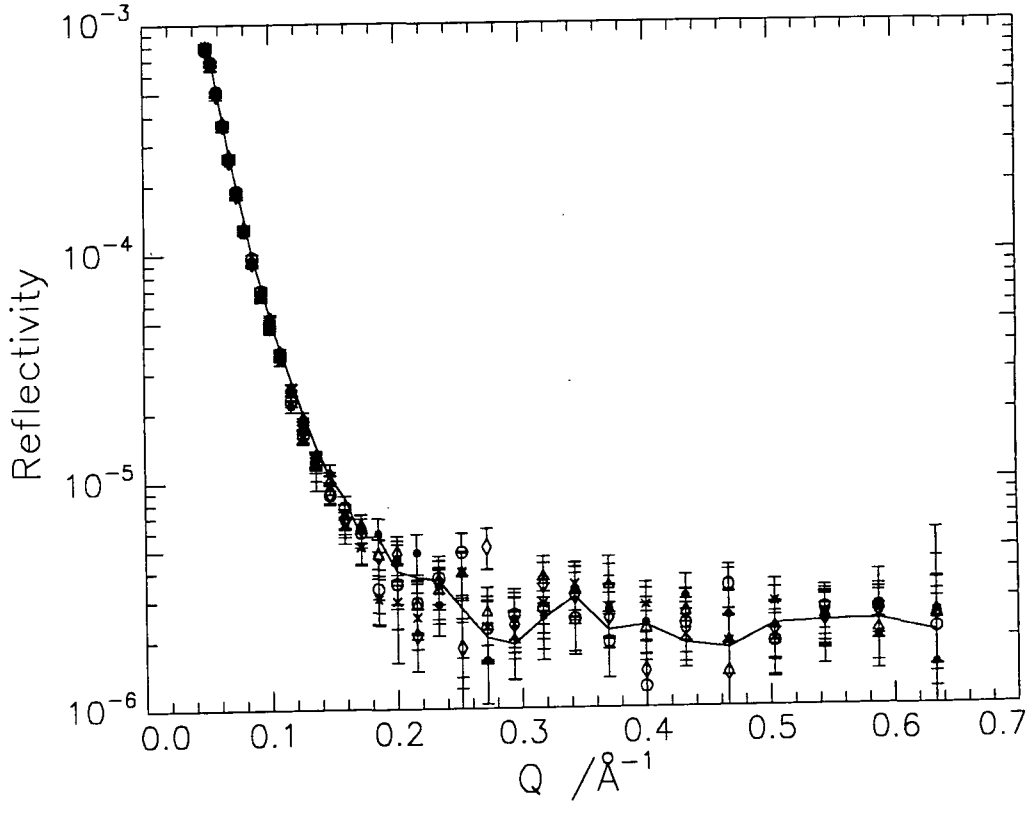

Figure 4.60(a): Reflectivity profiles for DMDL at 0.4mN m^{-1} on D_2O

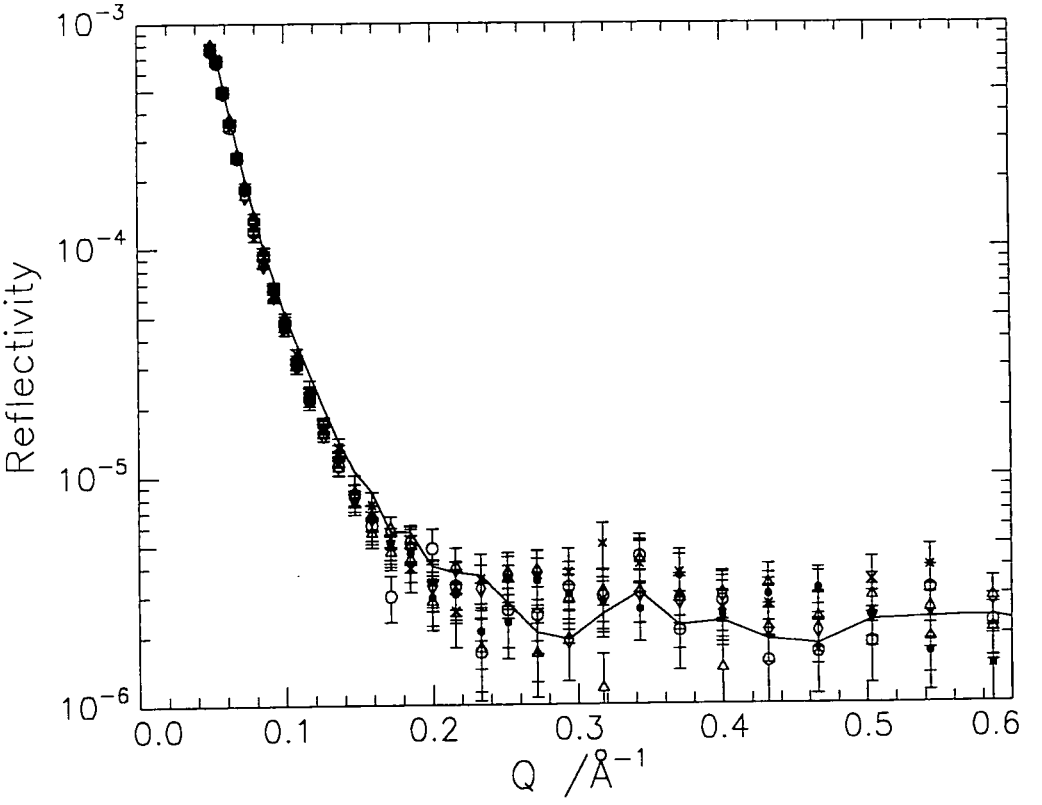

Figure 4.60(b): Reflectivity profiles for HMDL at 0.4mN m^{-1} on D_2O

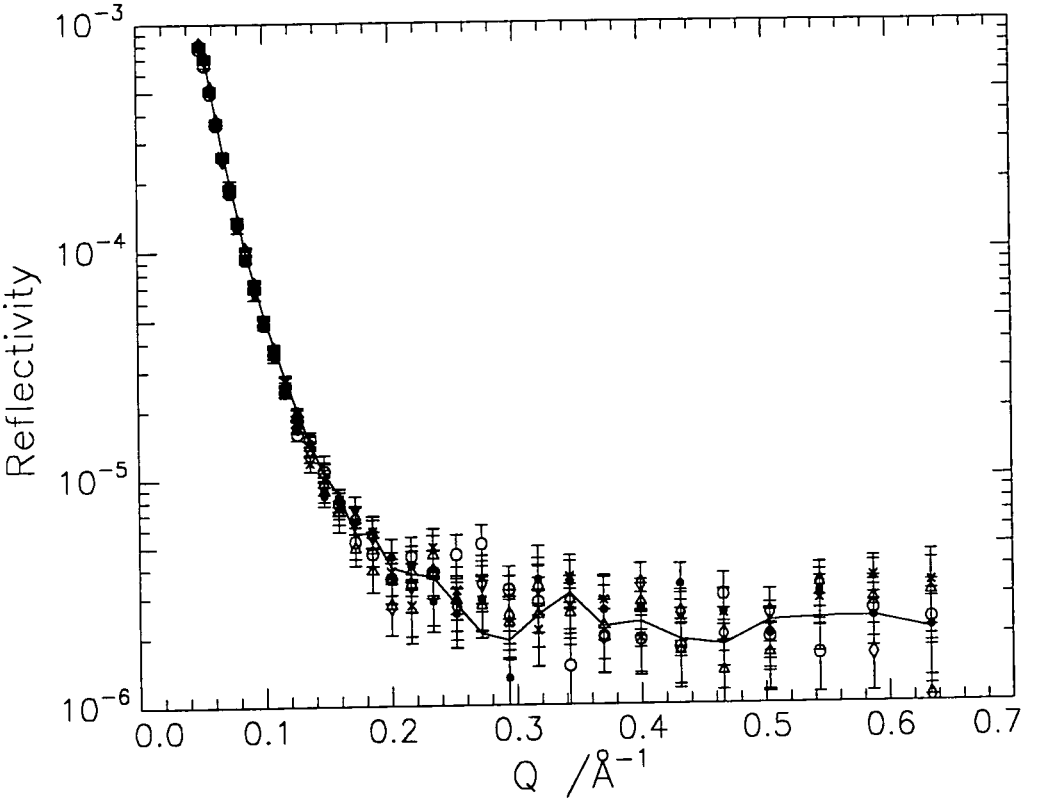

Figure 4.60(c): Reflectivity profiles for DMHL at 0.4mN m^{-1} on D_2O

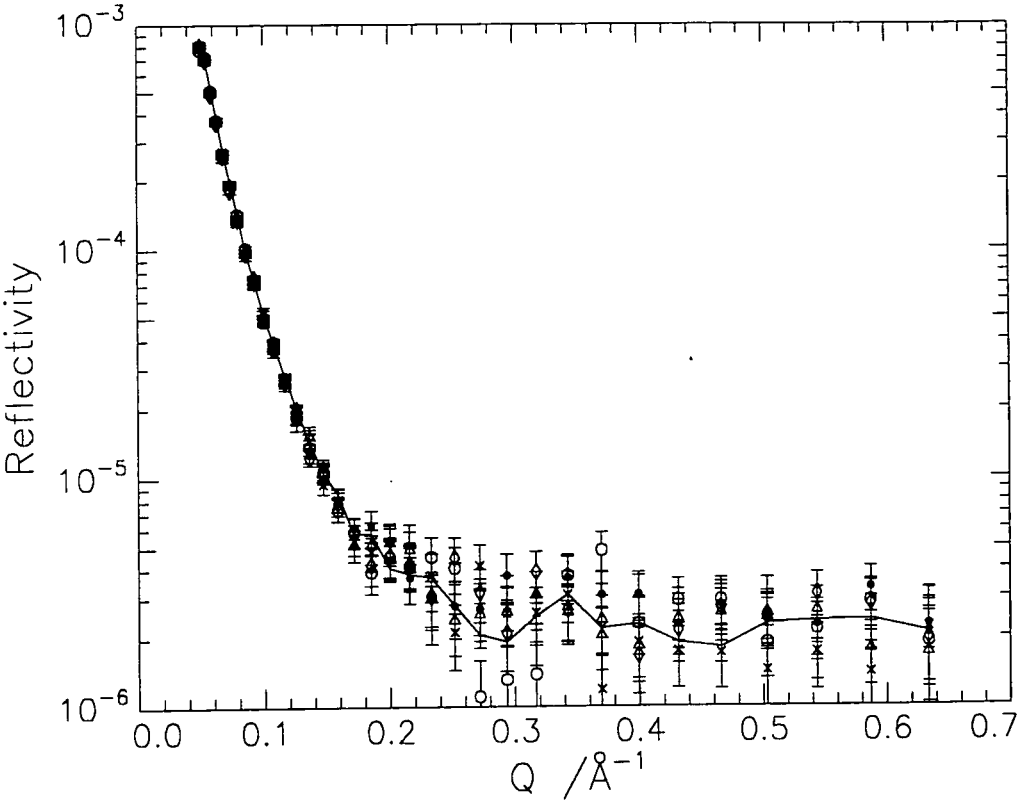

Figure 4.60(d): Reflectivity profiles for HMHL at 0.4mN m^{-1} on D_2O

The reflectivity profiles for the D_2O subphase all resemble that for clean D_2O, with the greatest deviation occurring for HMDL. This is the same pattern as that observed for the polymer monolayers, which suggests that the same reasoning can be used to explain the observed trends and hence the monomer monolayer appears to have a similar structure to the polymer. Little, or no change, is observed with time, which is as expected if the monolayer has a scattering length density profile similar to D_2O, so as the amount of monomer at the interface appears to decrease, exposing D_2O, no dramatic change will occur in the scattering length density profile normal to the interface.

As for the polymer, a two layer structure would seem to provide a more accurate description of the monomer distribution at the interface. This has been used to fit the data for the deuterated variations on a.c.m.w. and as for the single layer model, the first and sixth 15 minute runs are shown for DMDL and HMDL at each pressure (figures

4.61 to 4.63 (a) and (b)), whereas for DMHL, only the first run at 10 and 5mN m^{-1} produces sufficient signal, albeit weak, to allow fitting to take place (figures 4.61(c) and 5.62(c)). The parameters obtained from the fits are given in tables 4.19 to 4.21.

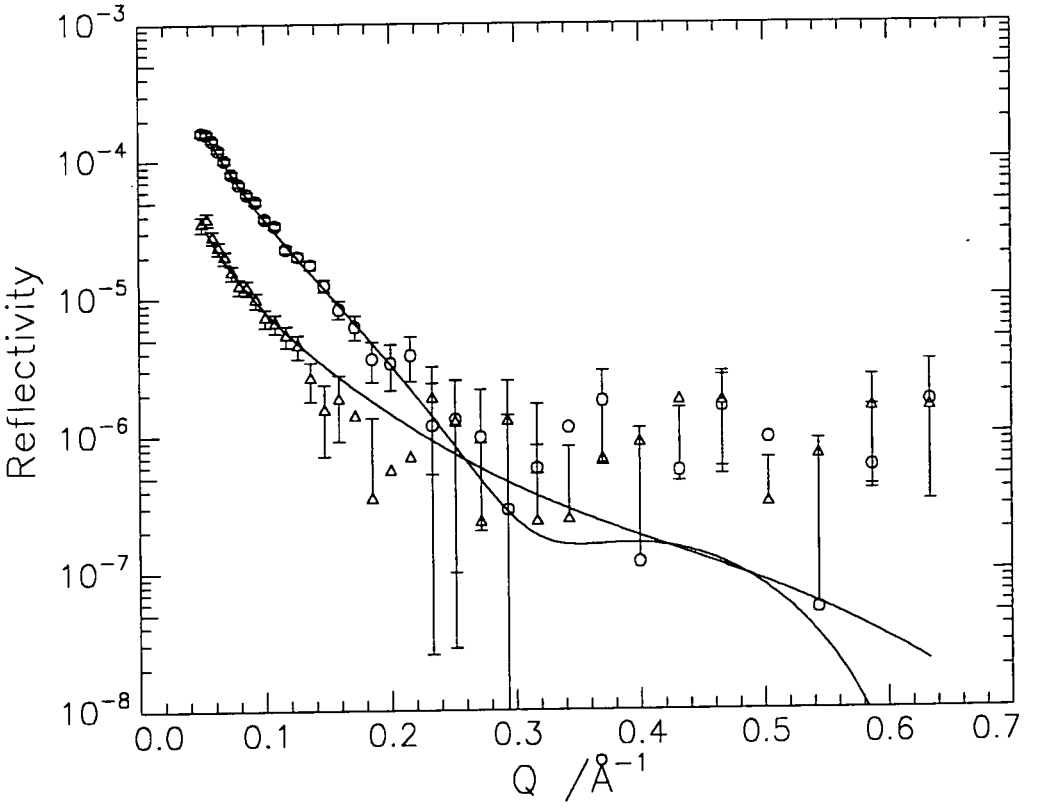

Figure 4.61(a): Reflectivity profiles for DMDL at 10mN m^{-1}, 1st 15 minute run (o), 6th 15 minute run (Δ) and two layer fit (—)

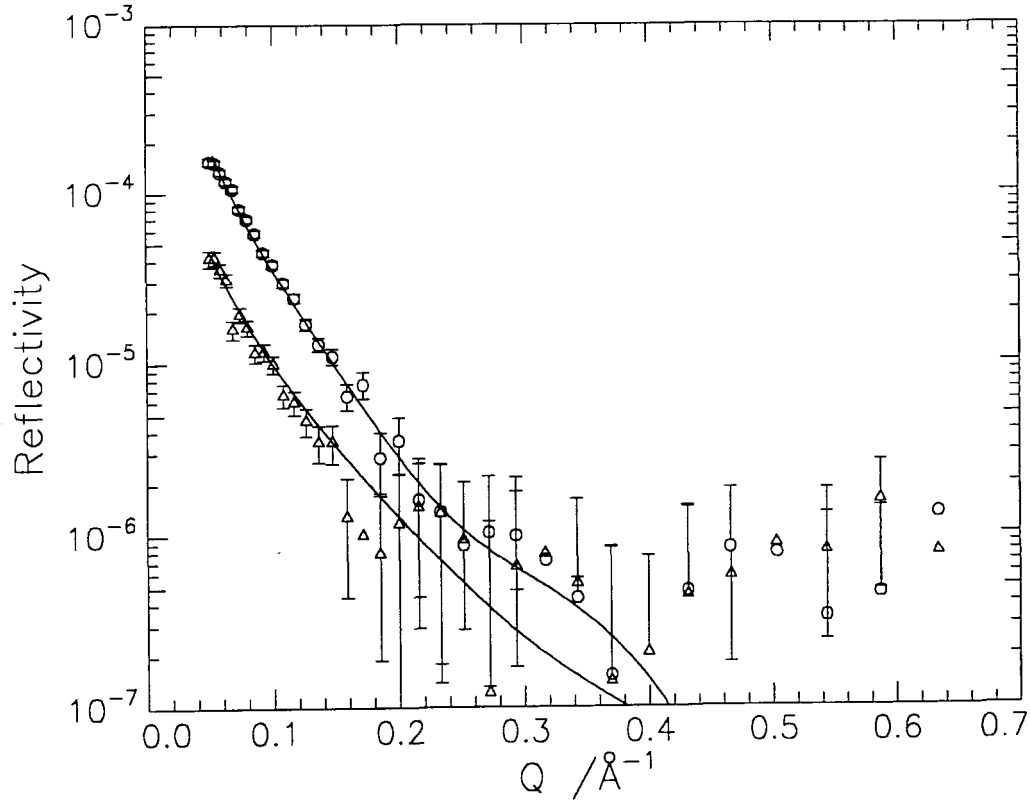

Figure 4.61(b): Reflectivity profiles for HMDL at 10mN m^{-1}, 1st 15 minute run (o), 6th 15 minute run (Δ) and two layer fit (—)

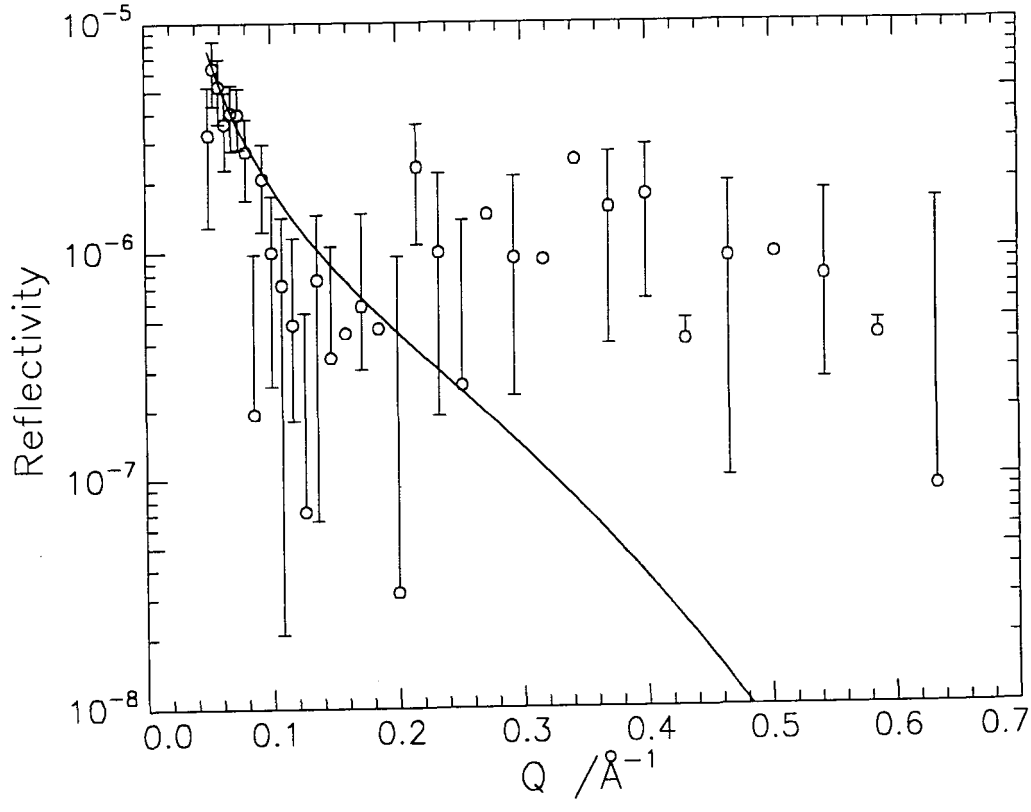

Figure 4.61(c): Reflectivity profiles for DMHL at 10mN m^{-1}, 1st 15 minute run (o) and two layer fit (—)

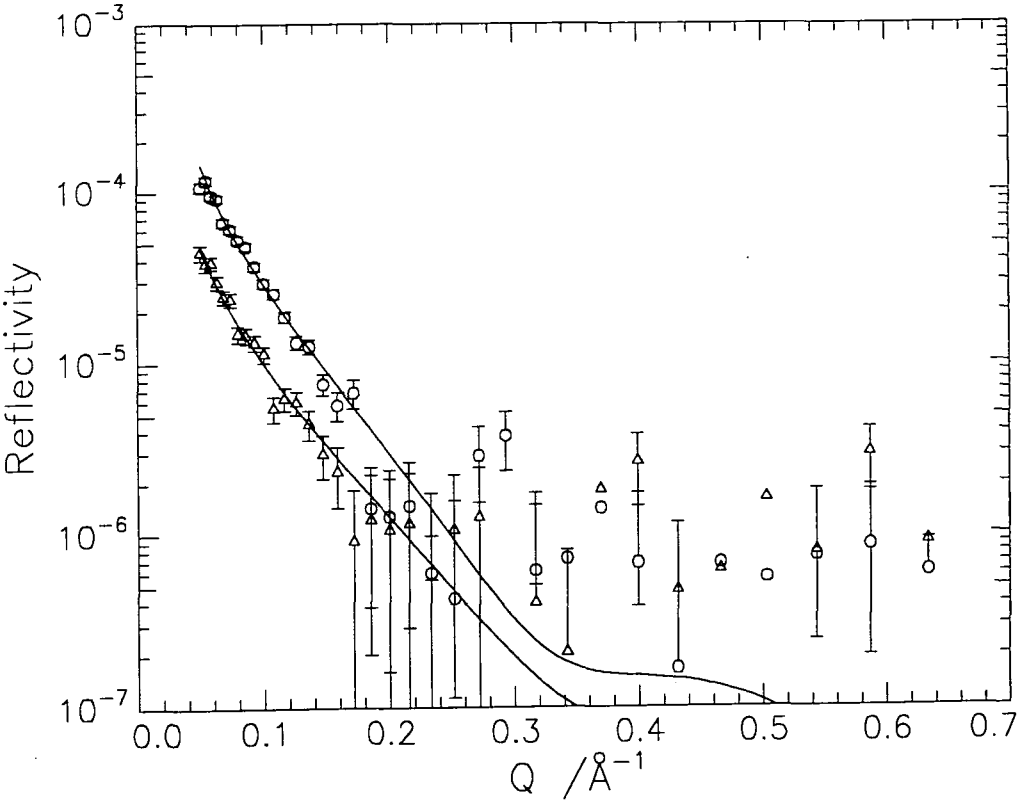

Figure 4.62(a): Reflectivity profiles for DMDL at 5mN m^{-1}, 1st 15 minute run (o), 6th 15 minute run (Δ) and two layer fit (—)

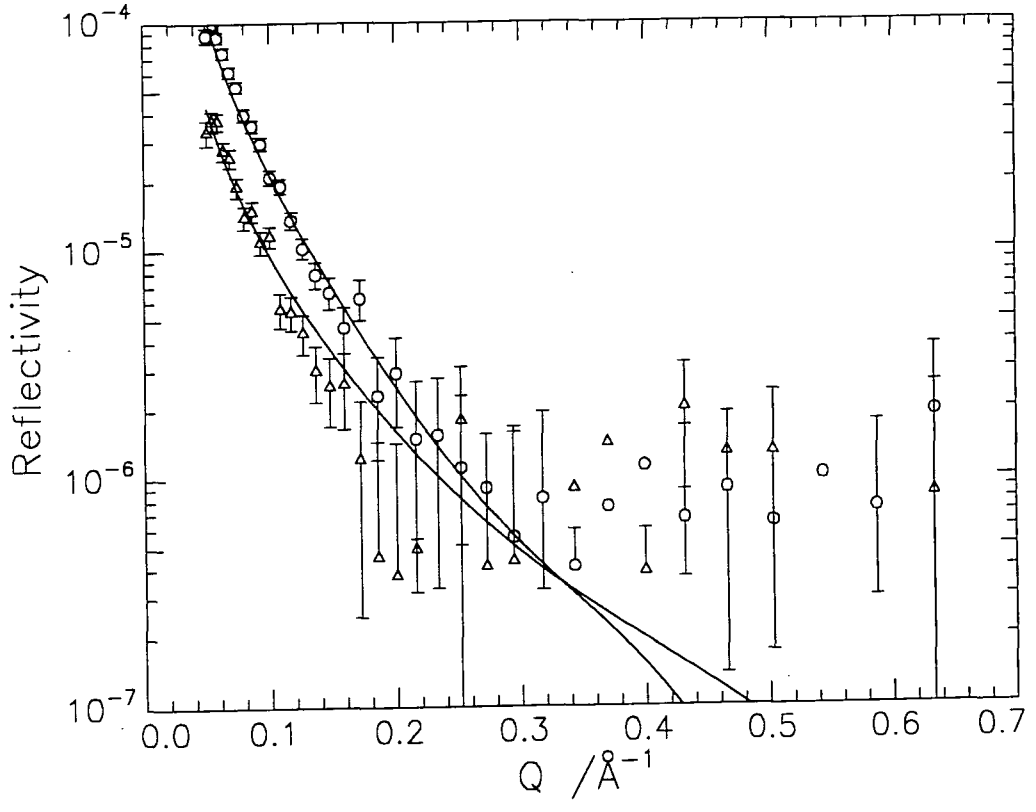

Figure 4.62(b): Reflectivity profiles for HMDL at 5mN m^{-1}, 1st 15 minute run (o), 6th 15 minute run (Δ) and two layer fit (—)

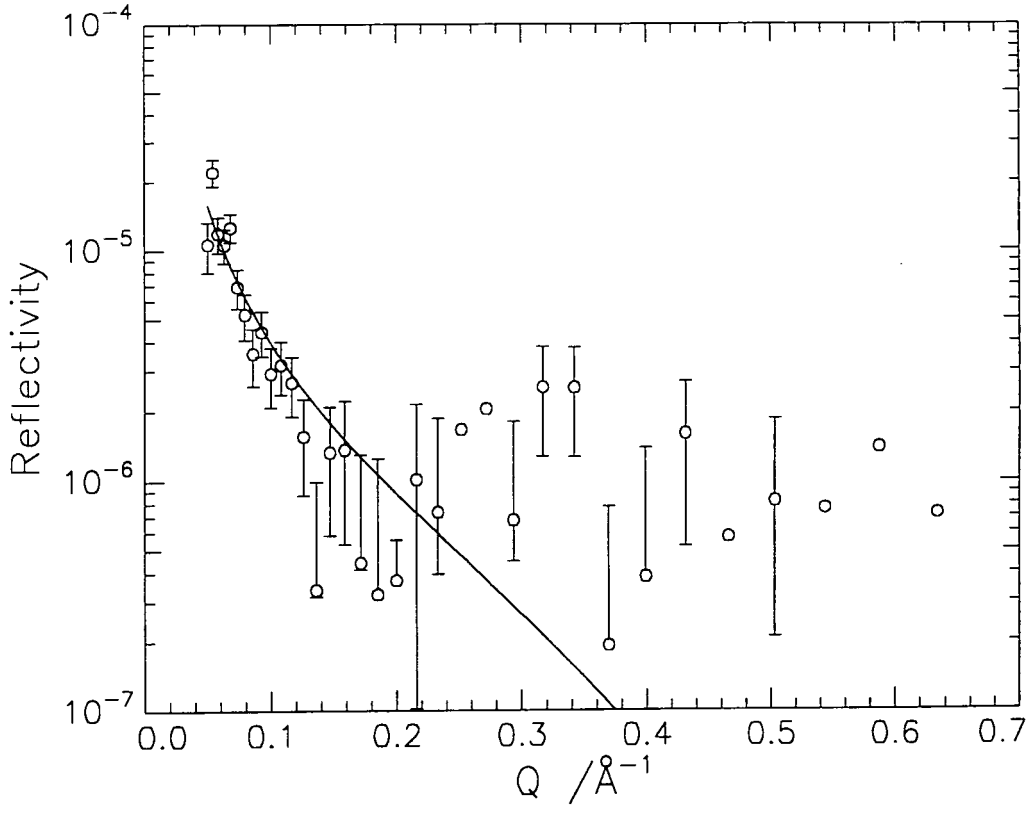

Figure 4.62(c): Reflectivity profiles for DMHL at 5mN m^{-1}, 1st 15 minute run (o) and two layer fit (—)

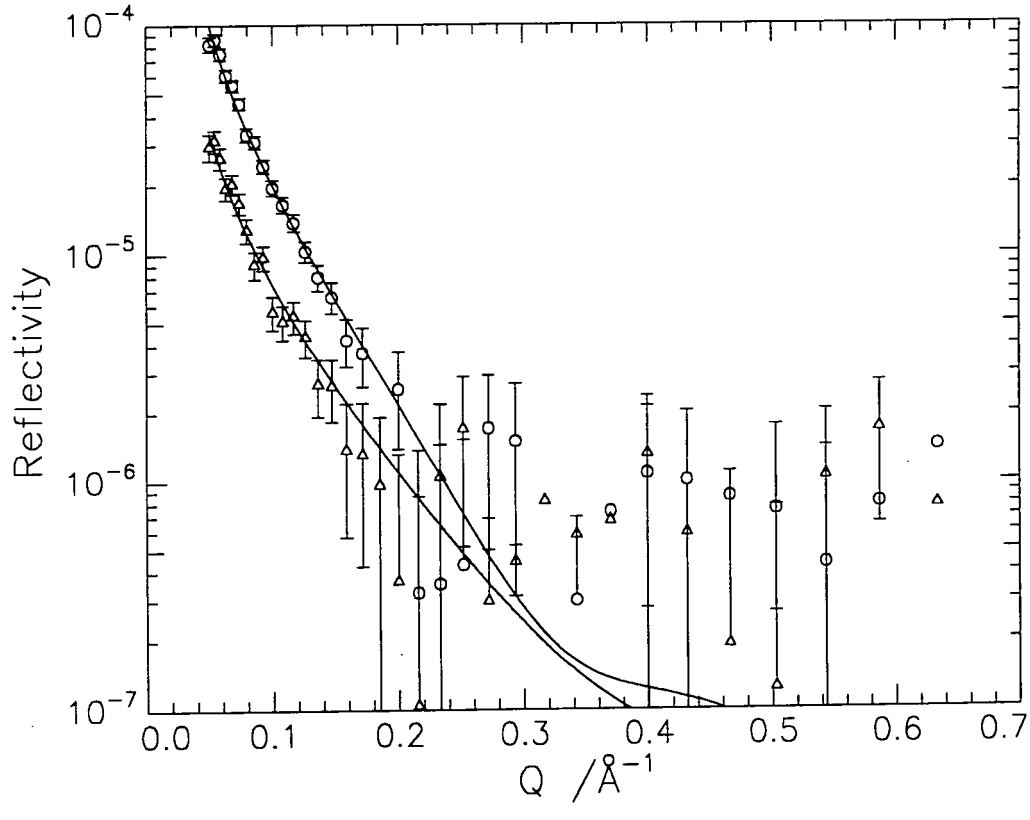

Figure 4.63(a): Reflectivity profiles for DMDL at 0.4mN m^{-1}, 1st 15 minute run (o), 6th 15 minute run (Δ) and two layer fit (—)

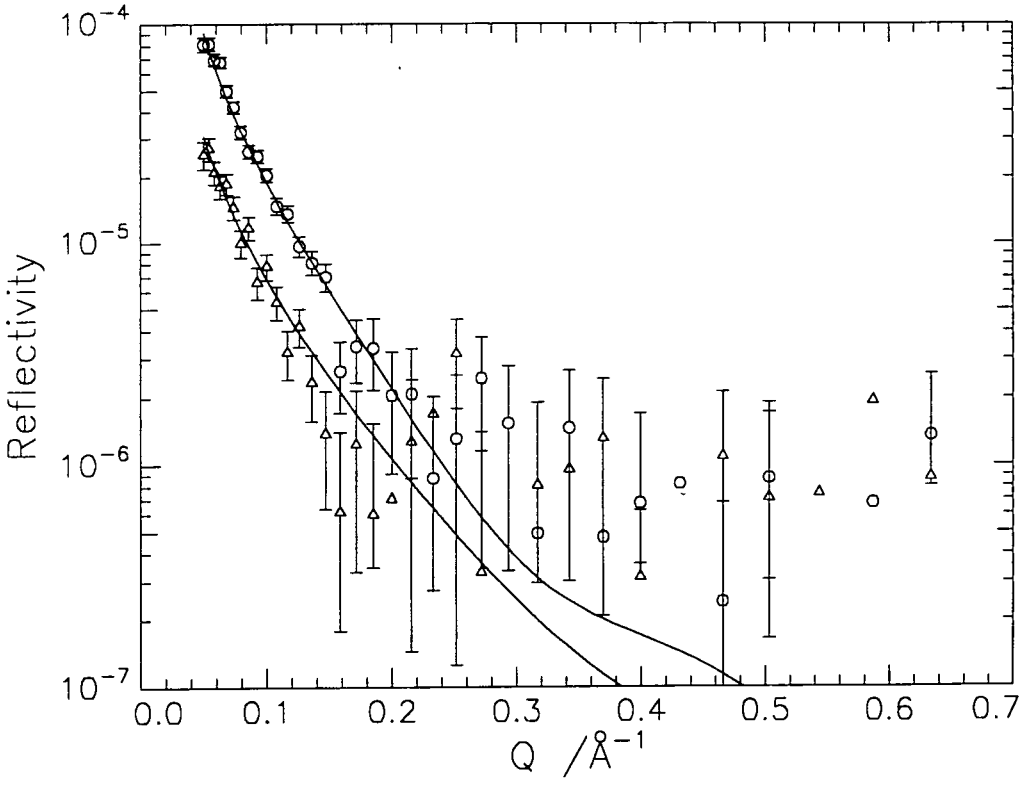

Figure 4.63(b): Reflectivity profiles for HMDL at 0.4mN m^{-1}, 1st 15 minute run (o), 6th 15 minute run (Δ) and two layer fit (—)

MONOMER	RUN NUMBER	LAYER 1		LAYER 2	
		d (Å)	ρ (Å^{-2} × 10^{-6})	d (Å)	ρ (Å^{-2} × 10^{-6})
DMDL	1	12.0	3.6	10.5	1.5
	2	9.0	3.3	9.0	1.2
	3	8.5	3.2	9.0	1.0
	4	8.0	3.0	9.0	0.9
	5	7.5	2.8	8.5	0.8
	6	7.0	2.7	8.0	0.8
HMDL	1	12.0	3.8	12	1.0
	2	10.0	3.5	10	0.8
	3	9.0	3.4	9.0	0.7
	4	8.5	3.2	9.0	0.6
	5	7.5	3.0	9.0	0.5
	6	7.5	2.8	9.0	0.5
DMHL	1	12	-0.1	10	1.7

Table 4.19: Parameters from two layer fits at 10mN m^{-1} on a.c.m.w.

MONOMER	RUN NUMBER	LAYER 1		LAYER 2	
		d (Å)	ρ ($Å^{-2} \times 10^{-6}$)	d (Å)	ρ ($Å^{-2} \times 10^{-6}$)
DMDL	1	11.0	3.3	10.0	1.4
	2	10.0	3.1	10.0	1.2
	3	9.5	3.0	9.5	1.1
	4	9.0	2.9	9.0	1.0
	5	8.5	2.8	8.5	0.9
	6	8.0	2.7	8.0	0.9
HMDL	1	11.0	3.3	11.0	0.8
	2	10.0	3.1	10.0	0.7
	3	9.5	3.0	9.5	0.6
	4	9.0	2.9	9.0	0.5
	5	8.5	2.8	8.5	0.4
	6	8.0	2.7	8.0	0.4
DMHL	1	12.0	-0.1	10.0	1.7

Table 4.20: Parameters from two layer fits at 5mN m^{-1} on a.c.m.w.

MONOMER	RUN NUMBER	LAYER 1		LAYER 2	
		d (Å)	ρ ($Å^{-2} \times 10^{-6}$)	d (Å)	ρ ($Å^{-2} \times 10^{-6}$)
DMDL	1	9.0	3.1	10.0	1.3
	2	8.5	3.1	10.0	1.1
	3	8.0	3.0	9.5	1.0
	4	7.5	2.8	9.5	0.9
	5	7.5	2.6	9.5	0.7
	6	7.0	2.5	9.5	0.7
HMDL	1	9.0	3.2	10.5	1.0
	2	8.5	3.0	10.0	1.0
	3	8.0	2.8	9.5	0.9
	4	7.5	2.8	9.5	0.8
	5	7.0	2.7	9.0	0.7
	6	7.0	2.5	9.0	0.6

Table 4.21: Parameters from two layer fits at 0.4mN m^{-1} on a.c.m.w.

From the parameters obtained for DMHL, layer 1 primarily contains the lauryl side chains as a negative scattering length density is obtained. The scattering length density values obtained for layer 1 for DMDL and HMDL are all lower than the value calculated for the pure deuterated lauryl ester group, this indicates that the alkyl chain region is penetrated by the subphase. The scattering length density value obtained for the methacrylate region is greatly reduced from the calculated value, indicating that the there is substantial immersion of the methacrylate region. All of the scattering length density values are lower than those obtained for the polymer which is as a result of the disappearance of LMA which leads to the decrease in the apparent scattering length density during the first 15 minute run, so the value obtained from the first run is below that for the polymer. For the subsequent runs the scattering length density and thickness appears to decrease, however, this may be misleading and could be a result of the coupled parameters. To account for the decrease in reflectivity any one of the four parameters could be decreased or all four decreased by a slight amount, either way the fits were indistinguishable, so the trend observed should be treated with caution.

The partial structure factor analysis has been attempted using the simplified version shown in equation 4.47 to obtain the layer thickness and separation of the whole monomer layer and the subphase, as well as using equation 4.25 to obtain information about the distribution of the methacrylate groups, lauryl ester groups and the subphase. As for the polymer, both uniform layer and Gaussian models were used to fit partial structure factors relating to LMA and uniform layer and hyperbolic tangent models were used to fit the subphase partial structure factors. Examples of the fits obtained for the self partial structure factors from the simplified version are shown in figures 4.64 to 4.67 (a) and (b) and the parameters obtained are given in tables 4.22 to 4.27.

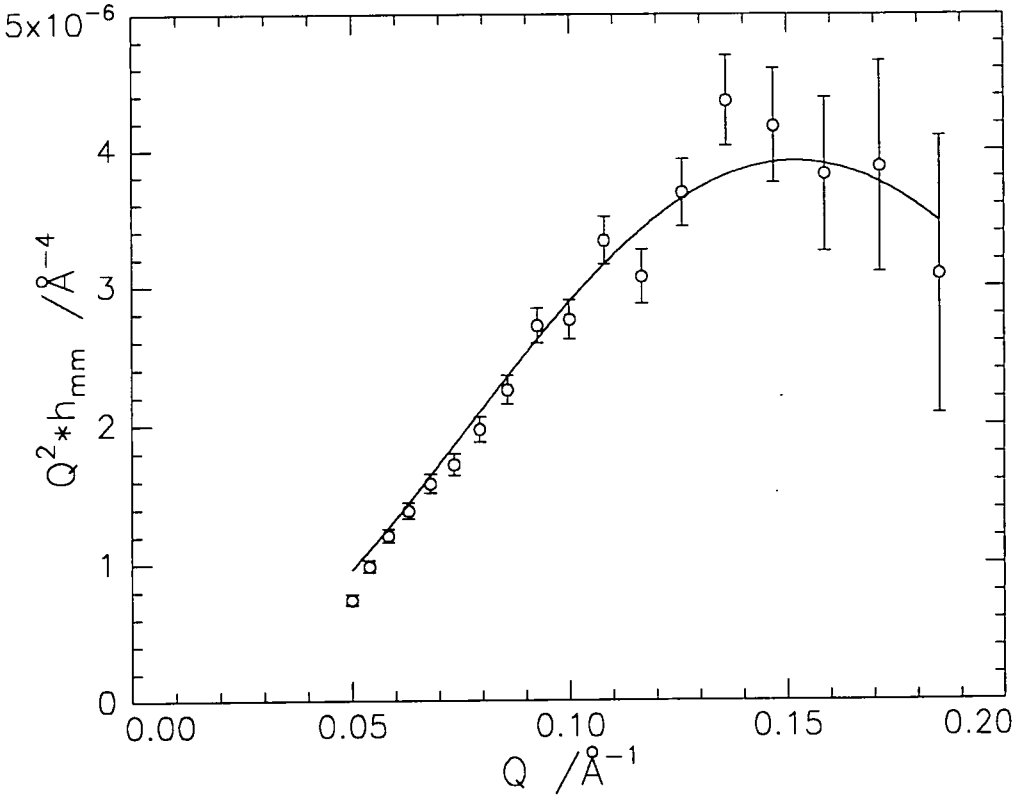

Figure 4.64(a): Monomer self partial structure factor, 1st 15 minutes at 10mN m^{-1} single uniform layer

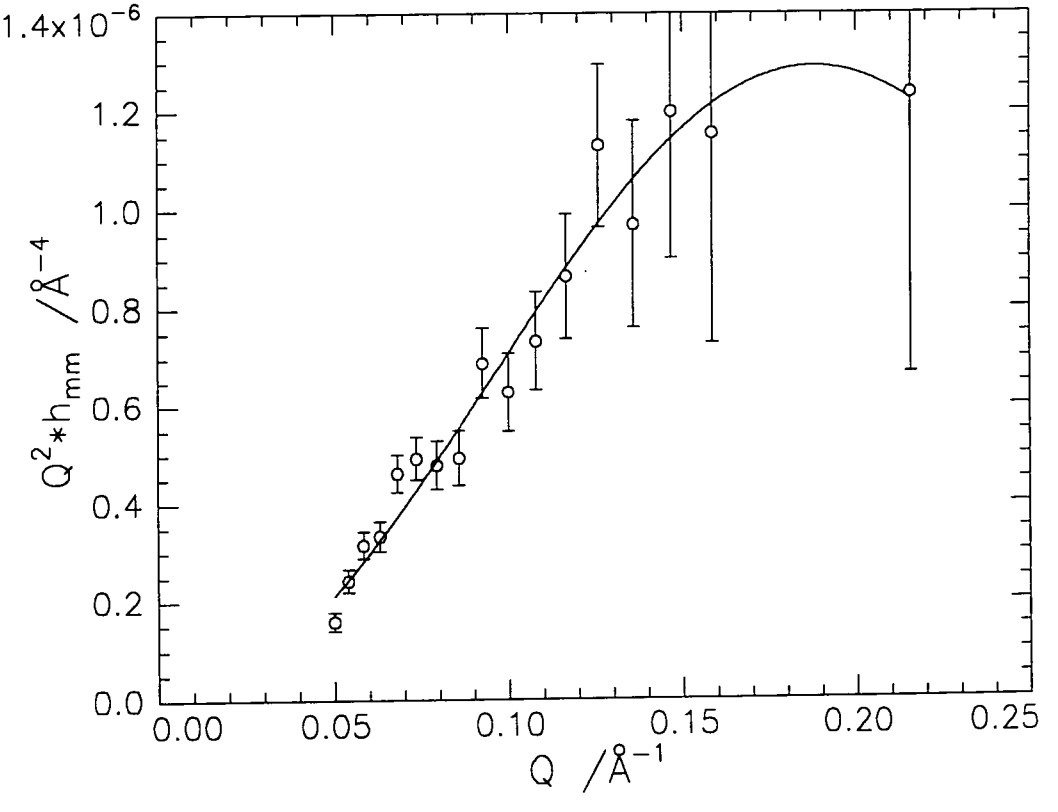

Figure 4.64(b): Monomer self partial structure factor, 6th 15 minutes at 10mN m^{-1} single uniform layer

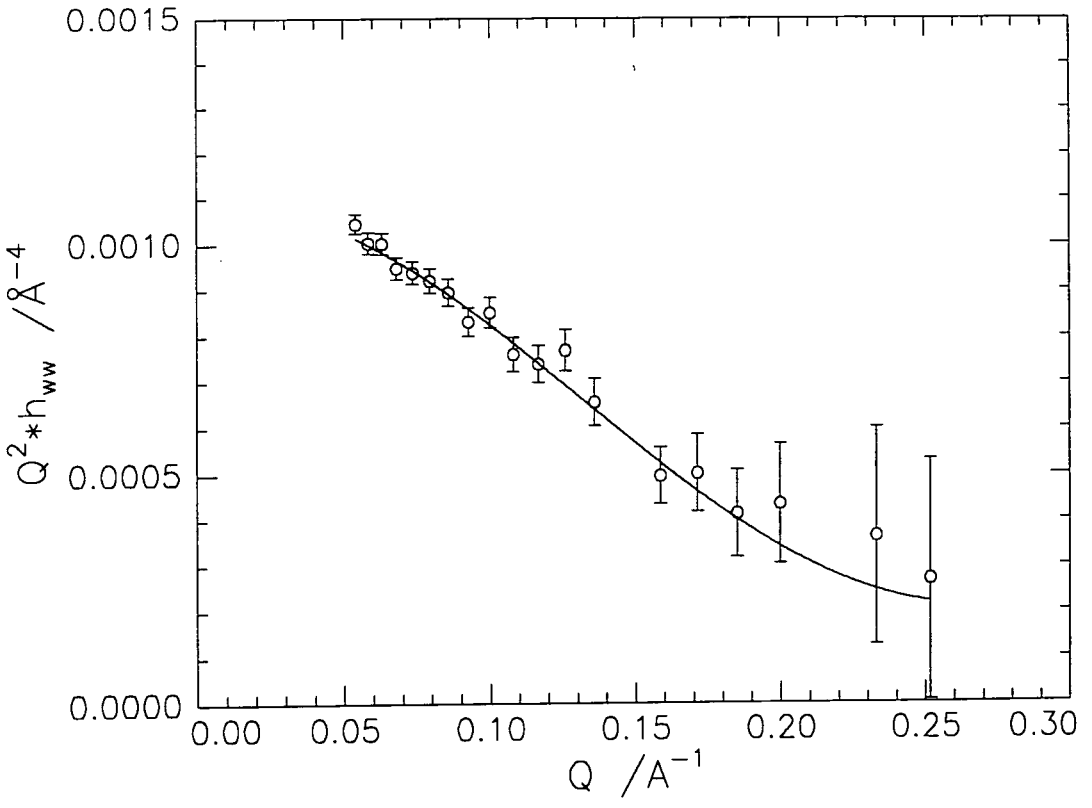

Figure 4.65(a): Subphase self partial structure factor, 1st 15 minutes at 10mN m^{-1} single uniform layer

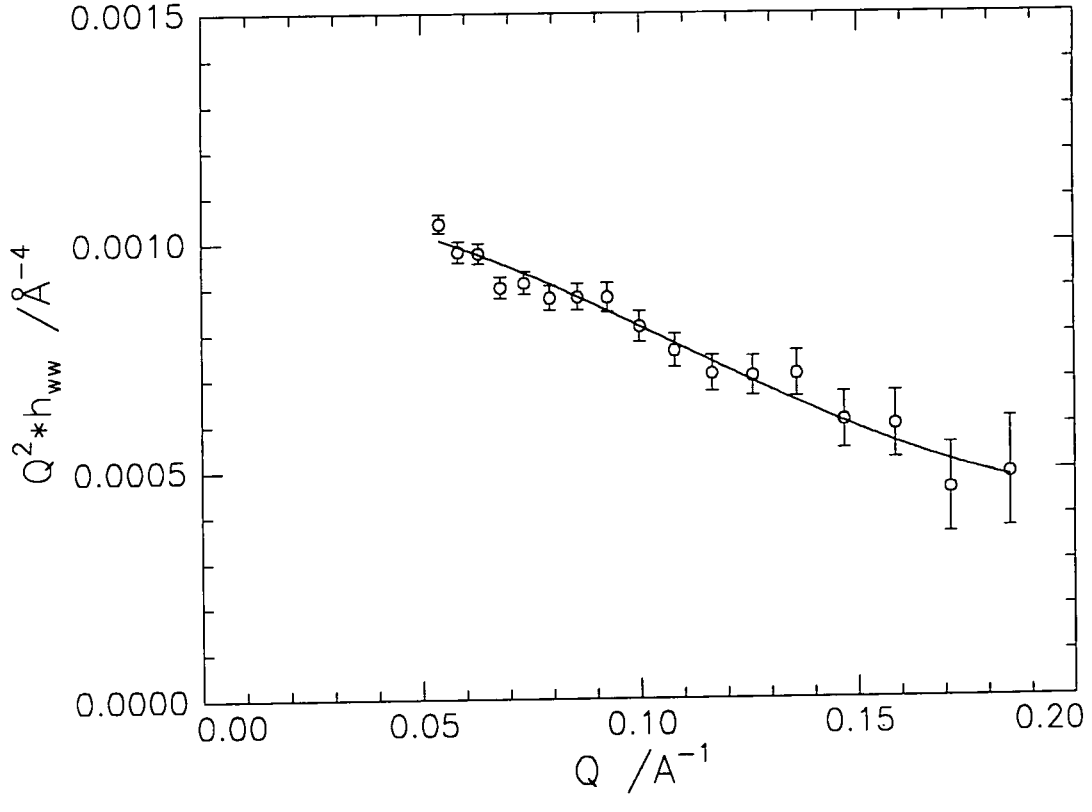

Figure 4.65(b): Subphase self partial structure factor, 6th 15 minutes at 10mN m^{-1} single uniform layer

RUN NUMBER	d_m (Å)	n_{m1} ($\times 10^{-4}$ Å^{-3})	d_w (Å)	n_{w1} ($\times 10^{-3}$ Å^{-3})
1	19.2	10.0	11.1	4.8
2	19.1	7.5	15.5	2.2
3	14.6	7.7	12.3	5.1
4	12.7	7.6	15.5	2.8
5	11.4	7.0	12.4	3.0
6	11.0	7.0	13.5	2.9

Table 4.22: Parameters from uniform layer fits to self partial structure factors at 10mN m^{-1}, m denotes monomer and w the subphase

RUN NUMBER	d_m (Å)	n_{m1} ($\times 10^{-4}$ Å^{-3})	d_w (Å)	n_{w1} ($\times 10^{-3}$ Å^{-3})
1	19.8	8.5	16.4	2.7
2	18.0	7.6	13.4	3.5
3	20.0	6.4	10.9	7.8
4	16.2	7.1	16.1	2.9
5	16.1	6.5	14.6	2.8
6	16.0	5.9	13.8	3.9

Table 4.23: Parameters from uniform layer fits to self partial structure factors at 5mN m^{-1}, m denotes monomer and w the subphase

RUN NUMBER	d_m (Å)	n_{m1} ($\times 10^{-4}$ Å^{-3})	d_w (Å)	n_{w1} ($\times 10^{-3}$ Å^{-3})
1	18.4	7.4	12.0	4.7
2	15.8	7.8	13.7	2.6
3	14.3	7.8	8.7	8.0
4	17.0	5.8	12.2	3.4
5	15.7	5.5	12.0	3.8
6	15.2	5.4	12.5	3.0

Table 4.24: Parameters from uniform layer fits to self partial structure factors at 0.4mN m^{-1}, m denotes monomer and w the subphase

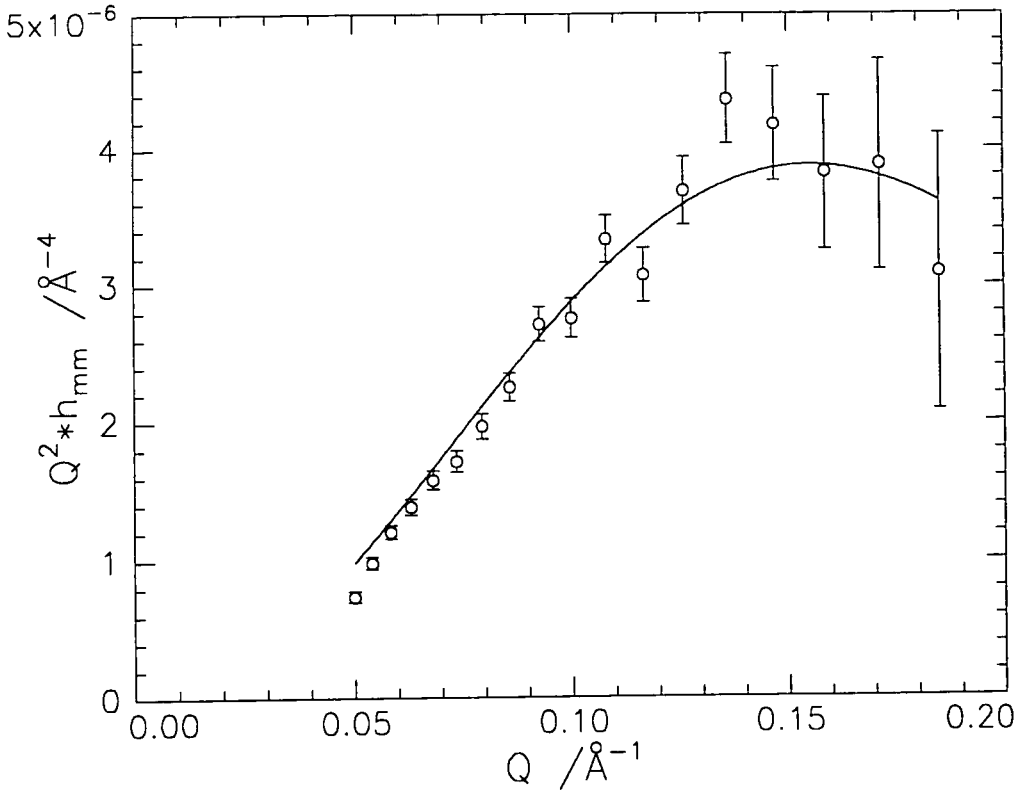

Figure 4.66(a): Monomer self partial structure factor, 1st 15 minutes at 10mN m^{-1} Gaussian distribution model

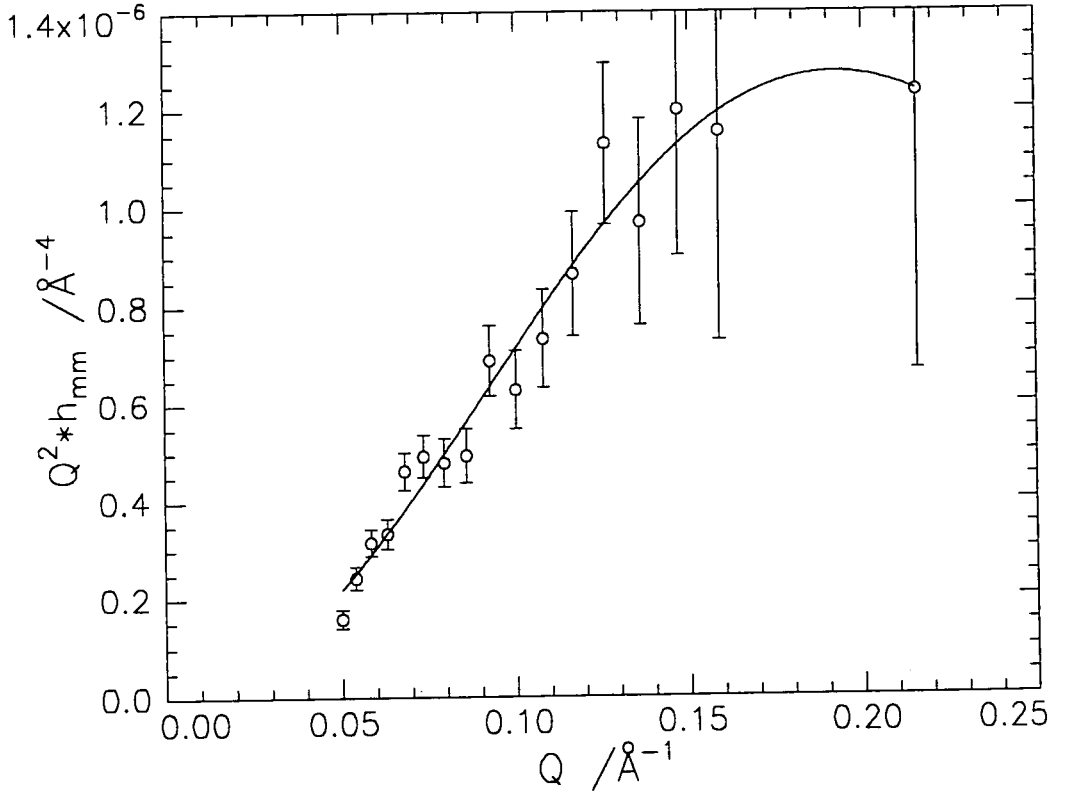

Figure 4.66(b): Monomer self partial structure factor, 6th 15 minutes at 10mN m^{-1} Gaussian distribution model

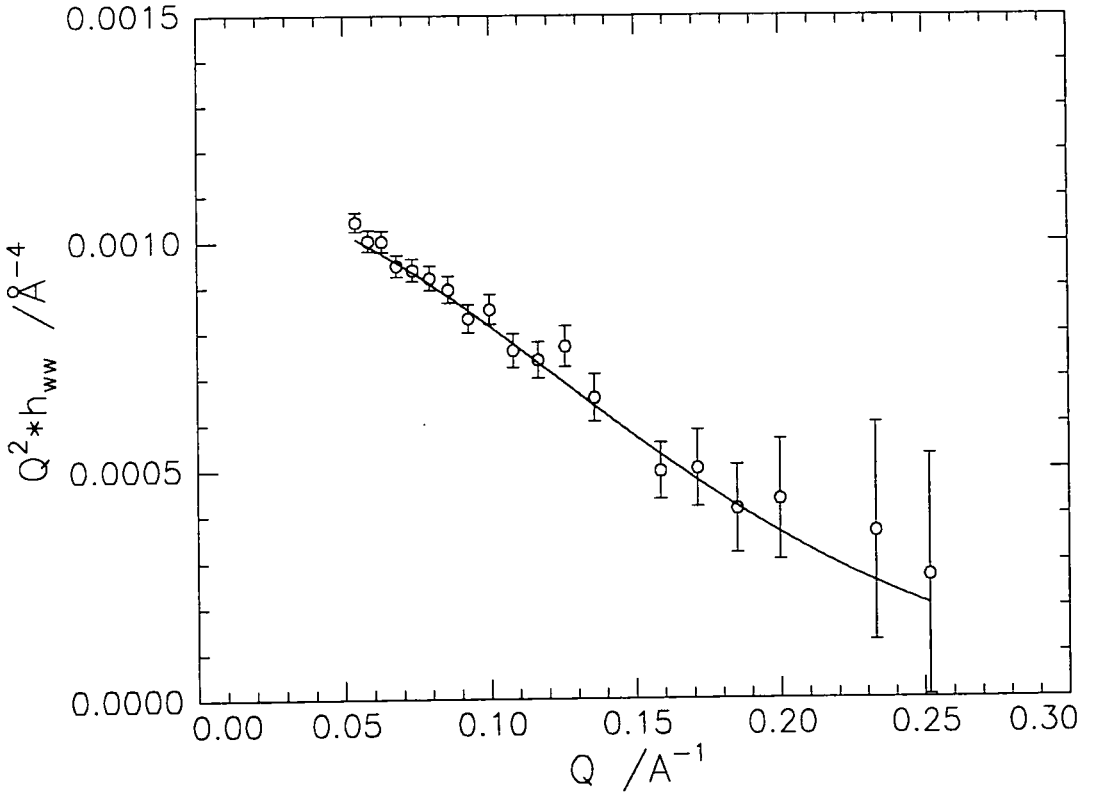

Figure 4.67(a): Subphase self partial structure factor, 1st 15 minutes at 10mN m^{-1} tanh distribution model

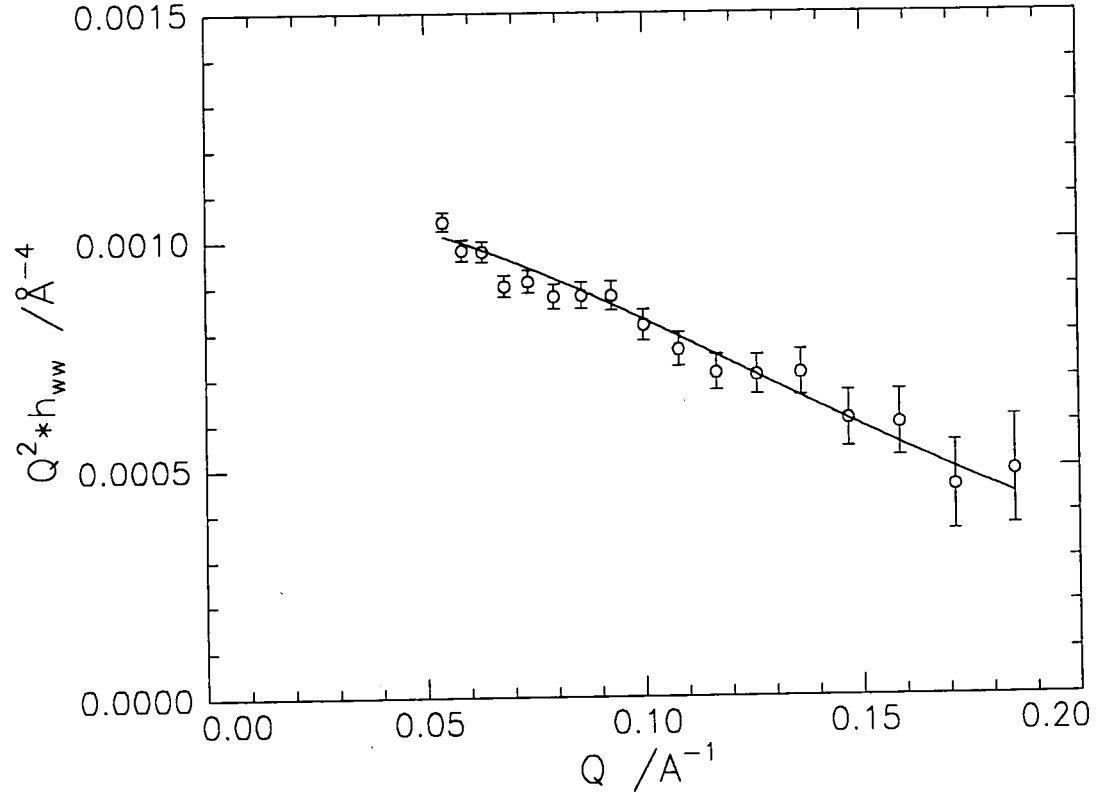

Figure 4.67(b): Subphase self partial structure factor, 6th 15 minutes at 10mN m^{-1} tanh distribution model

RUN NUMBER	σ_m (Å)	n_{m1} ($\times 10^{-4}$ Å^{-3})	ξ_w (Å)
1	15.0	14.0	4.0
2	15.7	10.0	3.2
3	12.2	11.0	4.6
4	11.6	9.6	4.3
5	14.2	7.5	3.8
6	15.4	6.26	4.0

Table 4.25: Parameters from Gaussian and tanh fits to self partial structure factors at 10mN m^{-1}, m denotes monomer and w the subphase

RUN NUMBER	σ_m (Å)	n_{m1} ($\times 10^{-4}$ Å^{-3})	ξ_w (Å)
1	17.7	11.0	4.6
2	16.5	9.8	4.1
3	18.3	8.3	5.1
4	13.7	9.6	4.3
5	14.0	8.5	3.9
6	15.5	7.1	4.6

Table 4.26: Parameters from Gaussian and tanh fits to self partial structure factors at 5mN m^{-1}, m denotes monomer and w the subphase

RUN NUMBER	σ_m (Å)	n_{m1} ($\times 10^{-4}$ Å^{-3})	ξ_w (Å)
1	15.4	10.0	4.6
2	13.7	10.0	4.3
3	12.0	9.9	3.8
4	14.2	7.9	4.2
5	13.4	7.3	4.6
6	16.2	5.9	4.7

Table 4.27: Parameters from Gaussian and tanh fits to self partial structure factors at 0.4mN m^{-1}, m denotes monomer and w the subphase

The parameters obtained from the monomer self partial structure factors using the uniform layer and Gaussian distribution models can be used to calculated the surface concentration using equations 4.34 and 4.37 respectively. The calculated values for both models are given in tables 4.28 to 4.30 together with the theoretical concentration calculated from the amount of monomer deposited on to the surface.

RUN NUMBER	Γ_{uni} (mg m^{-2})	Γ_{Gau} (mg m^{-2})	Γ_{calc} (mg m^{-2})
1	0.9	0.9	1.90
2	0.7	0.7	
3	0.5	0.5	
4	0.5	0.5	
5	0.4	0.4	
6	0.4	0.4	

Table 4.28: Surface concentrations calculated using the uniform layer (Γ_{uni}) and Gaussian model (Γ_{Gau}) parameters compared to the theoretical surface concentration (Γ_{calc}) at 10mN m^{-1}

RUN NUMBER	Γ_{uni} (mg m^{-2})	Γ_{Gau} (mg m^{-2})	Γ_{calc} (mg m^{-2})
1	0.79	0.8	1.07
2	0.64	0.7	
3	0.61	0.6	
4	0.55	0.6	
5	0.49	0.5	
6	0.44	0.5	

Table 4.29: Surface concentrations calculated using the uniform layer (Γ_{uni}) and Gaussian model (Γ_{Gau}) parameters compared to the theoretical surface concentration (Γ_{calc}) at 5mN m^{-1}

RUN NUMBER	Γ_{uni} (mg m^{-2})	Γ_{Gau} (mg m^{-2})	Γ_{calc} (mg m^{-2})
1	0.64	0.64	0.82
2	0.58	0.59	
3	0.52	0.50	
4	0.46	0.47	
5	0.41	0.41	
6	0.39	0.40	

Table 4.30: Surface concentrations calculated using the uniform layer (Γ_{uni}) and Gaussian model (Γ_{Gau}) parameters compared to the theoretical surface concentration (Γ_{calc}) at 0.4mN m^{-1}

It is not possible to distinguish between the fits obtained using the different models and the parameters produced by each model show no sign of a consistent trend, apart from an overall decrease in the polymer number density from run 1 to 6, although the variation is erratic. The surface concentrations do show a consistent decrease which agrees with the trend observed in the concentrations calculated from the single uniform layer fits. The parameters for the water layer appear to vary randomly, however, from the uniform layer parameters, although the thicknesses and number densities vary, the amount of water in the interfacial region remains fairly constant as whenever a small thickness is obtained the number density is high and vice versa, which indicates that the variation in thickness does not change the amount of water present but only the density of the water in the interfacial layer.

The separation of the two distributions can be calculated using equation 4.44 in the same way as for the polymer components and the subphase. Examples of the fits obtained are shown in figures 4.68 to 4.70 (a) and (b).

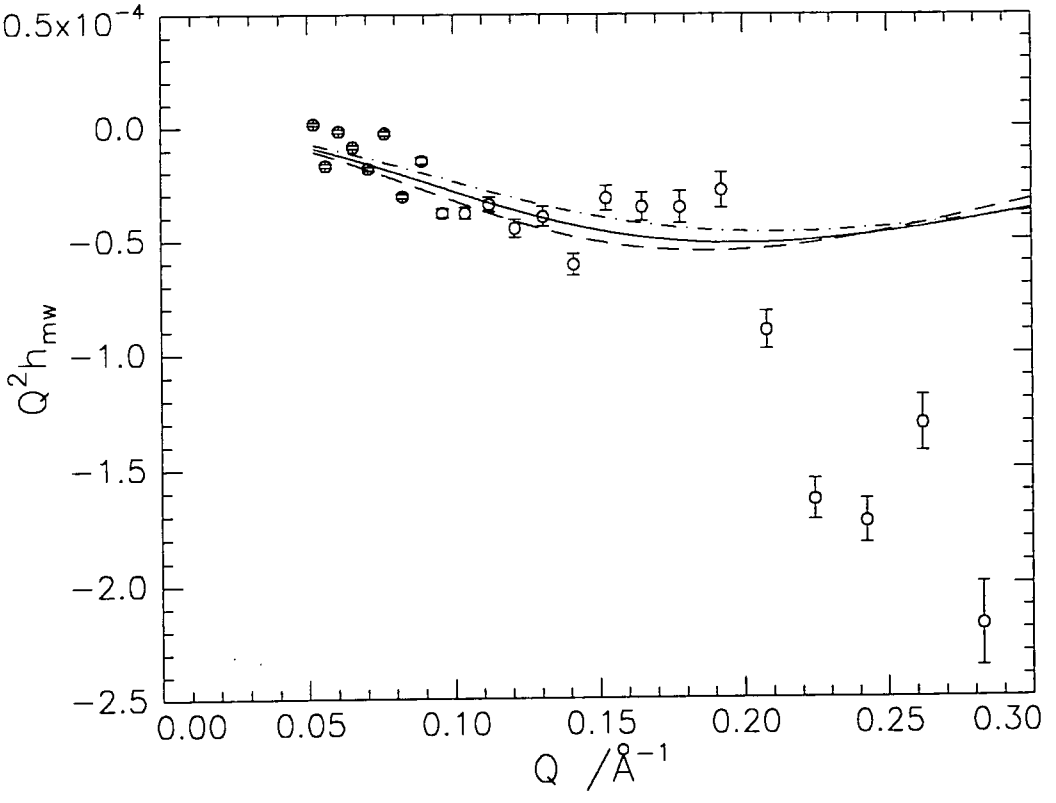

Figure 4.68(a): Cross partial structure factor for monomer and subphase, 1st 15 minute run at 10mN m^{-1}, experimental data (o) and lines are calculated cross term with different δ, δ = 7Å (– –), δ = 6Å (—) and δ = 5 Å (– · –)

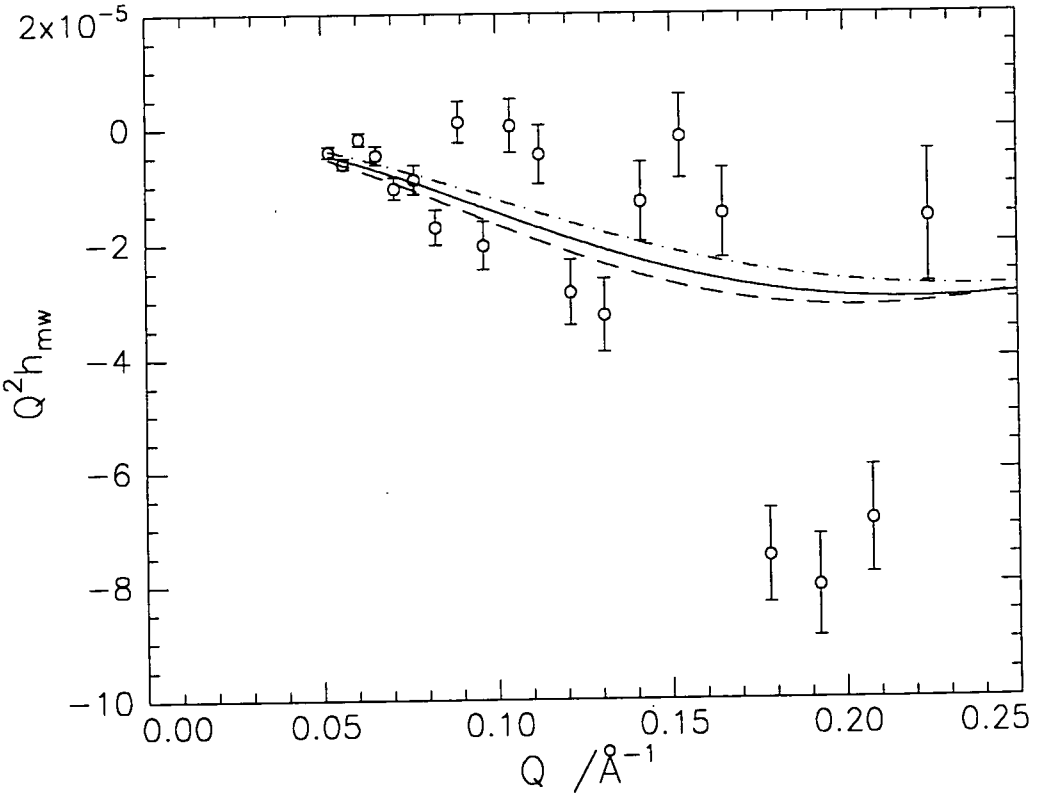

Figure 4.68(b): Cross partial structure factor for monomer and subphase, 6th 15 minute run at 10mN m^{-1}, experimental data (o) and lines are calculated cross term with different δ, δ = 7Å (– –), δ = 6Å (—) and δ = 5Å (– · –)

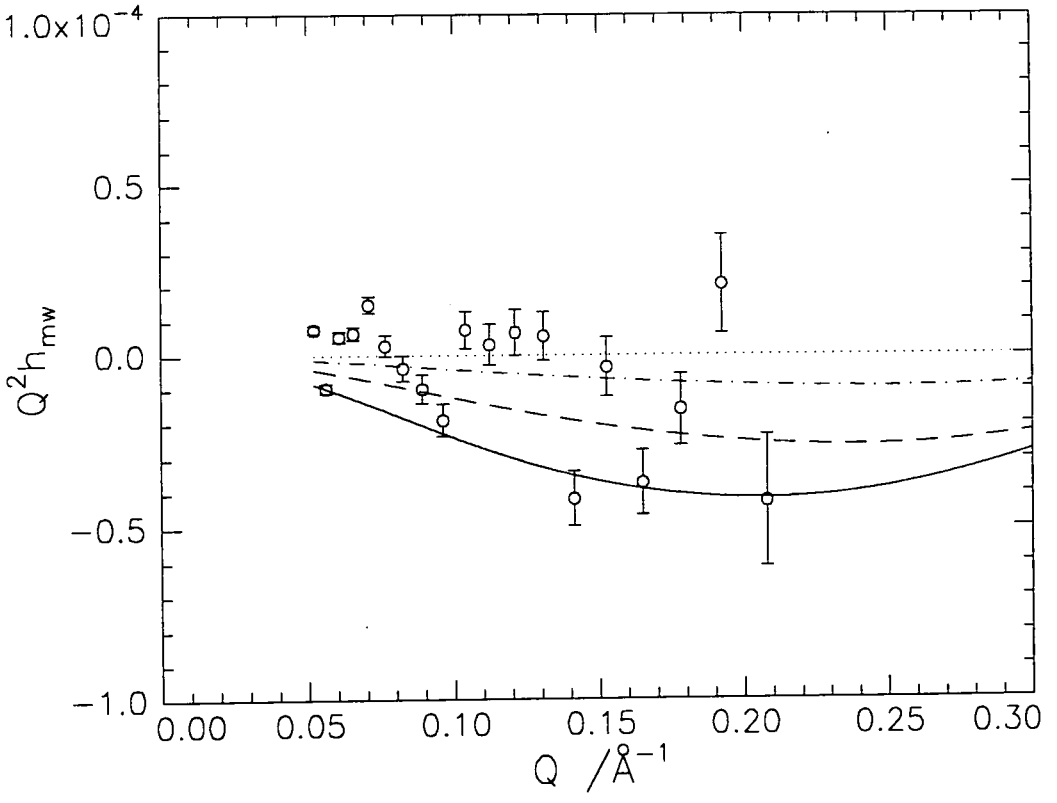

Figure 4.69(a): Cross partial structure factor for monomer and subphase, 1st 15 minute run at 5mN m^{-1}, experimental data (o) and lines are calculated cross term with different δ, δ = 6Å (—), δ = 3Å (– –), δ = 1Å (– · –) and δ = 0Å (· · ·)

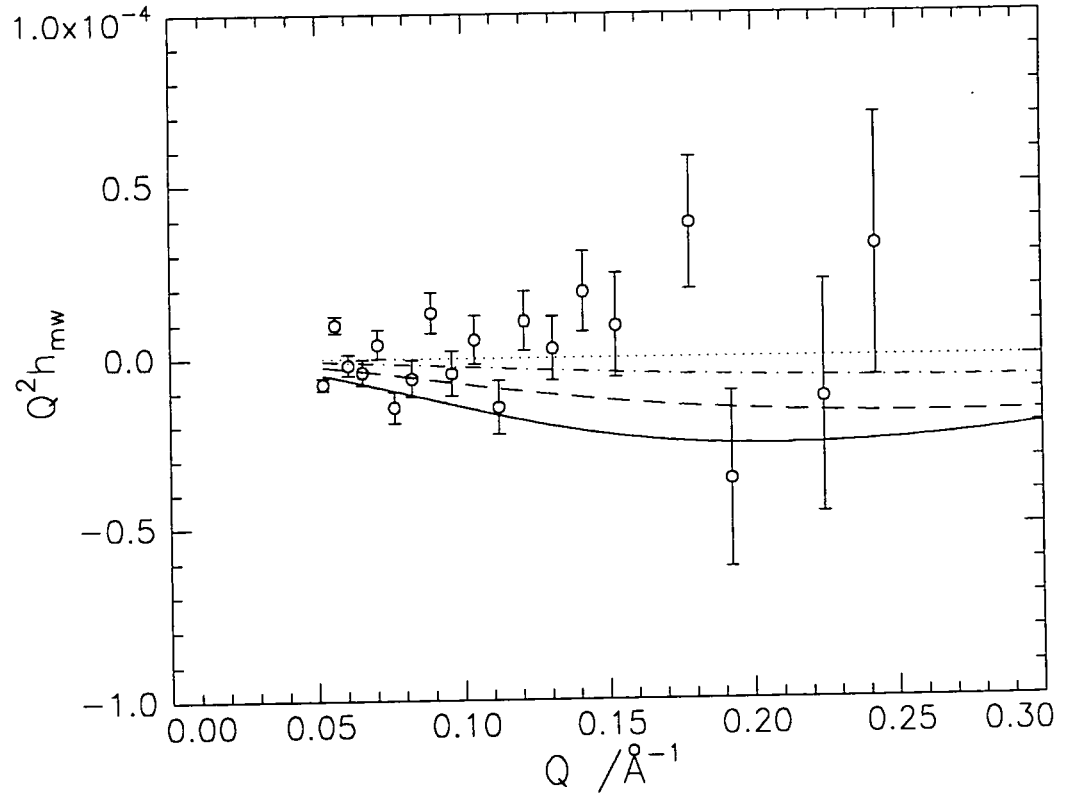

Figure 4.69(b): Cross partial structure factor for monomer and subphase, 6th 15 minute run at 5mN m^{-1}, experimental data (o) and lines are calculated cross term with different δ, δ = 6Å (—), δ = 3Å (– –), δ = 1Å (– · –) and δ = 0Å (· · ·)

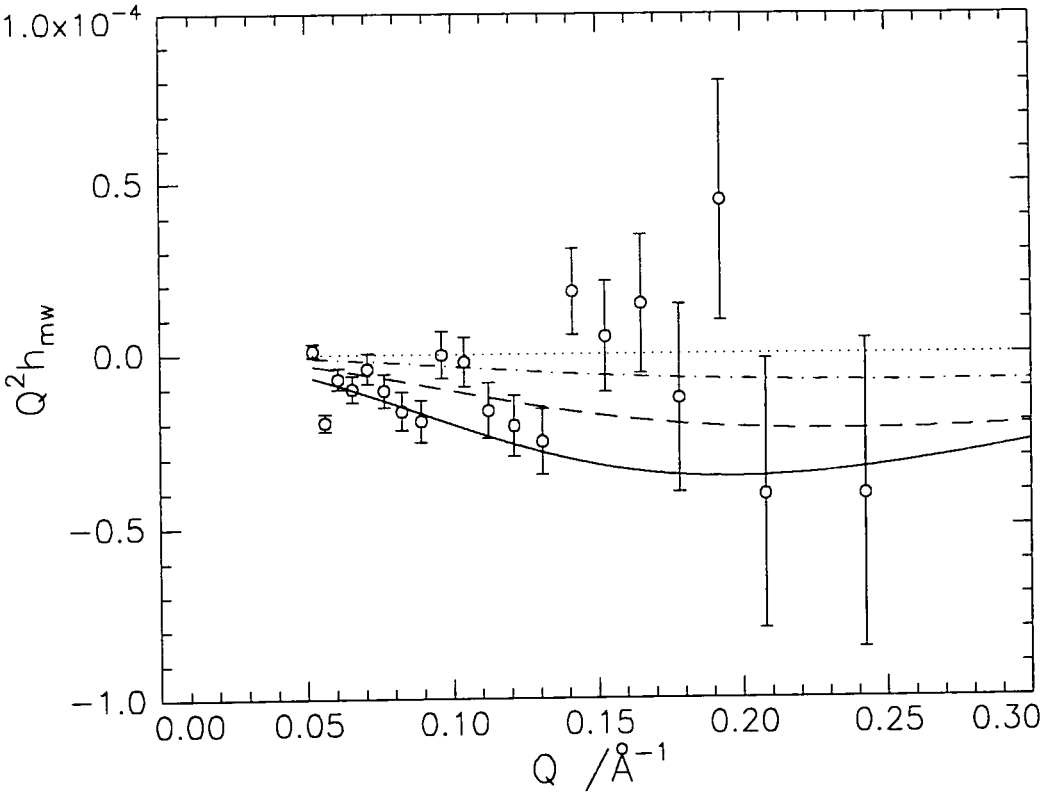

Figure 4.70(a): Cross partial structure factor for monomer and subphase, 1st 15 minute run at 0.4mN m^{-1}, experimental data (o) and lines are calculated cross term with different δ, δ = 6Å (—), δ = 3Å (– –), δ = 1Å (– · –) and δ = 0Å (· · ·)

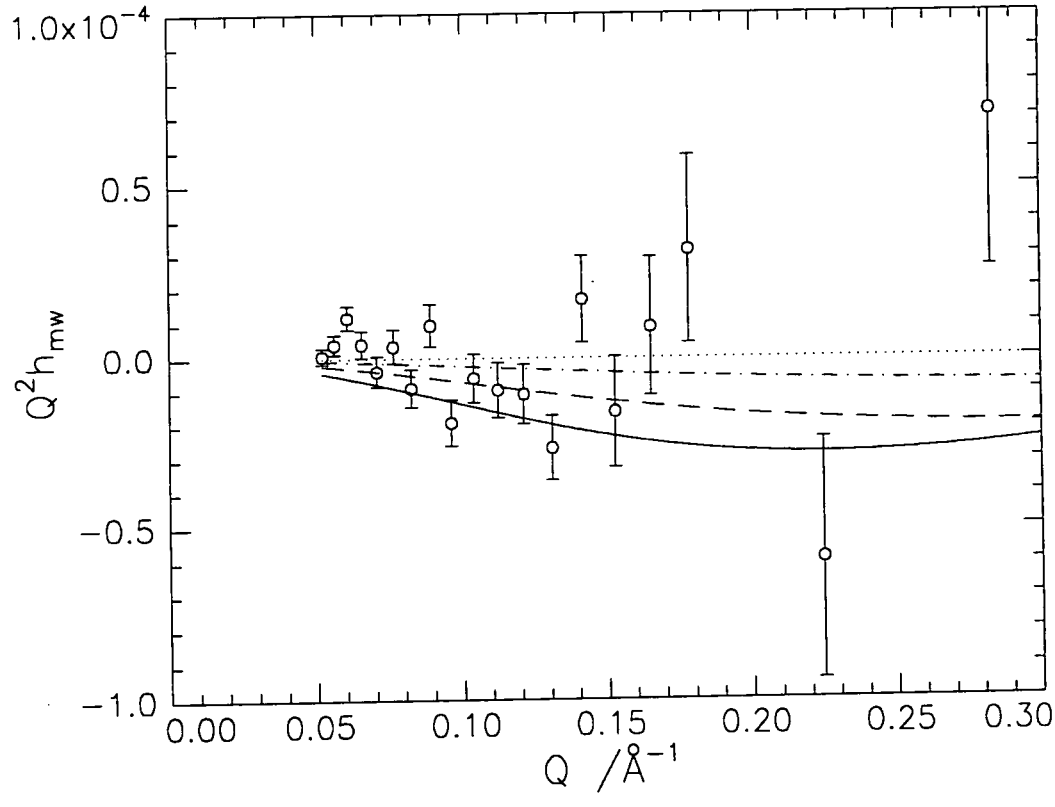

Figure 4.70(b): Cross partial structure factor for monomer and subphase, 6th 15 minute run at 0.4mN m^{-1}, experimental data (o) and lines are calculated cross term with different δ, δ = 6Å (—), δ = 3Å (– –), δ = 1Å (– · –) and δ = 0Å (· · ·)

All of the cross partial structure factor data are scattered, so good fits can not be obtained. At 10mN m^{-1}, the data for the first 15 minute run produced the best data and the fit suggests that δ is circa 6Å and with time the data becomes more scattered and no fit can be obtained (figure 4.68(b)). For all of the remaining runs the data is too scattered to obtain an accurate estimate of δ, however it is possible to conclude that δ is less than 6Å and the data is roughly scattered around $\delta = 0$Å.

The full version of the kinematic approximation in equation 4.25, which makes full use of the different contrast conditions, has been used to try and obtain the distributions of the methacrylate and lauryl ester groups relative to each other and the water subphase to enable the monomer structure at the interface to be compared to that for the polymer. Due to the diminishing reflectivities which occurred for each monomer the use of the full version of the kinematic approximation is limited. Only the first 15 minute run at 10mN m^{-1} produced sufficiently good data for the methacrylate self term to be fitted and even then it is not too reliable. The partial structure factor data for the last runs at 5 and 10mN m^{-1} for both components was too poor to fit reliably and this was also found to be the case for all the runs at 0.4mN m^{-1}. The fact that the 0.4mN m^{-1} data was poor is not surprising as the initial reflectivities obtained at this surface pressure were similar to those obtained for the last runs at the two higher pressures. The monomer partial structure factor data has been fitted with uniform layer and Gaussian distribution models and the water data has been fitted with uniform layer and hyperbolic tangent distribution models. As the fits obtained over the available Q range were indistinguishable, and the Gaussian and hyperbolic tangent distribution models are more realistic, only these results are shown. Figures 4.71 (a) to (c) and 4.72 to 4.74 (a) and (b) show the self partial structure factors obtained for the first and fifth runs and the parameters obtained are given in tables 4.31 and 4.32.

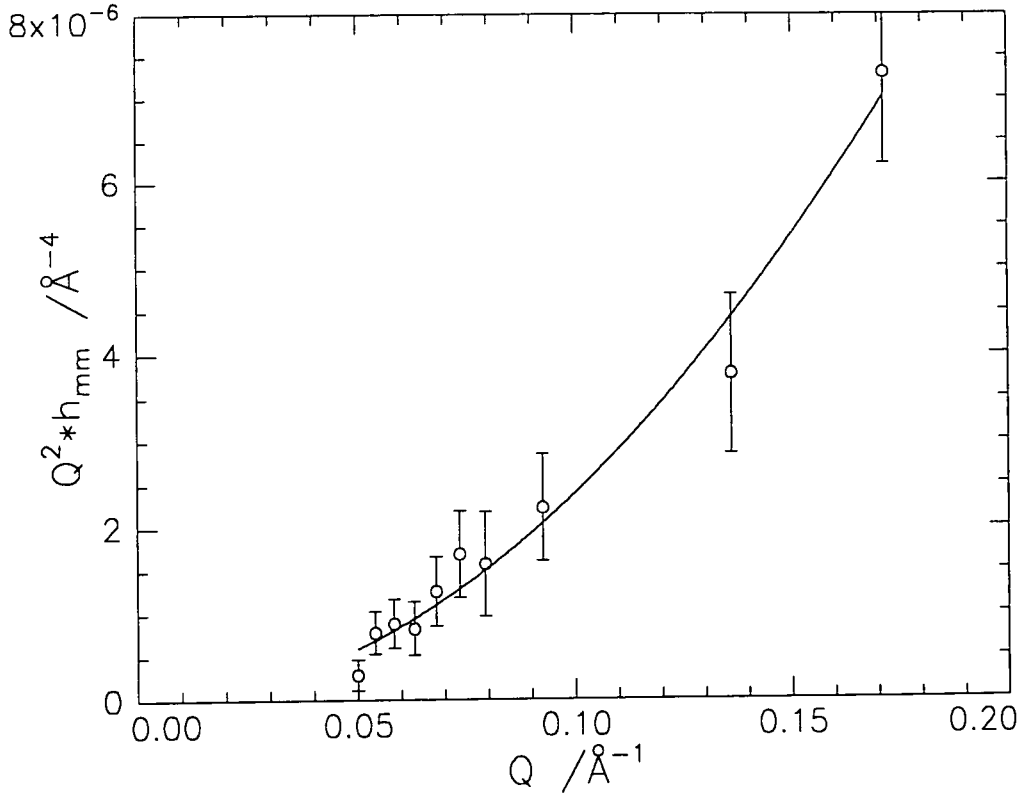

Figure 4.71(a): Methacrylate self partial structure factor for the 1st 15 minute run at 10mN m^{-1}

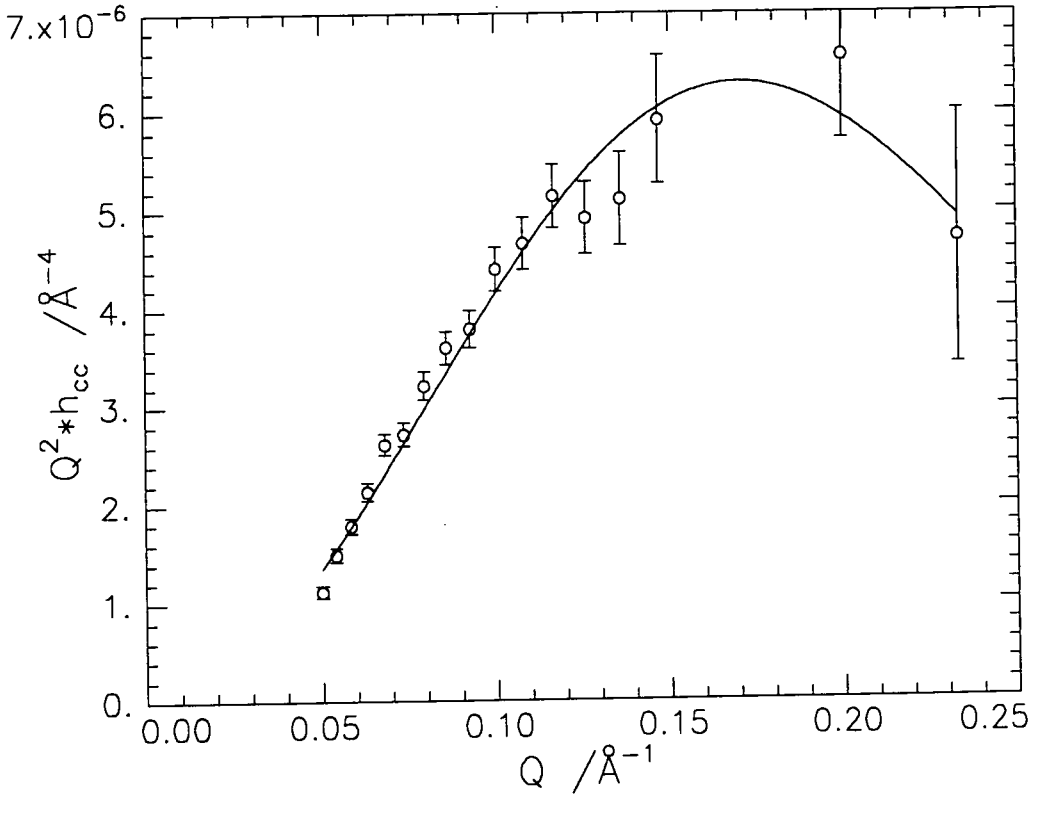

Figure 4.71(b): Lauryl ester side chain self partial structure factor for the 1st 15 minute run at 10mN m^{-1}

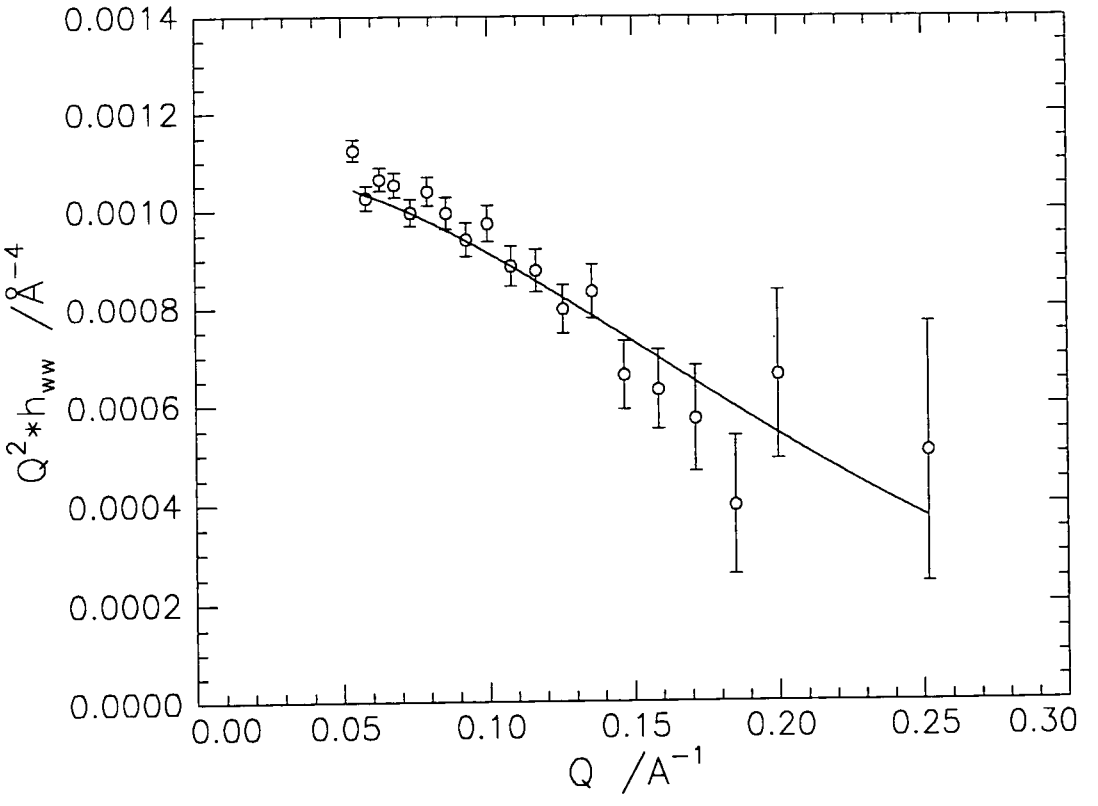

Figure 4.71(c): Water self partial structure factor for the 1st 15 minute run at 10mN m^{-1}

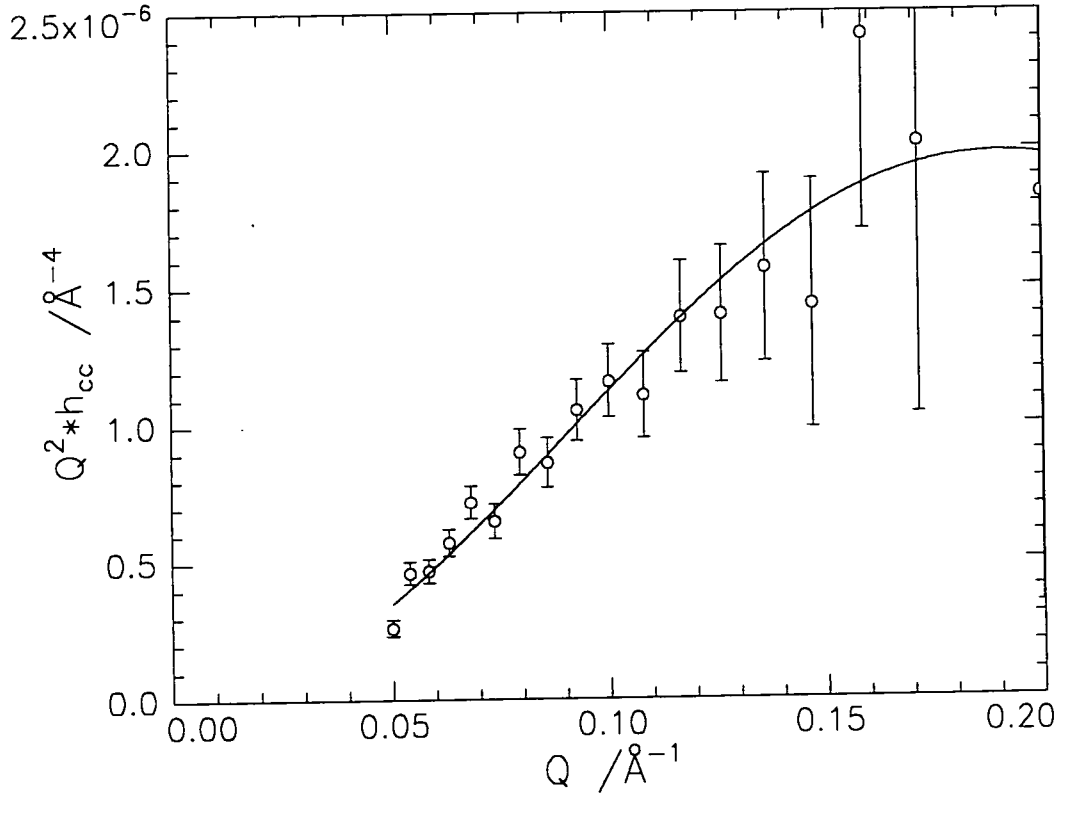

Figure 4.72(a): Lauryl ester side chain self partial structure factor for the 5th 15 minute run at 10mN m^{-1}

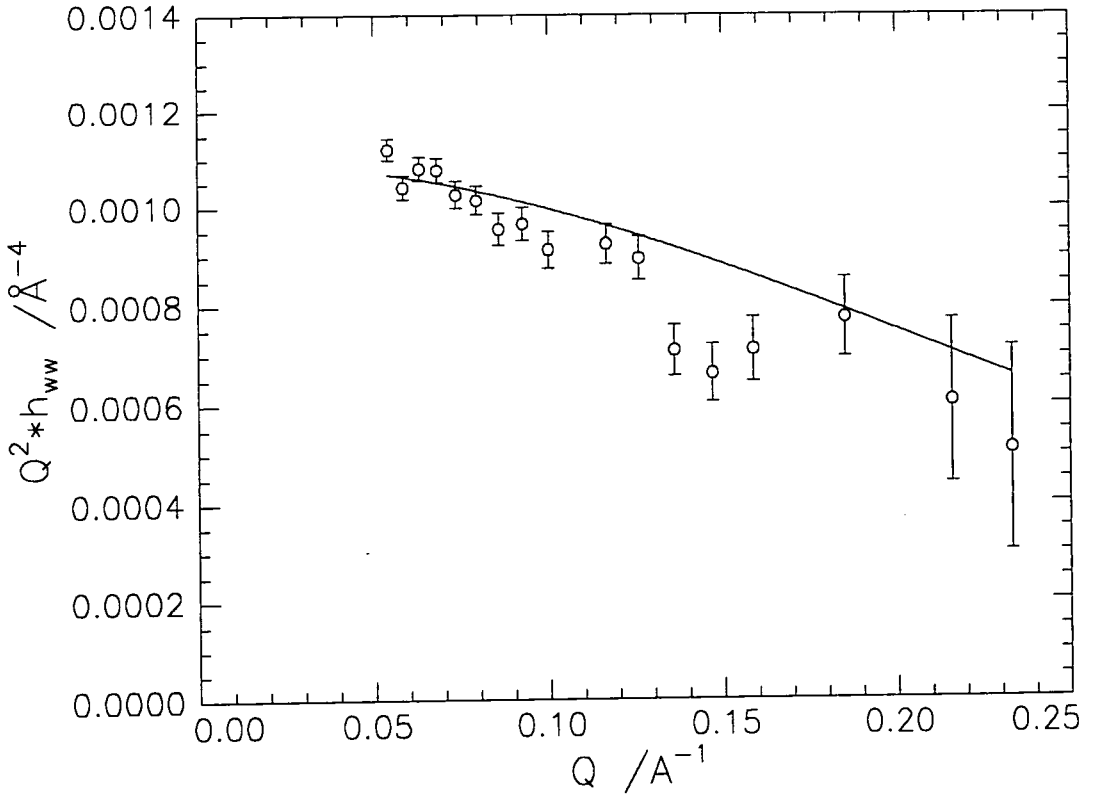

Figure 4.72(b): Water self partial structure factor for the 5th 15 minute run at 10mN m^{-1}

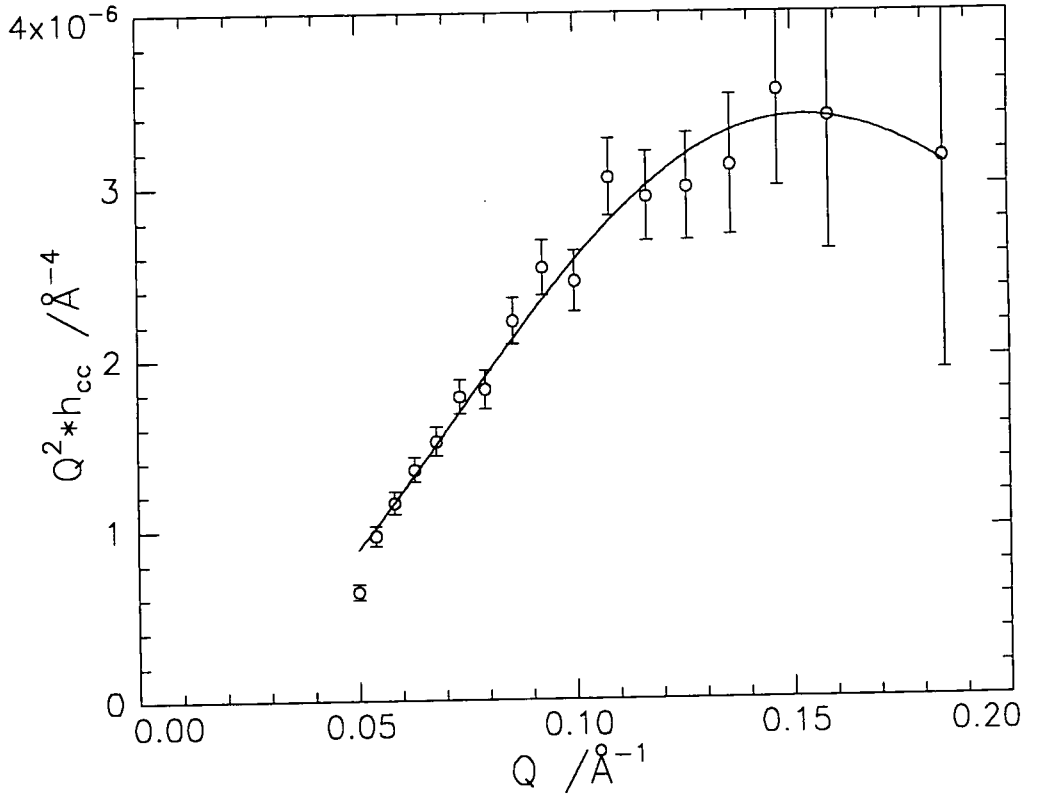

Figure 4.73(a): Lauryl ester side chain self partial structure factor for the 1st 15 minute run at 5mN m^{-1}

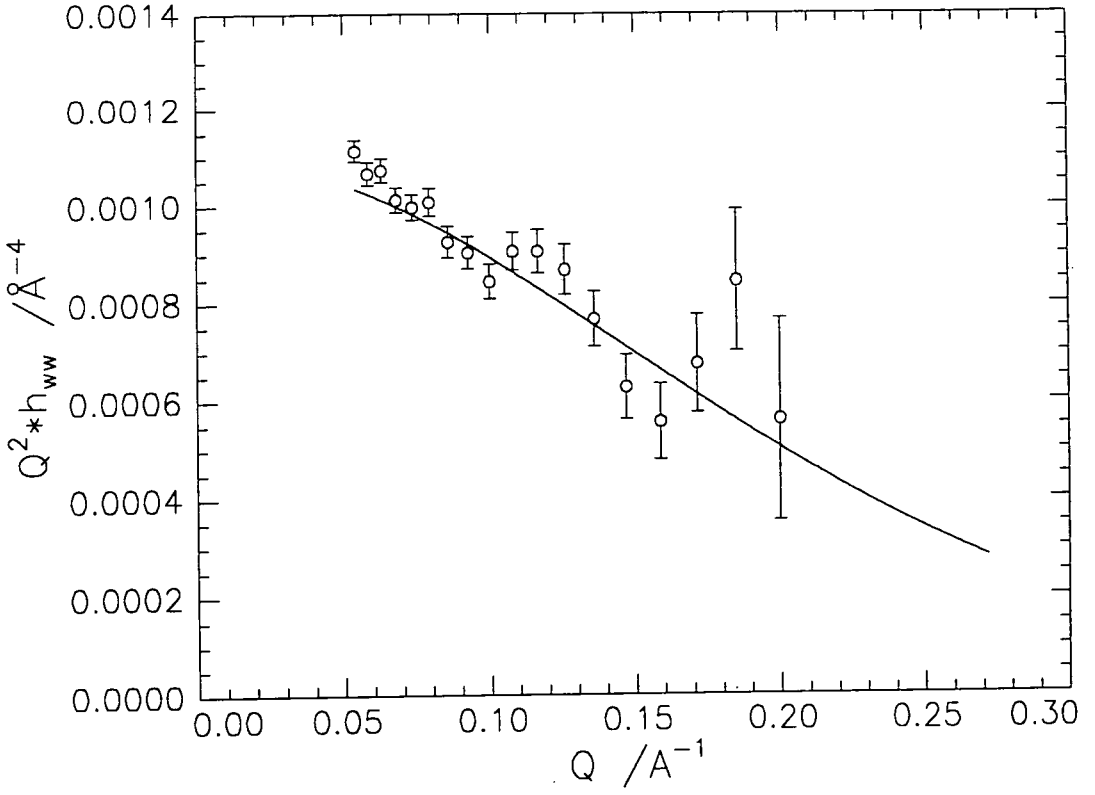

Figure 4.73(b): Water self partial structure factor for the 1st 15 minute run at 5mN m^{-1}

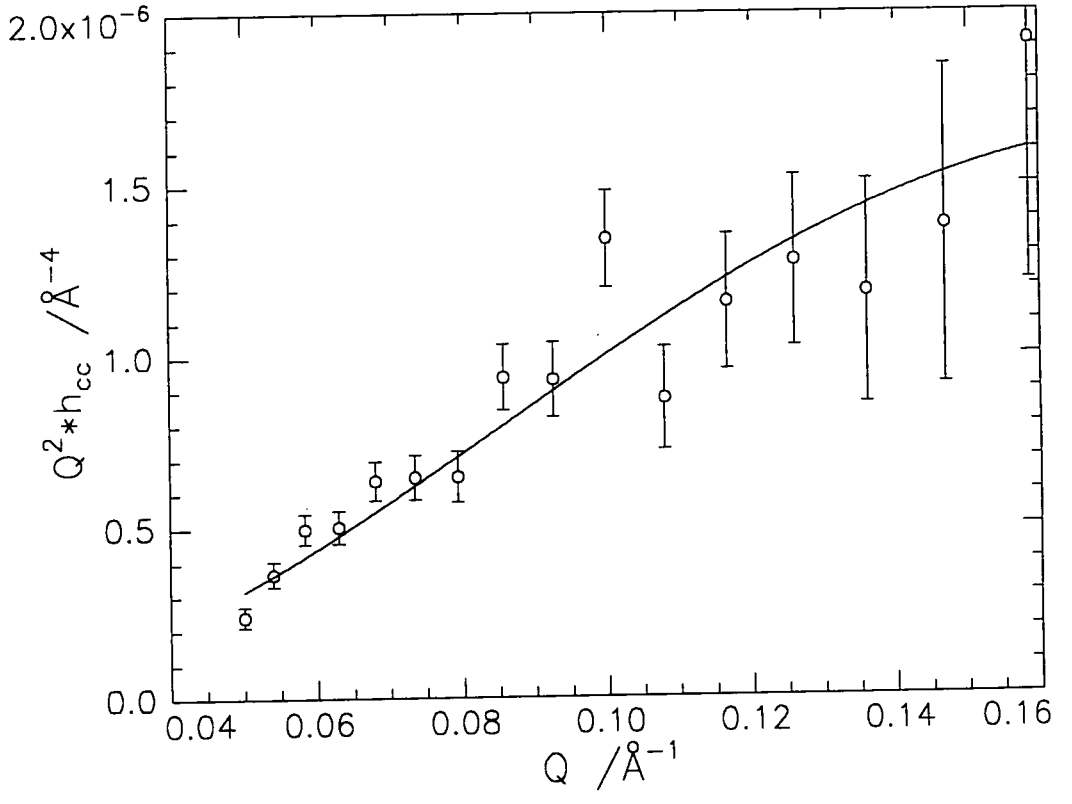

Figure 4.74(a): Lauryl ester side chain self partial structure factor for the 5th 15 minute run at 5mN m^{-1}

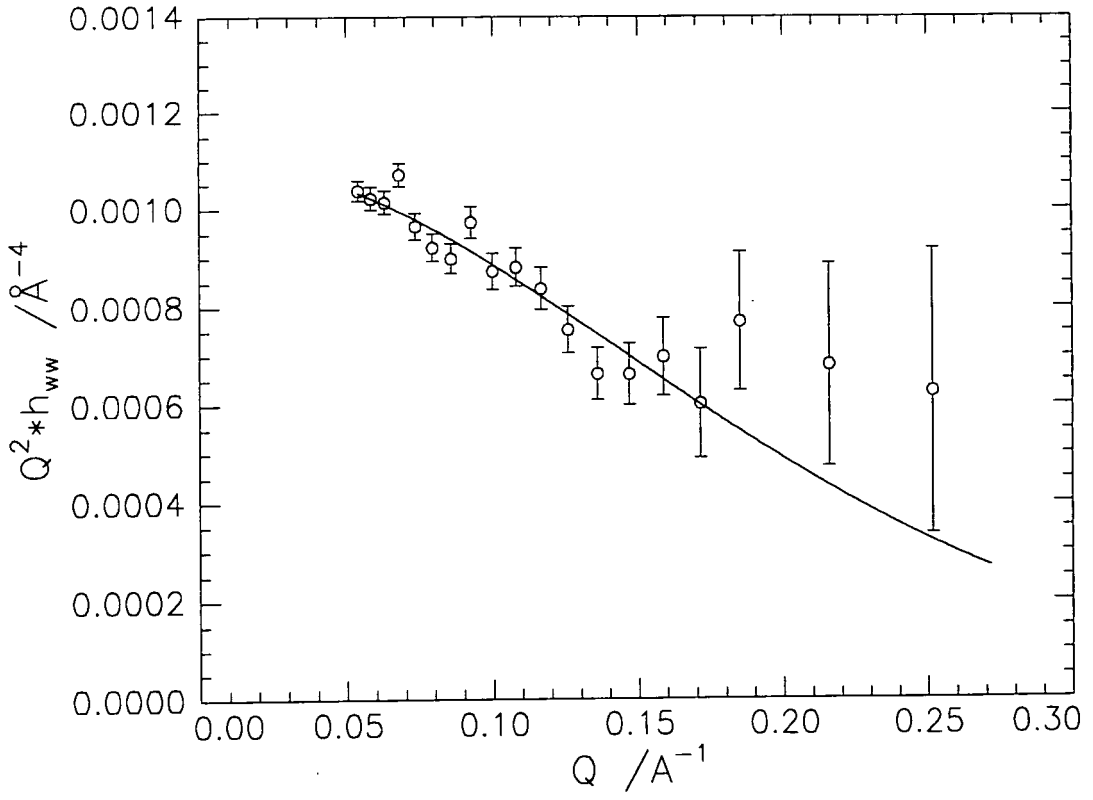

Figure 4.74(b): Water self partial structure factor for the 5th 15 minute run at 5mN m^{-1}

RUN N°	σ_m (Å)	n_{m1} (×10^{-3} Å^{-3})	Γ_m (mg m^{-2})	σ_c (Å)	n_{c1} (×10^{-3} Å^{-3})	Γ_c (mg m^{-2})	ξ_w (Å)
1	7.4	2.6	0.7	15.0	1.6	1.0	3.9
2	–	–	–	10.1	1.9	0.8	3.93
3	–	–	–	10.9	1.5	0.7	4.7
4	–	–	–	15.0	1.0	0.6	4.5
5	–	–	–	9.8	1.2	0.5	3.4

Table 4.31: Parameters from self partial structure factors at 10mN m^{-1} and the corresponding surface concentrations, m denotes methacrylate, c the lauryl ester chains and w the subphase water.

RUN N°	σ_c (Å)	n_{c1} ($\times 10^{-3}$ Å^{-3})	Γ (mg m^{-2})	ξ_w (Å)
1	16.8	1.2	0.8	4.4
2	13.4	1.3	0.7	3.9
3	8.6	1.7	0.6	4.6
4	5.2	2.3	0.5	3.9
5	14.6	0.8	0.5	3.8

Table 4.32: Parameters from self partial structure factors at 5mN m^{-1} and the corresponding surface concentrations, c denotes the lauryl ester chains and w the subphase water.

The same trend of decreasing surface concentration with time is again observed together with random fluctuations of the distribution width, σ and the number density. However, whenever σ is high, this is accompanied by a decrease in the number density and with time the overall decrease in the amount of material 'visible' can be observed by comparing different runs at each surface pressure with similar σ and noting that the number density is lower for the later run.

The separations between each component can be found in the same way as that used for the polymer. Due to the lack of information about the methacrylate component it is not possible to obtain the separations between the two monomer components and the methacrylate component and the water. Even for the first 15 minute run at 10mN m^{-1}, no fit was obtained to the cross partial structure factors involving the methacrylate component, so only the separation between the lauryl ester side chains and the subphase could be obtained. The resulting fits to the cross terms for the first and fifth 15 minute runs are shown in figures 4.75 and 4.76 (a) and (b).

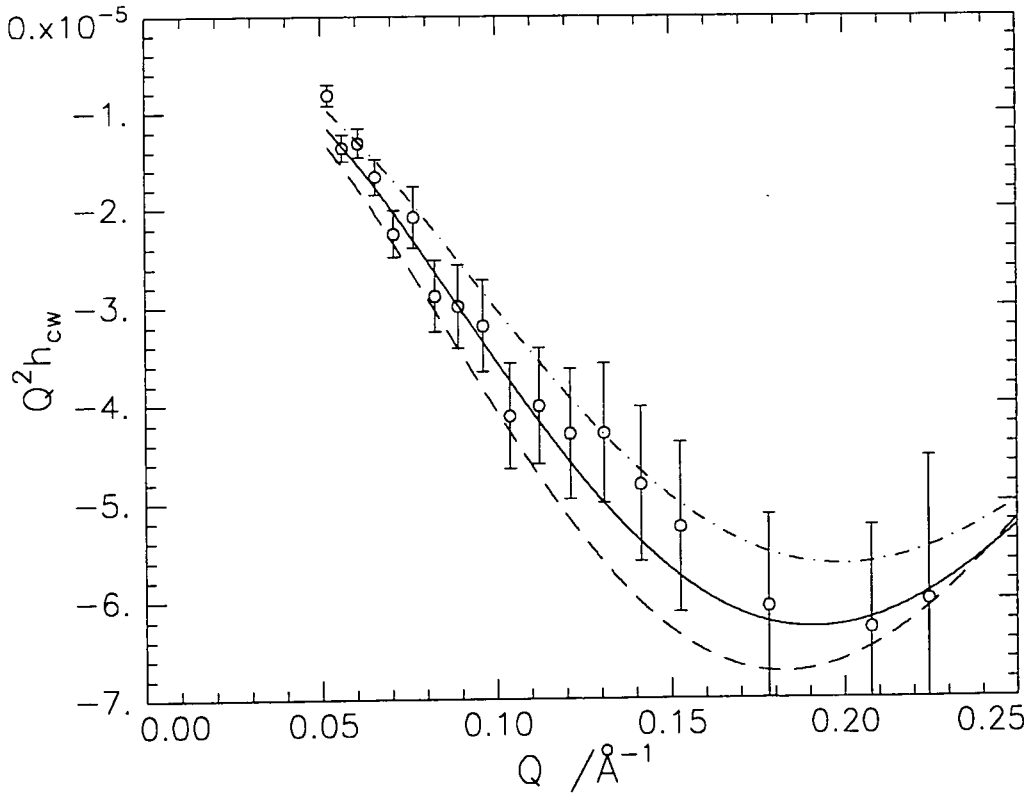

Figure 4.75(a): Cross partial structure factor for lauryl side chains and water, 1st 15 minute run at 10mN m^{-1}. δ = 7 (– –), δ = 6 (—), δ = 5 (– · –)

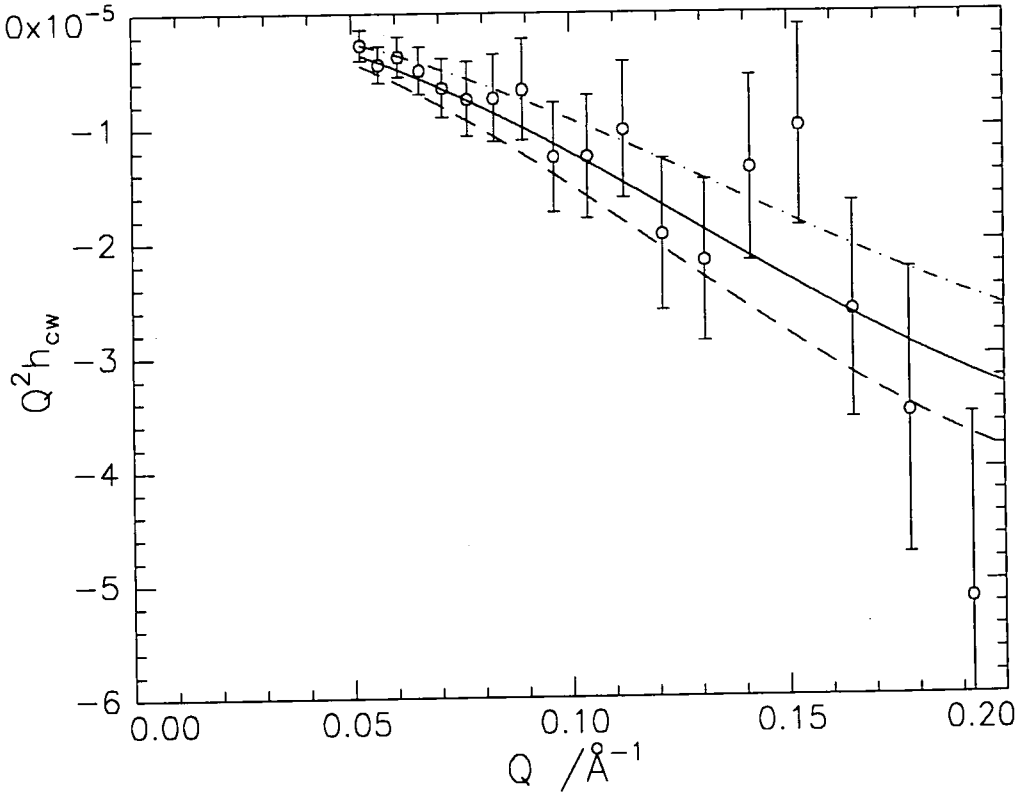

Figure 4.75(b): Cross partial structure factor for lauryl side chains and water, 5th 15 minute run at 10mN m^{-1}. δ = 5 (– –), δ = 4 (—), δ = 3 (– · –)

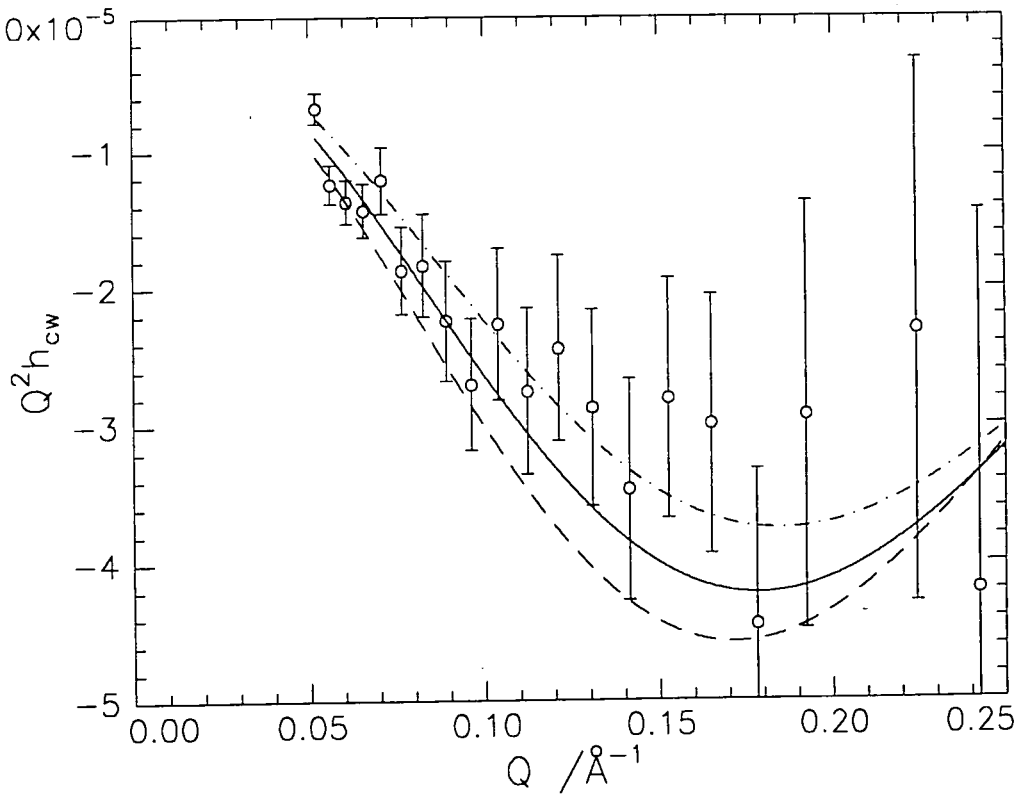

Figure 4.76(a): Cross partial structure factor for lauryl side chains and water, 1st 15 minute run at 5mN m^{-1}. δ = 7 (– –), δ = 6 (––), δ = 5 (– · –)

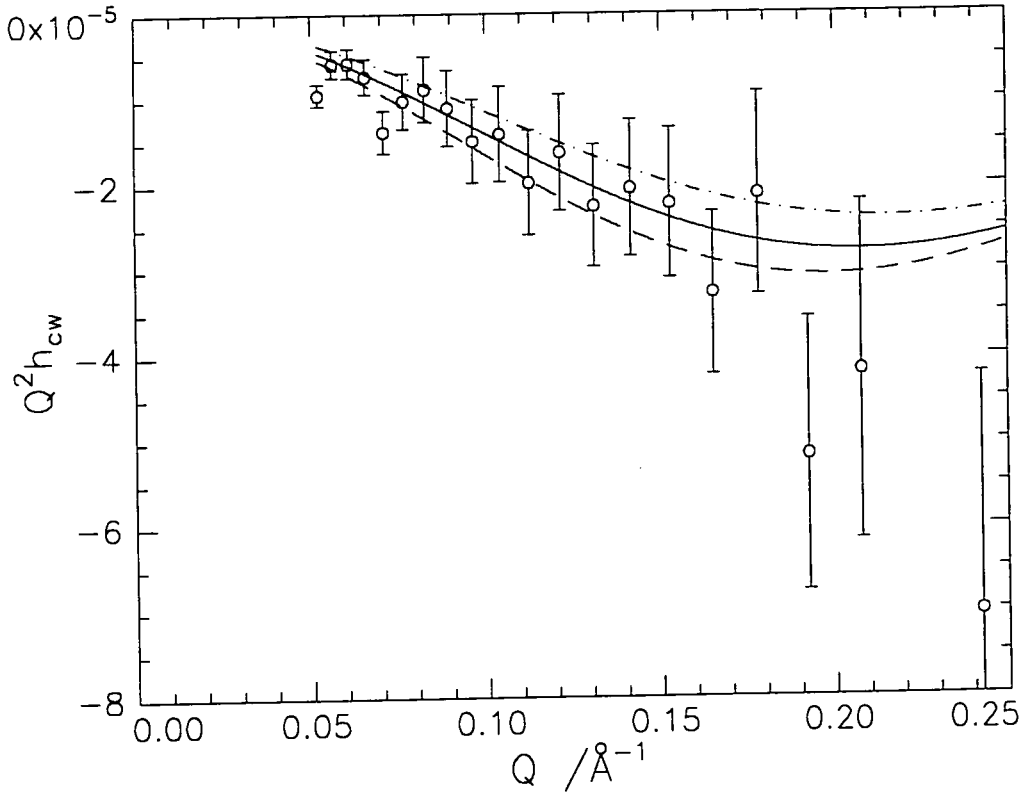

Figure 4.76(b): Cross partial structure factor for lauryl side chains and water, 5th 15 minute run at 5mN m^{-1}. δ = 5 (– –), δ = 4 (––), δ = 3 (– · –)

The values of δ were found to decrease at both surface pressures, from circa 6Å for the first 15 minute run, to 5Å for the second run and then remaining at circa 4Å for the next three runs. The changes which occur from run to run can be viewed in terms of the distributions of the lauryl ester groups and the subphase and this is shown in figures 4.77 and 4.78 (a) to (e) where the solid line represents the subphase distribution and the dotted line the lauryl ester groups. The overall decrease in the amount of monomer present at the interface can be observed in figures 4.77 and 4.78 by the decrease in area under the ester chain distribution.

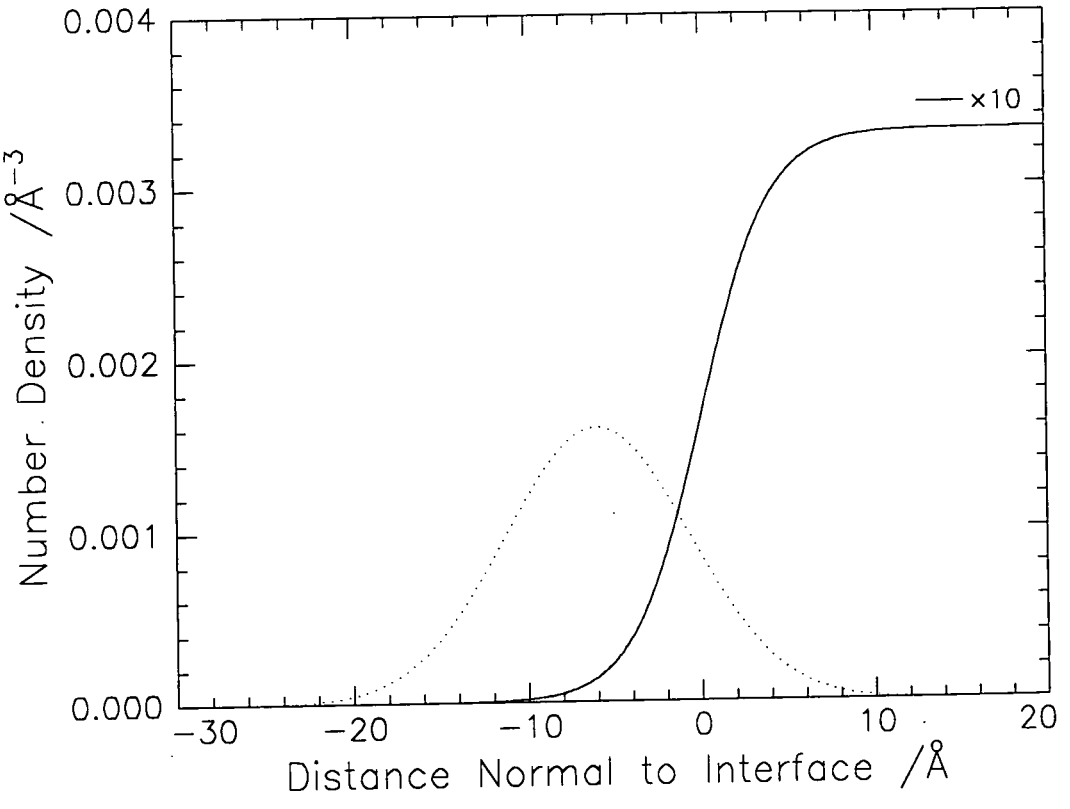

Figure 4.77(a): Distribution of the lauryl ester groups and the subphase for the 1st 15 minute run at 10mN m^{-1}

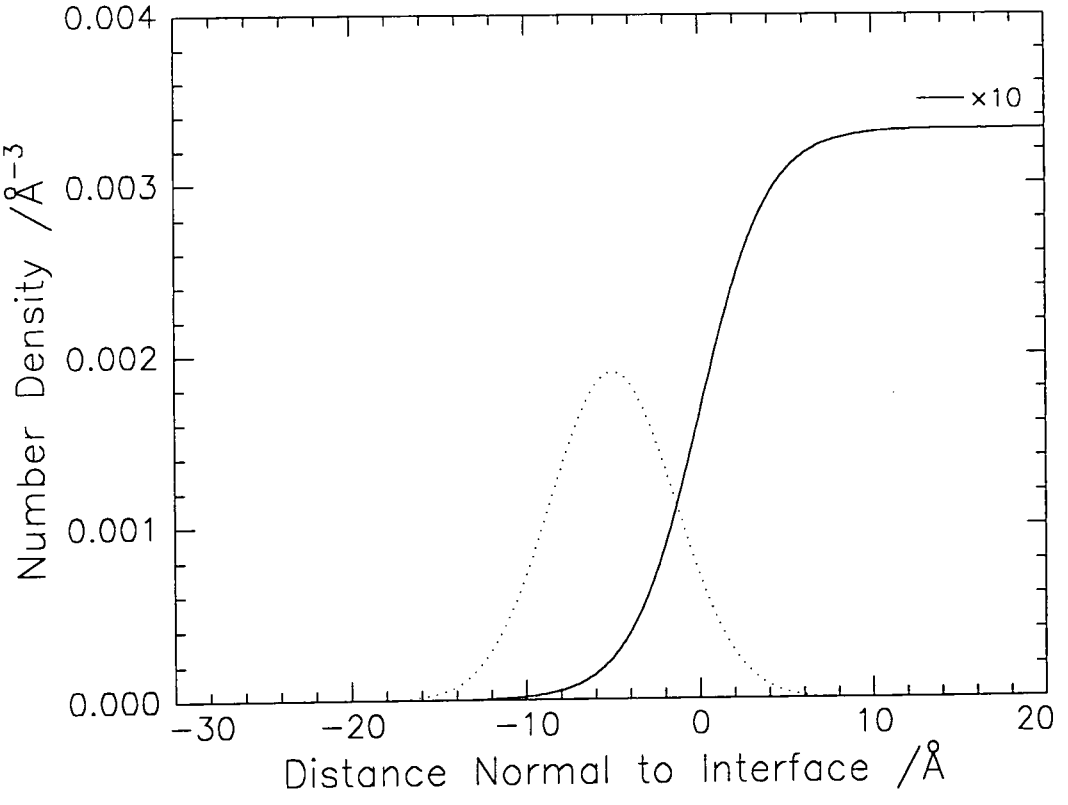

Figure 4.77(b): Distribution of the lauryl ester groups and the subphase for the 2nd 15 minute run at 10mN m^{-1}

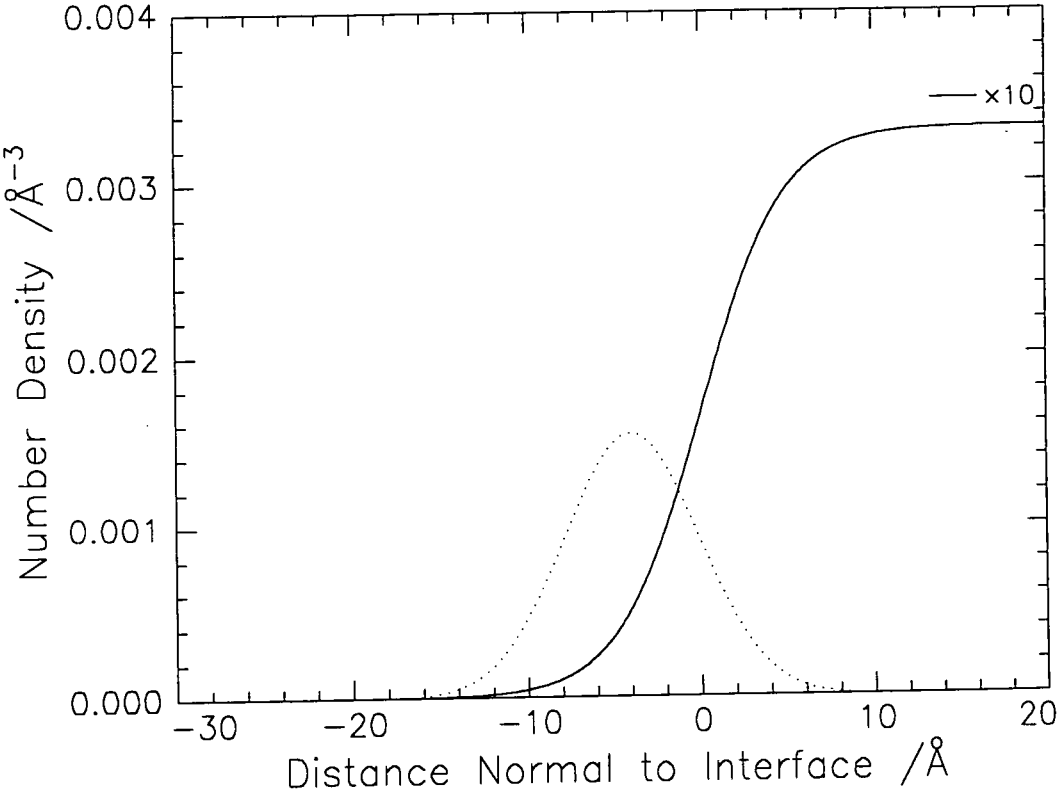

Figure 4.77(c): Distribution of the lauryl ester groups and the subphase for the 3rd 15 minute run at 10mN m^{-1}

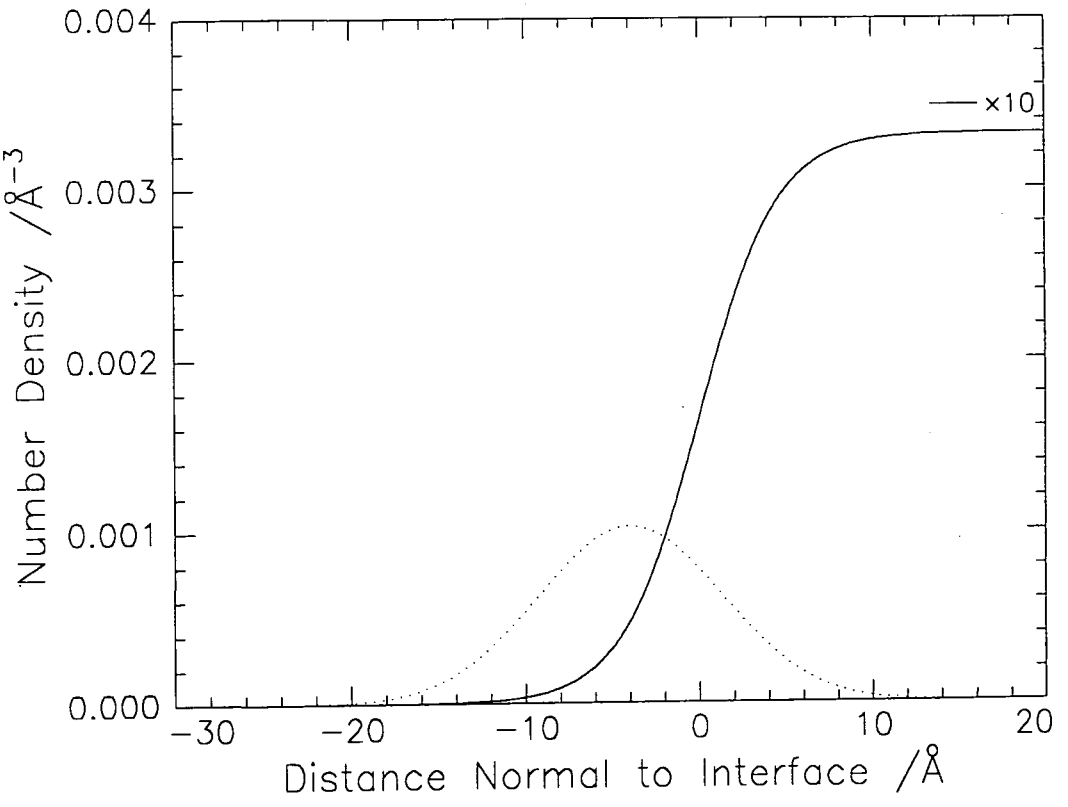

Figure 4.77(d): Distribution of the lauryl ester groups and the subphase for the 4th 15 minute run at 10mN m^{-1}

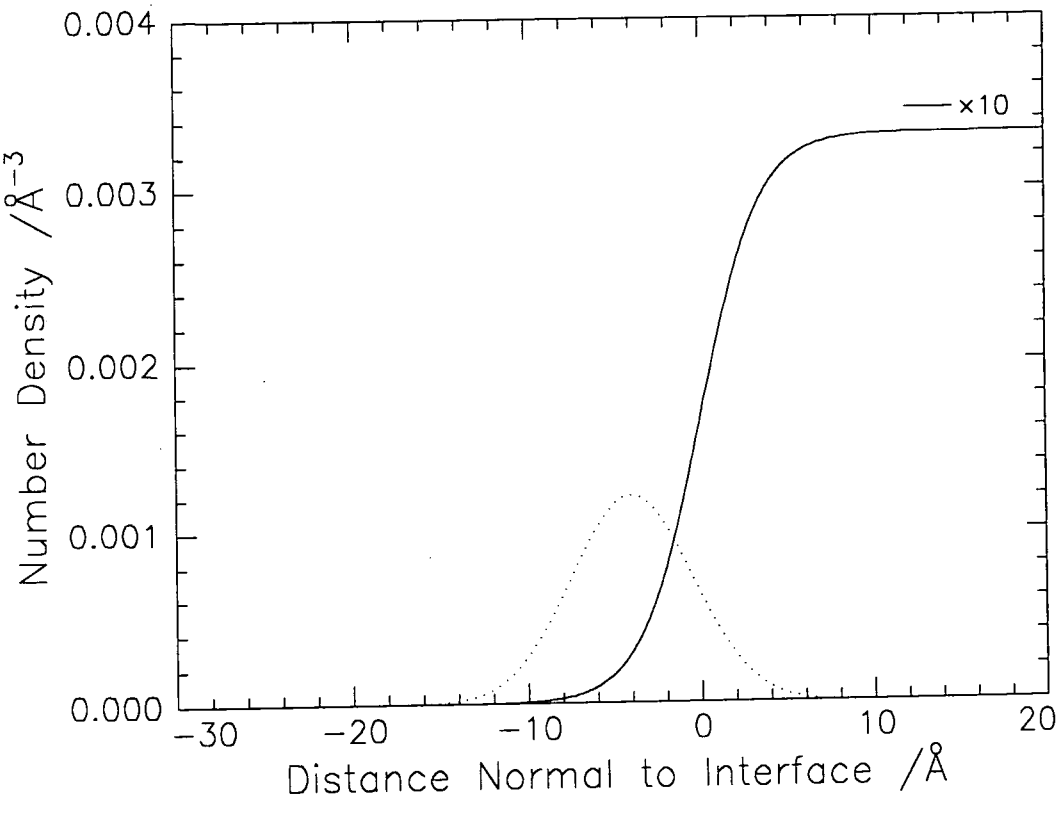

Figure 4.77(e): Distribution of the lauryl ester groups and the subphase for the 5th 15 minute run at 10mN m^{-1}

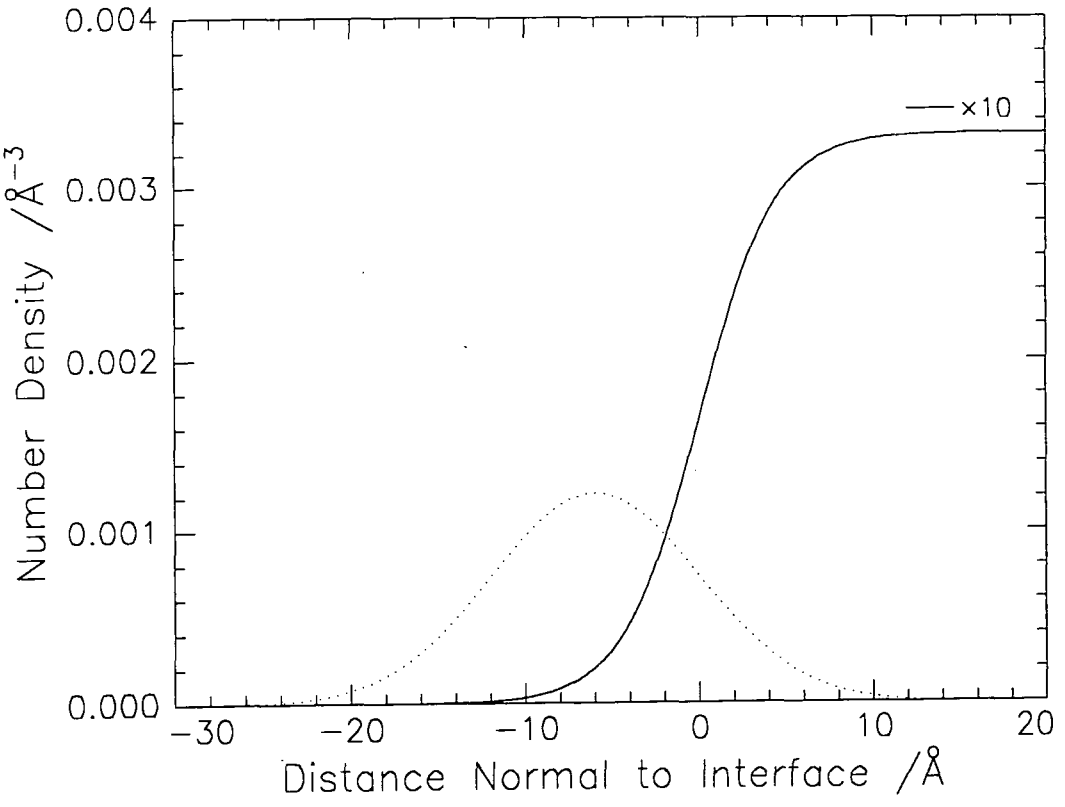

Figure 4.78(a): Distribution of the lauryl ester groups and the subphase for the 1st 15 minute run at 5mN m^{-1}

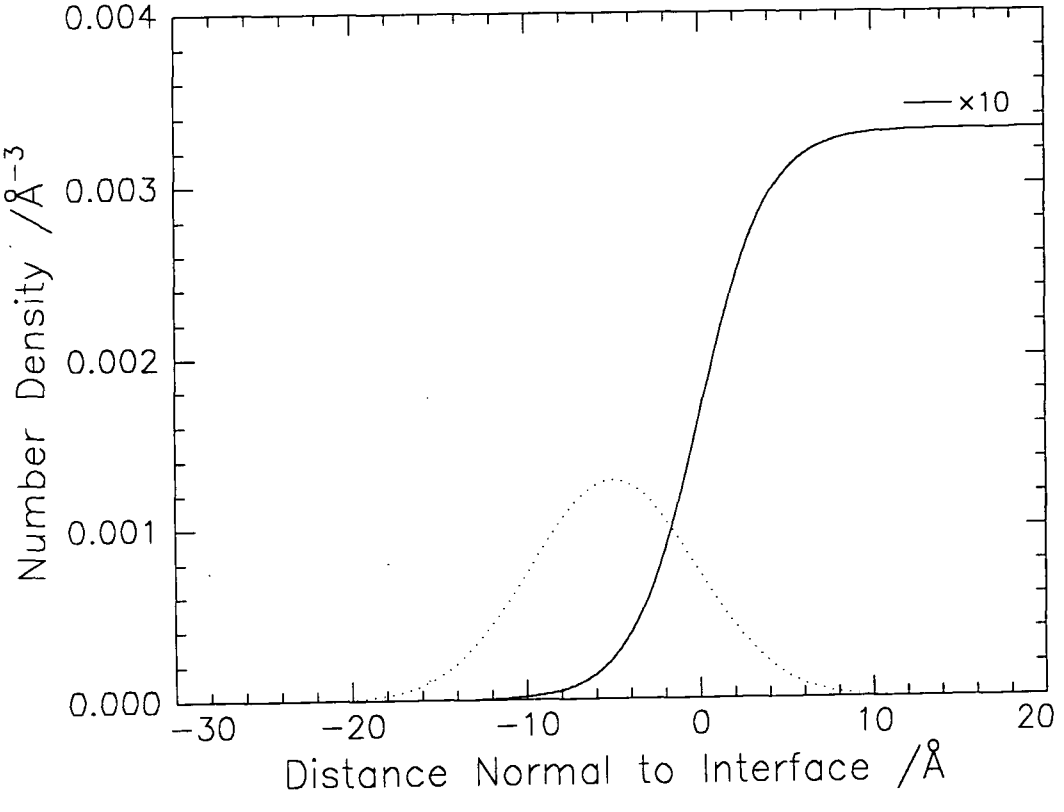

Figure 4.78(b): Distribution of the lauryl ester groups and the subphase for the 2nd 15 minute run at 5mN m^{-1}

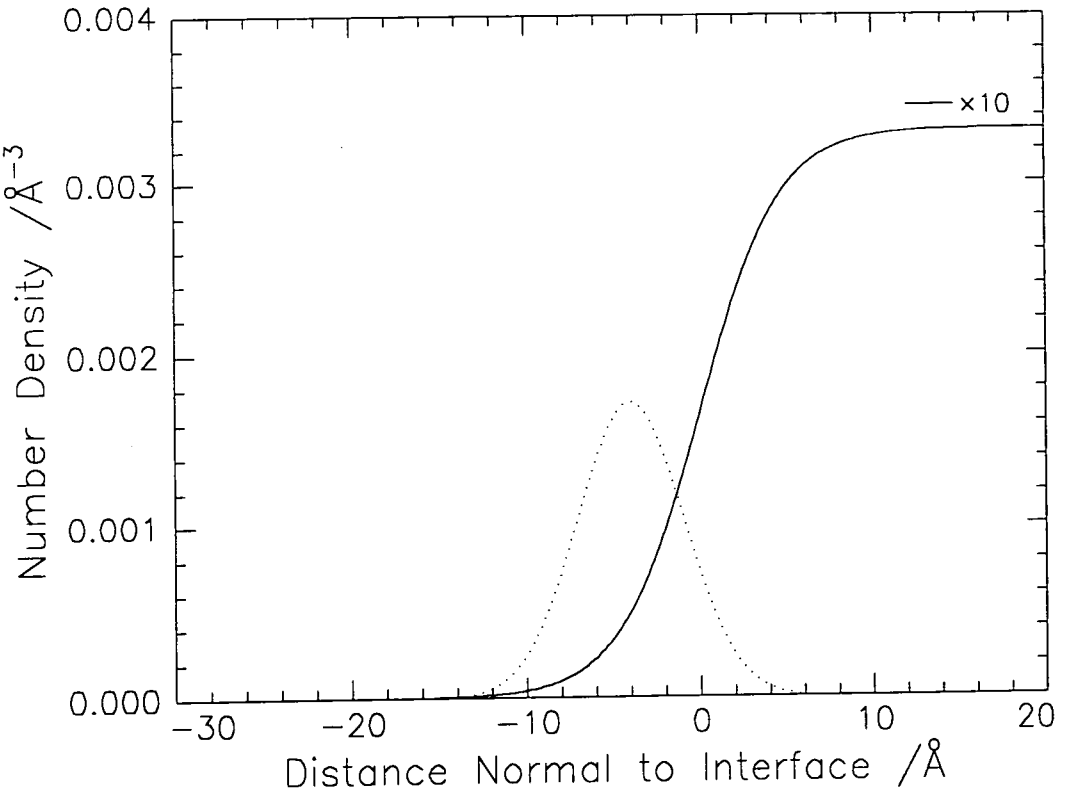

Figure 4.78(c): Distribution of the lauryl ester groups and the subphase for the 3rd 15 minute run at 5mN m^{-1}

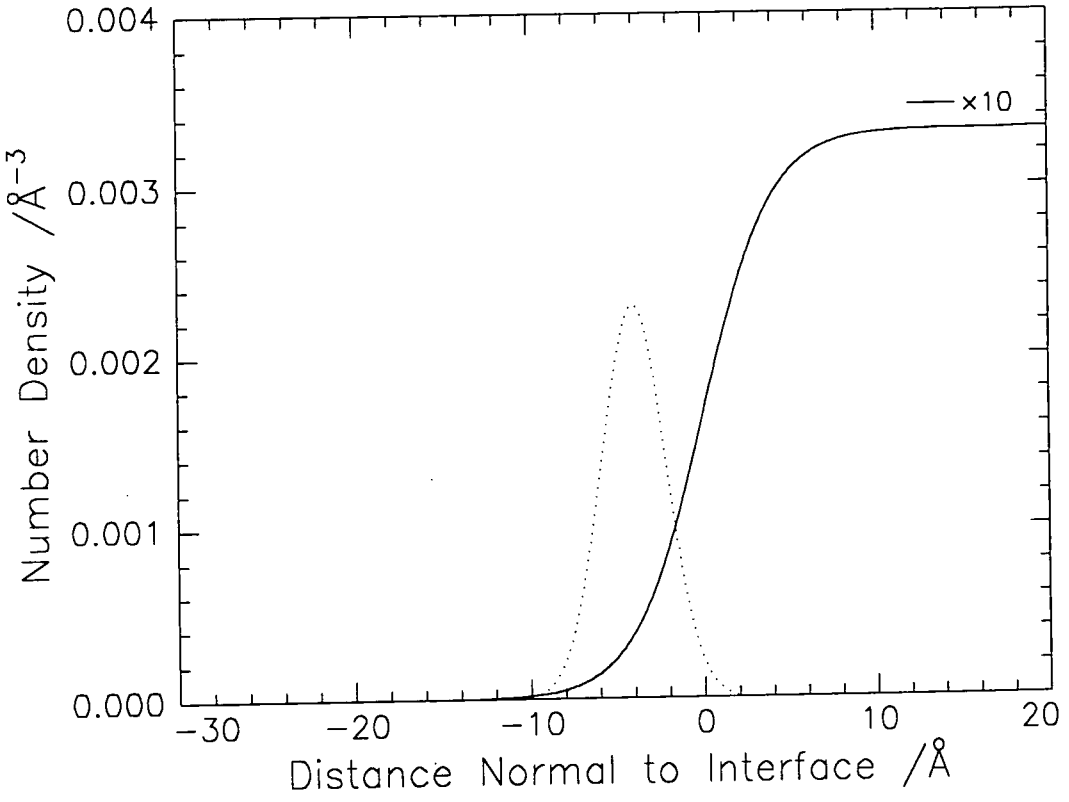

Figure 4.78(d): Distribution of the lauryl ester groups and the subphase for the 4th 15 minute run at 5mN m^{-1}

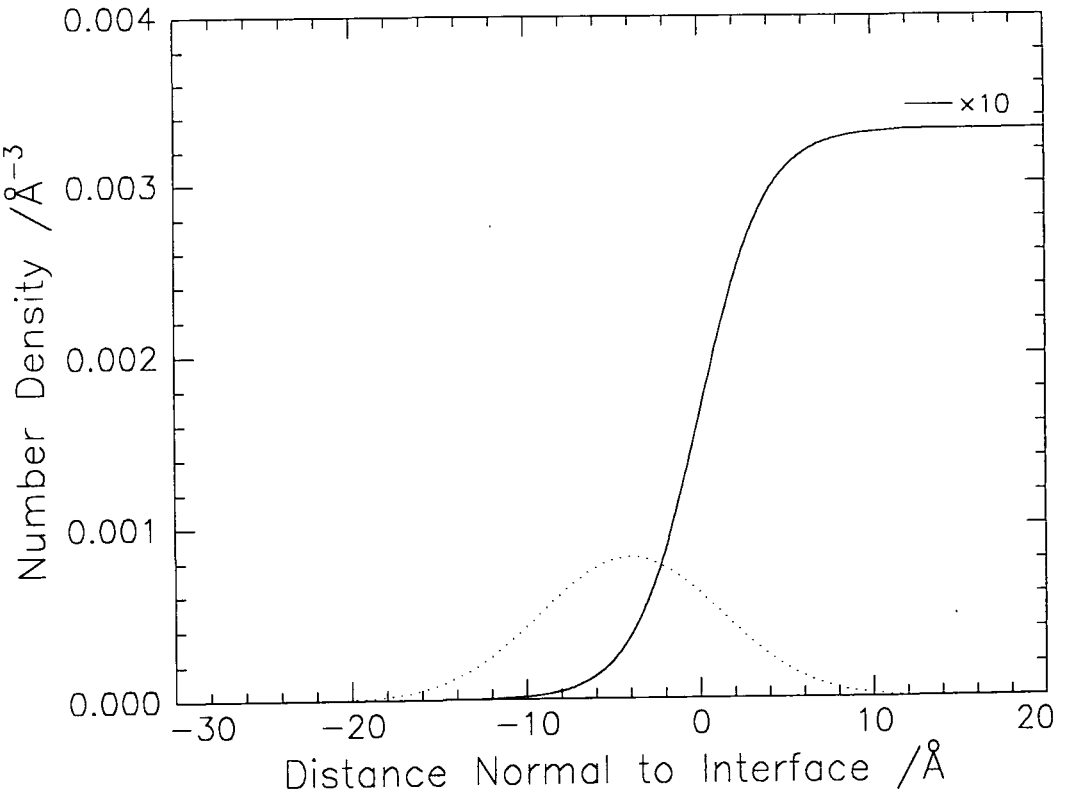

Figure 4.78(e): Distribution of the lauryl ester groups and the subphase for the 5th 15 minute run at 5mN m^{-1}

For the first 15 minute run at 5 and 10mN m^{-1} the lauryl ester group distribution has a similar size and position relative to the subphase as for the polymer. This may indicate that the organisation of the whole molecule is similar to that obtained for the monomer units in the polymer, as in order to accommodate the position of the ester groups in the monomer the methacrylate component will have to be forced into the subphase, as for the polymer. Unlike the polymer, LMA does not remain stable and the decrease in the apparent surface concentration is accompanied by a change in the distribution of the ester groups with the penetration of the layer by the subphase increasing with time. The instability of the LMA monolayer is due to the hydrophobicity of the molecules which leads to contraction of the monolayer into small lenses at the interface (this is a conclusion reached from the SQELS study in the following chapter), whereas for PLMA such contraction is limited due to the backbone. Initially there is a

rapid 'disappearance' of LMA which is due to the migration of molecules to form the lenses and exposes bare subphase, which in the case of a.c.m.w. reduces the reflectivity. A constant surface concentration is achieved at each surface pressure which corresponds to the completion of lens formation, so on average over the area 'visible' to the neutrons there is a constant amount of LMA and bare subphase which produces the effect of a constant surface concentration which is reduced from the theoretical surface concentration. As the molecular distribution is varying, the reflectivity profiles obtained will be an average of the various distributions sampled during the 15 minutes, so this may account for the random variations in layer thickness. The trends observed in the thickness and number density (or scattering length density) can not be assigned directly to structural changes in the LMA molecules within the layer due to the observed changes being due to lens formation, resulting in parameters from the data analysis which are not solely due to the molecules, but are averages between exposed subphase and the lens. For example, although from the values of δ would seem to indicate that the monolayer becomes closer to the subphase, this decrease is more likely due to the exposure of bare subphase which will have no contribution to the cross term and will lower the apparent value of δ. A constant value will be reached when lens formation is complete which will be a weighted average between the lenses present and the amount of bare subphase. The distribution of the molecules within the lenses can not be determined due to the area over which the neutrons impinge on the interface being larger than the lens dimensions and also the motion of the lenses on the surface would average the structure even if a small diameter beam was available.

4.5 Conclusions

For PLMA model fitting and consideration of the reflectivity profiles obtained on D_2O suggest that a two layer model is the minimum number that can be used to realistically represent the polymer distribution at the interface. It was also evident that two such layers do not occupy completely separate spatial regions, but overlap to a certain degree. In addition, the monolayer is penetrated by the subphase, not only the methacrylate region which is nearer to the subphase, but also the lauryl ester region.

By applying the kinematic approximation and maximising the utilisation of contrast variation, the distribution of the two polymer components could be quantified. The methacrylate backbone was almost wholly immersed in the subphase forming a narrow region which can be described by a Gaussian distribution of segments with a standard deviation of circa 6Å. The lauryl substituents are approximately evenly distributed, with half of their distribution being in the air and half in the subphase, with a small proportion which can extend slightly deeper into the subphase than the backbone plane. This can be attributed to rotations about the main chain backbone bonds which can result in some of the side chains being forced deeper into the subphase before rotations about bonds in the alkyl substituents eventually enable the hydrophobic substituents to reach the air phase. Little change is observed in the polymer structure as the surface pressure is increased, which may be as a result of the small change in surface concentration associated with the increase, so no change in the molecular packing is required. The increase in surface tension is due to the aggregation of polymer islands, at $0.5 mN\ m^{-1}$ the islands will be more or less compacted together in a homogeneous film and the increase in surface pressure occurs as the islands penetrate each other. The

resulting film consists of chains with the same configurations as those in the isolated islands as no change is observed from 0.5 to 10mN m^{-1}.

It did not prove possible to compare the structure of the polymer monolayer to that of the LMA monolayer to see if the same organisation was present even though the restrictions of the backbone had been removed. This was due to the instability of the monomer monolayer, however, from the lauryl chain partial structure for the first 15 minute run at 5 and 10mN m^{-1} the monomer may have originated with a similar distribution to that of the polymer, before lens formation disrupted the monolayer structure.

4.6 References

1. Born, M., Wolf, E., *Principles of Optics*, Pergamon Press, Oxford, 1970
2. Heavens, O.S., *Optical Properties of Thin Films*, Butterworths, London, 1955
3. Lekner, J., *Theory of Reflection*, Martinus Nijhoff, 1987
4. Highfield, R.R., Thomas, R.K., Cummins, P.G., Gregory, D.P., Mingins, J., Hayter, J.B., Scharpf, O., *Thin Solid Films*, 165, **99**, 1987
5. Croce, P., Nevot, L., *Phys. Appl.*, 761, **15**, 1980
6. Crowley, T.L., Lee, E.M., Simister, E.A., Thomas, R.K., *Physica B*, 143, **173**, 1991
7. Crowley, T.L., *Physica A*, 354, **95**, 1993
8. Henderson, J.A., Richards, R.W., Penfold, J., Shackleton, C., Thomas, R.K., *Polymer*, 3284, **32**, 1991
9. Henderson, J.A., Richards, R.W., Penfold, J., Thomas, R.K., *Acta Polymer*, 184, **44**, 1993
10. Lu, J.R., Simister, E.A., Lee, E.M., Thomas, R.K., Rennie, A.R., Penfold, J., *Langmuir*, 1837, **8**, 1992
11. Lu, J.R., Li, Z.X., Su, T.J., Thomas, R.K., Penfold, J., *Langmuir*, 2408, **9**, 1993
12. Lee, E.M., Thomas, R.K., Penfold, J., Ward, R.C., *J. Phys. Chem.*, 381, **93**, 1989
13. Lee, E.M., Simister, E.A., Thomas, R.K., Penfold, J., *J. Phys. Chem.*, 1373, **96**, 1992

5. SURFACE QUASI - ELASTIC LIGHT SCATTERING (SQELS)

5.1 Theoretical Background

A liquid surface is not perfectly smooth but is continually roughened by thermal agitation at the molecular level. This causes spontaneous propagation of low amplitude (~ 2Å), high frequency capillary waves at the air - liquid interface, when a surface film is present dilational modes also occur. The surface light scattering is dominated by the capillary waves which are governed by the interfacial tension (γ), however, the dilational waves, which are governed by the dilational modulus (ε) of the interface, are coupled to the capillary waves so ε has an indirect effect on the capillary waves. The temporal evolution of the waves is reflected in the time domain spectrum of the scattered light and as the wave evolution is governed by the interfacial visco-elastic properties, suitable fitting to an experimentally generated time domain spectrum of the scattered light can provide information about the visco-elastic properties of the interface.

The random surface waves can be Fourier decomposed into a set of modes and the displacement of the surface from its equilibrium plane (defined as the x - y plane) for each mode can be described by:

$$\xi(x,t) = \xi_o \exp[i(qx + \omega t)] \qquad 5.1$$

where $q = 2\pi/\Lambda$ = surface wavenumber

Λ = wavelength of surface wave

ω = wave frequency

The surface behaves as a weak diffraction grating for light approaching in the x - z plane and some of the incident light is scattered through an angle $\delta\theta$ with reference to the specularly reflected beam(figure 5.1).

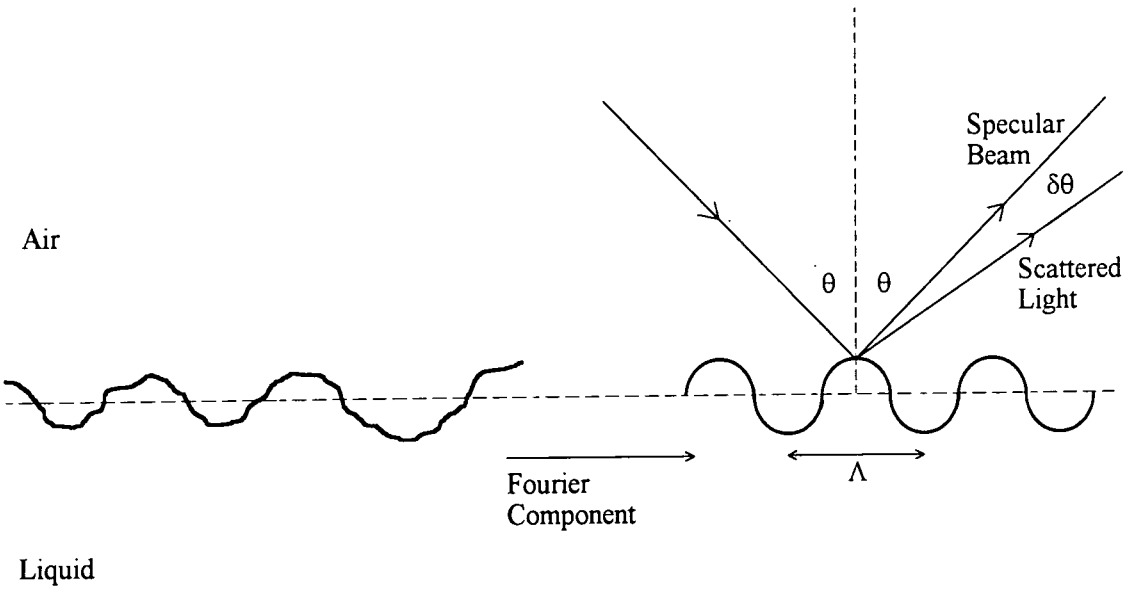

Figure 5.1: Light scattered at air - water interface

For the small angles of scatter involved in SQELS it is found that

$$q = 2k_o \sin(\delta\theta/2).\cos\theta \qquad 5.2$$

where $2k_o\sin(\delta\theta/2) = K$, the scattering vector.

SQELS experiments can be carried out either by measuring the time domain correlation function or the spatial power spectrum of the scattered light as a function of real frequency. For the case of time domain spectral analysis of scattered light, a mode of real wave vector q is selected and the complex frequency ω ($= \omega_o + i\Gamma$, where ω_o = wave propagation frequency and Γ = time domain damping constant) is measured.

The dispersion equation of the interfacial waves relates ω to q and to the material properties of the system. For a free liquid surface the equation is [1,2]

$$D(\omega) = (i\omega + 2\upsilon q^2)^2 + gq + \gamma q^3/\rho - 4\upsilon^2 q^3(q^2 + i\omega/\upsilon)^{1/2} = 0 \qquad 5.3$$

where γ = surface tension

υ = kinematic viscosity = η/ρ

g = gravitational acceleration

ρ = density of liquid

For sufficiently short wavelengths the gravitational term may be neglected and the equation can be reduced to

$$D(S) = (S+1)^2 + Y - (2S+1)^{1/2} = 0 \qquad 5.4$$

where $S = i\omega / 2\upsilon q^2$

$Y = \gamma / 4\upsilon^2 \rho q^2 = \gamma\rho / 4\eta^2 q$

Y represents the balance between driving forces and dissipative forces in wave propagation

$$Y = \frac{\text{restoring force} \times \text{inertial force}}{(\text{damping force})^2} \qquad 5.5$$

Numerical solutions of the dispersion equation show that for $Y > 0.145$ it has complex conjugate roots, corresponding to propagating capillary modes. Below this value two real roots are found, corresponding to overdamping of the surface motions.

A first order approximation to the solution of equation 5.3 gives the wave propagation frequency, ω_o, as

$$\omega_o^2 = \gamma q^3/\rho \qquad 5.6$$

and the wave damping as

$$\Gamma = 2\upsilon q^2 \qquad 5.7$$

The spectrum of light scattered by the capillary waves is just the power spectrum of the waves of the relevant q^3

$$P(\omega) = -\frac{kT}{\pi\omega}\cdot\frac{\rho}{4\eta^2 q^3}\,\mathrm{Im}\left\{\frac{1}{D(\omega)}\right\} \qquad 5.8$$

The spectrum is approximately Lorentzian in shape and is characterised by a peak frequency f_s and width Δf_s (full width at half peak height), corresponding to the real and imaginary parts of the complex frequency of the capillary waves (ω). Using photon correlation techniques, the correlation function $g(\tau)$ measured in the time domain is simply the Fourier transform of $P(\omega)$.

For a liquid surface supporting a monolayer the dispersion equation is modified to include terms for the physical properties of the monolayer, the modified equation is [4,5]

$$D(\omega) = [\varepsilon q^2 + i\omega\eta(q + m)]\,[\gamma q^2 + i\omega\eta(q + m) - \omega^2\rho/q] - [i\omega\eta(q - m)]^2 = 0 \qquad 5.9$$

where $m = Re(q^2 + i\omega\rho/\eta)^{1/2}$

γ = surface tension

η = viscosity

ρ = density of the liquid

ε = dilational modulus of the monolayer = $\Gamma(d\pi/d\Gamma)$

A = molecular area in the film

For a monolayer covered surface the spectrum of scattered light is an explicit function of the surface properties γ and ε[4]

$$P(\omega) = -\frac{kT}{\pi\omega} Im\left\{\frac{i\omega\eta(q+m)+\varepsilon q^2}{D(\omega)}\right\} \qquad 5.10$$

The responses to shear stress normal to the interface (expressed via γ) and to in-plane dilational stress (ε) may both include viscous elements, which can be incorporated by expansion of the two surface moduli[6]

$$\gamma = \gamma_o + i\omega\gamma' \qquad 5.11$$

$$\varepsilon = \varepsilon_o + i\omega\varepsilon' \qquad 5.12$$

where the real parts are elastic moduli, γ_o corresponding to the classical surface tension and ε_o, the dilational modulus, corresponds to the Gibbs static elasticity and is defined as $\Gamma(d\pi/d\Gamma)$. The imaginary parts incorporate the surface viscosities, neither of which is the conventional surface viscosity which governs shear stress in the plane of the surface. These two viscosities govern the shear transverse to the surface (γ') and dilation in that plane (ε').

5.1.1 Data Fitting

The measured correlation function can be fitted with a Fourier transform of the power spectrum. If a Lorentzian P(ω) is used the Fourier transform is

$$G(\tau) = B + A\cos(\omega_o\tau)\exp(-\Gamma\tau) \qquad 5.13$$

where A and B are amplitude and background factors respectively. The actual P(ω) is not exactly Lorentzian and Earnshaw and McGivern [7] have shown that this function does not well represent the observed correlation functions, producing large and non-random residuals indicating systematic differences in shape between the observed and fitted functions.

The exact form of P(ω) is a skewed Lorentzian which has been broadened due to instrumental effects. Earnshaw and McGivern have included both these effects in their fitting function which produced

$$G(\tau) = B + A\cos(\omega_o\tau + \phi)\exp(-\Gamma\tau) \times \exp(-\beta^2\tau^2/4) + C\exp(-\alpha\tau) + D\tau^2 \qquad 5.14$$

where ϕ is a phase term which accounts for the skewing of the Lorentzian and the Gaussian multiplicative term in β represents the instrumental line broadening. The final two terms in the correlation function account for two effects which may influence the observed data. When the correlator sample time is less than 2μs the first few points follow an exponential decay. Earnshaw [8] has attributed this to after pulsing in the photomultiplier which occurs on such a fast time scale it is not observed for sample times greater than 2μs if the first point if the correlation function is omitted. This decay is

accounted for by the $C\exp(-\alpha\tau)$ term which only needs to be included for short sample times. The background of the correlation functions, B, was found to always exceed the theoretical value due to slow mechanical motions of the liquid surface which occur despite vibration isolation of the trough. If very long sample times are used these slow motions can be observed and the corresponding correlation function is seen to vary roughly cosinusoidally. If these slow motions occur to a large extent this additional background appears as a droop in the correlation function for the capillary waves. The effect of this additional background is incorporated by adding the term $D\tau^2$, which is the first term of the cosine expansion. This function (equation 5.14) provides values of ω_o and Γ, which have been shown to be unbiased [7].

There is no simple, unique relationship between ω_o and Γ and the four surface properties which affect capillary waves (i.e. γ_o, γ', ε_o and ε'). The gross effects are known, the surface tension γ_o mainly affects the wave frequency ($\omega_o \approx \gamma_o q^3/\rho$) and the transverse shear viscosity γ' increases the wave damping until at sufficiently large values of γ' the capillary waves do not propagate. The modulus ε affects the capillary waves indirectly and leads to difficulties in determining ε_o and ε' precisely via light scattering from capillary waves, except in the region $\varepsilon_o \sim 0.16\gamma_o$, where the two modes resonate. As the ε_o/γ_o ratio is increased (γ_o fixed) up to this resonance point the wave frequency and damping both increase and when ε_o becomes greater than $0.16\gamma_o$ the frequency and damping are decreased until $\varepsilon_o \sim 0.45\ \gamma_o$ when further increases in the ε_o/γ_o ratio have little effect on either property. The effect of ε' depends on the ε_o/γ_o ratio. Below $\varepsilon_o \sim 0.25\gamma_o$ increasing ε' decreases the frequency and above this point it increases the frequency. The damping is increased up to $\varepsilon_o \sim 0.1\gamma_o$ and then as ε_o is increased the

damping is decreased by increasing ε'. This occurs up to $\varepsilon_o \sim 0.5\gamma_o$, above this point ε' has little effect on the damping.

Earnshaw and his co-workers have developed a method to determine the four surface properties directly from a single correlation function [8]. This is achieved by fitting the data with a correlation function for which the damped cosine time dependence in equation 5.14 is replaced by the Fourier transform of $P(\omega)$ formulated as a function of the four surface parameters

$$G(\tau) = B + A(FT[P(\omega| X_j)]) \times \exp(-\beta^2\tau^2/4) + C\exp(-\alpha\tau) + D\tau^2 \qquad 5.15$$

where X_j represents the four surface properties

The last three terms account for the same effects as in equation 5.14

5.2 Experimental

Surface quasi - elastic light scattering experiments were carried out on an instrument constructed in Durham which is shown schematically in figure 5.2. It was built around the same Langmuir trough used for the surface pressure - area isotherms which was described earlier. The optical components were purchased from Ealing Electro - Optics, Watford, UK, and were all standard components to fit their triangular bench mounts.

The laser used was a Siemens He/Ne laser, model number LGK 7626, with a power rating of 30mW and light polarised normal to the plane of incidence. Due to space limitations the laser had to be placed beside the optical path. A series of mirrors were used to deflect the beam first up (m_1), then across (m_2) and finally down the optical path (m_3). This series of reflections changed the polarisation of the light ,so a half wave plate at 45° was used to change the polarisation. A Polaroid filter ensured that only light of the correct polarisation was used.

The beam of light then passed through a pin hole, about 1.5mm in diameter, to remove any flare light before passing through lens l_1 which focused the beam passing through the diffraction grating (purchased from Data Sites Ltd, UK, with 10μm wide lines and an inter - line spacing of 100 μm). Lens l_2 then reconverged the divergent diffraction orders into a single spot which is incident on the water surface, hence the reference beams were coherent with the scattered light out of the zero - order beam. The light was directed onto the liquid surface by a 'periscope' arrangement of mirrors (m_4 and m_5) which first reflected the beam upwards and then downwards onto the surface, 90° from the original direction.

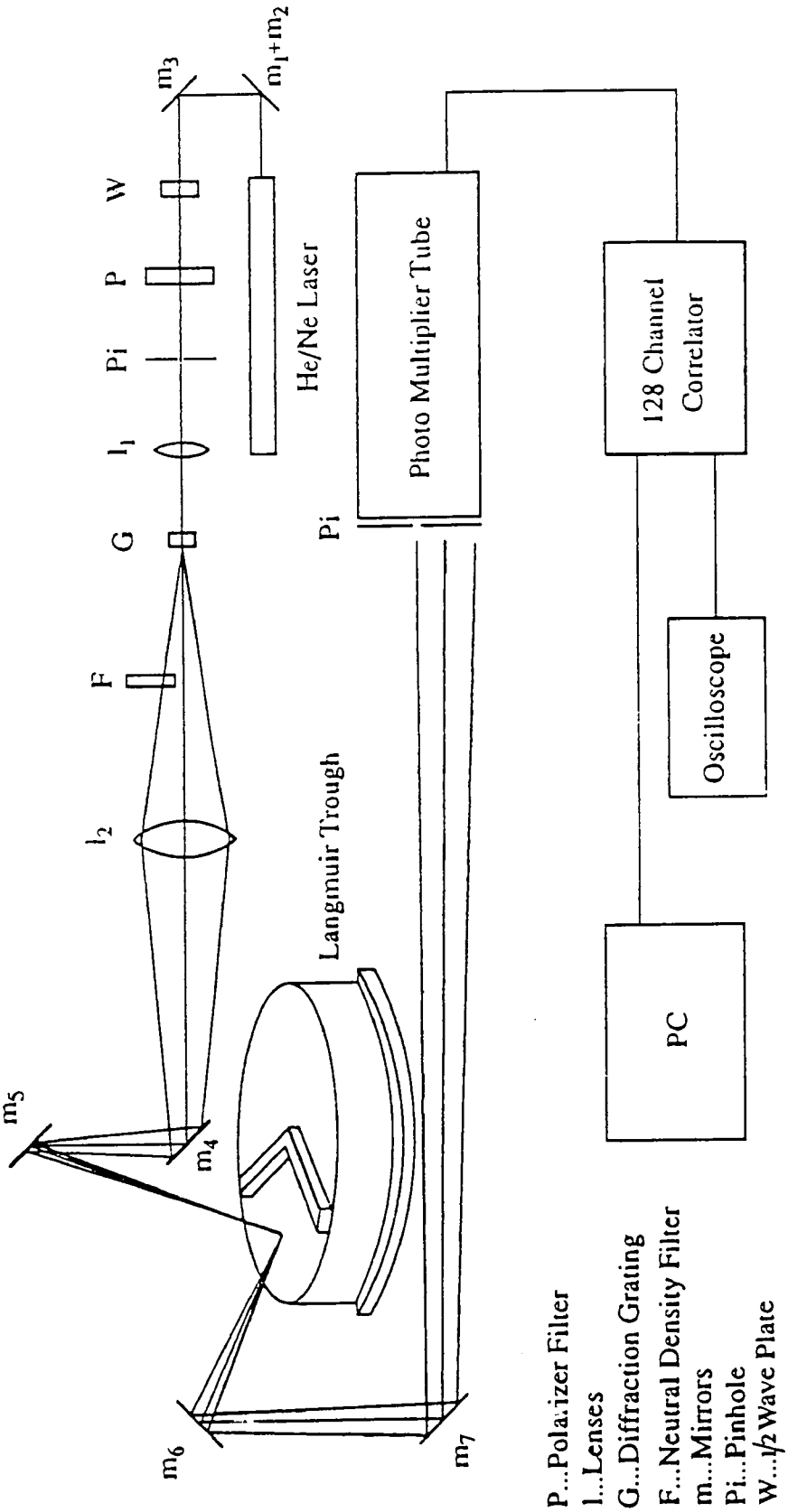

Figure 5.2: Schematic diagram of the SQELS set up

The reflected beam was collected by a similar arrangement of mirrors (m_6 and m_7) and directed horizontally towards the photo multiplier tube, which was approximately 2m from mirror m_7. This distance allowed the series of diffracted beams to separate and they appeared as a horizontal row of spots, with a bright central spot due to the specular reflection from the main undiffracted, zero - order beam. The series of specularly reflected diffraction beams provide heterodyne mixing beat signals for the scattered light from the zero - order beam falling on the detector pinhole at the same angle. Thus by tilting mirror m_7 slightly, a given diffraction order, and hence wavenumber, q, could be selected by directing the beam into the photo multiplier tube. The neutral density filter attenuated the diffraction orders to an intensity where the heterodyne beating effect was maximised and due to the low intensity of the diffracted beams, the scattering can be considered as arising from the zero - order beam. A neutral density 3 filter was used for diffraction spots two and three and a neutral density 4 filter for higher diffraction orders since the scattered intensity decreases as the scattering angle increases, so the intensity of the higher diffraction orders has to be decreased to obtain a suitable ratio of heterodyne reference beam intensity(I_R) to scattered intensity(I_S) for heterodyne detection to occur. If I_R is excessively large, random fluctuations of I_R dominate the time dependence.

The output of photodetection events from the photo multiplier tube was analysed using a 128 channel correlator (Malvern, UK, model K7025) with sample times between 2 and 18μs. The measured signal was displayed as it was obtained on an oscilloscope. Operation of the correlator was controlled via a PC which also stored the data files.

Whenever a particular diffraction spot was used, a clean water surface was analysed to determine the corresponding q value. The first spot was not used as light flared from the edge of the neutral density filter encroached across this spot and the high q limit was determined by the drop off in scattered intensity as the scattering angle

increased, which resulted in much longer run times being needed for the higher diffraction orders and poorer data quality. This is shown in figure 5.3(a) and (b), the data for spot 2 was collected in 30s with a sample time of 18μs and for spot 8, 1100s were used with a sample time of 2μs.

By fitting the correlation functions with the damped cosine function in equation 5.14 values of the wave propagation frequency, ω_o, and damping, Γ, can be obtained. The values of ω_o and Γ for a particular diffraction spot can be used to calculate the q value using the approximate formulae of equations 5.6 and 5.7. The data for the polymer monolayers was analysed by fitting with this equation as well as using equation 5.15 to obtain the visco - elastic parameters.

For studies on PLMA monolayers, three approaches were undertaken:

1. At a fixed surface concentration on the high and low plateau of the surface pressure -area isotherm (1.8 and 0.2mg m^{-2} respectively), repetitive runs were carried out for about two hours to monitor changes in properties with time.

2. At a fixed q value, a range of surface concentrations from 0.2 to 2mg m^{-2} were studied. Ten repeated runs at each concentration were obtained and the average of each parameter and the standard deviation were calculated.

3. At a fixed concentration, q was varied to obtain data for possible frequency dependence of the viscoelastic parameters.

SQELS was also carried out on monolayers of the monomer LMA in an attempt to compare the visco - elastic properties of two materials with the same basic chemical unit but with different restrictions on the packing of the molecules at the interface. Three surface concentrations were studied, 0.3, 1.5 and 3mg m^{-2}, which correspond to the π = 0 region of the surface pressure - area isotherm, half way up the steep increase in surface pressure and the high surface pressure region respectively.

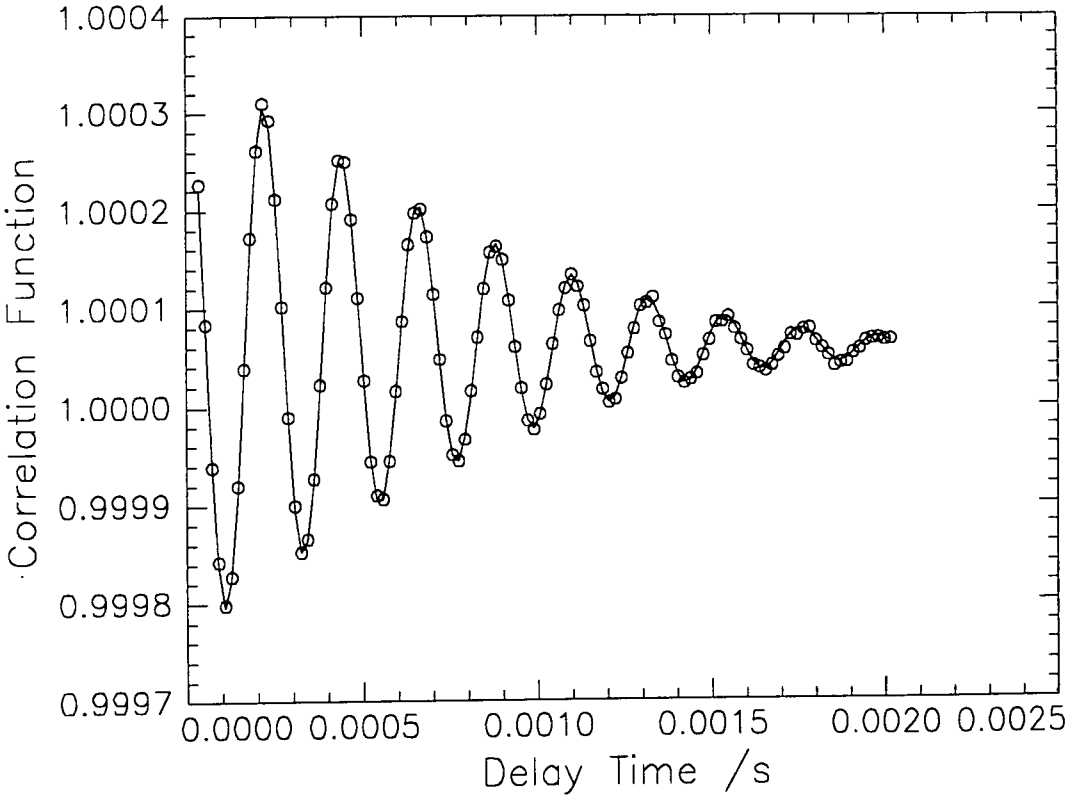

Figure 5.3(a): Correlation function for water using spot 2

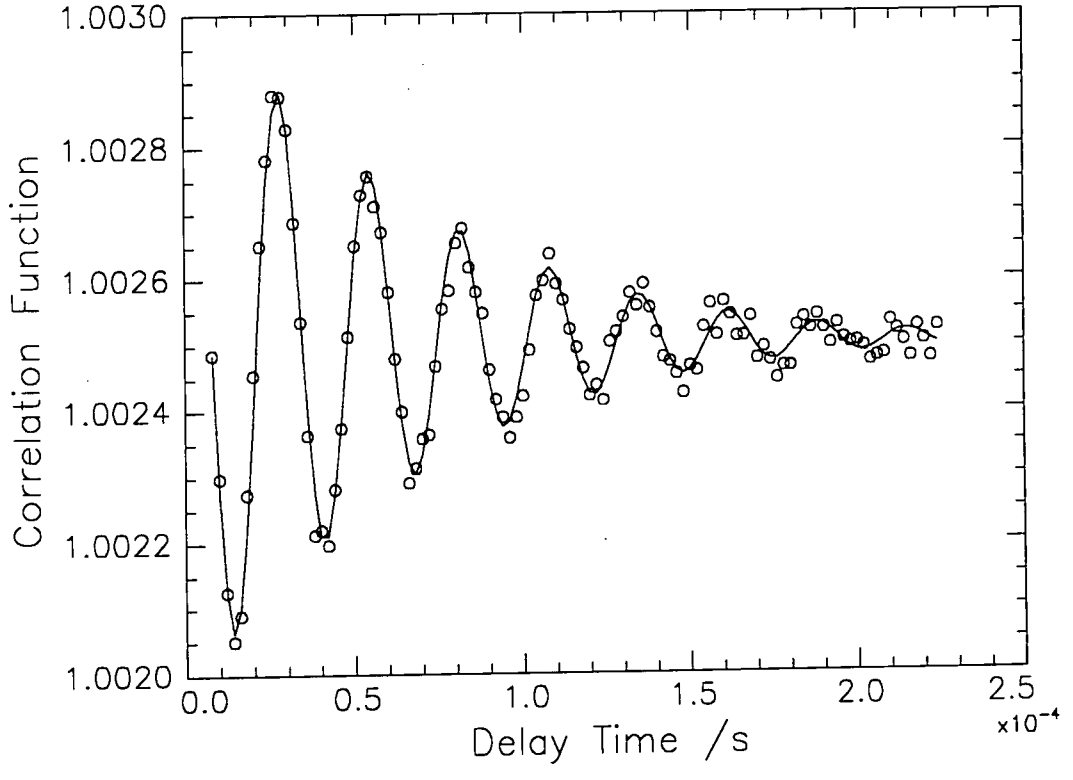

Figure 5.3(b): Correlation function for water using spot 8

5.3 SQELS on PLMA Monolayers

5.3.1 Time Dependant Studies

Figures 5.4 and 5.5 (a) show two correlation functions from a set of ten 90s runs for q = 226.2cm^{-1} and at a surface concentration of 0.6mg m^{-2}, which is in region 1 of the surface pressure - area isotherm. The solid lines are fits to the data using the cosine function in equation 5.14 and the residuals of each fit are also shown in figures 5.4 and 5.5 (b).

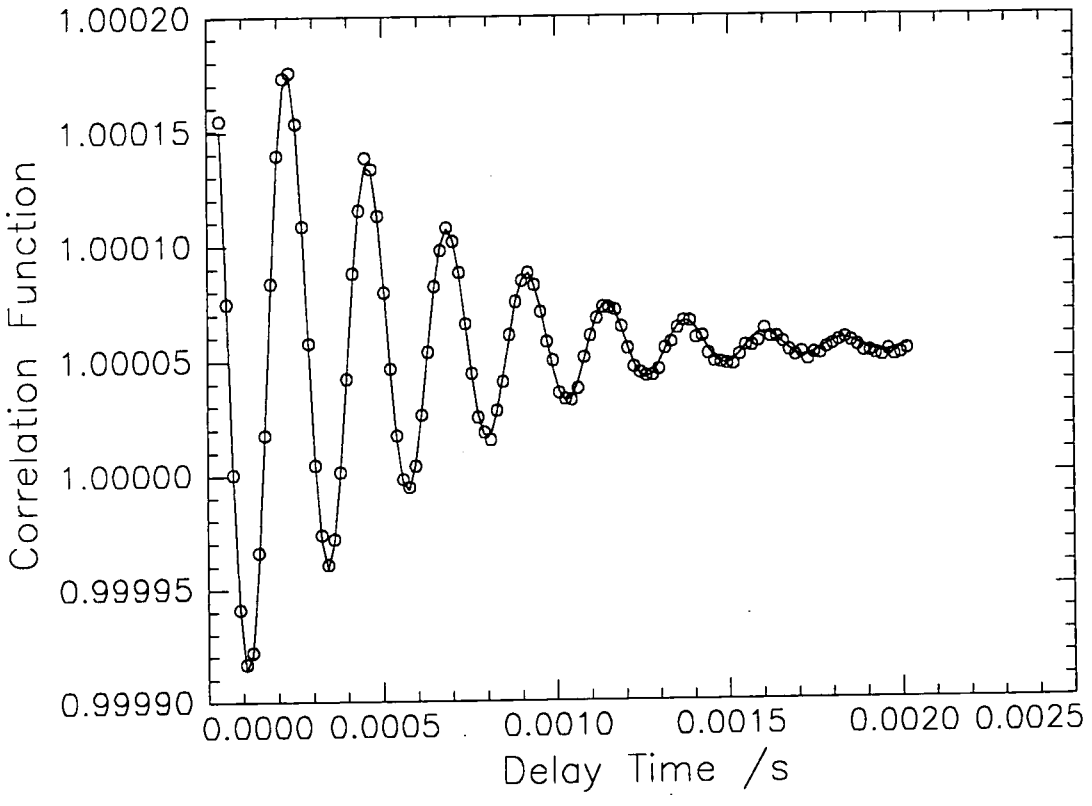

Figure 5.4(a): Correlation function at 0.6mg m^{-2} - 8th run of 10

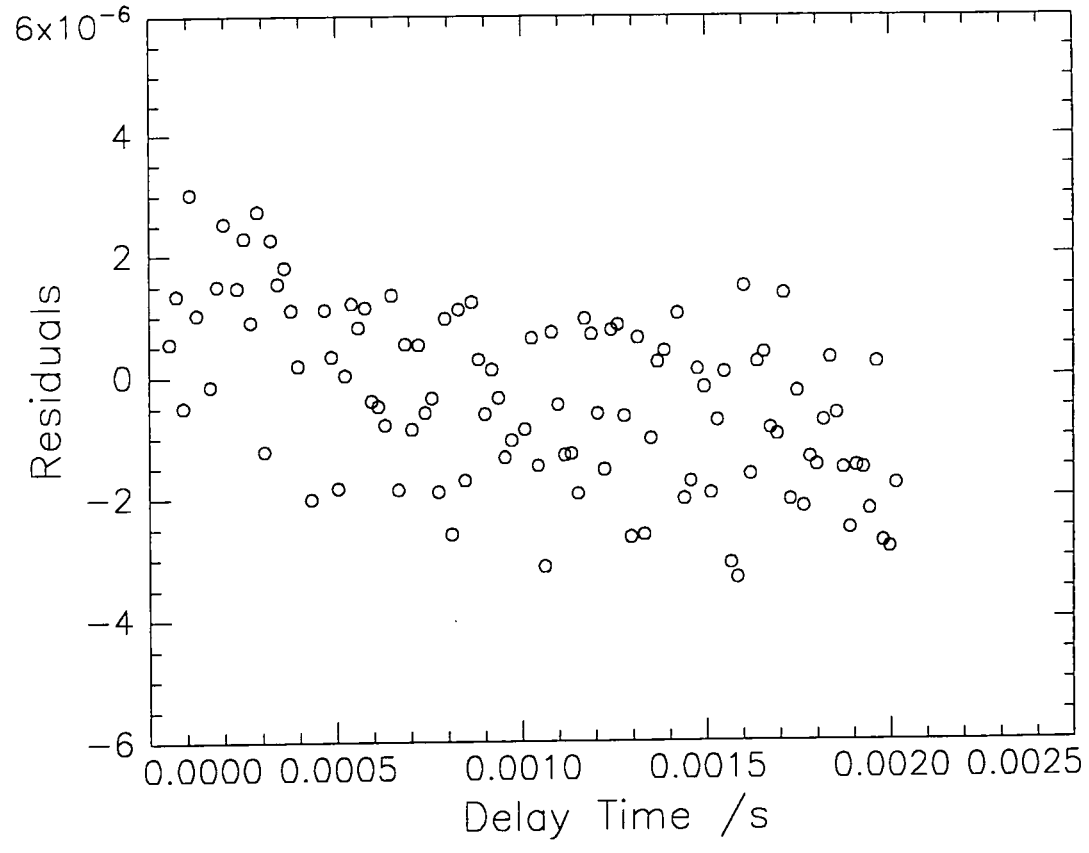

Figure 5.4(b): Residuals at 0.6mg m^{-2} - 8th run of 10

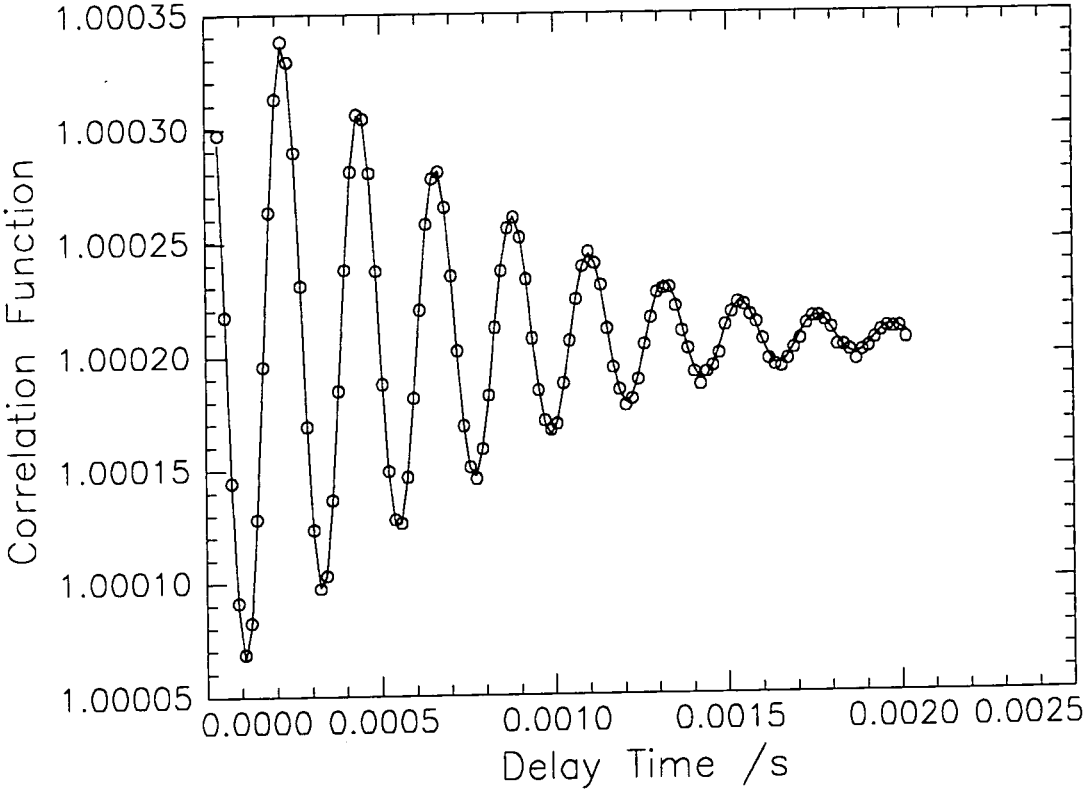

Figure 5.5(a): Correlation function at 0.6mg m^{-2} - 5th run of 10

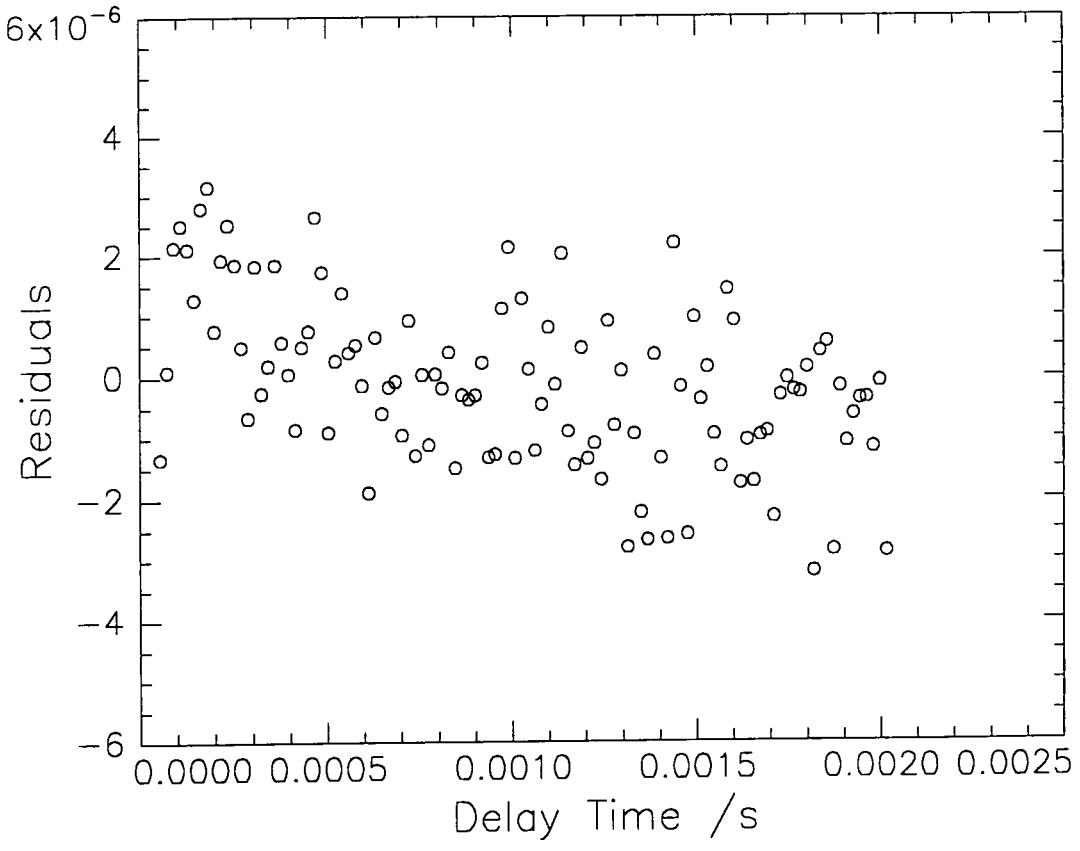

Figure 5.5(b): Residuals at 0.6mg m^{-2} - 5th run out of 10

The frequency of the correlation function is slightly changed, however, the change in the amplitude of the oscillations is more noticeable, being more damped in figure 5.4(a) than in 5.5(a). When all ten correlation functions were fitted using equation 5.14 these observations were quantified, with values of the propagation frequency (ω_o) and wave damping (Γ) being obtained. The values of ω_o and Γ varied between two extreme values, one of which corresponded to the value for water. This is shown in figures 5.6 and 5.7, where the frequency and damping found for water at this q were about 28800s^{-1} and 805s^{-1} respectively. For ten runs, each of 100s duration at 0.2mg m^{-2} and for q = 291cm^{-1}, a similar pattern of variation was observed, as is shown in figure 5.8 where the damping of clean water was found to be 1490s^{-1}.

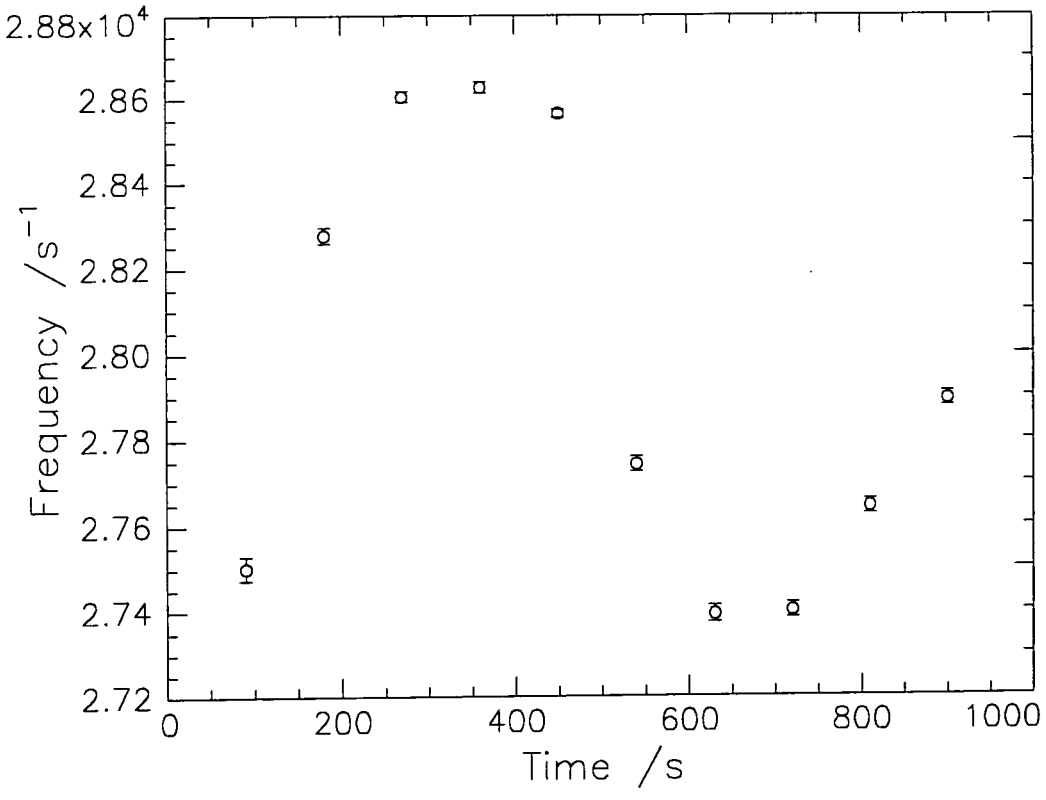

Figure 5.6: Variation in frequency at 0.6mg m^{-2}

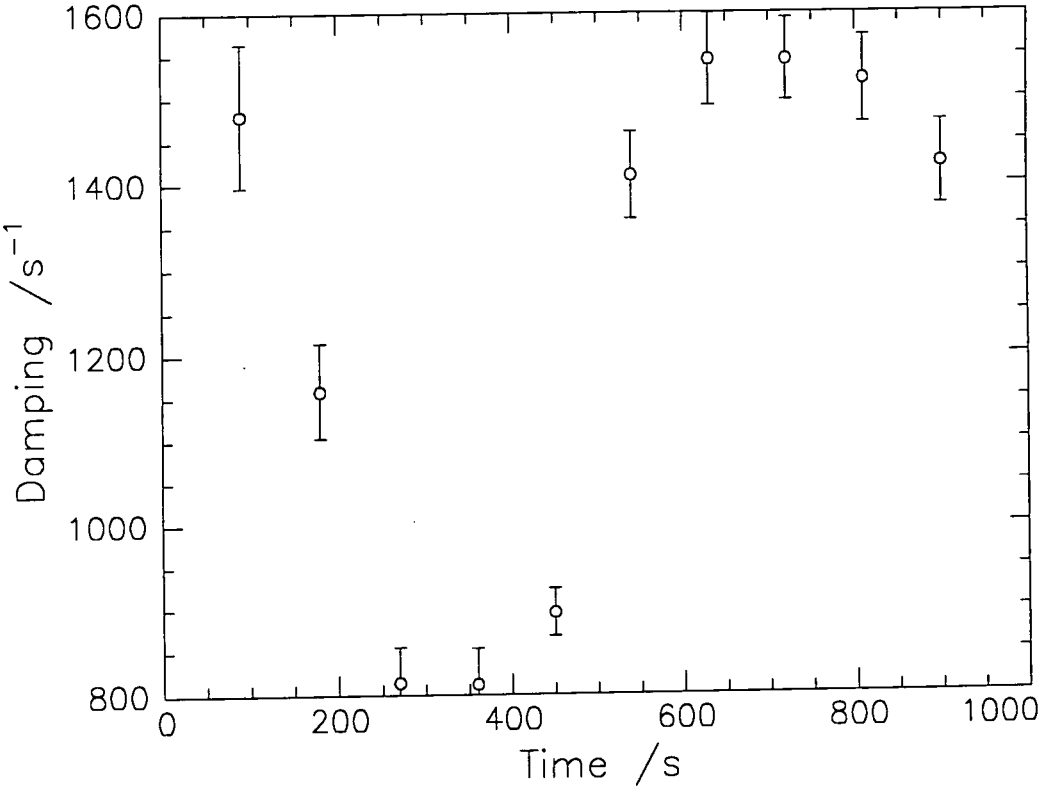

Figure 5.7: Variation in damping at 0.6mg m^{-2}

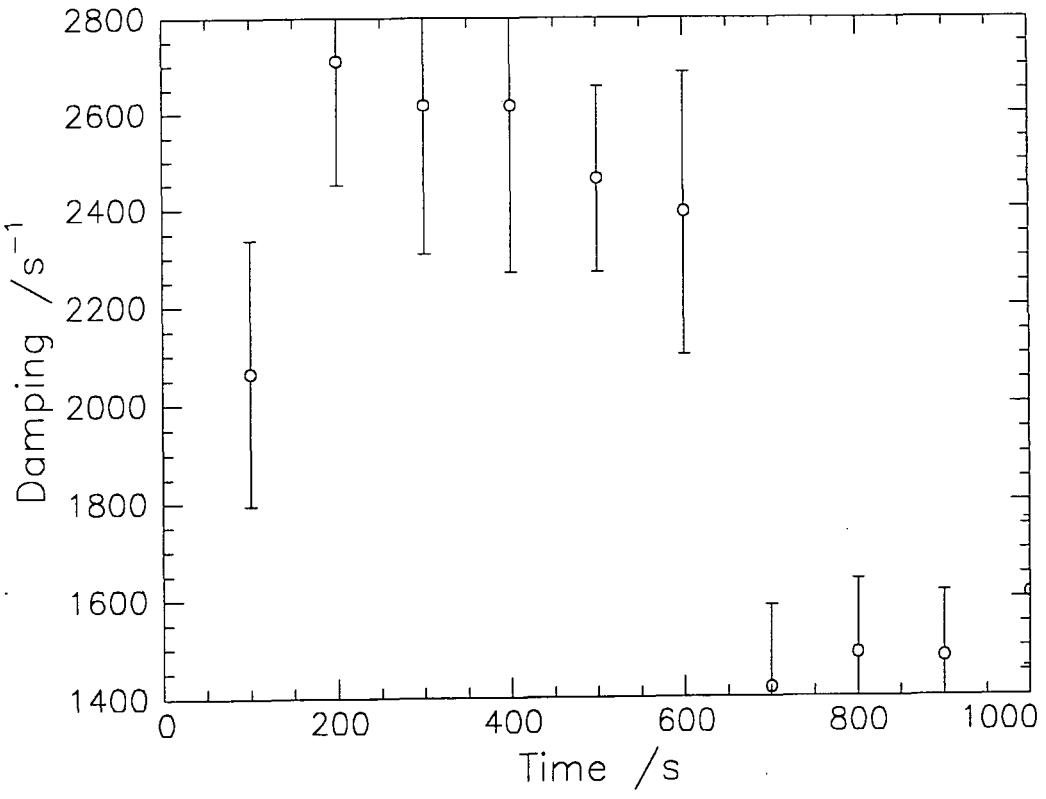

Figure 5.8: Variation in damping at 0.2mg m^{-2}

Repetitive runs covering a much longer time scale were carried out, 240 runs, each lasting 60s at 0.2mg m^{-2} (region 1) and 50 runs of 150s duration at 1.8mg m^{-2} (region 3) for q = 291cm^{-1}. The resulting variations in damping are compared in figure 5.9. The values at 1.8mg m^{-2} are much more stable, which according to the description of the isotherm corresponds to a continuous monolayer at this surface concentration, compared to the varying values obtained at 0.2mg m^{-2}, which showed similar variation to the shorter time scale runs.

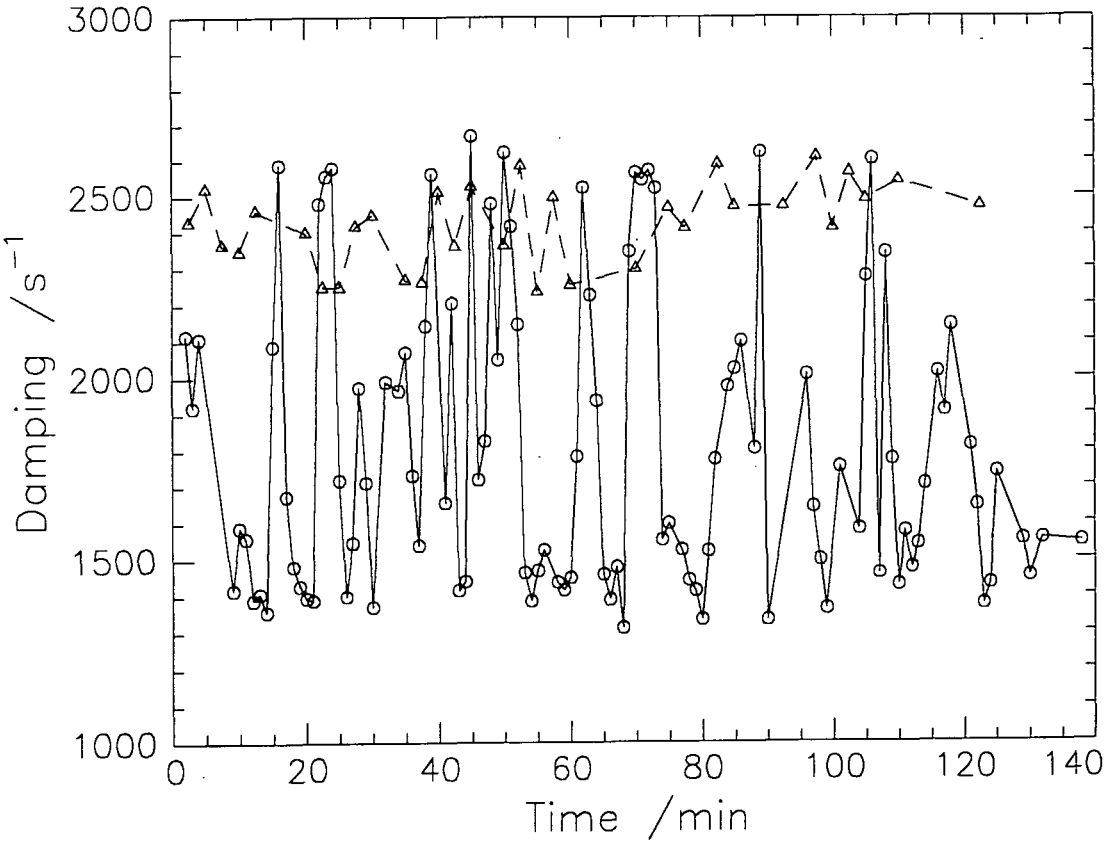

Figure 5.9: Variation in damping at 0.2mg m^{-2} (—) and 1.8mg m^{-2} (- -)

Such fluctuations as those observed here have been attributed to the coexistence of separated domains of different phases [9] in the interfacial layer. The results observed here agree with the description of the monolayer behaviour used to explain the shape of the isotherm. The changes in damping (and frequency) are caused by the condensed polymer islands drifting into and out of the illuminated area on the liquid surface and when the polymer island is present it acts as a blanket, increasing the damping of the capillary waves (and decreasing their propagation frequency).

The fact that fluctuations are observed gives an indication of the size of the condensed polymer islands. Two cases can be considered, with islands either smaller than the dimensions of the illuminated area or vice versa, as shown in figure 5.10 (a) and (b).

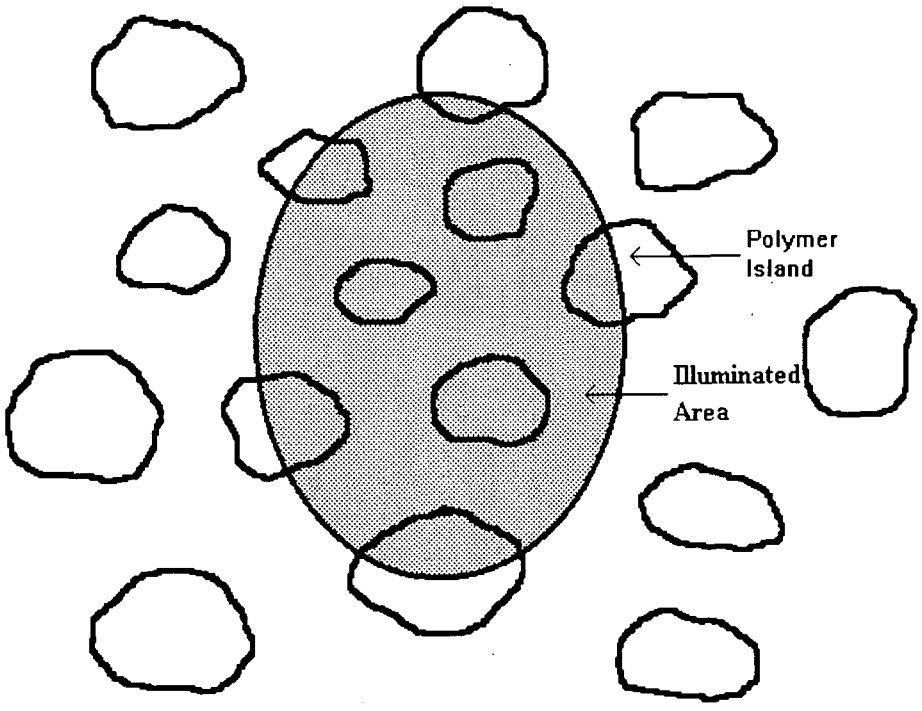

Figure 5.10 (a): Polymer islands on the surface of water with dimensions less than the illuminated area.

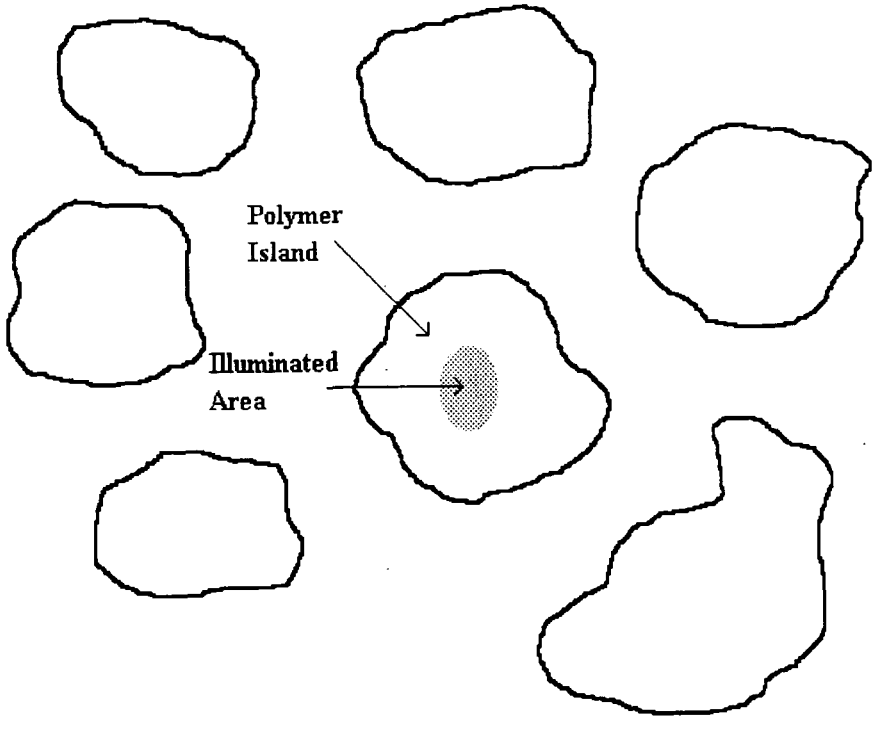

Figure 5.10 (b): Polymer islands on the surface of water with dimensions greater than the illuminated area.

The situation shown in figure 5.10(a) cannot be the case for PLMA as this would produce only small fluctuations in the values for ω_o and Γ somewhere between the values expected for clean water and complete monolayer coverage, weighted towards one or the other depending on the ratio of islands to clean water in the illuminated area. To obtain the large fluctuations in damping coefficient observed here, which vary between values for clean water and polymer, the islands must be greater in dimensions than the illuminated area so that the laser illuminates one phase at a time (figure 5.10(b)). This places a minimum size on the islands that is equal to the dimensions of the laser beam spot on the surface, which forms an ellipse of axes 3 and 7mm.

In figure 5.8 the transition from polymer to water at 600s takes place during the course of one 100s run, during which time the domain edge must have completely crossed the illuminated area otherwise an intermediate damping value would have been obtained. Between 0 and 200s, such an intermediate value occurs as the polymer island is not completely illuminated. On average it takes about 150s for the edge of an island to completely clear the illuminated area, which will require the island to move about 5mm (average distance from the axes of the ellipse illuminated), this gives a velocity of 33μm s^{-1}. The time in each phase is about 400s, so this suggests a dimension of about 13mm for the polymer island. The same rationale can be applied to figure 5.7. Here it took two runs to switch between phases which equals 180s, giving a velocity of 28μm s^{-1}. Each phase was illuminated for about 300s giving a mean island dimension of about 8mm.

These values are not definitive answers and they do not mean that all the islands at 0.2mg m^{-2} are 13mm and those at 0.6mg m^{-2} are 8mm in size. All of the islands at each surface concentration would not be expected to be the same size due to the random nature of the spreading process, so domains will form differently every time a monolayer

is deposited. Figures 5.7 and 5.8 only show one transition relating to one island passing through the beam, so they give a limited impression of the interfacial layer and only allow the dimensions of one island to be determined. In figure 5.9, which runs over a much longer time scale, the data at 0.2mg m^{-2} show that it is not as simplistic as this. The presence of a range of island sizes show up as differences in the persistence time of the highest values of damping. The longest spell spent in the high damping regime occurs between 70 to 74 minutes and then drops to the water value within 60 seconds. Using the same beam dimension of 5mm, this corresponds to a polymer island dimension of 20mm. The shortest time with a high damping value is 60 seconds which also falls to the water value in 60 seconds, corresponding to a polymer dimension of 5mm.

Likewise, the gaps between islands also vary, as can be seen from the different lengths of time elapsed with a damping value equal to that of water. The longest time with just water present was between 54 and 61 minutes, which corresponds to a dimension of 35mm. The shortest time was 60 seconds, which corresponds to 5mm.

Apart from the two extreme values of damping for polymer layer and clean water there are intermediate values at about $2000s^{-1}$. There are two possible explanations for these values. The first is that an area of islands which are smaller than the beam dimensions pass into the illuminated area and produce damping values between the two extremes as was mentioned earlier. The second is that an island is partly illuminated and skirts across the edge of the beam. When an intermediate value persists (between 31 and 33 minutes for example) this can be explained by either an island drifting half way into the beam and then continuing to drift, but never fully entering the illuminated area, before drifting away, or by an area of small islands drifting through the beam.

Reports of similar behaviour have been described by Earnshaw *et al* [9] for monolayers of pentadecanoic acid, PDA. Fluctuations in damping were used to estimate

the size of the condensed phases to be circa 11mm, similar to the dimensions observed here for PLMA. In a range of six polymers studied by Kawaguchi *et al* [10], PMMA was found to be the only one to display biphasic behaviour, this has since been investigated [11] and variations in damping similar to those for PLMA were observed over nine hours, although no estimate of the condensed phase dimensions were made. In each case, strong inter - molecular cohesion must dominate the monolayer properties.

5.3.2 Surface Concentration Variation at a Fixed q

The equilibrium static monolayer behaviour, determined from the surface pressure - area isotherm, can be compared to the dynamic properties of the monolayer that are determined by SQELS at a range of surface concentrations. At each concentration, ten correlation functions were obtained and each was analysed using equations 5.14 and 5.15. The results for the ten runs were averaged and the standard deviation of each set was calculated and used as the error.

Figures 5.11 and 5.12 show the variation of the propagation frequency and damping respectively.

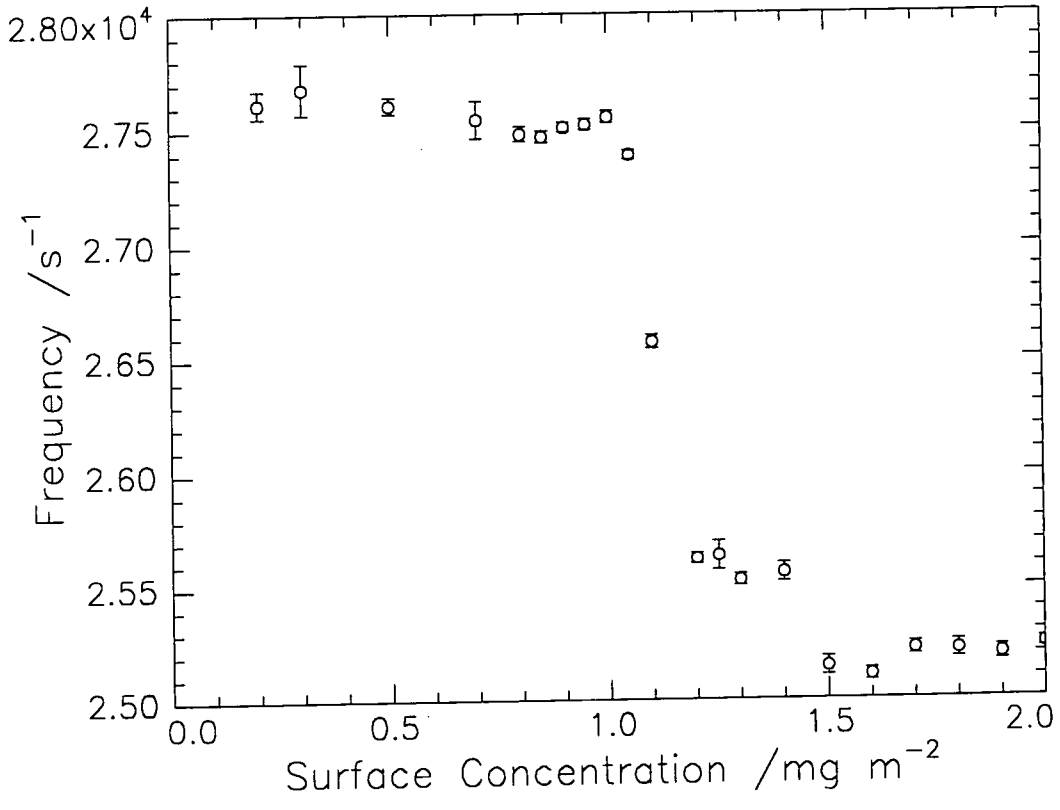

Figure 5.11: Variation of propagation frequency with surface concentration

propagation frequency for water = 28575 ± 206s^{-1}

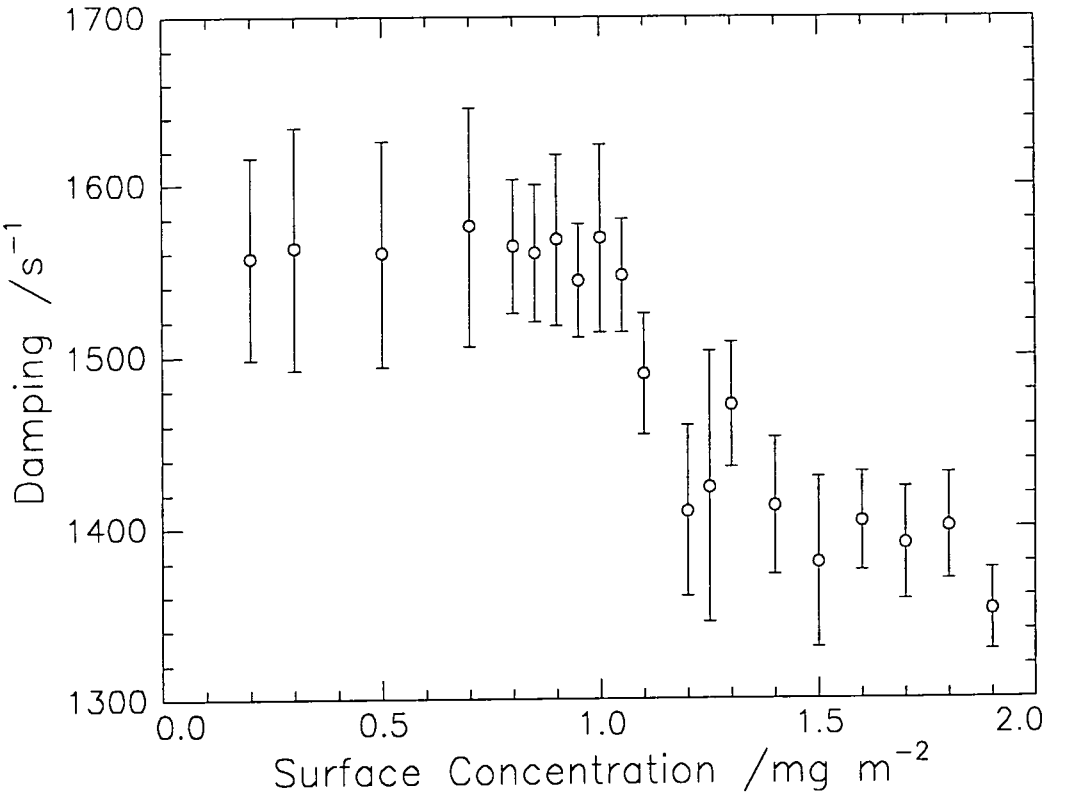

Figure 5.12: Variation of damping with surface concentration

damping for water = 795 ± 20s^{-1}

The variation in capillary wave frequency with concentration follows the change in surface tension, which is not too surprising as the tension mainly affects the wave frequency, in rough accord with the approximate relation $\omega_o^2 \approx \gamma_o q^3/\rho$. The damping also shows a decrease at the surface concentration range corresponding to the transition in the surface pressure - area isotherm. This is the opposite to what might have been expected, as more polymer on the surface should presumably lead to more damping of the surface waves. This apparent anomaly will be discussed further later.

By fitting the correlation data using equation 5.15, the four visco-elastic parameters have been determined at each surface concentration. An example of the fits obtained and the corresponding residuals are shown in figures 5.13(a) and (b), with the values obtained shown in figures 5.14 to 5.17.

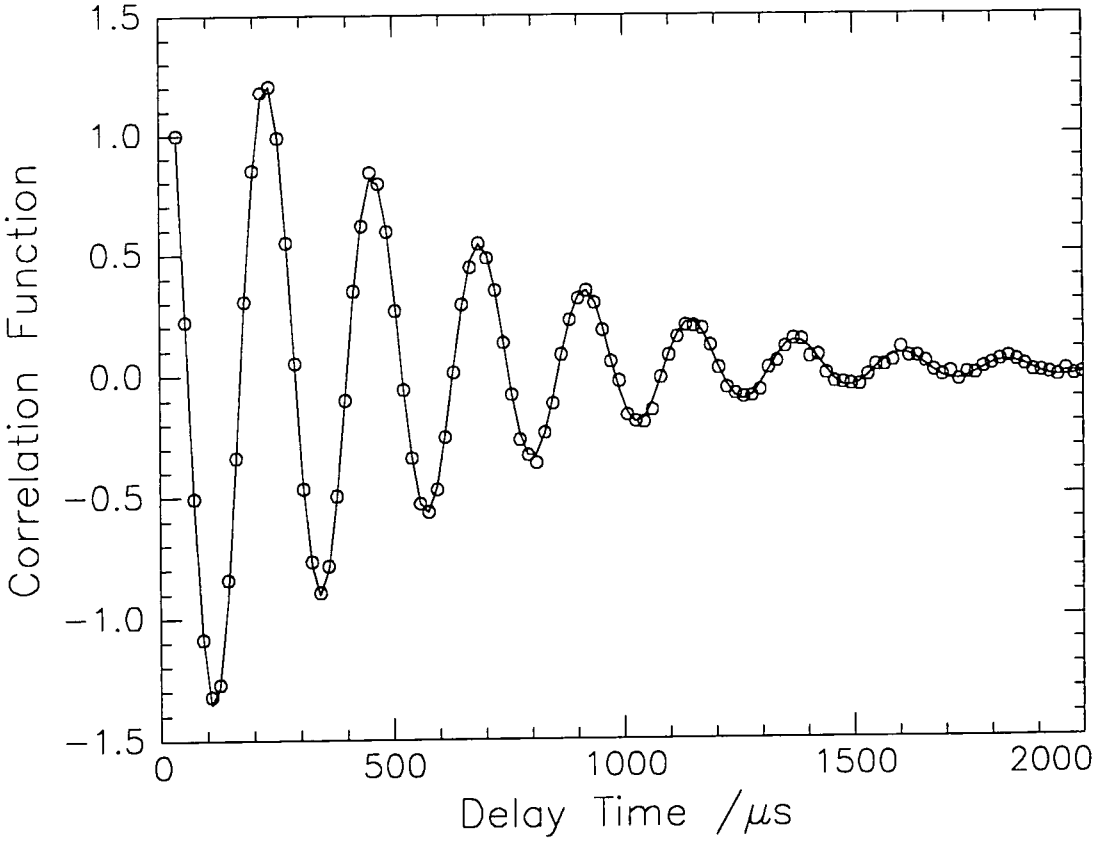

Figure 5.13(a): Example of fit to correlation data using equation 5.15

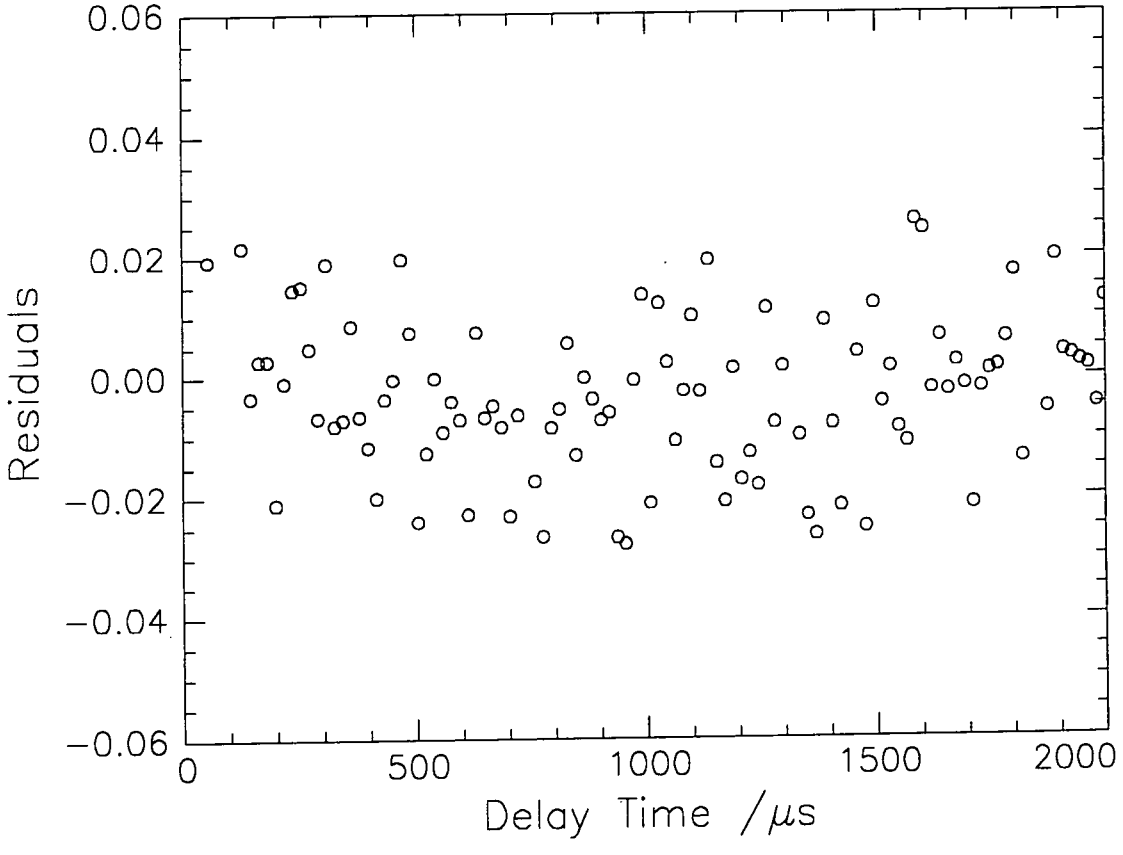

Figure 5.13(b): Residual of the fit shown in figure 5.13(a)

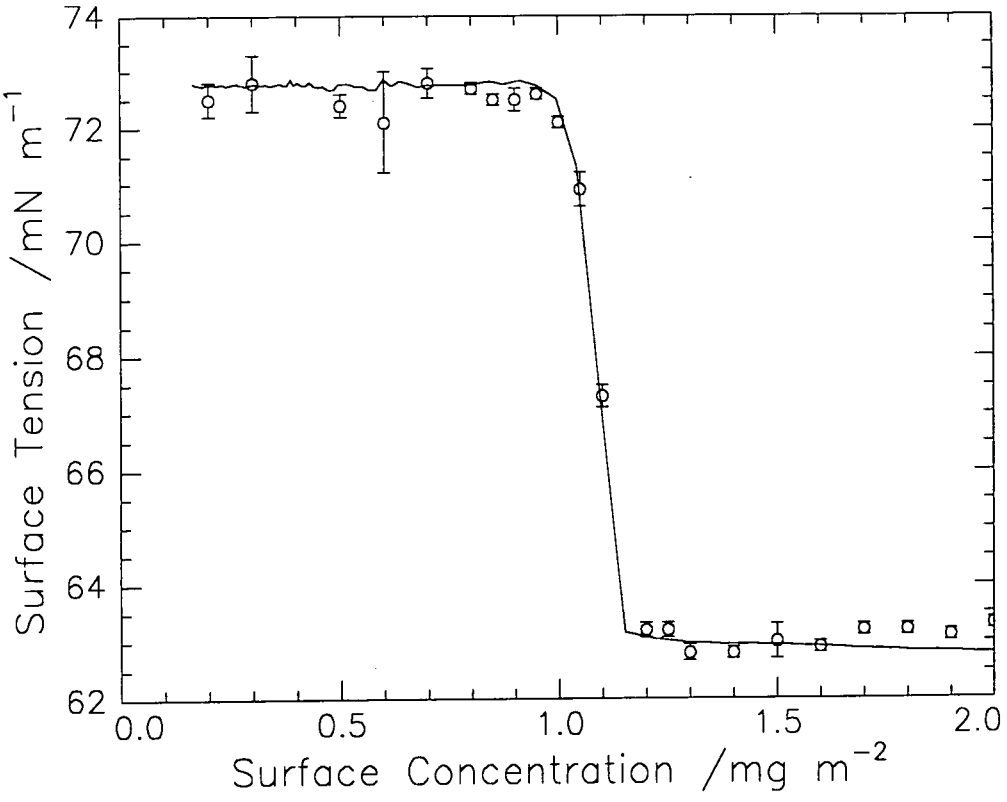

Figure 5.14: SQELS values of surface tension (o) compared with values from the surface pressure - area isotherm (—)

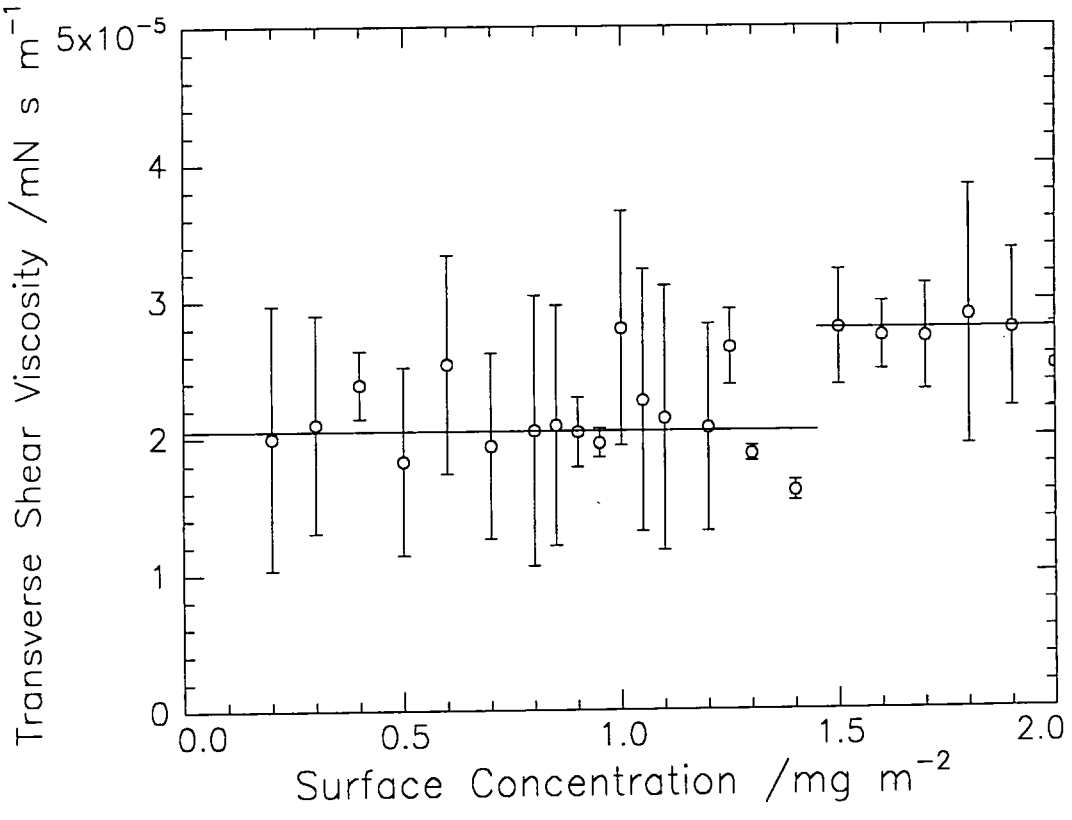

Figure 5.15: Variation in transverse shear viscosity with two regions of different viscosities shown by solid lines.

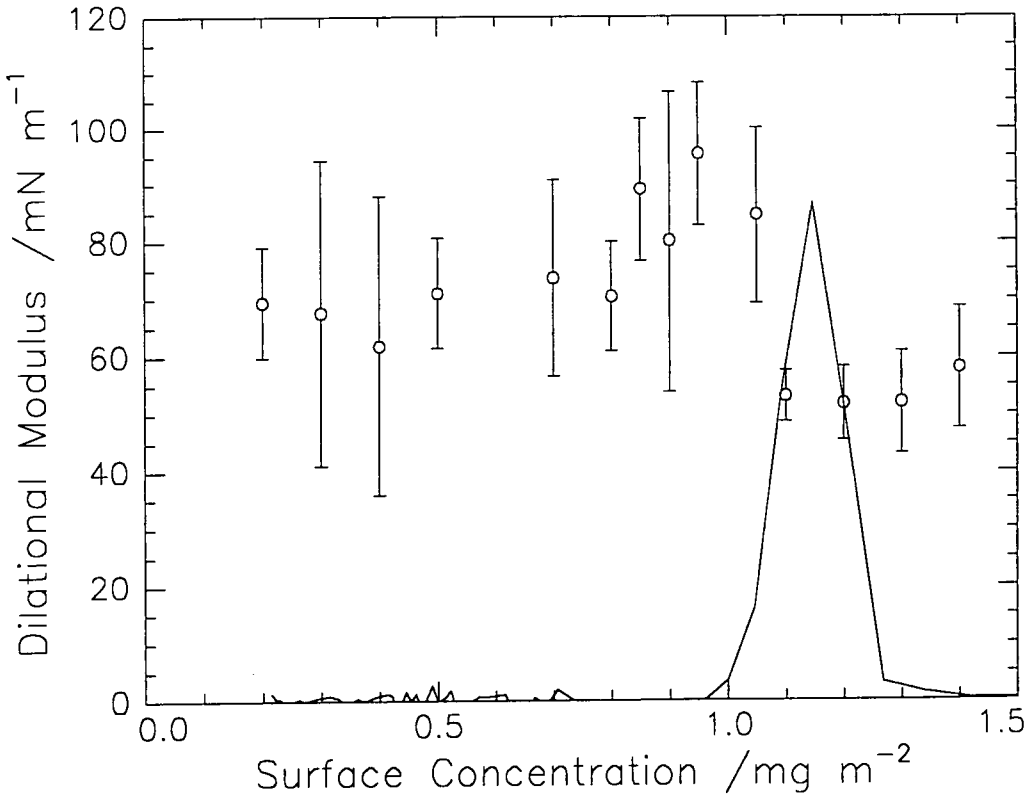

Figure 5.16: SQELS dilational modulus (o) compared to static elasticity (—) calculated from the surface pressure - area isotherm

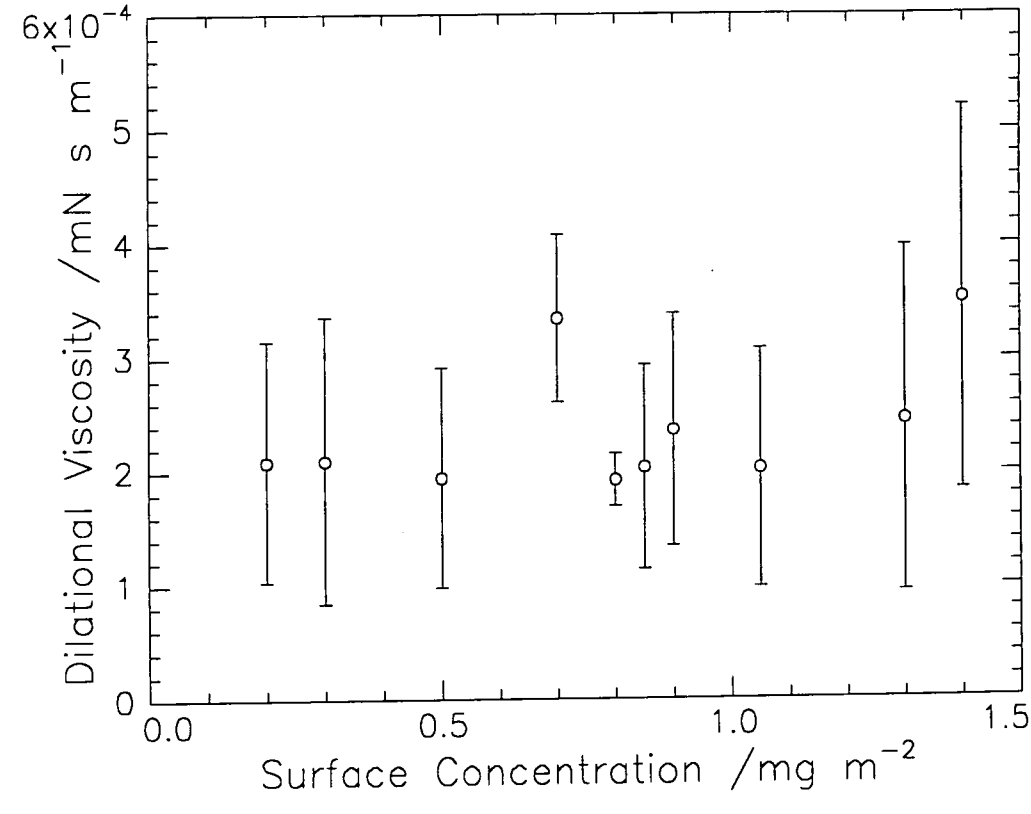

Figure 5.17: Variation of dilational viscosity with surface concentration

The values obtained for the dynamic surface tension from SQELS are generally in good agreement with those determined from the surface pressure -area isotherm (γ = 72.8 - π). The most significant deviation of the two sets of results occurs at high surface concentrations (> 1.2mg m^{-2}), but this can be accounted for by considering how the SQELS experiments were carried out. A known volume of polymer was deposited on to the water surface and compressed to the appropriate area to give the desired surface concentration for every value required. From repeated measurements of the isotherms it was observed that the high surface pressure plateau occurred at slightly different values of surface pressure each time and as the SQELS experiments were carried out on a new monolayer each time the values of surface tension obtained will vary slightly due to the high plateau occurring at a slightly different value each time. Theoretically this could be overcome by using one monolayer for all the surface concentrations by compressing it step by step and having the Wilhelmy plate in the water to monitor the static surface pressure and then comparing this to the SQELS values of surface tension. The drawbacks with doing this are that the monolayer would have to be left on the surface for about five hours, during which time a considerable amount of dust will have settled on the surface which causes flaring of the light and destabilises the monolayer which may lead to premature collapse, also, leaving the Wilhelmy plate in the water can disturb the water surface since it is susceptible to air currents. As the values from both techniques agree this suggests that the surface tension has no frequency dependence as the SQELS γ_o is determined from the high frequency capillary waves and the isotherm is the static measurement of γ_o. This will be dealt with fully in the next section.

At first sight the transverse shear viscosity appears more or less constant across the surface concentration range. However, as indicated by the solid lines in figure 5.15, there may in fact be two distinct values, with a jump at 1.5mg m^{-2}, which corresponds to

the point at which an observation was made during the experiments. At 1.5mg m^{-2} and above, stratifications became visible in the illuminated area on the water surface. Such stratifications are connected with the formation of a layered structure which indicates that the monolayer is no longer in a 2-D state when it is compressed beyond this point. This will create more polymer - polymer interactions, hence, increasing the resistance of the layer to respond to the fluctuations caused by the capillary waves, which manifests itself as an increase in the viscosity. Earnshaw has associated the film viscosity with chain - chain interactions and this was supported by data from lipid bilayers formed from glycerol mono - oleate. When the bilayer was formed from decane solution it retains a large quantity of solvent and γ' was negligible, whereas for solvent free bilayers, γ' had finite values [12]. The difference occurs due the decane enabling the acyl chains to move freely, whereas in the solvent free bilayer, the chains had more steric resistance to chain movement. This would seem to support the idea that the increase in γ' observed here is as a result of the departure from the 2-D state which leads to an increase in chain - chain interactions.

The dynamic dilational modulus from SQELS can be compared to the Gibbs static elasticity which is calculated from the surface pressure - area isotherm using the equation $\varepsilon_s = \Gamma(d\pi/d\Gamma)$, the comparison of the two is shown in figure 5.16. There is clearly a large difference between the two which reflects the response of the monolayer to the slow compression used to obtain the isotherm and the high frequency stress applied to the monolayer due to the capillary waves. The value of the dilational elasticity is effectively a measure of the monolayer compressibility, so the classical elasticity which is zero at all surface concentrations, except at the transition point, indicates that the monolayer has little resistance to compression and only when the polymer islands contact each other is there any resistance to compression, but this is overcome when the chains

inter - penetrate and the elasticity returns to zero. This is not surprising as PLMA is well above its T_g and would not be expected to appear as a rigid, incompressible monolayer. From the SQELS experiments the monolayer appears incompressible right across the surface concentration range, contradicting what is obtained from the classical elasticity. This indicates that the polymer monolayer has insufficient time for the chains to relax in response to the high frequency perturbations and, therefore, appears incompressible.

It was noted earlier that the damping decreased after the transition point and as the damping essentially amplifies variations of the dilational modulus this must be due to a change in the dilational properties of the monolayer. This is shown by a decrease in the dilational modulus at the transition point. From 0.8 to 1mg m^{-2} there is a slight increase in the dilational modulus which can be attributed to the initial contact of the polymer islands and after this point there is a decrease and the monolayer appears more compressible. On initial contact of the polymer islands there will be an increase in the resistance to further compression until the chains rearrange to accomodate the inter - penetration of molecules from adjacent islands. Once this rearrangement has taken place the resistance to further compression will be lowered.

The final parameter, the dilational viscosity, shows no particular trend and appears constant around 2×10^{-4}mN s m^{-1} (figure 5.17). At the concentration where the monolayer departs from the 2-D state there maybe the onset of an increase in the viscosity which would be due to the same effect as the increase in the transverse shear viscosity. The data above 1.5mg m^{-2} could not be used to determine values of the dilational viscosity as the fitting routine produced large and constant values (in the order of thousands) which were clearly nonsensical. This is probably due to the highly elastic nature of the monolayer at these high surface concentrations which makes the technique insensitive to the dilational viscosity.

The propagation frequency for various systems that have been studied (i.e. poly(ethylene oxide) (PEO), poly(tetrahydrofuran) (PTHF), poly(vinyl acetate) (PVAc), poly(methyl acrylate) (PMA), poly(tertiary butyl methacrylate) (PtBMA) [10], glycerol mono - oleate (GMO) [13], the surfactants cetyltrimethylammonium (CTAB) and sodium dodecyl sulphate (SDS) [14]) all showed the same trend with increasing surface concentration, which was, a plateau of constant frequency at low surface concentrations that corresponded to the propagation frequency of clean water and then as the concentration increased further the frequency decreased, essentially tracking the profile of the surface tension. For PMMA [10] and pentadecanoic acid (PDA) [9] the low surface concentration plateau was found to have a frequency below that of clean water, this has also been found here for PLMA, with a low concentration plateau value circa $1000s^{-1}$ below the value obtained for clean water. This has been attributed to the biphasic nature of the monolayers at low surface concentrations, where the condensed phase causes the premature drop in wave frequency.

The damping variation shows a similar divide between the range of materials studied as for the frequency. The majority, as before, show similar characteristics, with a peak being obtained in the damping at a certain surface concentration which corresponds to the point where the condition for resonance between the capillary and dilational modes is satisfied, i.e. $\varepsilon_o / \gamma_o = 0.16$. No peak is observed for PDA and PMMA which is also the case found here for PLMA. This reflects the fact that ε_o is relatively large and constant across the range of surface concentrations, so ε_o / γ_o was always greater than 0.16 and the resonance condition was never passed through.

The surface tension values obtained from SQELS are generally in close agreement with the static values obtained from Wilhelmy plate measurements (e.g. PMMA [10,11], PtBMA[10], PDA[15], GMO [13], CTAB and SDS[14]). This indicates that the high

frequency capillary waves are governed by the equilibrium (static) tension. The local tension will vary during each cycle of the wave, as the dilation and compression of the surface film changes the local surface concentration and hence the surface tension, but the cycle averaged value, as detected by SQELS, is just the equilibrium tension. The greatest variation occurs in the low surface concentration regions for PMMA, PDA and PLMA which was observed in this work. This is attributed to the biphasic nature of the monolayer in these regions. PEO produces SQELS values of γ_0 which are consistently circa 2 - 4mN m^{-1} higher than the static values [11] and when PEO is incorporated into a diblock copolymer with PMMA the same effect is observed [16], although the features of the static isotherm are reproduced in the SQELS values.

The values of the transverse shear viscosity for PMMA are scattered below 1mg m^{-2} ($\pi = 0$) and the range of values is approximately 1.5 to 5 $\times$ 10^{-5} mN s m^{-1}. Above this point γ' is fairly constant at circa 1.5 $\times$ 10^{-5} mN s m^{-1} [11]. The range of values are of the same order of magnitude as those obtained for PLMA, indicating that the response of both polymers to shear stress transverse to the interface is similar. Spread monolayers of PEO initially have values of γ' of the same order of magnitude as PMMA and PLMA, but at a surface concentration of circa 0.5mg m^{-2} γ' increases rapidly to a maximum of ~ 4 $\times$ 10^{-5} mN s m^{-1} at 0.6mg m^{-2} [11]. This corresponds to the point in the isotherm where PEO penetrates the subphase. For a diblock copolymer of PMMA and PEO a peak occurs at 1.5mg m^{-2} which coincides with a transition in the isotherm where the structure changes and the PEO block is forced into the subphase and as a result, greater chain - chain interactions occur [16]. These two cases show that γ' is sensitive to changes in monolayer structure. For PLMA, at the transition in the isotherm, no change in γ' occurred, indicating that no structural changes occurred during the transition, which supports the observations made in the neutron reflectivity experiments. The change that

does occur for PLMA is at a surface concentration of 1.5mg m^{-2}, where it appears that the monolayer departs from a 2-D structure. The layered chains above this point result in greater resistance to shearing transverse to the interface.

PDA [15], GMO [13] and solutions of the soluble surfactant CTAB [14], all show similar trends for γ' as the surface concentration increases, indicating that the response to shear stress transverse to the film plane is similar for spread monolayers and for adsorbed layers. At low surface concentrations, the values for γ' were maximal ($\sim 0.7 \times 10^{-5}$ mN s m^{-1} for PDA and CTAB, $\sim 1.4 \times 10^{-5}$ mN s m^{-1} for GMO) and then falls as the surface concentration is increased. This behaviour seems counter - intuitive, going against the association of greater values of viscosity with increasing inter - molecular interactions. However, γ' relates to high frequency perturbations and little is known of the underlying molecular mechanisms and relaxation processes, so other factors may account for this apparent anomaly. In general γ' is lower for these low molecular weight materials than that for PLMA. This is probably due to extra freedom to move for the low molecular weight material, whereas movement transverse to the interface is more restricted for PLMA due to the polymer backbone.

Values of the dilational modulus ε_o for PMMA occur in the range of 50 to 100mN m^{-1} across the whole surface concentration range [10], in direct contrast to the static elasticity which is zero except for a peak where the surface pressure increases. This is similar behaviour to that observed for PLMA and it appears that the long side chains have little effect on the response to compression in the plane of the monolayer. In comparison, polymers which form more expanded monolayers (e.g. PEO, PTHF, PVAc and PMA [10]) do not show this behaviour and the static and SQELS ε_o agree up to the maximum in the peak of the static ε_o. At concentrations above that where the peak occurs, qualitative agreement is still obtained, although the SQELS ε_o tends to be slightly

higher (by ~ 4mN m^{-1}) due to the monolayers departing from 2-D conformations by chain looping, or possibly macroscopic collapse. The low molecular weight materials discussed here show similar behaviour, with the static ε_o increasing from zero to a maximum and then returning to zero. The SQELS ε_o is generally non - zero at low surface concentrations and increases as the static ε_o increases and continues to increase as the static ε_o decreases. The SQELS ε_o reaches a maximum of about 80 100mN m^{-1} and remains high even when the static ε_o is zero. This discrepancy at high surface concentrations is due to the molecules at high surface concentrations being orientated perpendicular to the interface and compacted together, this causes the monolayer to appear rigid as it resists the high frequency compressional perturbations.

The values for the dilational viscosity ε' for PMMA [10] are similar to those for PLMA in as much as there is no particular trend and they are fairly constant across the surface concentration range. PEO is not so straight forward, ε' increases to circa 1.5mN s m^{-1} at a concentration of 0.6mg m^{-2}, which may be due to the same reason as for the peak observed for γ', however, after this point there is a sudden fall to negative values of ε',which become more positive as the surface concentration increases from 0.6 mg m^{-2} to 1mg m^{-2} [11]. Negative values have been found at all concentrations for the soluble surfactants CTAB and SDS [14]. ε' directly reflects dissipative effects within a system which increase the damping of the dilational waves, therefore, negative values must thus correspond to reduced damping of the dilational surface modes from the value corresponding to $\varepsilon' = 0$. ε' is considered as an 'effective' value only, due to the fact that processes occur at the surface of surfactant solutions which are not accounted for in $P(\omega)$ (i.e. diffusive exchange). This results in force fitting of an inappropriate form to the data and only effective values of ε' are obtained. Similar rational can be applied to explain the negative values for PEO which occur at the point where the chains penetrate

the water subphase and form a brush - like structure. Fluctuations caused by the capillary waves vary the local surface concentration (high concentration in the trough of a wave and low at the crest) and variations in the microscopic density of water in the subphase lead to osmotic swelling and deswelling of the brush layer. These fluctuations could be viewed as the polymeric equivalent of diffusive exchange that occurs for the surfactants. ε' for a diblock copolymer of PMMA and PEO showed similar behaviour as for γ', with a peak at circa 1.6mg m^{-2} [16], which may indicate similarities in the underlying mechanisms and this would lead to the fact that an increase in ε' for PLMA above 1.5mg m^{-2} may be expected. PMA and PVAc show an increase in ε' as ε_o increases, but it continues to increase after monolayer collapse [10], presumably due to increased chain - chain interactions as segments leave the interface. This supports the view that ε' would be expected to increase for PLMA as it departs from 2-D conformations above 1.5mg m^{-2}. For the low molecular weight spread layers of PDA [15] and GMO [13] ε' was small ($\leq 10^{-5}$ mN s m^{-1}) and constant and then increases by an order of magnitude to circa 3×10^{-4}mN s m^{-1} at the highest surface concentrations, corresponding to the conventional pattern of increasing viscosity as interactions increase.

5.3.3 Frequency Dependence of Surface Properties

A range of capillary wave frequencies from 28000 to 230000s^{-1} were used to investigate the visco - elastic relaxation of the monolayer. Two surface concentrations were studied, 0.85mg m^{-2}, which is just before the transition in the isotherm, and 2mg m^{-2} which is on the high surface pressure plateau. These two concentrations allow any differences in behaviour between the low and high surface pressure regions to be determined. The values obtained for the surface tension and transverse shear viscosity at both concentrations are shown in figures 5.18 to 5.21.

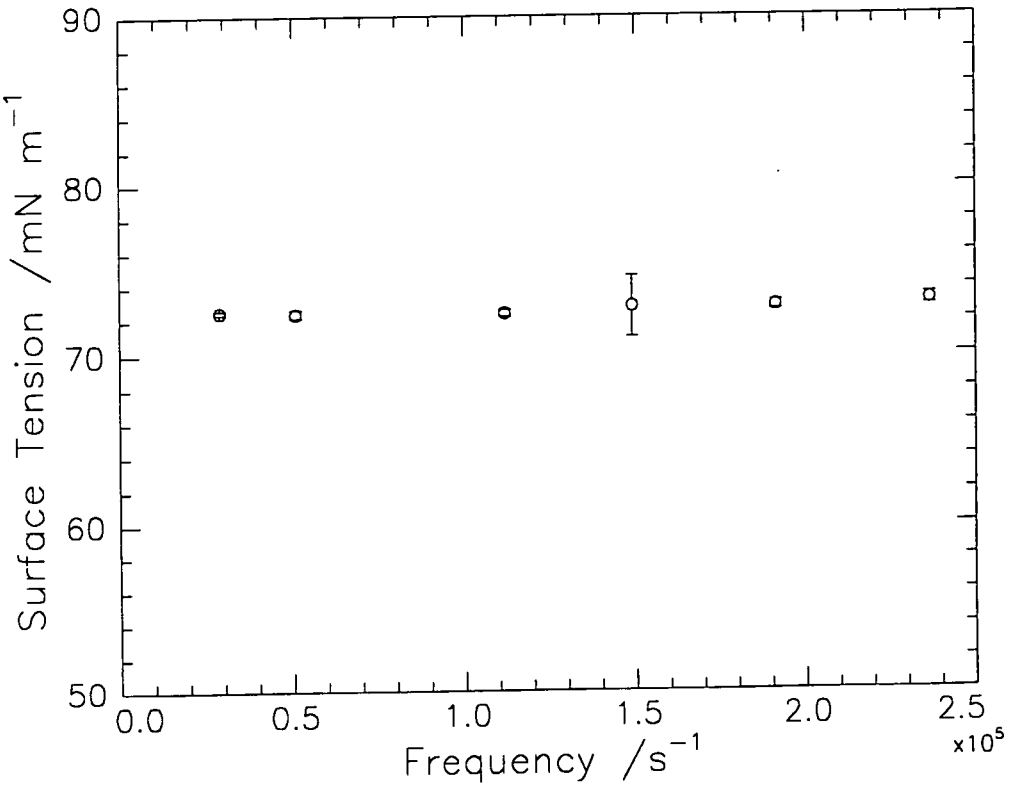

Figure 5.18: Surface tension values obtained at 0.85mg m^{-2}

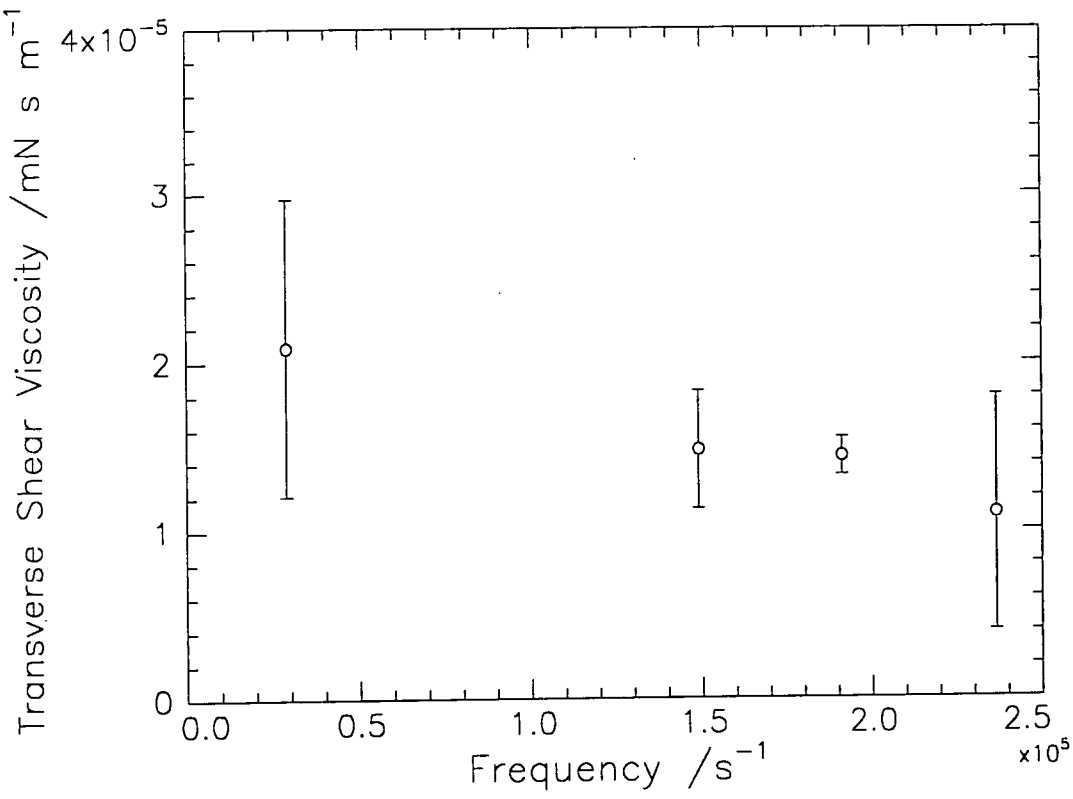

Figure 5.19: Transverse shear viscosity values obtained at 0.85mg m^{-2}

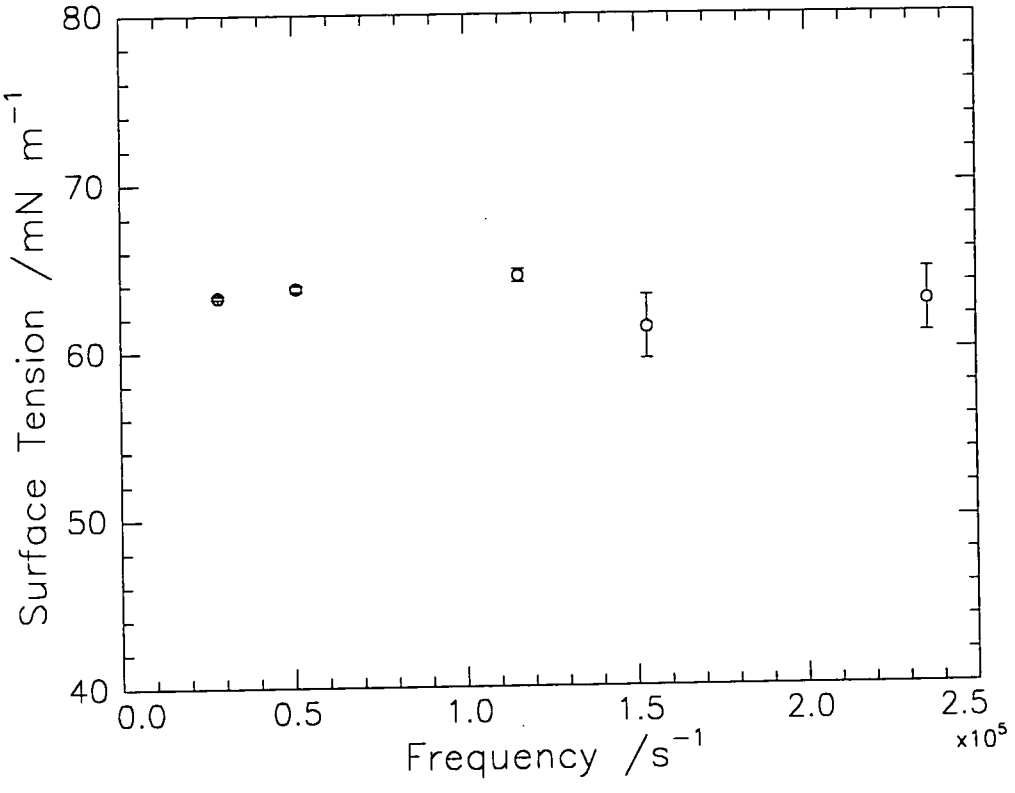

Figure 5.20: Surface tension values obtained at 2.0mg m^{-2}

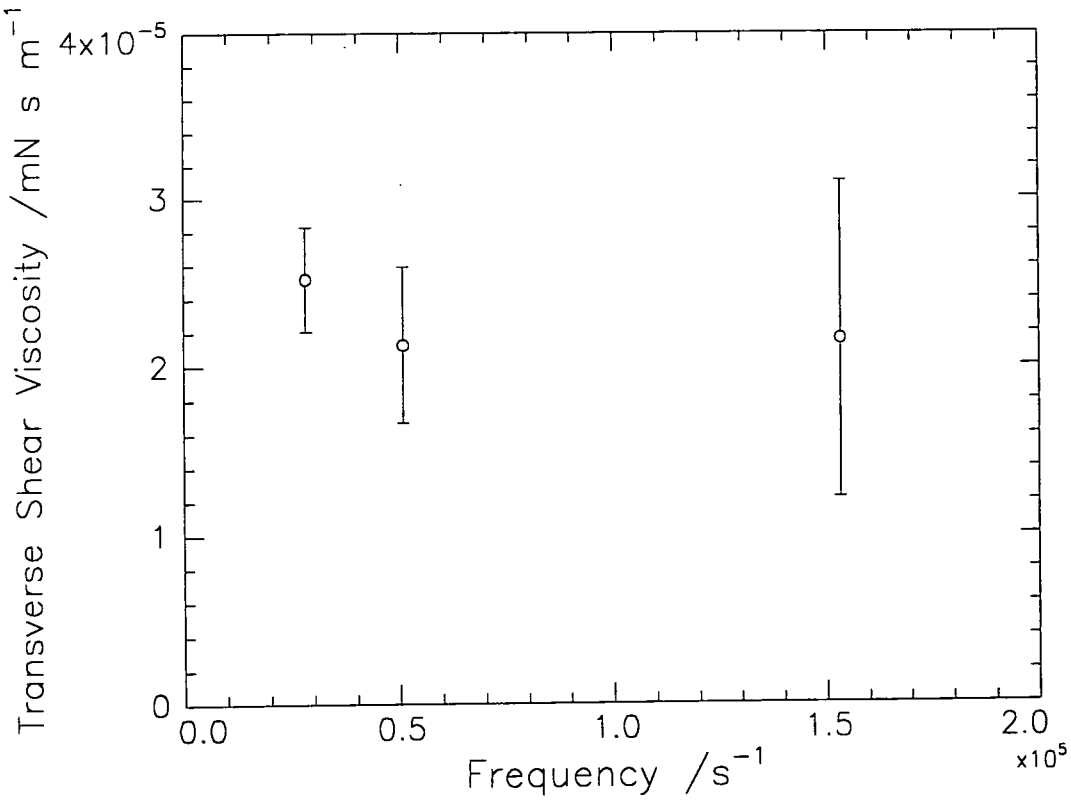

Figure 5.21: Transverse shear viscosity values obtained at 2.0mg m^{-2}

In conventional rheological notation [17], an oscillatory stress ($T(t) = T^* e^{i\omega t}$) and the resulting strain ($u(t) = u^* e^{i\omega t}$) are related via a complex dynamic modulus $G^*(\omega)$:

$$T^* = [G'(\omega) + iG''(\omega)]u^* \qquad 5.16$$

This can be considered the case here with the capillary waves providing the oscillatory stress. $G'(\omega)$, which is known as the storage modulus, can be identified with the elastic components of the visco - elastic moduli, i.e. γ_o (or ε_o) and $G''(\omega)$, which is known as the loss modulus, corresponds to $\omega\gamma'$ (or $\omega\varepsilon'$). There are no microscopic theories of interfacial rheological relaxation, however, for linear visco - elasticity, combinations of simple rheological models can be used which exhibit arbitrary frequency dependencies of G^*. Earnshaw [13] has used two such models, the Maxwell fluid and the

Voigt visco - elastic solid. The Maxwell fluid model is characterised by an exponential relaxation of $G'(\omega)$ and $G''(\omega)$, described by

$$G'(\omega) = G_e + G[(\omega^2\tau^2)/(1 + \omega^2\tau^2)] \quad 5.17$$

$$G''(\omega) = G[(\omega\tau)/(1 + \omega^2\tau^2)] \quad 5.18$$

where G_e is the equilibrium static elastic modulus determined from the Wilhelmy plate and G is the strength of the relaxation process, so γ_o and γ' should show a frequency dependence if Maxwell fluid behaviour is apparent. The Voigt model is described by

$$G'(\omega) = G \quad 5.19$$

$$G''(\omega) = G\omega\tau \quad 5.20$$

and no frequency dependence is predicted for $G'(\omega)$ and $G''(\omega)/\omega$, therefore γ_o and γ' should show no frequency dependence if the monolayer behaves as a Voigt visco - elastic solid.

At 0.85mg m^{-2}, the surface tension remains constant across the whole frequency range studied and the transverse shear viscosity, although it appears to have a slight decrease, this is within the error on each point and can be taken as constant. This indicates that the monolayer behaves as a Voigt solid. At 2mg m^{-2} the same behaviour is observed and the slight variations in the surface tension values are due to new monolayers being used for each frequency as was described in the last section.

From the equations used to describe the Voigt model, 5.19 and 5.20, the relaxation time, τ, associated with the monolayer is,

$$\tau = \gamma' / \gamma_o \qquad 5.21$$

Relaxation times calculated using equation 5.21 at each surface concentration are shown in figure 5.22.

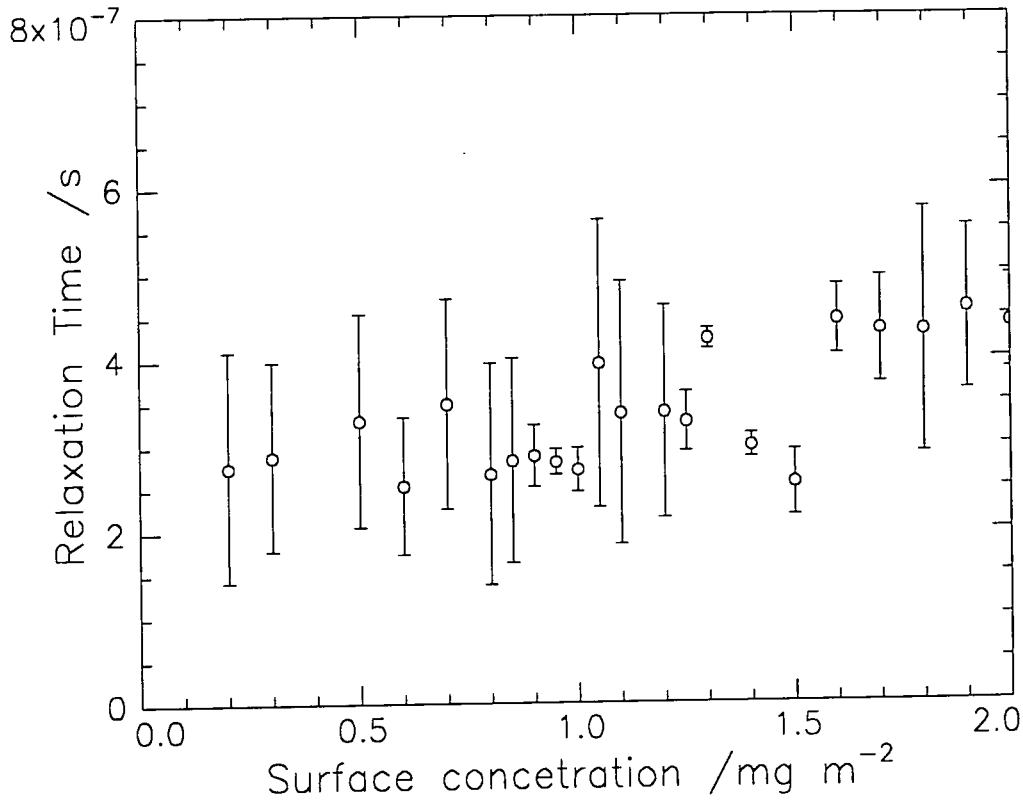

Figure 5.22: Relaxation times of PLMA monolayer as a function of surface concentration

The relaxation times are fairly constant at circa 3×10^{-7}s up to a concentration of 1.5mg m^{-2}, where after the relaxation time shows a jump to circa 4.5×10^{-7}s, which can be attributed to the increase observed in γ' which will result in longer times for the monolayer to relax. The range of relaxation times covered for PLMA are almost identical to those found for PMMA (circa $2 - 7 \times 10^{-7}$s) [11], which is also described by a Voigt model. This would tend to suggest that the relaxation for both polymers arises from similar molecular processes. The relaxation times for both polymers are circa an

order of magnitude smaller than that for PEO spread layers [11] and for a linear PEO - PMMA diblock copolymer [16], both of which show Maxwell fluid model frequency dependencies. This indicates that the PEO block relaxation properties dominate those of the PMMA block and the result is that the diblock copolymer has relaxation characteristics similar to those of PEO spread layers. Attaching long side chains to the methacrylate backbone on the other hand, appears not to induce any different behaviour than that observed for PMMA.

Frequency dependent studies on glycerol monooleate (GMO) monolayers [13], bilayers [18] and pentadecanoic acid (PDA) monolayers [15] have shown that γ_o and γ' in each case are consistent with a Maxwell model. For GMO monolayers τ was found to be 9μs and for the bilayer it was 37μs, while for PDA monolayers τ = 20μs. The behaviour of these films are consistent with acyl chain melting and the time scales are compatible with values from temperature jump studies of bilayer transitions [19]. The differences between the three relaxation times are due to steric effects. In the bilayer the apposed lipid films hinder movement of the chains and cause the larger τ value. For PDA the more closely packed fully saturated chains are more hindered than the unsaturated oleate chains of GMO. PLMA shows no relaxation processes due to the presence of long alkyl side chains, due to the fact that if the side chains did have an effect they would presumably cause similar relaxation behaviour as that observed for the fatty acids. The lack of side chain effect could be due to greater steric crowding in the condensed polymer monolayer and the extra restrictions placed on movement due to the backbone.

5.4 SQELS on LMA Monolayers

Three surface concentrations were studied at q = 331cm^{-1} and at each concentration ten runs were carried out. At 0.3mg m^{-2} each run was 90s long, at 1.5mg m^{-2} the duration of each run was 160s and at 3mg m^{-2} each run was 120s long. Examples of the correlation functions obtained at each concentration are shown in figures 5.23(a) to 5.27(a), where the solid lines are fits to the data using the cosine function in equation 5.14, and the residuals of each fit are shown in figures 5.23(b) to 5.27(b).

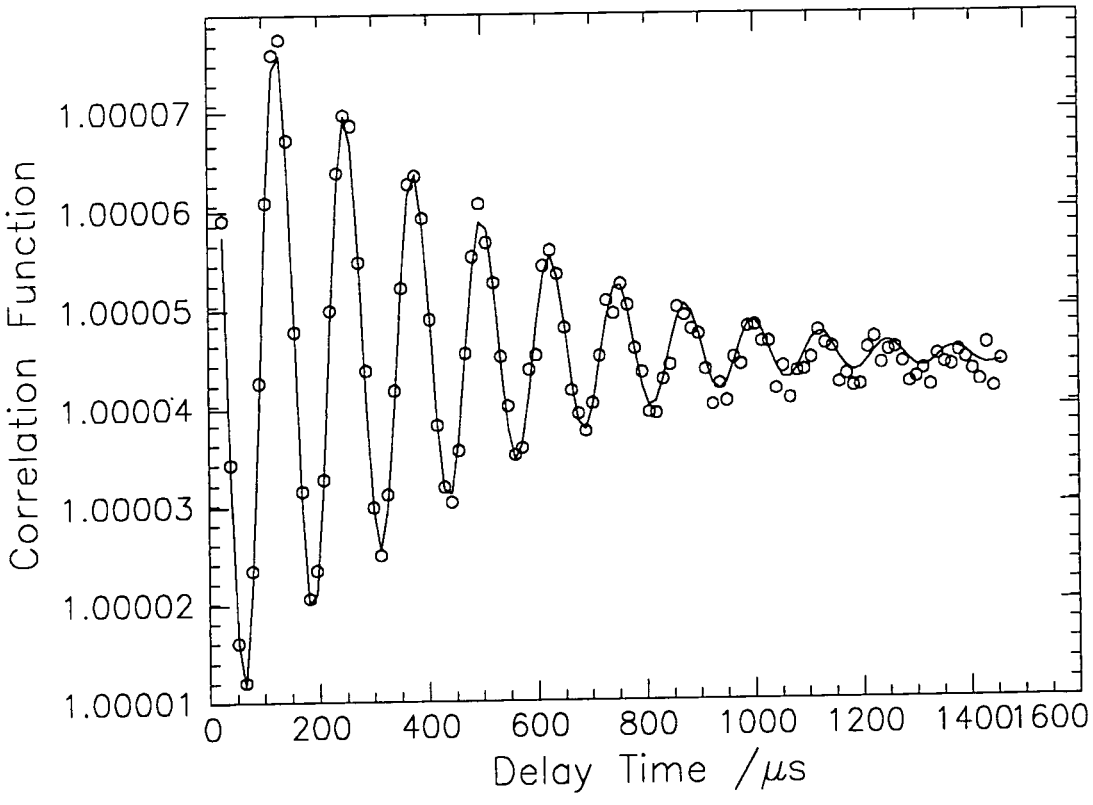

Figure 5.23(a): Correlation function at 0.3mg m^{-2}

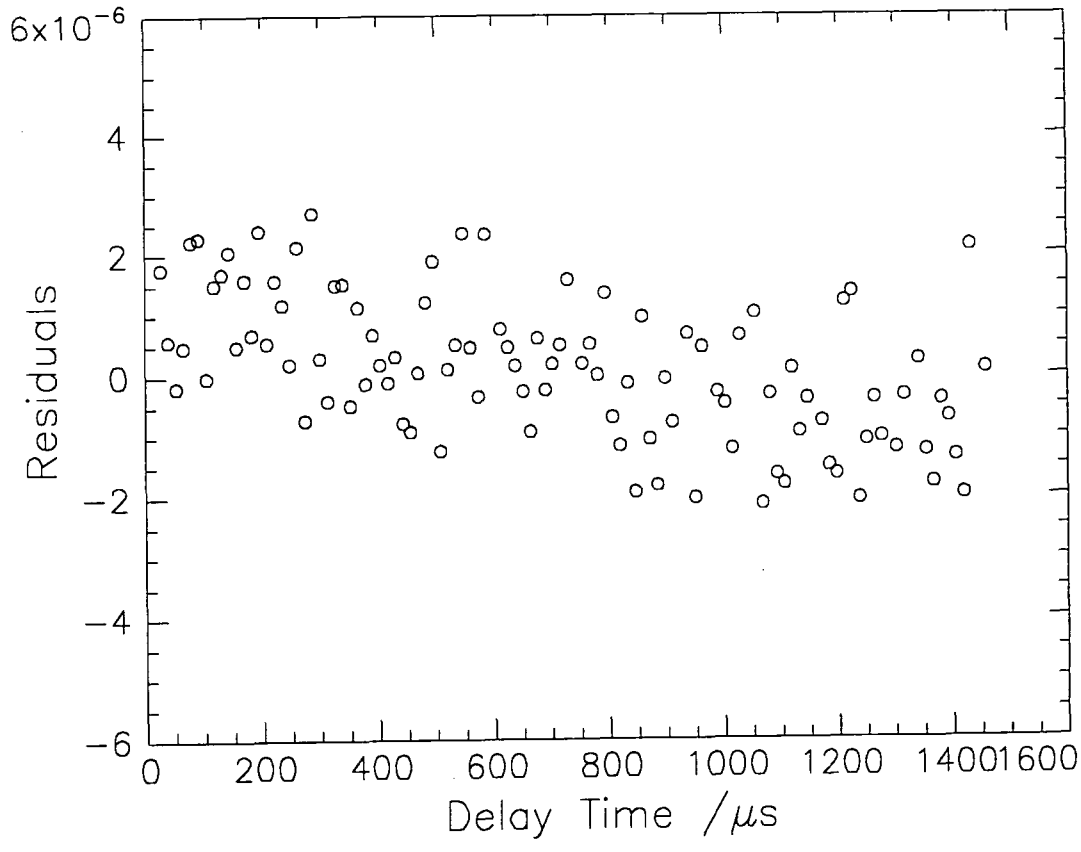

Figure 5.23(b): Residuals at 0.3mg m^{-2}

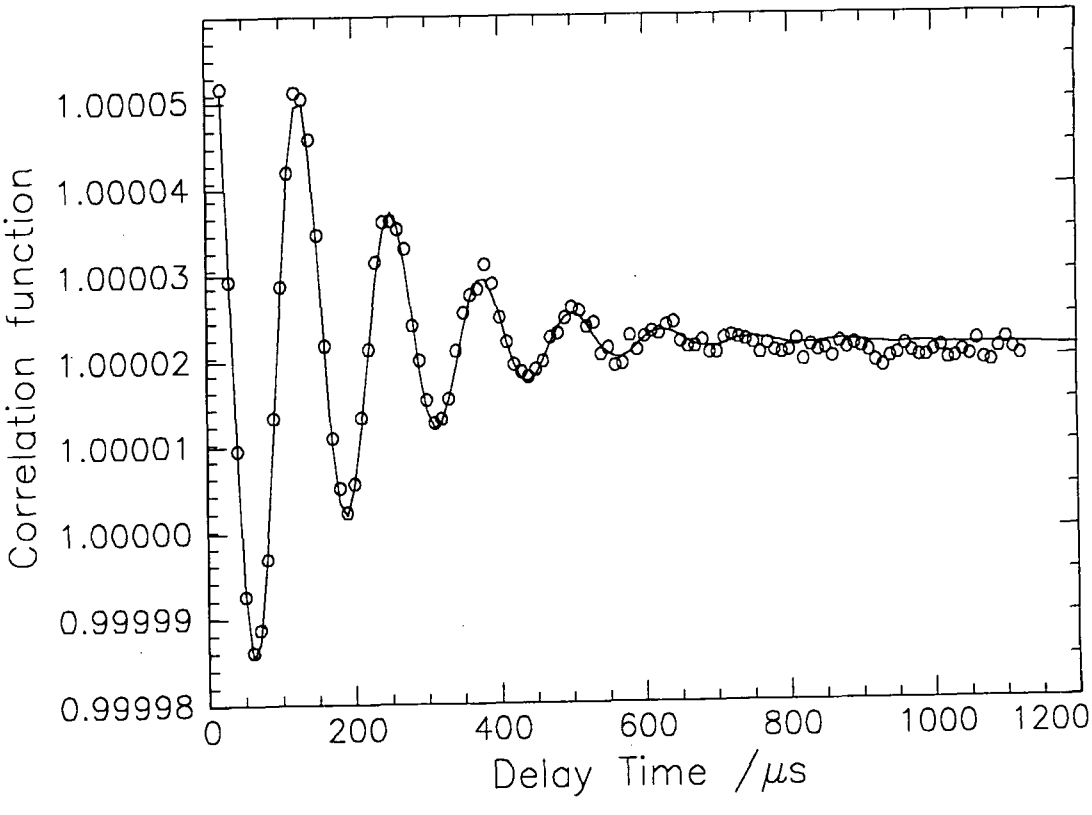

Figure 5.24(a): Correlation function at 1.5mg m^{-2} - 1st run of 10

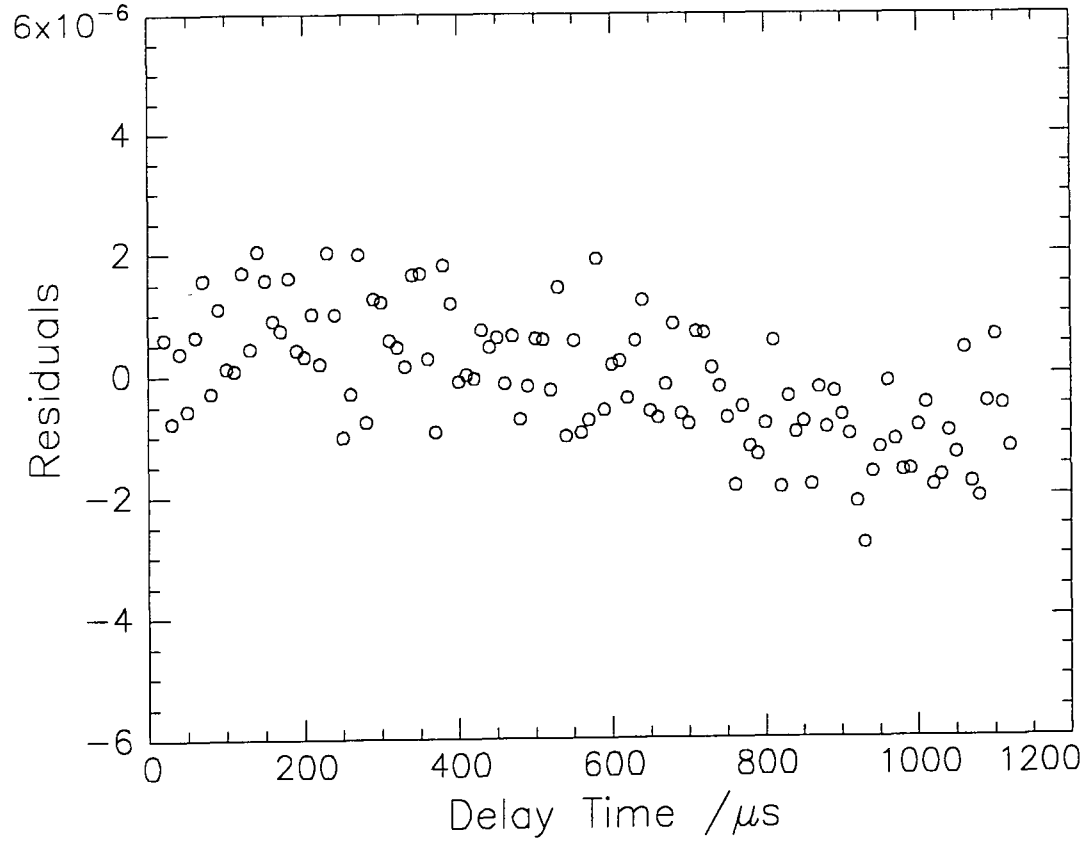

Figure 5.24(b): Residual at 1.5mg m^{-2} - 1st run of 10

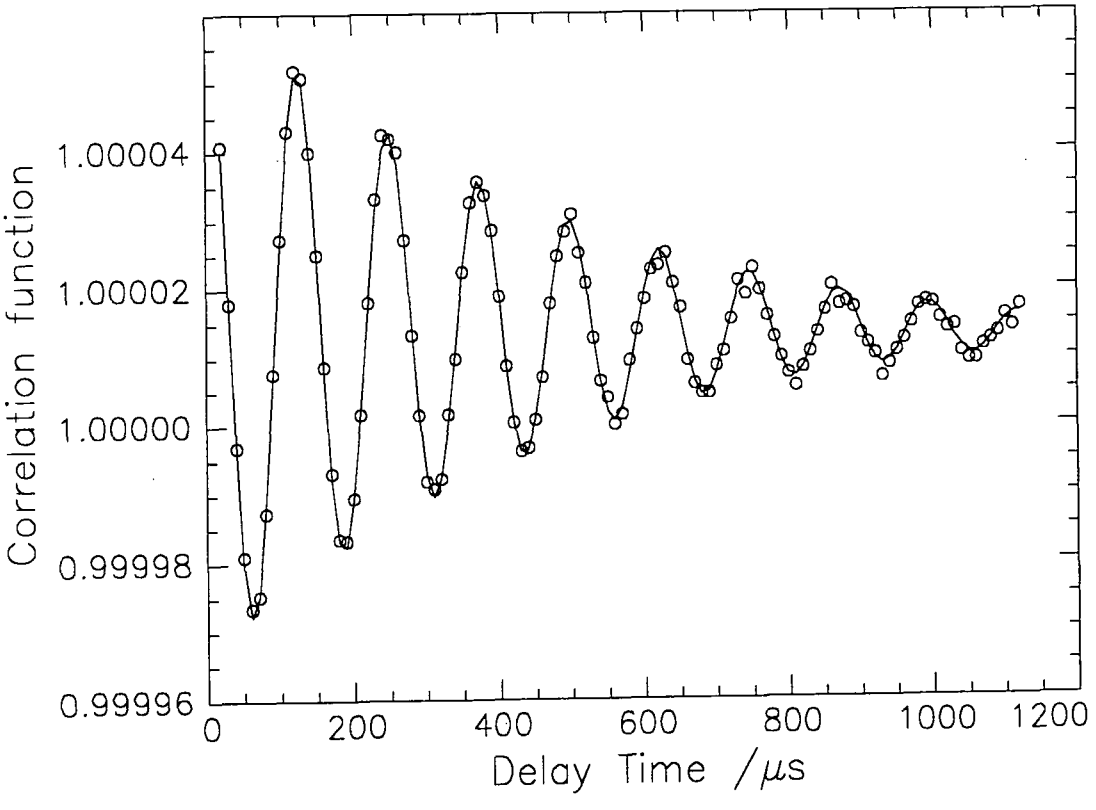

Figure 5.25(a): Correlation function at 1.5mg m^{-2} - 9th run of 10

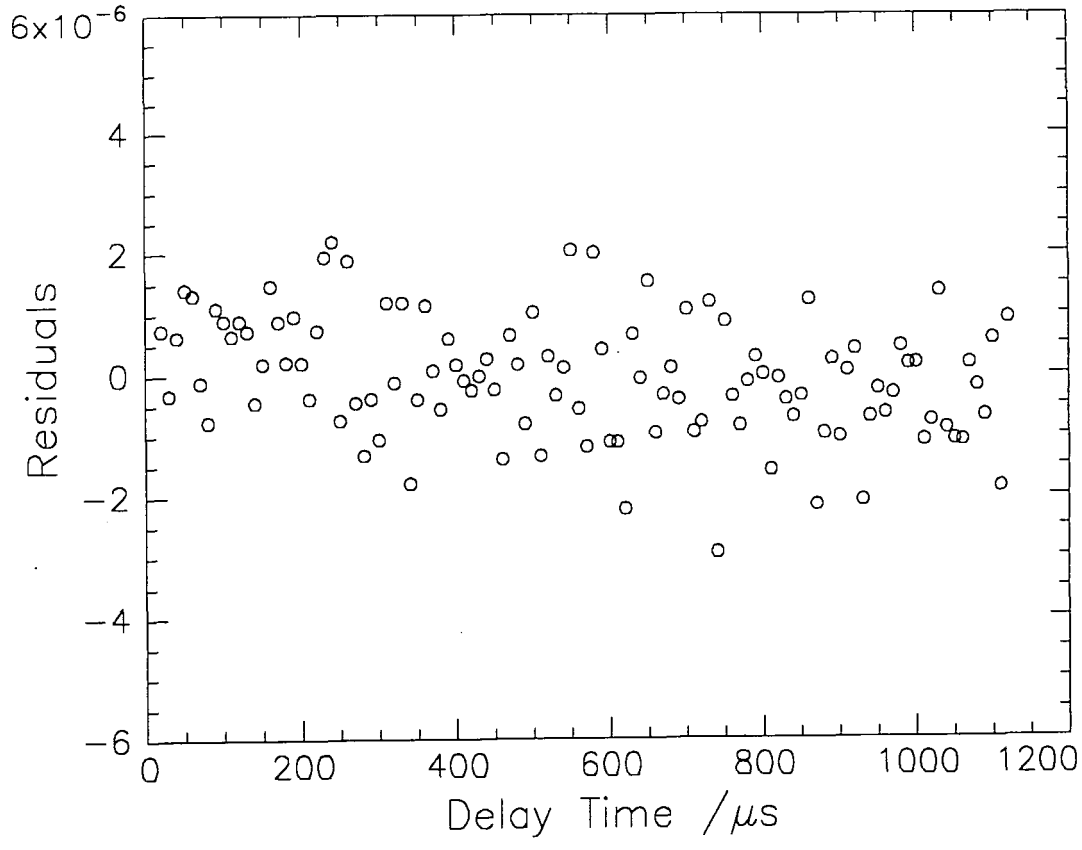

Figure 5.25(b): Residual at 1.5mg m^{-2} - 9th run of 10

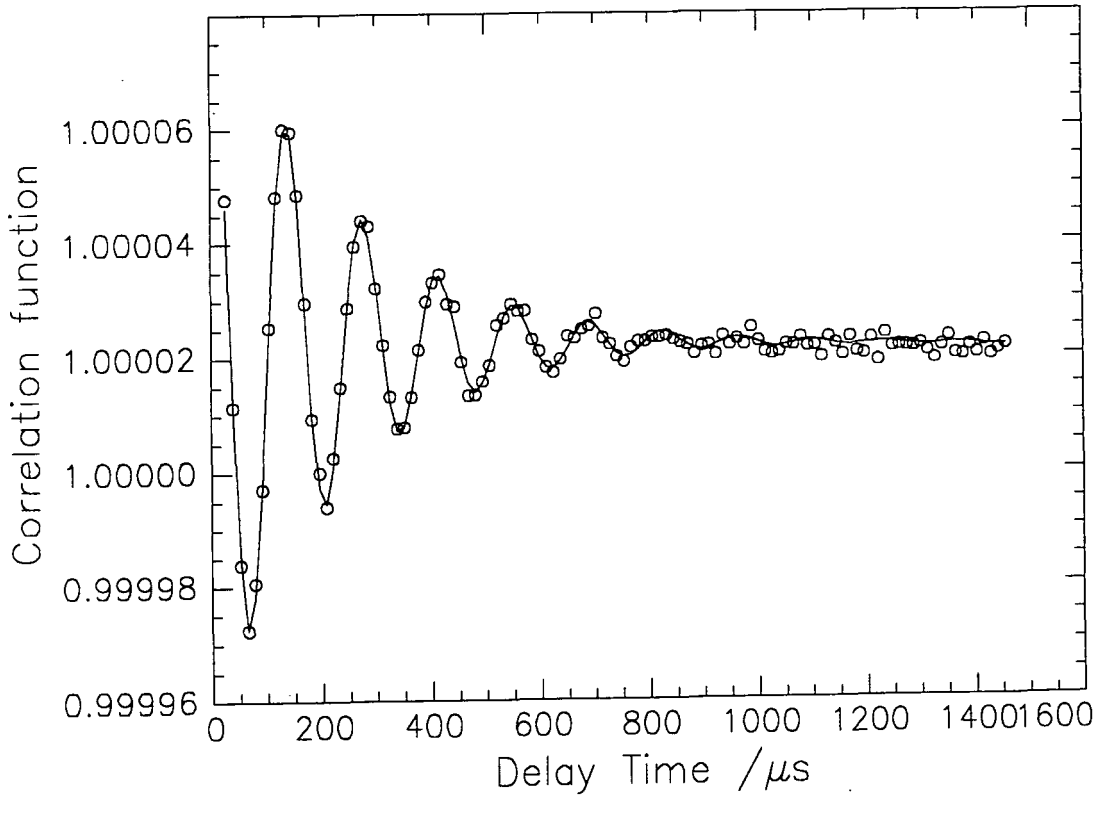

Figure 5.26(a): Correlation function at 3mg m^{-2} - 3rd run of 10

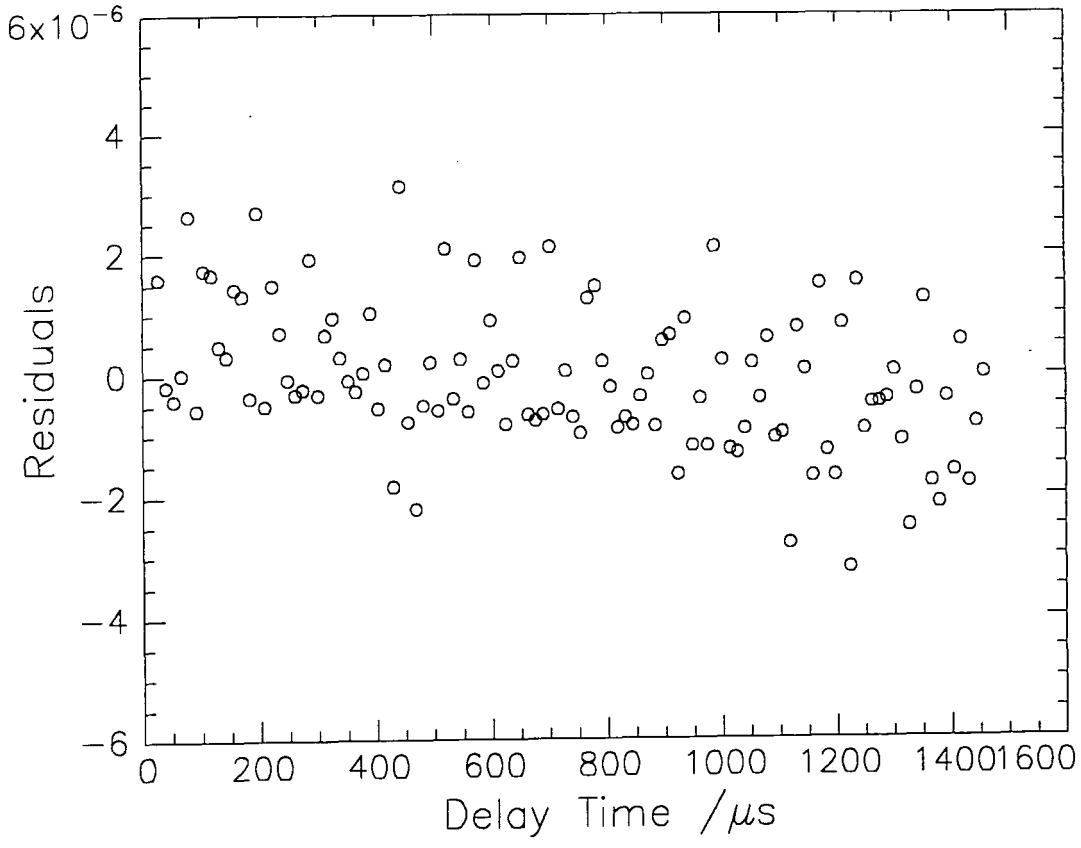

Figure 5.26(b): Residual at 3mg m^{-2} - 3rd run of 10

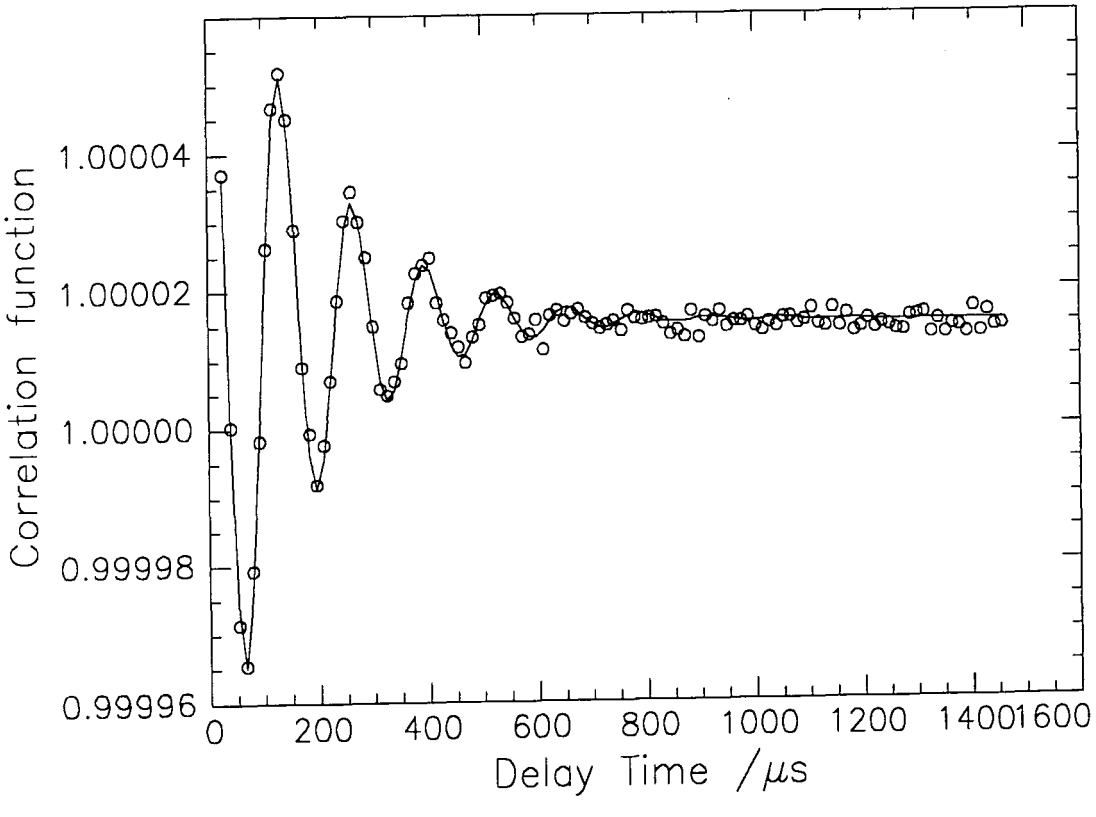

Figure 5.27(a): Correlation function at 3mg m^{-2} - 8th run of 10

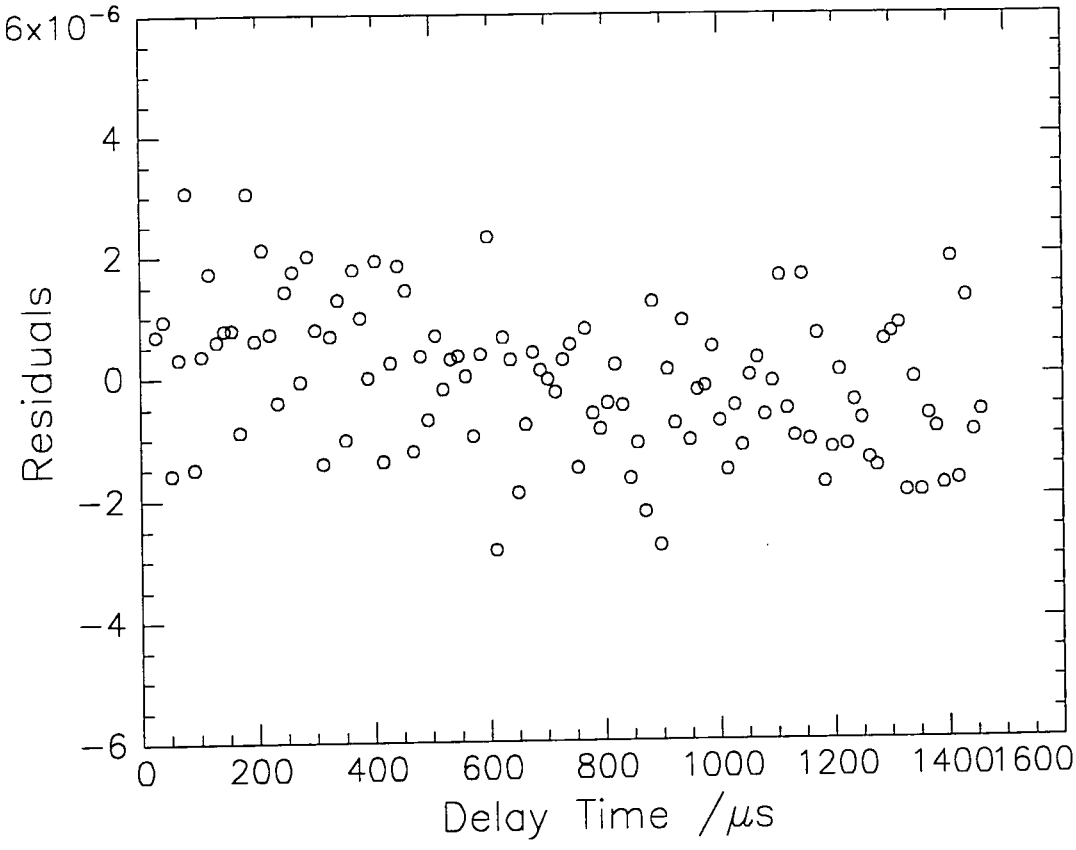

Figure 5.27(b): Residual at 3mg m^{-2} - 8th run of 10

At 0.3mg m^{-2}, all ten correlation functions were similar, whereas at 1.5mg m^{-2} there was a noticeable decrease in the damping observed in the correlation functions as time went by. At 3mg m^{-2} the damping appeared to increase slightly for the runs towards the end of the set of ten. There was no visible change in the propagation frequency, although a slight change would be expected to accompany the changes in damping. The values obtained for the propagation frequency and wave damping from the fits of all the correlation functions at each surface concentration show the changes observed with time and are shown in figures 5.28 to 5.33. The values obtained for the propagation frequency and damping for clean water at this q were 51000 ± 500s^{-1} and 1780 ± 60s^{-1} respectively.

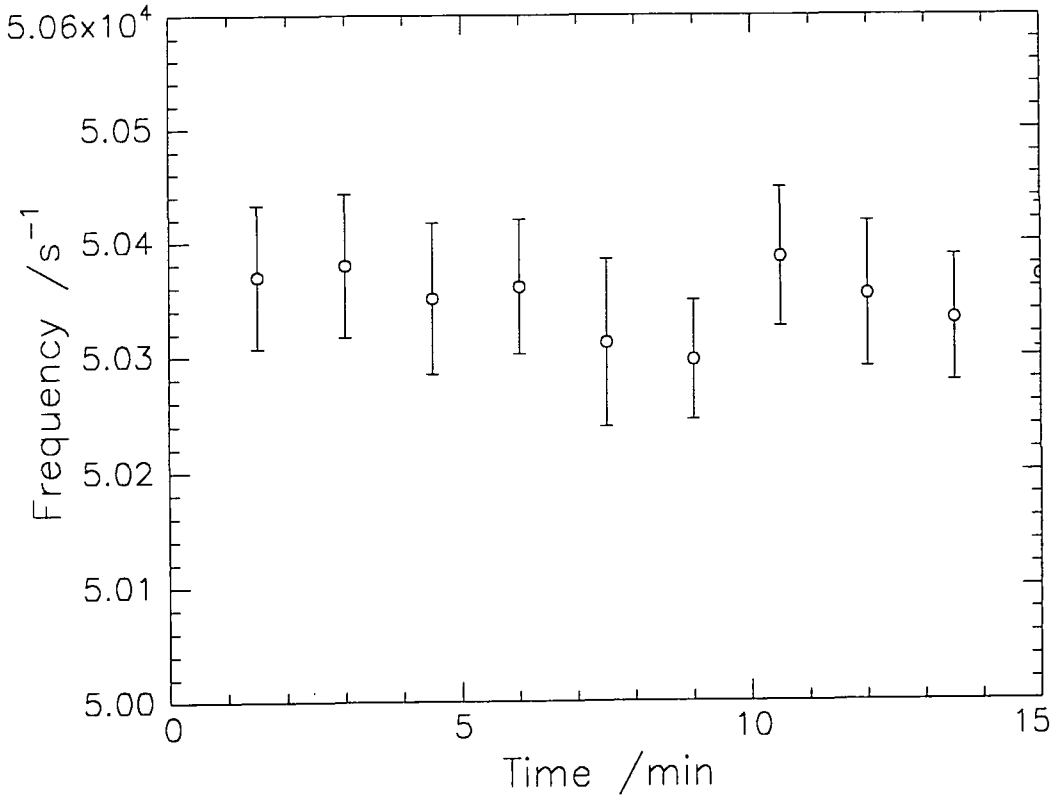

Figure 5.28: Variation in frequency at 0.3mg m^{-2}

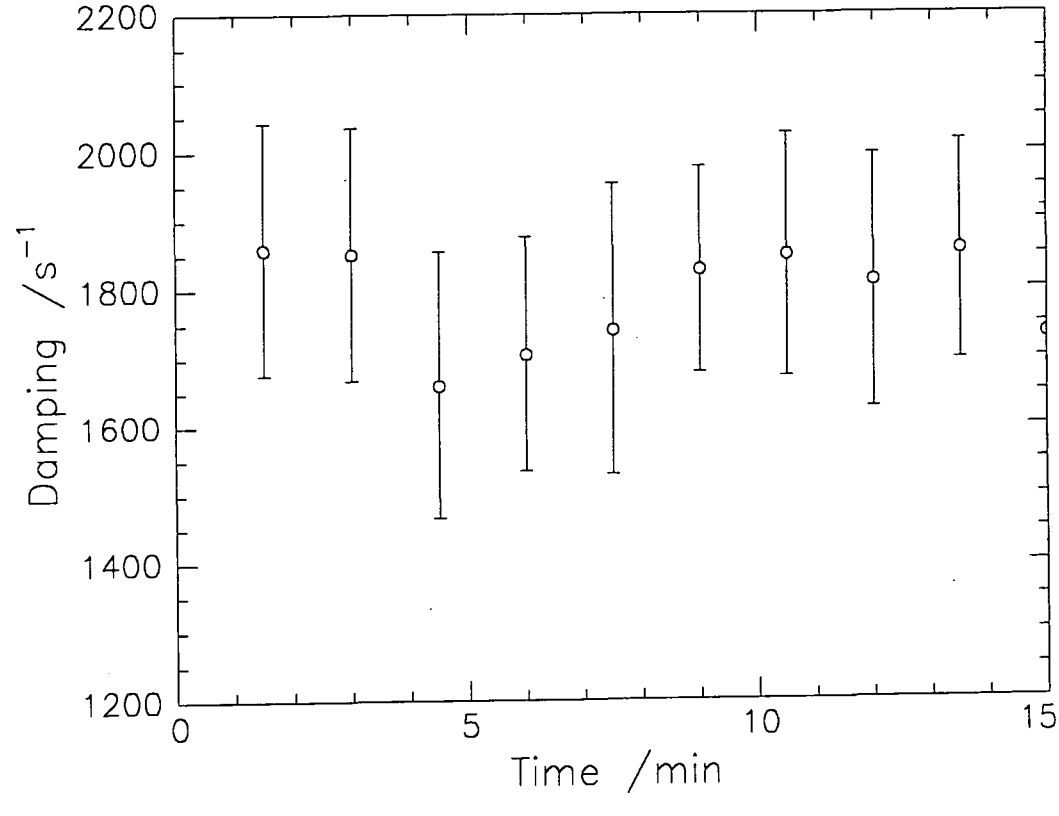

Figure 5.29: Variation in damping at 0.3mg m^{-2}

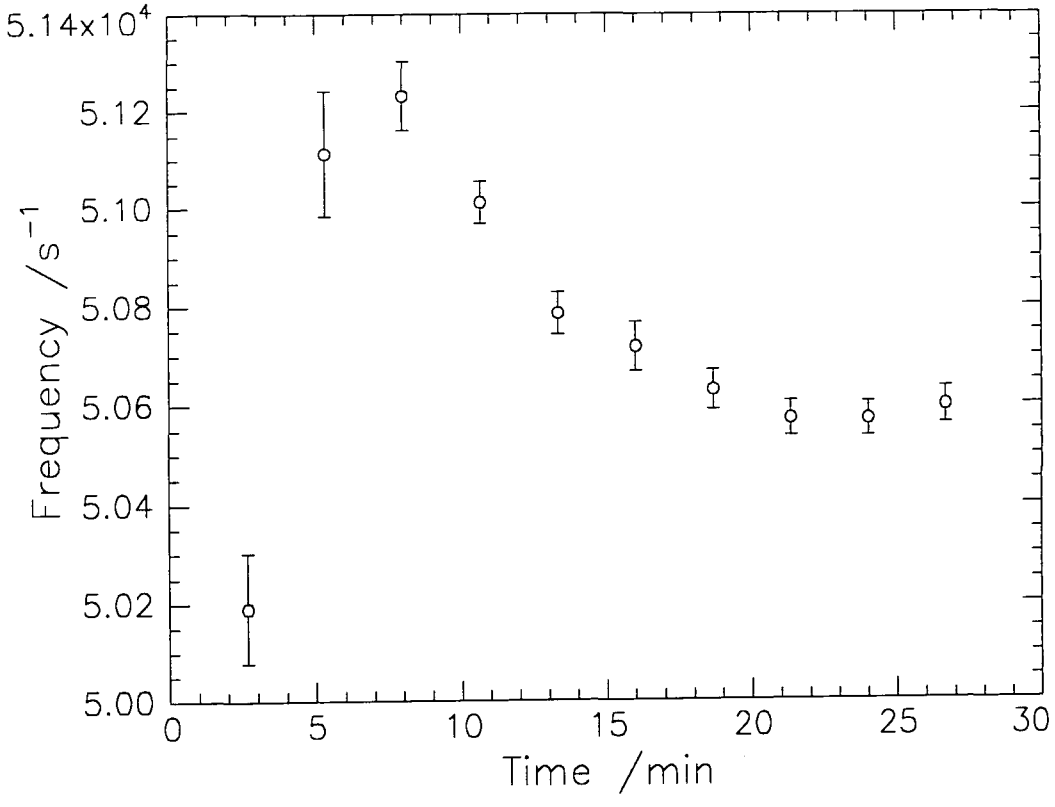

Figure 5.30: Variation in frequency at 1.5mg m^{-2}

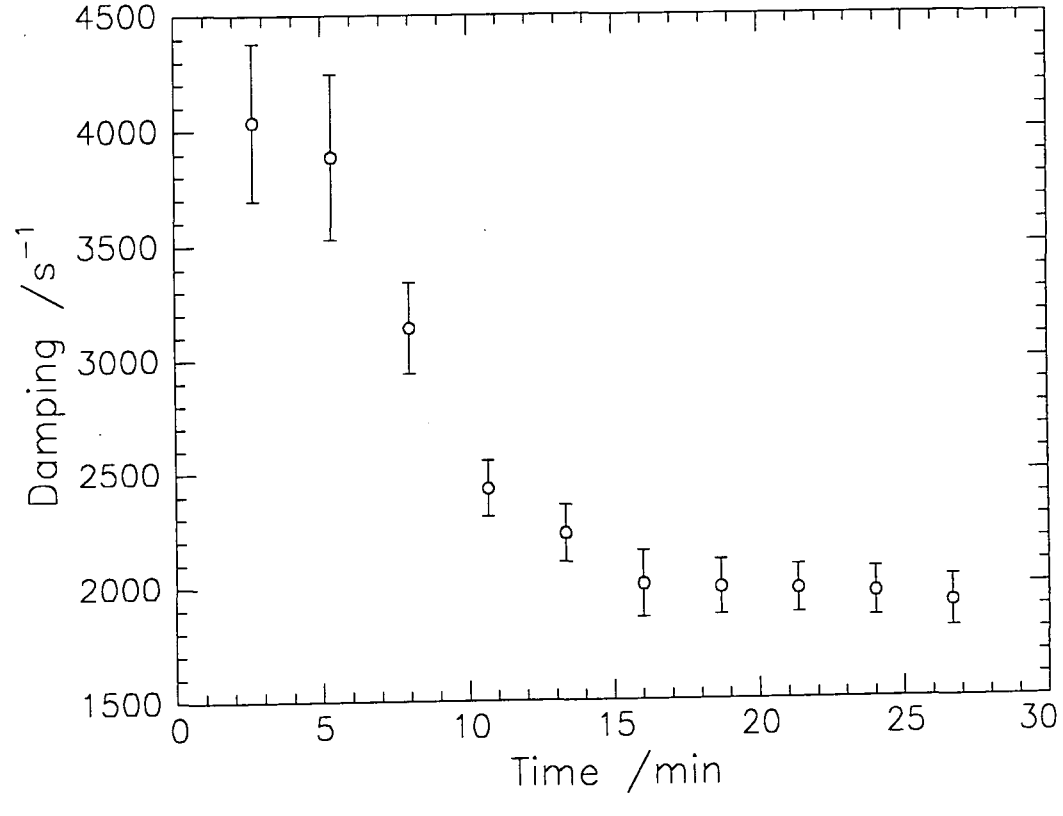

Figure 5.31: Variation in damping at 1.5mg m^{-2}

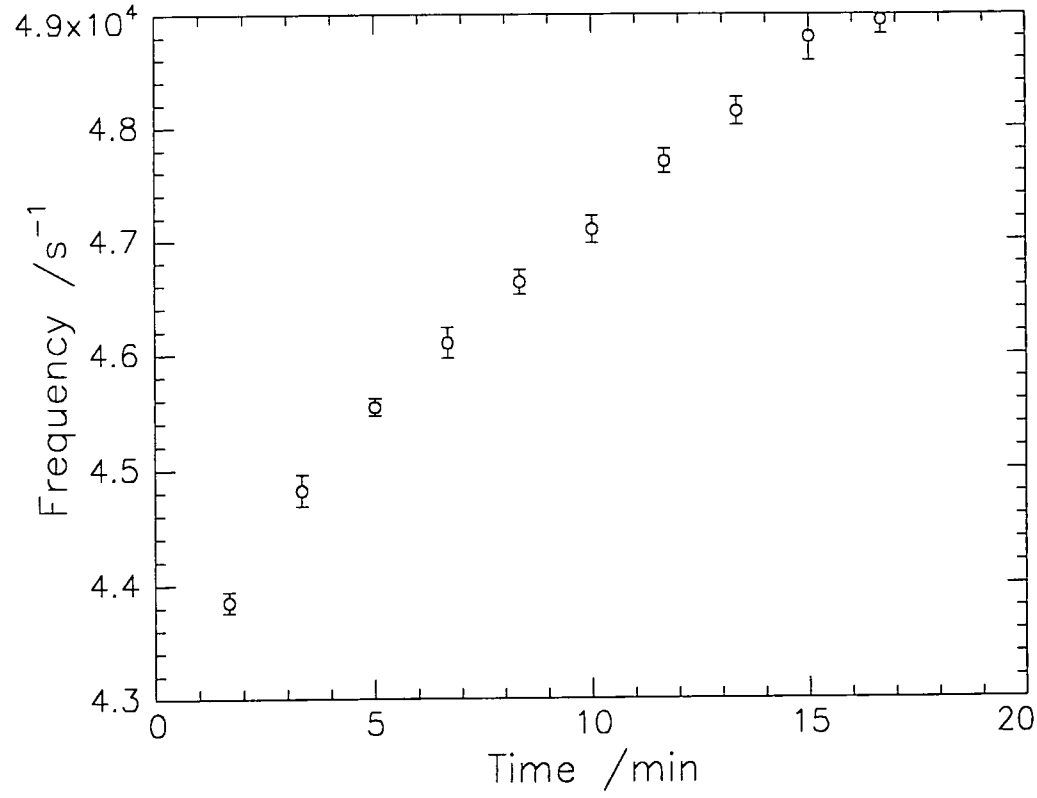

Figure 5.32: Variation in frequency at 3mg m^{-2}

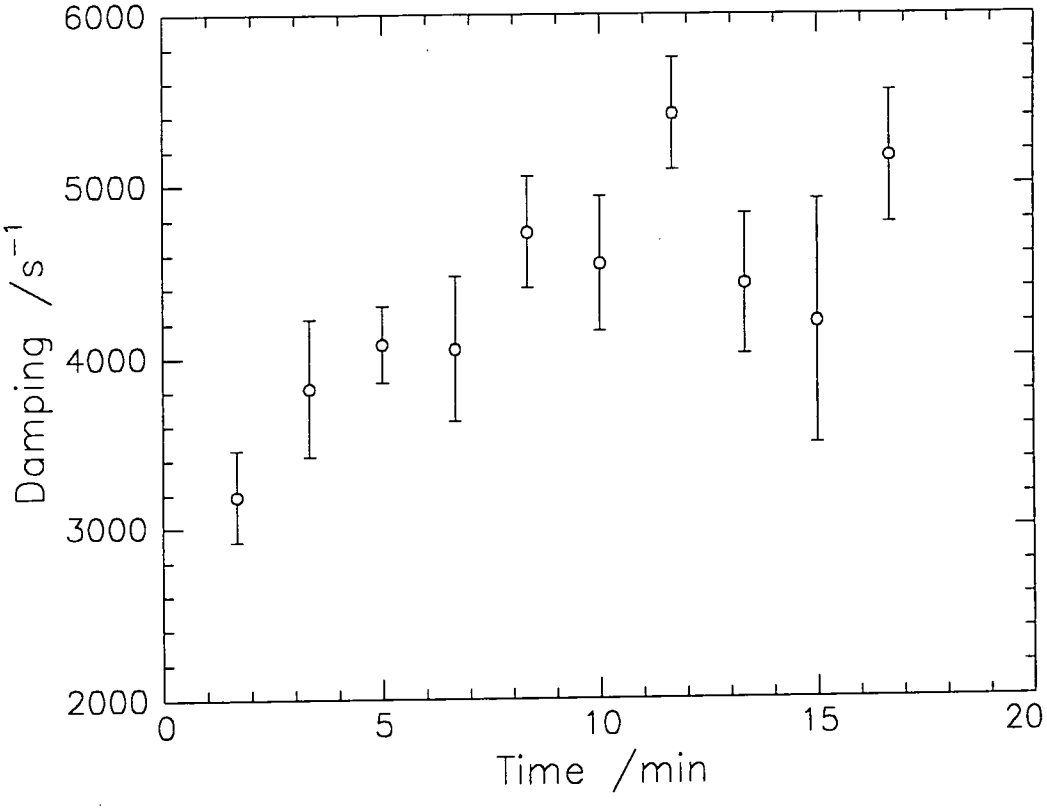

Figure 5.33: Variation in damping at 3mg m^{-2}

At 0.3mg m^{-2} both the frequency and the damping remain fairly constant for all ten runs, with values close to those of clean water. The damping at 1.5mg m^{-2} shows a dramatic decrease up to 10 minutes and then begins to plateau at a value similar to that obtained at 0.3mg m^{-2}. The frequency at 1.5mg m^{-2} increases, as would be expected from the decrease in damping, and then plateaus, although this occurs after a slight decrease in the frequency. Over a similar time scale at 3mg m^{-2} the trend seems to be reversed, with both the damping and frequency increasing with time.

A longer time scale was used at 3mg m^{-2} to see if similar behaviour occurred, but at a slower rate, which might be expected due to the extra material present at the interface. 50 runs, each of 120s duration, were carried out and the resulting variations of the propagation frequency and wave damping are shown in figures 5.34 and 5.35.

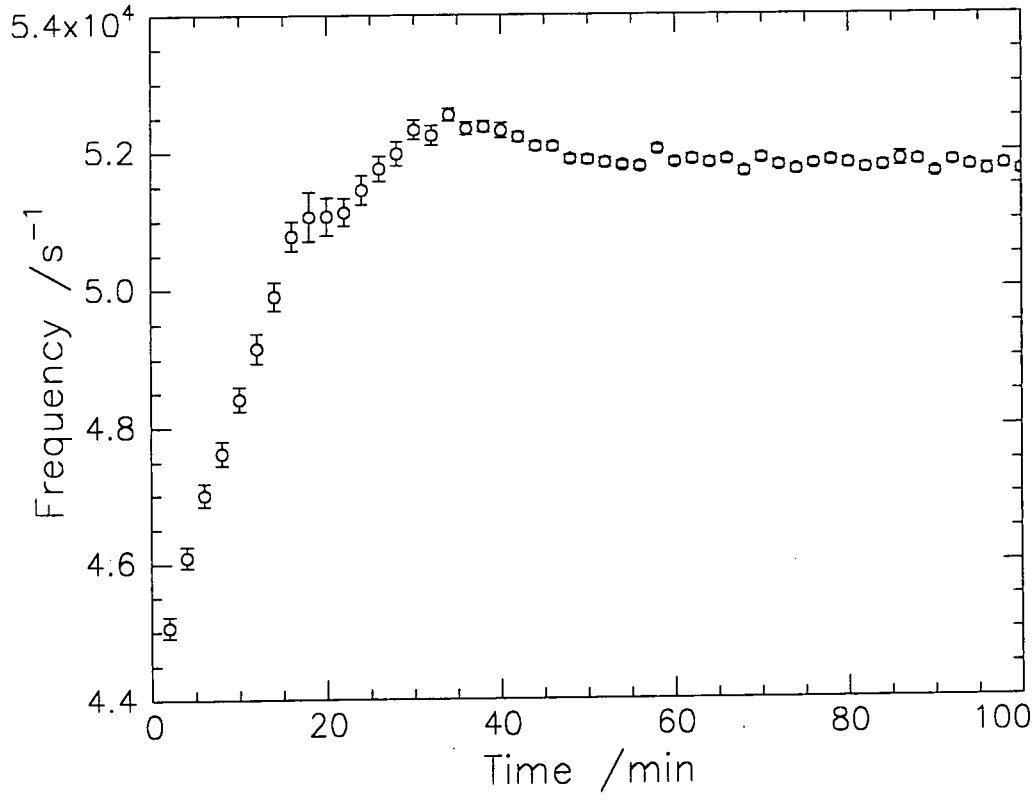

Figure 5.34: Variation in frequency at 3mg m^{-2}

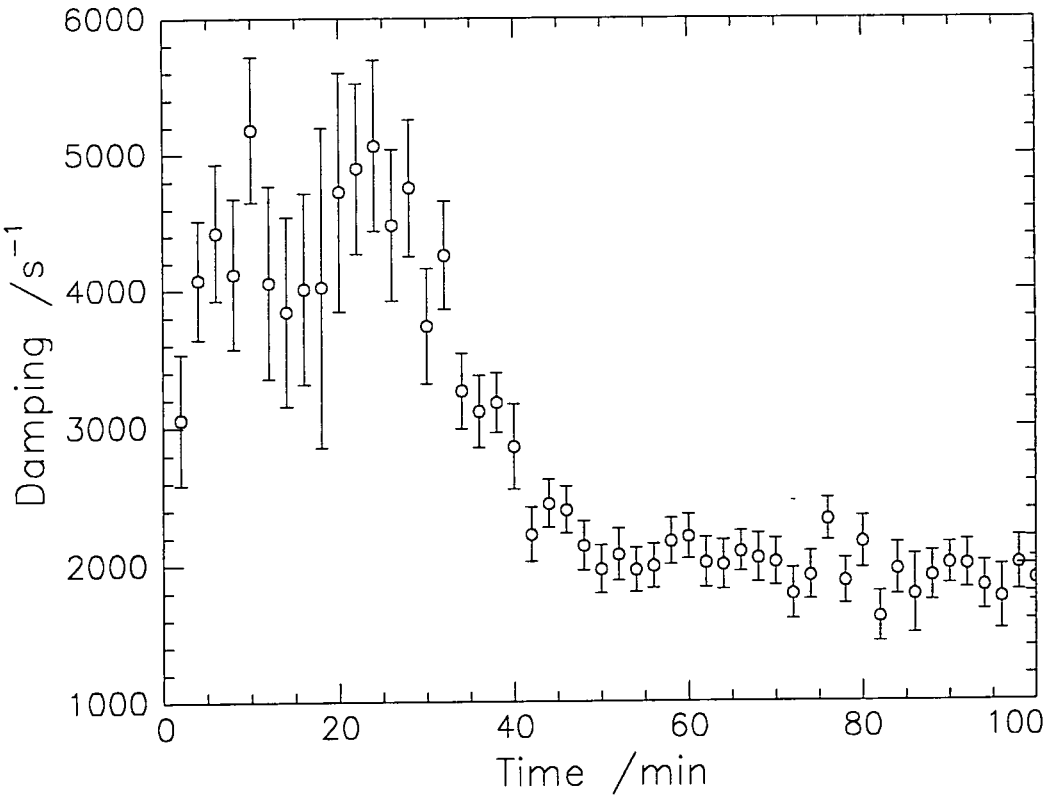

Figure 5.35: Variation in damping at 3mg m^{-2}

As expected, over a longer time scale the monolayer behaved similarly to that at 1.5mg m^{-2} and after a longer period attained plateau values of frequency and damping similar to the two lower concentrations. These results seem to indicate that a relaxation process of some kind occurs and the monolayer reverts to a state similar to that at 0.3mg m^{-2}.

All of the correlation functions were also fitted using equation 5.15 to obtain the four visco - elastic parameters and examples of the fits obtained are shown in figures 5.36(a) to 5.40(a) with the residuals of each fit shown in figures 5.36(b) to 5.40(b).

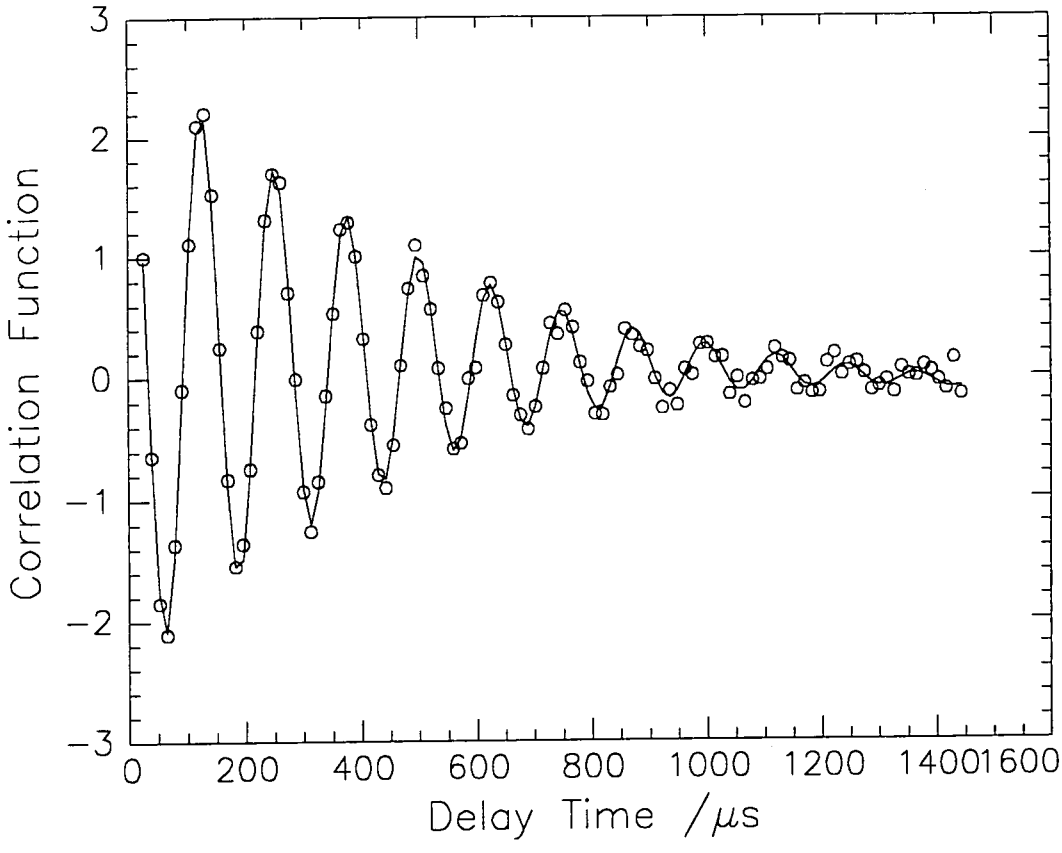

Figure 5.36(a): Correlation function at 0.3mg m^{-2}

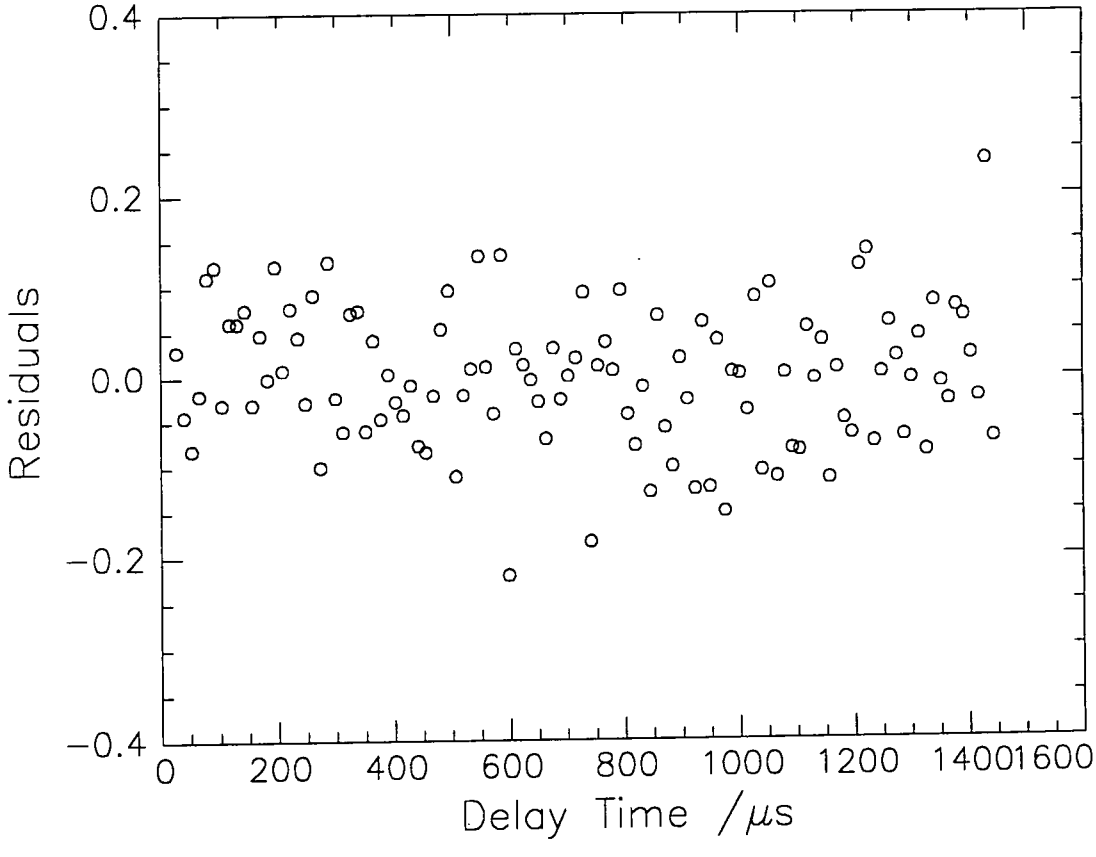

Figure 5.36(b): Residuals at 0.3mg m^{-2}

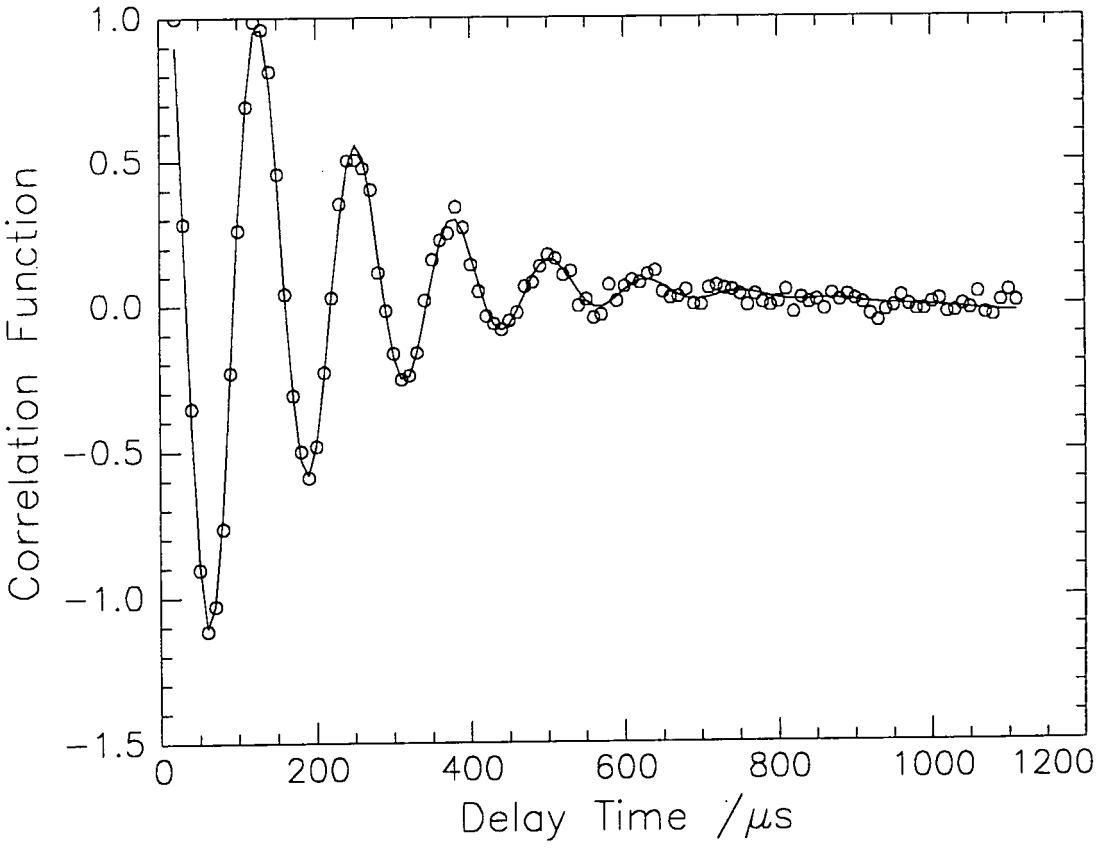

Figure 5.37(a): Correlation function at 1.5mg m^{-2} - 1st run of 10

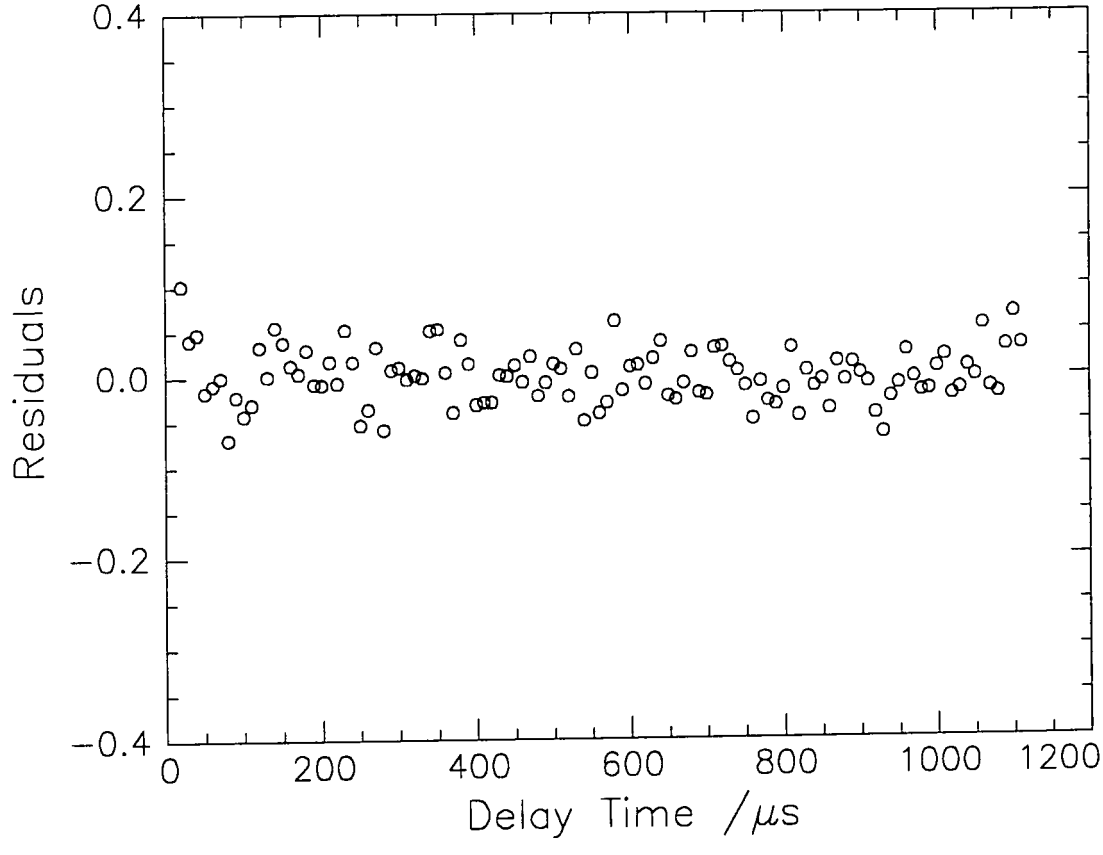

Figure 5.37(b): Residuals at 1.5mg m^{-2} - 1st run of 10

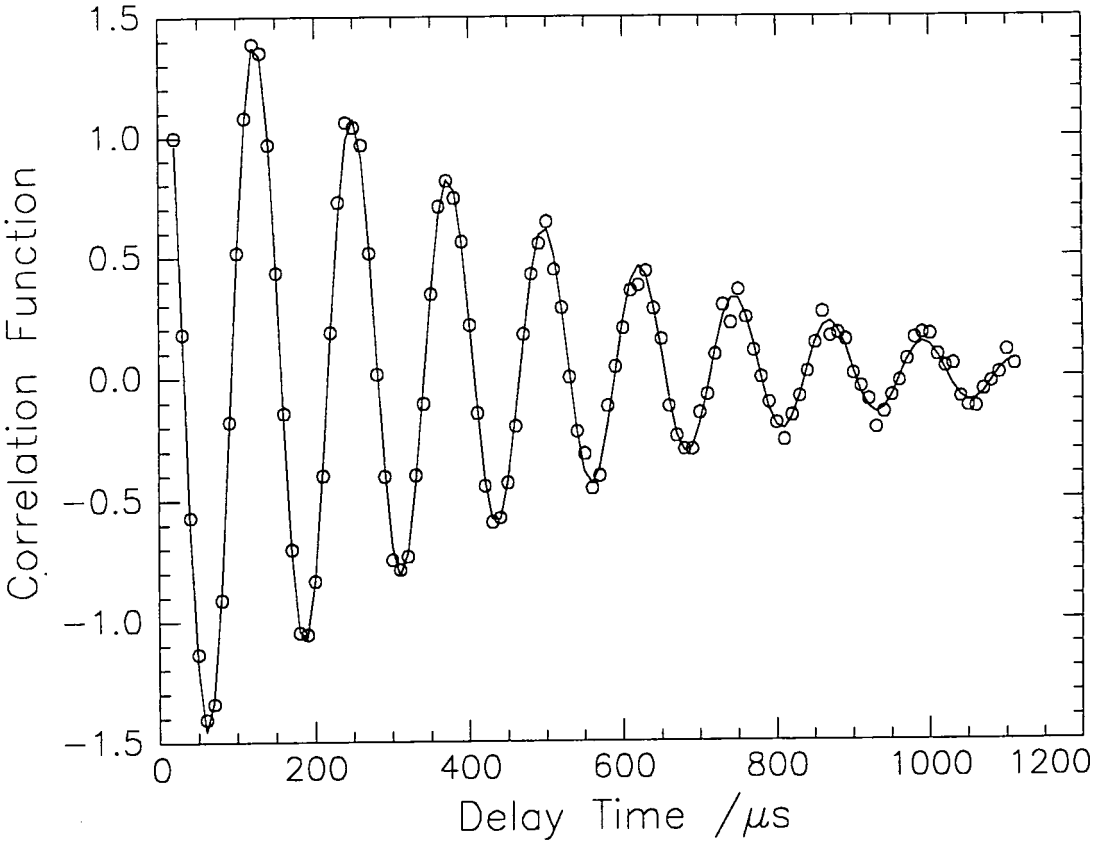

Figure 5.38(a): Correlation function at 1.5mg m^{-2} - 9th run of 10

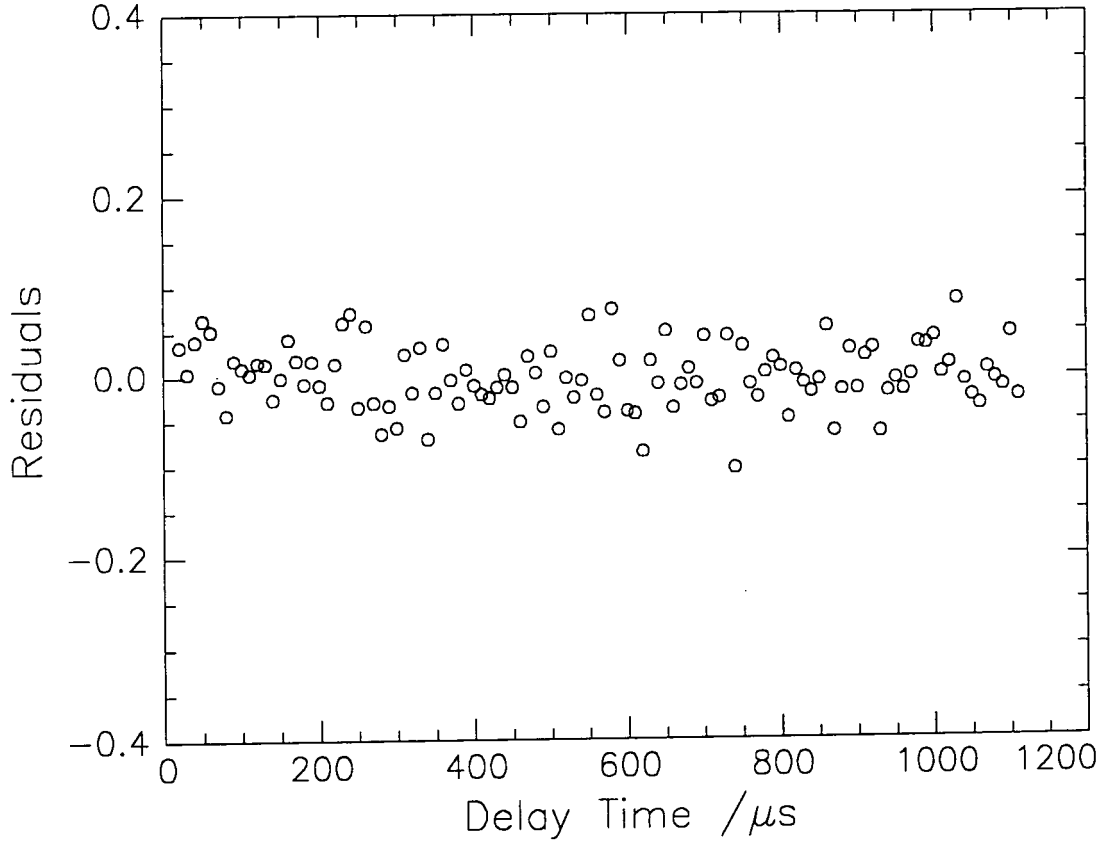

Figure 5.38(b): Residuals at 1.5mg m^{-2} - 9th run of 10

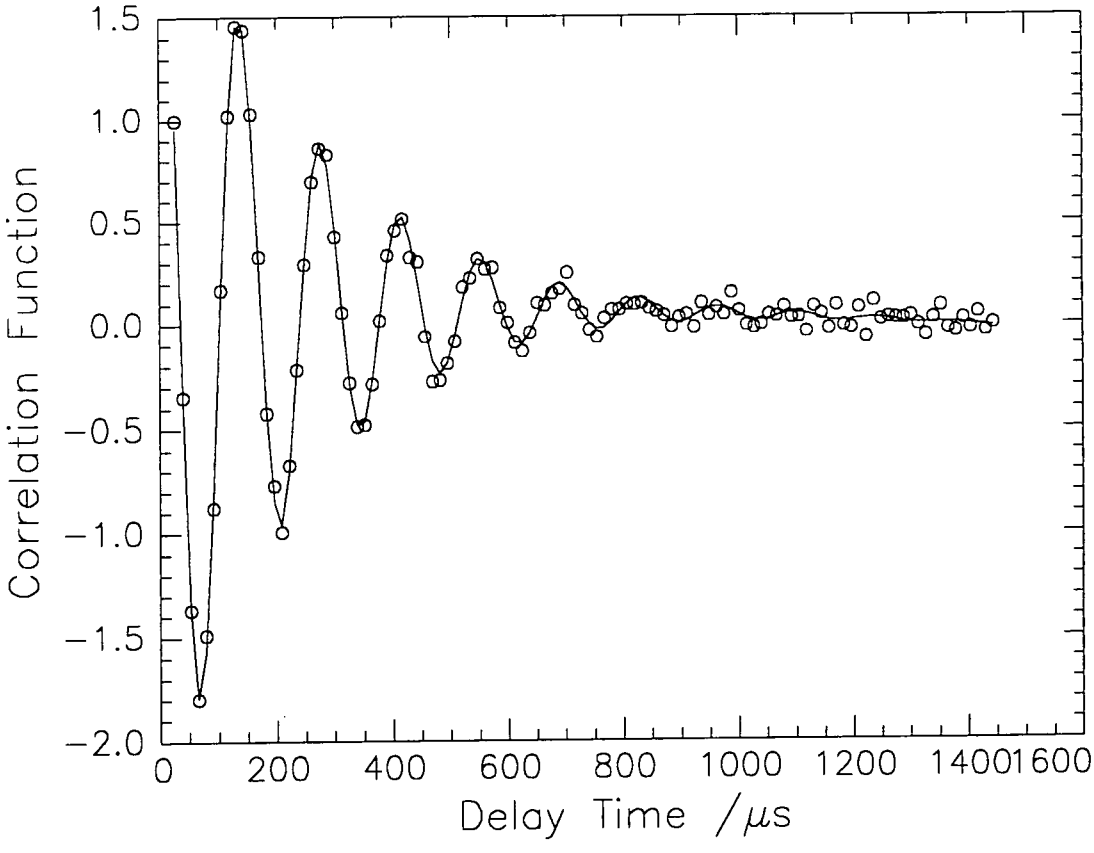

Figure 5.39(a): Correlation function at 3mg m^{-2} - 3rd run of 10

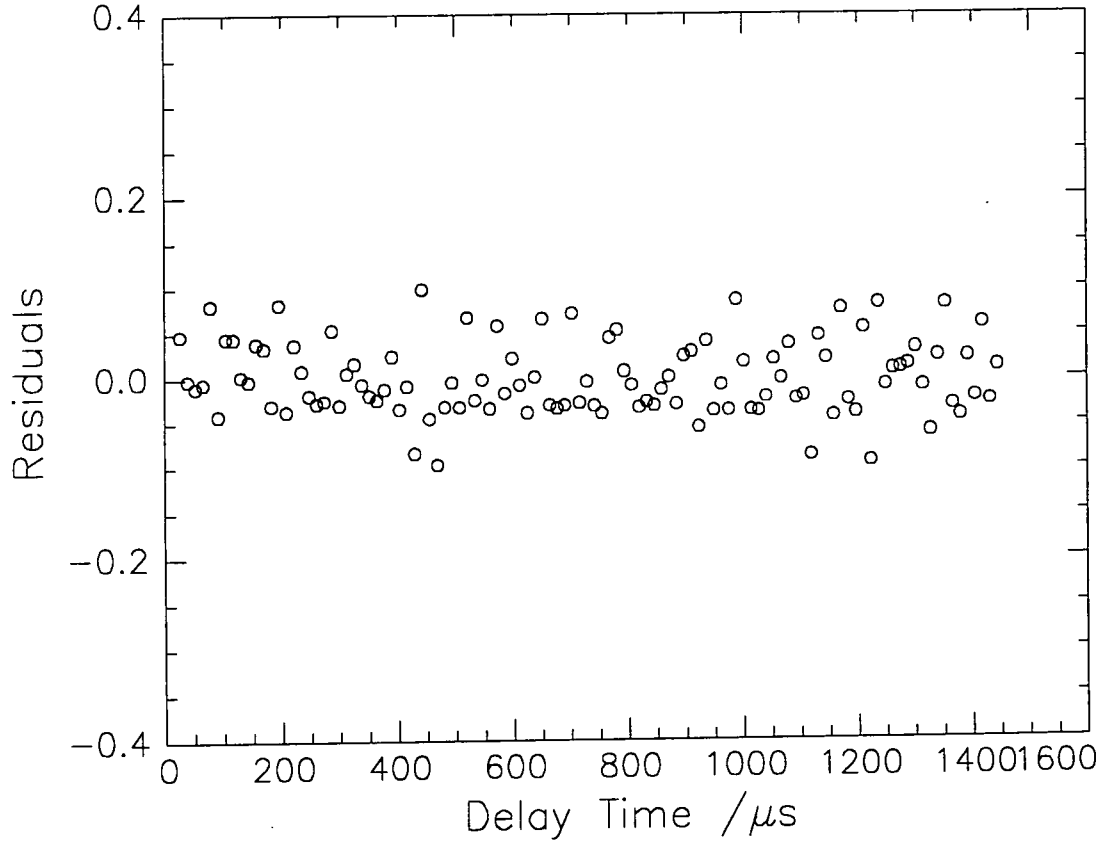

Figure 5.39(b): Residuals at 3mg m^{-2} - 3rd run of 10

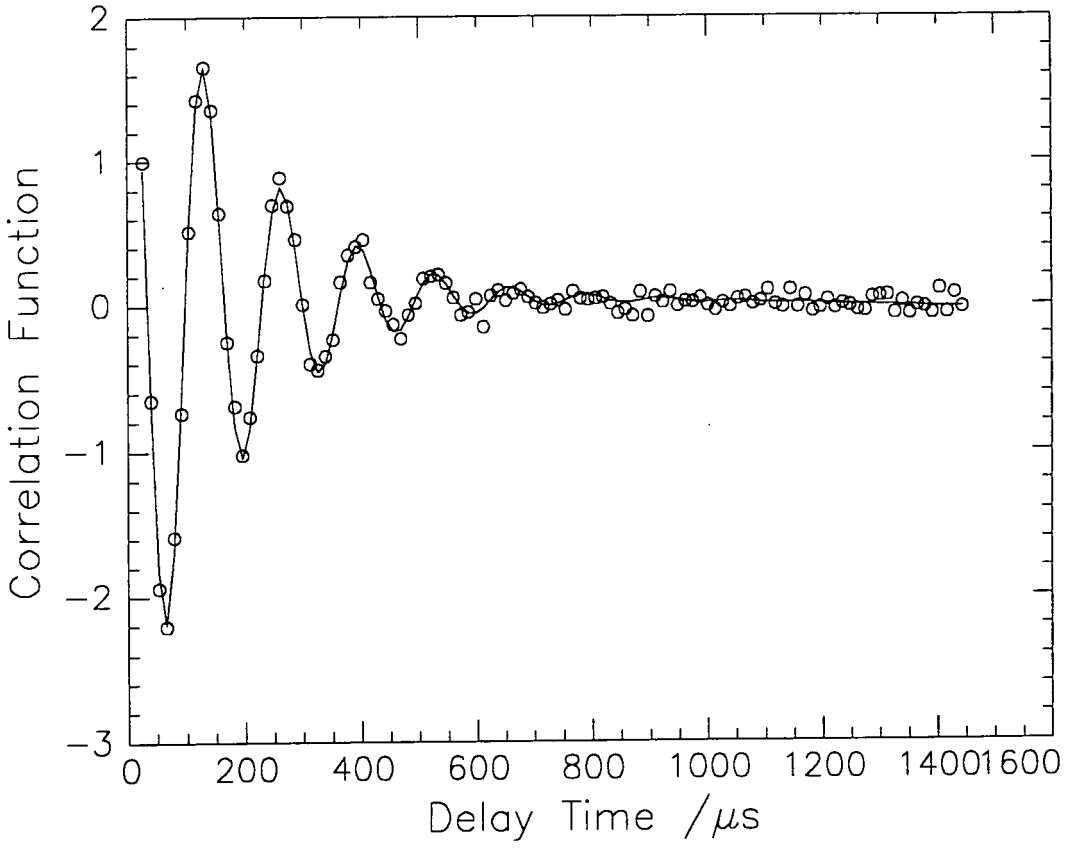

Figure 5.40(a): Correlation function at 3mg m^{-2} - 8th run of 10

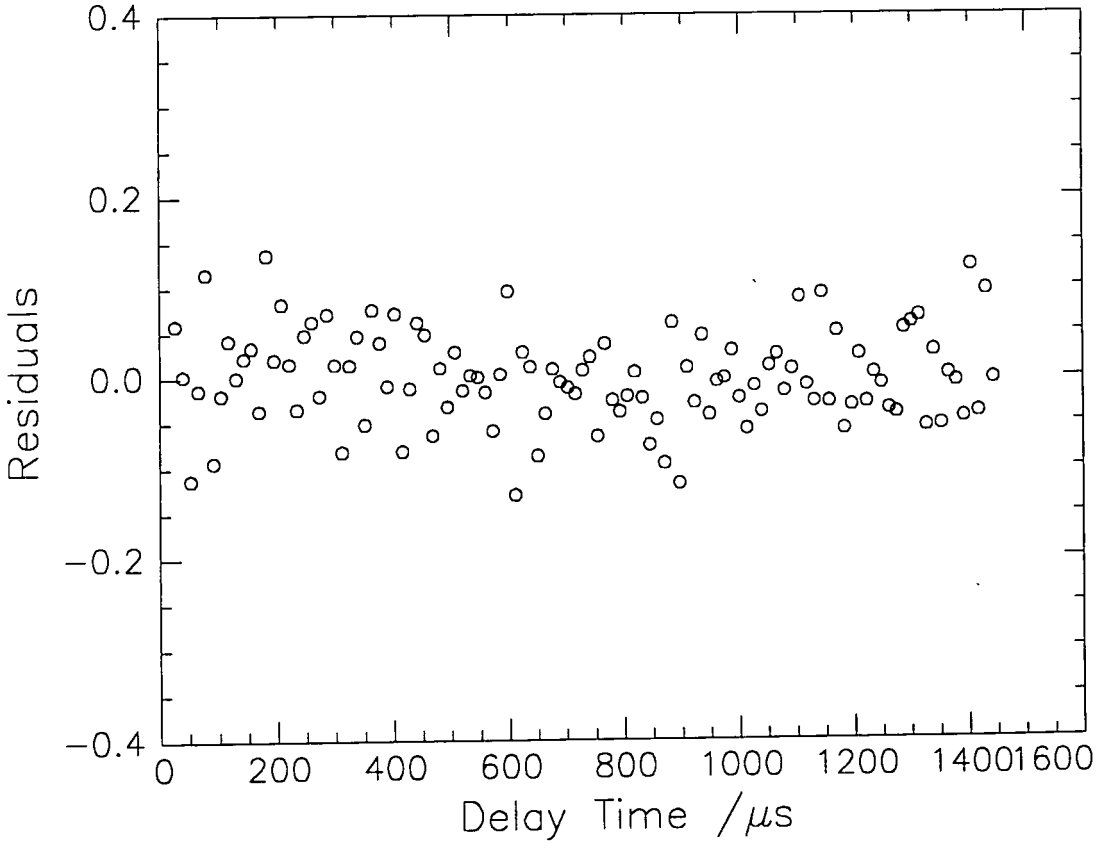

Figure 5.40(b): Correlation function at 3mg m^{-2} - 8th run of 10

At each concentration values for the surface tension and transverse shear viscosity were determined successfully, whereas the dilational modulus and viscosity were only obtained at 3mg m^{-2}. At the other concentrations, unrealistically large ($\geq 10^6$) and constant values were obtained due to the fact that the determination of ε_o and ε' is sensitive to noise on the data and if the system is well away from the resonance condition, then the coupling between the capillary and dilational modes is reduced and SQELS is insensitive to the dilational modes. The values obtained are shown in figures 5.41 to 5.50.

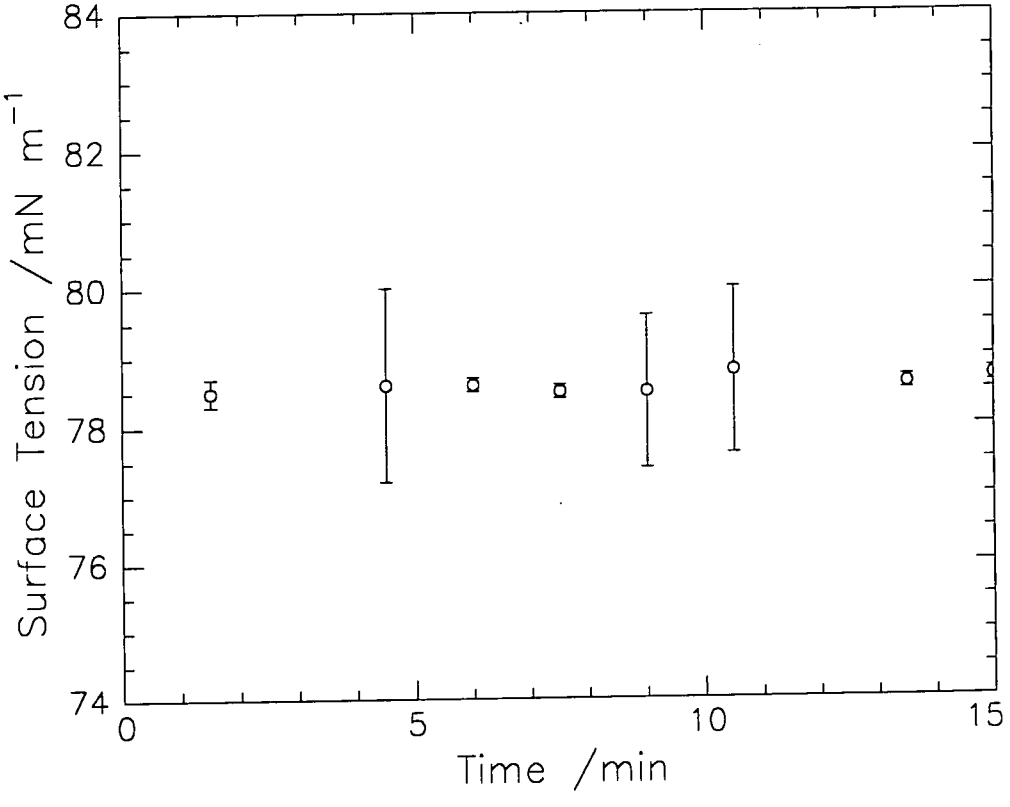

Figure 5.41: Variation of the surface tension at 0.3mg m^{-2}

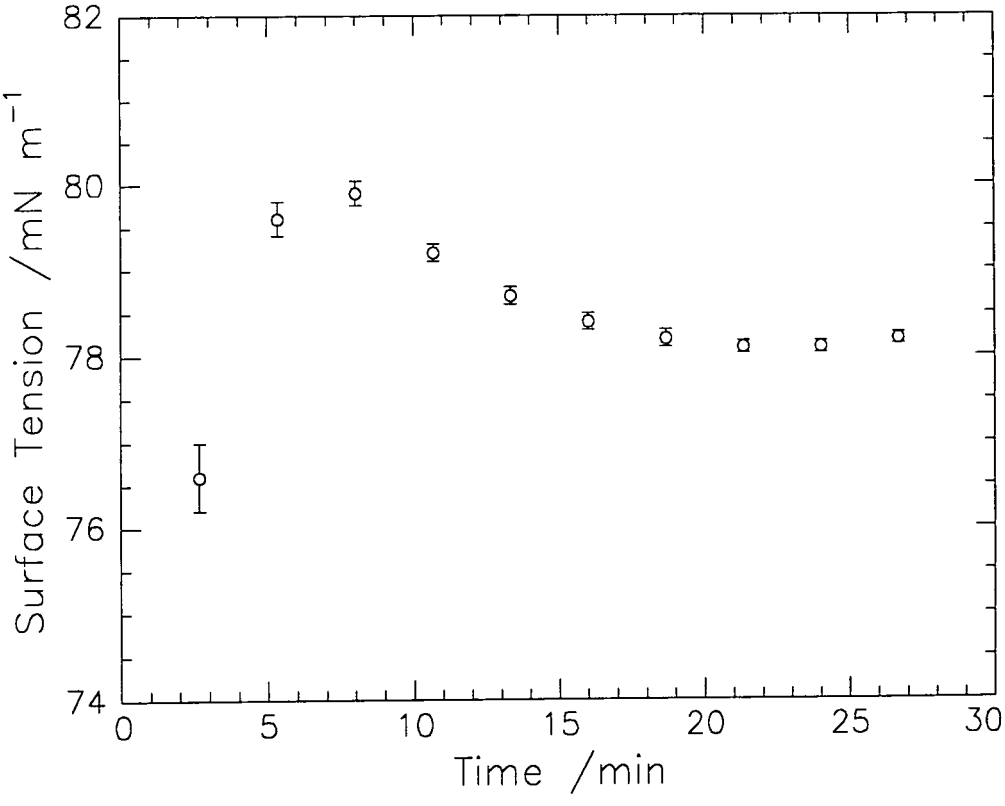

Figure 5.42: Variation of the surface tension at 1.5mg m^{-2}

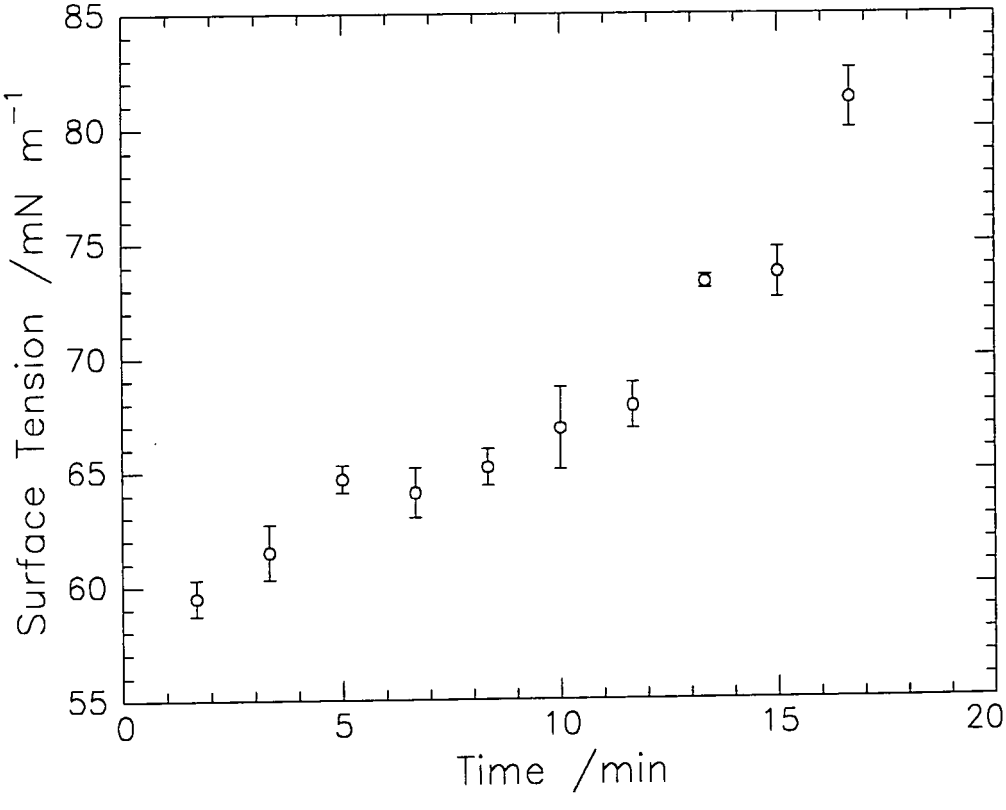

Figure 5.43: Variation of the surface tension at 3mg m^{-2}

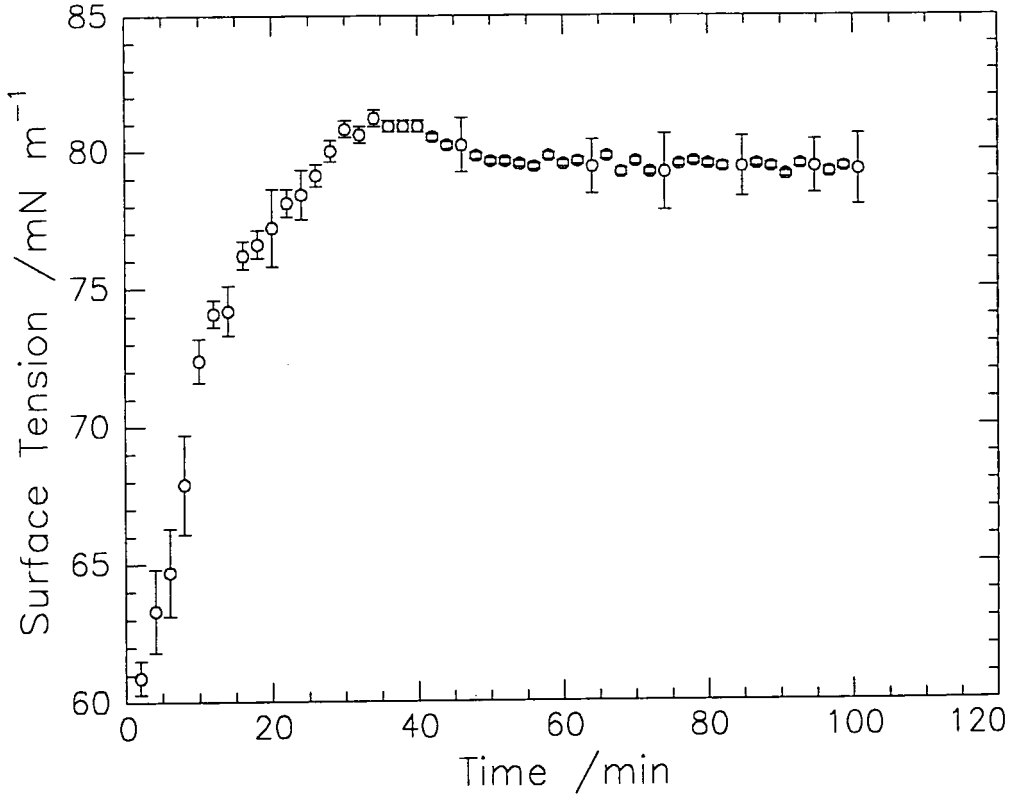

Figure 5.44: Variation of the surface tension at 3mg m^{-2} over a longer time

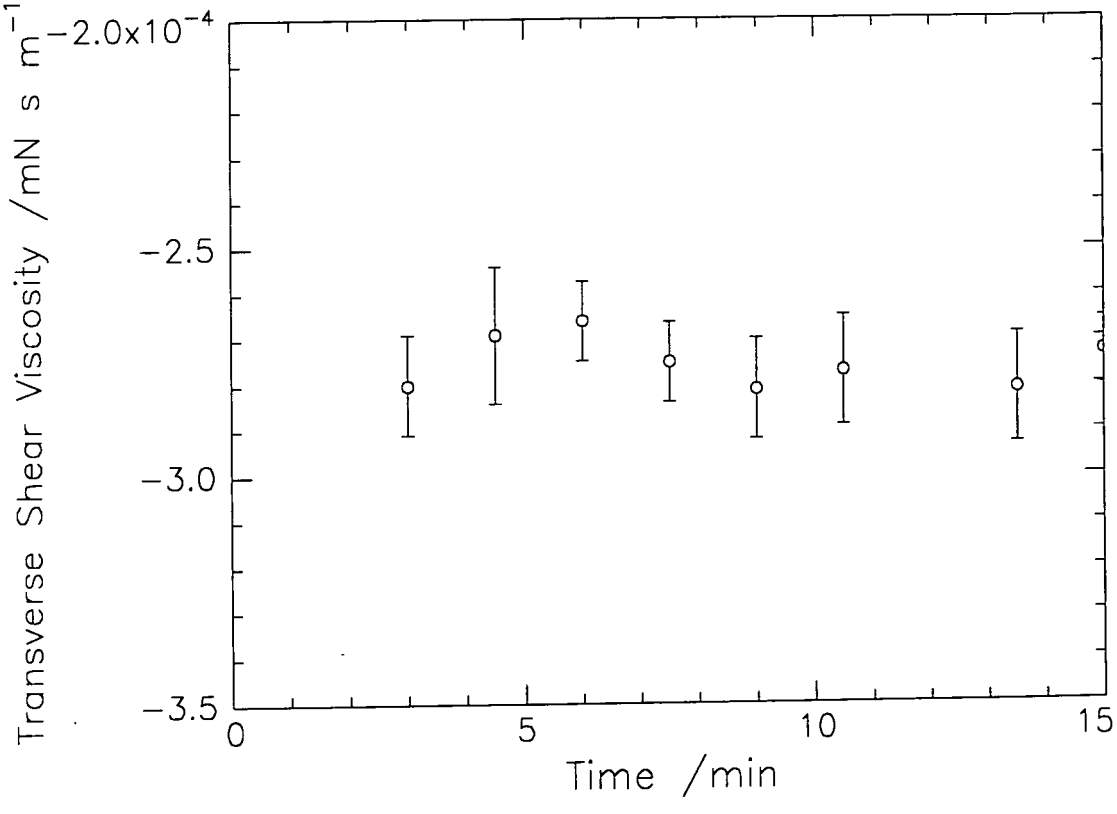

Figure 5.45: Variation of the transverse shear viscosity at 0.3mg m^{-2}

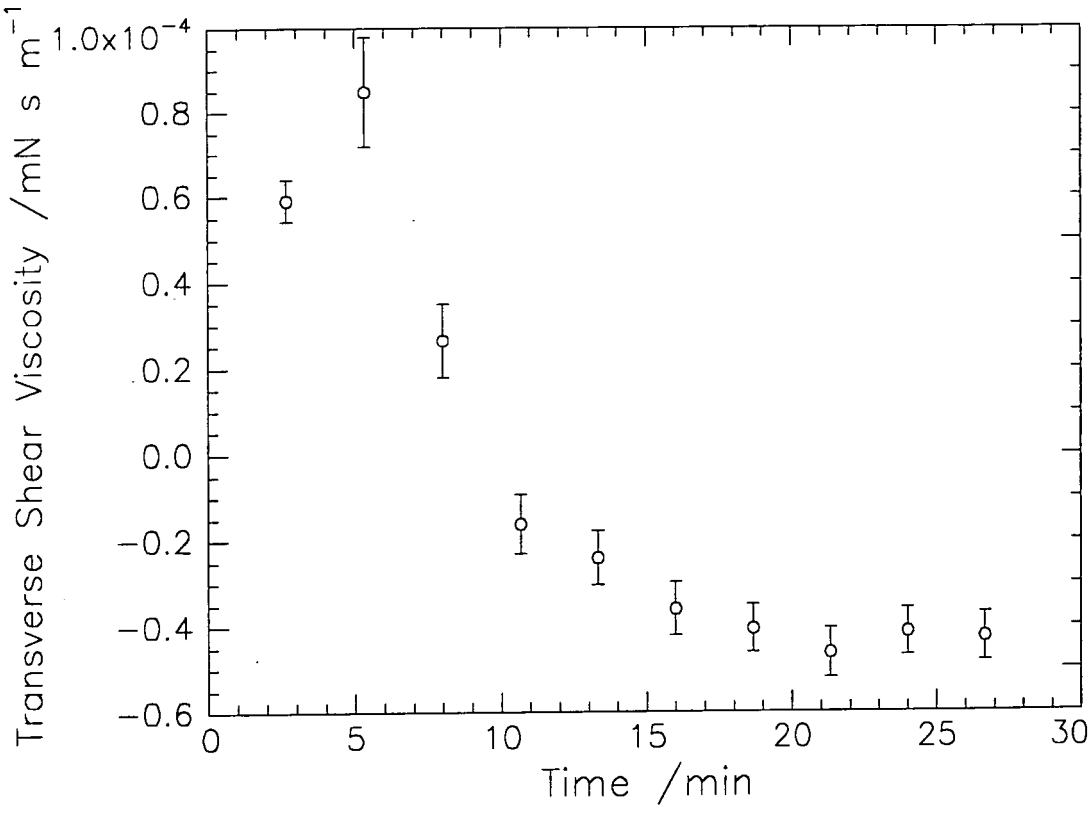

Figure 5.46: Variation of the transverse shear viscosity at 1.5mg m^{-2}

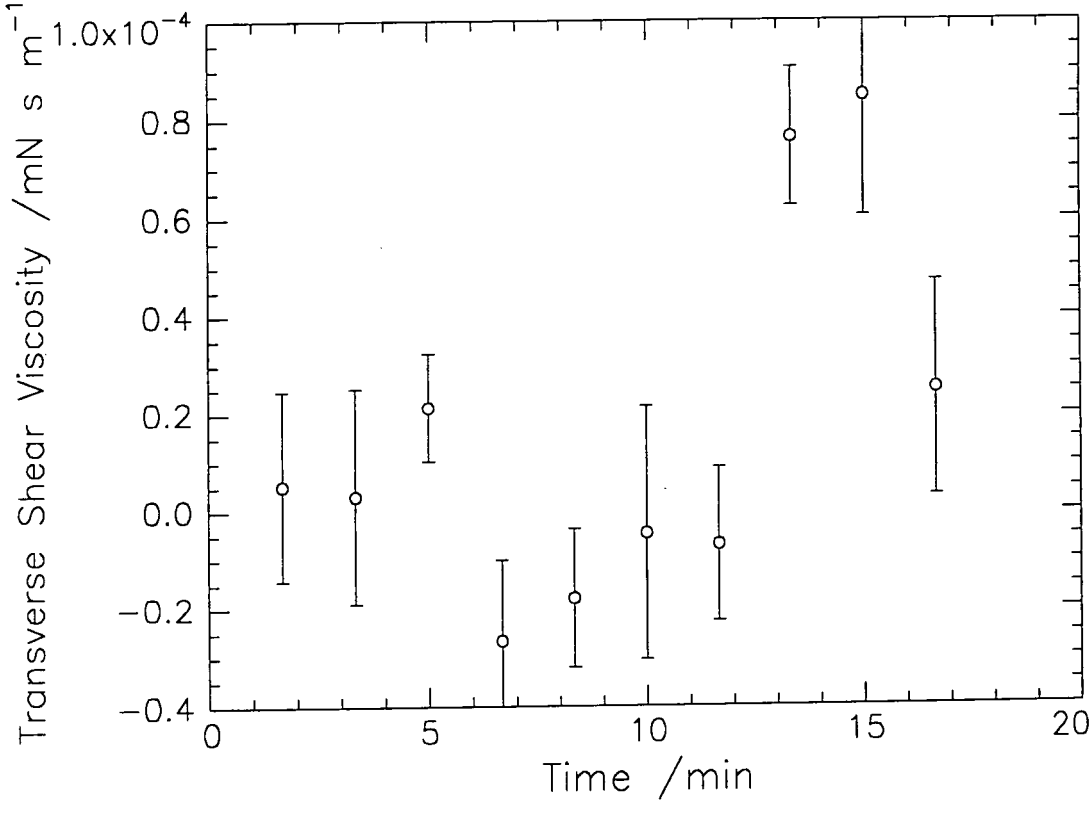

Figure 5.47: Variation of the transverse shear viscosity at 3mg m^{-2}

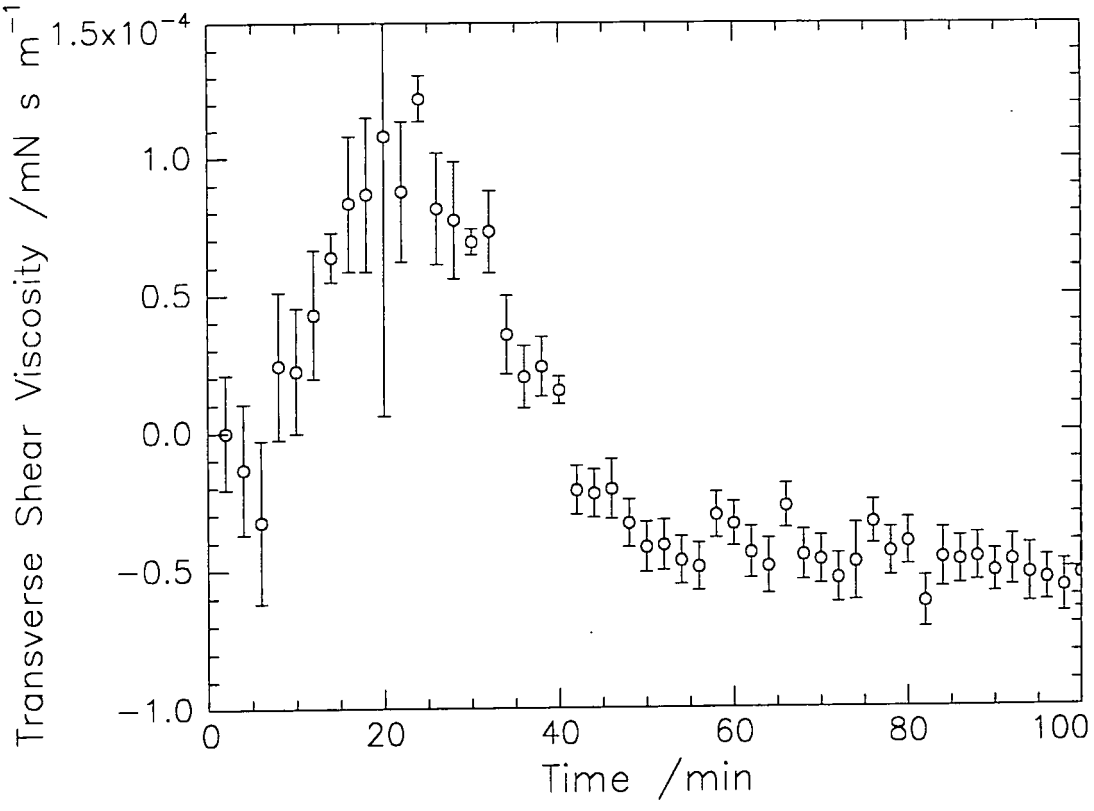

Figure 5.48: Variation of the transverse shear viscosity at 3mg m^{-2} over a longer time

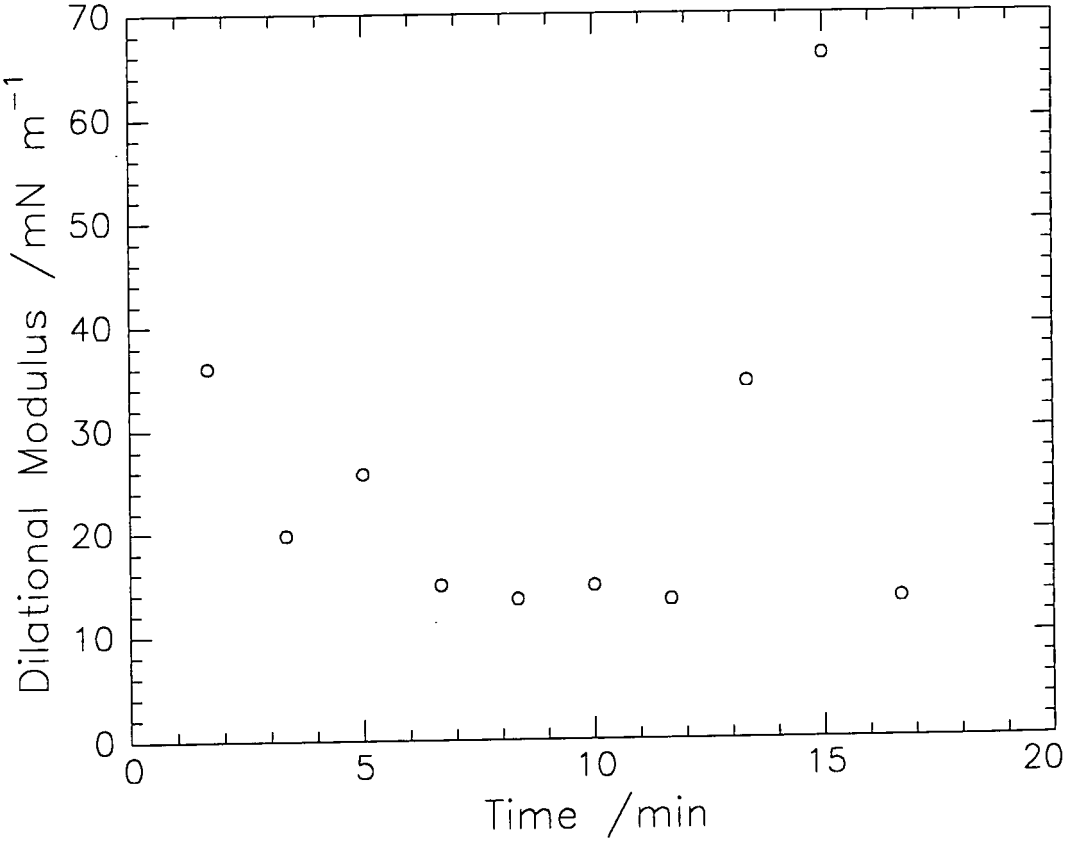

Figure 5.49: Variation of the dilational modulus at 3mg m^{-2}

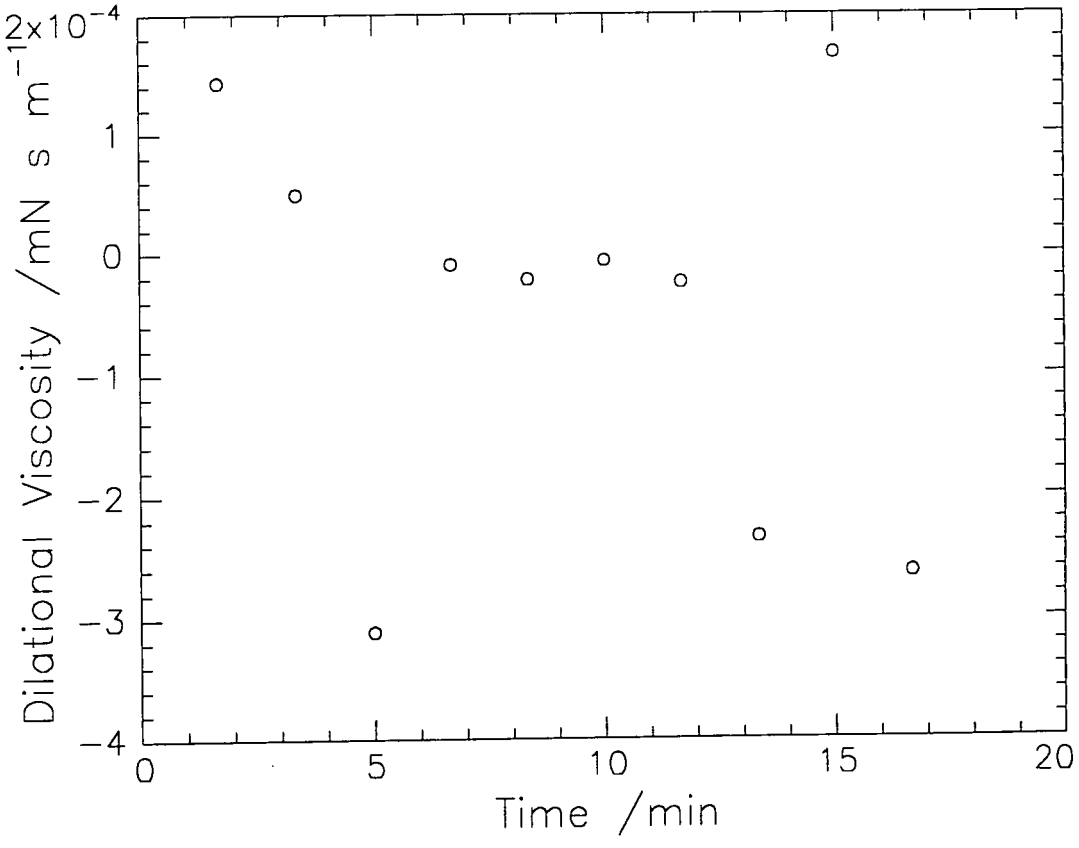

Figure 5.50: Variation of the dilational viscosity at 3mg m^{-2}

Both γ_o and γ' show the same trend as that observed for the frequency and damping, i.e. at 0.3mg m^{-2} the values are constant and at the other two concentrations, with time (longer for 3mg m^{-2} than for 1.5mg m^{-2}), the values become constant at similar values as for 0.3mg m^{-2}. The dilational modulus and viscosity values are difficult interpret due to the lack of errors associated with each value. This is due to the fitting routine which does not return sensible values for these errors whenever it is used, and not just in this case.

The value at which γ_o plateaus is about 79mN m^{-1}, which seems a physically impossible value which is greater than the surface tension of clean water and corresponds to a surface pressure of -6mN m^{-1}. This indicates that the processes occurring at the interface must be imparting greater structure and order to the interfacial region and

hence making it less expandable and a greater force would be required to increase the surface area, i.e. increased surface tension by definition.

γ' at 1.5 and 3mg m^{-2} show an increase followed by a decrease in value. The maximum value in both cases is circa 1×10^{-4}mN s m^{-1}, which is nearly an order of magnitude greater than the constant value obtained for PLMA. This indicates a considerable increase in molecule - molecule interactions at the interface which then decrease with time, eventually reaching negative values of γ'. As mentioned earlier, negative values may indicate that it is only an effective value, due to processes occurring at the interface which are not accounted for in the form used for $P(\omega)$ in the fitting routine. The effect of γ' is to increase the damping of the capillary waves, so a negative value indicates that a process is occurring that leads to a greater decrease in damping relative to the value of damping corresponding to $\gamma' = 0$.

There could be three possible causes for these observations, firstly, the LMA may be dissolving in the subphase, secondly, the LMA may be evaporating and thirdly, the LMA may be forming lenses on the surface. The first option seems unlikely due to the hydrophobic, oily nature of LMA, in addition, the results of a ^{1}H NMR carried out on D_2O which had a layer of HMHL monomer placed on top of it, shaken, and left to stand for five days, showed no sign of the presence of hydrogenous material in the D_2O. This means that option one can be discounted. Evaporation of the LMA from the interface would also appear unlikely due to LMA having a boiling point of 142°C at 4mm Hg (from Aldrich), which corresponds to circa 280°C at 760mm Hg. The vapour pressure (v.p.) of LMA could not be found in the literature, however, in Stull's list of vapour pressures [20] for over 1200 organic compounds, the values for various 12 carbon compounds were obtained. To obtain a v.p. of 1mmHg for each compound the following temperatures would be required, Dodecane 47°C, lauraldehyde 78°C, lauryl

alcohol 91°C and lauric acid 121°C. LMA would have a v.p. somewhere in this range, probably towards the top end of this range of temperatures due to the extra mass of the molecule. Options one and two would also give no explanation for observations such as the high value obtained for the surface tension, as both options result in loss of material from the interface, which would result in an increase in surface tension, but not beyond that of clean water. This leaves lens formation as the likely process occurring at the interface.

At 0.3mg m^{-2} there was no change in any of the parameters, indicating that when there is only a small amount of material at the interface it must be distributed in the form of lenses. When higher surface concentrations are used there must be so much monomer present that it is forced to spread over the surface, however, with time it eventually contracts and forms lenses. At 3mg m^{-2} it was observed that the changes occurred after a longer time delay, this is presumably due to the increased amount of material that has to move during the formation of the lenses.

During the formation of the lenses the molecules must migrate towards each other and this will lead to localised thickening of the layer and increased molecule - molecule interactions, this corresponds to the initial increase in the transverse shear viscosity. As lens formation nears completion, increasing amounts of subphase will be exposed, so on average the transverse shear viscosity of the area illuminated by the laser will decrease. At the same point in time, circa 15 minutes at 3mg m^{-2}, the dilational modulus also peaks corresponding to an increase in the rigidity of the layer in response to the high frequency dilational perturbations. This too can be accounted for in terms of increased molecule - molecule interactions which result in the monolayer having insufficient time to respond to the high frequency perturbations, hence it appears rigid. Once the lens formation is complete all the parameters tend to the value expected for

water, which will be due to a balance between bare subphase and lenses being illuminated, hence the damping, transverse shear viscosity and dilational modulus decrease and the surface tension increases. However, the surface tension increases to a value greater than that for pure water and the transverse shear viscosity drops below zero. Therefore, once the lenses have formed they must modify the interfacial region, perhaps by moving around, or by systematically growing and decaying. These processes are not accounted for in the dispersion equation and hence in $P(\omega)$, so there are no parameters to alter the fit and allow for the dynamic processes of the lenses. This leads to force fitting of the data and to obtain a fit the values of γ_o and γ' are forced to seemingly unrealistic values, i.e. they are effective values only. Also, as no variation with time is observed for the frequency or damping, the lens dimensions must be smaller than the illuminated area as discussed for PLMA in section 5.3.1.

From the isotherm studies, it is known that the nature of the monolayer is affected by changes in temperature. At 40°C the isotherm is typical of a very condensed monolayer, whereas at 25°C, which was the temperature at which the SQELS experiments were carried out, the isotherm was typical of an expanded monolayer. If the monolayer was left for one hour at 25°C and then compressed it produced an isotherm with the same features as those found at 40°C. Therefore, an increase in temperature must increase the mobility of the molecules so at 40°C lens formation is almost instantaneous and an isotherm for a condensed monolayer is produced, whereas at lower temperatures more time is required for the molecules to migrate into lenses.

In a similar SQELS study, Kawaguchi *et al* [21] studied spread monolayers of vinyl stearate and poly (vinyl stearate), although the monomer formed stable monolayers, there were still differences observed in the behaviour of the monomer and polymer. The changes in the propagation frequency and wave damping occurred at different surface

coverages, below 30Å^2/molecule for the monomer and at 55Å^2/segment for the polymer, reflecting the differences in packing at the interface. Such comparisons are made impossible in this case due to the instability of the LMA monolayer.

5.5 Conclusions

PLMA displays similar properties to those of PMMA, despite the addition of long side chains, whereas combining PMMA with PEO in a diblock copolymer introduces additional behaviour characteristic of PEO spread monolayers. Also the fact that PMMA is well below its T_g (circa 100°C for syndiotactic PMMA) and PLMA is well above its T_g does not seem to introduce any drastic differences in the behaviour of the polymer monolayers. PLMA shows differences between the static and dynamic dilational elasticities due to the condensed nature of the polymer in the monolayer which results in it having insufficient time to respond to the high frequency compressions, whereas during the slow rate of compression used to obtain the isotherm, the molecules have time to interpenetrate.

The polymer and monomer monolayers show vastly different behaviour. The carbonyl group and ester oxygen in the monomer must not be sufficiently hydrophilic to balance the hydrophobic side chain and maintain a stable spread layer. The polymer does not show such a drastic contraction of the molecules at the interface which is due to the restrictions placed on the configuration of the polymer molecule due to the backbone. The fact that the hydrophilic portion of the molecule is insufficiently hydrophilic to spread the monomer, the same must be true for the polymer, so it is no surprise that the polymer does not spread, but forms islands instead.

5.6 SQELS References

1. Lamb, H., in *Hydrodynamics*, p.627, 6th Edition, New York, 1945
2. Levich, V.G., in *Physiochemical Hydrodynamics*, p.603, Prentice - Hall, Englewood Cliffs, New Jersey
3. Bouchiat, M.A., Meunier, J., *J. Physique*, 561, **32**, 1971
4. Langevin, D., Meunier, J., Chatenay, D., *Surfactants in Solution*, Eds. Mittal, K.L., Lindman, B., Plenum, New York, 1991, **3**, 1984
5. Lucassen - Reynders, E.H., Lucassen, J., *Adv. Colloid Int. Sci.*, 330, **114**, 1969
6. Goodrich, F.C., *Proc. R. Soc. Lond.*, 341, **A374**, 1981
7. Earnshaw, J.C., McGivern, R.C., *J. Coloid and Interface Sci.*, 36, **123**, 1988
8. Earnshaw, J.C., McGivern, R.C., McLaughlin, A.C., Winch, P.J., *Langmuir*, 649, **6**, 1990
9. Earnshaw, J.C., Winch, P.J., *J. Phys.: Condens. Matter 1*, 7187, 1989
10. Kawaguchi, M., Sauer, B., Yu, H., *Macromolecules*, 1735, **22**, 1989
11. Taylor, M.R., Richards, R.W., submitted to *J. Chem. Soc.: Faraday Trans 2*
12. Earnshaw, J.C., Crilly, J.F., *Biophys. J.*, 197, **41**, 1983
13. Earnshaw, J.C., McGivern, R.C., Winch, P.J., *J. Phys., France*, 1271, **49**, 1988
14. Earnshaw, J.C., McCoo, E., *Langmuir*, 1087, **11**, 1995
15. Earnshaw, J.C., Winch, P.J., *J. Phys.: Condens. Matter 2*, 8499, 1990
16. Rochford, B.R., Richards, R.W., Taylor, M.R., Submitted to *Macromolecules*
17. Ferry, J.D., *Viscoelastic Properties of Polymers*, 3rd edition, J. Wiley, New York, 1980
18. Earnshaw, J.C., Crawford, G.E., *Biophys. J.*, 87, **52**, 1987
19. Genz, A., Holzwarth, J.F., *Coll. Polymer Sci.*, 484, **263**, 1985

20. Stull, D.R., *Ind. and Eng. Chem.*, 517, **39**, 1947

21. Kawaguchi, H., Chen, Y.-L., Yu, H., Zografi, G., *Langmuir*, 31, **3**, 1987

6. SMALL ANGLE NEUTRON SCATTERING

6.1 Theoretical Background

The basis of neutron scattering is the measurement of the intensity of neutrons which have been scattered through various angles by encounters with the nuclei present in a sample. Following the usual convention for neutron experiments, the variation in scattered intensity is determined as a function of the scattering vector Q (= $(4\pi/\lambda)\sin\theta$). The scattering properties of neutrons are analogous to those for electro - magnetic radiation, this can be visualised by remembering that neutrons have wave properties as well as their particulate nature, which are related via de Broglie's formula

$$\lambda = h/mv \qquad 6.1$$

where h is Planck's constant and λ is the wavelength associated with a particle in terms of its mass (m) and velocity (v). The velocity of neutrons used in the experiments correspond to a wavelength in the order of 10^{-10}m, so they are ideal for investigating structures at the atomic or molecular level.

The most important interaction between the sample and the incident neutrons is that between the neutrons and the nucleus. When such an interaction takes place with a nucleus that is vibrating, rotating or translating, there is a finite probability that an exchange of energy may occur. If this occurs the neutron is said to be inelastically scattered and the neutron may gain energy from or lose energy to the molecular motion. The quantised energy associated with vibrations is comparable to the energy of the neutrons, so if a quantum of vibrational energy is gained or lost, distinct shifts in the

neutron energy occur. The quantised energy levels associated with rotational and translational motions are negligibly small compared to the neutron energies and any exchange involving these motions leads to broadening of the initial neutron energy distribution. If no exchange of energy takes place when the neutrons are scattered by the nucleus, then the process is said to be elastic and the scattered neutrons depend only on the static structure of the sample.

The nature of the neutron - nucleus interaction determines the scattering properties of a material. Although the form of this interaction is not known, it is a short range interaction (~ 10^{-13}m) with dimensions less than the wave length of the incident neutrons, so the scattering contains only an S - wave component and is isotropic. It is characterised by a single parameter b, the scattering length, and can be modelled using the Fermi - pseudo potential, which for the interaction between a neutron and a nucleus, is given by

$$V(r) = -\frac{h^2}{2\pi m} b\,\delta(\mathbf{r}-\mathbf{R}) \qquad 6.2$$

where **R** is the position of the scattering nucleus, **r** is a position vector and $\delta(x)$ is the Dirac delta function.

The probability of a neutron being scattered somewhere in all space is termed the cross section and is represented by σ. In neutron scattering experiments it is the partial differential scattering cross section which is measured and this describes the fraction of neutrons that are scattered into a solid angle $d\Omega$ (equal to $\sin\theta d\theta d\phi$), shown in figure 6.1. For a small solid angle, the number of neutrons scattered into the angle per second depends on their energy (E), the orientation of $d\Omega$ and on the intensity of the beam, I_o

(defined by the number of neutrons per unit area and per unit time), so the partial differential cross section is given by

$$I_o \frac{d^2\sigma}{d\Omega dE} d\Omega dE \qquad 6.3$$

For elastic scattering, no energy change takes place during the scattering process so equation 6.3 can be simplified to give

$$I_o \frac{d\sigma}{d\Omega} d\Omega \qquad 6.4$$

where $d\sigma/d\Omega$ is known as the differential scattering cross section.

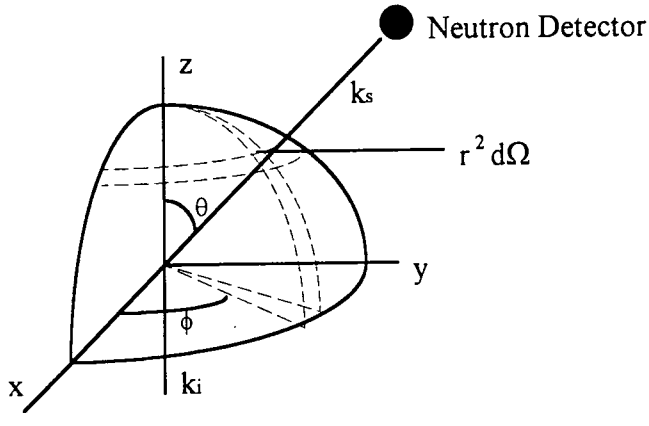

Figure 6.1: The geometry of neutron scattering for an incident neutron with initial wavevector k_i and scattered wavevector k_s

Elastic scattering has two components, coherent and incoherent scattering. The coherent scattering arises from spatial correlations between nuclei with the same scattering length, but different from the bulk of the sample, for example if some polymer

molecules are deuterated. This leads to interference effects between waves scattered from the labelled nuclei and the coherent scattering contains the structural information which can be described in terms of structure factors S(Q) which are characteristic of the chain configurations. Incoherent scattering occurs if there are no spatial correlations between nuclei, then the scattering obtained is random, isotropic and has no dependence on Q, so no structural information is obtained from incoherent scattering.

The differential scattering cross section can be split into coherent and incoherent contributions

$$\frac{d\sigma}{d\Omega} = \left(\frac{d\sigma}{d\Omega}\right)_{coh} + \left(\frac{d\sigma}{d\Omega}\right)_{incoh} \qquad 6.5$$

where

$$\left(\frac{d\sigma}{d\Omega}\right)_{coh} = \left|\bar{b}\right|^2 \left|\sum_j \exp\left(iQ.R_j\right)\right| \qquad 6.6$$

$$\left(\frac{d\sigma}{d\Omega}\right)_{incoh} = N\overline{\left|b - \bar{b}\right|^2} \qquad 6.7$$

where R_j is the position of nuclei j and N is the number of nuclei in the sample. Both the coherent and incoherent scattering depend on the scattering lengths of the nuclei present in the sample, however, when scattering from polymer chains is being considered the Q range does not extend high enough for the internal structure of the monomers to be investigated, so the scattering from monomer segments, or groups of labelled atoms within the monomer, is considered where the scattering lengths of each

group are b_H for the hydrogenous atoms and b_D for the deuterated atoms. The coherent scattering component, represented as I(Q), follows the general form

$$I(Q) = \left(\frac{b_H}{v_H} - \frac{b_D}{v_D}\right)^2 S(Q) \qquad 6.8$$

where v_i is the volume of the hydrogenous and deuterated components and S(Q) is the scattering structure factor. de Gennes[1] has calculated S(Q) for polymer blends using the incompressible random phase approximation which gives

$$S^{-1}(Q) = \frac{1}{\phi N_A g_D(R_{gA}, Q)} + \frac{1}{(1-\phi) N_B g_D(R_{gB}, Q)} - 2\chi_{FH} \qquad 6.9$$

where ϕ is the volume fraction of component A and as the blend is assumed to be incompressible, $(1-\phi)$ is the volume fraction of component B, N_i is the degree of polymerisation of the component and χ_{FH} is the Flory - Huggins interaction parameter[2], defined as

$$\chi_{FH} = \frac{z_c\left(2\varepsilon_{AB} - \varepsilon_{AA} - \varepsilon_{BB}\right)}{2k_B T} \qquad 6.10$$

where ε_{ij} are the nearest neighbour pair exchange interaction energies between monomer i and j and z_c is the co - ordination number. $g_D(R_g,Q)$ is the Debye function[3] which describes the intensity of scattering from a single Gaussian polymer chain with radius of gyration R_g

$$g_D(R_g, Q) = \left(\frac{2}{u^2}\right)(\exp(-u) + u - 1) \qquad 6.11$$

where $u = Q^2R_g^2$. Therefore, the coherent elastic neutron scattering for a blend with segment volumes v_A and v_B and scattering lengths b_A and b_B is given by[4]

$$I(Q) = v_o\left(\frac{b_A}{v_A} - \frac{b_B}{v_B}\right)^2\left(\frac{v_o}{\phi N_A v_A g_D(R_{gA}, Q)} + \frac{v_o}{(1-\phi) N_B v_B g_D(R_{gB}, Q)} - 2\chi\right)^{-1} \qquad 6.12$$

where v_o is a reference volume given by

$$v_o = \left(\frac{\phi}{v_A} + \frac{(1-\phi)}{v_B}\right)^{-1} \qquad 6.13$$

In equation 6.12 the Flory - Huggins interaction parameter has been replaced by an effective interaction parameter χ as the interaction parameter determined from small angle neutron scattering is not the simple χ_{FH} given by equation 6.10, but is a function of composition and molecular weight.

6.2 Experimental

The samples used for the SANS experiments were mixtures of each of the deuterated isomeric variations with the fully hydrogenous PLMA in 10/90% w_D/w_H proportions and 100% samples of each PLMA variations. The mixtures were prepared by weighing out the appropriate masses of each polymer, then dissolving the polymer in 2 - butanone and mixing the solutions of the polymers to produce the desired polymer mixture. The amount of solvent used was limited so that the final mixed solution was approximately 5% w/v. This solution was then poured into methanol, which precipitates the mixed polymer, the methanol removed and the remaining polymer dried under vacuum at 40°C. The polymer samples then had to be placed between two quartz discs (circa 1mm thick) which were separated by a 1mm thick Teflon washer (internal diameter circa 13mm). Due to the viscous, tacky nature of PLMA, the best method to achieve this was to place one of the quartz plates on a flat surface with the Teflon washer on top of it. A quantity of PLMA was then deposited in the centre of the plate, weights placed around the edge of the washer and then the polymer was allowed to flow to fill the remaining space which took circa 24 to 48 hours depending on the amount of air trapped in the polymer which had to migrate to the surface. Once a homogeneous layer was formed the level was noted and more polymer was added if required, as a slightly convex surface was required before the second plate could be placed on top to ensure no air was present in the sample. Once the polymer was between the quartz plates, the plate/polymer combination was placed in a brass holder, with a diameter slightly greater than the quartz plates, and then a brass ring was screwed down to firmly hold the plates together, ensuring no polymer could escape. To make sure no damage was inflicted on the quartz plates, Teflon rings were placed on the base of the brass holder and on top of

the outer quartz plate before the sample was screwed in. The brass holder was then placed into an aluminium ring (outer diameter circa 50mm) which was the correct size to fit the sample holder.

The small angle neutron scattering experiments were carried out using the LOQ diffractometer at the UK pulsed neutron source, ISIS, at the Rutherford Appleton Laboratories, Didcot, Oxfordshire and it is shown schematically in figure 6.2.

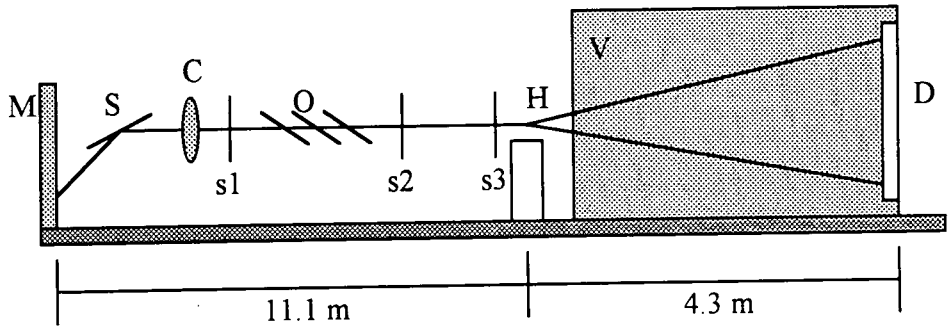

Figure 6.2: Schematic diagram of the LOQ diffractometer

The incident neutron beam initially passes through a liquid hydrogen moderator (M) to reduce the energy of the neutrons produced in the spallation process. The emerging beam contains a wide spread of energies (and hence wavelengths) which has to be narrowed by selecting a particular range. The initial selection is carried out by the Soller bending mirror (S) which deflects all but the shortest wavelength neutrons (< 2Å) and this also prevents the detector (D) from being in the direct line of the neutron source which reduces the background radiation. The chopper (C) operated at 50Hz and selects a wavelength range of 2 to 10Å, any longer wavelength neutrons originating from earlier pulses are removed by the frame overlap mirrors (O). The neutrons are collimated by three apertures (s1, s2 and s3) which can be varied in dimension, in this case a beam of

10mm was produced at the sample position. The samples were placed in a nine position sample holder (H) which could be temperature controlled with a sinusoidal variation of $\pm 2^{\circ}C$ at each selected temperature. The position of the rack was driven by the LOQ CAMAC electronics after initial alignment using a laser which was coincident with the neutron beam. The neutron flight path from the source to the sample position and from the sample position to the detector are evacuated to minimise the loss of neutrons due to collisions between the neutrons and air molecules. The flight path from the sample to the detector is simply an evacuated vacuum tank (V) which is placed in front of the detector. Both flight paths are heavily shielded by solid steel and borated wax to reduce the background radiation. The neutrons scattered by the sample are detected by an area detector (D) which consists of $^{3}He\text{-}CF_4$ filled $1cm^2$ pixels which are combined to produce an active area of 64cm by 64cm. The detector area together with the wavelength range and the geometry of LOQ produces an available Q range of 0.01 to 0.17Å^{-1}.

Each sample was run at 25, 65 and $125^{\circ}C$ and at each temperature two measurements were made. Firstly, the transmission of the sample was determined by placing a small collimation aperture in the incident beam and a scintillation monitor immediately after the sample position. This measurement, in conjunction with a similar measurement of the neutron beam without the sample, are used to calculate the transmission. Secondly, the small angle scattering was measured using the area detector and this is a function of θ, where 2θ is the scattering angle from the direct beam, ϕ, the azimuthal angle, and λ, the neutron wavelength. The raw data was then corrected for the incident beam flux, detector efficiency and sample transmission, in addition the data is converted from a function of wavelength and θ to a function of Q. Finally, as the data is radially isotropic the data can be radially averaged to leave the data as a function of Q

only, I(Q). These transformations were carried out using the COLETTE program at the Rutherford - Appleton Laboratory.

To obtain absolute scattering intensities from the scattering data, further calibration has to be carried out. For pulsed neutron sources the scattering from polymer blends has been used for the calibration of SANS data [5] because they produce very strong scattering at low Q and this is important as it minimises the time required for the calibration measurement. The scattering from a blend containing 0.47 volume fraction of deuterated poly(styrene) in hydrogenous poly(styrene) was used in these experiments and a random copolymer of deuterated poly(styrene) and hydrogenous poly(styrene) with the same volume fraction of deuterated poly(styrene) as the blend was used to measure the background scatter for the blend. The polystyrene blend data, after background subtraction, was fitted using the incompressible random phase approximation (equation 6.12) using the FORTRAN program BANTAM [6], allowing the normalisation constant and the radii of gyration for the hydrogenous and deuterated components to vary, but with the constraint $R_{gD} = R_{gH}$. Polystyrene is known to scatter in an ideal manner according to the Debye function [7] and the constants used in the fit were $b_H = 2.328\times10^{-12}$cm, $b_D = 10.660\times10^{-12}$cm, the reference volume = 1.725×10^{-22}cm^3, the average degree of polymerisation was 800 (determined from SEC results in tetrahydrofuran) and χ was fixed at zero. The value of the normalisation constant (k_n) was found to be 0.642 and R_g was equal to 66.4Å, the fit to the experimental data is shown in figure 6.3. To convert the raw data obtained from COLETTE to absolute units, the data is multiplied by $1 / k_n$, all of the data obtained from the experiments has been converted using this procedure.

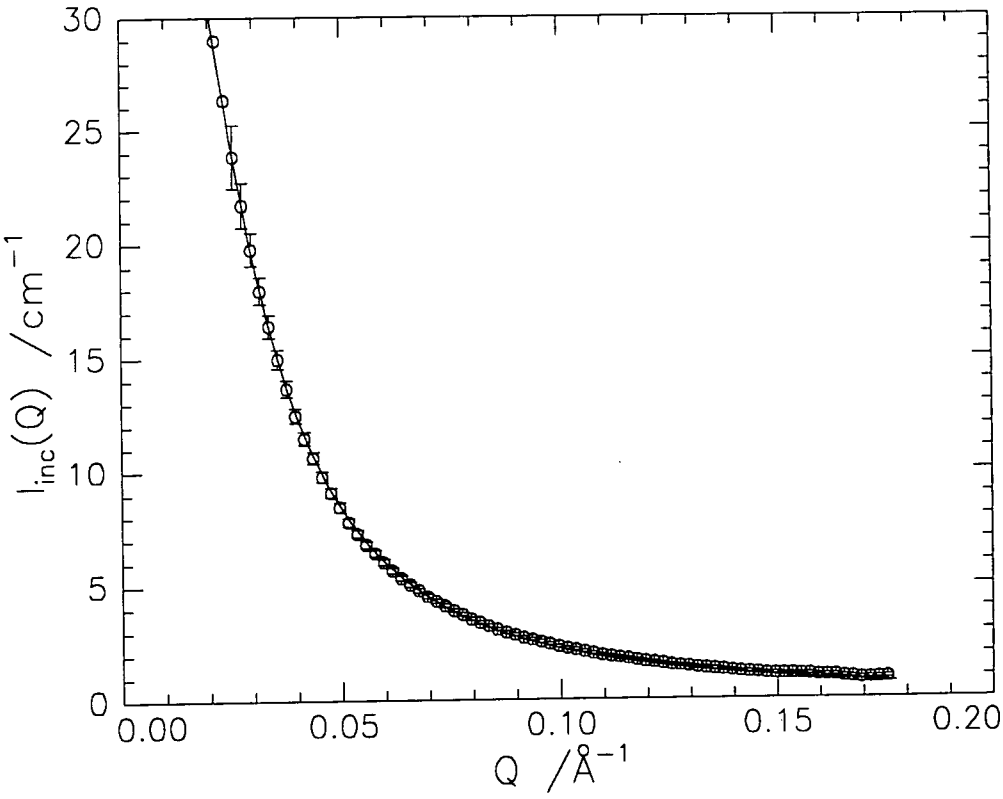

Figure 6.3: Fit to the calibration sample data (o) using the incompressible random phase approximation (—)

There are several sources of error involved with this calibration procedure which may produce inaccuracies in the normalisation constant. The first source of error in the determination of k_n arises from the value used for the degree of polymerisation which was determined from the molecular weights of the polymers obtained from SEC measurements in THF, however, if the results from SEC measurements in chloroform were used, which produced a lower molecular weight and therefore a lower degree of polymerisation, a 20% increase occurred in the value obtained for k_n . The values from the THF instrument were used as it has a double detection system, both refractive index and viscosity, whereas the chloroform machine only has a single refractive index detector. A second source of error arises due to uncertainty in the densities and, therefore, in the value of the segmental volume used. The final source of error is due to the assumption that χ is equal to zero, which may be valid for the scattering of low

molecular weight polymers according to Wignall [5], however, for the d-PS/h-PS system χ has been given by Bates [8] in the range 1.6 to 3.7×10^{-4} which lead to k_n values which are around 10% lower than for $\chi = 0$. The effects of each of these sources of error have been studied [9] and the main one was found to be the inaccuracy in the molecular weight determination, however, as the same uncertainty applies to all the corrected data it should all be on the same relative scale.

To obtain the elastic coherent scattering of the polymer mixtures the background scattering has to be subtracted. This background consists of elastic incoherent and inelastic incoherent scattering from the sample and the quartz plates containing the sample. To obtain the background, samples of the pure hydrogenous and deuterated isotopic variations were run at each temperature corresponding to those for the mixtures. The scattering cross section from each of the pure polymers was combined together in the same ratio as each mixture for which the background is needed and as the pure polymers show no elastic coherent scattering, the resulting summation is a measure of all the incoherent and inelastic scattering produced by the mixtures. The sum of the scattering from the pure polymers was then subtracted from the scattering of the mixture, which also results in the scattering from the quartz plates being removed as all the samples used identical plates. Figure 6.4 shows the incoherent scattering for each of the pure isotopic variations of PLMA at room temperature, similar patterns were obtained at the two higher temperatures. The fact that hydrogen has a much larger incoherent scattering power than deuterium is clearly visible from the increasing incoherent scattering levels as the amount of hydrogen increases in the polymer.

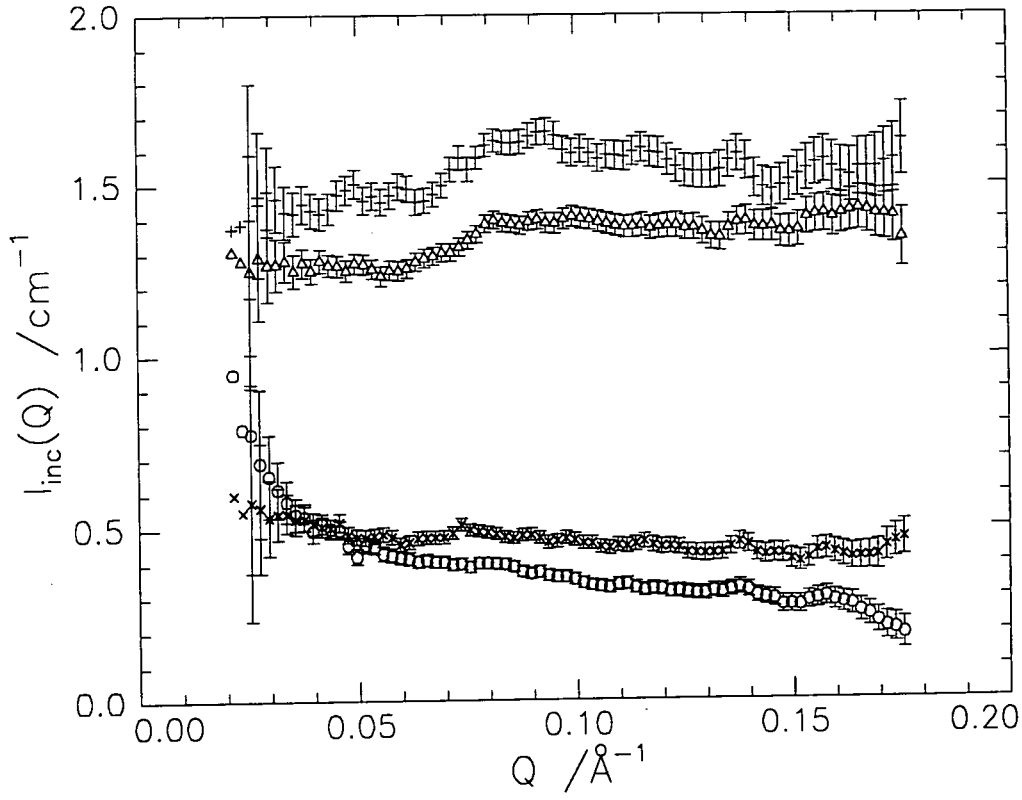

Figure 6.4: Incoherent scattering from the pure polymer samples at 25°C, DMDL (o), HMDL (×), DMHL (Δ) and HMHL (+)

6.3 Results

As for the reflectivity experiments, the maximum value for the scattering data at low Q followed the trend expected from consideration of the scattering lengths of the deuterated monomers. This is illustrated in figures 6.5(a) to (c), where the scattering data for each of the polymer mixtures at each temperature is shown.

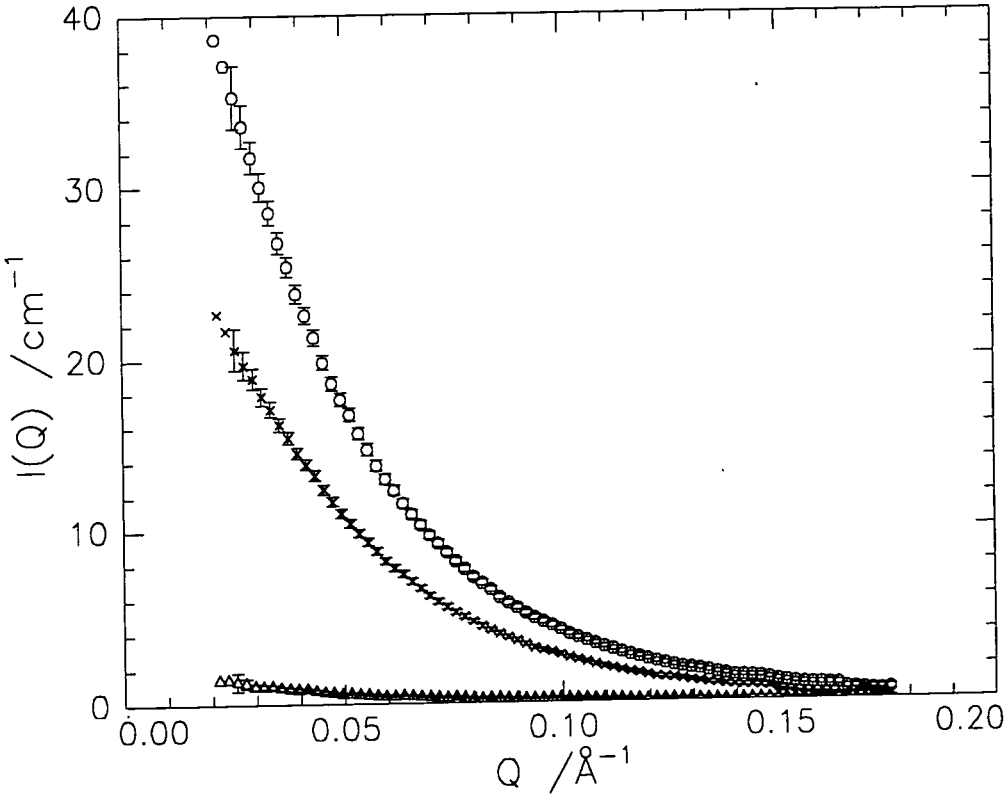

Figure 6.5(a): Scattering data for each of the polymer mixtures at 25°C, DMDL (o), HMDL (×) and DMHL (Δ)

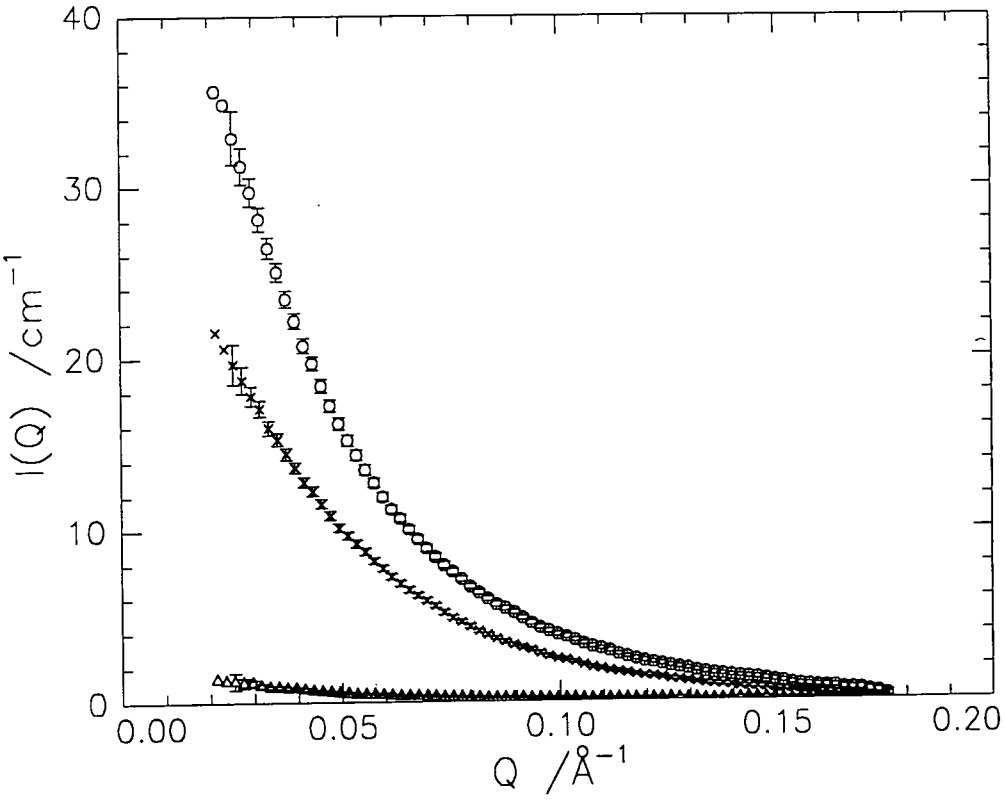

Figure 6.5(b): Scattering data for each of the polymer mixtures at 65°C, DMDL (o), HMDL (×) and DMHL (Δ)

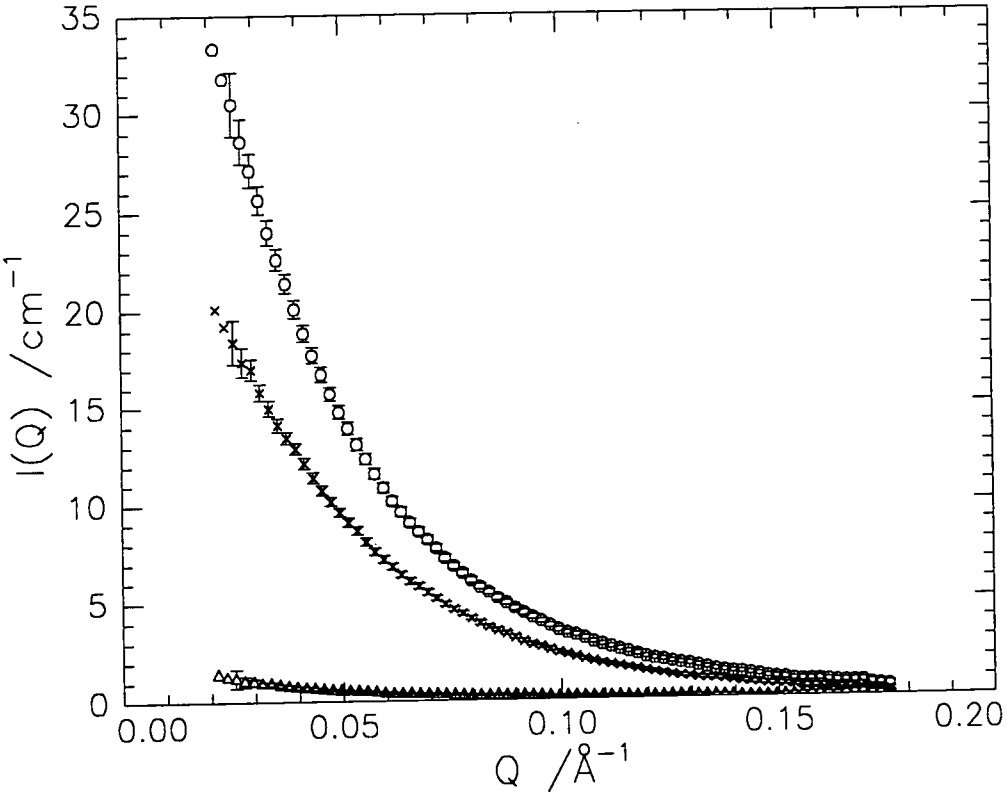

Figure 6.5(c): Scattering data for each of the polymer mixtures at 125°C, DMDL (o), HMDL (×) and DMHL (Δ)

The effect of temperature on the scattering patterns is shown in figures 6.6 (a) to (c).

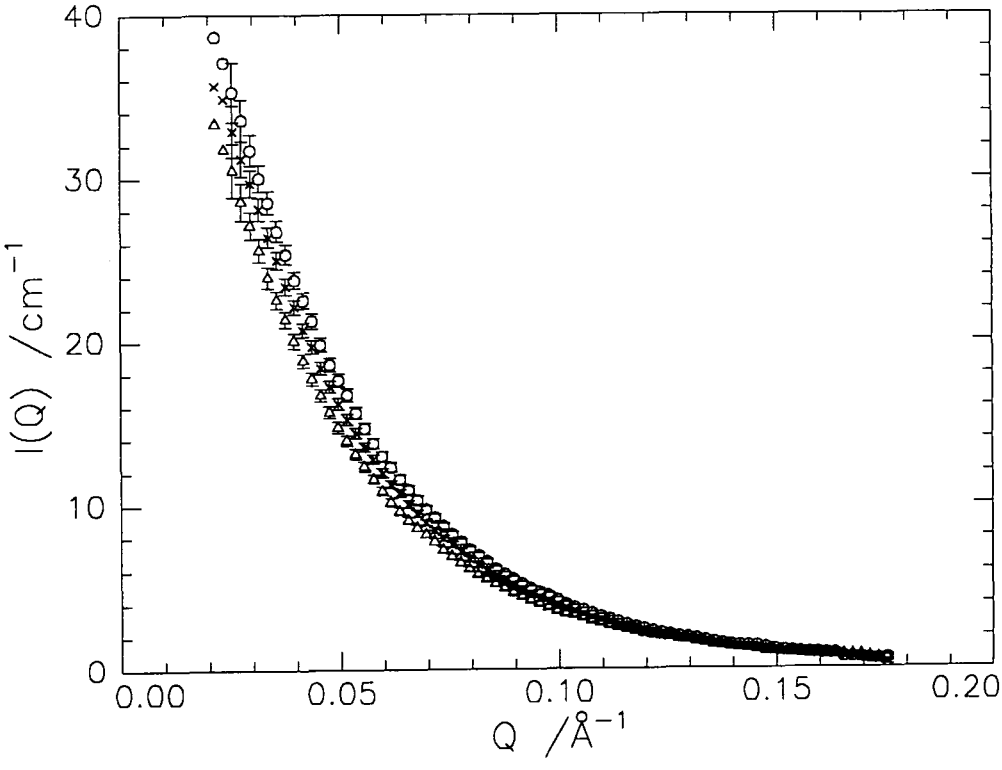

Figure 6.6(a): Scattering from DMDL mixtures at 25°C(o), 65°C (×) and 125°C (Δ)

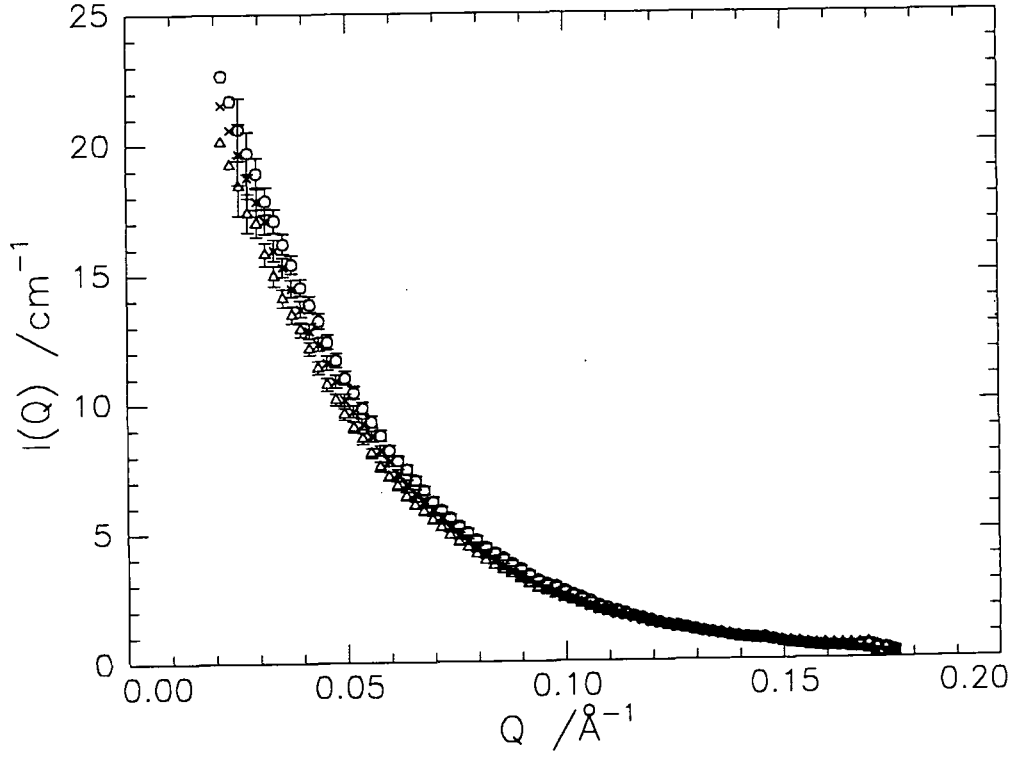

Figure 6.6(b): Scattering from HMDL mixtures at 25°C (o), 65°C (×) and 125°C (Δ)

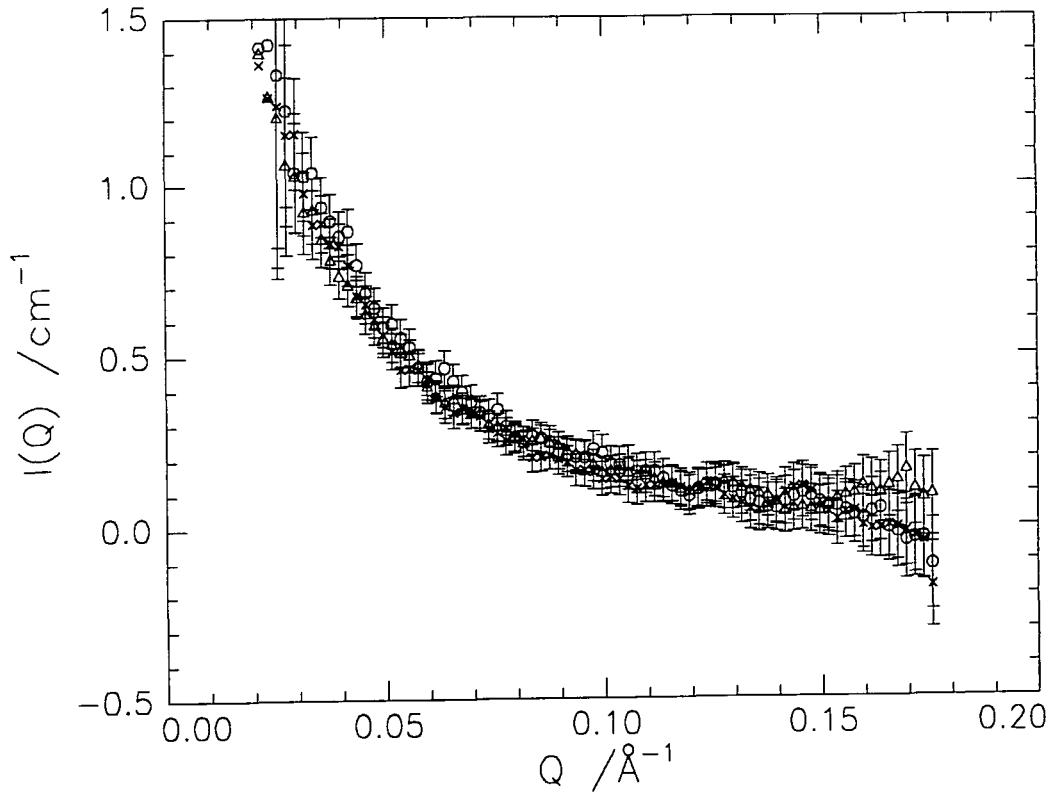

Figure 6.6(c): Scattering from DMHL mixtures at 25°C (o), 65°C (×) and 125°C (Δ)

The radius of gyration at each temperature for PLMA can be determined from the DMDL mixture scattering data by plotting the data as 1/I(Q) versus Q^2 according to the expression by Zimm

$$\frac{1}{I(Q)} = \frac{1}{I(0)}\left(1 + Q^2 R_{g,z}^2\right) \qquad 6.14$$

This produces a linear plot in the low Q region ($Q < R_g^{-1}$) where the expression is valid, from which the z average radius of gyration can be obtained. Such a Zimm plot is shown in figure 6.7.

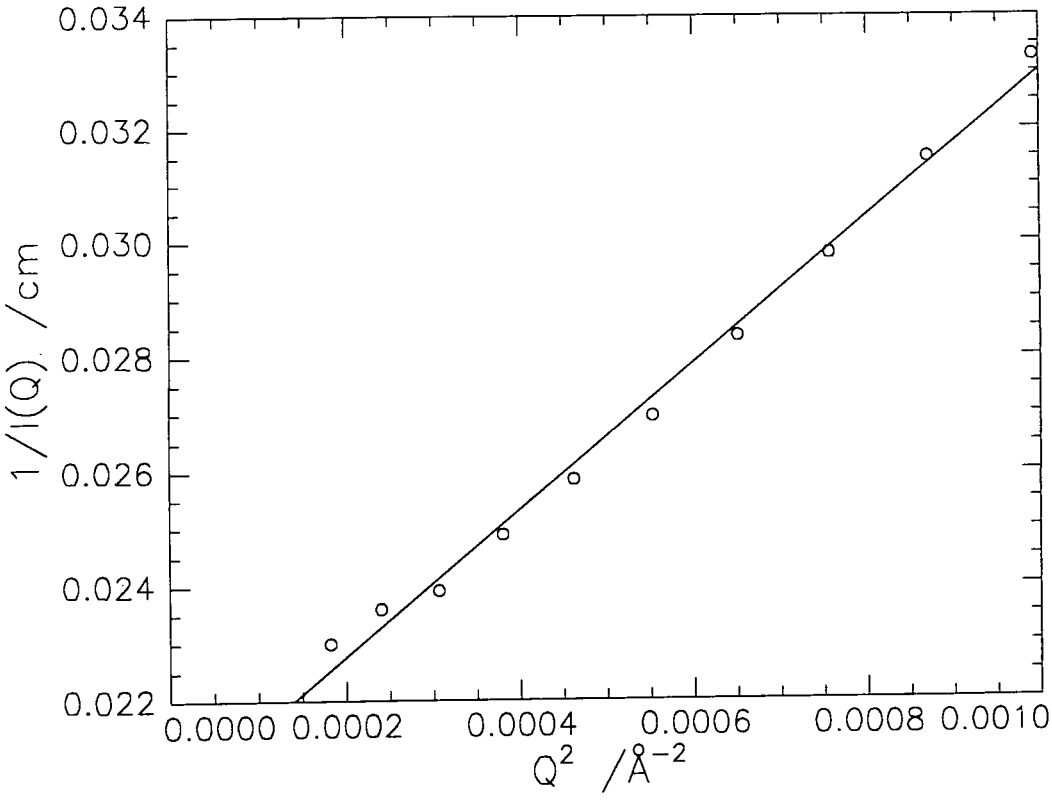

Figure 6.7: Zimm plot of DMDL data at 25°C with a least squares fit

The values of the z average radius of gyration obtained can be converted to the weight average radius of gyration, $R_{g,w}$, which are required for further calculations, using the relationship

$$R_{g,z}\left(\frac{h+1}{h+2}\right) = R_{g,w} \qquad 6.15$$

where $h = (M_w / M_n - 1)^{-1}$. The values of $R_{g,w}$ can be used to calculate $\langle r^2 \rangle_o$, which is the average mean square of the polymer chain end to end distance of the unperturbed dimension, using the relationship

$$\langle r^2 \rangle_o = 6R_{g,w}^2 \qquad 6.16$$

The values for $R_{g,w}$ and $\langle r^2 \rangle_o$ determined at each temperature are given in table 6.1.

TEMPERATURE / °C	$R_{g,w}$ /Å	$\langle r^2 \rangle_o$ / Å
25	32.9	6495
65	34.1	6977
125	36.0	7776

Table 6.1: Values of the weight average radius of gyration and mean square end to end distance for PLMA at each temperature

The radii of gyration for HMDL and DMHL can be determined in the same way as for DMDL and the values obtained are given in table 6.2.

POLYMER	TEMPERATURE / °C	$R_{g,w}$ / Å
HMDL	25	33.3
	65	33.6
	125	33.9
DMHL	25	43.4
	65	32.7
	125	46.0

Table 6.2: Radius of gyration values determined from the data for HMDL and DMHL

The values obtained for HMDL are of the same order as those obtained for DMDL, but do not show the same increase. This indicates that although the polymer molecule as a whole expands as the temperature is increased, the correlations between

the positions of the atoms in the side chains remain fairly constant, so when only the scattering from the side chains is used to determine the radius of gyration no major increase is observed. The radius of gyration values obtained from the DMHL data are less certain due to the poor signal to noise ratio, so it is not possible to say if the trend observed is valid, which would seem unlikely as the value at 65°C is much lower than the other two.

The values of $\langle r^2 \rangle_o$ can be used to determine the effect of short range and steric interactions on the dimensions of the polymer chains. These effects can be expressed via the characteristic ratio, C_∞, or the steric parameter, σ. C_∞ provides an indication of the degree to which the short range effects cause the polymer chains to expand and is given by the ratio of the experimentally determined mean square end to end distance, $\langle r^2 \rangle_o$, to the value calculated for the mean square end to end distance in the absence of any interactions (freely jointed chain), r_f^2, which is given by

$$r_f^2 = nl^2 \qquad 6.17$$

where n is the number of bonds in the polymer chain and l is the length of the bonds. σ represents the effect of steric hindrances on the average chain dimensions. It is expressed in terms of the square root of the ratio between $\langle r^2 \rangle_o$ and the mean square end to end distance calculated for a chain which has restrictions placed on its configuration due to the valence angles (θ) between each chain atom (freely rotating chain), which is given by

$$\langle r^2 \rangle_{of} = nl^2 \left(\frac{1 - \cos\theta}{1 + \cos\theta} \right) \qquad 6.18$$

For an all carbon backbone, $\theta \approx 109^{\circ}$ and $\cos\theta = -1/3$, so equation 6.18 becomes

$$\langle r^2 \rangle_{of} = 2nl^2 \qquad 6.19$$

The values calculated for C_∞ and σ at each temperature are given in table 6.3.

TEMPERATURE /°C	C_∞	σ
25	10.01	2.24
65	10.77	2.32
125	12.00	2.45

Table 6.3: Characteristic ratio and steric parameter for PLMA at each temperature

With increasing temperature the dimensions of the chains increase as the main chains and the lauryl side chains become more mobile. The values obtained here for PLMA can be put into context by considering the literature values for a range of straight chain methacrylates (from Polymer Handbook, Brandrup and Immergut 3rd edition) shown in table 6.4

POLYMER	TEMP /°C	C_∞	σ	TECHNIQUE AND SOLVENT
PMMA	25	7.50	1.94	VS in various solvents
PbutylMA	23	8.50	2.06	LS in 2 - propanol
PhexylMA	33	10.50	2.29	VS in 2 - propanol
PoctylMA	20	9.60	2.19	VS in butanol
"	17	10.40	2.28	LS in butanol
PLMA	13	12.90	2.54	VS in isopropyl acetate
"	30	13.40	2.59	VS in pentanol

Table 6.4: Literature values of C_∞ and σ for various methacrylates, key to techniques used is VS = viscosity measurements and LS = light scattering

From table 6.4 it can be observed that the values of the parameters obtained are not only temperature dependant but also vary depending on the technique used in their determination. Generally, the values of C_∞ and σ increase as the size of the ester group increases, which indicates that the degree of chain extension increases as the ester group chain length increases. The values determined from the SANS experiments for PLMA are in the region between those for poly (octyl methacrylate) and PLMA found in the literature which are given in table 6.4. The discrepancy is probably due to the vastly different techniques used to determine these values, with the literature values being obtained by experiments on dilute solutions, so polymer - solvent interactions will be the main limiting restriction on the chain dimensions, whereas the parameters determined here are due to chains in the solid state and, therefore, will have greater restrictions placed on the chain configurations, hence the values of C_∞ and σ determined from the SANS experiments are lower than the literature values, indicating that the chains are not as expanded.

The temperature dependence of $\langle r^2 \rangle_o$ can be determined from the slope of a plot of $\ln\langle r^2 \rangle_o$ versus temperature, which is shown in figure 6.8.

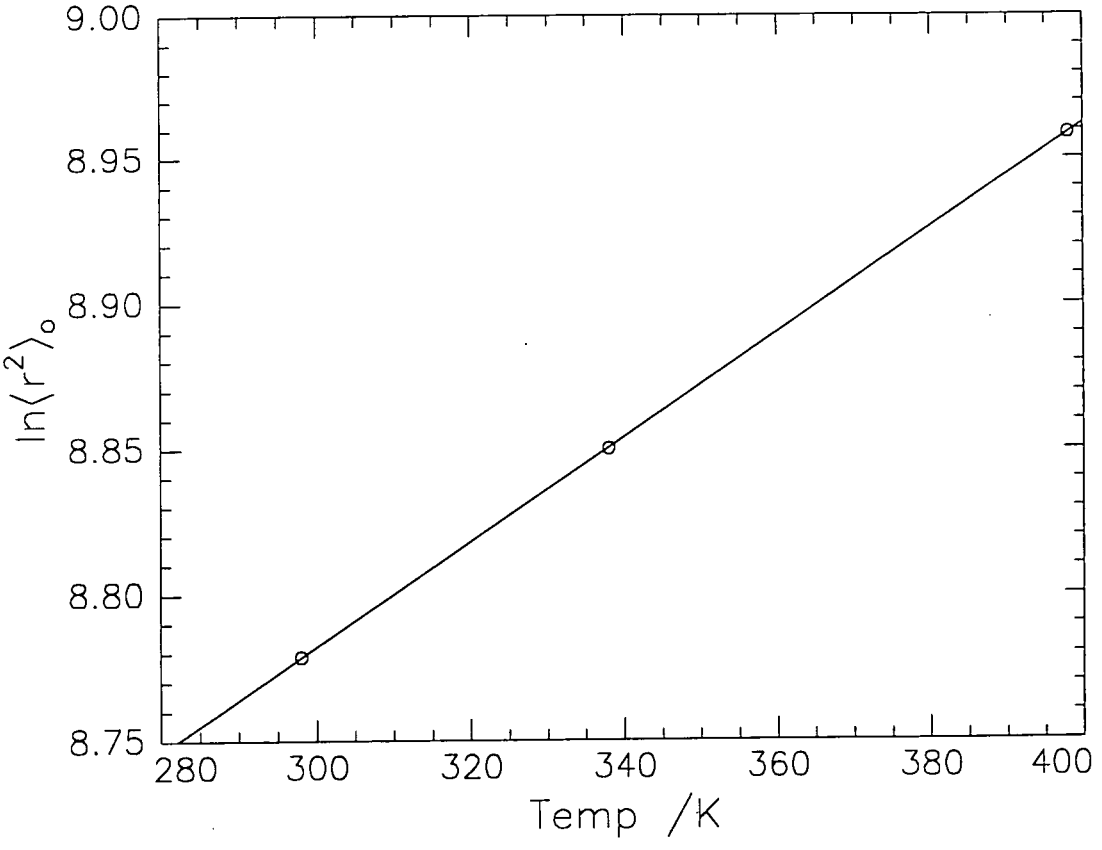

Figure 6.8: Temperature dependence of $\langle r^2 \rangle_o$, solid line is a least squares fit to data

For PLMA $d \ln\langle r^2 \rangle_o / d T$ was found to be 1.8×10^{-3} deg^{-1}, which can be compared to the literature values (from Polymer Handbook, Brandrup and Immergut 3rd edition) obtained for various methacrylates given in table 6.5.

POLYMER	$d \ln\langle r^2 \rangle_o / d T$ ($\times 10^{-3}$ deg^{-1})
PMMA	0.1
PbutylMA	2.5
PhexylMA	2.2
PoctylMA	2.2
PlaurylMA	2.6

Table 6.5: Literature values for various methacrylates

All of the literature values were determined by stress - temperature experiments in which strips of crosslinked polymer are placed in a stress relaxation balance and stretched to a constant elongation (α). The force on the balance is then measured as the temperature is varied, and this leads to the value of $\langle r^2 \rangle_o$ via the equation

$$F = \Phi N k T \left[\alpha - (1/\alpha)^2 \right] \qquad 6.20$$

where F is the force per unit original cross sectional area, N is the number of network chains per cubic centimetre, k is Boltzmann's constant, T is the absolute temperature and Φ is given by

$$\Phi = \frac{\langle r^2 \rangle_i}{\langle r^2 \rangle_o} \qquad 6.21$$

where $\langle r^2 \rangle_i$ is the mean square distance between network junctures. As before, the value obtained from the SANS experiments is within the expected range, although it is slightly less than the literature values. This will most likely be due to the different techniques used to obtain the values and once again the values obtained in this study are more direct, being obtained from chains which are distributed in their natural bulk environment.

The scattering data has been fitted using the incompressible random phase approximation (equation 6.12) which allows the value of the interaction parameter, χ, to be determined and a fit to the data is shown in figure 6.9.

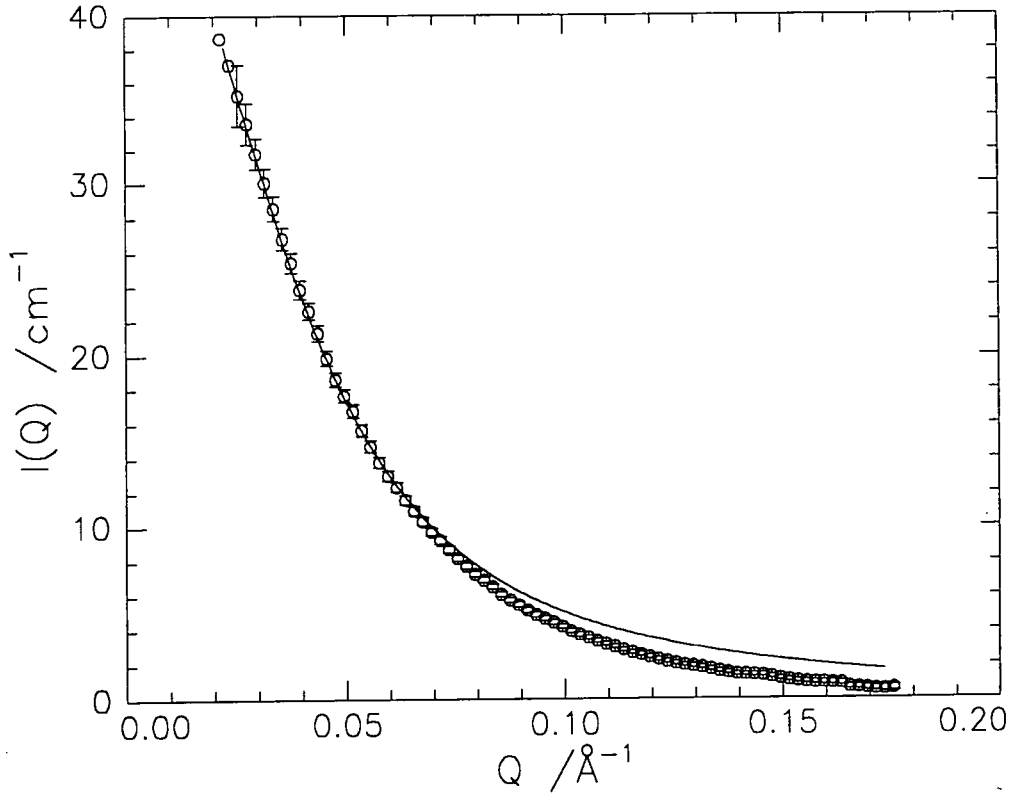

Figure 6.9: Scattering data for DMDL mixture at 25°C (o) with fit from the incompressible random phase approximation (—)

The deviation between the data and the fit occurs due to the polymer chains not behaving as a Gaussian coil, which is the model described by the Debye function (equation 6.11) used in the incompressible random phase approximation. The deviation becomes more apparent when the data is reploted in Kratky form, i.e. $I(Q)\times Q^2$ versus Q, as is shown in figure 6.10. The deviation between the data and the fits in figures 6.9 and 6.10 arises due to the bulky nature of the lauryl ester side chains leading to increased steric hindrance to rotations about the main chain bonds. In doing so, many main chain configurations are high in energy and are not favoured, so the polymer chains can not behave as simple Gaussian coils and have a much more complicated geometry. The effect of the side chains in determining the chain configuration can be confirmed by comparing the scattering data to that obtained for PMMA which has the same main chain bonds but with small ester groups. The Kratky plot for PMMA shows only a very slight

droop at Q greater than circa 0.1, indicating that the chains are in closer agreement to the Gaussian coil structure, so the droop observed for PLMA must be due to the influence of the side chains on the main chain configurations.

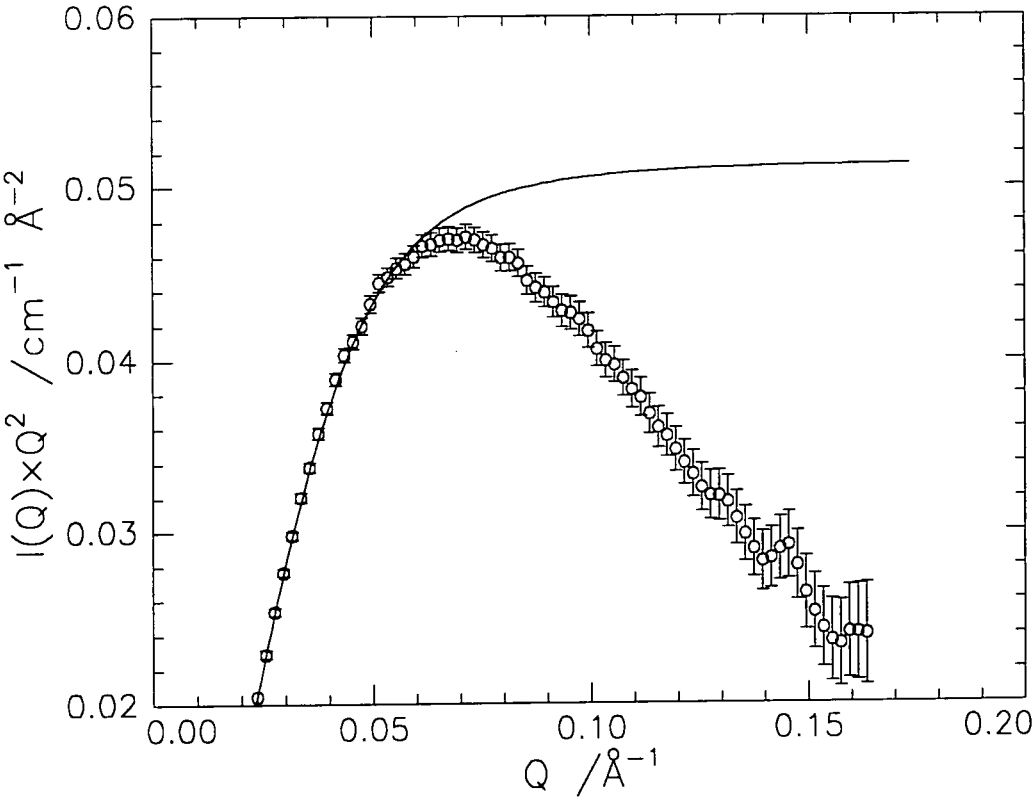

Figure 6.10: Kratky plot of the DMDL mixture data and fit at 25°C

The values of χ obtained from the fits at each temperature are given in table 6.6 and the values determined here are in line with the values calculated for other isotopic systems, e.g. syndiotactic PMMA $\chi \approx 5\times10^{-3}$ at 300K.

TEMPERATURE /°C	χ /$\times10^{-3}$
25	5.64
65	4.42
125	3.22

Table 6.6: χ values determined at each temperature

The main objective for carrying out this scattering study was to compare the experimental scattering data with that calculated from a computer model of PLMA in a similar way to that carried out for PMMA[9]. From computer generated molecular models of PMMA the scattering was calculated for each of three scattering centres within each monomer unit, these being the α methyl group, the ester methyl group and the backbone methylene. The scattering calculated for the ester group reproduced the experimental scattering, whereas the other two centres produced scattering curves which increased (in Kratky plot format). This demonstrated that the scattering was dominated by the ester group. For PLMA scattering centres on the backbone and side chains could be used and then compared to the experimental scattering data for the corresponding isotopic variations of PLMA. If the calculated scattering for each centre matched that for the corresponding isotopic variation then the computer model of the configuration of the PLMA chains must be close to that which is adopted in the real polymer sample, so a picture of the structure could be obtained instead of using mathematical models and fitting to experimental data. However, unlike for PMMA which is easily modelled using rotational isomeric state calculations to obtain a chain with a realistic configuration, for PLMA the software could not cope with a polymer with 12 carbon side groups and even when a compromise was used, which involved using a six carbon side chain, problems arose during the calculation of the statistical weights for each rotational angle. The various problems encountered have precluded the fulfilment of the main objective of the experiments.

The Kratky plot for HMDL showed the same characteristics as that obtained for DMDL, i.e. a big droop occurred, whereas for DMHL, although the signal is much weaker, no such droop is observed, these Kratky plots are shown in figures 6.11 and 6.12.

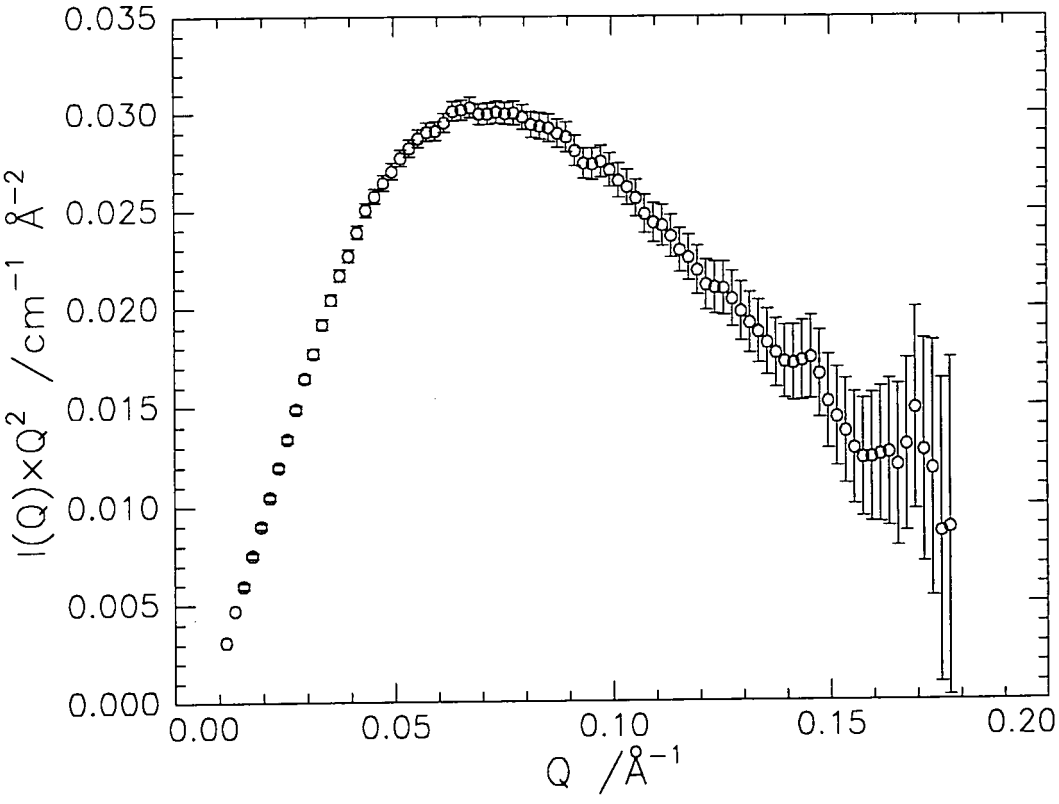

Figure 6.11: Kratky plot of the HMDL mixture data at 25°C

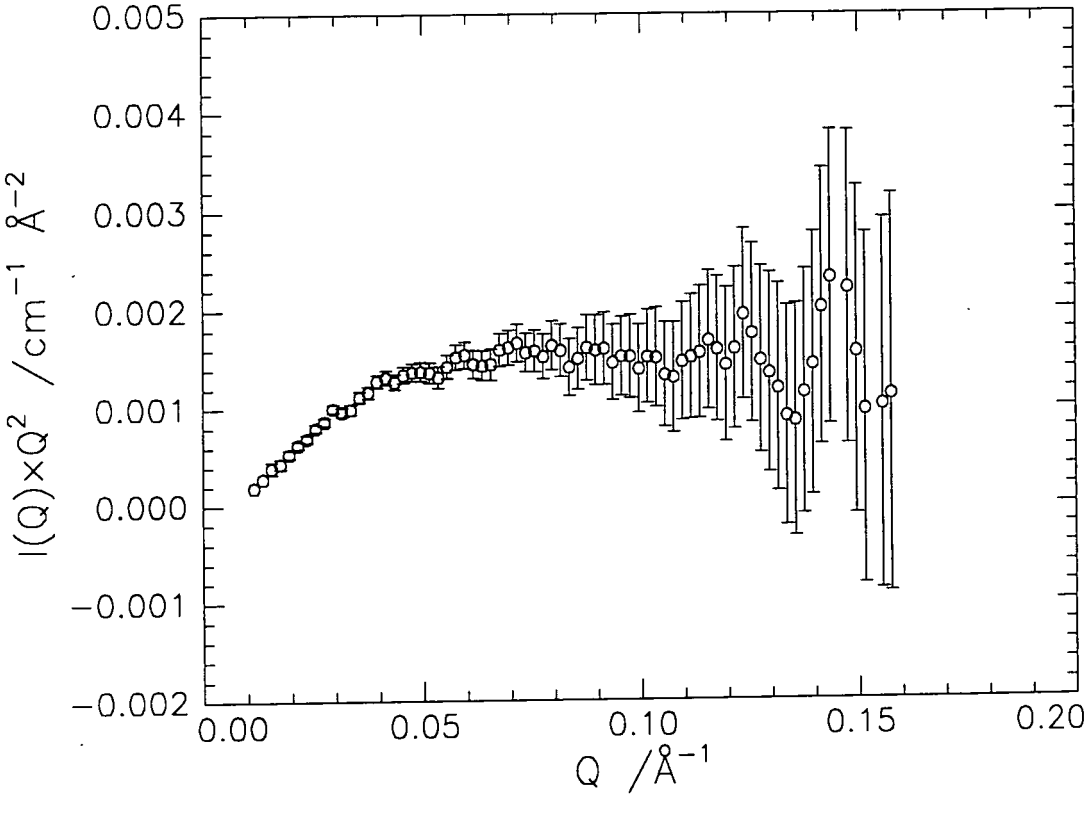

Figure 6.12: Kratky plot of the DMHL mixture data at 25°C

This indicates that, as for PMMA, the scattering is dominated by the ester side chains and when the scattering from the methacrylate part of the polymer only is considered, a flatter Kratky plot is obtained, similar to PMMA. However, the signal due to the backbone is so weak its contribution is lost in the scattering from DMDL due to the side chain domination.

6.4 Conclusions

Although the main objective of this section has proved impossible to carry out it is possible to conclude that the configuration of PLMA is determined by the steric effects due to the lauryl ester groups. This imparts a complex packing of the molecules in the solid phase which manifests itself as a drastic deviation from the scattering predicted by the incompressible random phase approximation which is based on the chains behaving as an ideal Gaussian coil.

6.5 References

1. de Gennes, P.G., *Scaling Concepts in Polymer Physics*, Cornell Univ. Press, Ithaca, New York, 1979
2. Flory, P.J., *Principles of Polymer Chemistry*, Cornell Univ. Press, Ithaca, New York, 1953
3. Debye, P., *J. Physical Colloid Chem.*, 18, **51**, 1947
4. Shibayama, M., Yang, H., Stein, R.S., Han, C.C., *Macromolecules*, 2179, **18**, 1985
5. Wignall, G.D., Bates, F.S., *J. Applied Crystallography*, 28, **20**, 1987
6. Program written by I. Hopkinson, Durham
7. Rawiso, M., Duplessix, R., Picot. C., *Macromolecules*, 630, **20**, 1987
8. Bates, F.S., Wignall, G.D., *Physical Review Letters*, 1429, **57(12)**, 1986
9. Hopkinson, I, *Ph.D. Thesis*, Durham, 1994

7. CONCLUSIONS AND SUGGESTIONS FOR FURTHER WORK

One of the initial ideas behind the project was to investigate the effect of tacticity on the behaviour and structure of PLMA monolayers. Tacticity may have been expected to have an effect due to the observations made on the behaviour and structure of stereotactic isomers of PMMA. However, due to synthetic problems, it proved impossible to obtain the stereoisomers of PLMA. These problems may be possible to overcome with more work, enabling the effect, if any, of tacticity to be investigated.

The nature of the isotherm for PLMA is similar to syndiotactic PMMA in that it forms a condensed monolayer and has an abrupt increase in surface pressure. Whereas the surface pressure for syndiotactic PMMA continues to increase more gradually after the abrupt increase, for PLMA the surface pressure plateaus. This may be due to PLMA being well above its T_g, hence allowing easier interpenetration of the polymer chains. Both polymers produce a value of υ, the critical scaling exponent, equal to 0.53, indicating that both polymers are in less than theta conditions. The monomer, LMA, was also studied to compare the behaviour and structure of the monolayer formed from LMA to that of PLMA. Both systems consist of the same chemical units, but one has restrictions due to the polymer backbone. The initial isotherms showed that this was not going to be possible as the LMA monolayers were unstable and the molecules contracted to form lenses. This instability is due to the dominant hydrophobicity of the lauryl ester groups. The PLMA monolayers appear stable due to the restrictions placed on the monomer units due to the backbone, however, the dominant hydrophobic nature results in the polymer forming macroscopic islands (~ 5 - 20mm in dimension) at low surface concentrations. Further investigations could be carried out using the various fractions of PLMA obtained to investigate at what molecular weight the transition in behaviour

occurs, or if a gradual transition takes place. Also, methacrylates with different ester lengths could be used to determine how the change in hydrophobicity affects the behaviour, i.e. tilt the balance of domination towards the hydrophilic groups.

A second objective of the project was to apply the kinematic approximation, together with the maximum utilisation of contrast variation, to obtain a detailed picture of the organisation of PLMA and LMA at the air - water interface. This proved successful for PLMA with the resulting structure consisting of the methacrylate backbone almost totally submerged, the reverse of that observed for PMMA and about 50% of the side chains mixed with the backbone in the subphase before rotations about carbon - carbon bonds allow the ester groups to protrude into the air. Due to rotations about main chain bonds, a small proportion of the side chains are forced to a lower spatial plane than the backbone. The LMA monolayer structure was to be compared to that obtained for the polymer, however, the instability of the monolayer prevented this from being possible. Results from the first 15 minute runs carried out on the LMA monolayers indicate that the initial structure of the monolayer may have resembled that of PLMA. Future areas of work on PLMA monolayers could include the analysis of non - specularly reflected neutrons (effectively in plane diffraction) which may give information on the topography of the monolayer. Neutron reflection could be carried out on LMA monolayers at temperatures approaching $0^{\circ}C$, as it is known from the isotherms that lower temperatures decrease the rate of lens formation, so it may be possible to maintain a stable film for sufficient time to obtain reasonable reflectivity profiles. This would require more elaborate equipment to prevent condensation, for example the Langmuir trough could be placed in a temperature controlled enclosure, so the surrounding air temperature could be decreased.

The SQELS experiments on PLMA monolayers showed no dramatic behaviour, no viscous relaxation occurred and the monolayer could be represented as a Voigt solid. The only change that occurred in the visco - elastic parameters coincided with the point where the monolayer departed from a two - dimensional state. SQELS allowed the biphasic nature of the monolayer at low surface concentrations to be investigated and it was possible to determine the dimensions of the islands and the separations between them. Again, the study of the LMA monolayer was hindered by its instability, however, the formation of the lenses could be followed in real time by monitoring the changes in the visco - elastic parameters, especially the transverse shear viscosity. Each of the higher surface concentrations studied tended towards the values obtained for the lowest surface concentrations studied with time. The additional properties introduced due to the dynamic nature of the lenses being present on the surface resulted in effective values being obtained for γ_o and γ' as the dispersion equation does not include terms to account for such a situation. The observation that all the visco - elastic parameters tended to go to those obtained for the low surface concentration agrees with the observation in the neutron reflectivity, which was that the apparent surface concentration always decreased to circa 0.4mg m^{-2}, which is close to the low concentration used in the SQELS experiments of 0.3mg m^{-2}. This indicates that regardless of the initial concentration, after lens formation the average surface coverage similar resulting in similar visco - elastic parameters. SQELS experiments could be carried out on PLMA monolayers over a greater range of q to investigate if viscous relaxation occurs on a time scale outside the range studied here. For LMA monolayers the effect of temperature could be used to produce more stable monolayers, allowing a full investigation to be carried out.

For the PLMA and LMA monolayers the technique of surface potential fluctuations could be used to investigate differences in the surface coverage.

Alternatively, fluorescence microscopy could be used if a suitable fluorescent marker could be obtained, this allows the distribution of the molecules at the interface to be directly pictured.

The work on the solid phase configuration requires more work on the computer modelling to investigate the various parameters and deduce their effect to enable the successful construction of PLMA molecular models.

APPENDIX A: GLOSSARY OF SYMBOLS

CHAPTER 1: INTRODUCTION

γ_o	surface tension of clean water
γ	measured surface tension with monolayer present
h	Planck's constant (= 6.626×10^{-34} J s)
k_i	initial neutron wavevector
k_f	final neutron wavevector
λ	neutron wavelength
π	surface pressure (= $\gamma_o - \gamma$)
Q	scattering vector
R_g	radius of gyration
υ	critical scaling exponent

CHAPTER 2: SYNTHESIS

$\overline{M}_n$	number average molecular weight
$\overline{M}_w$	weight average molecular weight
T_g	glass transition temperature

CHAPTER 3: SURFACE PRESSURE - AREA ISOTHERMS

a	monomer length
A	surface area for which the surface pressure equals π
A_o	extrapolated area at zero pressure or limiting area per segment
A_2	second virial coefficient
$A_{2,2}$	two dimensional second virial coefficient

β $$\left[\frac{\left\{1-\frac{2}{z}\left(1-\frac{1}{r}\right)\right\}\left(1-\frac{A_0}{A}\right)\frac{A_0}{A}}{\left\{1-\frac{2}{z}\left(1-\frac{1}{r}\right)\frac{A_0}{A}\right\}^2}\left(\eta^2-1\right)+1\right]^{1/2}$$

c concentration in polymer solution theory

c^* concentration at the transition from dilute to semi - dilute solution behaviour, concentration of initial chain overlap

c^{**} concentration at the transition from semi - dilute to concentrated solution behaviour

ϕ polymer volume fraction

ϕ^* polymer volume fraction at the transition from dilute to semi - dilute solution behaviour

ϕ^{**} polymer volume fraction at the transition from to semi - dilute to concentrated solution behaviour

γ surface tension

Γ surface concentration

Γ^* surface concentration at the transition from dilute to semi - dilute behaviour

Γ^{**} surface concentration at the transition from semi - dilute to concentrated behaviour

η $\exp(\omega/zk_BT)$

k_B Boltzmann constant ($1.380 \times 10^{-23} J K^{-1}$)

M polymer molecular weight

N degree of polymerisation

π surface pressure

π_o k_BT/A_o

r number of segments in one molecule

R_g radius of gyration

T absolute temperature

T_g glass transition temperature

τ reduced temperature

υ critical scaling exponent

υ_θ theta condition value of scaling exponent

ω interchain cohesion

ψ_θ	scaling exponent
z	co - ordination number of monomer units in polymer

CHAPTER 4: NEUTRON REFLECTIVITY

b_i	scattering length of species I
β	optical path length of beam in the interfacial film
d	film thickness at interface
δ_{ij}	separation between distributions I and j
Γ_c	surface concentration
h(Q)	structure factor
$h_{ii}(Q)$	self partial structure factor
$h_{ij}(Q)$	cross partial structure factor
$I(\lambda)$	reflected intensity with roughness
$I_o(\lambda)$	reflected intensity without roughness
k_o	incident neutron wavevector
k_o'	scattered neutron wavevector
λ	wavelength of neutron beam
m	monomer molecular weight
$[M_j]$	characteristic matrix for the j^{th} layer
$[M_R]$	matrix for the reflectivity
n	neutron refractive index
n_i	number density of species I
N_A	Avagadro's number
Q	scattering vector
θ	angle of incidence of neutron beam on the surface
θ_c	critical angle of incidence
r_{ij}	Fresnel coefficient at the i j interface
R	reflectivity
ρ	scattering length density
ρ_a	absorption cross section density
σ	full width of Gaussian distribution at height n_{i1}/e

$\langle\sigma\rangle$ root mean square roughness

ξ subphase interfacial width parameter

CHAPTER 5: SURFACE QUASI - ELASTIC LIGHT SCATTERING

A amplitude factor

B instrumental background

$D(\omega)$ dispersion expression

$\delta\theta$ deviation from specular angle

Δf_s full width at half peak height

ε static dilational modulus

ε_o dilational modulus

ε' dilational viscosity

f_s peak frequency of spectrum of scattered light

ϕ phase term to account for non Lorentzian spectrum of scattered light

g gravitational acceleration (= 9.81m s^{-2})

$g(\tau)$ correlation function in time domain

G strength of relaxation process

G_e equilibrium static elastic modulus

$G(\tau)$ measured auto - correlation function

$G^*(\omega)$ complex dynamic modulus

$G'(\omega)$ storage modulus

$G''(\omega)$ loss modulus

γ surface tension

γ_o transverse shear modulus (corresponds to classical surface tension)

γ' transverse shear viscosity

Γ damping constant

Γ_c surface concentration

η viscosity

I_R intensity of reference beam

I_S intensity of scattered beam

k Boltzmann constant (1.380×10^{-23} J K^{-1})

K	scattering vector
Λ	wavelength of surface wave
$P(\omega)$	power spectrum
π	surface pressure
q	surface wavenumber
θ	angle of light incidence
ρ	density of liquid
T	absolute temperature
T_g	glass transition temperature
T*	oscillatory stress modulus
τ	relaxation time
u*	oscillatory strain modulus
υ	kinematic viscosity
ω	complex capillary wave frequency
ω_o	wave propagation frequency
ξ	displacement of surface from its equilibrium plane

CHAPTER 6: SMALL ANGLE NEUTRON SCATTERING

α	elongation of polymer sample
b	scattering length of nucleus
C_∞	characteristic ratio
χ	effective Flory - Huggins interaction parameter
χ_{FH}	Flory - Huggins interaction parameter
$d\Omega$	solid angle into which neutrons are scattered
$\frac{d^2\sigma}{d\Omega dE}$	partial differential cross section
$\frac{d\sigma}{d\Omega}$	differential cross section
$\delta(x)$	Dirac delta function
E	energy of neutron
ε_{ij}	nearest neighbour pair potentials

F	force per unit original cross sectional area
ϕ	volume fraction
$g_D(R_g,Q)$	Debye function for polymer with radius of gyration R_g
h	Planck's constant
I_o	intensity of incident neutron beam
$I(Q)$	coherent elastic neutron scattering
k_b	Boltzmann constant($1.380 \times 10^{-23} J K^{-1}$)
k_i	initial neutron wavevector
k_s	scattered neutron wavevector
k_n	normalisation constant for LOQ data
l	length of bond
λ	neutron beam wavelength
m	mass of particle
n	number of bonds in polymer chain
N	number of network chains per cubic centimetre
N	number of nuclei in sample
N_i	degree of polymerisation of component I
Q	scattering vector
θ	scattering angle
θ	valence bond angle
$\mathbf{r}$	general position vector
$\mathbf{R}$	position vector of scattering nucleus
$R_{g,i}$	radius of gyration of component i
$R_{g,w}$	weight average radius of gyration of component
$R_{g,z}$	z average radius of gyration of component
r_f^2	mean square end to end distance of a polymer chain in the absence of any interactions (freely jointed chain)
$\langle r^2 \rangle_{of}$	mean square end to end distance of a polymer chain which has restrictions placed on its configuration due to valence angles between chain atoms (freely rotating chain)
$\langle r^2 \rangle_o$	mean square end to end distance of a polymer chain in its unperturbed dimension
$\langle r^2 \rangle_i$	mean square distance between network junctures

$S(Q)$	scattering structure factor
σ	total scattering cross section of a nucleus
σ	steric parameter
T	absolute temperature
v	velocity
v_i	segmental volume of species i
$V(r)$	Fermi -pseudo potential for interaction between neutron and nucleus
z_c	co - ordination number

APPENDIX B: LECTURES, CONFERENCES AND COURSES ATTENDED

UNIVERSITY OF DURHAM
Board of Studies in Chemistry

COLLOQUIA, LECTURES AND SEMINARS FROM INVITED SPEAKERS

1992

October 15 Dr M. Glazer & Dr. S. Tarling, Oxford University & Birbeck College, London
It Pays to be British! - The Chemist's Role as an Expert Witness in Patent Litigation

October 20 Dr. H. E. Bryndza, Du Pont Central Research
Synthesis, Reactions and Thermochemistry of Metal (Alkyl) Cyanide Complexes and Their Impact on Olefin Hydrocyanation Catalysis

October 22 Prof. A. Davies, University College London
The Ingold-Albert Lecture The Behaviour of Hydrogen as a Pseudometal

October 28 Dr. J. K . Cockcroft, University of Durham
Recent Developments in Powder Diffraction

October 29 Dr. J. Emsley, Imperial College, London
The Shocking History of Phosphorus

November 4 Dr. T. P. Kee, University of Leeds
Synthesis and Co-ordination Chemistry of Silylated Phosphites

November 5 Dr. C. J. Ludman, University of Durham
Explosions, A Demonstration Lecture

November 11 Prof. D. Robins†, Glasgow University
Pyrrolizidine Alkaloids : Biological Activity, Biosynthesis and Benefits

November 12 Prof. M. R. Truter, University College, London
Luck and Logic in Host - Guest Chemistry

November 18 Dr. R. Nix†, Queen Mary College, London
Characterisation of Heterogeneous Catalysts

November 25 Prof. Y. Vallee. University of Caen
Reactive Thiocarbonyl Compounds

November 25 Prof. L. D. Quin†, University of Massachusetts, Amherst
Fragmentation of Phosphorous Heterocycles as a Route to Phosphoryl Species with Uncommon Bonding

November 26 Dr. D. Humber, Glaxo, Greenford
AIDS - The Development of a Novel Series of Inhibitors of HIV

December 2 Prof. A. F. Hegarty, University College, Dublin
Highly Reactive Enols Stabilised by Steric Protection

December 2 Dr. R. A. Aitken†, University of St. Andrews
The Versatile Cycloaddition Chemistry of $Bu_3P.CS_2$

December 3 Prof. P. Edwards, Birmingham University
The SCI Lecture - What is Metal?

December 9 Dr. A. N. Burgess†, ICI Runcorn
The Structure of Perfluorinated Ionomer Membranes

1993

January 20 Dr. D. C. Clary†, University of Cambridge
Energy Flow in Chemical Reactions

January 21 Prof. L. Hall, Cambridge
NMR - Window to the Human Body

January 27 Dr. W. Kerr, University of Strathclyde
Development of the Pauson-Khand Annulation Reaction : Organocobalt Mediated Synthesis of Natural and Unnatural Products

January 28 Prof. J. Mann, University of Reading
Murder, Magic and Medicine

February 3 Prof. S. M. Roberts, University of Exeter
Enzymes in Organic Synthesis

February 10 Dr. D. Gillies†, University of Surrey
NMR and Molecular Motion in Solution

February 11 Prof. S. Knox, Bristol University
The Tilden Lecture Organic Chemistry at Polynuclear Metal Centres

February 17 Dr. R. W. Kemmitt†, University of Leicester
Oxatrimethylenemethane Metal Complexes

February 18 Dr. I. Fraser, ICI Wilton
Reactive Processing of Composite Materials

February 22 Prof. D. M. Grant, University of Utah
Single Crystals, Molecular Structure, and Chemical-Shift Anisotropy

February 24	Prof. C. J. M. Stirling†, University of Sheffield Chemistry on the Flat-Reactivity of Ordered Systems
March 10	Dr. P. K. Baker, University College of North Wales, Bangor 'Chemistry of Highly Versatile 7-Coordinate Complexes'
March 11	Dr. R. A. Y. Jones, University of East Anglia The Chemistry of Wine Making
March 17	Dr. R. J. K. Taylor†, University of East Anglia Adventures in Natural Product Synthesis
March 24	Prof. I. O. Sutherland†, University of Liverpool Chromogenic Reagents for Cations
May 13	Prof. J. A. Pople, Carnegie-Mellon University, Pittsburgh, USA *The Boys-Rahman Lecture* Applications of Molecular Orbital Theory
May 21	Prof. L. Weber, University of Bielefeld Metallo-phospha Alkenes as Synthons in Organometallic Chemistry
June 1	Prof. J. P. Konopelski, University of California, Santa Cruz Synthetic Adventures with Enantiomerically Pure Acetals
June 2	Prof. F. Ciardelli, University of Pisa Chiral Discrimination in the Stereospecific Polymerisation of Alpha Olefins
June 7	Prof. R. S. Stein, University of Massachusetts Scattering Studies of Crystalline and Liquid Crystalline Polymers
June 16	Prof. A. K. Covington, University of Newcastle Use of Ion Selective Electrodes as Detectors in Ion Chromatography
June 17	Prof. O. F. Nielsen, H. C. Ørsted Institute, University of Copenhagen Low-Frequency IR - and Raman Studies of Hydrogen Bonded Liquids
September 13	Prof. Dr. A.D. Schlüter, Freie Universität Berlin, Germany Synthesis and Characterisation of Molecular Rods and Ribbons
September 13	Dr. K.J. Wynne, Office of Naval Research, Washington, USA Polymer Surface Design for Minimal Adhesion
September 14	Prof. J.M. DeSimone, University of North Carolina, Chapel Hill, USA Homogeneous and Heterogeneous Polymerisations in Environmentally Responsible Carbon Dioxide
September 28	Prof. H. Ila, North Eastern Hill University, India Synthetic Strategies for Cyclopentanoids via Oxoketene Dithioacetals

October 4 Prof. F.J. Feher†, University of California, Irvine, USA
Bridging the Gap between Surfaces and Solution with Sessilquioxanes

October 14 Dr. P. Hubberstey, University of Nottingham
Alkali Metals: Alchemist's Nightmare, Biochemist's Puzzle and Technologist's Dream

October 20 Dr. P. Quayle†, University of Manchester
Aspects of Aqueous ROMP Chemistry

October 27 Dr. R.A.L. Jones†, Cavendish Laboratory, Cambridge
Perambulating Polymers

November 10 Prof. M.N.R. Ashfold†, University of Bristol
High Resolution Photofragment Translational Spectroscopy : A New Way to Watch Photodissociation

November 17 Dr. A. Parker†, Rutherford Appleton Laboratory, Didcot
Applications of Time Resolved Resonance Raman Spectroscopy to Chemical and Biochemical Problems

November 24 Dr. P.G. Bruce†, University of St. Andrews
Structure and Properties of Inorganic Solids and Polymers

December 1 Prof. M.A. McKervey†, Queen's University, Belfast
Synthesis and Applications of Chemically Modified Calixarenes

December 8 Prof. O. Meth-Cohn†, University of Sunderland
Friedel's Folly Revisited - A Super Way to Fused Pyridines

December 16 Prof. R.F. Hudson, University of Kent
Close Encounters of the Second Kind

1994

January 26 Prof. J. Evans†, University of Southampton
Shining Light on Catalysts

February 2 Dr. A. Masters†, University of Manchester
Modelling Water Without Using Pair Potentials

February 9 Prof. D. Young†, University of Sussex
Chemical and Biological Studies on the Coenzyme Tetrahydrofolic Acid

February 16 Prof. K.H. Theopold, University of Delaware, USA
Paramagnetic Chromium Alkyls : Synthesis and Reactivity

February 23 Prof. P.M. Maitlis†, University of Sheffield
Across the Border : From Homogeneous to Heterogeneous Catalysis

March 2	Dr. C. Hunter†, University of Sheffield Noncovalent Interactions between Aromatic Molecules
March 9	Prof. F. Wilkinson, Loughborough University of Technology Nanosecond and Picosecond Laser Flash Photolysis
March 10	Prof. S.V. Ley, University of Cambridge New Methods for Organic Synthesis
March 25	Dr. J. Dilworth, University of Essex Technetium and Rhenium Compounds with Applications as Imaging Agents
April 28	Prof. R. J. Gillespie, McMaster University, Canada The Molecular Structure of some Metal Fluorides and Oxofluorides: Apparent Exceptions to the VSEPR Model.
May 12	Prof. D. A. Humphreys, McMaster University, Canada Bringing Knowledge to Life
October 5	Prof. N. L. Owen, Brigham Young University, Utah, USA Determining Molecular Structure - the INADEQUATE NMR way
October 19	Prof. N. Bartlett, University of California Some Aspects of Ag(II) and Ag(III) Chemistry
November 2	Dr P. G. Edwards, University of Wales, Cardiff The Manipulation of Electronic and Structural Diversity in Metal Complexes - New Ligands
November 3	Prof. B. F. G. Johnson, Edinburgh University Arene - Metal Clusters - DUCS Lecture
November 9	Dr J. P. S. Badyal, University of Durham Chemistry at Surfaces, A Demonstration Lecture
November 9	Dr G. Hogarth, University College, London New Vistas in Metal Imido Chemistry
November 10	Dr M. Block, Zeneca Pharmaceuticals, Macclesfield Large Scale Manufacture of the Thromboxane Antagonist Synthase Inhibitor ZD 1542
November 16	Prof. M. Page, University of Huddersfield Four Membered Rings and b-Lactamase
November 23	Dr J. M. J. Williams, University of Loughborough New Approaches to Asymmetric Catalysis

December 7 Prof. D. Briggs, ICI and University of Durham
Surface Mass Spectrometry

1995

January 11 Prof. P. Parsons, University of Reading
Applications of Tandem Reactions in Organic Synthesis

January 18 Dr G. Rumbles, Imperial College, London
Real or Imaginary 3rd Order non-Linear Optical Materials

January 25 Dr D. A. Roberts, Zeneca Pharmaceuticals
The Design and Synthesis of Inhibitors of the Renin-Angiotensin System

February 1 Dr T. Cosgrove, Bristol University
Polymers do it at Interfaces

February 8 Dr D. O'Hare, Oxford University
Synthesis and Solid State Properties of Poly-, Oligo- and Multidecker Metallocenes

February 22 Prof. E. Schaumann, University of Clausthal
Silicon and Sulphur Mediated Ring-opening Reactions of Epoxide

March 1 Dr M. Rosseinsky, Oxford University
Fullerene Intercalation Chemistry

March 8 Nikki Chesters, Wayne Devonport & Penelope Herbertson, University of Durham 1995 Graduate Seminar Series

March 15 Janet Hopkins, Brian Rochford & Graham Rivers, University of Durham
1995 Graduate Seminar Series

March 22 Dr M. Taylor, University of Auckland, New Zealand
Structural Methods in Main Group Chemistry

April 26 Dr M. Schroder, University of Edinburgh
Redox Active Macrocyclic Complexes : Rings, Stacks and Liquid Crystals

May 3 Prof. E. W. Randall, Queen Mary and Westfield College
New Perspectives in NMR Imaging

May 4 Prof. A. J. Kresge, University of Toronto
The Ingold Lecture - Reactive Intermediates : Carboxylic Acid Enols and Other Unstable Species

May 10 George Bates, Steve Carss, Martyn Coles, University of Durham
1995 Graduate Seminar Series

May 17	Graham McKelvey, Richard Towns & Tim Thompson, University of Durham 1995 Graduate Seminar Series
May 31	Rob Spink, Ian Reynolds & Nick Haylett, University of Durham 1995 Graduate Seminar Series
June 7	Abdulla Ahmed, Mike Chan & Alex Eberlin, University of Durham 1995 Graduate Seminar Series
June 14	Iain May, Leela Sequeira & Gareth Williams, University of Durham 1995 Graduate Seminar Series
June 21	Oliver Greenwood, Mike Chalton & Alex Roche, University of Durham 1995 Graduate Seminar Series
July 5	Alan Gilbert, Emma Rivers & Simon Lord, Univeristy of Durham 1995 Graduate Seminar Series
July 12	Martin Ryan, Steven Dunn & R Samadi, Univeristy of Durham 1995 Graduate Seminar Series

† Invited specially for the graduate training programme.

The author has also attended the following lectures in the IRC in polymer Science and Technology International Seminar Series.

1993

March 16	Prof. J.M.G. Cowie (Heriot-Watt University), at Bradford University High Technology in Chains : The Role of Polymers in Electronic Applications and Data Processing
April 1	Prof. H. W. Speiss (Max-Planck Institut for Polymerforschung, Mainz), at Durham University. Multidimensional NMR Studies of Structure and Dynamics of Polymers.
June 2	Prof. F. Ciardelli (University of Pisa), at Durham University Chiral Discrimination in the Stereospecific Polymerisation of α-olefins.
June 8	Prof. B. E.Eichinger (BIOSYM Technologies Inc. San Diego), at Leeds University. Recent PolymerModeling Results and a look into the Future.
July 6	Prof. C. W. Macosko (University of Minnesota, Minneapolis), at Bradford University Morphology Development in Immiscible Polymer Blending

CONFERENCES, MEETING AND COURSES ATTENDED BY THE AUTHOR

January 1993	IRC Polymer Engineering Course, Bradford University
March 1993	IRC Polymer Physics Course, Leeds University
April 1993	Macro Group (U.K) Family Meeting, Lancaster University
September 1993	Neutron Beam User's Meeting, Sheffield University*
September 1993	Polymers at Interfaces, Bristol University
December 1993	RSC - Faraday Division (Colloid and Interface Science Group) Dynamics of Surfactant Monolayers, London
April 1994	Macro Group (UK) Family Meeting, Birmingham University*
September 1994	Faraday Discussion, Bristol University*

* Poster presentation by the author

PUBLICATIONS

Reynolds, I., Richards, R.W., to be published in *Macromolecules*, November 1995